SEISMIC HAZARD OF THAILAND AND BI-DIRECTIONAL RESPONSE SPECTRA

Mr. Chitti Palasri

A Dissertation Submitted in Partial Fulfillment of the Requirements
for the Degree of Doctor of Philosophy Program in Civil Engineering
Department of Civil Engineering
Faculty of Engineering
Chulalongkorn University
Academic Year 2012

ความเสี่ยงภัยแผ่นดินไหวของประเทศไทยและสเปกตรัมผลตอบสนองสองทิศทาง

นายจิตติ ปาลศรี

วิทยานิพนธ์นี้เป็นส่วนหนึ่งของการศึกษาตามหลักสูตรปริญญาวิศวกรรมศาสตรดุษฎีบัณฑิต

สาขาวิชาวิศวกรรมโยธา ภาควิชาวิศวกรรมโยธา

คณะวิศวกรรมศาสตร์ จุฬาลงกรณ์มหาวิทยาลัย

ปีการศึกษา 2555

Thesis Title	SEISMIC HAZARD OF THAILAND AND BI-DIRECTIONAL RESPONSE SPECTRA
By	Mr. Chitti Palasri
Field of Study	Civil Engineering
Thesis Advisor	Assistant Professor Anat Ruangrassamee, Ph.D.

Accepted by the Faculty of Engineering, Chulalongkorn University in Partial Fulfillment of the Requirements for the Doctoral Degree

…………………………………… Dean of the Faculty of Engineering
(Associate Professor Boonsom Lerdhirunwong, Dr.Ing.)

THESIS COMMITTEE

…………………………………… Chairman
(Professor Panitan Lukkunaprasit, Ph.D.)

…………………………………… Thesis Advisor
(Assistant Professor Anat Ruangrassamee, Ph.D.)

…………………………………… Examiner
(Associate Professor Supot Teachavorasinskun, Ph.D.)

…………………………………… Examiner
(Assistant Professor Chatpan Chintanapakdee, Ph.D.)

…………………………………… External Examiner
(Associate Professor Nakhorn Poovarodom, Ph.D.)

จิตติ ปาลศรี : ความเสี่ยงภัยแผ่นดินไหวของประเทศไทยและสเปกตรัมผลตอบสนองสองทิศทาง. (SEISMIC HAZARD OF THAILAND AND BI-DIRECTIONAL RESPONSE SPECTRA) อ.ที่ปรึกษาวิทยานิพนธ์หลัก: ผศ.ดร.อาณัติ เรืองรัศมี, 360 หน้า.

เมื่อเกิดเหตุการณ์แผ่นดินไหวขึ้น คลื่นแผ่นดินไหวจากแหล่งกำเนิดที่ตั้งอยู่บนชั้นหินดานจะเคลื่อนที่ผ่านชั้นดินไปยังโครงสร้างซึ่งชั้นดินนั้นสามารถเปลี่ยนแปลงคุณสมบัติของคลื่นได้ ดังนั้นจึงต้องพิจารณา 3 ส่วนได้แก่ การวิเคราะห์ความเสี่ยงภัยแผ่นดินไหวเชิงความน่าจะเป็น ผลกระทบจากการขยายคลื่นแผ่นดินไหวผ่านชั้นดิน และผลกระทบจากการสั่นไหวของโครงสร้างจากคลื่นแผ่นดินไหวสองทิศทาง

งานวิจัยนี้ได้พัฒนาแผนที่เสี่ยงภัยแผ่นดินไหวของประเทศไทยและบริเวณใกล้เคียง ข้อมูลแผ่นดินไหวที่ใช้วิเคราะห์เป็นข้อมูลตั้งแต่ปี ค.ศ.1912 ถึง ค.ศ. 2009 จากกรมอุตุนิยมวิทยาและสำนักงานสำรวจทางธรณีวิทยาของสหรัฐอเมริกา และใช้สมการลดทอนแผ่นดินไหวที่ให้ค่าใกล้เคียงกับผลตรวจวัดความเร่งในประเทศไทย ผลของการวิเคราะห์แสดงเป็นแผนที่เสี่ยงภัยแผ่นดินไหวเชิงความน่าจะเป็นสำหรับค่าความเร่งในแนวราบสูงสุดที่ชั้นหินดาน และสเปกตรัมความเร่งที่มีโอกาสเกิน 10% และ 2% ในรอบ 50 ปี สำหรับโอกาสเกิน 10% ในรอบ 50 ปี ความเร่งในแนวราบสูงสุดมีค่าประมาณ 0.25g ทางภาคเหนือ 0.15g ทางภาคตะวันตก และ 0.03g ในบริเวณกรุงเทพมหานคร ส่วนสเปกตรัมความเร่งที่คาบการสั่น 0.2 วินาทีมีค่าประมาณ 0.6g ทางภาคเหนือ 0.3g ทางภาคตะวันตก และ 0.06g ในบริเวณกรุงเทพมหานคร และสเปกตรัมความเร่งที่คาบการสั่น 1.0 วินาทีมีค่าประมาณ 0.15g ทางภาคเหนือ 0.08g ทางภาคตะวันตก และ 0.03g ในบริเวณกรุงเทพมหานคร ค่าความเร่งในแนวราบสูงสุดและสเปกตรัมความเร่งสำหรับโอกาสเกิน 2% ในรอบ 50 ปีมีค่าประมาณ 1.6 ถึง 2 เท่าของค่าความเร่งในแนวราบสูงสุดและสเปกตรัมความเร่งสำหรับโอกาสเกิน 10% ในรอบ 50 ปี

สำหรับการศึกษาผลกระทบของการขยายคลื่นแผ่นดินไหวในชั้นดิน ได้ทำการหาค่าความเร็วคลื่นเฉือนจากการทดสอบดาวน์โฮลจำนวน 6 หลุมเพื่อพัฒนาสมการหาค่าความเร็วคลื่นเฉือนในบริเวณภาคเหนือและกรุงเทพมหานคร จากนั้นทำการวิเคราะห์หาอัตราการขยายคลื่นแผ่นดินไหวในชั้นดิน 33 จุดในจังหวัดเชียงใหม่ เชียงราย กาญจนบุรี และกรุงเทพมหานคร พบว่าอัตราการขยายความเร่งสูงสุดที่ผิวดินสามารถมีค่าถึง 2 เท่าได้หากเป็นบริเวณที่ความเร็วคลื่นเฉือนที่ 30 เมตรมีค่าน้อยกว่า 200 เมตรต่อวินาที

ในงานวิจัยนี้ได้นำเสนอผลตอบสนองของแผ่นดินไหวสองทิศทางซึ่งเรียกว่า “สเปกตรัมความเร่งที่พิจารณาผลของแผ่นดินไหวสองทิศทาง” โดยจำลองโครงสร้างในระบบขั้นความเสรีเท่ากับสอง และใช้คลื่นแผ่นดินไหวจำนวน 86 ชุดในการวิเคราะห์ กำหนดให้แกนหลักของคลื่นแผ่นดินไหวคือแกนที่มีค่าความรุนแรงของแอเรียสสูงสุด และแกนรองของคลื่นเป็นแกนที่ตั้งฉากกับแกนหลัก ค่าเฉลี่ยบวกหนึ่งเท่าของค่าเบี่ยงเบนมาตรฐานของอัตราส่วนของสเปกตรัมความเร่งมีค่าเท่ากับ 1.18 โดยเมื่อนำค่าดังกล่าวไปใช้ออกแบบพบว่า ได้ค่าสเปกตรัมความเร่งมากกว่าการวิเคราะห์ด้วยวิธี SRSS และ CQC3 ประมาณ 16% ในด้านที่มีคาบธรรมชาติสั้นกว่า

ภาควิชา …วิศวกรรมโยธา…………… ลายมือชื่อนิสิต ……………………………………..

สาขาวิชา …วิศวกรรมโยธา………….. ลายมือชื่อ อ.ที่ปรึกษาวิทยานิพนธ์หลัก ………………….

ปีการศึกษา …2555…………………

5071853021 : MAJOR CIVIL ENGINEERING

KEYWORDS: BI-DIRECTIONAL EARTHQUAKE / SEISMIC HAZARD / SOIL AMPLIFICATION / DESIGN SPECTRA / GROUND MOTION

CHITTI PALASRI: SEISMIC HAZARD OF THAILAND AND BI-DIRECTIONAL RESPONSE SPECTRA. ADVISOR: ASST. PROF. ANAT RUANGRASSAMEE, Ph.D., 360 pp.

When an earthquake occurs, a ground motion propagates from a seismic source where the epicenter locates on bedrock to structures located on soil layers which can modify characteristics of the motion. Therefore, a lot of factors need to be considered such as the probabilistic seismic hazard analysis, the effect of soil amplification for the wave propagation and the effects of bi-directional excitations on structures.

The probabilistic seismic hazard map of Thailand and neighboring areas is developed. Earthquakes recorded from 1912 to 2009 by the Thai Meteorological Department and US Geological Survey are used in the analysis. The attenuation models which give good correlations with actual measured accelerations are used in predicting peak horizontal accelerations in Thailand. Maps of peak horizontal and spectral accelerations on bedrock with 2% and 10% probabilities of exceedance in 50 years are developed. For 10% probability of exceedance in 50 years, the maximum peak horizontal accelerations are about 0.25g in northern Thailand, 0.15g in western Thailand, and 0.03g in Bangkok. The spectral accelerations at the period of 0.2s are about 0.6g in northern Thailand, 0.3g in western Thailand, and 0.06g in Bangkok. And, the spectral accelerations at the period of 1.0s are about 0.15g in northern Thailand, 0.08g in western Thailand, and 0.03g in Bangkok. For 2% probability of exceedance in 50 years, the peak horizontal accelerations and the spectral accelerations are about 1.6 to 2.0 times the peak horizontal accelerations and spectral accelerations with 10% probability of exceedance in 50 years.

For the effect of soil amplification study, seismic downhole tests were conducted at 6 sites in the northern Thailand and Bangkok to develop the relationship for predicting shear wave velocity in the areas. Soil response analysis was done for 33 sites in Chiangmai, Chiangrai, Kanchanaburi, and Bangkok to obtain the amplification factors. The amplification factors of peak ground acceleration are as large as 2.0 at locations where Vs30 is less than 200 m/s.

This study also clarifies the effects of bi-directional excitations on structures and proposes the response spectra called "bi-directional pseudo-acceleration response spectra." A simplified analytical model of a two-degree-of-freedom system was employed. 86 ground motion records were used in the analysis. The axis with the largest Arias intensity is referred to as the major axis and that perpendicular to the major axis is referred to as the minor axis. For design purposes, the mean plus a standard deviation of acceleration ratio response spectrum is proposed as 1.18. The proposed method is more conservative than 16%, SRSS and CQC3-rules for the direction with a shorter period.

Department:…Civil Engineering………… Student's Signature ………………………..

Field of Study:…Civil Engineering……. Advisor's Signature ……………………..

Academic Year:…2012…………………

ACKNOWLEDGEMENTS

First, I would like to express my sincere gratitude to my advisor, Asst. Prof. Anat Ruangrassamee for many advices, kindness, encouragement, and continuous support throughout this research. I wish to express to him all my gratitude. I would also like to express my deepest appreciations to Prof. Panitan Lukkunaprasit, Asst. Prof. Chatpan Chintanapakdee, Assoc. Prof. Supot Teachavorasinskun, Assoc. Prof. Nakhorn Poovarodom for their valuable guidance, constructive comments and to be committees of my dissertation defense. Their suggestions and comments help this research more completely.

I would like to acknowledge the EU-NICE Erasmus Mundus scholarship to give me a chance for 12 months to research at the University G. D'Annunzio Chieti-Pescara, Italy. This is very useful in broadening my experience and exchanging knowledge with Prof. Enrico Spacone, Prof. Guido Camata and Dr. Cristina Cantagallo who are experts in this research area. I am deeply grateful for their guidance and support.

I would like to acknowledge the Meteorology Department of Thailand, Asian Institute Technology, Chiangmai University and Wat Chedi Luang Woraviharn for the in-situ test and also hearted thanks to Asst. Prof. Worapan Nantawong and Mr. Panu Uthaisri for preparing some test equipments for in-situ test in the North of Thailand. The financial support was funded by the Department of Rural Roads, Ministry of Transport and Office of the Higher Education Commission for the in-situ test are highly acknowledged.

I sincerely thank to the members of Center of Excellence on Earthquake Engineering and Vibration, Chulalongkorn University is also acknowledged. Especially, Mr. Siripol Siripala for his suggestions and Mr. Wissanu Hattha for the earthquake data and the in-situ testing are highly appreciated.

Finally, special thanks go to my family for their patience and support throughout my life.

CONTENTS

Page

LIST OF TABLES

page

LIST OF FIGURES

Page

Page

Page

Page

Page

CHAPTER I
INTRODUCTION

1.1 Problem Statement

When an earthquake occurs, a ground motion propagates from a seismic source to structures. Therefore, a lot of factors need to be considered such as the probabilistic seismic hazard analysis, the effect of soil amplification for the wave propagation and the effects of bi-directional excitations on structures.

In Thailand, earthquakes occasionally occur in the northern and western parts of Thailand that are considered as active tectonic regions. Especially, there are several active faults in the north of Thailand such as the Mae-Chan fault, Thoen-Long-Prae faults, Payao fault and in the west of Thailand such as the Sri Sawat fault and Three Pagoda fault. Some earthquakes caused structural damages in Chiang Rai and Bangkok. For example, the September 11th, 1994 earthquake with a local magnitude (M_L) of 5.1 had an epicenter near Pan District, Chiang Rai. The earthquake caused structural damage to the Pan hospital. The May 16th, 2007 earthquake with a moment magnitude (M_W) of 6.3 had an epicenter in Laos. The earthquake caused structural damage to a school in Chiang Rai. At present, the availability of updated earthquake catalogs can support the proper selection of attenuation models. So, the seismic hazard maps showing peak horizontal accelerations can be developed with sound attenuation models and updated information. The seismic hazard map can be used as a guideline to design structures resisting earthquakes in Thailand.

The hazard maps are developed for a rock site. Hence, the effect of soil amplification needs to be considered. In this study, the formulation to estimate shear wave velocities is developed and soil amplification is investigated by the one dimentional equivalent linear method.

Under strong ground motions, structures are excited horizontally and vertically in a complicated manner. Oliva and Clough (1987) conducted shaking table tests to investigate bi-directional inelastic response of a reinforced concrete frame and found that column strength was reduced and the response demand was increased comparing with uni-directional response. Wong et. al. (1993) studied the bi-axial behavior of circular reinforced concrete columns under different displacement orbits and found that the columns under bi-axial bending had more reduction of strength and stiffness than those under uni-axial bending. In summary, the strength of structures under bi-directional excitations is less than that under uni-directional excitation.

So far, bi-directional responses have not been investigated for a wide range of natural periods of structures in orthogonal directions, critical angles of incidence, and strong ground motions. The research was conducted to address the issues and the bi-directional pseudo-acceleration response spectrum was proposed.

1.2 Objectives

The objectives of this study are

1. To develop the probabilistic seismic hazard map for Thailand.

2. To develop the relations among shear wave velocities, SPT N-values and undrained shear strengths for Bangkok and the northern Thailand

3. To determine the soil amplification of the north and west of Thailand and Bangkok.

4. To develop bi-directional response spectra for near field and far field waves.

1.3 Scopes and Limitations

- <u>Probabilistic Seismic Hazard Map</u>

1. The earthquakes catalogs were collected by the Thai Meteorological Department (TMD) and US Geological Survey (USGS). Earthquake events in the catalogs date 1912 to 2009 in the area covering 0^{o}N to 30^{o}N and 88^{o}E to 110^{o}E.

2. Seismic source zones in Thailand was proposed by Saithong et al. (2004)

3. The attenuation models by Sadigh et al. (1997) and Idriss (1993) are weighed equally and used for the active tectonic regions. The Petersen’s (2004) attenuation model modified from Youngs et al. (1997) is used for subduction zones.

4. The 2% and 10% probability of exceedance in 50 years are considered in developing probabilistic seismic hazard maps.

- Soil Response Analysis

1. The downhole seismic test is used for determining shear wave velocities of 3 boreholes in Bangkok and 3 boreholes in the north of Thailand.

2. The equivalent linear method is used to analyze the effect of soil amplification.

- Bi-directional Response Spectra

1. The ground motions are collected from the website of PEER Strong Motion Database [http://peer.berkeley.edu/smcat/search.html]. There are 86 of near field waves and far field waves. The ground motions vary in the soil types of the earthquake stations.

2. Ground motions are considered in the orthogonal directions.

3. Torsional effect is neglected.

4. The response of structures is considered in the elastic range.

CHAPTER II

LITERATURE REVIEWS

2.1 Probabilistic Seismic Hazard Map

Warnitchai and Lisantono (1996) proposed a seismic hazard map of Thailand using the earthquake data recorded from 1910 to 1989 and the seismic source zones proposed by the Southeast Asia Association of Seismology and Earthquake Engineering (Nutalaya et al., 1985). The attenuation model by Esteva and Villaverde (1973) was used to estimate peak accelerations. From Figure 2-1, the peak horizontal acceleration with 10% probability of exceedance in 50 years was determined to be 0.25 g in western and northern Thailand. The peak horizontal acceleration was 0.05 g in Bangkok.

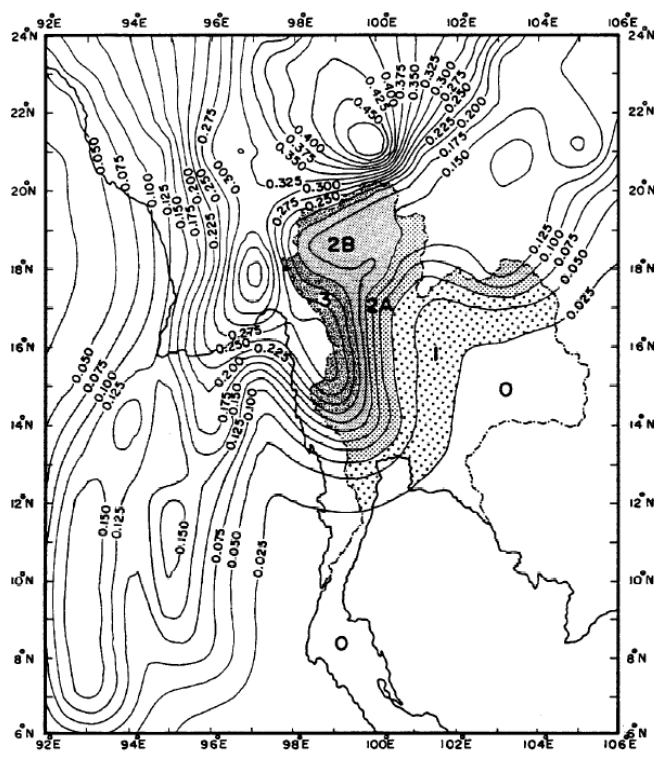

Figure 2-1 Map showing contours of peak groung acceleration (in units of g) with 10% probability of exceedance in 50 years. (Warnitchai and Lisantono, 1996)

Petersen et al. (2004) developed seismic hazard maps for Sumatra, Indonesia and the southern Malaysian Peninsula. The seismic source zones were generated from EHB catalog (Engdahl, van der Hilst, and Buland, 1998), ISC catalog (various Bulletins of the International Seismological Centre), and PDE catalog (various Preliminary Determination of Epicenters catalogs of the US Geological Survey). They modified the attenuation model originally proposed by Youngs et al (1997) to give a good fit with measured accelerations for a distance larger than 200 km from subduction earthquakes. The peak ground accelerations with 2% and 10% probability of exceedance in 50 years for rock sites were determined as shown in Figure 2-2. The peak ground acceleration with 2% probability of exceedance in 50 years ranges from 0.1 g to 1 g across Sumatra and becomes less than 0.2 g for the Malaysian Peninsula.

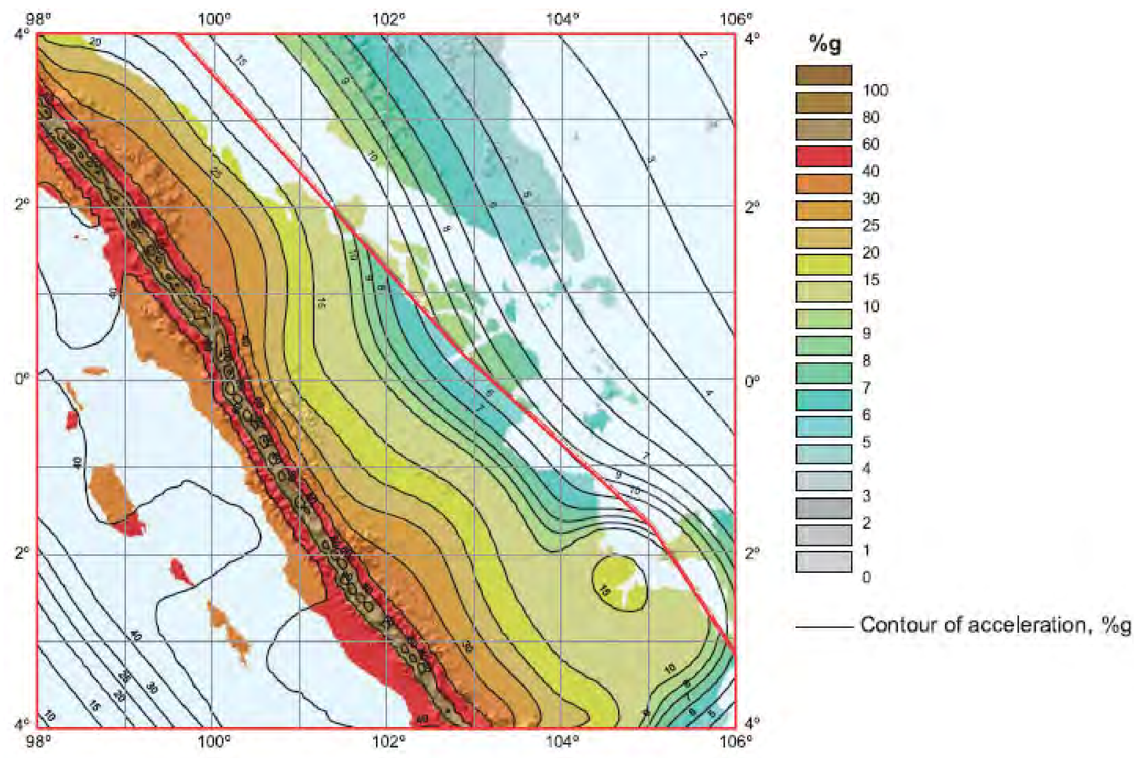

Figure 2-2 Map showing contours of peak groung acceleration (in units of g) with 10% probability of exceedance in 50 years for Sumatra, Indonesia and the southern Malaysian Peninsula. (Petersen et al., 2004)

Chintanapakdee et al. (2008) studied suitable attenuation models for Thailand by comparing measured ground accelerations with various available attenuation models. Peak horizontal accelerations were obtained from 163 ground motions recorded by the Thai Meteorological Department from 45 earthquakes with moment magnitudes between 4.7 to 6.3 and distances ranging from 231 to 2090 km. Measured peak horizontal accelerations were compared with attenuation relationships. The square root of mean of square (RMS) of differences between estimated peak horizontal accelerations and actual accelerations was computed to indicate the goodness of fit as Figure 2-3. They found that the relationships proposed by Idriss (1993) and Sadigh et al. (1997) had the lowest RMS for crustal earthquakes.

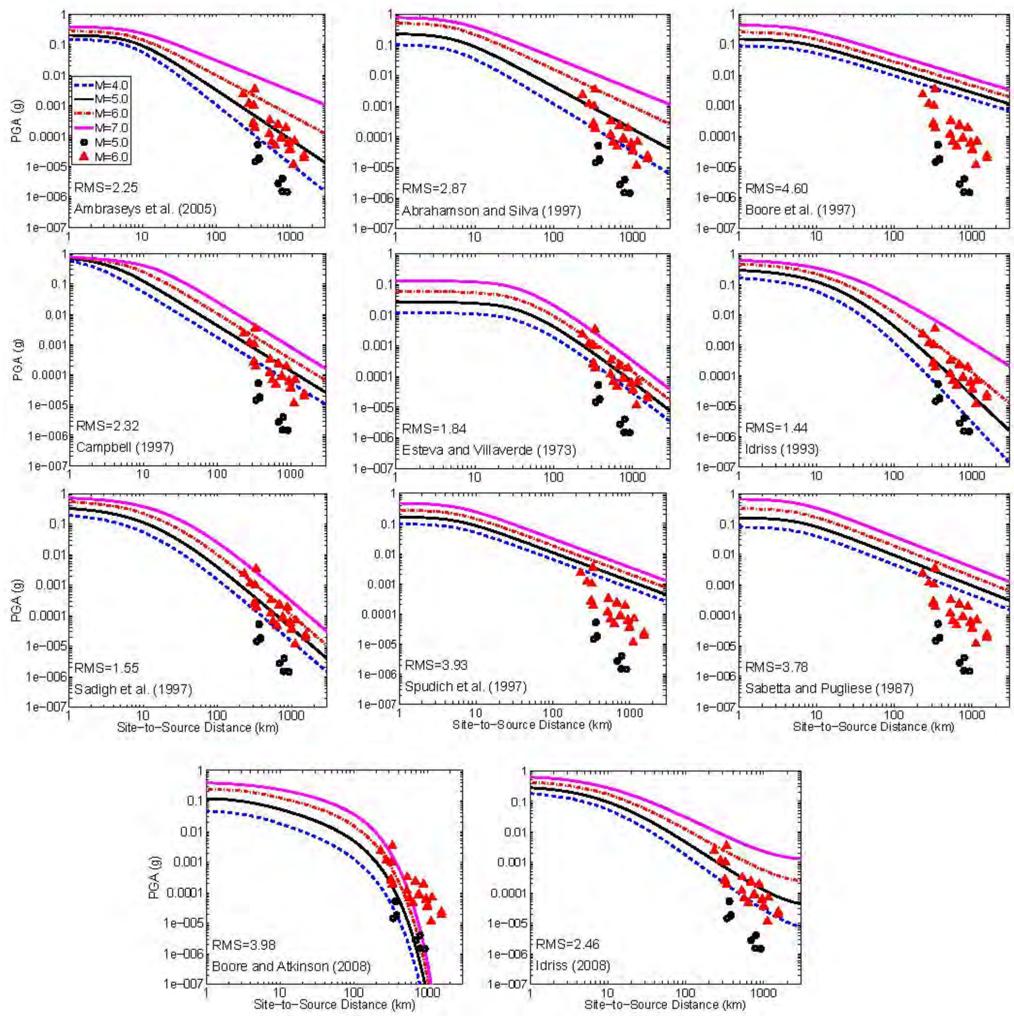

Figure 2-3 Comparison of attenuation curves for active tectonic regions and recorded PGA on rock sites in Thailand from shallow crustal earthquakes. (Chintanapakdee et al., 2008)

Seismic source zones are usually derived from tectonics, earthquake catalogs, and studies on active faults in a particular area. Seismic source zones in Thailand was recently proposed by Saithong et al. (2004) as shown in Figure 2-4. Active tectonic regions in northern Thailand consist of Zones E, F and I where Chiang Mai, Chiang Rai, Mae Hong Sorn provinces are located in. The active tectonic region in western Thailand consists of Zone J which covers Kanchanaburi province. The study by Fenton et al. (2003) indicates that active faults in the zones are capable to generate earthquakes with maximum magnitudes of up to 7.5.

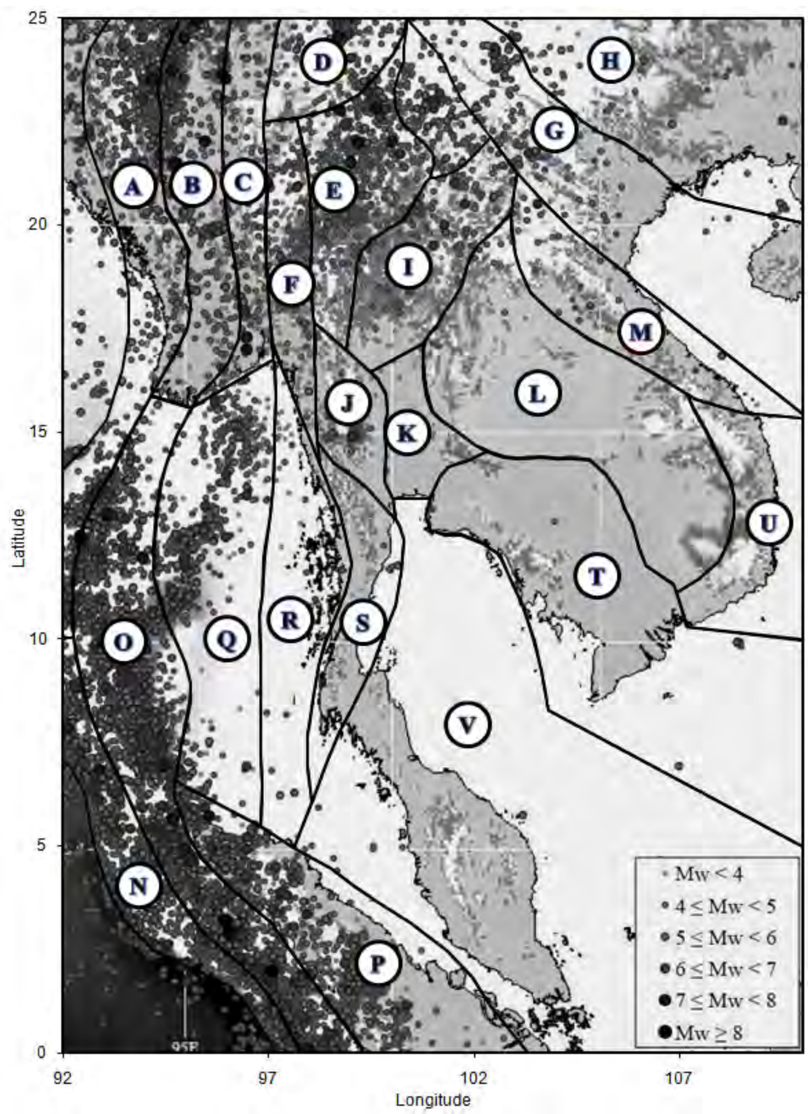

Figure 2-4 Seismic source zones in Thailand and neighboring areas (Saithong et al., 2004)

2.2 Soil Amplification in Thailand

Ashford et al. (1997) studied the amplification of ground acceleration in Bangkok which locates on the soft clay layer. The equivalent linear method was used in this study. They considered the horizontal acceleration on bedrocks at 0.02g, 0.05g, 0.07g and 0.10g. The bedrocks were defined at the level of 80 m, 160 m and 300 m, respectively. This study could be summarized that the Bangkok clay can amplifies the earthquake acceleration about 3-7 times of the acceleration at bedrock which is quite close to the measured amplification from the Mexico city and the Gulf of San Francisco.

Tuladhar et al. (2004) studied about the seismic microzonation of Bangkok by using Microtremor observations more than 150 sites around Bangkok. They found that the predominant periods are from 0.8s to 1.2s for Bangkok soil near the Gulf of Thailand and less than 0.4s for the areas outside that. The results from this study are displayed that the long period structures such as tall buildings and long span bridges which are located in Bangkok takes higher response of earthquakes than the short period structures.

2.3 Bi-directional Response

Takizawa and Aoyama (1976) studied the biaxial effects in modeling earthquake response of R/C structures by comparing between the results from R/C columns test with biaxial and uniaxial loading. The model of R/C column can be shown in Figure 2-5. The loads were applied by displacement controls in uniaxial and biaxial as shown in Figure 2-6. From the results in Figure 2-7, the strength of R/C columns after yielding under the biaxial displacement control was lower than in the uniaxial displacement control.

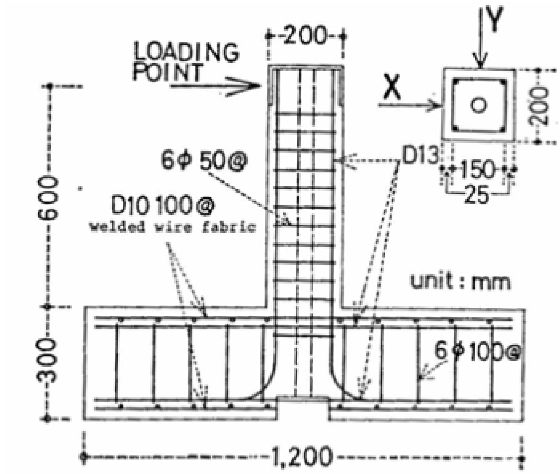

Figure 2-5 Elevation and section of test specimens (Takizawa and Aoyama, 1976)

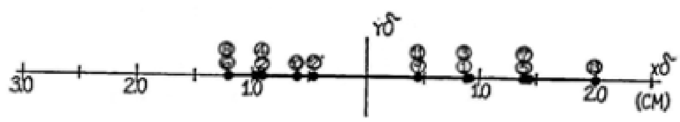

(a)

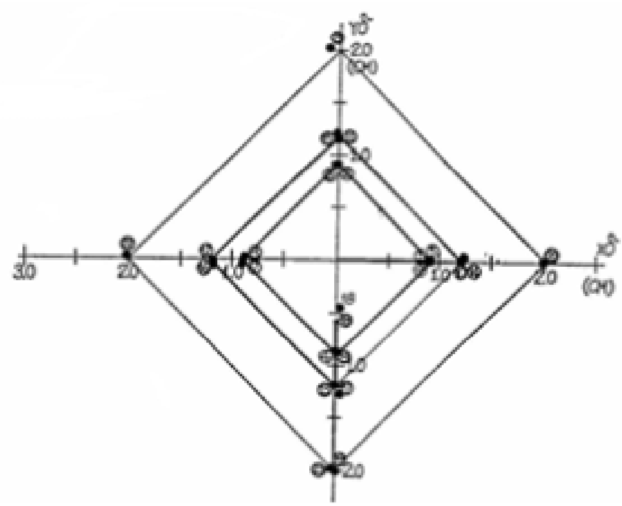

(b)

Figure 2-6 Compulsory deflection paths (Takizawa and Aoyama, 1976)

(a) Uniaxial displacement control (b) Biaxial displacement control

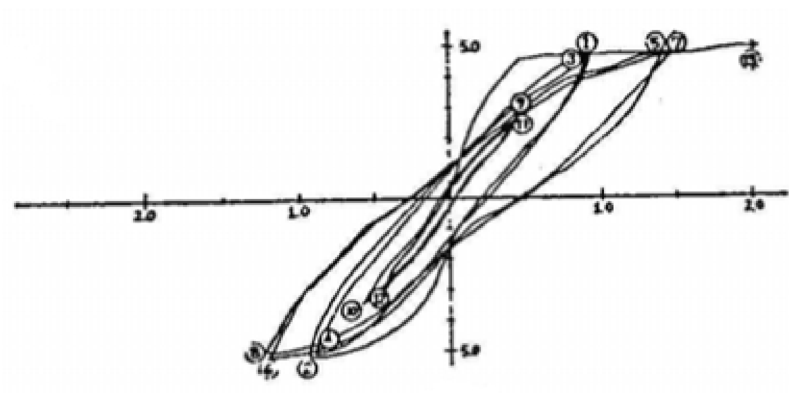

(a)

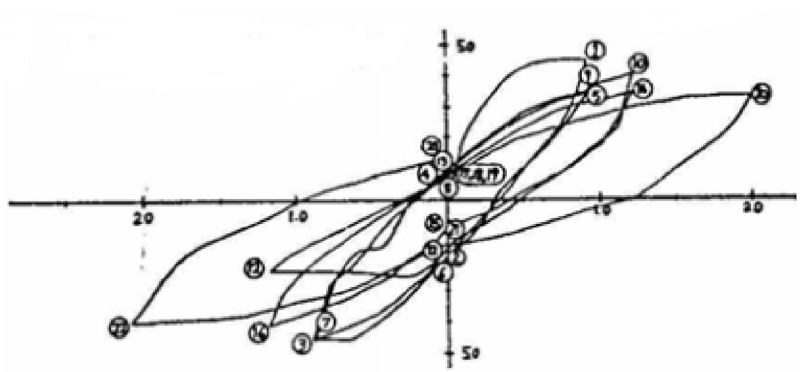

(b)

Figure 2-7 Comparison of load-deflection curves (Takizawa and Aoyama, 1976)

(a) Uniaxial displacement control (b) Biaxial displacement control

Oliva and Clough (1987) studied about the biaxial seismic response of R/C frames by comparison of the biaxial response from the shaking table test of R/C frame having rectangular columns as shown in Figure 2-8 with the uniaxial response using computerized analysis. The displacement record of 1952 Taft N69W earthquake was applied in this test. From the Figure 2-9, the biaxial stiffness of the first story column after yielding is decreased more than the uniaxial response. The results can be summarized in the Table 2-1. It is seem that the biaxial response of the first floor relative displacement in strong axis is higher than the uniaxial response. The torsion occurred only in the biaxial response because of the unsymmetrical stiffness when a column at corner cracked by biaxial loading. They summarized that the predicted uniaxial deformation demands were lower than measured in the biaxial test 32% for floor displacements, 60% for column flexural deformations in transverse axis and 16% for floor displacements, 20% for column flexural deformations in longitudinal axis.

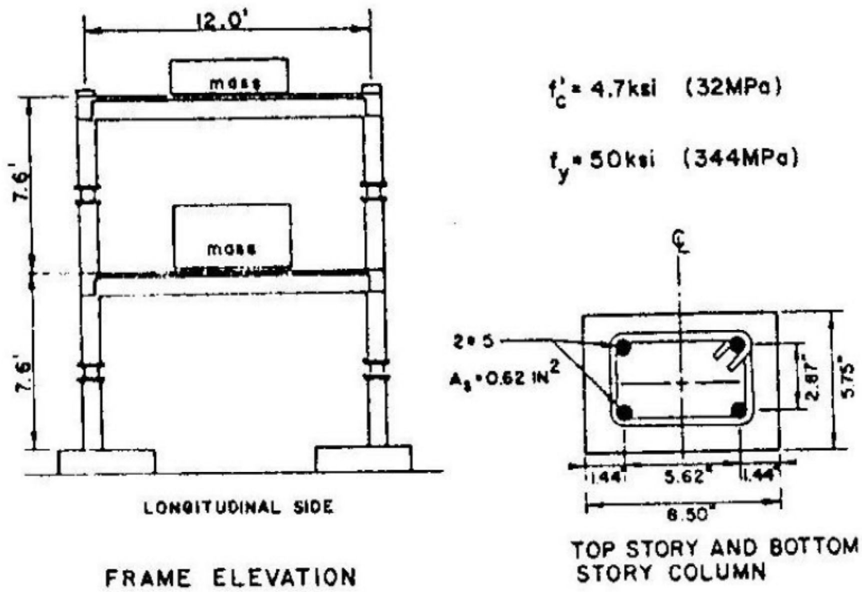

Figure 2-8 Test frame and column section dimensions (Oliva and Clough, 1987)

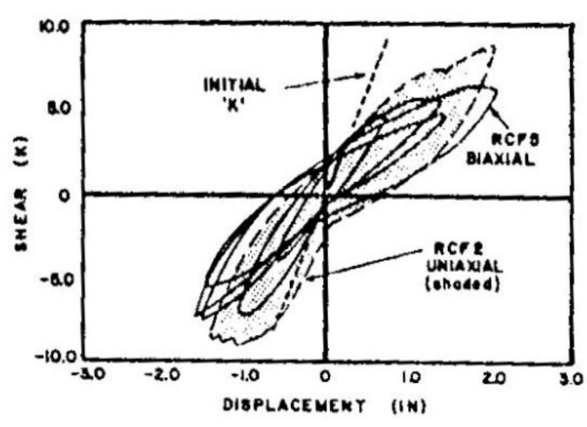

Figure 2-9 Shear versus top strong axis displacement of the first story column (Oliva and Clough, 1987)

Table 2-1 Comparison of frames' response data (Oliva and Clough, 1987)

Frame	First floor peak acceleration (g)	First floor relative displacement (in.)	Torsion (rad)
Biaxial-weak axis	0.306	1.54	0.043
Biaxial-strong axis	0.684	2.12	0.043
Uniaxial	0.798	2.04	None

Magliulo and Ramasco (2007) studied the seismic response of three-dimensional r/c multi-storey frame building under uni- and bi-directional input ground motions. The structural model is same as Verzelletti et al.'s (1994) test structure that can be displayed in Figure 2-10. The numerical results were compared with the experimental results for calibrating the model as Figure 2-11. That got a good correlation with the experimental results. So, the numerical model was suitable for other sensitivity study. The effects of bi-directional input motions were studied by comparing with the response of uni-directional input motions. The results can be shown in Figure 2-12 and 2-13. 'Uni-dir Y' means that the primary component of ground motion is applied in the global reference Y direction and, 'Bi-dir Y' means that the primary component of ground motion is applied in the global reference Y direction and also the secondary component of ground motion is applied in the global reference X direction. From Figure 2-12 and 2-13, the average base shears and displacement under bi-directional excitation are larger than with those under uni-directional excitation about 10%. It seems that the 30% combination rule for the response of bi-directional excitation of ground motion is conservative. From Figure 2-14, the local damage due to secondary component is larger than with uni-directional component. Therefore, the secondary component should not be neglect.

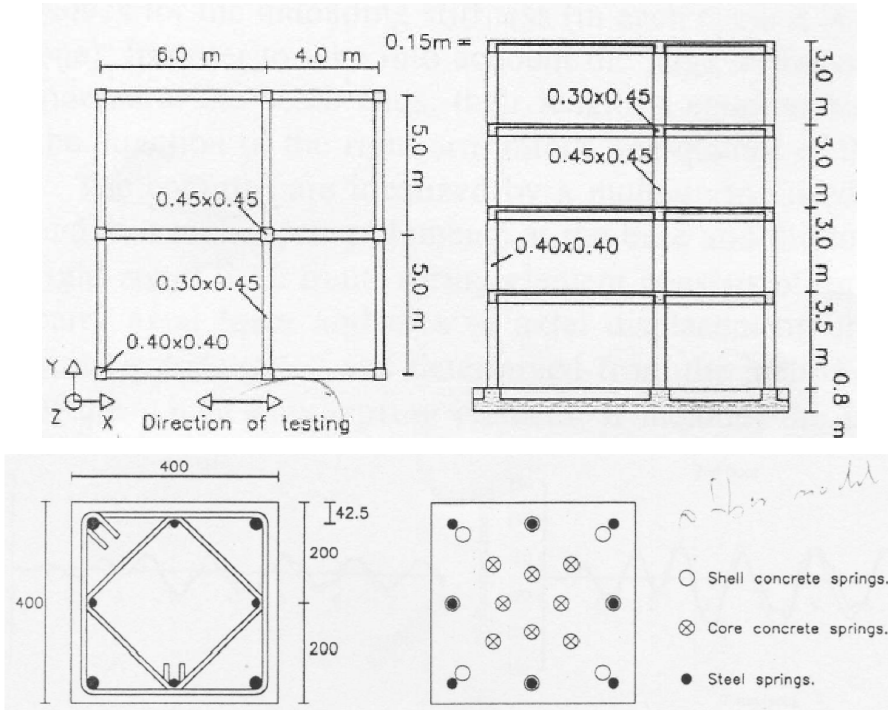

Figure 2-10 Reference test building, geometry and modeling of a corner column section (Magliulo and Ramasco, 2007)

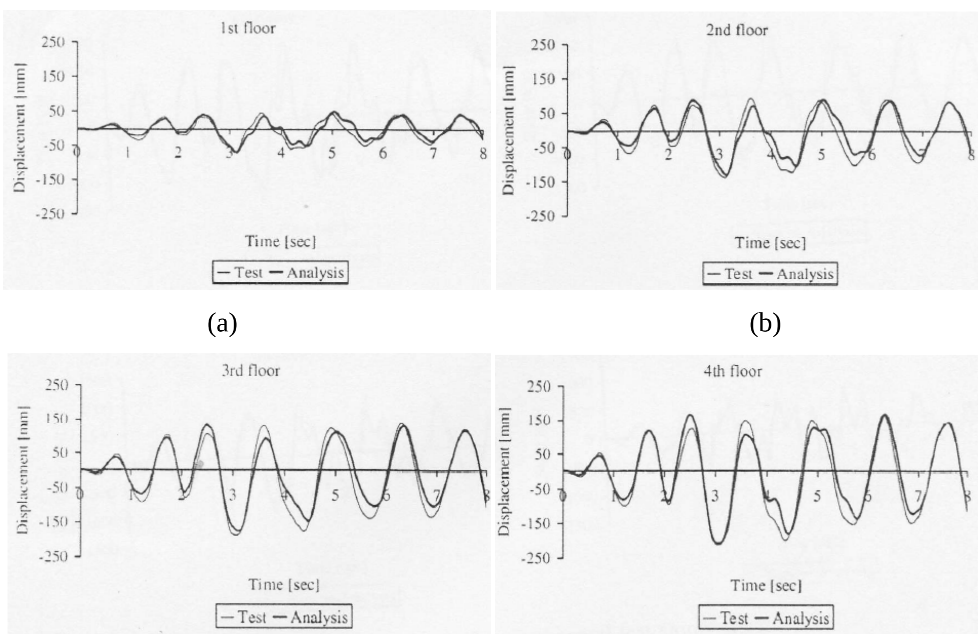

(a) (b)

(c) (d)

Figure 2-11 Numerical vs experimental test floor displacements (Magliulo and Ramasco, 2007)

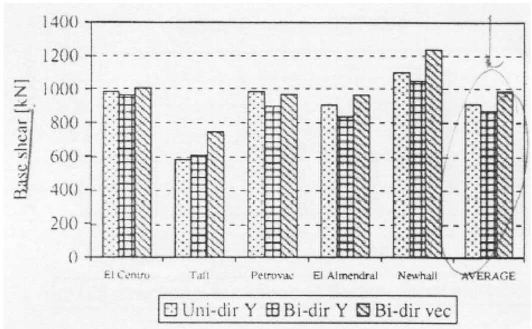

(a)

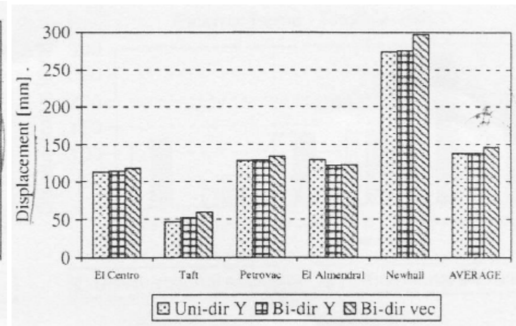

(b)

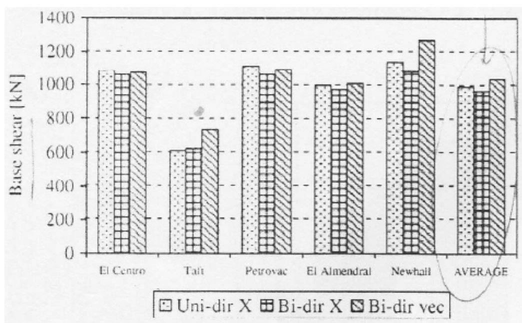

(c)

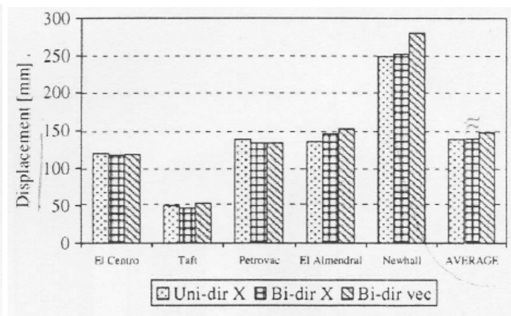

(d)

Figure 2-12 Maximum base shears and displacements of the upper floor centre of mass. (Magliulo and Ramasco, 2007)

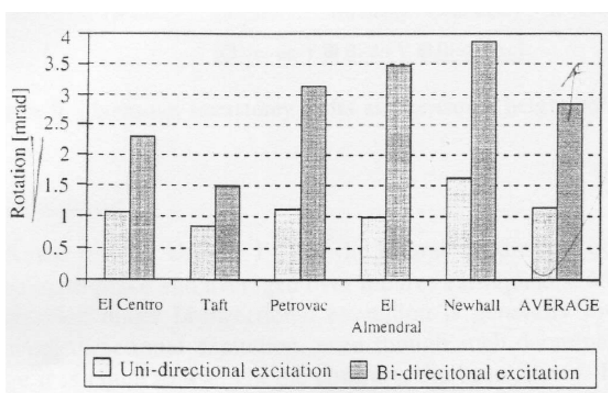

Figure 2-13 Maximum top floor rotations (Magliulo and Ramasco, 2007)

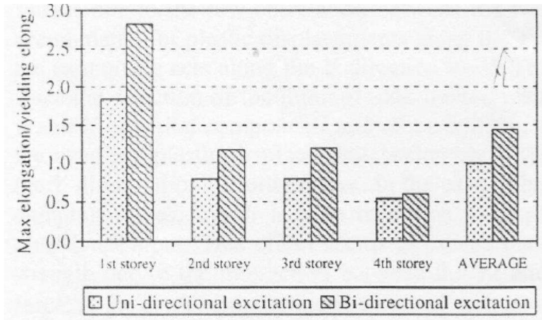

(a)

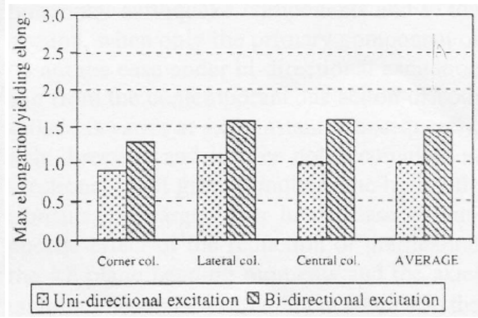

(b)

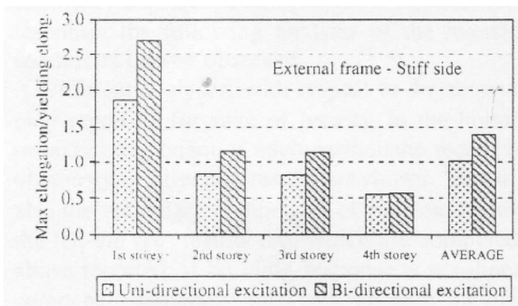

(c)

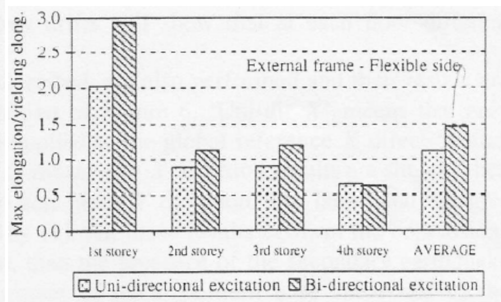

(d)

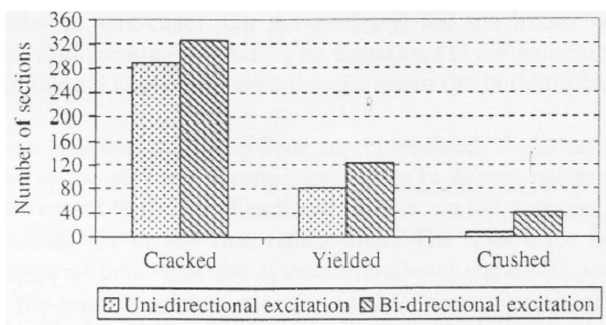

(e)

Figure 2-14 Averaged reinforcement plastic demand (Magliulo and Ramasco, 2007)

(a) storeys (b) column position (c) stiff side frame for each story, (d) flexible side frame for each storey (e) damage of the column sections.

2.4 Ground Motion

Malhotra (1999) determined the response of buildings to near-field pulse-like ground motions in acceleration, velocity and displacement histories. The Imperial Valley, 1979, Sylmar, 1994 and the synthetic earthquakes which are near-field pulse-like ground motions were compared with the Elcentro, 1940 earthquake which does not contain the pulse as shown in Figure 2-15. It is seem that the acceleration-sensitive region which the response of structure related with the ground acceleration of the pulse-like ground motions are wider than the ground motions which do not contain the pulse. The response spectra of those ground motions can be displayed in the Figure 2-16. The PGV/PGA and PGD/PGV ratios for the four ground motions were compared in Table 2-2. From the comparison of Figure 2-16 and Table 2-2, the spectral amplitudes in various regions depend on the PGA, PGV and PGD which the higher PGV/PGD ratio leads to wider acceleration-sensitive region and lower PGD/PGV ratio leads to wider displacement-sensitive region.

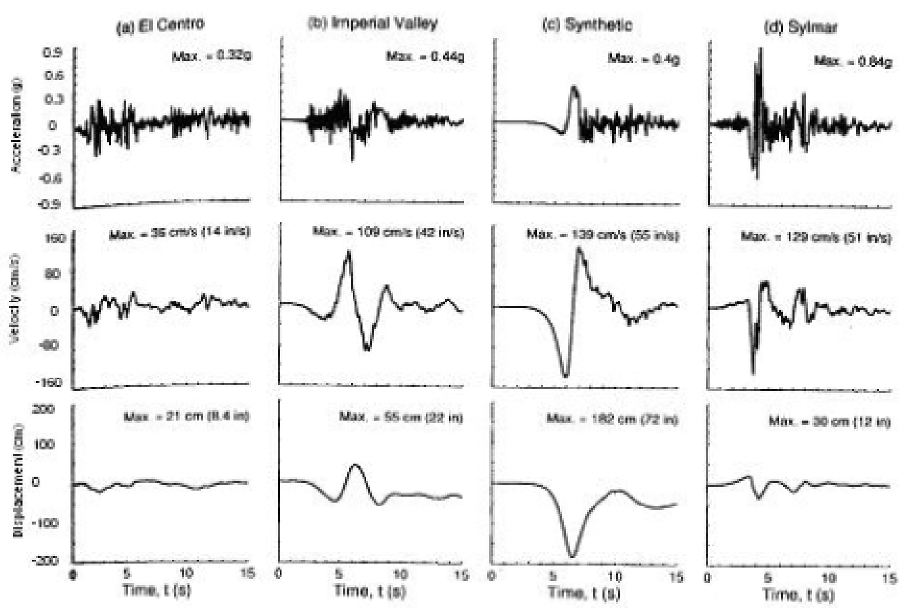

Figure 2-15 Acceleration, velocity and displacement histories of three recorded and one synthetic near-field ground motions (Malhotra, 1999)

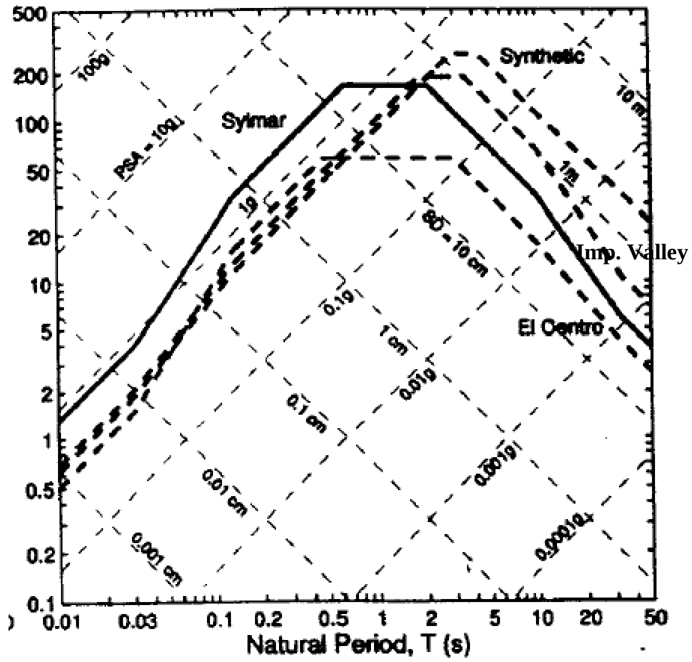

Figure 2-16 Tripartite plots of 5 percent damped smooth elastic response spectra of three recorded and one synthetic near-field ground motions (Malhotra, 1999)

Table 2-2 PGV/PGA and PGD/PGV values for near-field ground motions (Malhotra, 1999)

Ground motions	PGV/PGA	PGD/PGV
1940 El Centro	0.12 s	0.58 s
1979 Imperial Valley	0.25 s	0.50 s
1994 Sylmar	0.16 s	0.23 s
Synthetic	0.35 s	1.31 s

The effects of wide acceleration-sensitive region lead to highly maximum shear strain at the base, the first-story drift and the roof displacement as shown in Figure 2-17 and 2-18.

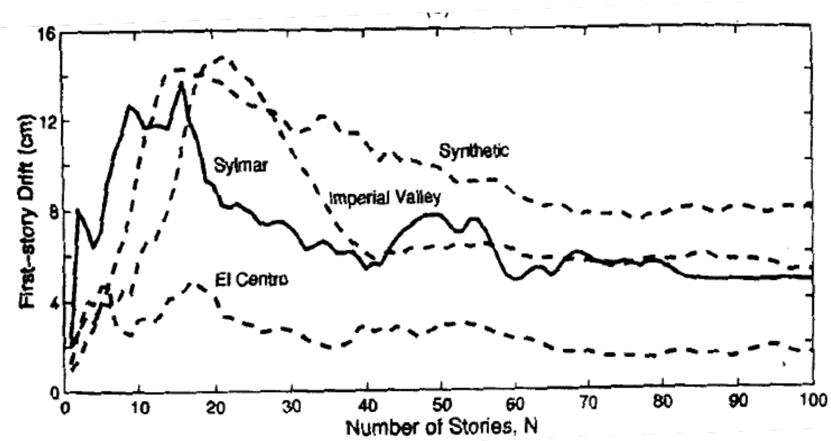

Figure 2-17 Drift spectra for three recorded and one synthetic near-field ground motions (Fundamental building period T_1=0.15N, damping ratio = 2%) (Malhotra, 1999)

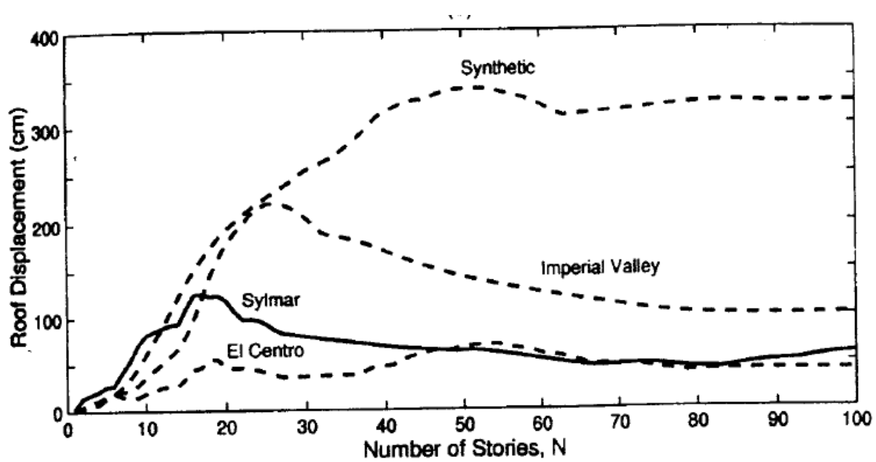

Figure 2-18 Roof displacement spectra for three recorded and one synthetic near-field ground motions (Fundamental building period T_1=0.15N, damping ratio = 2%) (Malhotra, 1999)

Chopra and Chintanapakdee (2001) compared the response of SDF systems to near-fault and far-fault earthquake motions in the context of spectra regions. This research uses Northridge, 1994 earthquake (NR94rrs) which is a near-field motion (epicenter 7.5 km) and Taft, 1952 earthquake which is a far-field motion (epicenter 43 km). From Figure 2-19, the response spectra of near-field motion in the fault-normal component are mostly higher than in the fault-parallel component but the response spectra of far-field motion in the fault-normal and fault-parallel component are quite close. The normalized PSA, PSV and PSD were shown in Figure 2-20. It is seem that the maximum responses in the fault-normal component are lower than in the fault-parallel component because of the number of cycles of ground motion as shown in Figure 2-21. The amplitude responses were higher when the number of cycles of ground motion increased.

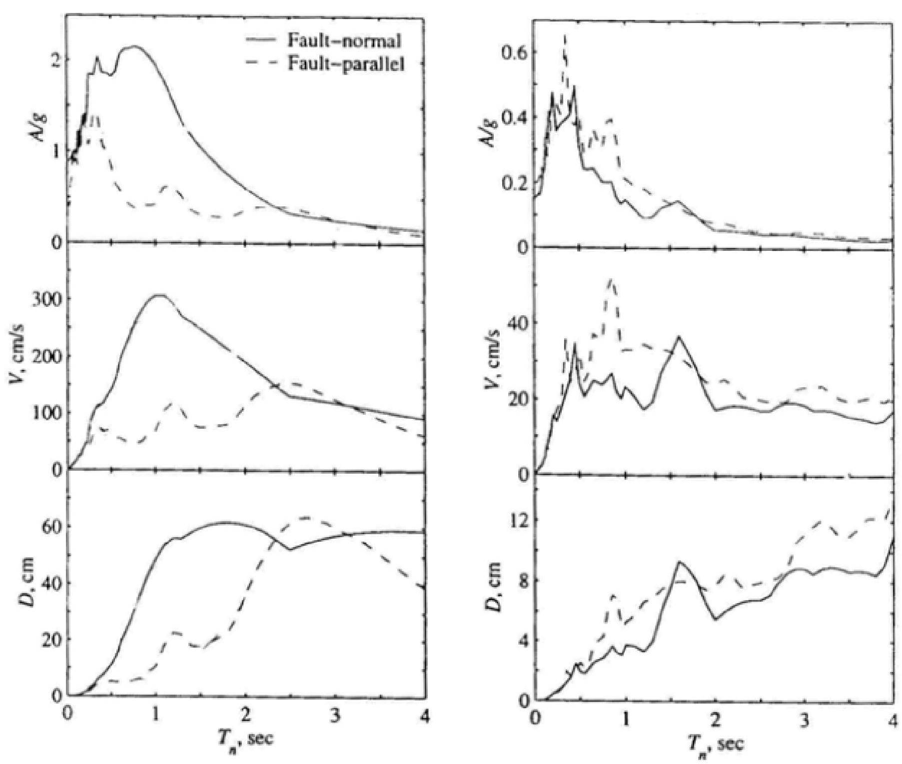

(a) NR94rrs (b) Taft

Figure 2-19 Response spectra for fault-normal and fault-parallel components, damping ratio = 5% (Chopra and Chintanapakdee, 2001)

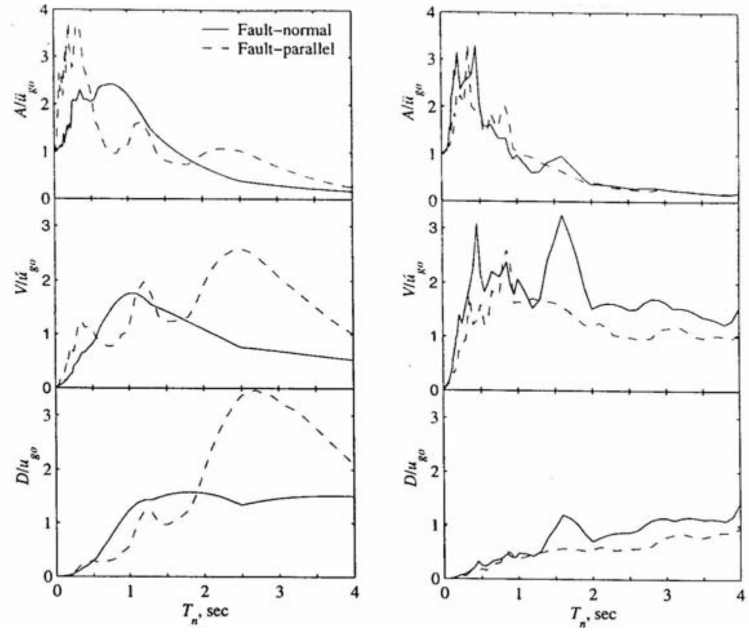

(a) NR94rrs and (b) Taft

Figure 2-20 Normalized response spectra for fault-normal and fault-parallel components, damping ratio = 5% (Chopra and Chintanapakdee, 2001)

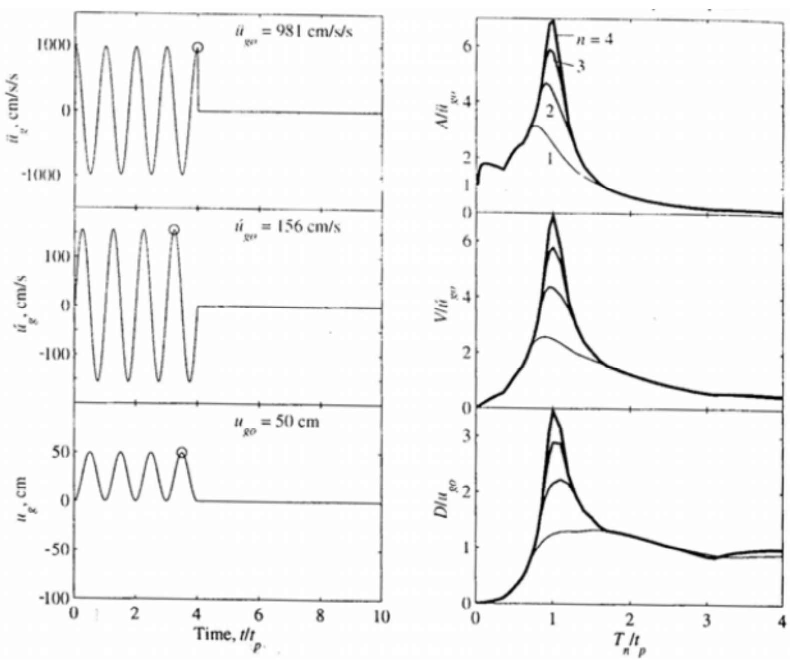

(a) (b)

Figure 2-21 Time histories and response spectra for four cycles of idealized motion with period t_p (Chopra and Chintanapakdee, 2001)

(a) Acceleration, velocity and displacement (b) Normalized response spectra

CHAPTER III

PROBABILISTIC SEISMIC HAZARD ANALYSIS

3.1 Introduction

Thailand has been affected by earthquakes with epicenters in neighboring countries as well as Thailand where some active faults exist. Most of active faults are located on the northern areas such as Mae Chan, Thoen, and Phayao faults; and the western areas such as Si Sawat and Three Pagodas faults as shown in Figure 3-1 Fenton et al. (2003) investigated several faults in northern and western Thailand and determined maximum earthquakes based on fault lengths. They found that some active faults in Thailand were capable to generate earthquakes with magnitudes of up to 7.5. A maximum magnitude of 7.5 was estimated for Mae Chan and Three Pagodas faults.

Thailand has experienced moderate earthquakes which caused damage to buildings in areas close to epicenters. The September 11th, 1994 earthquake which had a local magnitude (M_L) of 5.1 and an epicenter located approximately 15 km from Pan District, Chiang Rai Province caused shear failure of columns in a local hospital (Figure 3-2). The May 16th, 2007 earthquake with a moment magnitude of 6.3 and an epicenter near the Thai-Laos border caused damage to a school in Chiang Rai Province, located 109 km from the epicenter. Figure 3-3 shows shear failure in a column exposed from a masonry wall.

In designing structures, it is important to assure the safety and functionality of structures at various limit states and corresponding levels of seismic inputs, especially for important structures such as nuclear facilities and important lifelines. There is a need to develop a seismic hazard map with 2% probability of exceedance in 50 years which is widely used in various seismic design codes. This research is aimed to develop the seismic hazard map for Thailand for with 2% and 10% probability of exceedance in 50 years based on up-to-date earthquake catalogs and recent studies on appropriate attenuation relationships for Thailand and the region, The seismic hazard map can be used for earthquake-resistant design of structures in Thailand and neighboring countries.

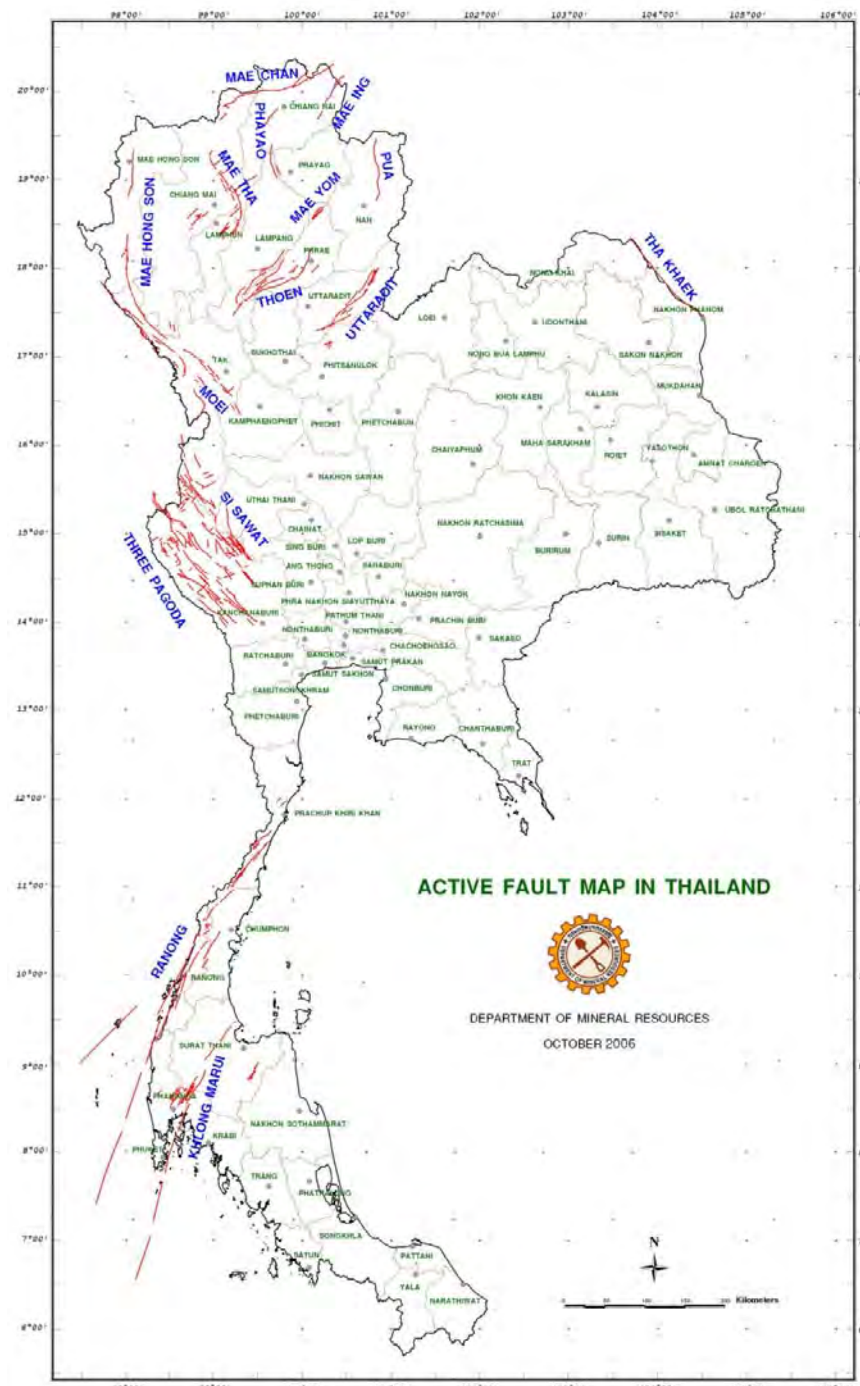

Figure 3-1 Map of active faults in Thailand

(Courtesy of Department of Mineral Resources, Ministry of Natural Resources and Environment)

Figure 3-2 Shear failure in short columns of the Pan hospital in the September 11th, 1994 earthquake (After Lukkunaprasit, 1995)

Figure 3-3 Shear failure in columns of a school in Chiang Rai province in the May 16th, 2007 earthquake

3.2 Theories

Cornell (1968) and Algermissen et al. (1982) developed the method of the probabilistic seismic hazard analysis. That has 4 principal sequences which can be summarized in Figure 3-4.

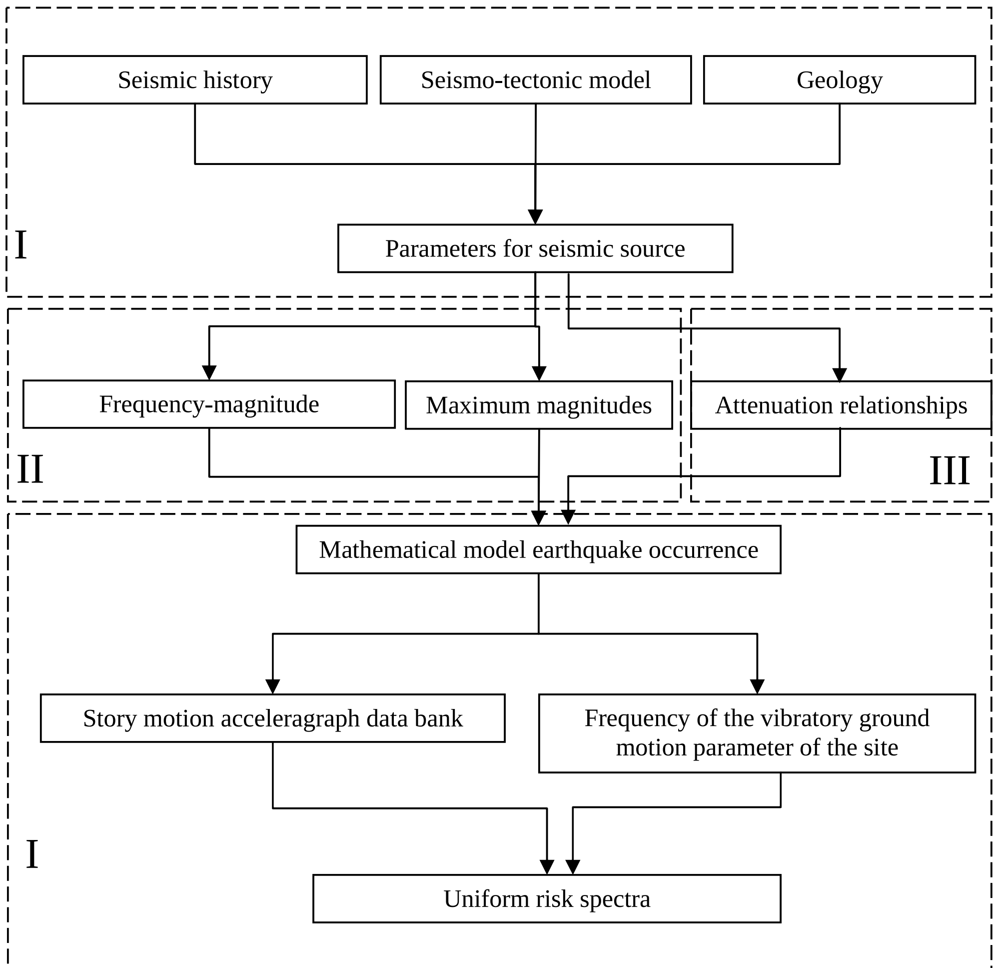

Figure 3-4 The algorithm of the probabilistic seismic hazard analysis

The details of this method consists of

1. The seismic source zones are usually derived from tectonic boundaries, earthquake catalogs, and faults study and the closest distance from seismic sources to site are determined.

The probabilities of distance can be found from

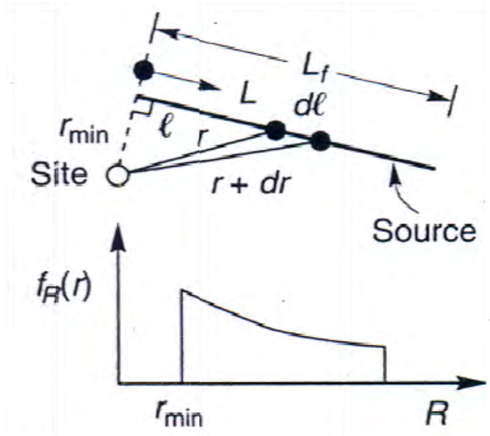

Figure 3-5 Determining the probability of distance from seismic source zone to site.

From Figure 3-5, the probability of event that occurs in the seismic source zone which is in the ranging of l to $l + dl$ is equal to the probability of event that occurs in the seismic source zone which is in the ranging of r to $r + dr$.

$$f_L(l)dl = f_R(r)dr \tag{3-1}$$

$$f_R(r) = f_L(l)\frac{dl}{dr} \tag{3-2}$$

$$l^2 = r^2 - r_{\min}^2 \tag{3-3}$$

$$f_L(l) = \frac{1}{L_f} \tag{3-4}$$

$$f_R(r) = \frac{r}{L_f\sqrt{r^2 - r_{\min}^2}} \tag{3-5}$$

where $f_L(l)$ is the probability of the distance from an earthquake that occurs in the seismic source zone to the point on the seismic source zone which is the closest to a station (l).

$f_R(r)$ is the probability of the distance from the seismic source zone to a station (r).

L_f is the length of the seismic source zone

2. The recurrence rates of earthquake magnitudes are determined in each source zone. The relation between the recurrence rates of earthquakes and magnitudes can be expressed in a form of the Gutenberg-Richter equation as

$$\log \lambda_m = a - bm \qquad (3\text{-}6)$$

where λ_m is The recurrence rates of earthquakes which the magnitudes are over m. (per a year)

a and b are constants.

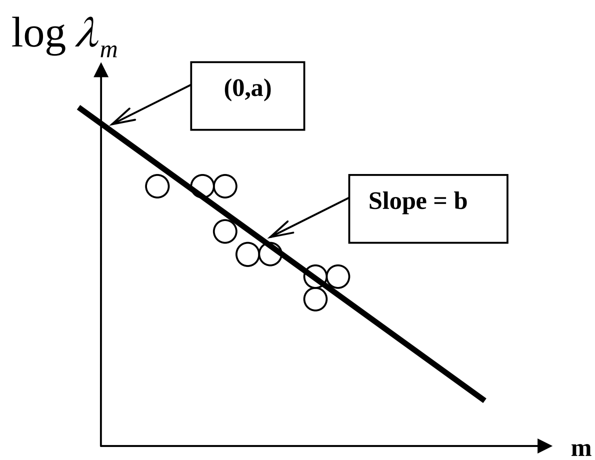

Figure 3-6 Determining the a and b values of the Gutenberg-Richter equation from the relation between the recurrence rates of earthquakes and magnitudes.

The probability of the recurrence rate (λ_m) of the earthquake magnitude (m) is determined from

$$\lambda_m = 10^{a-bm} = e^{\alpha - \beta m} \qquad (3\text{-}7)$$

where $\alpha = 2.303a$ and $\beta = 2.303b$ (3-8)

If the minimum magnitude of earthquake (m_0) is defined, the recurrence rate (λ_m) of the earthquake magnitude (m) will be derived following the McGuire and Arabasz (1990) equation.

$$\lambda_m = \upsilon \exp[-\beta(m - m_0)] \qquad ; \ m > m_0 \tag{3-9}$$

where $\upsilon = \exp(\alpha - \beta m_0)$ (3-10)

The probability of the recurrence rate can be set in the form of the cumulative distribution function (CDF) as

$$F_M(m) = P[M < m \mid M > m_0] = \frac{\lambda_{m0} - \lambda_m}{\lambda_{m0}} = 1 - e^{-\beta(m - m0)} \tag{3-11}$$

The Probability density function (PDF) or the probability of the recurrence rate (λ_m) of the earthquake magnitude (m) is

$$f_M(m) = \frac{d}{dm} F_M(m) = \beta e^{-\beta(m - m_0)} \tag{3-12}$$

If the minimum magnitude of earthquake is equal to m_0 and the maximum magnitude is $m_{\max}$, the recurrence rate (λ_m) of the earthquake magnitude (m) following the McGuire and Arabasz (1990) equation will be

$$\lambda_m = \upsilon \frac{\exp[-\beta(m - m_0)] - \exp[-\beta(m_{\max} - m_0)]}{1 - \exp[-\beta(m_{\max} - m_0)]}; \ m_0 < m < m_{\max} \tag{3-13}$$

From the Equation (3-13), the mean of annual rate can be plotted in Figure 3-7

From Figure 3-7, it seems that the means of annual rates are bounded like curves to zero at the maximum magnitude. The probability of the recurrence rate can be set in the form of the cumulative distribution function (CDF) as

$$F_M(m) = P[M < m \mid m_0 < M < m_{\max}] = \frac{1 - \exp[-\beta(m - m_0)]}{1 - \exp[-\beta(m_{\max} - m_0)]} \tag{3-14}$$

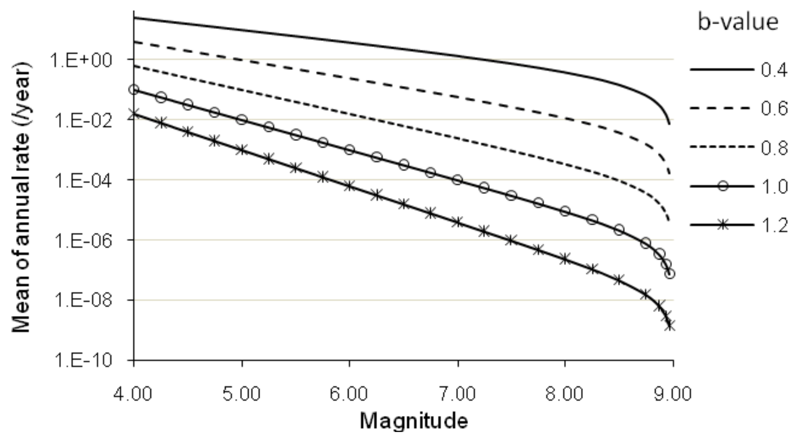

Figure 3-7 The relation between mean of annual rate and magnitude of earthquake from the equation of McGuire and Arabasz (1990) (a = 3)

The probability density function (PDF) or the probability of the recurrence rate (λ_m) of the earthquake magnitude (m) is

$$f_M(m) = \frac{\beta \exp[-\beta(m - m_0)]}{1 - \beta \exp[-\beta(m_{\max} - m_0)]} \tag{3-15}$$

which can be plotted in Figure 3-8

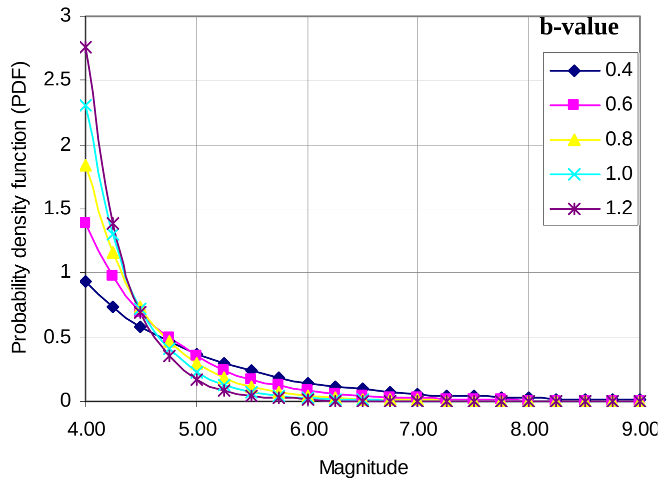

Figure 3-8 The probability of the recurrence rate (λ_m) of the earthquake magnitude (m) in various b-values

3. The suitable attenuation models are selected for finding peak horizontal acceleration. The probability of attenuation models can be determined by using the standard derivation that is defined in each attenuation model as shown in Figure 3-9.

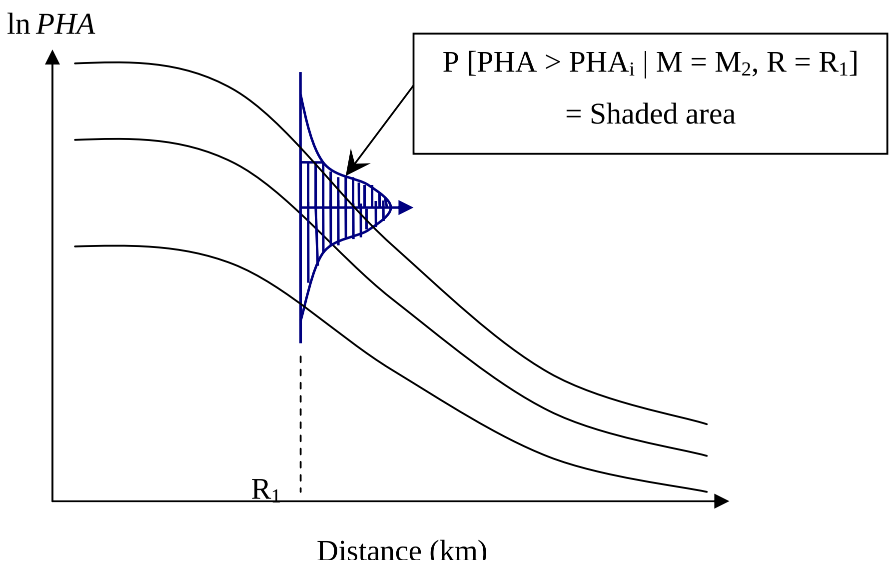

Figure 3-9 The probability of attenuation models

The probability of the normal distribution at ln x of the data which the mean is $\overline{ln\ x}$ and the standard deviation is σ_x can be expressed by the following equation.

$$f_x(x) = \frac{1}{x\sqrt{2\pi}\sigma_x}\exp\left[-\frac{1}{2}\left(\frac{\ln x - \overline{\ln x}}{\sigma_x}\right)^2\right] \quad (3\text{-}16)$$

4. The probabilities of all steps are combined and the peak horizontal accelerations are expressed on the used return periods which are 10% in 50 years or 475 years and 2% in 50 years or 2475 years.

3.3 Earthquake Records

The Thai Meteorological Department (TMD) has recorded earthquake events and compiled earthquake records consisting of origin times, locations, depths, and magnitudes. Earthquake events in the catalogs date 1912 to 2009 in the area covering 0^{o}N to 30^{o}N and 88^{o}E to 110^{o}E. Magnitudes in the catalogs are presented in a body-wave magnitude (m_b), a local magnitude (M_L), a surface-wave magnitude (M_S) and a moment magnitude (M_W). The event records in the catalog were obtained from US Geological Survey (USGS) from 1954, International Seismological Centre (ISC) from 1964, TMD from 1976 and other catalogs as shown in Figure 3-10. The earthquake magnitudes were converted to the moment magnitude (M_W) using the relations proposed by Scordilis (2006), Sipkin (2003) and Heaton et al. (1986) which are expressed by Table 3-1.

Table 3-1 The equations for converting other magnitude scales into moment magnitude

Magnitude scales	Magnitude Ranges	Equations	References
M_s	$3.0 \le M_s \le 6.1$	$M_w = 0.67\ M_s + 2.07$ (3-17)	Scordilis (2006)
	$6.2 \le M_s \le 8.2$	$M_w = 0.99\ M_s + 0.08$ (3-18)	Scordilis (2006)
m_b	$3.5 \le m_b \le 6.2$	$M_w = 0.85\ m_b + 1.03$ (3-19)	Scordilis (2006)
	$5.5 \le m_b \le 7.3$	$M_w = 1.46\ m_b - 2.42$ (3-20)	Sipkin (2003)
M_L	$M_L \le 6$	$M_w = M_L$ (3-21)	Heaton (1986)

An assumption in the seismic hazard analysis is that all earthquake events are independent. Thus, the earthquake events which are foreshocks and aftershocks must be eliminated before further analysis. The method proposed by Gardner and Knopoff (1974) was applied to eliminate foreshocks and aftershocks. Earthquakes with magnitudes less than a magnitude (M) within a duration (T) and a distance (L) are considered as foreshocks and aftershocks, expressed by the following equations:

$$\log T = 0.556\, M + 0.603 \text{ for } M < 6.4 \quad (3\text{-}22)$$

$$\log T = 0.062\, M + 2.512 \text{ for } M \ge 6.4 \quad (3\text{-}23)$$

$$\log L = 0.124\, M + 0.983 \quad (3\text{-}24)$$

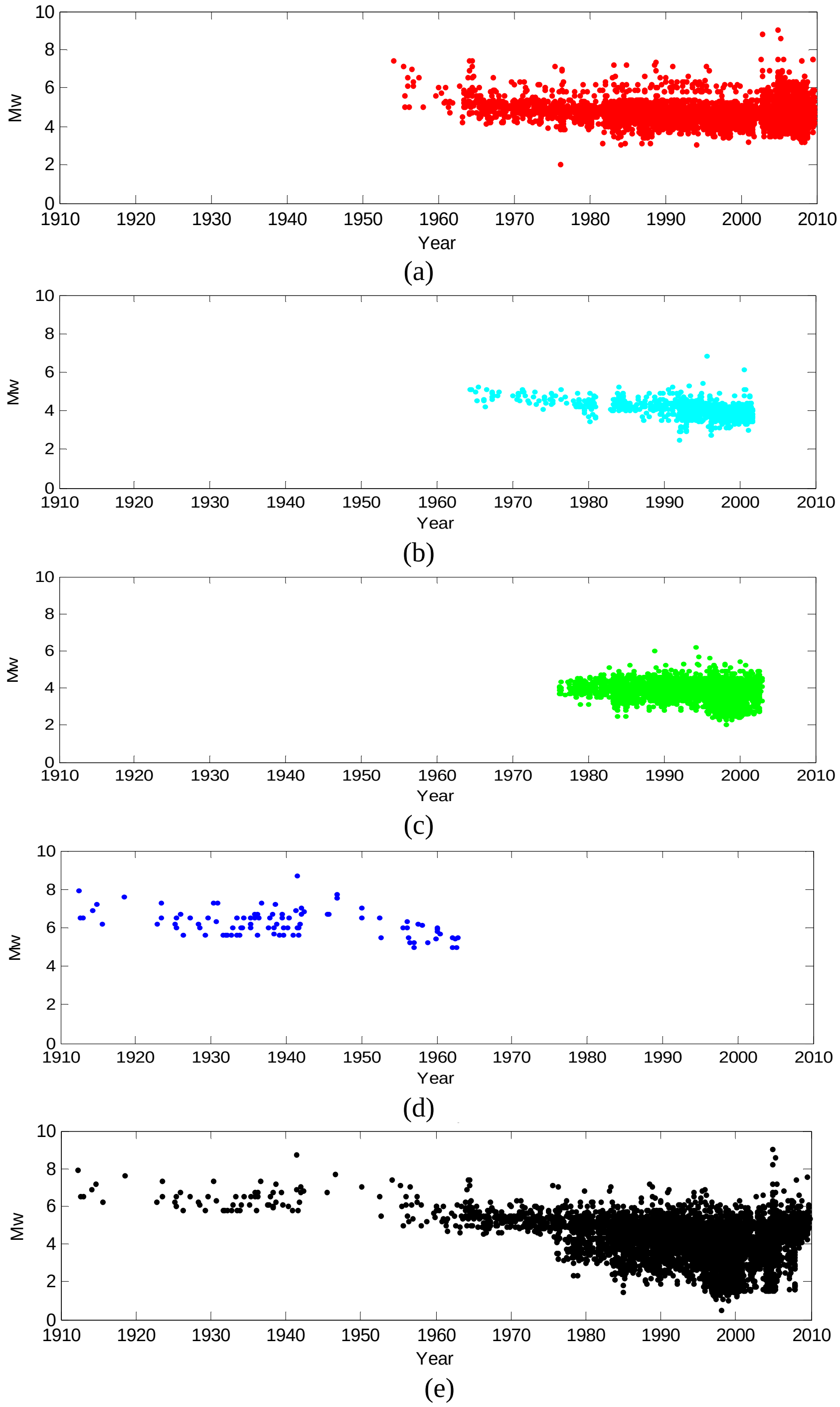

Figure 3-10 Recorded moment magnitudes versus years from various catalogs
(a) USGS, (b) ISC, (c) TMD, (d) Other catalogs, (e) All catalogs

Elimination of foreshocks and aftershocks reduces the number of earthquake events from 17,451 to 6,400 which are 37% of all data. An example of the elimination of foreshocks and aftershocks is shown in Figure 3-11. The seismicity map of main shocks during 1912-2009 is shown in Figure 3-12.

No.	YY	MM	DD	HR	MIN	SEC	LAT	LONG	DEPTH	Mw
8491	2003	7	12	9	40	34.7	4.04	95.33	33	3.9
8492	2003	7	13	23	38	51.4	12.56	95.63	33	5.1
8493	2003	7	16	11	5	33.4	27.38	100.3	33	4.3
8494	2003	7	16	17	48	38	1.97	98.84	124	4.2
8495	2003	7	21	15	16	31.9	25.98	101.29	10	6
8496	2003	7	21	19	21	10.7	6.68	93.6	10	5.6
8497	2003	7	22	0	9	38.6	25.96	101.19	10	4.4
8498	2003	7	22	6	21	14.2	6.71	93.5	10	4.9
8499	2003	7	22	21	41	55.4	6.7	93.15	10	4.7
8500	2003	7	23	4	42	30.1	26.05	101.21	10	4.3
8501	2003	7	23	23	52	41.9	25.97	101.27	10	4

(a)

No.	YY	MM	DD	HR	MIN	SEC	LAT	LONG	DEPTH	Mw
8491	2003	7	12	9	40	34.7	4.04	95.33	33	3.9
8492	2003	7	13	23	38	51.4	12.56	95.63	33	5.1
8493	2003	7	16	11	5	33.4	27.38	100.3	33	4.3
8494	2003	7	16	17	48	38	1.97	98.84	124	4.2
8495	2003	7	21	15	16	31.9	25.98	101.29	10	6
8496	2003	7	21	19	21	10.7	6.68	93.6	10	5.6
8499	2003	7	22	21	41	55.4	6.7	93.15	10	4.7

(b)

Figure 3-11 An example of the elimination of foreshocks and aftershocks

(a) All data before elimination of foreshocks and aftershocks

(b) Main shocks after elimination of foreshocks and aftershocks

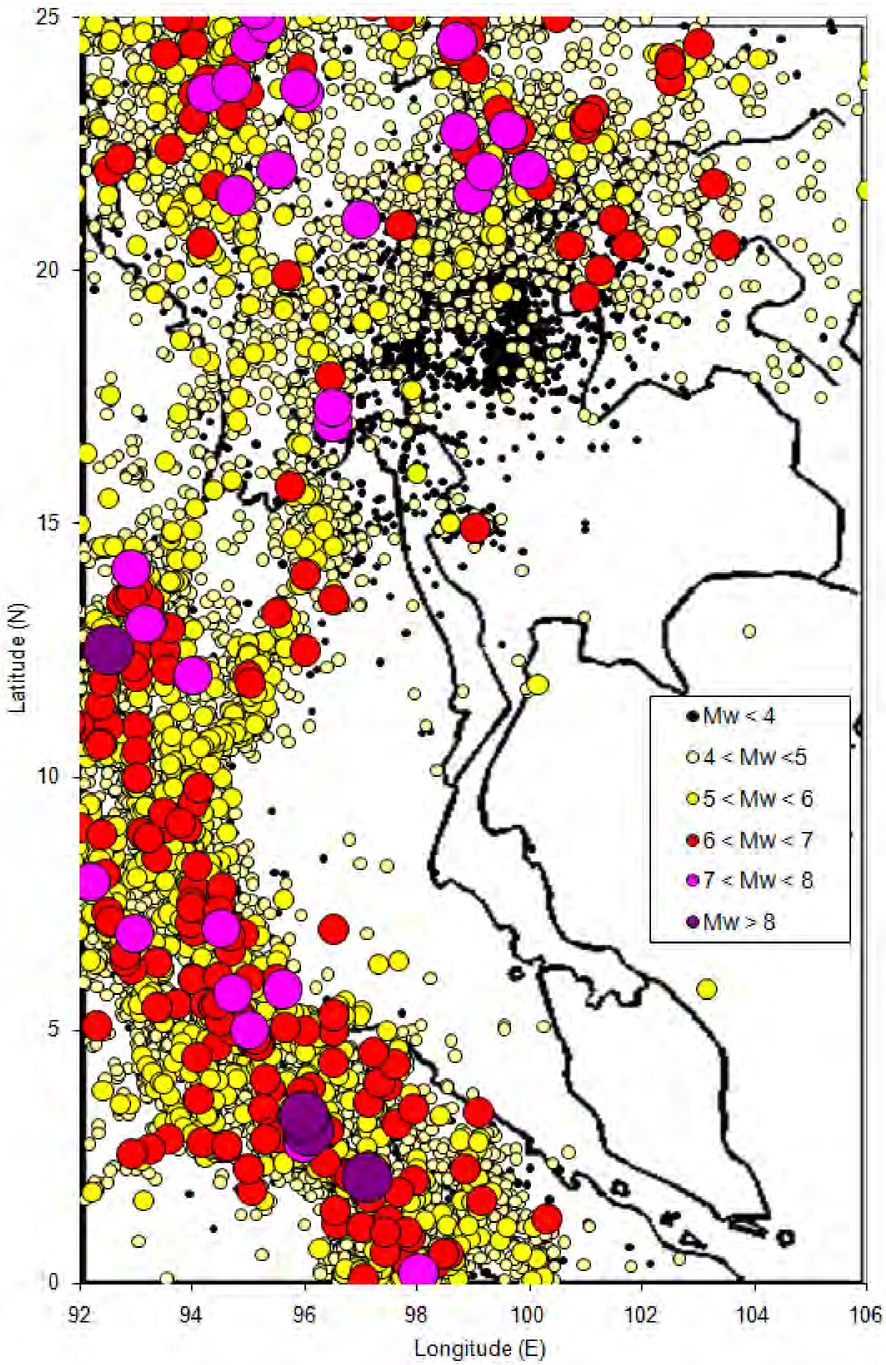

Figure 3-12 Seismicity in Thailand and neighboring area during 1912 – 2009 after elimination of foreshocks and aftershocks

3.4 Seismic Source Zones

Seismic source zones are usually derived from tectonics, earthquake catalogs, and studies on active faults in a particular area. Seismic source zones in Thailand were recently proposed by Saithong et al. (2004) as shown in Figure 3-13.

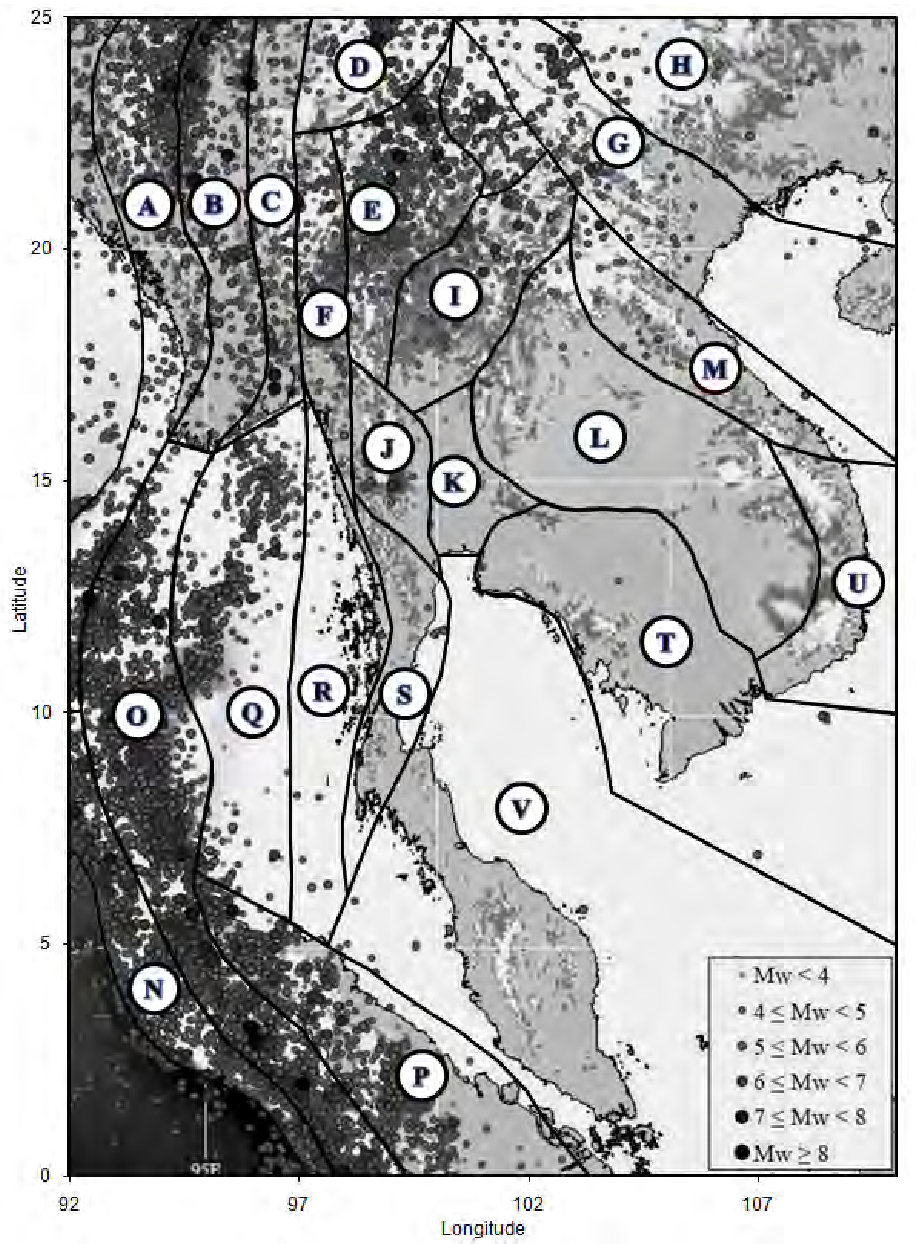

Figure 3-13 Seismic source zones in Thailand and neighboring areas

From the seismicity and the seismotectonic, the seismic source zone can be separated in 2 types.

1) Active tectonic regions consist of zones B, C, D, E, F, G, H, I, J, M, P, Q, R and W.

2) Subduction zones consist of zones A, N and O.

Active tectonic regions in northern Thailand consist of Zones E, F and I where Chiang Mai, Chiang Rai, Mae Hong Sorn provinces are located in. The active tectonic region in western Thailand consists of Zone J which covers Kanchanaburi province. The study by Fenton et al., 2003 indicates that active faults in the zones are capable to generate earthquakes with maximum magnitudes of up to 7.5.

3.5 Completeness of Data

Earthquake events recorded in the past may be incomplete because instruments could not detect small earthquakes. From 1954 to 2009, USGS recorded earthquakes with magnitudes greater than 3.5 as shown in Figure 3-10(a) but earthquakes with magnitudes less than 3.5 can be recorded by TMD since 1964 as shown in Figure 3-10(c). Incomplete data can result in under-estimation of recurrence rates. Hence, the completeness of data is analyzed before conducting hazard analysis. The method proposed by Stepp (1972) for determining the time period of complete data is used in the study. The equation that is used for this method can be expressed as

$$k(m) = \frac{n(m)}{T} \tag{3-25}$$

where $k(m)$ is the recurrence rate of earthquakes which the magnitude is equal to *m* in 1 year and $n(m)$ is the number of earthquakes which the magnitude is equal to *m* for the period *T* years (10 years ,20 years ,30 years...,).

The standard deviation) σ (can be determined by

$$\sigma = \frac{\sqrt{k(m)}}{\sqrt{T}} \tag{3-26}$$

The relation between the standard deviation) σ(and the period (T) can be plotted in the logarithm as Figure 3-14. The range of completeness data need to have the slope about -0.5.

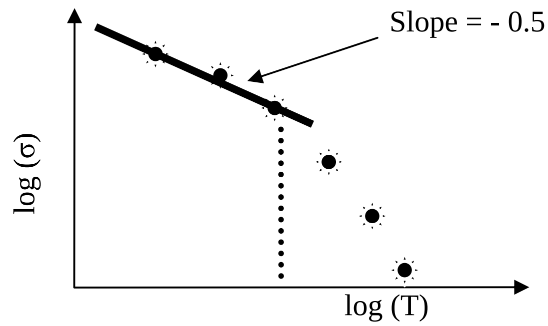

Figure 3-14 The logarithm relation between σ and T

The years after which the data is considered complete is summarized in Table 3-2. The table is divided into various zones and magnitude ranges.

Table 3-2 The year after which the data is considered complete.

Magnitude	**ZONE**																
	A	**B**	**C**	**D**	**E**	**F**	**G**	**H**	**I**	**J**	**M**	**N**	**O**	**P**	**Q**	**R**	**W**
2.75-2.95	1995		1990	1995	1985	1980			1985	1980					1985	1990	
3.00-3.20	1990	1985	1980	1995	1975	1975	1985		1975	1980					1980	2005	1995
3.25-3.45	1990	1975	1975	2000	1975	1975		1985	1985	1980	2000		1995	1995	1975	1985	1995
3.50-3.70	1980	1975	1975	1985	1975	1975	1980	1985	1975	1985	1985				1980	2005	1980
3.75-3.95	1995	1975	1975	1990	1975	1975	2005	1995	1980	2000	1975		1995		1980	1995	1980
4.00-4.20	1985	1975	1975	1975	1975	1975	1985	1990	1975	1985	1980	1985	1980	1985	1975	1990	1975
4.25-4.45	1980	1980	2005	1985	1975	1980	1975	2000	1980	2000	1990	1990	1980	1980	1980	1995	1975
4.50-4.70	2005	2000	1980	1960	1975	1985	1975	1990	1975	1985	1995	2005	2005	1995	2005	1985	1975
4.75-4.95	2005	1990	2005	1970	1985	1980	1985	1980	1975	2000	2005	2005	1985	2005	2005	2005	1980
5.00-5.20	1960	2000	2005	1980	1970	1980	1975	1990	1975	2005	2000	2000	1965	1990	1965	2005	2005
5.25-5.45	1965	1955	1960	2000	2005		1970	1995	2000			2000	1960	2005	1970	1960	1965
5.50-5.70	1960	1930		2000	2005		1965	1995	1980	1985		2005	1990	2000	1960	1960	1965
5.75-5.95	2005	2000	1985	1930	1980	1930	1925		1985	1980		1990	1945	1980	1960		1990
6.00-6.20	1925	2005	1995	1985	1955	2000	1930		1930			2005	1950	1925	1930		1975
6.25-6.45	2000	1990			2005				2005				2000	2005			1970
6.50-6.70	1935	1925		1985	1950		1912	1935	1925		1935	2000	2000	1912	1930		1920
6.75-6.95		1960	1990	1912	1995								1980	1940			
7.00-7.20	1935	1955		1975	1940							2000	1912				
7.25-7.45		1950	1930		1920								2005	1960			
7.50-7.70	2005		1945														
7.75-7.95						1912											
8.50-8.70													2000				
9.00-9.25																	

3.6 The Constants of Gutenburg-Richter Equation

The Gutenberg-Richter magnitude-frequency relation is determined for each source zone according to the following expression. (Gutenberg and Richter, 1954)

$$\log \lambda_m = a - bm \tag{3-27}$$

where λ_m is an average annual rate of exceedance of a magnitude m, a and b are parameters representing seismicity of a source zone. The a and b values of the Gutenberg-Richter equation are determined as shown in Figures 3-15 to 3-31. The result can be summarized in Table 3-3 which indicates a and b values of the Gutenberg-Richter relation and the maximum moment magnitude of each source zone based on the study by Fenton et al. (2003).

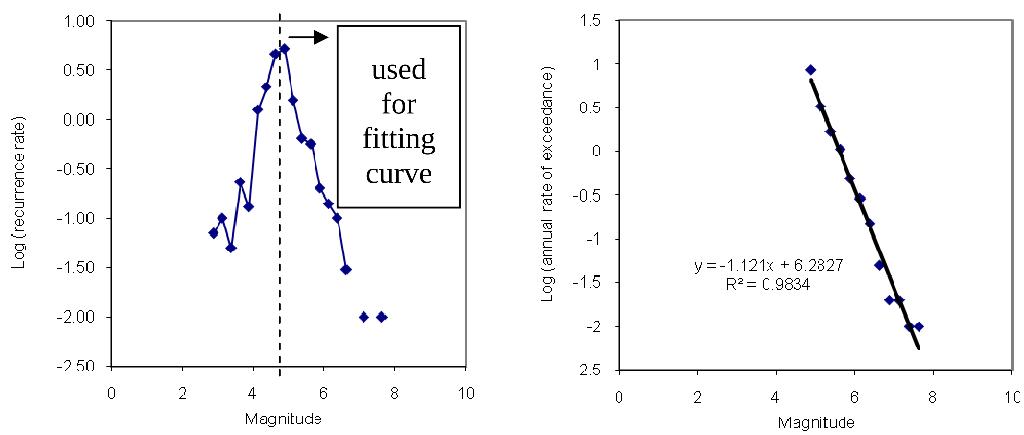

(a) (b)

Figure 3-15 Determining a and b values of Gutenberg-Richter equation for zone A

(a) Logarithm of recurrence rate of earthquake magnitudes

(b) Logarithm of annual rate of exceedance of earthquake magnitudes

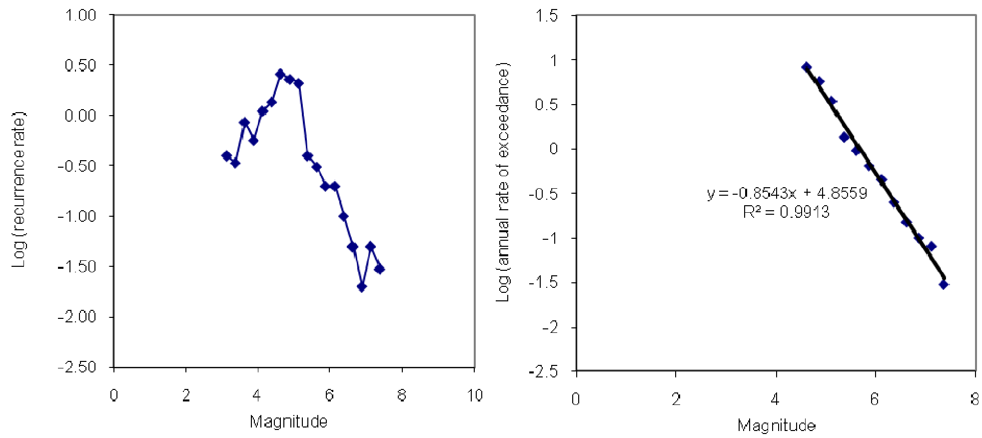

(a) (b)

Figure 3-16 Determining a and b values of Gutenberg-Richter equation for zone B

(a) Logarithm of recurrence rate of earthquake magnitudes

(b) Logarithm of annual rate of exceedance of earthquake magnitudes

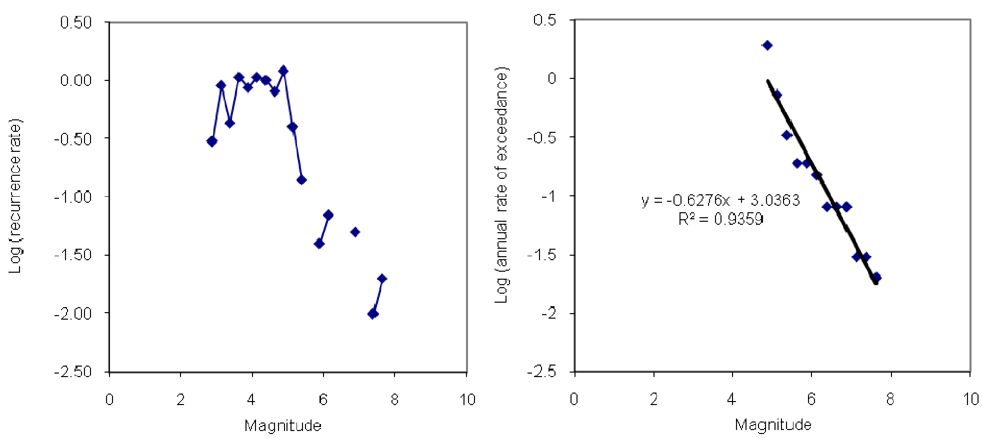

(a) (b)

Figure 3-17 Determining a and b values of Gutenberg-Richter equation for zone C

(a) Logarithm of recurrence rate of earthquake magnitudes

(b) Logarithm of annual rate of exceedance of earthquake magnitudes

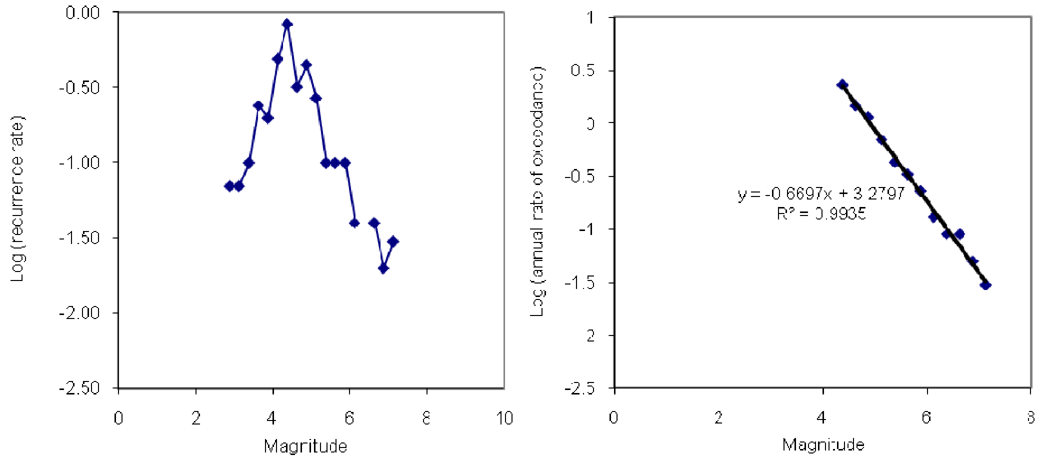

(a) (b)

Figure 3-18 Determining a and b values of Gutenberg-Richter equation for zone D

(a) Logarithm of recurrence rate of earthquake magnitudes

(b) Logarithm of annual rate of exceedance of earthquake magnitudes

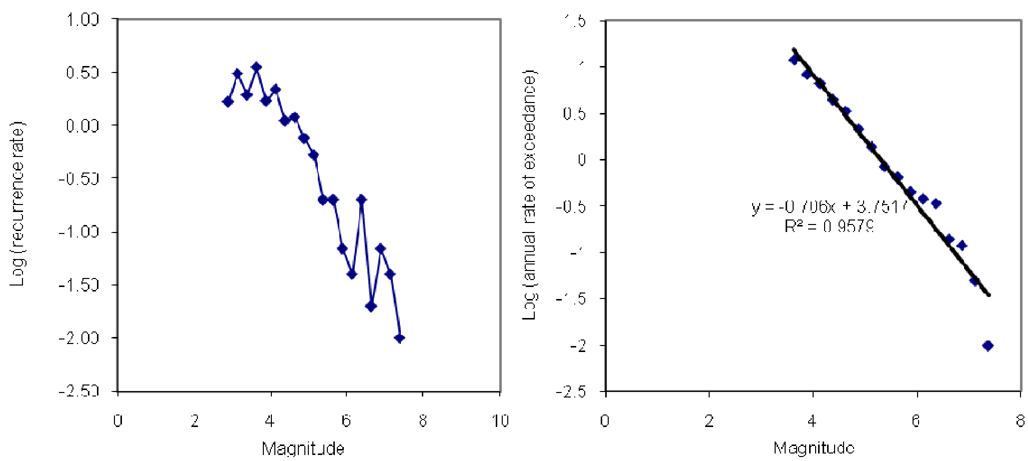

(a) (b)

Figure 3-19 Determining a and b values of Gutenberg-Richter equation for zone E

(a) Logarithm of recurrence rate of earthquake magnitudes

(b) Logarithm of annual rate of exceedance of earthquake magnitudes

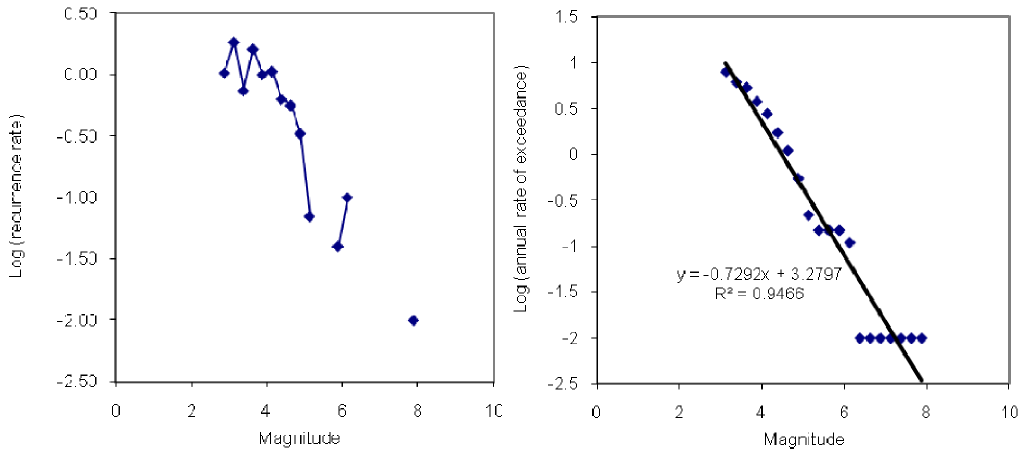

(a) (b)

Figure 3-20 Determining a and b values of Gutenberg-Richter equation for zone F

(a) Logarithm of recurrence rate of earthquake magnitudes

(b) Logarithm of annual rate of exceedance of earthquake magnitudes

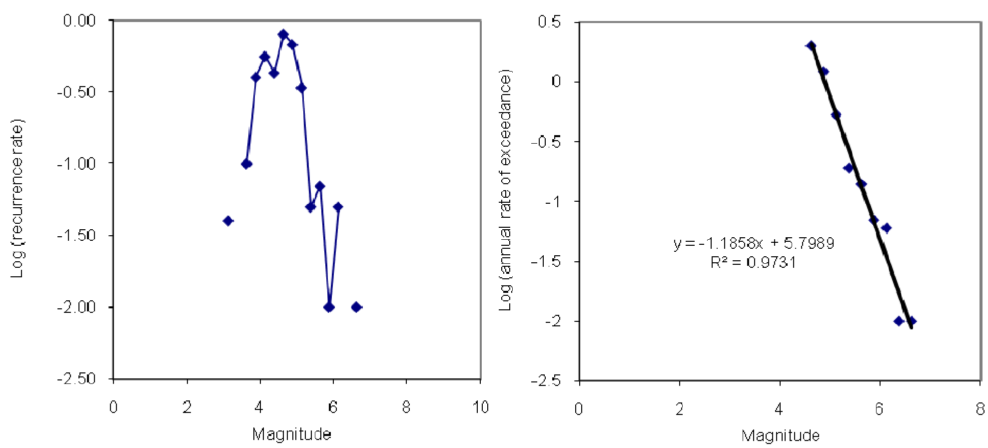

(a) (b)

Figure 3-21 Determining a and b values of Gutenberg-Richter equation for zone G

(a) Logarithm of recurrence rate of earthquake magnitudes

(b) Logarithm of annual rate of exceedance of earthquake magnitudes

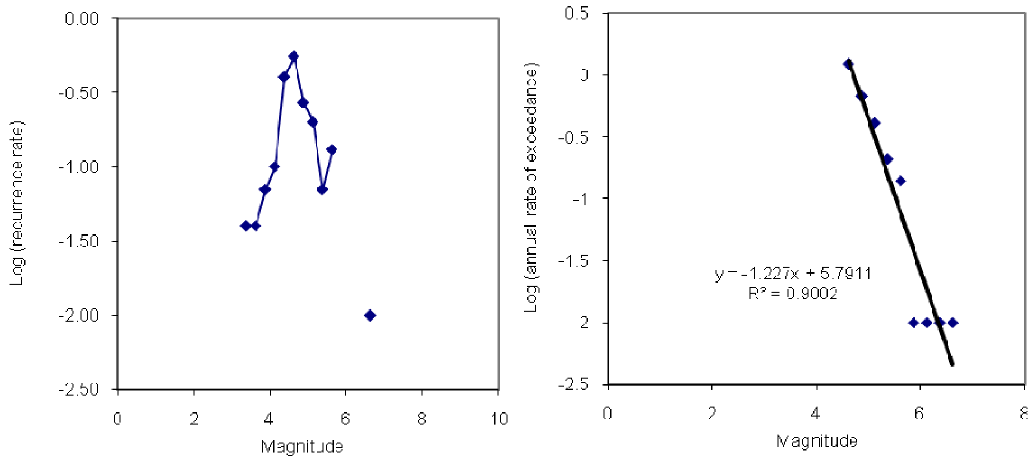

(a) (b)

Figure 3-22 Determining a and b values of Gutenberg-Richter equation for zone H

(a) Logarithm of recurrence rate of earthquake magnitudes

(b) Logarithm of annual rate of exceedance of earthquake magnitudes

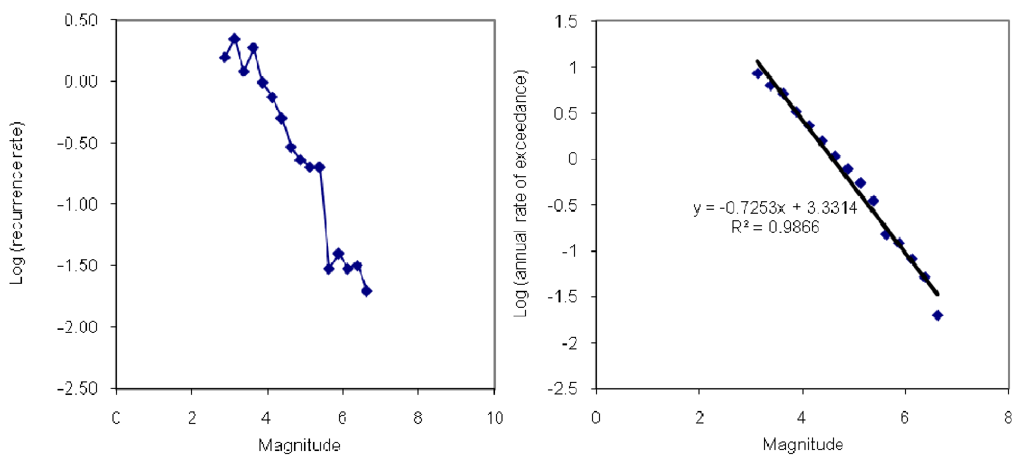

(a) (b)

Figure 3-23 Determining a and b values of Gutenberg-Richter equation for zone I

(a) Logarithm of recurrence rate of earthquake magnitudes

(b) Logarithm of annual rate of exceedance of earthquake magnitudes

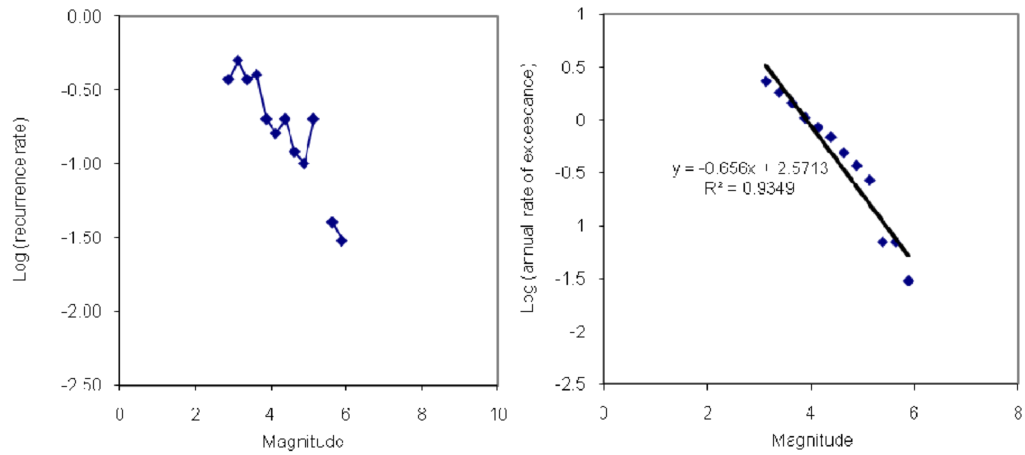

(a) (b)

Figure 3-24 Determining a and b values of Gutenberg-Richter equation for zone J

(a) Logarithm of recurrence rate of earthquake magnitudes

(b) Logarithm of annual rate of exceedance of earthquake magnitudes

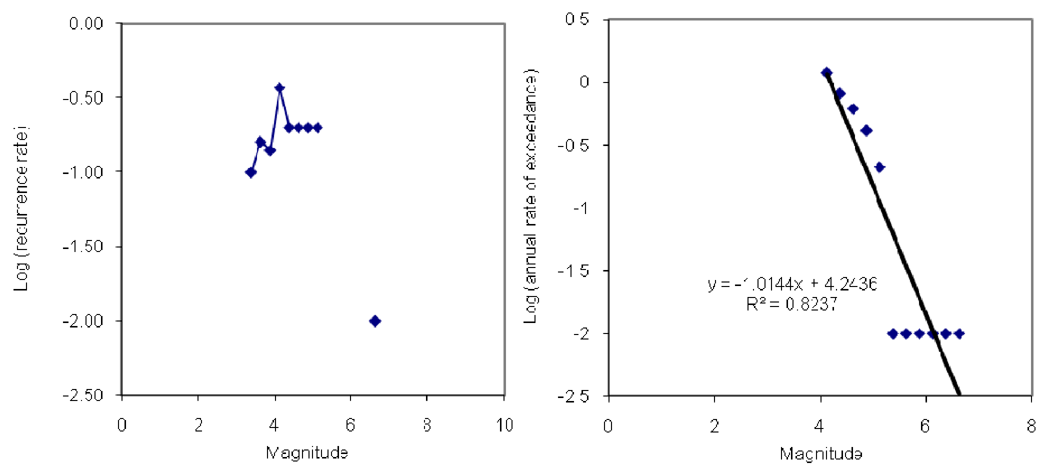

(a) (b)

Figure 3-25 Determining a and b values of Gutenberg-Richter equation for zone M

(a) Logarithm of recurrence rate of earthquake magnitudes

(b) Logarithm of annual rate of exceedance of earthquake magnitudes

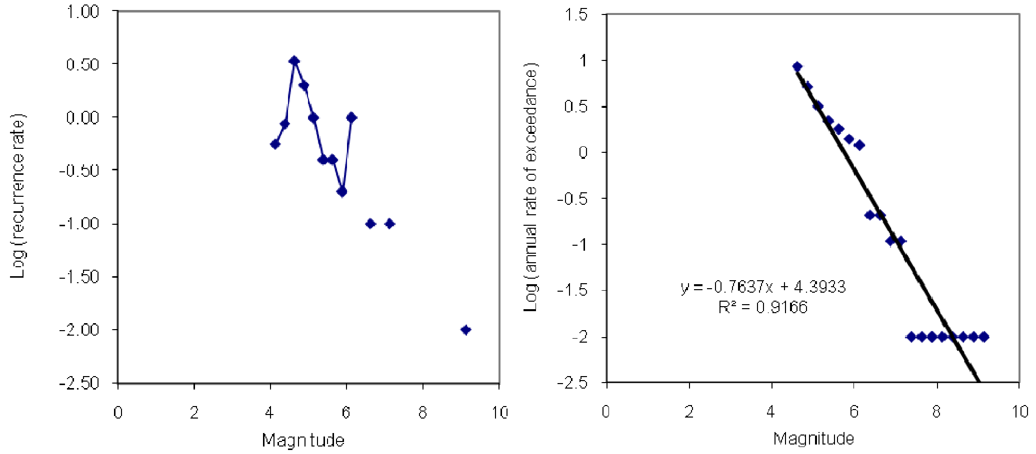

(a) (b)

Figure 3-26 Determining a and b values of Gutenberg-Richter equation for zone N

(a) Logarithm of recurrence rate of earthquake magnitudes

(b) Logarithm of annual rate of exceedance of earthquake magnitudes

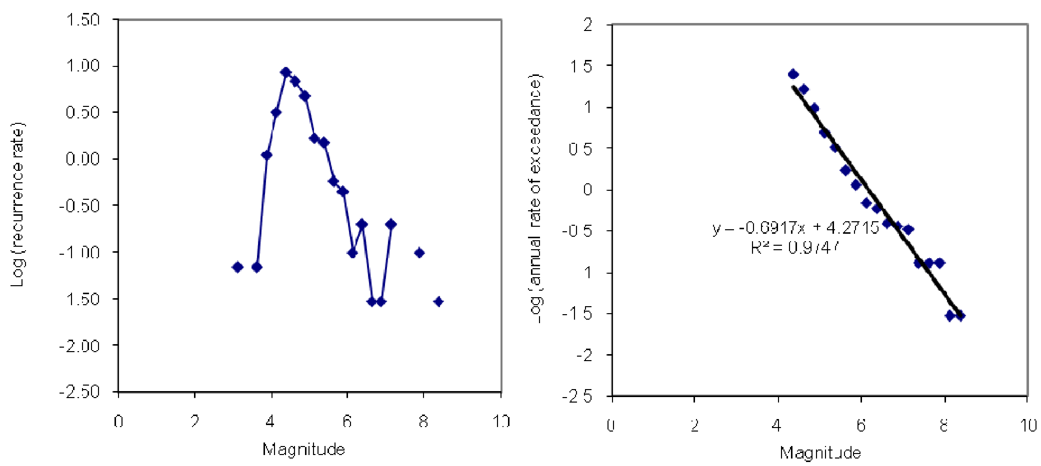

(a) (b)

Figure 3-27 Determining a and b values of Gutenberg-Richter equation for zone O

(a) Logarithm of recurrence rate of earthquake magnitudes

(b) Logarithm of annual rate of exceedance of earthquake magnitudes

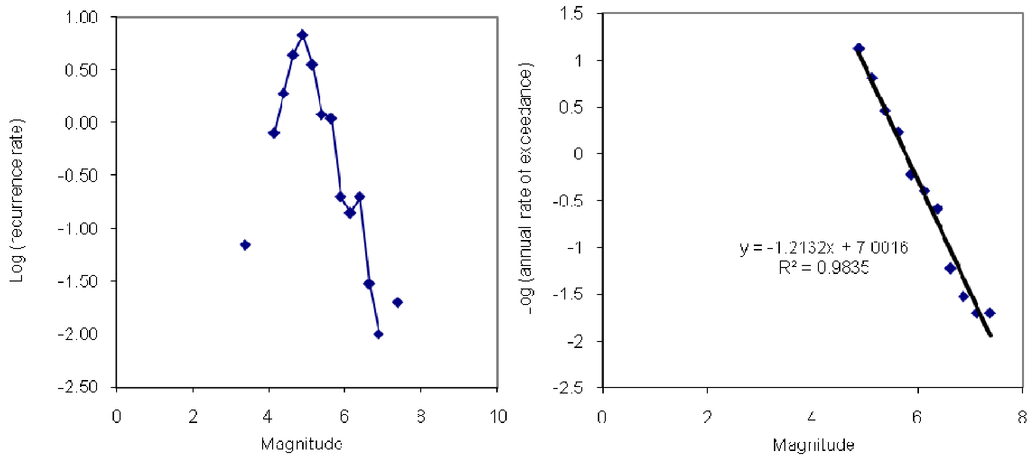

(a) (b)

Figure 3-28 Determining a and b values of Gutenberg-Richter equation for zone P

(a) Logarithm of recurrence rate of earthquake magnitudes

(b) Logarithm of annual rate of exceedance of earthquake magnitudes

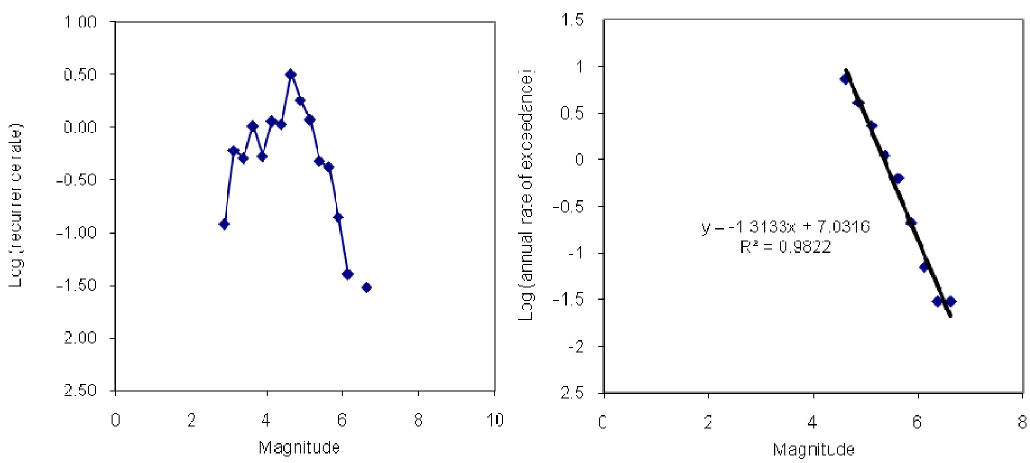

(a) (b)

Figure 3-29 Determining a and b values of Gutenberg-Richter equation for zone Q

(a) Logarithm of recurrence rate of earthquake magnitudes

(b) Logarithm of annual rate of exceedance of earthquake magnitudes

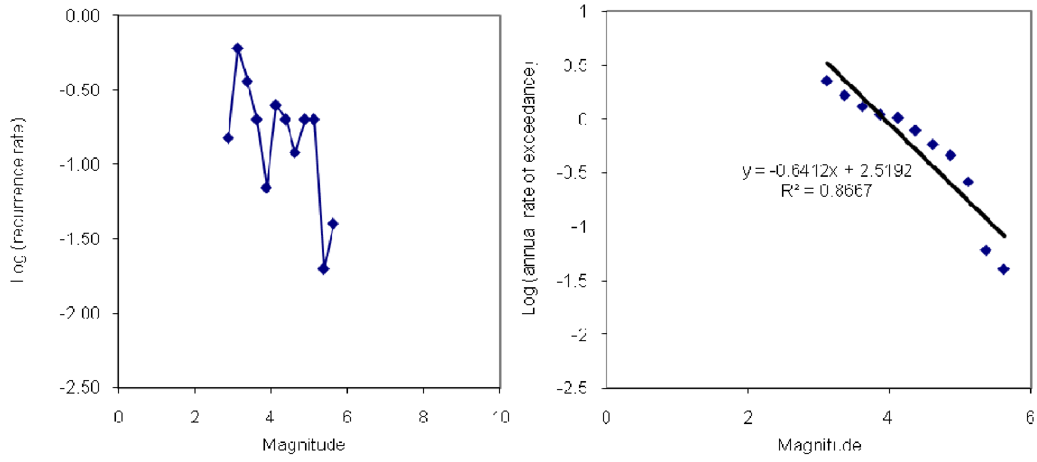

(a) (b)

Figure 3-30 Determining a and b values of Gutenberg-Richter equation for zone R

(a) Logarithm of recurrence rate of earthquake magnitudes

(b) Logarithm of annual rate of exceedance of earthquake magnitudes

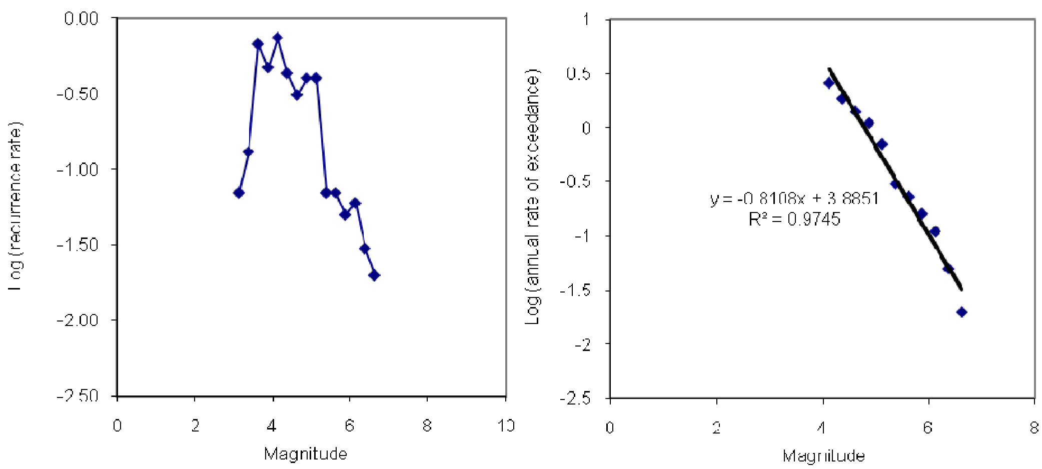

(a) (b)

Figure 3-31 Determining a and b values of Gutenberg-Richter equation for zone W

(a) Logarithm of recurrence rate of earthquake magnitudes

(b) Logarithm of annual rate of exceedance of earthquake magnitudes

Table 3-3 Source zones and parameters of seismicity in Thailand and neighboring areas.

Source Zones	No. of Events (1912-2009)	Parameters of Gutenberg-Richter Equation		Maximum Magnitude from Catalog
		a	b	
Zone A	473	6.283	1.121	7.5
Zone B	438	4.856	0.854	7.4
Zone C	262	3.036	0.628	7.7
Zone D	103	3.280	0.670	7.0
Zone E	827	3.752	0.706	7.3 (7.5)
Zone F	396	3.280	0.729	7.9
Zone G	110	5.799	1.186	6.5
Zone H	42	5.791	1.227	6.7
Zone I	783	3.331	0.725	6.7 (7.5)
Zone J	102	2.571	0.656	5.8 (7.5)
Zone M	34	4.244	1.014	6.7
Zone N	141	4.393	0.764	9.0
Zone O	948	4.272	0.692	8.7
Zone P	459	7.002	1.213	7.4
Zone Q	373	7.032	1.313	6.5
Zone R	49	2.519	0.641	5.7
Zone W	124	3.885	0.811	6.7

Remarks the value in the parenthesis is the moment magnitude from the study by Fenton et al. (2003).

3.7 Attenuation Models

Attenuation models for predicting peak horizontal accelerations from earthquake magnitudes and distances are crucial in the hazard analysis. The site condition of attenuation models used in the analysis is a rock site. Hence, the peak horizontal acceleration presented in the hazard map is for rock sites. A local site effect may need to be taken into account by soil response analysis in vulnerable areas.

Thailand has been affected by subduction earthquakes along the Sumatra subduction zone. Most of attenuation models for subduction zones were developed at the distance within a few hundred kilometers from epicenters. Petersen et al. (2004) modified the attenuation relationship originally proposed by Youngs et al. (1997) for the distance larger than 200 km by fitting the equation with accelerations measured at the distance larger than 200 km.. The proposed attenuation model is expressed as

$$\begin{aligned} \ln Y &= 0.2418 + 1.414M + C_1 + C_2(10-M)^3 + C_3 \ln(R_{rup} + 1.7818\exp(0.554M)) \\ &+ 0.00607H + 0.3846Z_r \qquad \text{Standard Deviation} = C_4 - C_5\, M \end{aligned} \tag{3-28}$$

$$\ln Y_{Modified}(M,R_{rup}) = \ln Y_{Youngs}(M,R_{rup}) - 0.0038(R_{rup} - 200) \tag{3-29}$$

where Y is the median spectral acceleration for 5% damping (g), or a peak horizontal acceleration (g), M is a moment magnitude, R_{rup} is the closest distance to the rupture plane (km), H is the depth of earthquake source (km), $Z_{\mathrm{r}} = 0$ for a crustal interplate region, $Z_{\mathrm{r}} = 1$ for a crustal intraplate region; and C_1, C_2, C_3, C_4, and C_5 are constants of the relationship. The original relationship by Youngs et al. (1997) is used for the distance less than 200 km and the modified relationship is used for the distance over 200 km. The attenuation model is used for earthquakes occurring in Zones A, N, and O.

Chintanapakdee et al. (2008) investigated suitability of various attenuation models in predicting peak horizontal accelerations in Thailand. The attenuation models by Sadigh et al. (1997) and Idriss (1993) gave predicted accelerations close to the observed data. Hence, the attenuation models by Sadigh et al. (1997) and Idriss (1993) are weighed equally and used for zones outside the subduction zones (Zones A, N, and O). The attenuation models by Sadigh et al. (1997) and Idriss (1993) are formulated in Eq. (3-30) and Eq. (3-31), respectively.

$$\begin{gathered}\ln Y = K_1 + K_2 M + K_3 (8.5 - M)^{2.5} + K_4 \ln[R_{rup} + \exp(K_5 + K_6 M)] + K_7 \ln(R_{rup} + 2) \\ \text{Standard Deviation} = 1.39\text{-}0.14\ M\end{gathered} \tag{3-30}$$

$$\begin{gathered}\ln Y = [\alpha_0 + \exp(\alpha_1 + \alpha_2 M)] - [\beta_0 + (\beta_1 + \beta_2 M)]\ln(R_{rup} + 20) + \varphi F \\ \text{Standard Deviation} = 1.39 - 0.14M\end{gathered} \tag{3-31}$$

where K_1, K_2, K_3, K_4, K_5, K_6, K_7, α_0, α_1, α_2, β_0, β_1, β_2, and φ are constants of the relationship, $F = 0$ for strike slip faults, $F = 0.5$ for oblique faults, and $F = 1$ for reverse faults.

3.8 Sample of Calculation

The probabilistic seismic hazard analysis developed by Cornel (1968) and Algermissen et al. (1982) needs to consider probabilities of 3 principal parameters which are the probability of distance from seismic source zones to site [P(R)], the probability of recurrence rate of earthquake magnitudes [P(M)] and the probability of peak horizontal acceleration from attenuation model [P(PHA|M,R)]. Hereafter, the peak horizontal acceleration at the latitude 13.85°N and longitude 100.57°E which locates in Bangkok is calculated as following.

3.8.1 Probability of distance from seismic source zones to site

The probabilities of distances can be calculated from the method in Figure 3-5 and equations (3-1) to (3-5). The probability density functions (PDF) from this calculation of all source zones are shown in Figure 3-32.

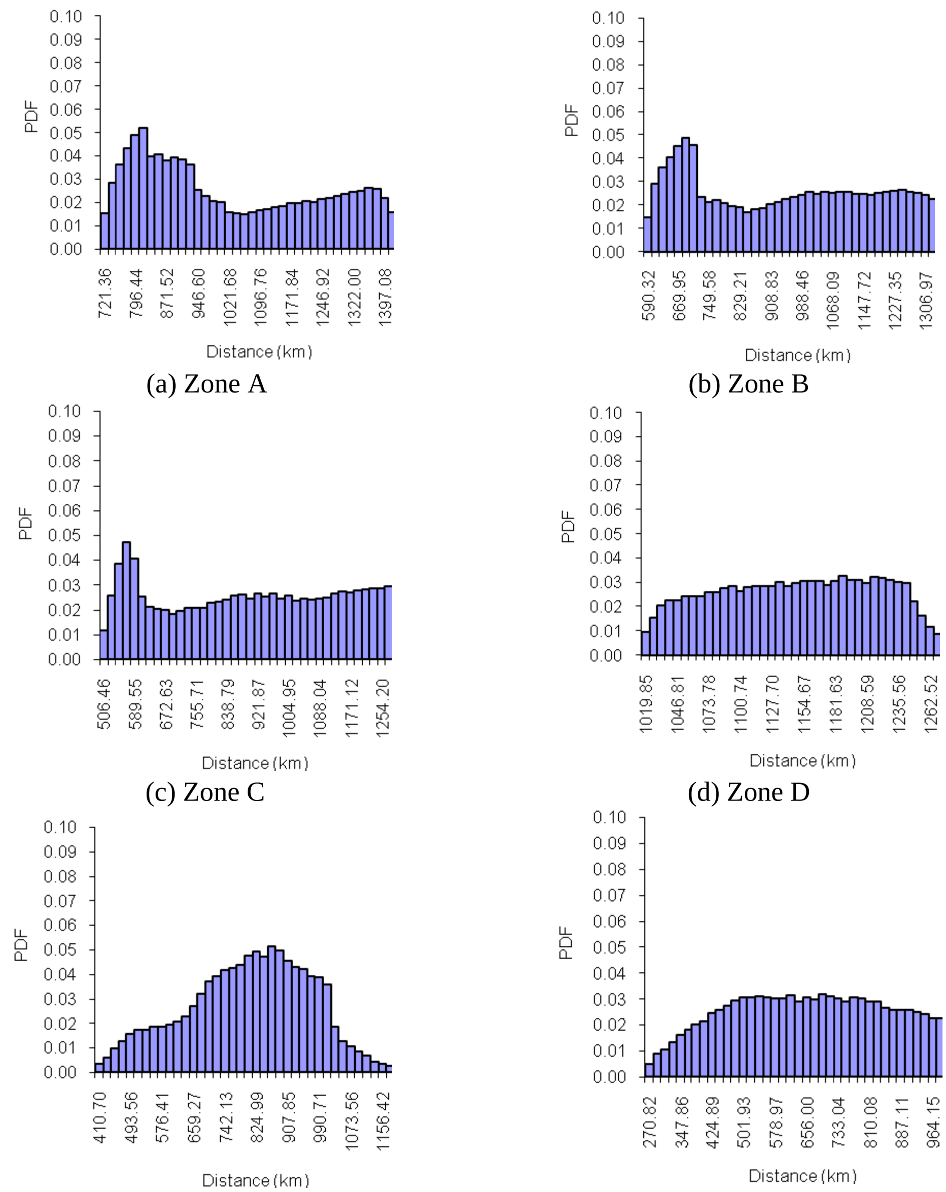

(a) Zone A (b) Zone B

(c) Zone C (d) Zone D

(e) Zone E (f) Zone F

Figure 3-32 (1) Probability density functions of distance from seismic source zones to site at the latitude 13.85°N and longitude 100.57°E

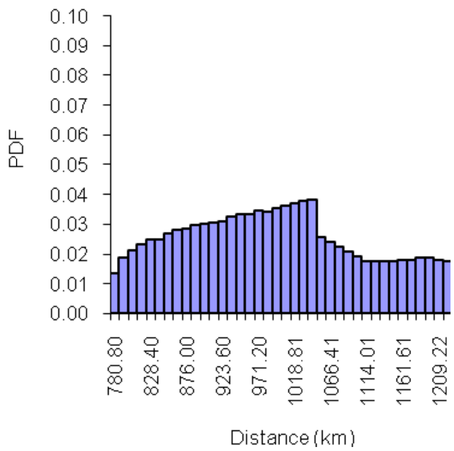

(g) Zone G

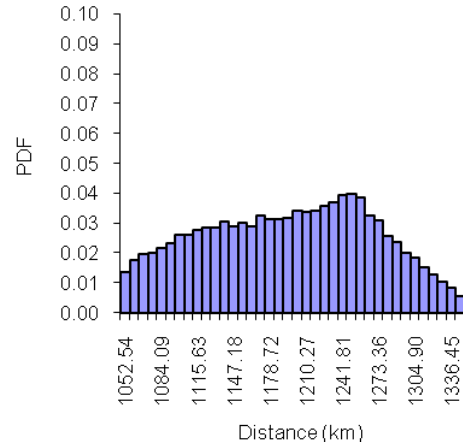

(h) Zone H

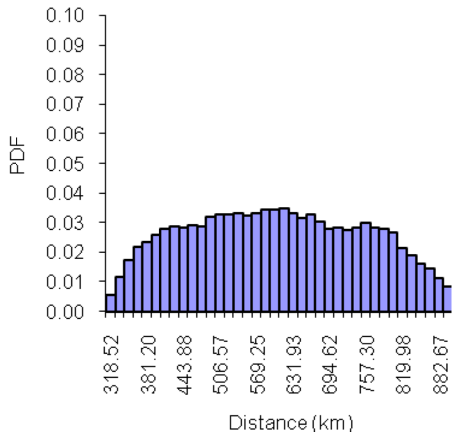

(i) Zone I

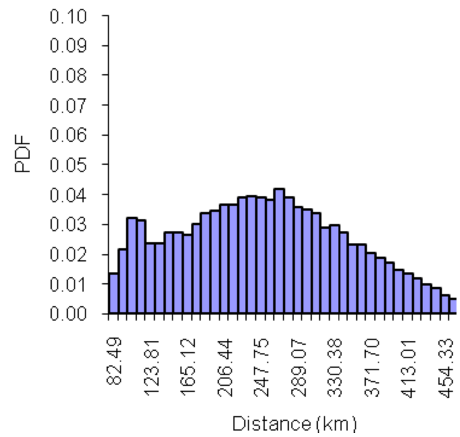

(j) Zone J

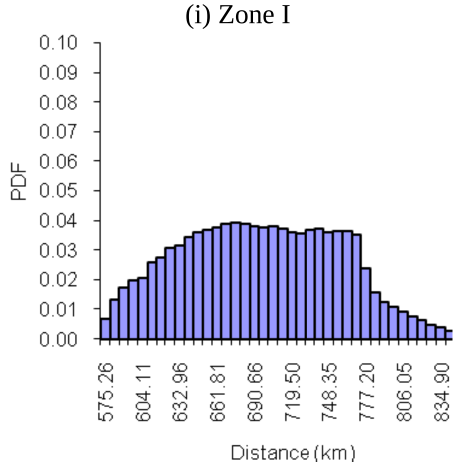

(k) Zone M

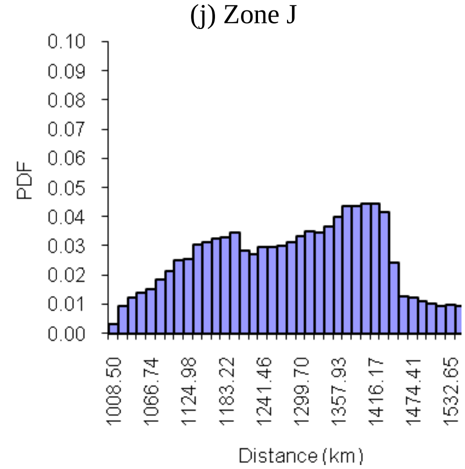

(l) Zone N

Figure 3-32(2) Probability density functions of distance from seismic source zones to site at the latitude 13.85°N and longitude 100.57°E

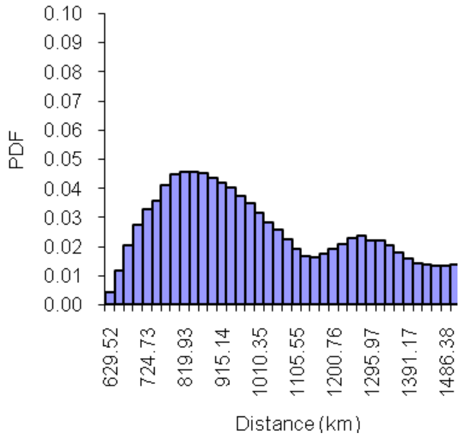

(m) Zone O

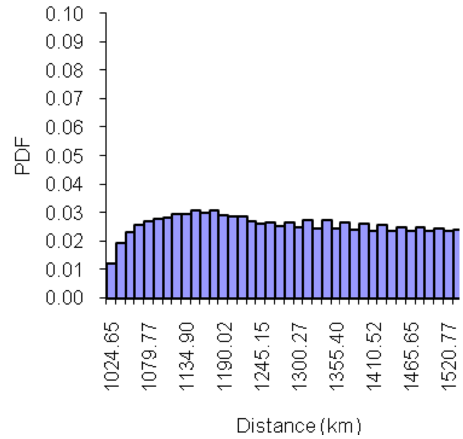

(n) Zone P

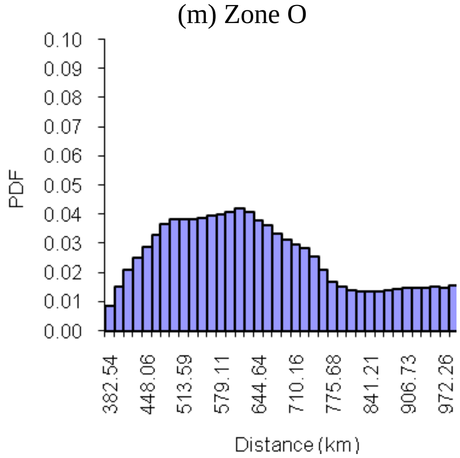

(o) Zone Q

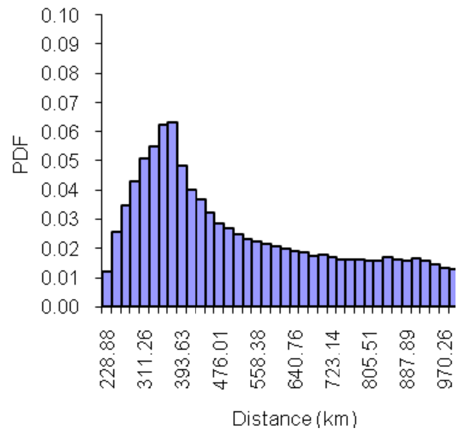

(p) Zone R

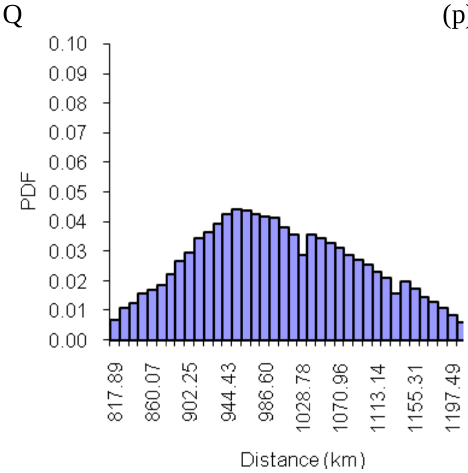

(q) Zone W

Figure 3-32(3) Probability density functions of distance from seismic source zones to site at the latitude 13.85°N and longitude 100.57°E

3.8.2 Probability of recurrence rate of earthquake magnitude

The magnitude of earthquakes depends on the characteristic of seismic source zone which is the a and b values of the Gutenburg-Richter equation. The probability density function of recurrence rate of earthquake magnitude can be determined from the equation 3-15. The results are shown in Figure 3-33.

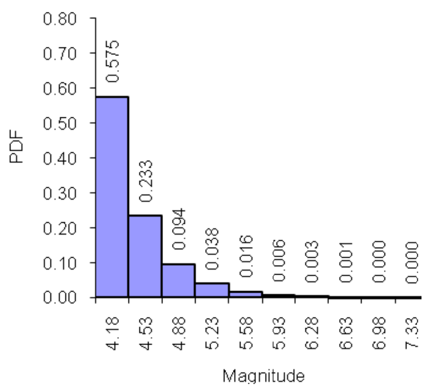

(a) Zone A

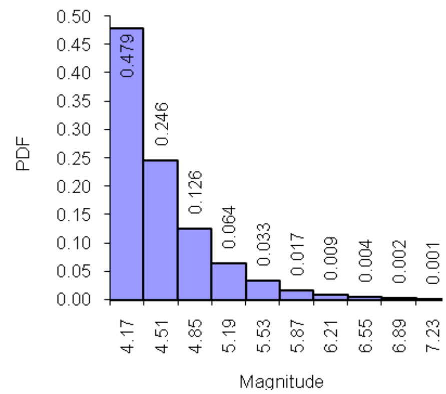

(b) Zone B

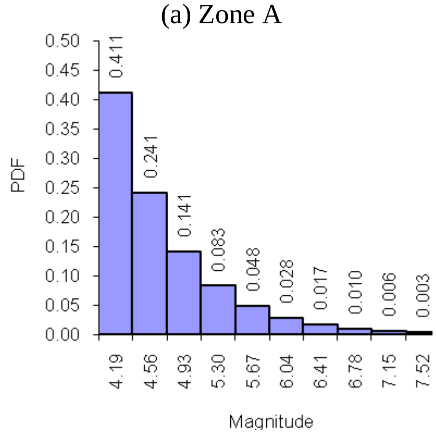

(c) Zone C

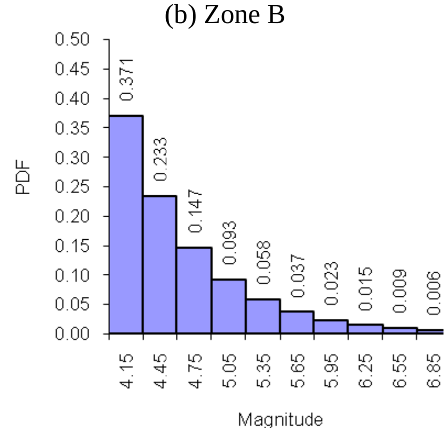

(d) Zone D

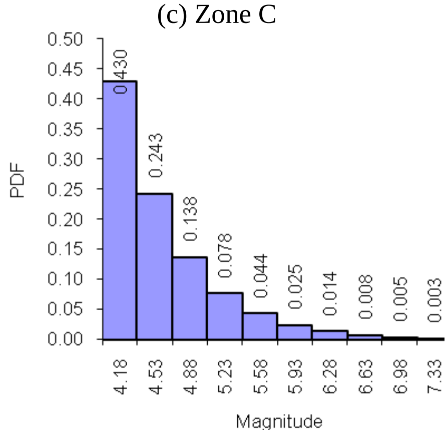

(e) Zone E

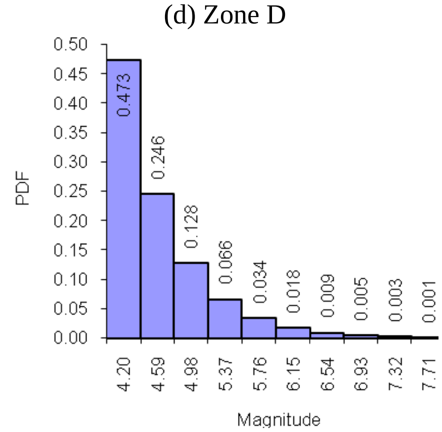

(f) Zone F

Figure 3-33 (1) Probability density functions of recurrence rate of earthquake magnitude

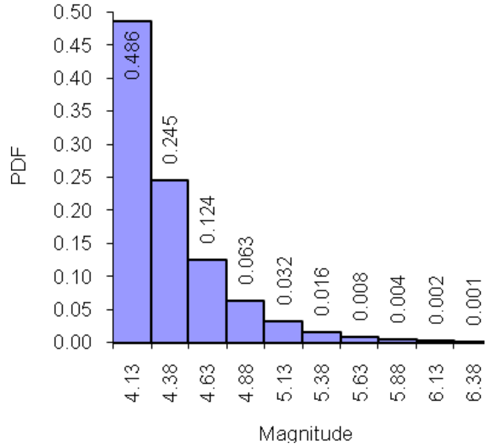

(g) Zone G

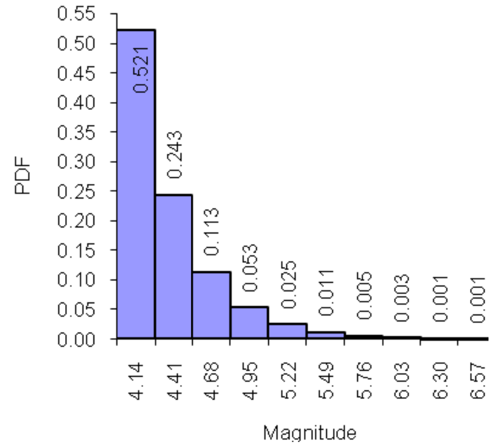

(h) Zone H

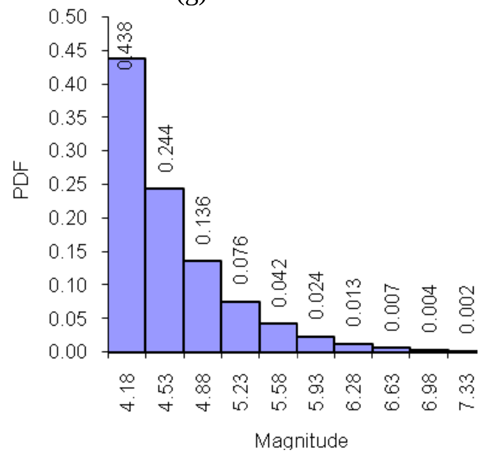

(i) Zone I

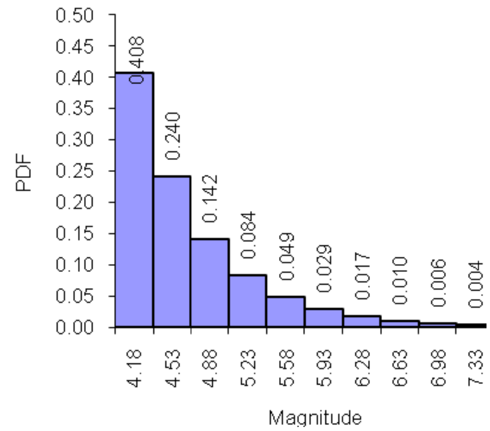

(j) Zone J

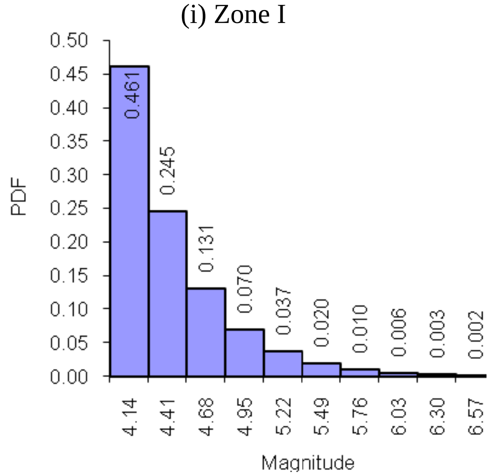

(k) Zone M

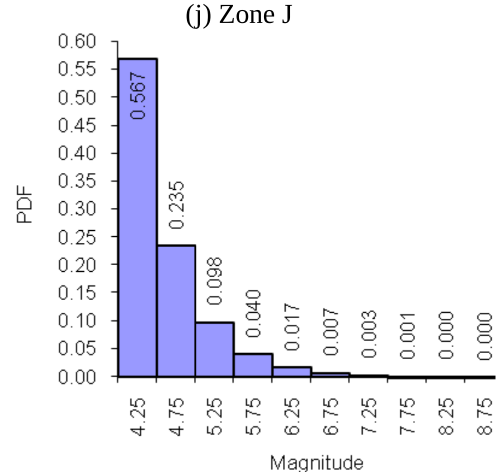

(l) Zone N

Figure 3-33(2) Probability density functions of recurrence rate of earthquake magnitude

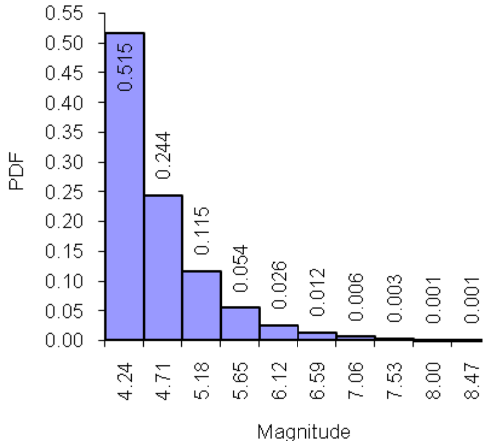

(m) Zone O

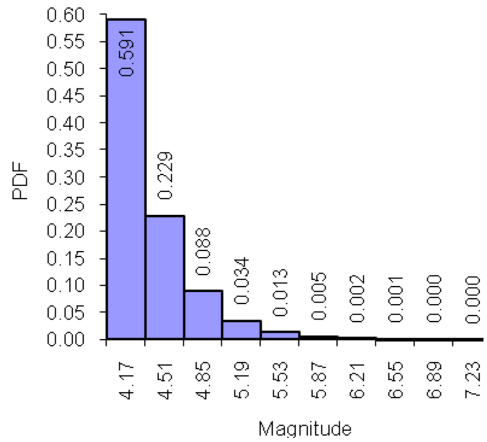

(n) Zone P

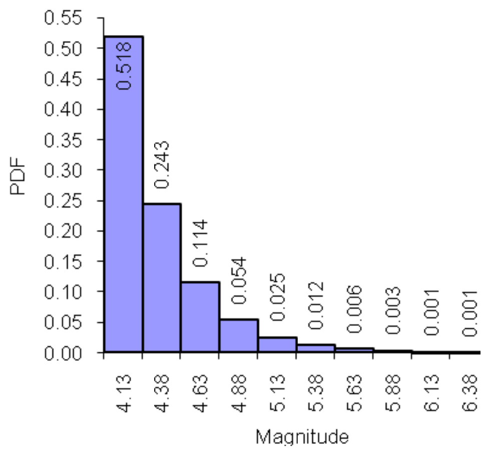

(o) Zone Q

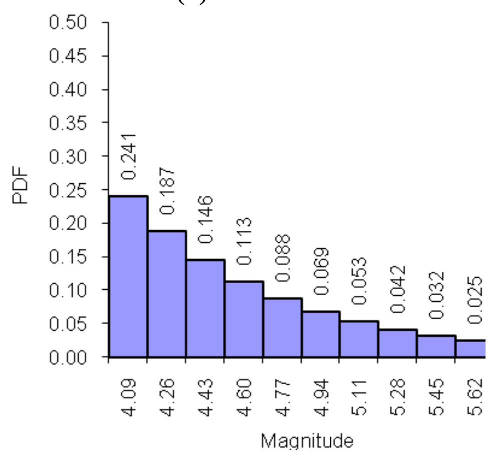

(p) Zone R

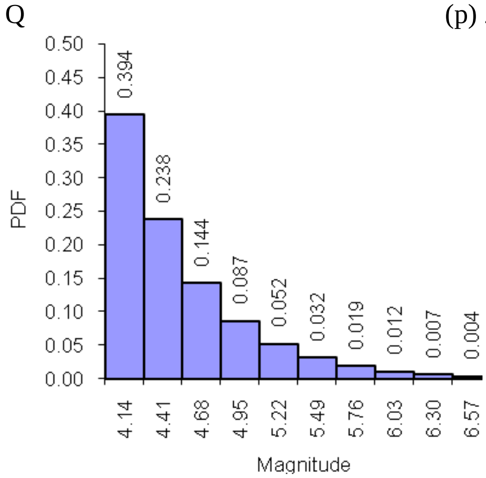

(q) Zone W

Figure 3-33(3) Probability density functions of recurrence rate of earthquake magnitude

3.8.3 Probability of peak horizontal acceleration

The probability of peak horizontal acceleration can be determined from the normal distribution of attenuation relationship which gives the standard deviation equation for each model. In this study, the distances from a source zone to a site are separated in 40 ranges of distances (n = 40). So, the results from Section 3.8.1 are 40 values of the probabilities of distances ($P(R_1)$, $P(R_2)$, $P(R_3)$, …, $P(R_n)$). The magnitudes of earthquakes in each source zone are separated in 10 ranges of magnitudes (m = 10). So, the results from Section 3.8.2 give 10 values of the probabilities of magnitudes ($P(M_1)$, $P(M_2)$, $P(M_3)$, …, $P(M_m)$). Therefore, the probability of peak horizontal acceleration can be calculated from n × m ordered pairs of distances (R_1, R_2, R_3,…, R_n) and earthquake magnitudes (M_1, M_2, M_3,…, M_m) which is equal to 400 data for a source zone. The peak horizontal accelerations are divided into 200 values from PHA = 0.005g to 1.995g. The examples of calculation are displayed as following.

For Zone A locates in subduction zone. The attenuation model of Youngs et al. (1997) is applied to determine the peak horizontal acceleration.

At the distance between 711.97 to 730.74 km and the earthquake magnitude between 4.00 to 4.32 → ln PHA = -3.626

The probability of horizontal acceleration for PHA≥0.005g by the normal distribution method is P_A [PHA ≥ 0.005g | 4.00≤M<4.32, 711.97≤R<730.74 km] = 2.181×10^{-7}

For Zone B locates in active tectonic region. The attenuation model of Sadigh et al. (1997) is applied to determine the peak horizontal acceleration.

At the distance between 580.37 to 600.27 km and the earthquake magnitude between 4.00 to 4.34 → ln PHA = -3.002

The probability of horizontal acceleration for PHA≥0.005g by the normal distribution method is P_B [PHA ≥ 0.005g |4.00≤M<4.34, 580.37≤R<600.27 km] = 6.14×10^{-9}

3.8.4 Combination of the probabilities

For Zone A The probability of exceedance of peak horizontal acceleration 0.005g for the distance between 711.97 to 730.74 km and the earthquake magnitude between 4.00 to 4.32 is

$\lambda_{A0.005g} = \upsilon_A * P_A$ [PHA $\geq$ 0.005g |4.00$\leq$M<4.32, 711.97$\leq$R<730.74 km] * P_A [711.97$\leq$R<730.74 km] * P_A [4.00$\leq$M<4.32]

$= (56.754)\ (2.181 \times 10^{-7})\ (1.536 \times 10^{-2})\ (0.575) = 1.093 \times 10^{-7}$ times/year

The annual rate of exceedance of peak horizontal acceleration 0.005g in zone A is

$\sum \lambda_{0.005g(zoneA)} = \upsilon_A * \{P_A$ [PHA $\geq$ 0.005g $|M_1, R_1$] * P_A [R_1] * P_A [M_1] + P_A [PHA $\geq$ 0.005g $|M_1, R_2$] * P_A [R_2] * P_A [M_1] + P_A [PHA $\geq$ 0.005g $|M_1, R_3$] * P_A [R_3] * P_A [M_1] + … + P_A [PHA $\geq$ 0.005g $|M_{10}, R_{40}$] * P_A [R_{40}] * P_A [M_{10}]$\}$ = 4.368×10^{-4} times/year

For Zone B The probability of exceedance of peak horizontal acceleration 0.005g for the distance between 580.37 to 600.27 km and the earthquake magnitude between 4.00 to 4.34 is

$\lambda_{B0.005g} = \upsilon_B * P_B$ [PHA $\geq$ 0.005g |4.00$\leq$M<4.34, 580.37$\leq$R<600.27 km] * P_B [580.37$\leq$R<600.27 km] * P_B [4.00$\leq$M<4.34]

$= (27.542)\ (6.14 \times 10^{-9})\ (1.467 \times 10^{-2})\ (0.479) = 1.188 \times 10^{-9}$ times/year

The annual rate of exceedance of peak horizontal acceleration 0.005g in zone B is

$\sum \lambda_{0.005g(zoneB)} = \upsilon_B * \{P_B$ [PHA $\geq$ 0.005g $|M_1, R_1$] * P_B [R_1] * P_B [M_1] + P_B [PHA $\geq$ 0.005g $|M_1, R_2$] * P_B [R_2] * P_B [M_1] + P_B [PHA $\geq$ 0.005g $|M_1, R_3$] * P_B [R_3] * P_B [M_1] + … + P_B [PHA $\geq$ 0.005g $|M_{10}, R_{40}$] * P_B [R_{40}] * P_B [M_{10}]$\}$= 9.741×10^{-8} times/year

The annual rate of exceedance of peak horizontal acceleration 0.005g for all zones is

$$\lambda_{0.005g} = \lambda_{0.005g\ (zoneA)} + \lambda_{0.005g\ (zone\ B)} + \ldots + \lambda_{0.005g\ (zone\ W)} = 0.061 \text{ times/year}$$

which identifies that the return period of the peak horizontal acceleration 0.005g at this site is equal to 1/0.061 = 16.4 years

The results from other peak horizontal accelerations ($\lambda_{0.005g}$, $\lambda_{0.015g}$, $\lambda_{0.025g}$,..., $\lambda_{1.995g}$) can be plotted into the hazard curves which are shown in Figure 3-34.

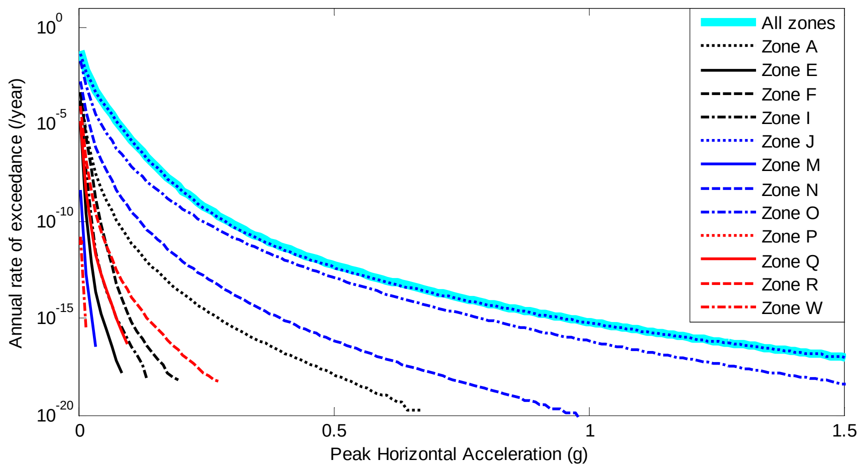

Figure 3-34 Hazard curves at the latitude 13.85°N and longitude 100.57°E

The 10% probability of exceedance in 50 year can be determined from

$$\lambda_y = \frac{\ln(1 - P[10\%])}{T} = \frac{\ln(1 - 0.1)}{50} = 0.00211 \text{ times/year} \qquad (3\text{-}32)$$

The hazard curves are deaggregated to find the contribution of source zones. It is seen that the seismic hazard curve of all zones is close to the hazard curve of Zone J which are displayed in Figure 3-34. For the 10% probability of exceedance in 50 years, the peak horizontal acceleration on bedrock at the latitude 13.85°N and longitude 100.57°E is equal to 0.022g.

For the earthquake resistant design of structures, the design spectra need to be considered at the 10% and 2% probabilities of exceedance in 50 years or the return periods 475 and 2475 years respectively. The response spectra in various periods can be summarized on the Table 3-4 and plotted in Figure 3-35.

Table 3-4 Spectral acceleration at the latitude 13.85°N and longitude 100.57°E

Period (s)	Spectral acceleration (Sa, g)	
	10 % Probability in 50 years (Return period 475 years)	2 % Probability in 50 years (Return period 2475 years)
0 (PGA)	0.022	0.037
0.2	0.054	0.091
0.5	0.044	0.079
1.0	0.028	0.051
2.0	0.015	0.027
3.0	0.009	0.016

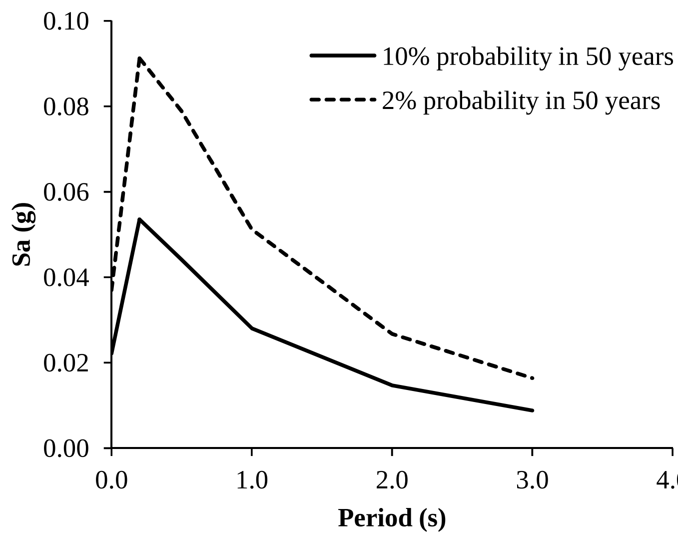

Figure 3-35 Spectral acceleration at the latitude 13.85°N and longitude 100.57°E

The seismic hazard curves which are the relation between the annual rate of exceedance and the peak horizontal acceleration for Chiang Mai (Point A), Kanchanaburi (Point B), and Bangkok (Point C) is presented in Figure 3-36. It is seen that the seismic hazard curve of Point A in northern Thailand is close to the hazard curve of Zone E, while the seismic hazard curves of Point B in western Thailand and Point C in Bangkok are close to the hazard curve of Zone J. It is clear that the seismic hazard in Bangkok is contributed by earthquakes in western Thailand.

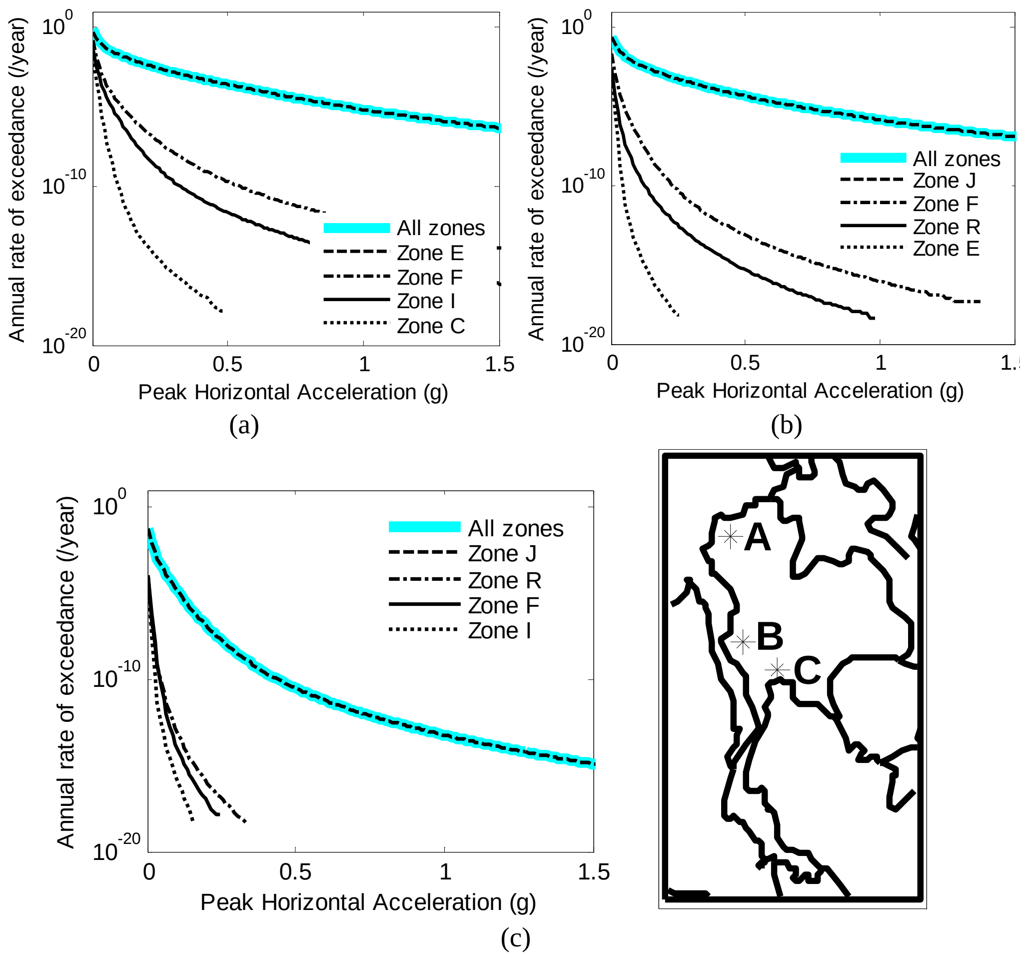

(c)

Figure 3-36 Seismic hazard curves at key locations

(a) Hazard curves at Point A (Chiang Mai)

(b) Hazard curves at Point B (Kanchanaburi)

(c) Hazard curves at Point C (Bangkok)

3.9 Probabilistic Seismic Hazard Maps

The peak horizontal accelerations are computed in the area ranging from 5^{o}N to 22^{o}N and 96^{o}E to 106^{o}E with a grid size of 0.25^{o}. The 2% and 10% probability of exceedance in 50 years are considered in developing probabilistic seismic hazard maps.

3.9.1 Effect of limits on maximum magnitudes

The effects of maximum magnitudes considered in each source zones on seismic hazard maps are investigated. The maximum magnitude is the upper limit set in the magnitude-frequency relation. Referring to Table 3-3, maximum moment magnitudes from the study of active faults by Fenton et al. (2003) for source zones E, I, and J are larger than those from the catalogs. Three cases of hazard maps in the comparison are:

- the hazard map having no limit on maximum magnitudes
- the hazard map using the maximum magnitudes determined from catalogs
- the hazard map using the maximum magnitudes determined from active faults

Figure 3-37 shows the comparison of the hazard maps using the Sadigh et al. (1997) attenuation relationship in the analysis. The peak horizontal acceleration for the analysis with no limit on maximum magnitudes of earthquakes in Figure 3-37(a) are larger than the peak horizontal acceleration for the analysis with maximum magnitudes derived from active faults in Figure 3-37(c). The difference is about 0.01g - 0.04g in northern Thailand and about 0.004g – 0.008g in western Thailand.

The peak horizontal accelerations for the analysis with maximum magnitudes from earthquake catalogs in Figure 3-37(b) are smaller than that the peak horizontal accelerations for the analysis with maximum magnitudes from active faults in Figure 3-37(c) by 0.014g in western Thailand and 0.004g in northern Thailand. It is seen that the effect of maximum magnitudes on seismic hazard is less significant because large earthquakes in Thailand have low probability. The maximum magnitudes based on the study of active faults are used for developing seismic hazard maps in this study.

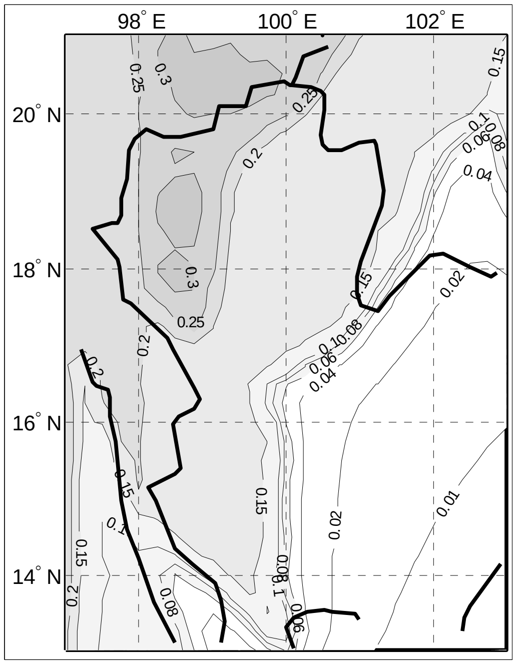

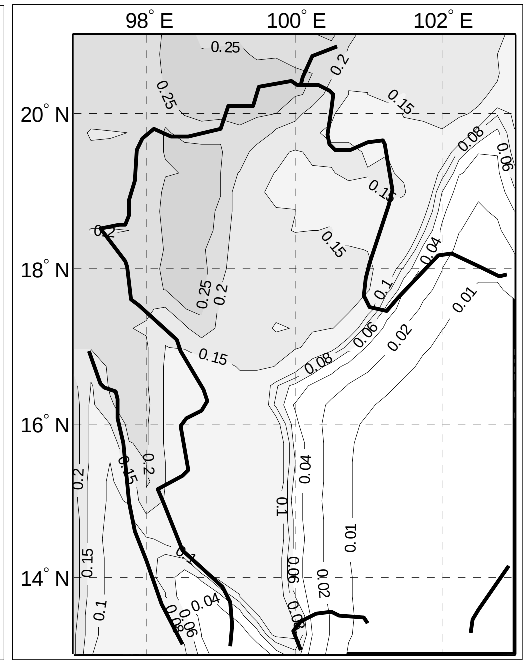

(a) (b)

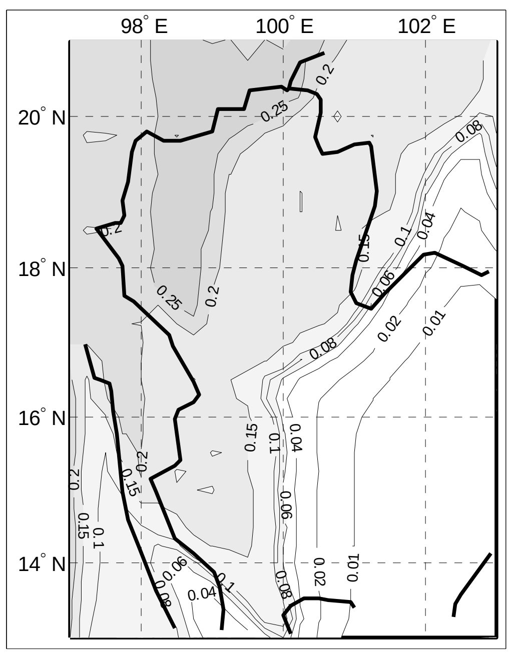

(c)

Figure 3-37 Seismic hazard maps of peak horizontal accelerations (g) considering different limits on maximum magnitudes

(a) No limit on maximum magnitudes

(b) Maximum magnitudes from the earthquake catalog

(c) Maximum magnitudes from study on active faults

3.9.2 Proposed probabilistic seismic hazard maps

The probabilistic seismic hazard maps representing peak horizontal accelerations at rock sites with 10% and 2% probability of exceedance in 50 years are developed. Figures 3-38(a) and 38(b) show the seismic hazard maps with 10% probability of exceedance in 50 years using attenuation models by Sadigh et al. (1997) and Idriss (1993) respectively. As the distance from a source zone with high seismicity increases, peak horizontal accelerations predicted by the Sadigh et al. (1997) model decreases at a higher rate than those predicted by the Idriss (1993) model. Therefore, the peak horizontal accelerations in eastern Thailand in Figure 3-38(a) are less than those in Figure 3-38(b) by about 0.002g – 0.006g.

The attenuation models by Sadigh et al. (1997) and Idriss (1993) are equally weighted to obtain the probabilistic seismic hazard maps as shown in Figure 3-39. For 10% probability of exceedance in 50 years, the maximum peak horizontal acceleration is about 0.25g in northern Thailand, about 0.15g in western Thailand, and about 0.02g in Bangkok. Comparing with the previous study by Warnitchai and Lisantono (1996), it is found that the maximum acceleration in northern Thailand is similar but the peak acceleration proposed in this study is lower by about 40% in western Thailand and about 60% in Bangkok. For the peak horizontal acceleration with 2% probability of exceedance in 50 years, the maximum accelerations are about 0.4 g in the northern part of Thailand and 0.04 g in Bangkok.

The spectral acceleration maps by using Sadigh et al. (1997)'s attenuation model for the periods 0.2s and 1.0s can be displayed in Figures 3-40 and 3.41 respectively. The spectral accelerations at the period of 0.2s are about 0.6g in northern Thailand, 0.3g in western Thailand, and 0.06g in Bangkok. And, the spectral accelerations at the period of 1.0s are about 0.15g in northern Thailand, 0.08g in western Thailand, and 0.03g in Bangkok. For 2% probability of exceedance in 50 years, the peak horizontal accelerations and the spectral accelerations are about 1.6 to 2.0 times the peak horizontal accelerations and spectral accelerations with 10% probability of exceedance in 50 years.

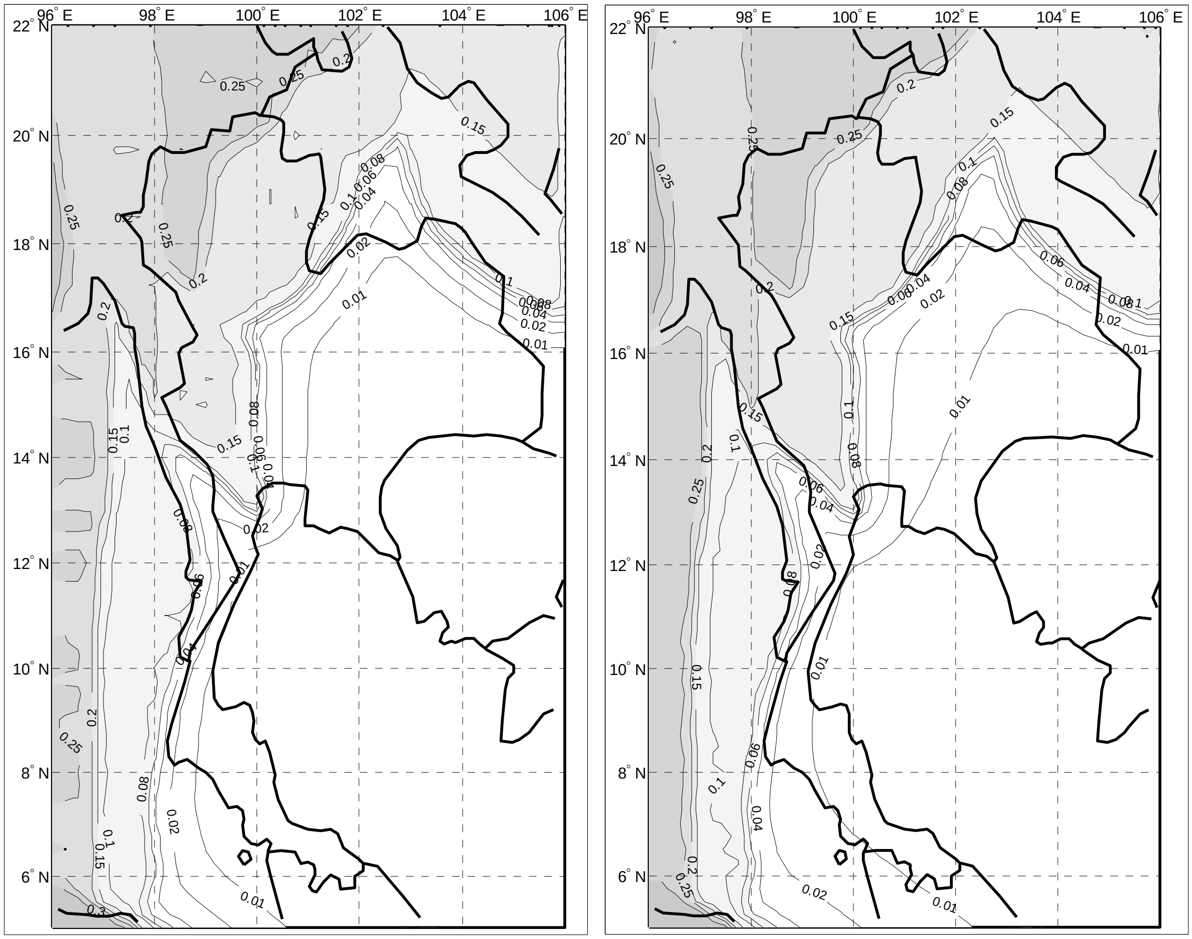

(a) (b)

Figure 3-38 Seismic hazard maps of peak horizontal accelerations with 10% probability of exceedance in 50 years (g)

(a) Using the attenuation model by Sadigh et al. (1997)

(b) Using the attenuation model by Idriss (1993)

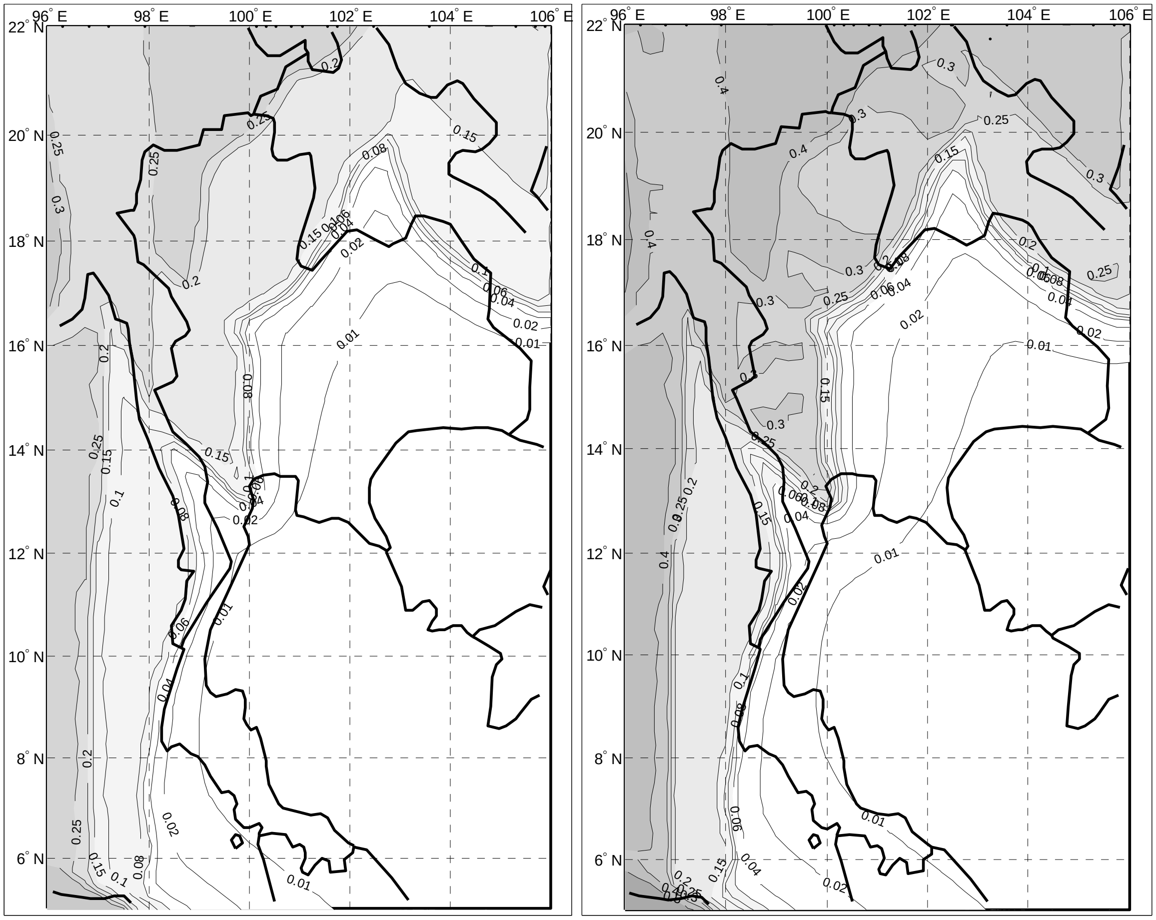

(a) (b)

Figure 3-39 Proposed probabilistic seismic hazard maps showing peak horizontal accelerations (g)

(a) 10% probability of exceedance in 50 years

(b) 2% probability of exceedance in 50 years

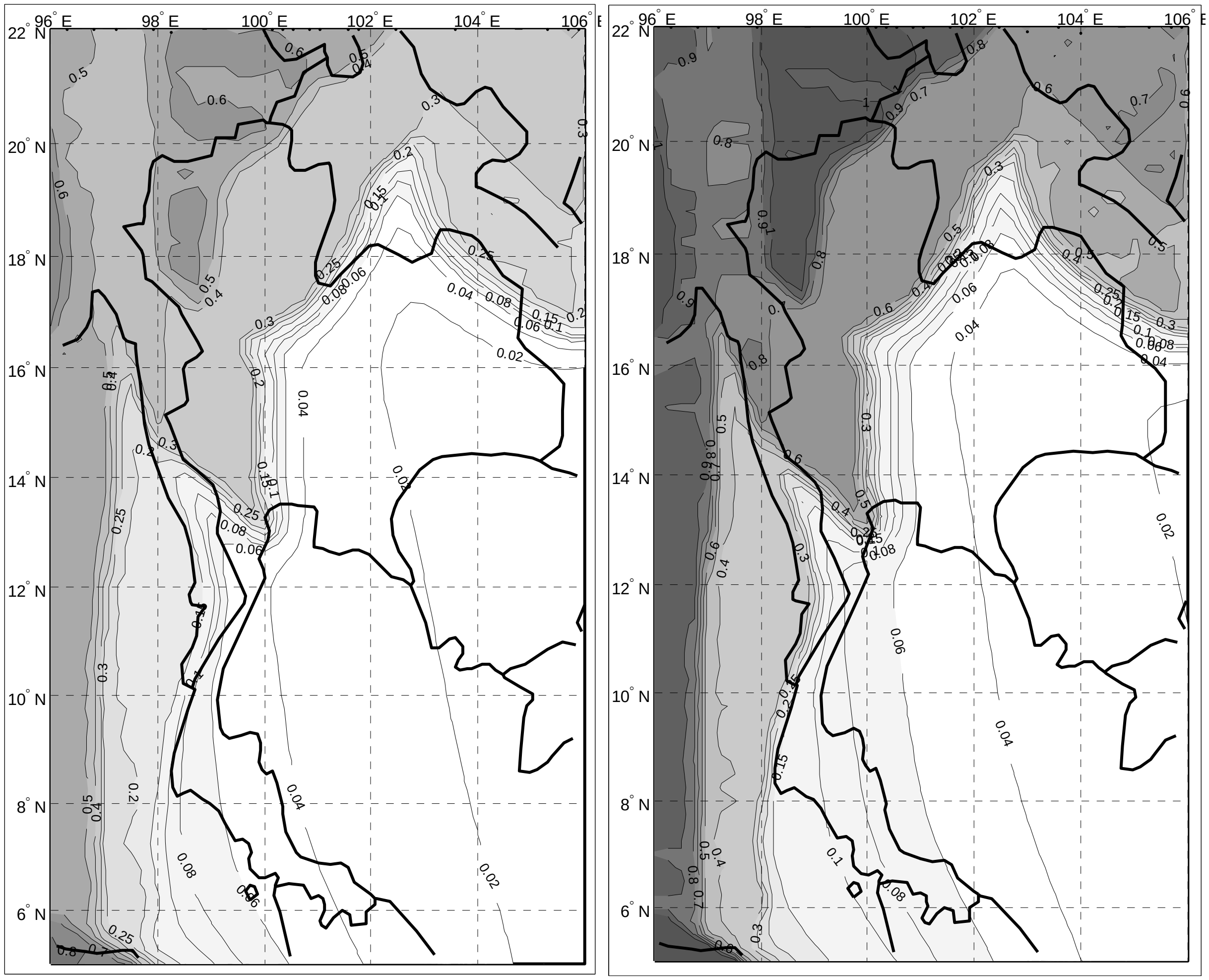

(a) (b)

Figure 3-40 Proposed probabilistic seismic hazard maps showing spectral accelerations (g) at the period 0.2 s

(a) 10% probability of exceedance in 50 years

(b) 2% probability of exceedance in 50 years

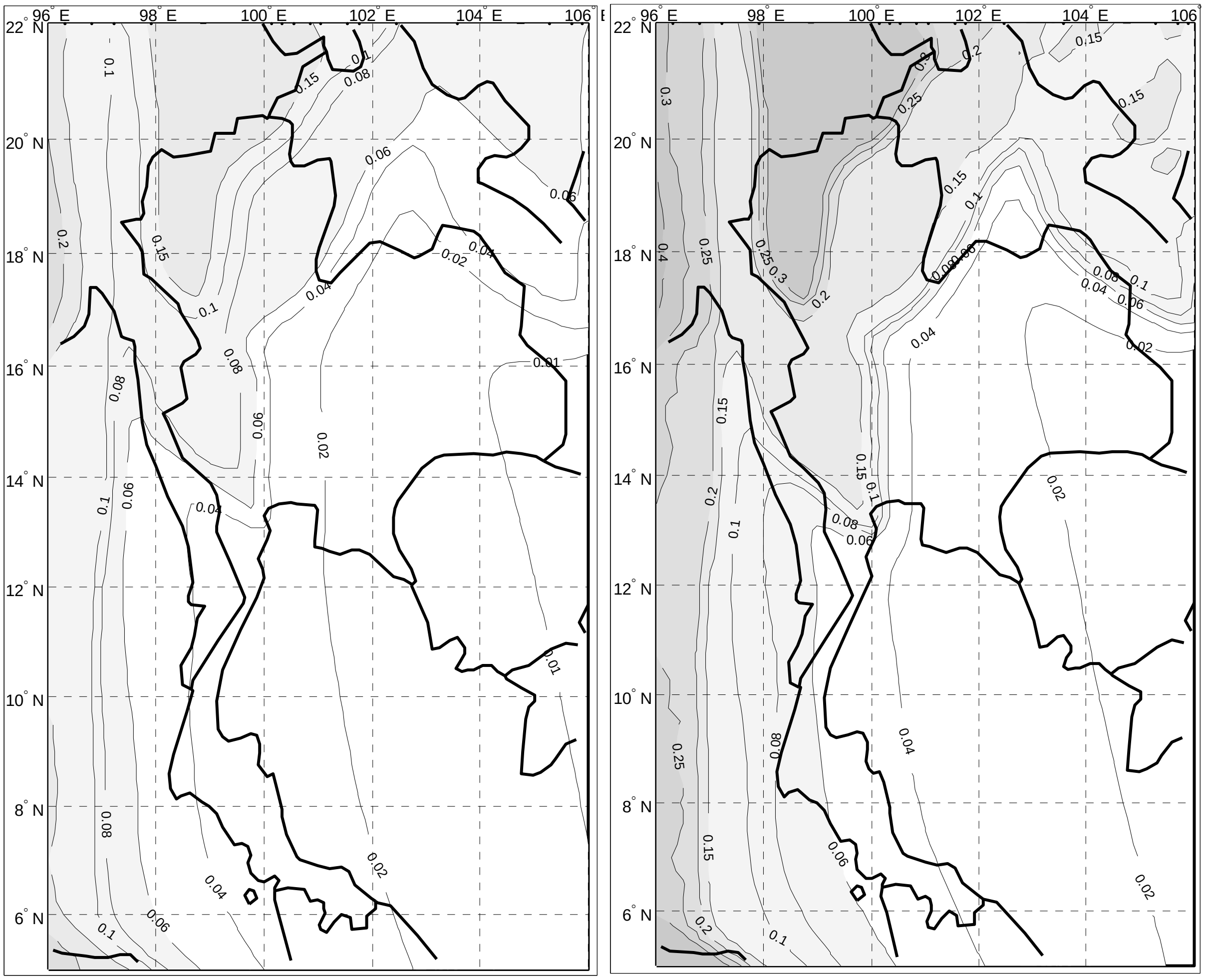

(a) (b)

Figure 3-41 Proposed probabilistic seismic hazard maps showing spectral accelerations (g) at the period 1.0 s

(a) 10% probability of exceedance in 50 years

(b) 2% probability of exceedance in 50 years

CHAPTER IV
EFFECT OF SOIL AMPLIFICATION

The peak horizontal accelerations which are given by the seismic hazard maps in Chapter III are suitable for bedrock. Therefore, the effect of soil amplification needs to be considered for the earthquake resistant-design of structures.

4.1 Dynamic Soil Properties

The seismic waves propagate through soil layers. The attenuated or amplified wave amplitudes depend on the properties of soil layers. The essential parameter for ground response analysis is the shear modulus of soil that is related to the shear wave velocity. Shear modulus can be determined in many ways such as unconfined compaction test, triaxial test for large strain and Wave propagation techniques for small strain, bender element for very small strain ($\leq 3.4 \times 10^{-4}$%) as shown in Figure 4-1.

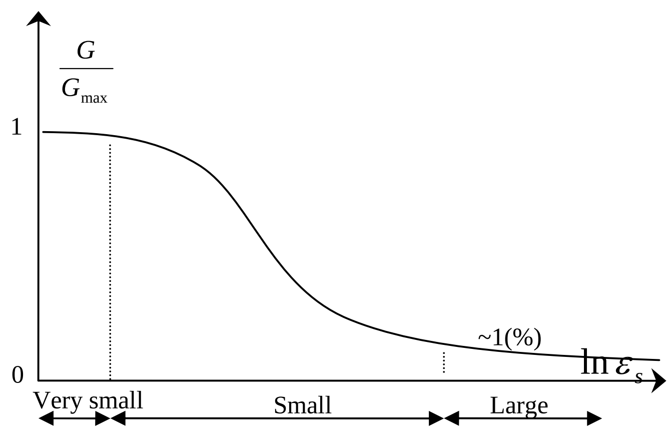

Figure 4-1 Graph of Modulus reduction curve displaying $\frac{G}{G_{\max}}$ with the various strain

The measured shear wave velocities (V_S) can be used to compute $G_{\max}$ as

$$G_{\max} = \rho V_S^2 \tag{4-1}$$

where ρ is the density of material.

The shear wave velocity can be estimated from the SPT N-value or undrained shear strength using available equations obtained from in-situ tests and laboratory tests in others. The relations among shear wave velocities, SPT N-values and undrained shear strengths of soils can be summarized in Table 4-1

Table 4-1 The relations among shear wave velocities, SPT N-values and undrained shear strengths of soils (Ashford et al, 1997)

Years	**Researchers**	**Equations**	**Units**	**Soil types**	**Locations**
1973	Ohsaki , Iwasaki	$V_s = 267\ N^{0.39}$	ft / sec	All	Japan
1982	Imai, Tonuchi	$V_s = 318\ N^{0.341}$	ft / sec	All	Japan
1983	Seed, Idriss, Arango	$V_s = 185\ N^{0.5}$	ft / sec	Sand	Japan
1983	Sykora, Stokoe	$V_s = 100.584\ N^{0.29}$	m / sec	All	Japan
1994	Dickenson	$V_s = 290(N+1)^{0.30}$	ft / sec	Sand	San Francisco
1994	Dickenson	$V_s = 18\left(S_u^{0.475}\right)$	ft / sec	Clay	San Francisco

From the Ashford et al's (1997) study, the suitable relation between shear wave velocities (V_s), and undrained shear strengths (S_u) of Bangkok soil is Dickenson's (1994) equation expressed as

$$V_s = 68.7 S_u^{0.475}\ \text{(m/s)};\ S_u\ \text{in t/m}^2 \tag{4-2}$$

Seed and Idriss (1970) studied the relation between the undrained shear strength (S_u) and Shear modulus (G) which can be expressed as

$$G_{max} = 2200\ S_u \tag{4-3}$$

Moreover, they studied the relations between the modulus ratio (G/G_{max}) and the damping ratio of sand with the values of shear strain by tests in the laboratory such as triaxial compression tests, simple shear tests, torsional shear tests and free vibration tests with soil specimens. The in-situ tests determined the shear wave velocities of soil sites. The results of this study can be shown as Figure 4-2

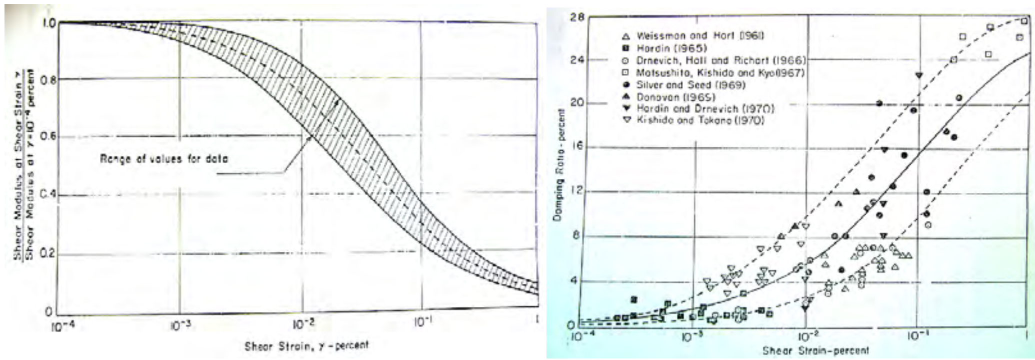

(a) (b)

Figure 4-2 Modulus reduction curve and Damping curve of sands (Seed and Idriss, 1970)

(a) Modulus reduction curve (b) Damping curve

Vucetic and Dobry (1991) studied the relations between the modulus ratio (G/G_{max}) and the damping ratio with the values of shear strain from 16 samples of clays. The function of over consolidation ratio (OCR) of clay specimens are ranging from 1 to 15. The results can be summarized that if the plastic index of clay increases, the modulus ratio will be increased but the damping ratio will be decreased. The relations between the modulus ratio (G/G_{max}) and the damping ratio of sand with the values of shear strain are shown in Figure 4-3

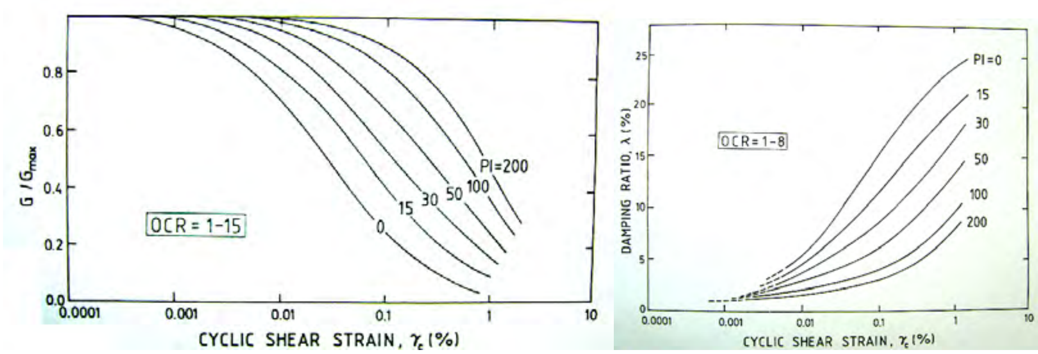

(a) (b)

Figure 4-3 Modulus reduction curve and Damping curve of clays (Vucetic and Dobry, 1991)

(a) Modulus reduction curve (b) Damping curve

4.2 Theories

Viscous damping is often used to represent this dissipation of elastic energy. For the purposes of viscoelastic wave propagation, soils are usually modeled as Kelvin-Voigt solids. (Kramer, 1996)

For Kelvin-Voigt model, a purely viscous damper and purely elastic spring connected in parallel as shown in the picture:

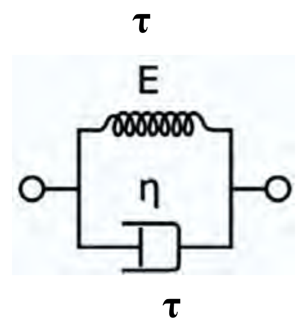

Figure 4-4 Kelvin-Voigt model

The model is arranged in parallel, the strains in each component are identical:

$$\gamma(t) = \gamma_S(t) = \gamma_D(t) \tag{4-4}$$

where γ is the shear strain of soil model

γ_S is the shear strain due to elastic material (modeled as soil spring) and

γ_D is the shear strain due to damping material (modeled as dashpot).

Similarly, the total force will be the sum of the forces in each component:

$$F_{Total} = F_S + F_D \tag{4-5}$$

where F_{Total} is the total force

F_S is the force in soil spring model

F_D is the force in dashpot

$$\tau(t)A = \tau_S(t)A + \tau_D(t)A$$

$$\tau(t) = G\gamma(t) + \eta\frac{\partial\gamma(t)}{\partial t} \tag{4-6}$$

where τ is the shear stress, γ is the shear strain, *G* is a shear modulus and η is the viscosity.

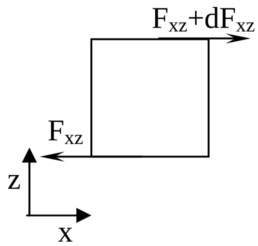

$$\gamma(t) = \frac{\partial u}{\partial z}$$

$$\sigma_{xz} = \tau(t)$$

$$\sum F_x = 0;$$

$$F_{xz} + dF_{xz} - F_{xz} - F_x = 0$$

$$F_x = F_{xz} + dF_{xz} - F_{xz}$$

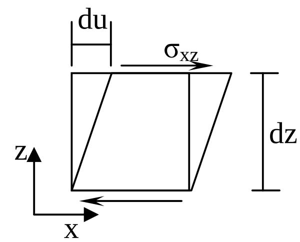

$$\rho dxdydz\frac{\partial^2 u}{\partial t^2} = \sigma_{xz}dxdy + \frac{\partial \sigma_{xz}}{\partial z}dz \cdot dxdy - \sigma_{xz}dxdy \quad (4\text{-}7)$$

where ρ is the density of material

The one-dimensional equation of motion

$$\rho\frac{\partial^2 u}{dt^2} = \frac{\partial \sigma_{xz}}{\partial z} \quad (4\text{-}8)$$

Substituting equation (4-7) into (4-8) with $\tau = \sigma_{xz}$ and $\gamma = \partial u/\partial z$

$$\rho\frac{\partial^2 u}{dt^2} = \frac{\partial \tau(t)}{\partial z} = \frac{\partial}{\partial z}\left(G\gamma(t) + \eta\frac{\partial \gamma(t)}{\partial t}\right)$$

$$\rho\frac{\partial^2 u}{dt^2} = \frac{\partial}{\partial z}(G\frac{\partial u}{\partial z} + \eta\frac{d}{dt}\frac{\partial u}{\partial z})$$

$$\rho\frac{\partial^2 u}{dt^2} = G\frac{\partial}{\partial z}\frac{\partial u}{\partial z} + \eta\frac{d}{dt}\frac{\partial}{\partial z}\frac{\partial u}{\partial z}$$

The governing equation becomes

$$\therefore \quad \rho\frac{\partial^2 u}{dt^2} = G\frac{\partial^2 u}{\partial z^2} + \eta\frac{\partial^3 u}{\partial z^2 \partial t} \quad (4\text{-}9)$$

Find the relation between the viscosity η and the shear modulus G

Energy dissipated in viscous damping

Consider the steady-state motion of SDOF system: $u(t) = u_0 \sin \omega t$

The energy dissipated by viscous damping in 1 cycle of harmonic vibration is

$$\Delta W = \int F_D du \quad (4\text{-}10)$$

$$\Delta W = \int_0^{2\pi/\omega} (c\dot{u})\dot{u}dt$$

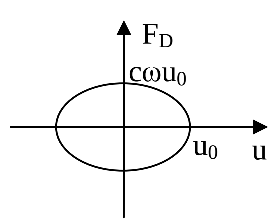

$$\Delta W = \int_0^{2\pi/\omega} c\dot{u}^2 dt$$

$$\Delta W = \int_0^{2\pi/\omega} c(u_0\omega\cos\omega t)^2 dt$$

$$\Delta W = cu_0^2\omega^2 \int_0^{2\pi/\omega} \cos^2 \omega t dt \quad ; \ \cos 2\theta = 2\cos^2\theta - 1$$

$$\Delta W = cu_0^2\omega^2 \int_0^{2\pi/\omega} \frac{\cos 2\omega t + 1}{2} dt$$

$$\Delta W = cu_0^2\omega\left(\frac{\sin 2\omega t}{4}\bigg|_0^{2\pi/\omega} + \frac{t}{2}\bigg|_0^{2\pi/\omega} \right)$$

$$\Delta W = cu_0^2\omega\pi \qquad ; c = \frac{2k\xi}{\omega_n}$$

$$\Delta W = 2\pi\xi k u_0^2 \frac{\omega}{\omega_n} \tag{4-11}$$

The strain energy

$$W = \int F_S du \tag{4-12}$$

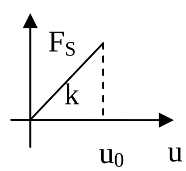

$$W = \int_0^{u_0} kudu = \frac{1}{2}ku^2\bigg|_0^{u_0} = \frac{1}{2}ku_0^2 \tag{4-13}$$

$\therefore ku_0^2 = 2W$ Substitutes into (4-11);

$$\Delta W = 4W\pi\xi \frac{\omega}{\omega_n}$$

$$\xi = \frac{1}{4\pi}\frac{\omega}{\omega_n}\frac{\Delta W}{W} \tag{4-14}$$

Equivalent viscous damping, matching dissipated energies at $\omega = \omega_n$ led to

$$\xi_{eq} = \frac{1}{4\pi}\frac{\Delta W}{W} \tag{4-15}$$

For a harmonic shear strain of form

$$\gamma(t) = \gamma_0 \sin\omega t \tag{4-16}$$

the shear stress will be

$$\tau(t) = G\gamma_0 \sin\omega t + \omega\eta\gamma_0 \cos\omega t \tag{4-17}$$

Equations (4-16) and (4-17) show the stress-strain loop of a Kelvin-Voigt solid is elliptical. The elastic energy dissipated in a single cycle is given by the area of the ellipse, or

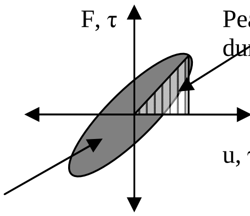

$$\Delta W = \int_0^{2\pi/\omega} \tau(t) \frac{\partial \gamma(t)}{\partial t} dt \qquad (4\text{-}18)$$

$$\Delta W = \int_0^{2\pi/\omega} (G\gamma_0 \sin\omega t + \omega\eta\gamma_0 \cos\omega t) \frac{\partial \gamma_0 \sin\omega t}{\partial t} dt$$

$$\Delta W = \int_0^{2\pi/\omega} (G\gamma_0 \sin\omega t + \omega\eta\gamma_0 \cos\omega t)\gamma_0 \omega \cos\omega t dt$$

$$\Delta W = \gamma_0^2 \int_0^{2\pi/\omega} (\omega G \sin\omega t \cos\omega t + \omega^2 \eta \cos^2 \omega t) dt$$

$\sin 2\theta = 2\sin\theta\cos\theta$ and $\cos 2\theta = 2\cos^2\theta - 1$

$$\Delta W = \gamma_0^2 \int_0^{2\pi/\omega} (\omega G \frac{\sin 2\omega t}{2} + \omega^2 \eta \frac{\cos 2\omega t + 1}{2}) dt$$

$$\Delta W = \gamma_0^2 \left(-\frac{G}{4}\cos 2\omega t \Big|_0^{2\pi/\omega} + \frac{\omega\eta}{4}\sin 2\omega t \Big|_0^{2\pi/\omega} + \frac{\omega^2 \eta t}{2} \Big|_0^{2\pi/\omega} \right)$$

$$\Delta W = \gamma_0^2 \left(0 + 0 + \frac{\omega^2 \eta}{2} (\frac{2\pi}{\omega}) \right)$$

$$\Delta W = \pi\eta\omega\gamma_0^2 \qquad (4\text{-}19)$$

$$W = \frac{1}{2} G\gamma_0^2 \qquad (4\text{-}20)$$

Since the peak energy stored in the cycle from Eq. (4-15), then

$$\xi = \frac{1}{4\pi} \frac{\pi\eta\omega\gamma_0^2}{\frac{1}{2}G\gamma_0^2} = \frac{\eta\omega}{2G}$$

Rearrange to $\eta = \dfrac{2G}{\omega}\xi$ (4-21)

For harmonic waves, the displacements can be written as

$$u(z,t) = U(z)e^{i\omega t} \qquad (4\text{-}22)$$

Substituting (4-22) into (4-9);

$$\rho \frac{\partial^2 U(z)e^{i\omega t}}{dt^2} = G \frac{\partial^2 U(z)e^{i\omega t}}{\partial z^2} + \eta \frac{\partial^3 U(z)e^{i\omega t}}{\partial z^2 \partial t}$$

$$\rho U(z)\frac{\partial^2 e^{i\omega t}}{dt^2} = Ge^{i\omega t}\frac{\partial^2 U(z)}{\partial z^2} + \eta\frac{\partial^2 U(z)}{\partial z^2}\frac{\partial e^{i\omega t}}{\partial t}$$

$$-\rho\omega^2 U(z)e^{i\omega t} = Ge^{i\omega t}\frac{\partial^2 U(z)}{\partial z^2} + i\omega\eta e^{i\omega t}\frac{\partial^2 U(z)}{\partial z^2}$$

$$-\rho\omega^2 U(z) = (G + i\omega\eta)\frac{\partial^2 U(z)}{\partial z^2} \tag{4-23}$$

Given $G* = G + i\omega\eta$ is the complex shear modulus. (4-24)

Substituting (4-21) into (4-24);

$$G^* = G + i\omega\frac{2G}{\omega}\xi = G(1 + 2i\xi) \tag{4-25}$$

So, the Equation (4-23) becomes

$$-\rho\omega^2 U(z) = G^*\frac{\partial^2 U(z)}{\partial z^2}$$

$$\frac{\partial^2 U(z)}{\partial z^2} + \frac{\rho\omega^2}{G^*}U(z) = 0 \tag{4-26}$$

The equation of motion (4-26) has the solution

$$u(z,t) = Ae^{i(\omega t + \sqrt{\rho\omega^2/G*}z)} + Be^{i(\omega t - \sqrt{\rho\omega^2/G*}z)}$$

$$u(z,t) = Ae^{i(\omega t + \omega\sqrt{\rho/G*}z)} + Be^{i(\omega t - \omega\sqrt{\rho/G*}z)} \tag{4-27}$$

given $k* = \omega\sqrt{\rho/G*}$ is the complex wave number. (4-28)

Thus, harmonic horizontal motion of the bedrock will produce vertically propagation shear waves in the overlying soil. The resulting horizontal displacement can be expressed as

$$u(z,t) = Ae^{i(\omega t + k*z)} + Be^{i(\omega t - k*z)} \tag{4-29}$$

where A and B the amplitudes of waves traveling in the –z (upward) and +z (downward) direction.

For the uniform, damped soil on rigid rock can be shown in Figure 4-5. (Kramer, 1996)

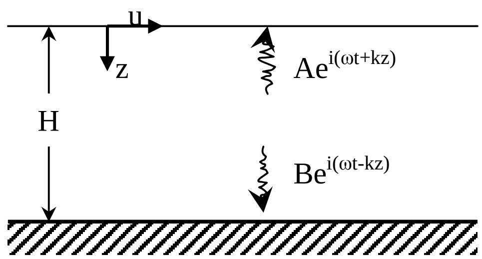

Figure 4-5 Uniform, damped Soil on Rigid Rock

The boundary condition at the free surface (z = 0)

$$\tau(0,t) = G\gamma(0,t) = G\frac{\partial u(0,t)}{\partial z} = 0 \tag{4-30}$$

Substituting (4-29) into (4-30) and differentiating yields

$$Gik*(Ae^{ik*(0)} - Be^{ik*(0)})e^{i\omega t} = Gik*(A-B)e^{i\omega t} = 0 \tag{4-31}$$

when A = B (nontrivially);

$$u(z,t) = A(e^{i(\omega t+k*z)} + e^{i(\omega t-k*z)}) = 2Ae^{i\omega t}(\frac{e^{ik*z}+e^{-ik*z}}{2})$$

$$u(z,t) = 2Ae^{i\omega t}\cos k*z \tag{4-32}$$

at z = 0; $u(0,t) = 2Ae^{i\omega t}\cos k*(0) = 2Ae^{i\omega t}$

at z = H; $u(H,t) = 2Ae^{i\omega t}\cos k*(H) = 2Ae^{i\omega t}\cos k*H$

The transfer function describes the ratio of displacement amplitudes at any two points in the soil layer. Choosing the top and the bottom layer gives the transfer function

$$F(\omega) = \frac{u(0,t)}{u(H,t)} = \frac{2Ae^{i\omega t}}{2Ae^{i\omega t}\cos k*H} = \frac{1}{\cos k*H} \tag{4-33}$$

$$G = \rho V_S^2; \qquad \rightarrow \qquad V_S = \sqrt{\frac{G}{\rho}} \tag{4-34}$$

if $G^* = G(1+2i\xi)$ → $V_S{*} = \sqrt{\dfrac{G(1+2i\xi)}{\rho}} = \sqrt{\dfrac{G}{\rho}}(1+i\xi)$

$$\therefore \qquad V_S{}^* = V_S(1+i\xi) \tag{4-35}$$

$$k^* = \frac{\omega}{V_S{}^*} = \frac{\omega}{V_S(1+i\xi)}$$

for small ξ → $k^* \approx \dfrac{\omega}{V_S}(1-i\xi) = k(1-i\xi)$ (4-36)

and finally, the transfer function, as

$$F(\omega) = \frac{1}{\cos k(1-i\xi)H} = \frac{1}{\cos \dfrac{\omega H}{V_S(1+i\xi)}} \tag{4-37}$$

Using the identity $|\cos(x+iy)| = \sqrt{\cos^2 x + \sinh^2 y}$, the transfer function can be expressed as

$$F(\omega) = \frac{1}{\sqrt{\cos^2 kH + \sinh^2 \xi kH}} \tag{4-38}$$

For small y: → $\sinh^2 y \approx y^2$, the transfer function can be simplified to

$$F(\omega) = \frac{1}{\sqrt{\cos^2 kH + (\xi kH)^2}} = \frac{1}{\sqrt{\cos^2(\omega H / V_S) + [\xi\omega H / V_S]^2}} \tag{4-39}$$

At the natural frequency point, the amplification will reach the local maximum. So, we can find the fundamental period of soil from the transfer function

From Equation (4-39), Plotting graph the relation between F(ω) and kH is

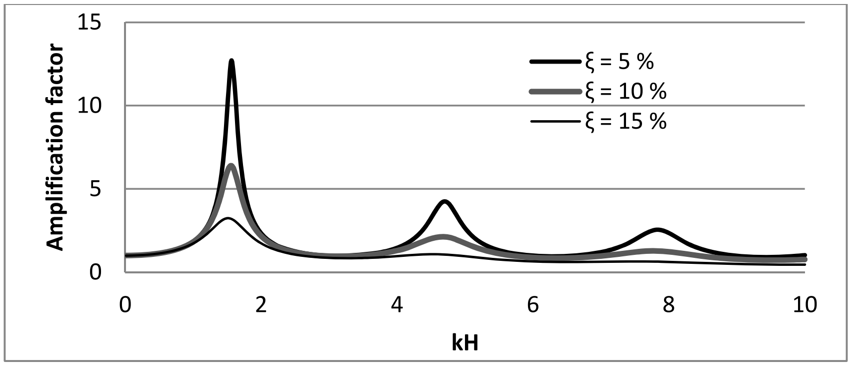

Figure 4-6 Influence of frequency on steady-state response of damped, linear elastic layer

$F(\omega)$ is maximum at cos (kH) = 1; → $kH = \pi/2 + n\pi$ → $\omega H/V_S = \pi/2 + n\pi$

So, the natural frequency of the soil deposit is given by

$$\omega_n \approx \frac{V_S}{H}\left(\frac{\pi}{2} + n\pi\right) \qquad n = 0, 1, 2, \ldots \qquad (4\text{-}40)$$

The greatest amplification factor gives the lowest natural frequency which is known as the fundamental frequency

$$\omega_0 = \frac{\pi}{2}\frac{V_S}{H} \qquad (4\text{-}41)$$

and also gives the characteristic site period,

$$T_S = \frac{2\pi}{\omega_0} = \frac{4H}{V_S} \qquad (4\text{-}42)$$

4.3 Seismic Downhole Test

The seismic downhole test is used for obtaining shear wave velocity by measuring the travelling time of elastic wave from the ground surface to some arbitrary depths beneath the ground. Ground vibration is generated at the ground surface by hammering the wooden plank securely anchored to the ground as shown in Figure 4-7.

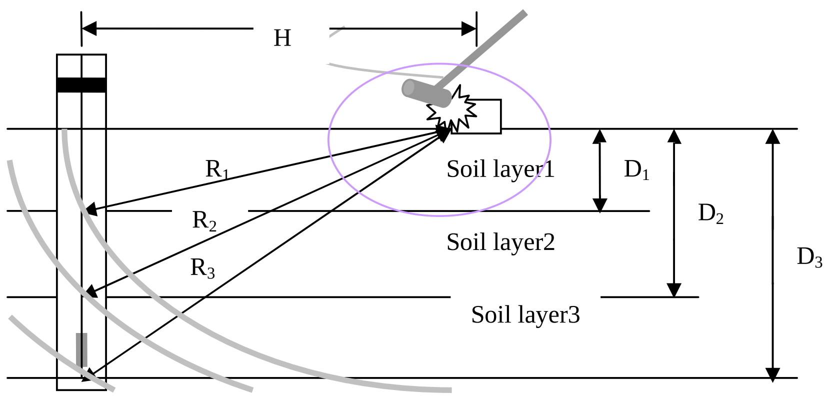

Figure 4-7 Generation of shear wave

A geophone is lowered into a borehole. Shear wave velocity V_s can be determined from

$$V_S = \Delta R / \Delta T \tag{4-43}$$

$$R_i = \sqrt{H^2 + D_i^2} \tag{4-44}$$

where H is the distance from the borehole to the plank, D_i is the depth of the geophone from the surface and R_i is the shortest distance from the geophone to the plank (the vibration source).

In this study, the downhole seismic test is used for determining shear wave velocities of 3 boreholes with the depth of 30 to 37 meter in Bangkok where most of soil types is soft clay and 3 boreholes with the depth of 13 to 22 meter in the north of Thailand where most of soil types is clayey sand. Data is collected at every 1 meter.

The 6 boreholes will be considered in this research. The locations of boreholes can be displayed in Figure 4-8. The SPT N-values and undrained shear strengths of boreholes can be shown in Figure 4-9 for Bangkok and Figure 4-10 for the Northern Thailand.

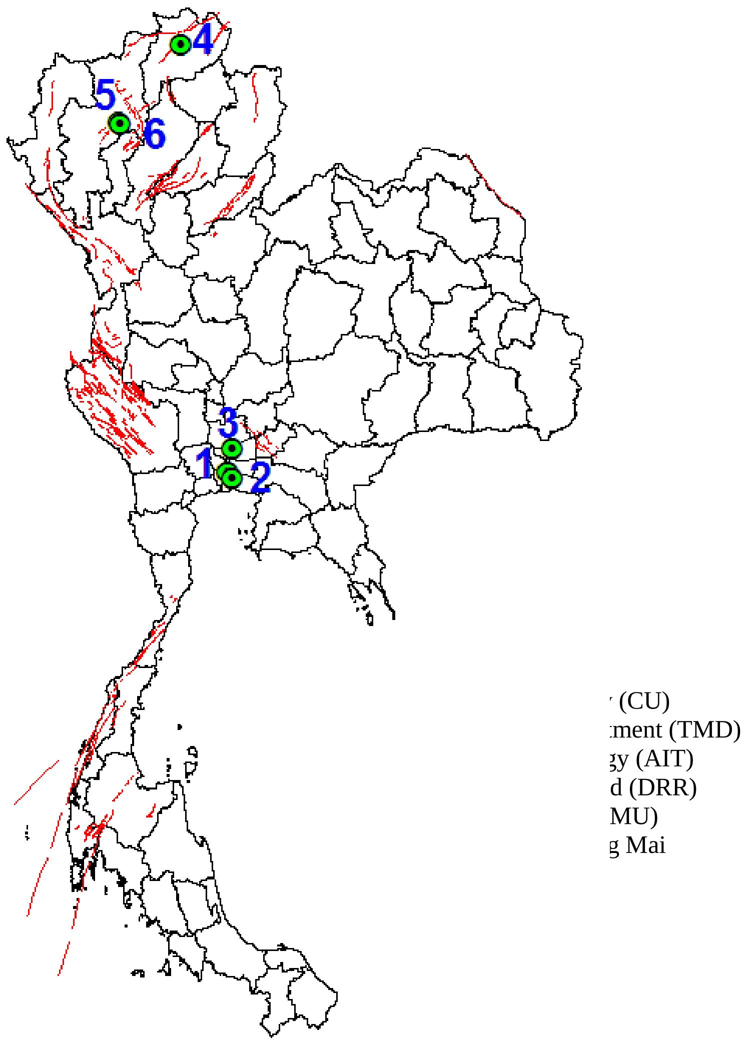

Figure 4-8 The locations of boreholes

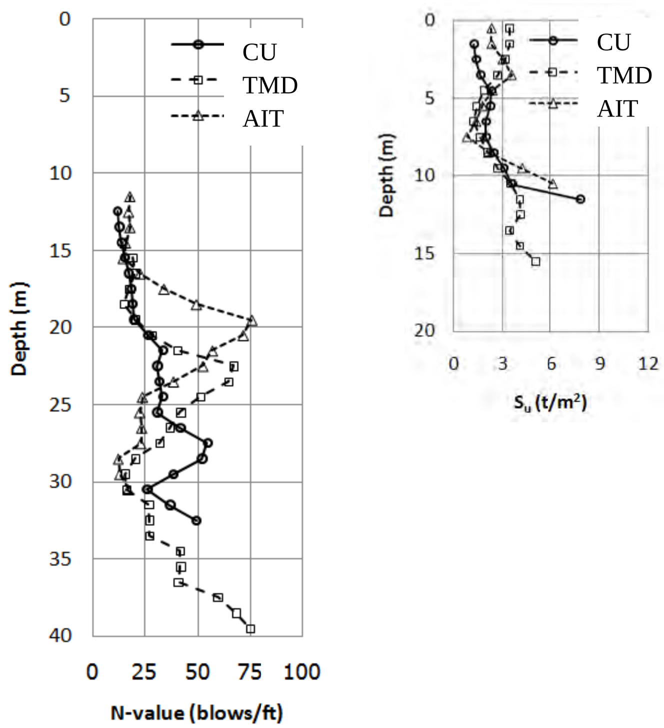

Figure 4-9 STP N-values and undrained shear strengths (Su) of boreholes in Bangkok.

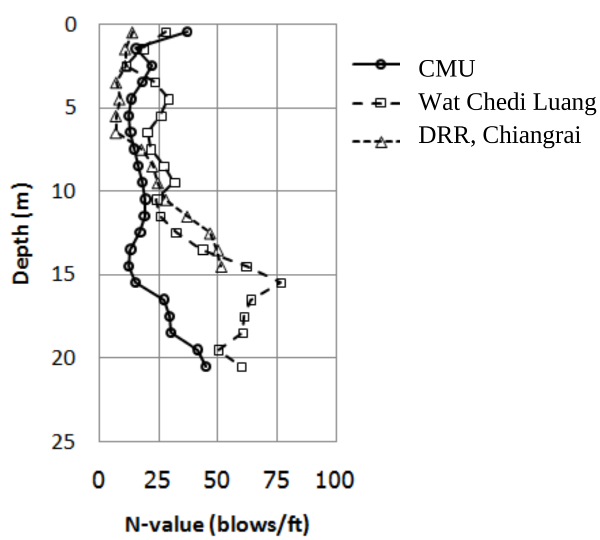

Figure 4-10 STP N-values of boreholes in the Northern Thailand

4.4 The Relations among N, S_u and V_s

The shear wave velocity (V_s) from seismic downhole test in Bangkok and the perimeter relates with undrained shear strength (Su) and SPT N-value (N) as shown in Figure 4-11 and 4-12 respectively. These equations are expressed as

$$V_s = 59.225\ S_u^{0.525} \tag{4-45}$$

$$V_s = 53.216\ N^{0.481} \tag{4-46}$$

where V_s is shear wave velocity (m/s)

S_u is undrain shear strength (t/m^2)

N is the number of blow counts per a foot for the standard penetration test.

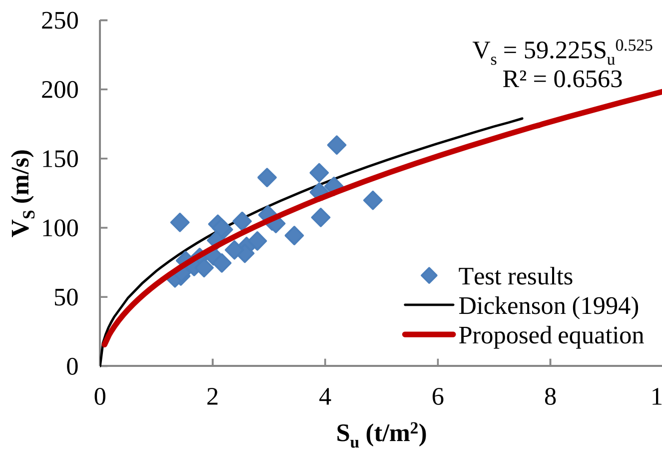

Figure 4-11 The relation between V_s and S_u of soft clay in Bangkok and the perimeter

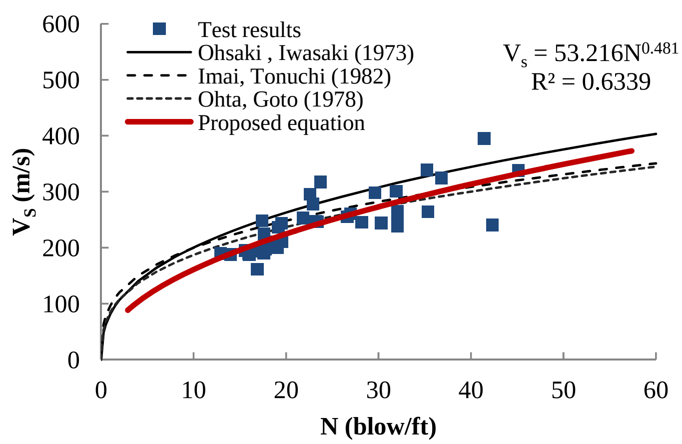

Figure 4-12 The relation between V_s and N of soft clay in Bangkok and the perimeter

From Figure 4-11, the relation between the shear wave velocity and the undrained shear strength of soft clay in Bangkok gives the shear wave velocity 10 % less than the shear wave velocity from equations developed by Dickenson (1994).

The shear wave velocities from the downhole test in the northern Thailand can be determined the relationship with SPT N-value (N) as shown in Figure 4-13. The equation is expressed as

$$V_s = 70.554\ N^{0.423} \qquad (4\text{-}47)$$

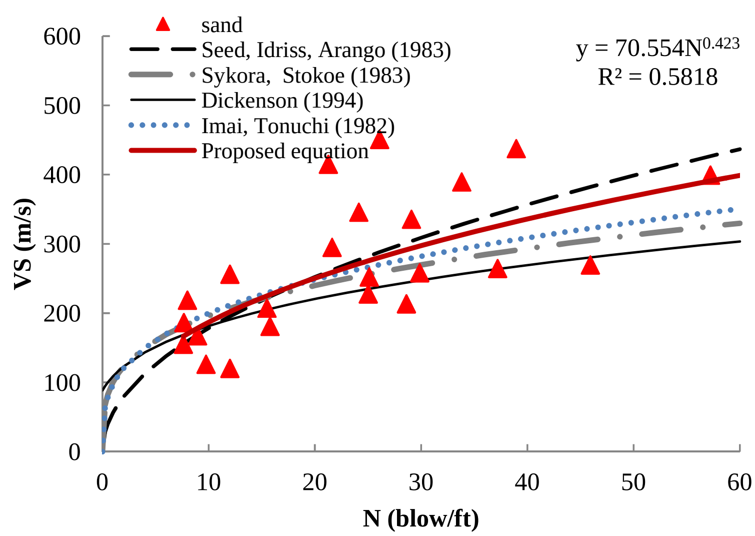

Figure 4-13 The relation between V_s and N of sand in the northern Thailand

4.5 Shear Wave Velocity Profiles

The shear wave velocities were obtained from the downhole test around -30 meters in Bangkok and -20 meters in Chiangmai as summarized in Appendix A. For the deeper soil layers, the shear wave velocities from 2sSPAC method (Pitakwong and Poovarodom, 2009) were applied (-20 meters) for Chiangmai University and Wat Chedi Luang which can be summarized in Table 4-2.

Table 4-2 Shear wave velocities from 2sSPAC method at Chiangmai University and Wat Chedi Luang (Pitakwong and Poovarodom, 2009)

Depth (m)	Shear wave velocities (m/s)	
	Chiangmai University	Wat Chedi Luang
20 – 30	539	307
30 – 40	640	368
40 – 50	683	427
50 – 60	703	458
60 – 70	734	466
70 – 80	801	462
80 - 90	873	453
> 90	903	447

The bedrock level of -90 meter where the shear wave velocity is over than 800 m/s was defined for Chiangmai University. And, the bedrock level of -60 meter where the shear wave velocity is equal to 466 m/s was defined for Wat Chedi Luang site.

For Bangkok and vicinity, the bedrock was assumed at -400 and -600 meters where the shear wave velocity is equal to 2000 m/s (Tuladhar and Warnitchai, 2003).

4.6 Soil Response Analysis of a Historical Event

The August 10, 2009, Andaman Islands earthquake, with magnitude of 7.5 occurred in the subduction zone between the India plate and the Burma plate which was 825 km far away from the west of Bangkok. The ground motions from this event were recorded by the Meteorology Department of Thailand (TMD) at Bangna station where the ground accelerations were collected at the level of -3m and -42m depths. The soil response analysis by the one dimensional equivalent linear method was conducted using PROSHAKE. The parameters for ground response analysis consist of shear wave velocities, unit weight, plastic indexes and thicknesses of soil layers which are expressed in Table 4-3. The shear wave velocities were obtained by the seismic downhole test that can be plotted in Figure 4-14.

Table 4-3 Soil profile of TMD (Bangna station)

Layer No.	Type of Sample	Depth, m	Thickness, m	Classification	Natural Water Content (%)	Su, t/m^2	SPT, N (Blow/ft)	Plastic Index (%)	Wet Unit Weight (t/m^3)	(Downhole) Vs (m/s)
1	ST	1.8	2.55	CH	37.0	3.44		32.00	1.86	81
2	ST	3.3	1.50	CH	65.0	2.90			1.67	90
3	ST	4.8	1.50	CH	54.0	1.63			1.72	69
4	ST	6.3	1.50	CH	71.0	1.17		39.00	1.64	60
5	ST	7.8	1.50	CH	88.0	1.75			1.56	90
6	ST	9.3	1.65	CH	84.0	2.56			1.56	93
7	ST	11.1	1.50	CH	69.0	4.01		62.00	1.63	118
8	ST	12.3	1.35	CH	67.0	4.27			1.61	144
9	ST	13.8	1.50	CH	37.0	3.24			1.86	159
10	ST	15.3	1.00	CH	36.0	5.07		36.00	1.75	217
11	SS	15.8	0.75	CH	31.0		19		1.88	214
12	SS	16.8	1.25	CH	33.0		21		2.00	191
13	SS	18.3	1.50	CH	37.0		14	30.00	2.00	208
14	SS	19.8	1.50	ML/SM	22.0		22		2.02	252
15	SS	21.3	1.50	CL	22.0		35	12.00	2.00	403
16	SS	22.8	1.50	SM	23.0		75		1.97	282
17	SS	24.3	1.50	SM	22.0		53		1.98	207
18	SS	25.8	1.50	SM	17.0		39		1.98	180
19	SS	27.3	1.50	SM	22.0		34		2.00	370
20	SS	28.8	1.50	CH	29.0		17	34.00	2.10	451
21	SS	30.3	1.50	CH	25.0		14		2.06	217
22	SS	31.8	1.50	CH	26.0		30		2.12	268
23	SS	33.3	1.50	CH	33.0		24	40.00	1.88	270
24	SS	34.8	1.50	CH	19.0		46		2.03	446
25	SS	36.3	1.50	CH	21.0		37		2.06	495
26	SS	37.8	1.50	SM/ML	18.0		65		2.01	550
27	SS	39.3	1.25	SM/ML	21.0		71		2.06	
28	SS	40.3	0.50	SM/ML	23.0		88		2.05	

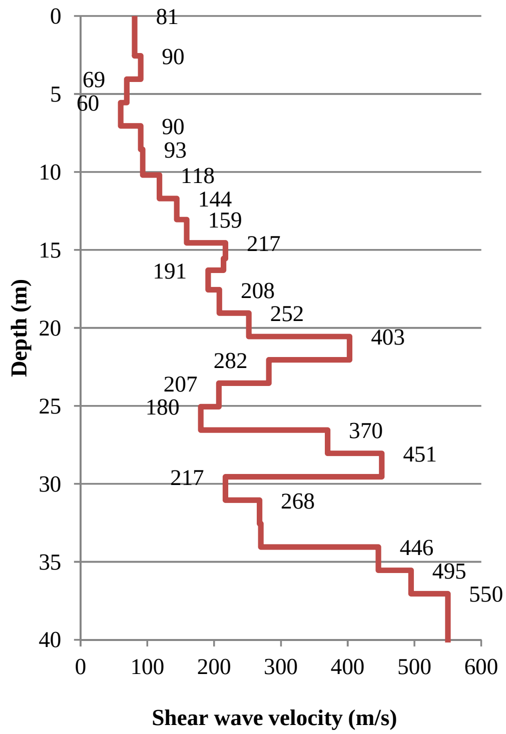

Figure 4-14 Shear wave velocity profile of TMD (Bangna Station)

The time histories of recorded motions at the depths of -3 meters and -42 meters can be shown in Figures 4-15 and 4-16. The recorded motion at -42 meters was defined as the input motion. The spectral acceleration of recorded motion at -42 meters depth can be shown as Figure 4-17.

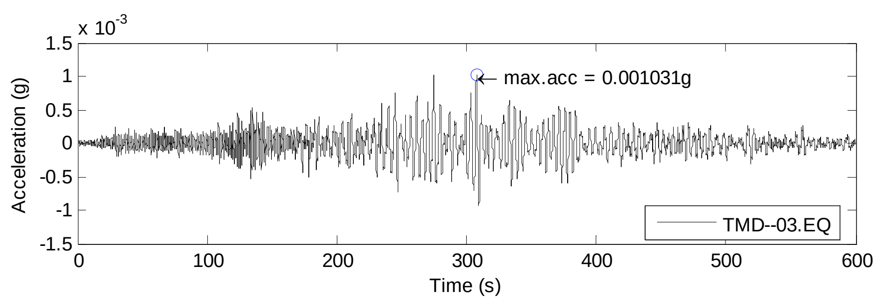

Figure 4-15 Acceleration time history of recorded motion from TMD at -3 meters depth

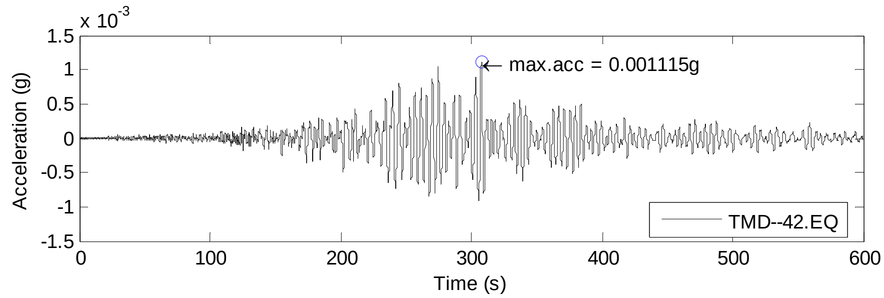

Figure 4-16 Acceleration time history of recorded motion from TMD at -42 meters depth

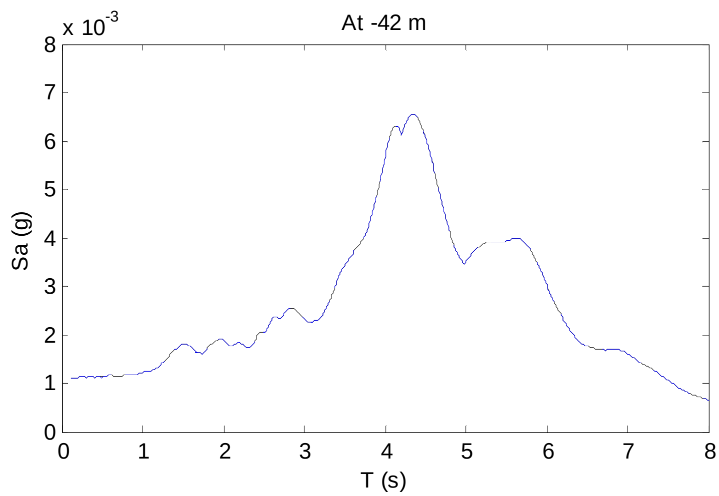

Figure 4-17 Spectral accelerations of the recorded motion at -42 meters depth

From the one dimensional equivalent linear method by PROSHAKE, the output motion of -3 meters depth can be shown in Figures 4-18. The spectral accelerations between recorded motions and analytical motions of -3 meters depth can be compared in Figures 4-19.

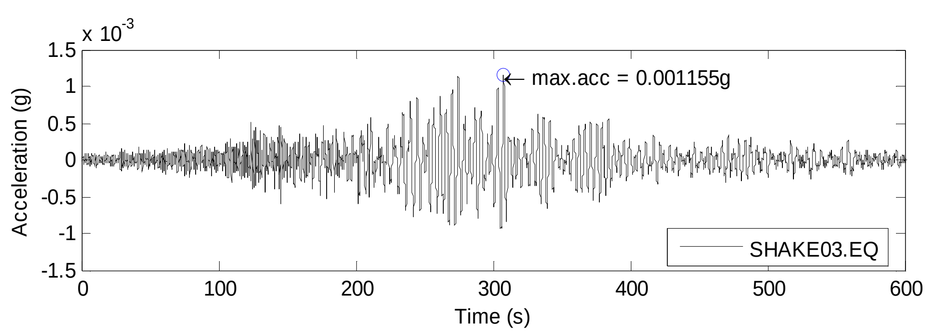

Figure 4-18 Acceleration time history of output motion at -3 meters depth

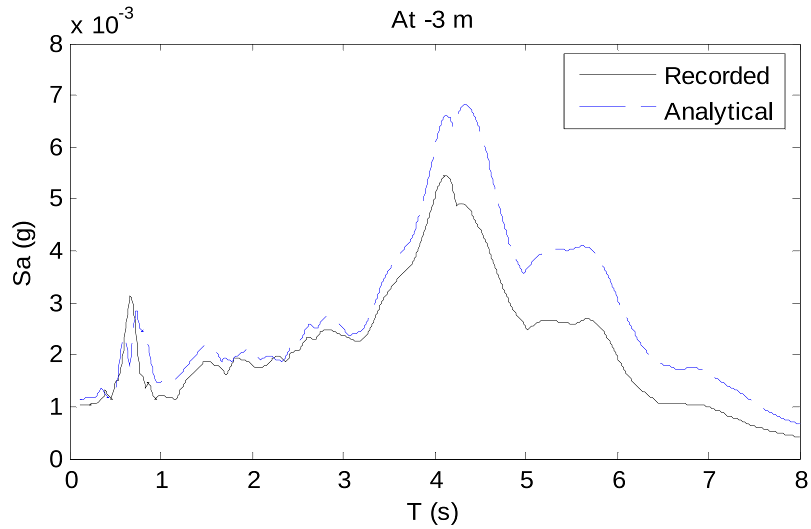

Figure 4-19 Comparison of spectral accelerations of the recorded and analytical motions at -3 meters depth

From Figure 4-19, it seems that the peak of spectral acceleration between 0 to 1 s is quite close to the recorded data.

4.7 Soil Amplification

The soil amplification factor is the ratio between a response of a surface ground motion and that response of an outcrop motion for peak ground acceleration (PGA) and spectral acceleration (S_a) in each period. The equation of soil amplification factor can be expressed as

$$\text{Soil amplification factor} = \frac{PGA\ or\ Sa_{output\ ground\ motion}}{PGA\ or\ Sa_{\ outcrop\ motion}} \tag{4-48}$$

This study aims to determine the distribution of soil amplification factors in regions which have various shear wave velocities at the first 30 meters depth of soil layers (Vs30).

The selected ground motions were selected from rock sites. The epicenters of those stations vary in the range of 20-230 km. The peak accelerations of outcrop motions were scaled to 0.05g. 10 earthquake outcrop motions which were used in this analysis are expressed in Table 4-4 and Figures 4-20 to 4-29.

Table 4-4 Selected outcrop motions

Name	Mw	Stations	Epicenter (km)	ID
San Fernando	6.6	Castaic Old Ridge Route	25	SOY
Kern County	7.4	Taft Lincoln School	41	KTX
Loma Preita	7.1	Diamond Heights	77	LDX
Kern County	7.4	Santa Barbara	88	KSX
Borah Peak	6.9	INEEL 99999 ANL	108	BIX
Hector Mine	7.1	Anza - Tripp Flats Training	120	HAX
San Fernando	6.6	Isabella Dam (Aux Abut)	134	SIX
Landers	7.3	San Gabriel E Grand Av	153	LGX
Hector Mine	7.1	Pacoima Kagel Canyon	197	HPX
San Fernando	6.6	Cholame-Shandon Array #2	223	SCX

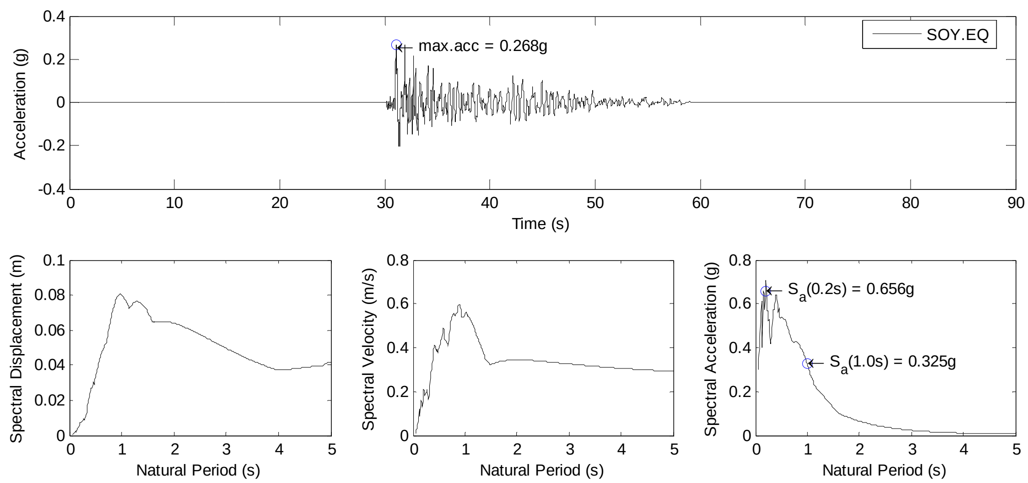

Figure 4-20 Acceleration time history and response spectra of San Fernando earthquakes from Castaic Old Ridge Route station

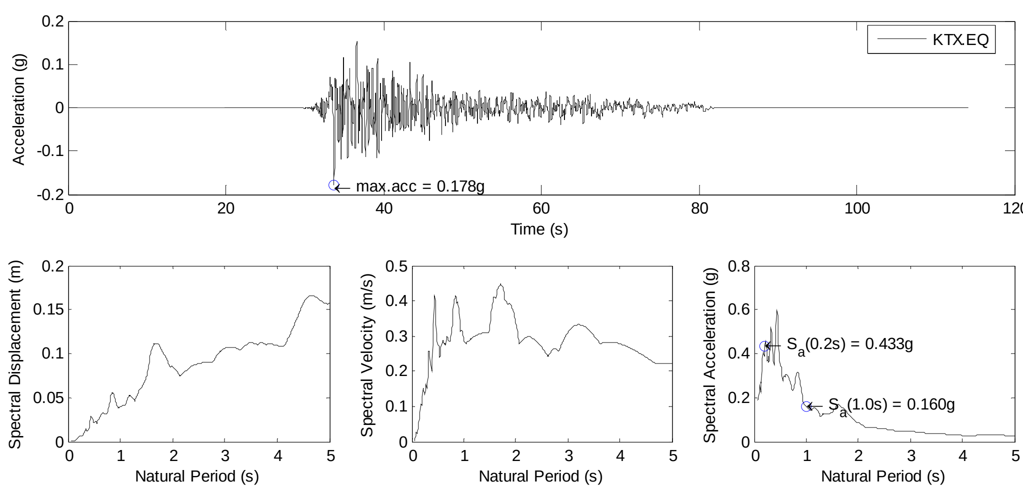

Figure 4-21 Acceleration time history and response spectra of Kern County earthquakes from Taft Lincoln School station

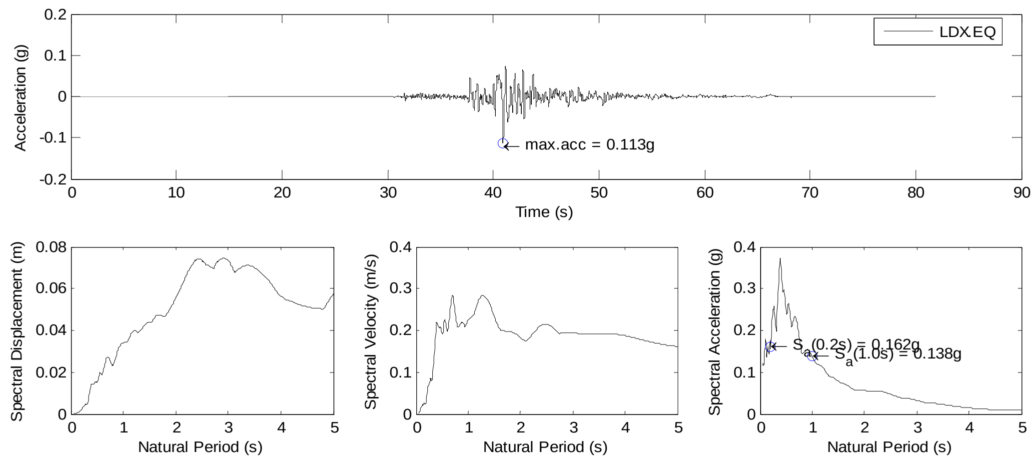

Figure 4-22 Acceleration time history and response spectra of Loma Preita earthquakes from Diamond Heights station

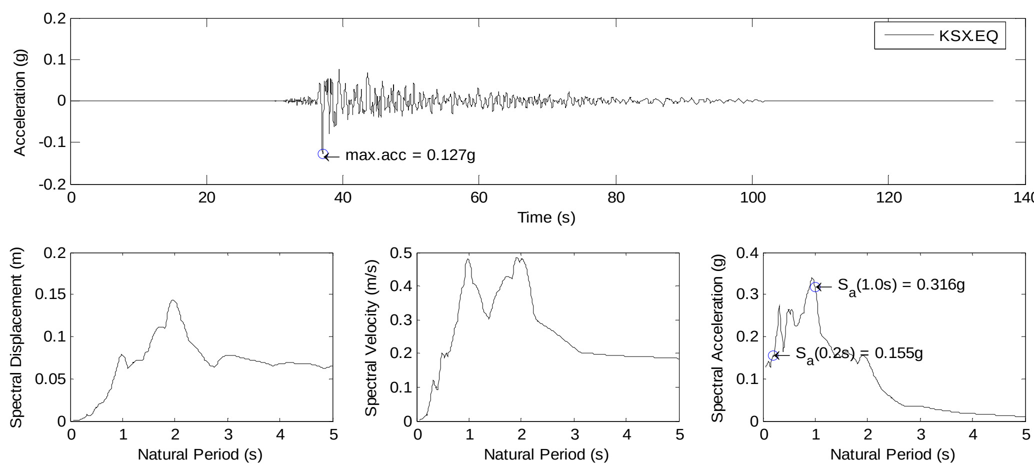

Figure 4-23 Acceleration time history and response spectra of Kern County earthquakes from Santa Barbara station

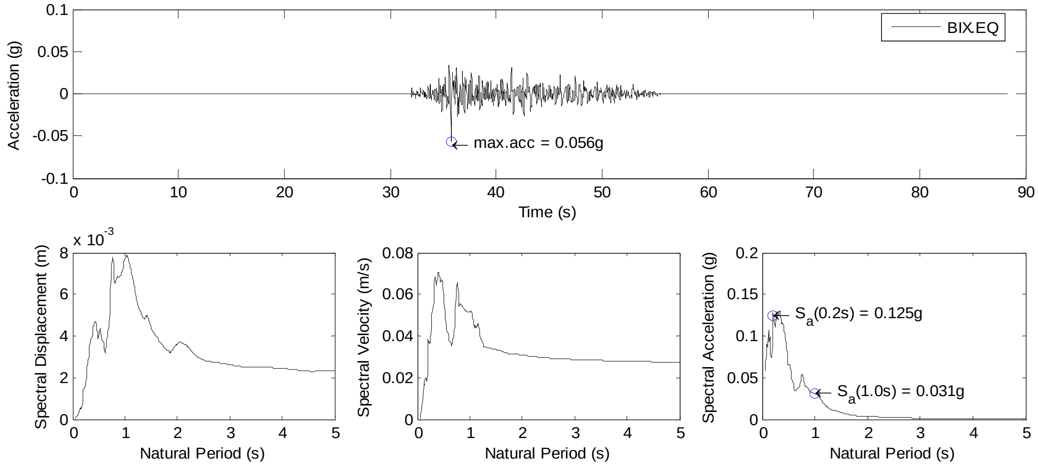

Figure 4-24 Acceleration time history and response spectra of Borah Peak earthquakes from INEEL 99999 ANL station

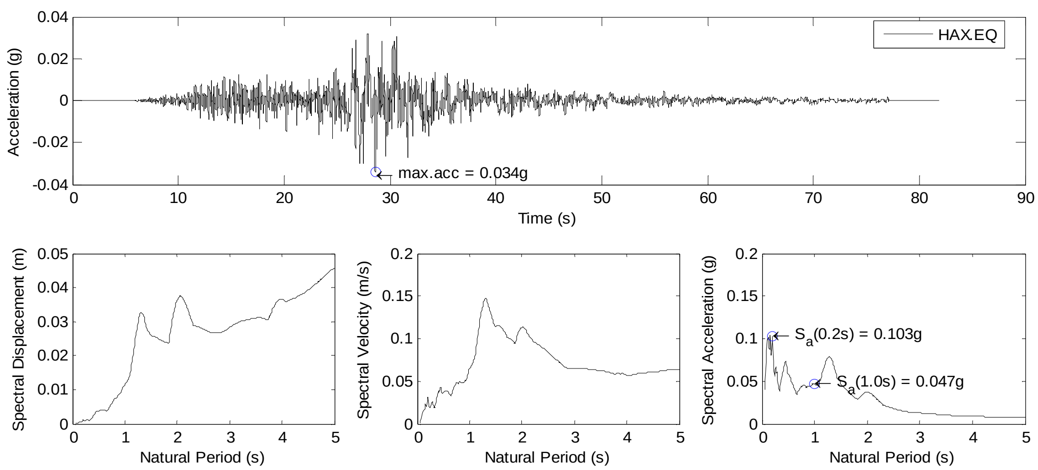

Figure 4-25 Acceleration time history and response spectra of Hector Mine earthquakes from Anza - Tripp Flats Training station

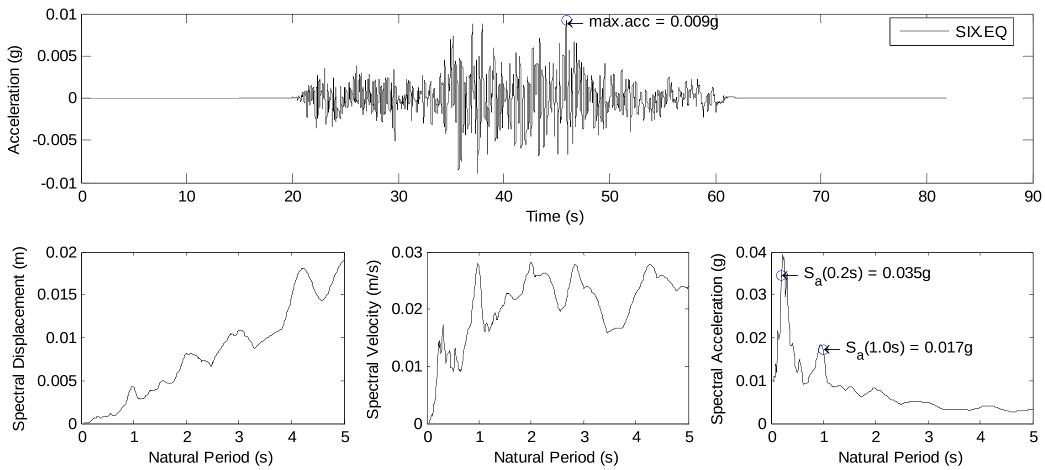

Figure 4-26 Acceleration time history and response spectra of San Fernando earthquakes from Isabella Dam station

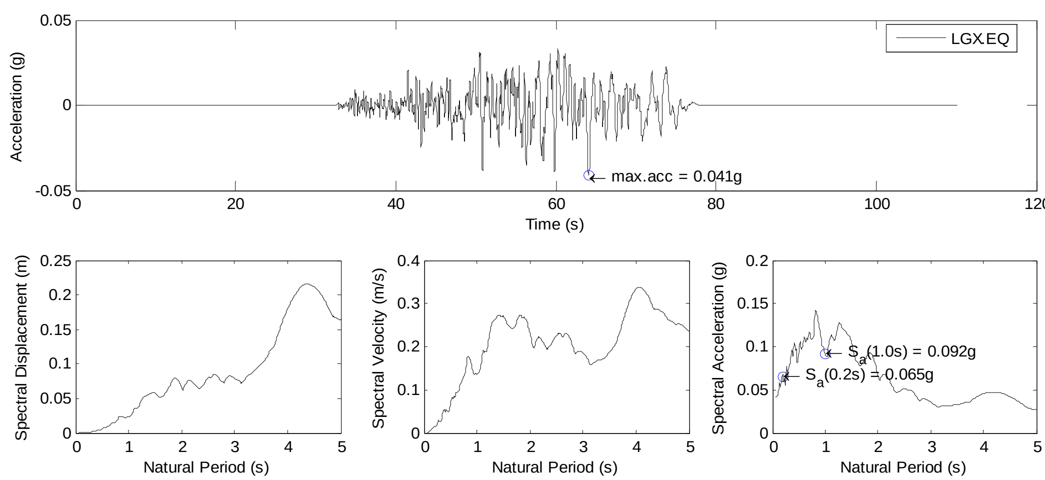

Figure 4-27 Acceleration time history and response spectra of Landers earthquakes from San Gabriel E Grand Av station

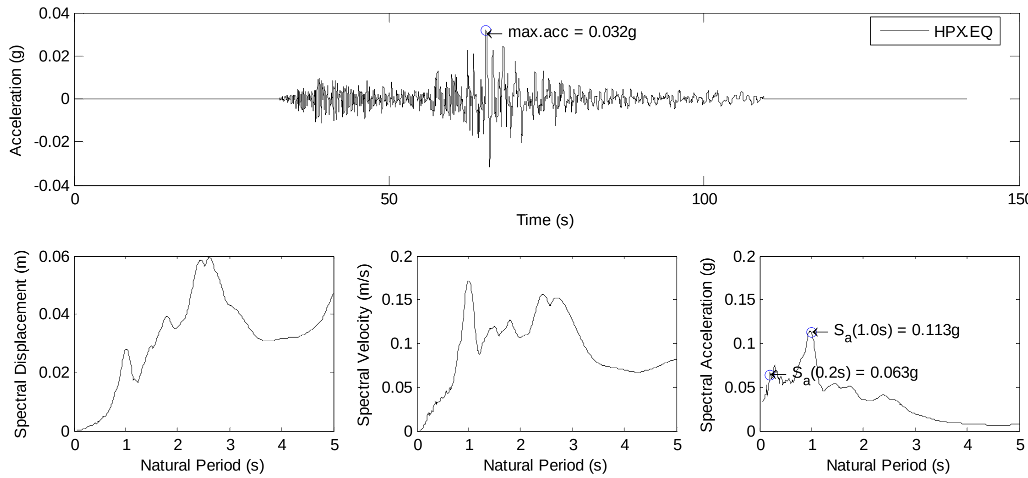

Figure 4-28 Acceleration time history and response spectra of Hector Mine earthquakes from Pacoima Kagel Canyon Route station

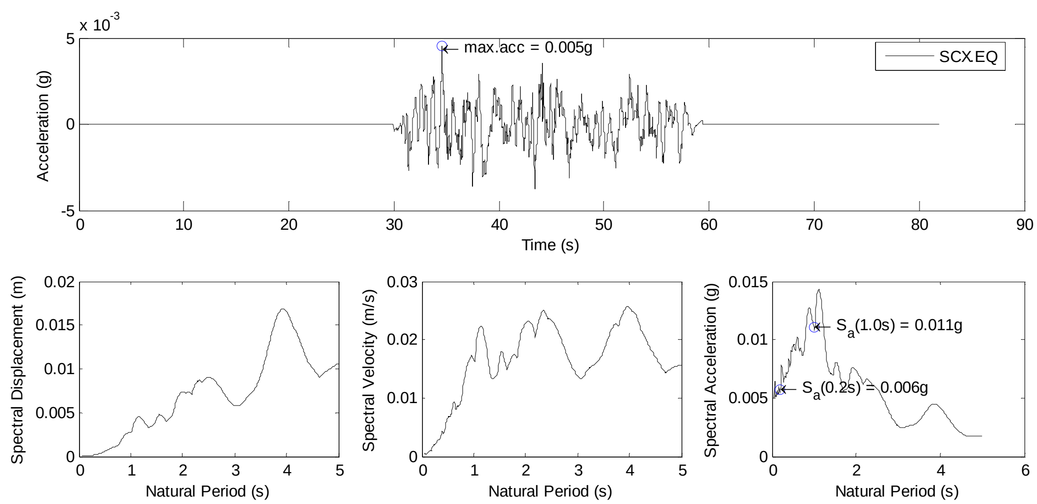

Figure 4-29 Acceleration time history and response spectra of San Fernando earthquakes from Cholame-Shandon Array #2 station

The results of Chiangmai and Wat Chedi Luang sites can be expressed in acceleration time histories and spectral accelerations of output ground motions which are shown in Figures 4-30 to 4-33. The soil amplification factor which is the ratio of the acceleration response between output and input motions can be summarized on Tables 4-5 and 4-6.

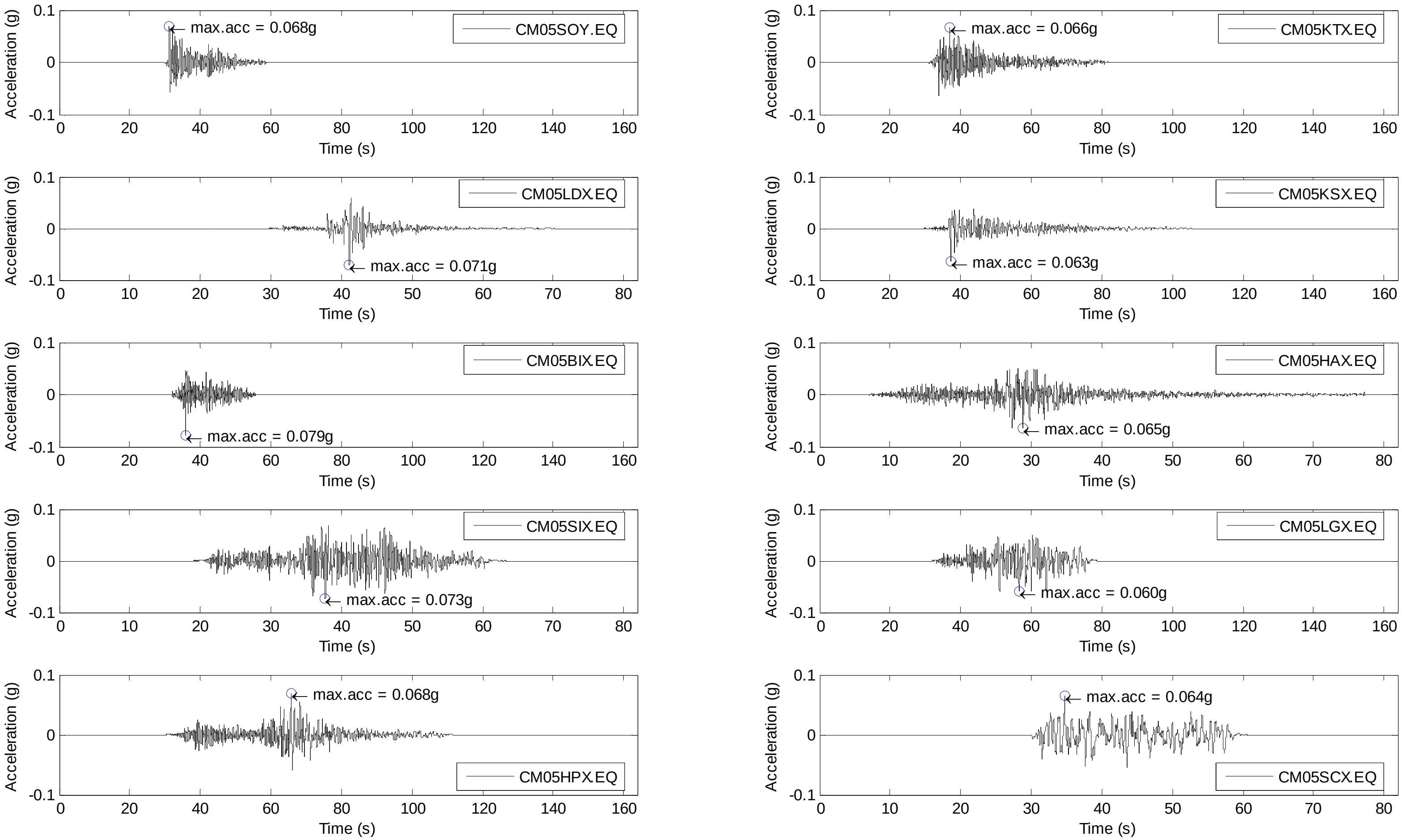

Figure 4-30 Acceleration time histories of output ground motions at Chiangmai University due to 0.05g input ground motions

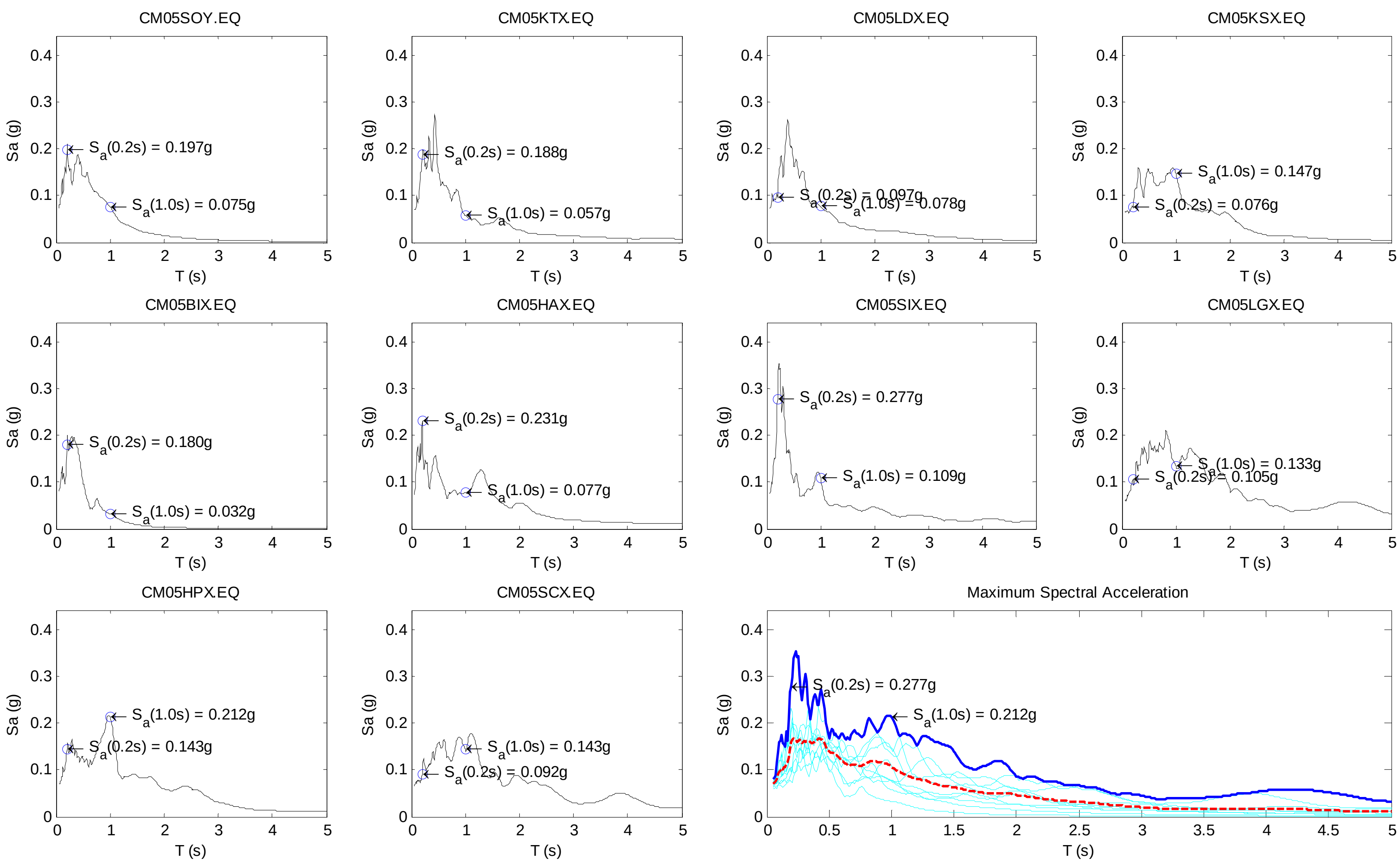

Figure 4-31 Spectral accelerations of output ground motions at Chiangmai University due to 0.05g input ground motions

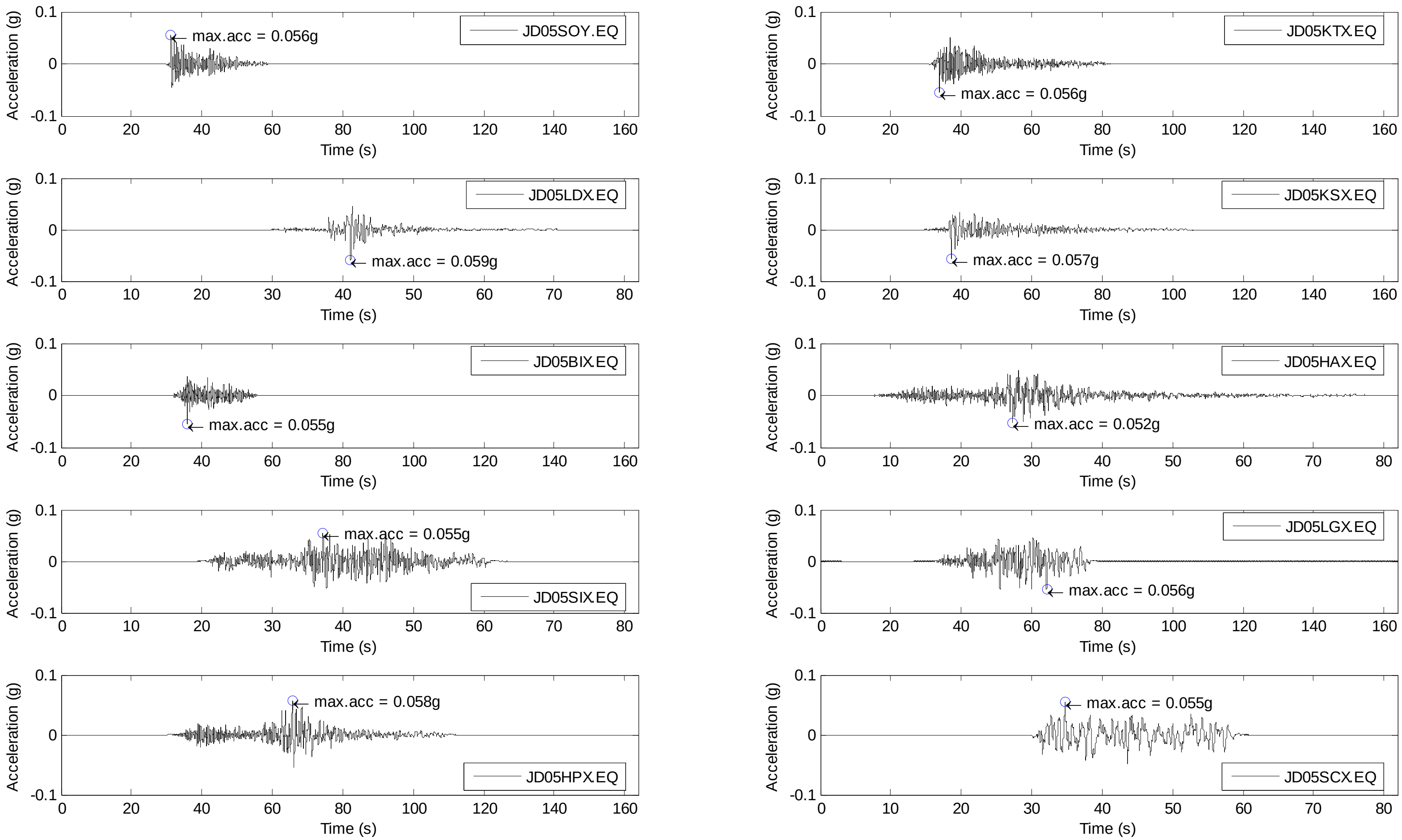

Figure 4-32 Acceleration time histories of output ground motions at Wat Chedi Luang due to 0.05g input ground motions

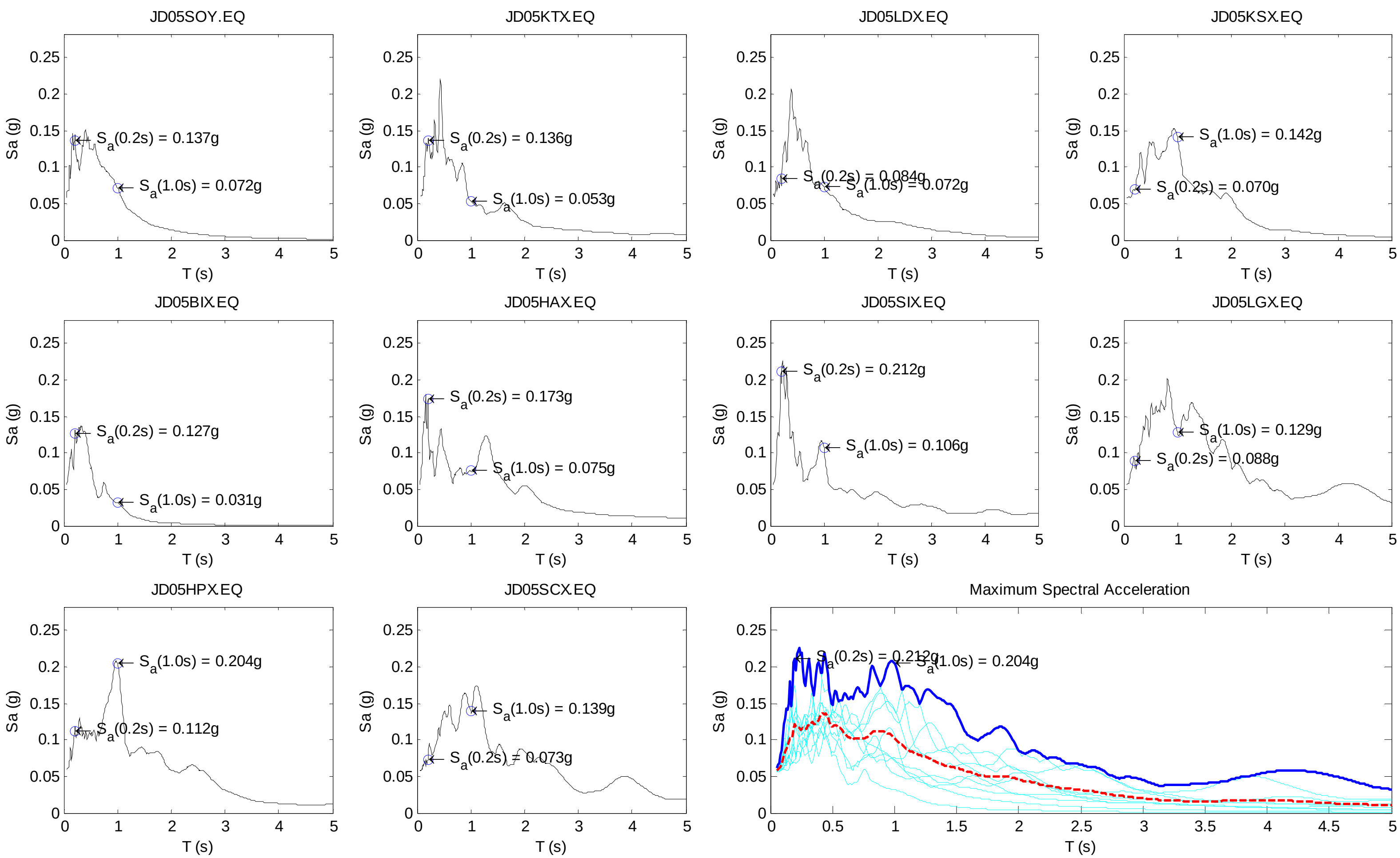

Figure 4-33 Spectral accelerations of output ground motions at Wat Chedi Luang due to 0.05g input ground motions

Table 4-5 Soil amplification factor at Chiangmai University due to input motions 0.05g

T (s)	SOY	KTX	LDX	KSX	BIX	HAX	SIX	LGX	HPX	SCX	Av.	Max.
0.0	1.357	1.320	1.412	1.258	1.573	1.296	1.453	1.199	1.365	1.286	**1.352**	**1.573**
0.2	1.612	1.545	1.352	1.233	1.618	1.527	1.469	1.328	1.431	1.447	**1.456**	**1.618**
0.5	1.417	1.521	1.534	1.494	1.641	1.426	1.536	1.451	1.418	1.495	**1.493**	**1.641**
1.0	1.241	1.269	1.272	1.176	1.162	1.126	1.166	1.183	1.187	1.162	**1.194**	**1.272**
1.5	1.157	1.129	1.092	1.076	1.278	1.092	1.072	1.096	1.072	1.060	**1.112**	**1.278**
2.0	1.194	1.090	1.050	1.049	1.279	1.045	1.057	1.049	1.040	1.045	**1.090**	**1.279**
2.5	1.191	1.038	1.055	1.058	1.361	1.032	1.065	1.019	1.028	1.029	**1.087**	**1.361**
3.0	1.210	1.037	1.022	1.037	1.382	1.019	1.006	1.022	1.016	1.022	**1.077**	**1.382**

Table 4-6 Soil amplification factor at Wat Chedi Luang due to input motions 0.05g

T (s)	SOY	KTX	LDX	KSX	BIX	HAX	SIX	LGX	HPX	SCX	Av.	Max.
0.0	1.124	1.123	1.184	1.141	1.090	1.035	1.094	1.113	1.150	1.108	**1.116**	**1.184**
0.2	1.117	1.115	1.168	1.136	1.145	1.147	1.127	1.112	1.121	1.144	**1.133**	**1.168**
0.5	1.253	1.291	1.293	1.301	1.361	1.218	1.299	1.293	1.233	1.309	**1.285**	**1.361**
1.0	1.186	1.182	1.188	1.137	1.126	1.105	1.139	1.143	1.142	1.129	**1.148**	**1.188**
1.5	1.115	1.090	1.063	1.062	1.185	1.078	1.060	1.078	1.059	1.048	**1.084**	**1.185**
2.0	1.139	1.061	1.036	1.041	1.181	1.035	1.044	1.040	1.032	1.038	**1.065**	**1.181**
2.5	1.139	1.026	1.043	1.044	1.232	1.027	1.039	1.016	1.023	1.024	**1.061**	**1.232**
3.0	1.151	1.024	1.018	1.028	1.241	1.012	1.008	1.018	1.012	1.018	**1.053**	**1.241**

The data of 33 boreholes which consist of depths, unit weights, soil classifications, plastic indexes, SPT N-values and undrained shear strengths were collected from the Department of Public Work and Town & Country Planning [http://www.dpt.go.th/soil/]. The SPT N-values and undrained shear strengths were converted to shear wave velocities by Equations (4-20) to (4-22). The locations and the soil amplification factor of 33 boreholes can be shown in Figures 4-34 to 4-37.

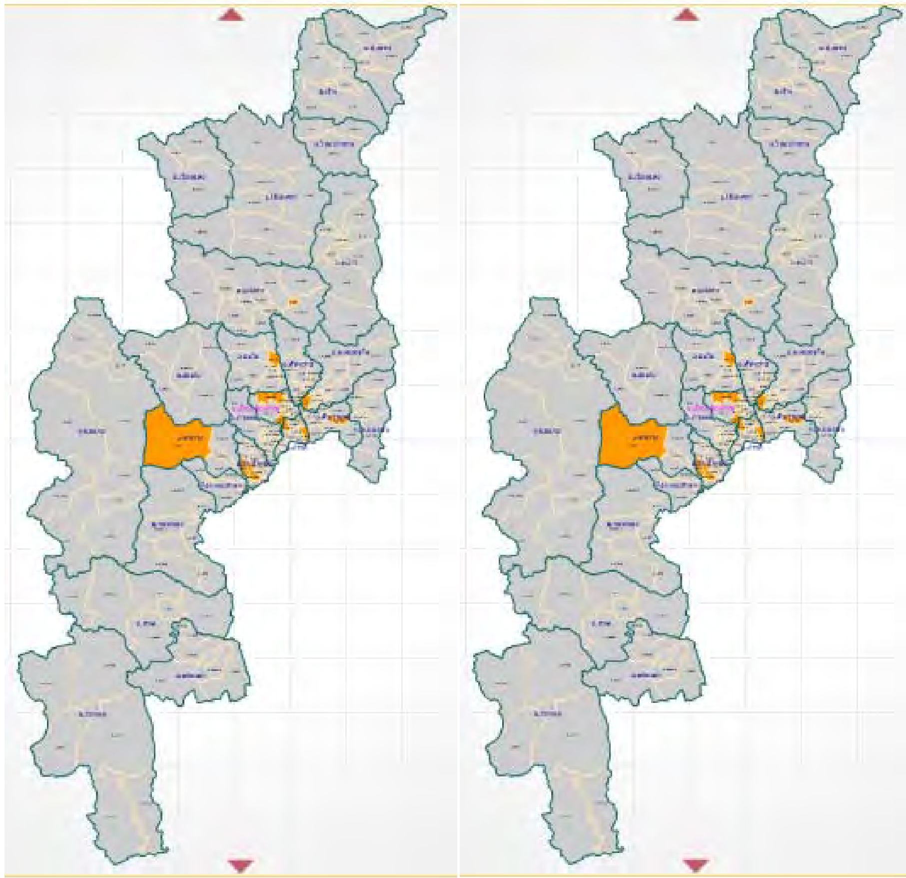

(a) (b)

Figure 4-34 Locations and soil amplification factors of PGA in Chiangmai
(a) Locations (b) Soil amplification factors of PGA

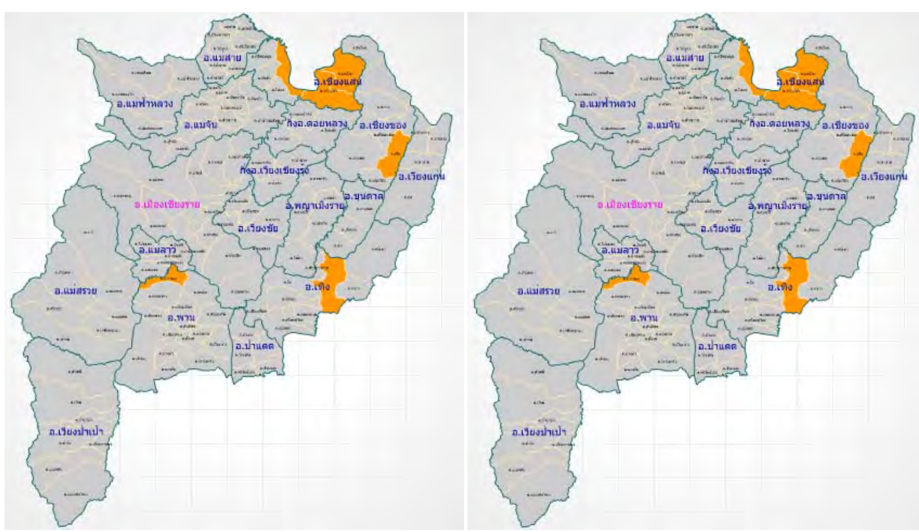

(a) (b)

Figure 4-35 Locations and soil amplification factors of PGA in Chiangrai
(a) Locations (b) Soil amplification factors of PGA

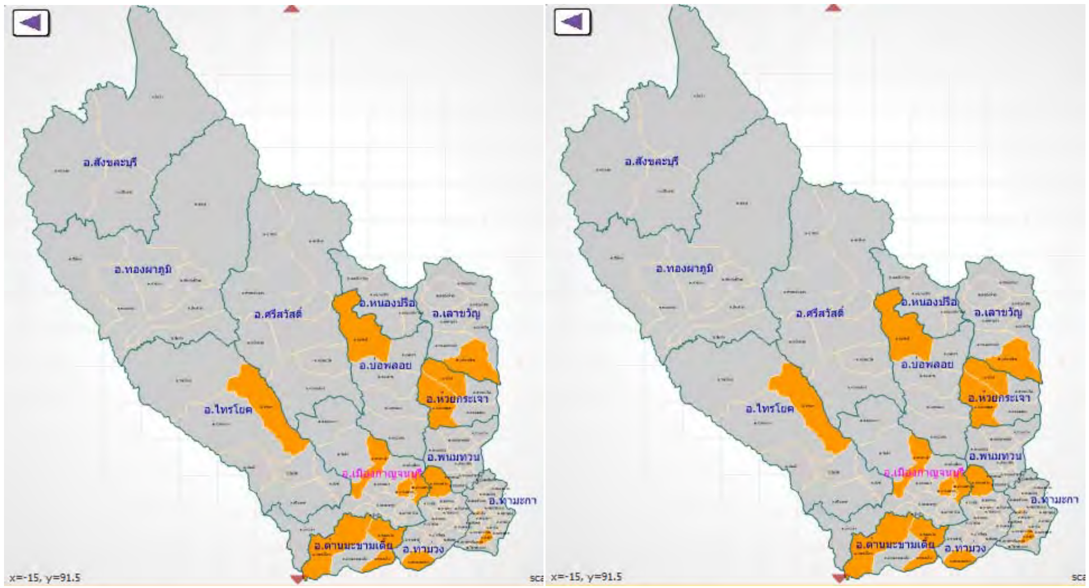

(a) (b)

Figure 4-36 Locations and soil amplification factors of PGA in Kanchanaburi
(a) Locations (b) Soil amplification factors of PGA

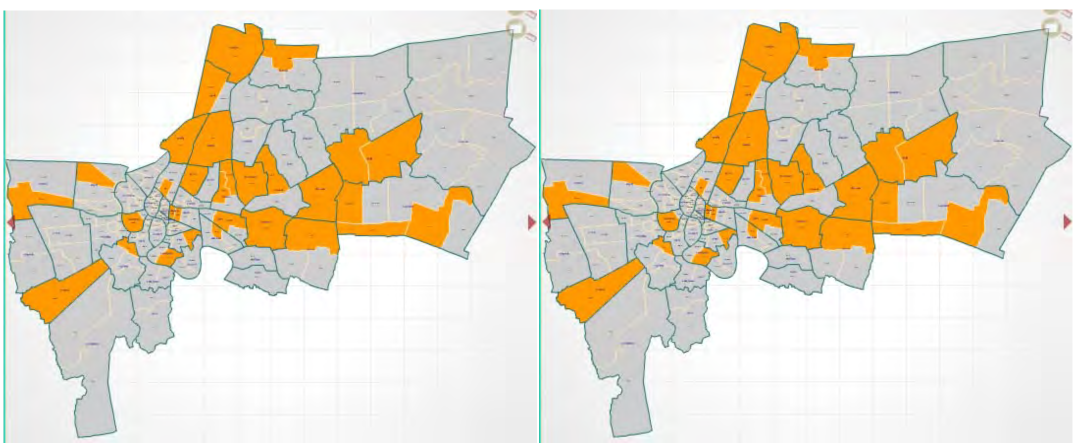

(a) (b)

Figure 4-37 Locations and soil amplification factors of PGA in Bangkok
(a) Locations (b) Soil amplification factors of PGA

Table 4-7 Summary of Vs30 and the amplification factors

Location	Vs30 (m/s)	Class	Amplification factors						
			PGA (T=0.0s)	S_a (T=0.2s)	S_a (T=0.5s)	S_a (T=1.0s)	S_a (T=1.5s)	S_a (T=2.0s)	S_a (T=3.0s)
CM01	302	D	1.115	1.055	1.185	1.178	1.113	1.083	1.065
CM02	395	C	1.344	1.718	1.160	1.047	1.033	1.023	1.022
CM03	314	D	1.270	1.503	1.246	1.067	1.043	1.030	1.027
CM04	278	D	1.462	1.460	1.543	1.142	1.085	1.063	1.071
CM05	324	D	1.127	1.239	1.123	1.038	1.024	1.016	1.015
CM06	309	D	1.090	1.178	1.042	1.010	1.006	1.003	1.004
CM07	402	C	1.750	2.371	1.426	1.101	1.068	1.051	1.079
CM08	575	C	1.008	1.010	1.002	1.001	1.000	1.000	1.001
CM09	342	D	1.146	1.269	1.068	1.022	1.014	1.009	1.009
CM10	249	D	1.685	1.650	1.736	1.167	1.106	1.089	1.112
CR01	306	D	1.196	1.385	1.112	1.034	1.022	1.015	1.015
CR02	341	D	1.223	1.361	1.234	1.066	1.041	1.029	1.026
CR03	308	D	1.415	1.523	1.421	1.106	1.068	1.045	1.059
CR04	294	D	1.259	0.904	2.012	1.275	1.144	1.125	1.122
CR05	280	D	1.456	1.121	2.248	1.284	1.150	1.145	1.147
CR06	274	D	1.589	2.338	1.178	1.050	1.038	1.029	1.029
KN01	181	D	1.471	1.549	1.434	1.117	1.071	1.052	1.055
KN02	330	D	1.447	2.007	1.165	1.048	1.034	1.026	1.025
KN03	417	C	1.146	1.117	1.024	1.008	1.005	1.002	1.003
KN04	428	C	1.175	1.230	1.045	1.015	1.010	1.006	1.007
KN05	323	D	1.010	1.042	1.015	1.001	1.000	0.999	1.000
KN06	484	C	1.011	1.010	1.003	1.001	1.001	1.000	1.001
KN07	280	D	1.629	1.946	1.363	1.099	1.064	1.047	1.047
KN08	385	C	1.076	1.088	1.018	1.006	1.004	1.002	1.002
BK01	129	E	1.686	1.101	1.443	3.307	3.573	2.737	3.028
BK02	142	E	1.112	0.711	1.041	1.762	2.519	2.803	3.618
BK03	149	E	1.244	0.930	0.977	1.711	3.381	3.062	2.452
BK04	130	E	1.598	1.019	1.430	2.744	4.356	3.302	2.479
BK05	150	E	1.837	1.226	1.636	3.746	3.006	2.199	2.010
BK06	164	E	1.955	1.261	2.073	3.440	2.710	2.066	1.918
BK07	181	D	1.969	1.612	2.663	2.636	1.988	1.790	2.491
BK08	135	E	1.484	0.928	1.449	2.760	3.419	3.151	3.454
BK09	138	E	1.149	0.805	0.888	2.197	2.945	2.856	3.222

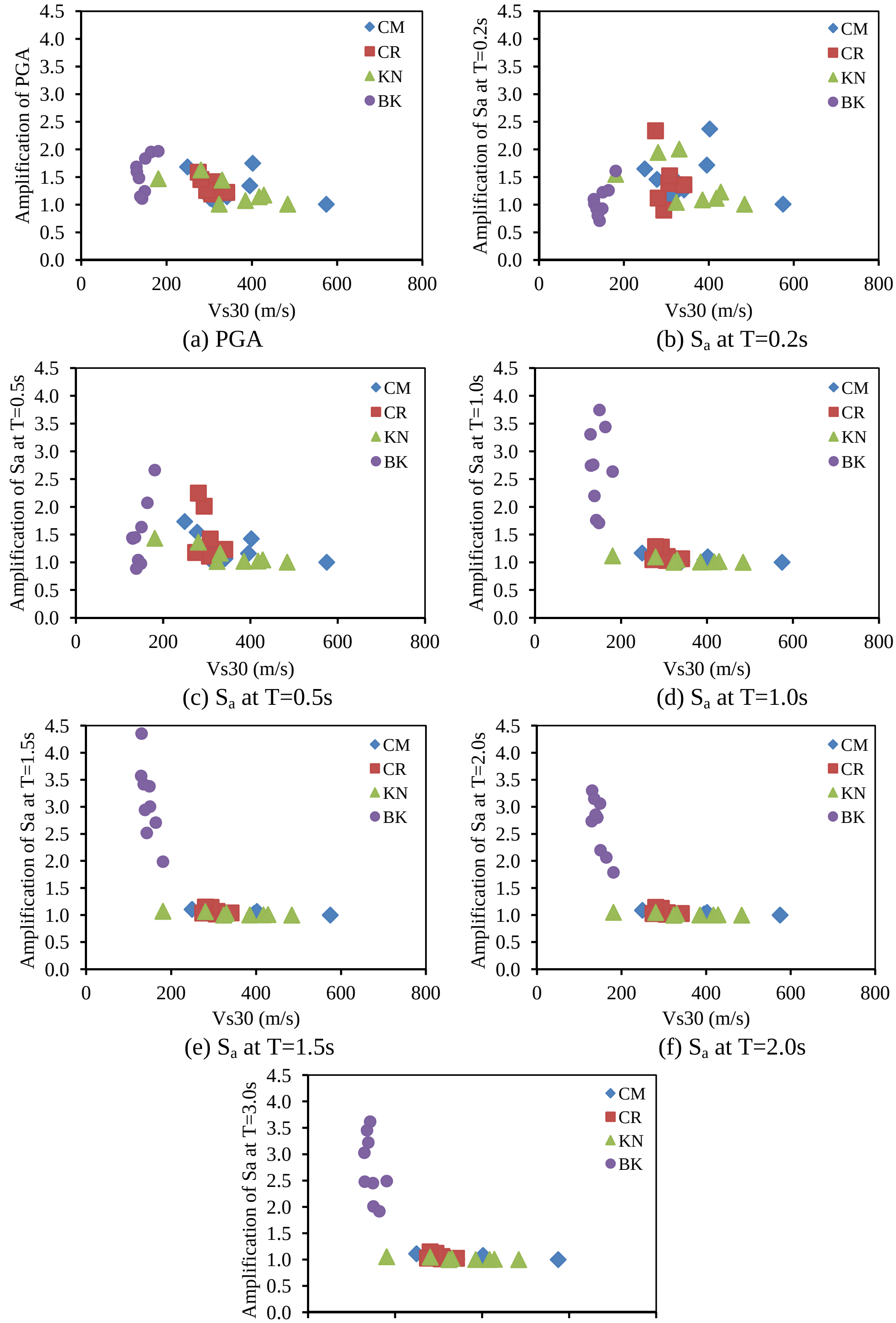

(a) PGA

(b) S_a at T=0.2s

(c) S_a at T=0.5s

(d) S_a at T=1.0s

(e) S_a at T=1.5s

(f) S_a at T=2.0s

(f) S_a at T=3.0s

Figure 4-38 The relation between soil amplification factors and Vs30

From Figure 4-38, it seems that the trend of soil amplification factors of PGA reduce with the increase of Vs30 and those factors are as large as 2.0 at locations where Vs30 is less than 200 m/s. The soil amplification factors of spectral accelerations at the periods less than 1.0 s can reach to 2.5 at locations where Vs30 is less than 400 m/s.

CHAPTER V

BI-DIRECTIONAL RESPONSE SPECTRA

5.1 Introduction

Under strong ground motions, structures are excited horizontally and vertically in a complicated manner. Oliva and Clough (1987) conducted shaking table tests to investigate bi-directional inelastic response of a reinforced concrete frame and found that column strength was reduced and the response demand was increased comparing with uni-directional response. Wong et al. (1993) studied the bi-axial behavior of circular reinforced concrete columns under different displacement orbits and found that the columns under bi-axial bending had more reduction of strength and stiffness than those under uni-axial bending. In summary, the strength of structures under bi-directional excitations is less than that under uni-directional excitation.

Analytical models for predicting bi-directional response have been developed and verified by experiments on sub-assemblages and frame structures. Takizawa and Aoyama (1976) proposed a hysteretic model with yield criteria to account for bi-axial bending. Zeris and Mahin (1991) verified the fiber-element model for determining bi-directional response by comparing the analytical results with experimental results from preceding studies. A multi-spring model was also applied in the correlation of actual and simulated results by Magliulo and Ramasco (2007). Responses of symmetrical and asymmetrical buildings under multi-component ground motions have been investigated extensively by numerical analyses (Magliulo and Ramasco, 2007), (Stefano et al., 1998), (Riddell and Santa-Maria, 1999), (Perus and Fajfar, 2005). Since the analyses were limited to certain structures, the results from various researchers were not conclusive on how much bi-directional excitation amplified structural responses.

In predicting seismic demands, the multi-component excitation is simplified and taken into account in seismic design by applying orthogonal components of strong motions along principal axes of structures independently and combining response by certain combination rules. The combination rules were extensively studied by many researchers.

Wilson et al. (1981) compared the Complete Quadratic Combination (CQC) method with the square-root-of-sum-of-square (SRSS) method. They suggested that the CQC method which reduced errors by considering the cross-correlation term had the advantage over the SRSS method.

Smeby and Der Kiureghian (1985) developed the modal combination rules by using the concepts of stationary random vibration and the model by Penzien and Watabe (1975) for the multi-component earthquake excitation.

Lopez and Torres (1997) determined the critical angles of ground motion incidence and the critical structural response by varying the spectral ratio for the horizontal components of ground motions. Lopez et al (2001) determined the critical response by the CQC3 combination rule considering all seismic incident angles.

Manun and Der Kiureghian (1998) compared the responses from CQC3, SRSS, 30% and 40% rules. According to Clough and Penzien (1993, page 658), the responses from 30% and 40% rules were calculated with $\gamma = 0.85$. They found that the responses from 40% rule were over than those from SRSS and CQC3 with $\gamma = 1.0$, but the responses from 30% rule are varied in the CQC3 and SRSS responses with γ over than 0.85. The responses from CQC3 with $\gamma = 1.0$ are equal to the responses from SRSS which are not depend on the different angle of the structure axes.

Fujita and Takewaki (2010) used the extended Penzien-Watabe model to determine the critical correlation of bi-directional ground motions. Their numerical analysis demonstrated that the response from the critically-correlated case was about 40% larger than that from the uncorrelated case.

The generalization of the effect of multi-directional excitations on structures was accomplished by applying the random vibration theory (Lopez and Torres, 1997), (Menun and Der Kiureghian, 1998), (Lopez et al., 2000), (Hernandez and Lopez, 2003). From the correlation or non-correlation of response in orthogonal directions, the maximum response and critical angle of incidence were derived. The studies showed the underestimation and overestimation of the combination rules used in seismic design codes. Heredia-Zavoni and Machicao-Barrionuevo (2004) found that soil conditions significantly affected the bi-directional response.

The effect of multi-directional excitations on structures has been generally investigated by applying the random vibration theory. By considering the correlation or non-correlation of response in orthogonal directions, the maximum response and critical angle of incidence were derived.

So far, bi-directional responses have not been investigated for a wide range of natural periods of structures in orthogonal directions, critical angles of incidence, and strong ground motions. The research was conducted to address the issues and the bi-directional pseudo-acceleration response spectrum was proposed.

5.2 Analytical Model

Buildings or bridges under bi-directional excitations can be modeled as a two-degree-of-freedom system as shown in Figure 5-1.

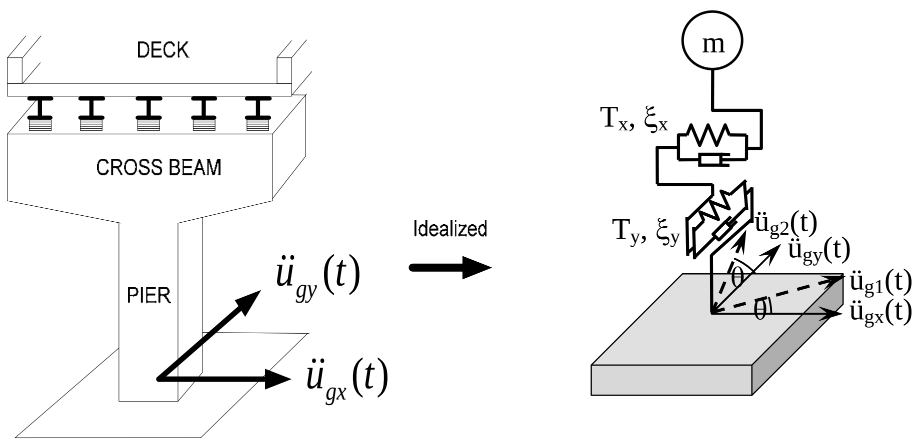

Figure 5-1 Idealized model for analysis

The system has translational degrees-of-freedom in two horizontal orthogonal directions which are usually the principal axes of a structure. Torsional movement is neglected in this model. And the response is assumed to be in the linear range of structural materials. The natural periods in the x- and y- axes are denoted as T_x and T_y, respectively. The damping ratios are denoted as ξ_x and ξ_y for the x- and y- axes, respectively. The system is subjected to two components of ground motions in the x- and y- axes. The angle of incidence of a strong ground motion is applied with respect to the x-axis at an angle of θ. Two components of a ground motion record can be transformed to the principal axes of the system by using the transformation expressed as

$$\begin{Bmatrix} \ddot{u}_{gx}(t) \\ \ddot{u}_{gy}(t) \end{Bmatrix} = \begin{bmatrix} \cos\theta & -\sin\theta \\ \sin\theta & \cos\theta \end{bmatrix} \begin{Bmatrix} \ddot{u}_{g1}(t) \\ \ddot{u}_{g2}(t) \end{Bmatrix} \tag{5-1}$$

where $\ddot{u}_{gx}(t)$ is the component of a ground motion transformed to the x-axis of the structure, $\ddot{u}_{gy}(t)$ is the component of a ground motion transformed to the y-axis of the structure, $\ddot{u}_{g1}(t)$ is a component of a ground motion with an angle of incidence equal to θ measured counter-clockwise from the x-axis of the structure, $\ddot{u}_{g2}(t)$ is another orthogonal component of a ground motion.

Since the system is linear and uncoupled between both axes, dynamic responses of in each axis can be expressed independently by the following equation of motion:

$$\begin{Bmatrix} \ddot{u}_x(t) \\ \ddot{u}_y(t) \end{Bmatrix} + \begin{bmatrix} \dfrac{4\pi\xi_x}{T_x} & 0 \\ 0 & \dfrac{4\pi\xi_y}{T_y} \end{bmatrix} \begin{Bmatrix} \dot{u}_x(t) \\ \dot{u}_y(t) \end{Bmatrix} + \begin{bmatrix} \dfrac{4\pi^2}{T_x^2} & 0 \\ 0 & \dfrac{4\pi^2}{T_y^2} \end{bmatrix} \begin{Bmatrix} u_x(t) \\ u_y(t) \end{Bmatrix} = -\begin{Bmatrix} \ddot{u}_{gx}(t) \\ \ddot{u}_{gy}(t) \end{Bmatrix} \tag{5-2}$$

5.3 Parameters in Analysis

To investigate the effect of bi-directional excitations on structural response, it is necessary to consider a wide range of parameters that represent typical structural properties. The natural period of the system in each principal axis is varied from 0.05 s to 4 s with an increment of 0.05 s to cover typical ranges of natural periods of structures. The damping ratio is assumed as 0.05 which is typical for reinforced-concrete structures.

Eighty-six ground motion records obtained from PEER Strong Motion Database were used in the analysis. Ground motions were recorded at stations located on various site conditions during earthquake events with epicentral distances not over than 223 km and magnitudes ranging from 5.2 to 7.6 which are expressed in Figure 5-2. Table 5-1 lists the ground motion records used in the study. Average shear wave velocities of upper 30-m soil layers denoted as Vs30 are available at all stations which are plotted with magnitudes in Figure 5-3. Site conditions of stations can be classified into various soil classes according to the NEHRP recommendations.

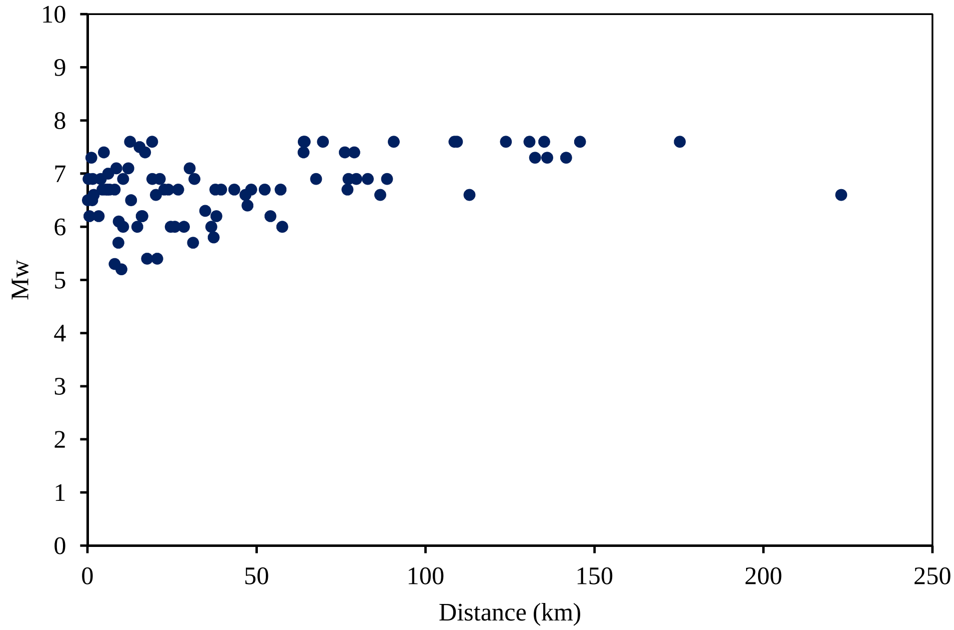

Figure 5-2 The distribution between Mw and Distance of selected ground motions

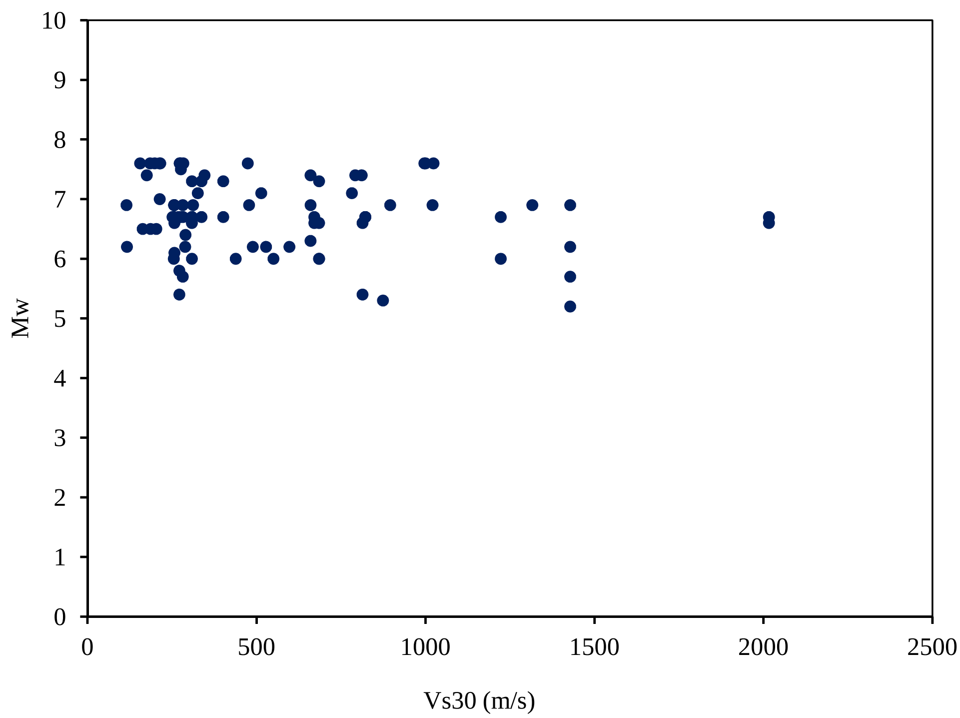

Figure 5-3 The distribution between Mw and Vs30 of selected ground motions

Table 5-1 Lists of the selected ground motions

No.	Earthquake	Mw	Station	Epicentral distance (km)	Vs30 (m/s)
1	San Fernando 1971/02/09 14:00	6.6	279 Pacoima Dam	1.8	2016.1
2	Northridge 1994/01/17 12:31	6.7	24207 Pacoima Dam (upper left)	8.0	2016.1
3	Kocaeli, Turkey 1999/08/17	7.4	Izmit	4.8	811
4	San Francisco 1957/03/22 19:44	5.3	1117 Golden Gate Park	8.0	874.0
5	Coyote Lake 1979/08/06 17:05	5.7	47379 Gilroy Array #1	9.1	1428
6	Hollister 1974/11/28 23:01	5.2	47379 Gilroy Array #1	10.0	1428
7	Loma Prieta 1989/10/18 00:05	6.9	47379 Gilroy Array #1	10.5	1428
8	Morgan Hill 1984/04/24 21:15	6.2	47379 Gilroy Array #1	16.2	1428
9	Kocaeli, Turkey 1999/08/17	7.4	Gebze	17.0	792
10	Lytle Creek 1970/09/12 14:30	5.4	111 Cedar Springs, Allen Ranch	20.6	813.5
11	Northridge 1994/01/17 12:31	6.7	90017 LA - Wonderland Ave	22.7	1222.5
12	Whittier Narrows 1987/10/01 14:42	6.0	90017 LA - Wonderland Ave	24.6	1222.5
13	Morgan Hill 1984/04/24 21:15	6.2	57217 Coyote Lake Dam (SW Abut)	0.5	597.1
14	Landers 1992/06/28 11:58	7.3	24 Lucerne	1.1	684.9
15	Morgan Hill 1984/04/24 21:15	6.2	1652 Anderson Dam (Downstream)	3.3	488.8
16	Loma Prieta 1989/10/18 00:05	6.9	16 LGPC	3.9	477.7
17	Cape Mendocino 1992/04/25 18:06	7.1	89005 Cape Mendocino	8.5	513.7
18	Whittier Narrows 1987/10/01 14:42	6.0	24461 Alhambra, Fremont Sch	14.7	550.0
19	Parkfield 1966/06/28 04:26	6.2	1438 Temblor pre-1969	16.0	527.9
20	San Fernando 1971/02/09 14:00	6.6	127 Lake Hughes #9	20.2	670.8
21	N. Palm Springs 1986/07/08 09:20	6.0	12206 Silent Valley - Poppet F	25.8	684.9
22	Northridge 1994/01/17 12:31	6.7	127 Lake Hughes #9	26.8	670.8
23	Imperial Valley 1979/10/15 23:16	6.5	5155 EC Meloland Overpass FF	0.1	186.2
24	Kobe 1995/01/16 20:46	6.9	0 Takarazuka	0.3	312.0
25	Imperial Valley 1979/10/15 23:16	6.5	942 El Centro Array #6	1.4	203.2
26	Kobe 1995/01/16 20:46	6.9	0 Takatori	1.5	256.0
27	Erzincan, Turkey 1992/03/13	6.7	95 Erzincan	4.4	274.5
28	Northridge 1994/01/17 12:31	6.7	74 Sylmar - Converter Sta	5.4	251.2
29	Northridge 1994/01/17 12:31	6.7	24279 Newhall - Fire Sta	5.9	269.1
30	Imperial Valley 1940/05/19 04:37	7.0	117 El Centro Array #9	6.1	213.4
31	Northridge 1994/01/17 12:31	6.7	77 Rinaldi Receiving Sta	6.5	282.3
32	Parkfield 1966/06/28 04:26	6.1	1015 Cholame #8	9.2	256.8
33	Whittier Narrows 1987/10/01 14:42	6.0	90071 West Covina - S Orange	10.5	308.6
34	Duzce, Turkey 1999/11/12	7.1	Bolu	12.0	326.0
35	Chi-Chi, Taiwan 1999/09/20	7.6	TCU110	12.6	212.7
36	Kocaeli, Turkey 1999/08/17	7.5	Duzce	15.4	276.0
37	Livermore 1980/01/27 02:33	5.4	57187 San Ramon - Eastman Kodak	17.6	271.4
38	Chi-Chi, Taiwan 1999/09/20	7.6	CHY025	19.1	277.5
39	Kobe 1995/01/16 20:46	6.9	0 Shin-Osaka	19.2	256.0
40	Kobe 1995/01/16 20:46	6.9	0 OSAJ	21.4	256.0
41	Northridge 1994/01/17 12:31	6.7	90016 LA - N Faring Rd	23.9	255.0
42	Whittier Narrows 1987/10/01 14:42	6.0	90016 LA - N Faring Rd	28.5	255.0
43	Imperial Valley 1979/10/15 23:16	6.5	5057 El Centro Array #3	12.9	162.9
44	Chi-Chi, Taiwan 1999/09/20	7.6	ILA063	69.6	996.5
45	Chi-Chi, Taiwan 1999/09/20	7.6	TAP065	130.8	1023.5
46	Chi-Chi, Taiwan 1999/09/20	7.6	TCU085	64.0	999.7
47	Loma Prieta 1989/10/18 00:05	6.9	58338 Piedmont Jr High	77.2	895.4
48	Loma Prieta 1989/10/18 00:05	6.9	58043 Point Bonita	88.6	1315.9
49	Loma Prieta 1989/10/18 00:05	6.9	58539 So. San Francisco, Sierra Pt.	67.6	1020.6
50	Northridge 1994/01/17 12:31	6.7	24399 Mt Wilson - CIT Seis Sta	37.8	821.7
51	Northridge 1994/01/17 12:31	6.7	24310 Antelope Buttes	48.4	821.7
52	Northridge 1994/01/17 12:31	6.7	24644 Sandberg - Bald Mtn	43.4	821.7

Table 5-1 Lists of the selected ground motions

No.	Earthquake	Mw	Station	Epicentral distance (km)	Vs30 (m/s)
53	San Fernando 1971/02/09 14:00	6.6	111 Cedar Springs, Allen Ranch	86.6	813.5
54	Chi-Chi, Taiwan 1999/09/20	7.6	TTN016	135.1	473.9
55	Duzce, Turkey 1999/11/12	7.1	1060 Lamont 1060	30.2	782.0
56	Kocaeli, Turkey 1999/08/17	7.4	Maslak	63.9	659.6
57	Landers 1992/06/28 11:58	7.3	90019 San Gabriel - E Grand Av	141.6	401.4
58	Loma Prieta 1989/10/18 00:05	6.9	58163 Yerba Buena Island	79.5	659.8
59	N. Palm Springs 1986/07/08 09:20	6.0	13199 Winchester Bergman Ran	57.6	684.9
60	Northridge 1994/01/17 12:31	6.7	90019 San Gabriel - E. Grand Ave.	39.5	401.4
61	San Fernando 1971/02/09 14:00	6.6	1035 Isabella Dam (Aux Abut)	113.0	684.9
62	Santa Barbara 1978/08/13	6.0	106 Cachuma Dam Toe	36.6	438.3
63	Victoria, Mexico 1980/06/09 03:28	6.3	6604 Cerro Prieto	34.8	659.6
64	Chi-Chi, Taiwan 1999/09/20	7.6	KAU037	145.7	283.2
65	Chi-Chi, Taiwan 1999/09/20	7.6	KAU081	175.2	272.6
66	Chi-Chi, Taiwan 1999/09/20	7.6	TTN012	90.6	272.6
67	Chi-Chi, Taiwan 1999/09/20	7.6	CHY012	64.2	198.4
68	Chi-Chi, Taiwan 1999/09/20	7.6	KAU073	123.8	215.0
69	Chi-Chi, Taiwan 1999/09/20	7.6	TAP006	109.3	184.8
70	Coalinga 1983/05/02 23:42	6.4	36227 Parkfield - Cholame 5W	47.3	289.6
71	Coyote Lake 1979/08/06 17:05	5.7	57191 Halls Valley	31.2	281.6
72	Kocaeli, Turkey 1999/08/17	7.4	Cekmece	76.1	346.0
73	Landers 1992/06/28 11:58	7.3	90071 West Covina - S Orange	132.4	308.6
74	Landers 1992/06/28 11:58	7.3	90073 Hacienda Heights - Colima	136.0	337.0
75	Livermore 1980/01/24 19:00	5.8	57063 Tracy - Sewage Treatm Plant	37.3	271.4
76	Loma Prieta 1989/10/18 00:05	6.9	57191 Halls Valley	31.6	281.6
77	Morgan Hill 1984/04/24 21:15	6.2	47125 Capitola	38.1	288.6
78	Northridge 1994/01/17 12:31	6.7	90090 Villa Park - Serrano Ave	76.9	308.6
79	Northridge 1994/01/17 12:31	6.7	90071 West Covina - S. Orange Ave	52.4	308.6
80	Northridge 1994/01/17 12:31	6.7	90073 Hacienda Hts - Colima Rd	57.1	337.0
81	San Fernando 1971/02/09 14:00	6.6	994 Gormon - Oso Pump Plant	46.7	308.4
82	San Fernando 1971/02/09 14:00	6.6	1015 Cholame-Shandon Array #8	223.0	256.8
83	Chi-Chi, Taiwan 1999/09/20	7.6	KAU011	108.6	155.3
84	Loma Prieta 1989/10/18 00:05	6.9	58117 Treasure Island	82.9	115.1
85	Kocaeli, Turkey 1999/08/17	7.4	Ambarli	78.9	175.0
86	Morgan Hill 1984/04/24 21:15	6.2	58375 APEEL 1 - Redwood City	54.1	116.4

5.4 Directivity of Ground Motions

In this study, the ground motions are considered in the horizontal direction. The selected ground motions were collected in the 2 horizontal directions which are perpendicular. An example is provided to illustrate the proposed response spectra. Figure 5-4 shows acceleration time histories and the orbital motion of the ground motion recorded at the Newhall Fire Station during the 1994 Northridge earthquake. The magnitude of the earthquake was 6.7 and the station was located about 6 km from the epicenter. The peak accelerations are 0.58 g and 0.59 g in two orthogonal components.

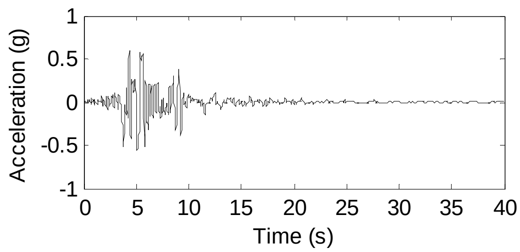

(a) X-component

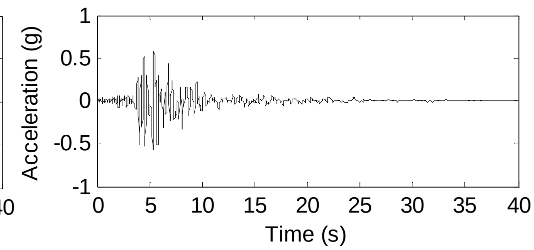

(b) Y-component

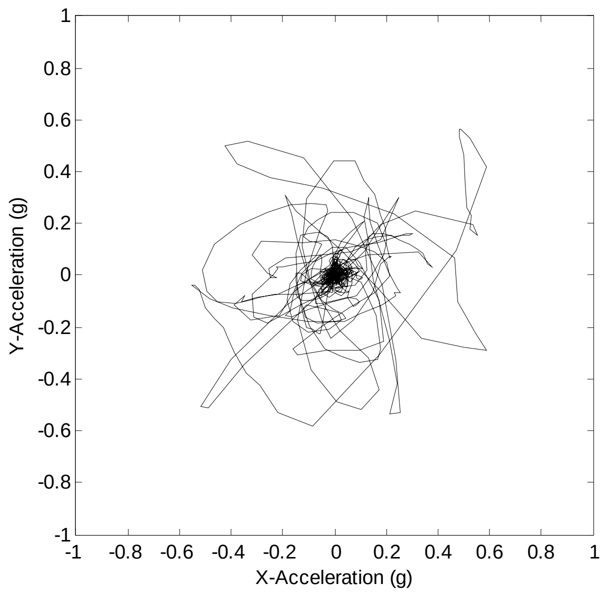

(c) Orbital motion

Figure 5-4 Ground motion at the Newhall Fire Station during the 1994 Northridge earthquake

The major and minor axes of ground motions cannot be known directly from the collected data. Although, the highest intensity of ground motions usually occurs in the perpendicular axis with the fault line, the maximum acceleration or other responses do not need to take place in the same direction.

Penzien and Watabe (1975) determined the principal axes of the 3-dimensional earthquake ground motions by using the orthogonal transformation which is used to determine the principal stress. They found that the principal axes direction of ground motions is quite close to the epicenter direction.

Dimova and Elenas (2002) studied the correlation between the fragility of linear and non-linear systems and seismic intensity parameters. Arias intensity (1970), Housner spectral intensity (1952), Kappos spectral intensity (1990) and Nau/Hall spectral intensity were determined from 20 recorded motions which were not picked in other directions that maybe give the higher responses. Thus, the Arias intensity and the Housner spectral intensity are considered in the several angles of the horizontal axes.

The Arias intensity I is expressed as (Arias, 1970):

$$I = \frac{\pi}{2g}\int_0^\infty \ddot{u}_g(t)^2\,dt \qquad (5\text{-}3)$$

where $\ddot{u}_g(t)$ is the time history of a ground acceleration record.

The Housner spectral intensity SI is expressed as (Housner, 1952):

$$SI = \int_{0.1}^{2.5} S_v(T,\xi)\,dT \qquad (5\text{-}4)$$

where $S_v(T,\xi)$ is the pseudo-velocity spectrum.

The Arias intensities and the Housner spectral intensities of 86 recorded ground motions can be determined from the equation (5-3) and (5-4) respectively. The relation of those is plotted in Figure 5-5.

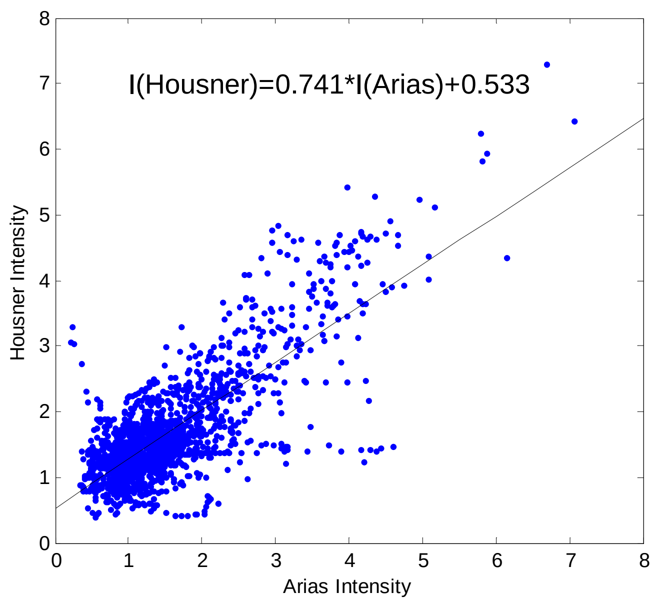

Figure 5-5 The relation between Arias intensity and Housner spectral intensity

The major and minor directions are defined from the largest and smallest intensities respectively taken from the variation of the angle reflects. The results from 86 ground motions are plotted in Figure 5-6. The average of the different major angles is about 2.09^{o} that is shown in Figure 5-7. It seems that the major axes by Arias intensity and Housner spectral intensity are quite near. Therefore, the Arias intensity is applied to determine the major axis of ground motions.

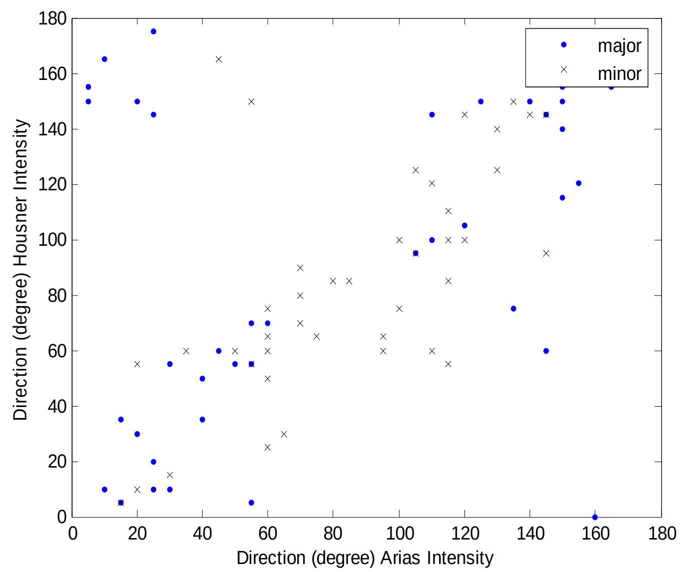

Figure 5-6 The relation of major and minor angles of ground motions between Housner spectral intensity and Arias intensity

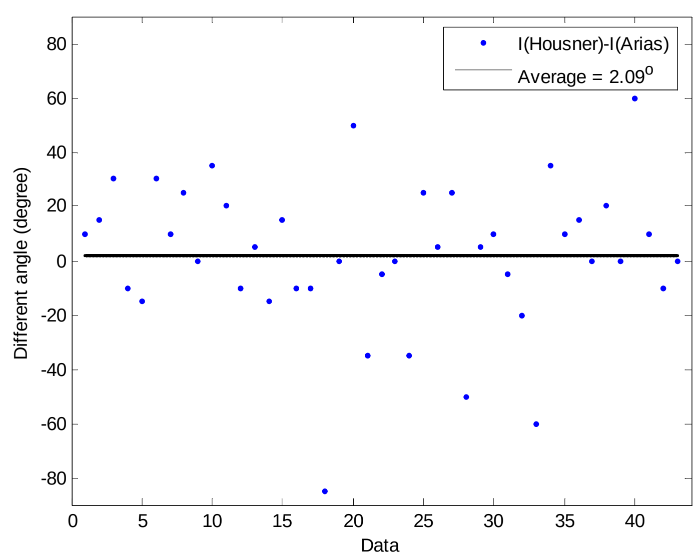

Figure 5-7 The difference of major angle of ground motions between Housner spectral intensity and Arias intensity

Ground motions are usually recorded with respect to the reference axes of strong motion accelerometers. It is common that ground motions recorded with respect to the axes may not result in the largest structural response. To find the axis in which the response is likely to be the largest, the Arias intensity is determined for all directions. Referring to Equation (5-1), the horizontal component with the largest Arias intensity is assigned here as $\ddot{u}_{g1}(t)$ and that perpendicular to the axis with the smallest Arias intensity is $\ddot{u}_{g2}(t)$. The axis with the largest Arias intensity is referred to as the major axis and that perpendicular to the major axis is referred to as the minor axis. The angle of incidence θ shown in Figure 5-1 is varied from 0 to 180 degrees with an interval of 5 degrees, measured counterclockwise from the x-axis of the structure. The variation of the angle reflects the fact that a ground motion may excite a structure at any direction with respect to the principle axes of the structure.

Figure 5-8 shows Arias Intensities computed at various angles measured with respect to the original axis of a strong motion accelerometer. The Arias intensity is largest at an angle of 30 degrees. Figure 5-9 shows acceleration time histories and the orbital motion with respect to the major and minor axes.

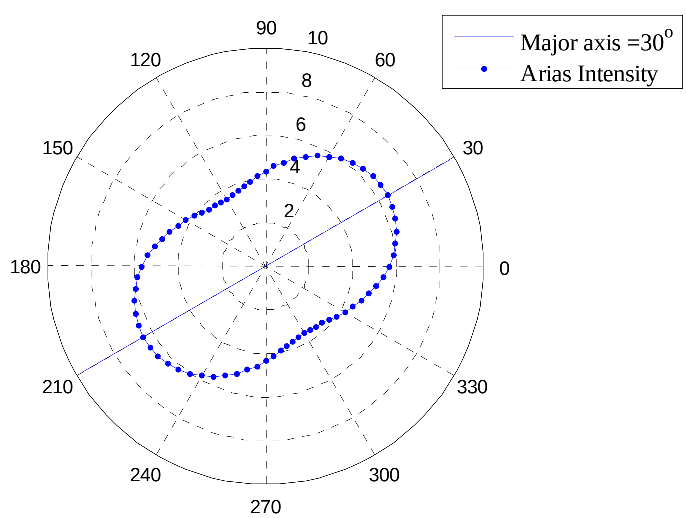

Figure 5-8 Arias Intensities at various angles of the ground motion recorded at the Newhall Fire Station

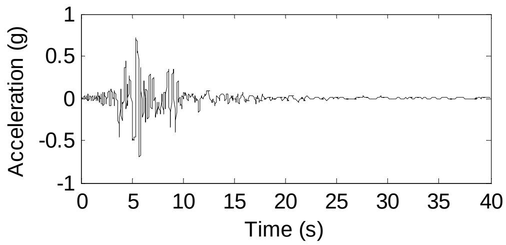

(a) X-component

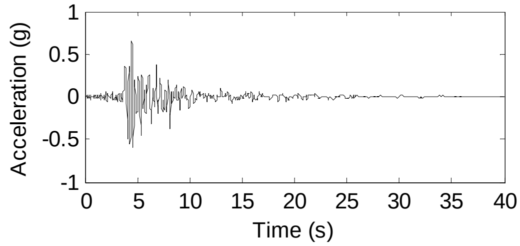

(b) Y-component

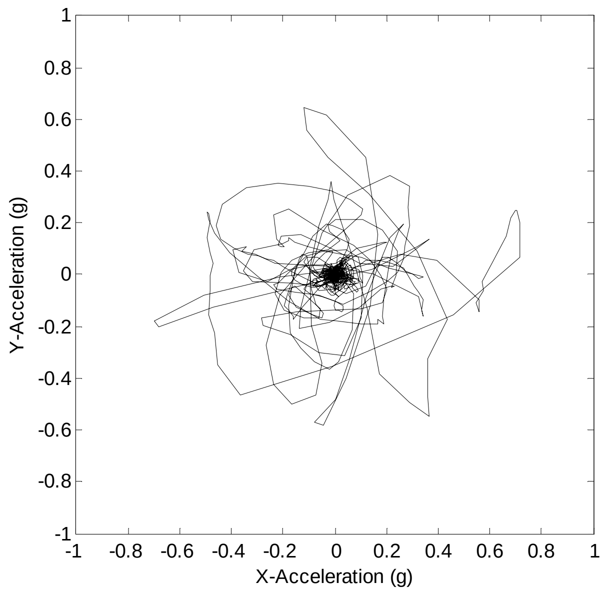

(c) Orbital motion

Figure 5-9 Ground motion after aligning axes

5.5 Definition of Bi-Directional Pseudo Acceleration Respones Spectra

Simultaneous displacements in the x- and y-axes of a structure result in an orbit of motions. The bi-directional pseudo-acceleration in terms of the resultant pseudo-acceleration $a_r(t)$ computed from orbital displacements is defined as

$$a_r(t) = \sqrt{\left(\left(\frac{2\pi}{T_x}\right)^2 u_x(t)\right)^2 + \left(\left(\frac{2\pi}{T_y}\right)^2 u_y(t)\right)^2} \tag{5-5}$$

The response spectrum of bi-directional pseudo-accelerations can be obtained from the maximum resultant pseudo-accelerations for various combinations of T_x, T_y, and θ as

$$S_A^r(T_x, T_y, \theta) = \max_t \left| a_r(t) \right| \tag{5-6}$$

The response spectrum is referred to as “the bi-directional pseudo-acceleration response spectrum.” The bi-directional pseudo-acceleration response spectrum is presented as a three-dimensional graph with the maximum resultant pseudo-acceleration as its vertical axis and the natural periods in the x- and y- axes of the structures as its horizontal axes.

Since the angle of incidence is unpredictable, it is conservative to consider the angle of incidence resulting in the maximum response. The response spectrum obtained from the maximum values considering all angles of incidence can be expressed as

$$\tilde{S}_A^r(T_x, T_y) = \max_\theta \left| S_A^r(T_x, T_y, \theta) \right| \tag{5-7}$$

The conventional acceleration response spectrum is represented in a three-dimensional graph as

$$S_A(T_x, T_y) = \max\left(S_A(T_x), S_A(T_y) \right) \tag{5-8}$$

where $S_A(T_x)$ is the pseudo-acceleration response spectrum of the ground motion in the major axis for various T_x, and $S_A(T_y)$ is the pseudo-acceleration response spectrum of the ground motion in the major axis for various T_y.

The ratio of Equation (5-7) to Equation (5-8) represents the amplification factor when considering the bi-directional excitation. The acceleration ratio response spectrum is expressed as

$$R_A(T_x, T_y) = \frac{\tilde{S}_A^r(T_x, T_y)}{S_A(T_x, T_y)} \tag{5-9}$$

In addition to the bi-directional response, it is equally important to know the direction of the maximum bi-directional pseudo-acceleration with respect to the principal axes of the structure. The direction that the maximum pseudo-acceleration occurs is computed for the structure with a particular combination of natural periods, an angle of incidence, and a ground motion record. The direction is measured counter-clockwise from the x-axis of the system. The direction response spectrum $\alpha(T_x, T_y, \theta)$ is defined as the direction that the maximum pseudo-acceleration occurs. Since the angle of incidence for a certain ground motion is unpredictable, the direction that the maximum pseudo-acceleration occurs should be considered for all possible angles of incidence. The direction response spectrum considering all angles of incidence is denoted as $\tilde{\alpha}(T_x, T_y)$.

5.6 Response Spectra for Typical Ground Motion Records

The acceleration time histories on the major and minor axes correspond to $\ddot{u}_{g1}(t)$ and $\ddot{u}_{g2}(t)$, respectively as written in Equation (5-1). Figure 5-8 shows the relative displacement, pseudo velocity, and pseudo acceleration response spectra at various angles measured relative to the major axis. It is obvious that the response spectra for the major axis are larger than response spectra for other angles at most natural periods while the response spectra for the minor axis are smaller than response spectra for other angles at most natural periods.

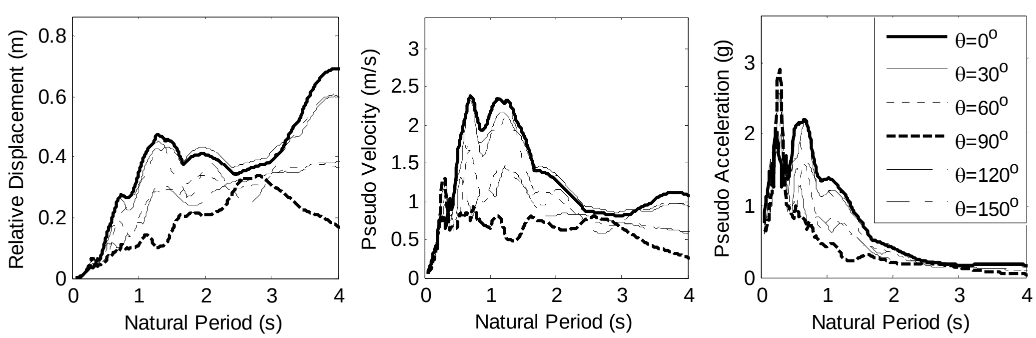

(a) Spectral displacement (b) Spectral velocity (c) Spectral acceleration

Figure 5-10 Response spectra at various angles measured relative to the major axis

The ground motion is applied to a structure with T_x = 2.0 s, T_y = 0.5 s at θ = 0 degree. Figure 5-11 shows the pseudo-acceleration orbit of the structure. The resultant pseudo-acceleration $S_A^r(T_x = 2.0, T_y = 0.5, \theta = 0)$ is 8.6 m/s^2 at an angle of 71.8 degrees while the maximum pseudo-accelerations in the x- and y- axes are 4.0 m/s^2 and 8.2 m/s^2, respectively. It is obvious that the resultant pseudo-acceleration is larger than the pseudo-accelerations in the principal axes of the structure. If the ground motion record is applied to the system with different combinations of natural periods, $S_A^r(T_x, T_y, \theta)$ at θ = 0 degree can be computed as shown in Figure 5-12. It should be noted that $S_A^r(T_x, T_y = 0, \theta = 0)$ is the same as the acceleration response spectrum for the major axis and $S_A^r(T_x = 0, T_y, \theta = 0)$ is the same as the acceleration response spectrum for the minor axis.

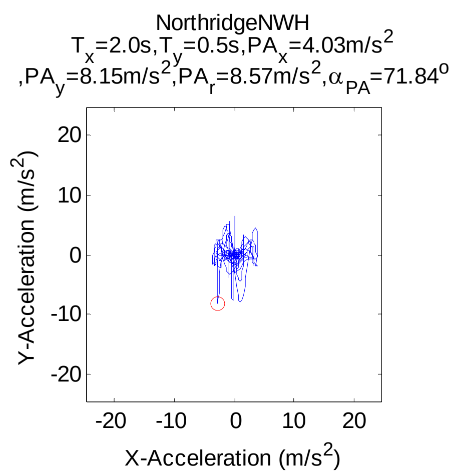

Figure 5-11 Pseudo-acceleration orbit for T_x = 2.0 s, T_y = 0.5 s

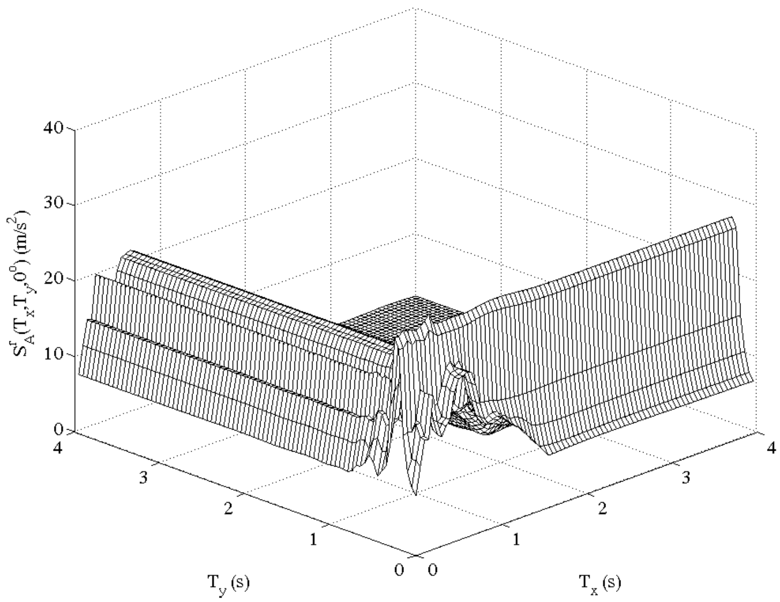

Figure 5-12 Bi-directional acceleration response spectra at 0 degree

Since the structure may be subjected to the ground motion record acting at any angle of incidence, $S^r_A(T_x,T_y,\theta)$ is computed for various angles as shown in Figure 5-13. It is seen that the maximum resultant acceleration for a particular combination of natural periods may occur at different angles of incidence. It is important to note that $S^r_A(T_x,T_y,\theta=0)$ is equal to $S^r_A(T_x,T_y,\theta=180)$. For design purposes, maximum values should be used by considering all angles of incidence. $\tilde{S}^r_A(T_x,T_y)$ for the ground motion record is shown in Figure 5-14. The maximum resultant pseudo-acceleration is about 30 m/s^2. It is important to note that the response spectrum is symmetric about the line $T_x = T_y$. $S_A(T_x,T_y)$ is the maximum value of the uni-directional pseudo-acceleration in x-axis ($S_A(T_x)$) or y-axis ($S_A(T_y)$) that can be shown in Figure 5-15. The response spectrum is also symmetric about the line $T_x = T_y$. $R_A(T_x,T_y)$ which represents the amplification of the maximum resultant pseudo-acceleration is presented in Figure 5-16. The value is larger than one and the maximum value is 1.34 for this ground motion record.

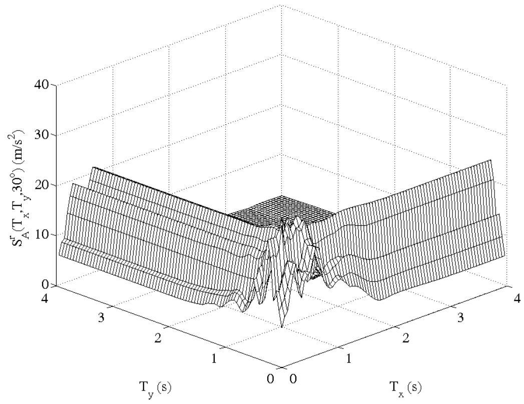

(a) 30 degrees

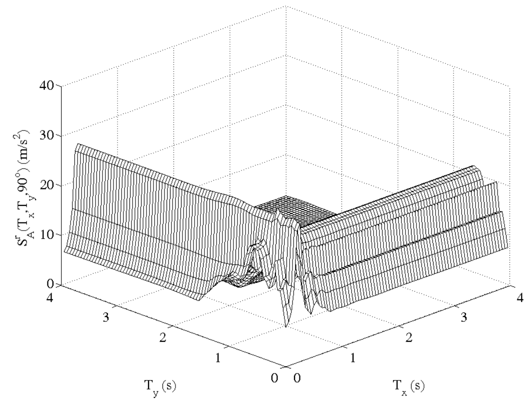

(b) 90 degrees

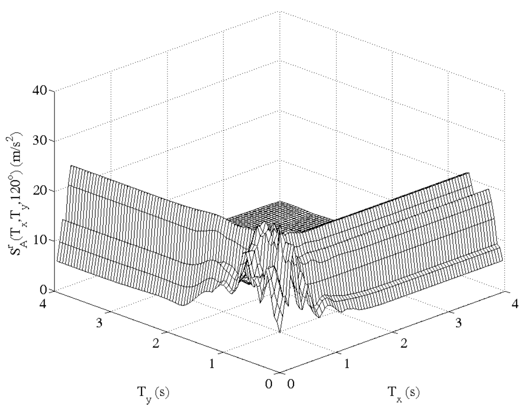

(c) 120 degrees

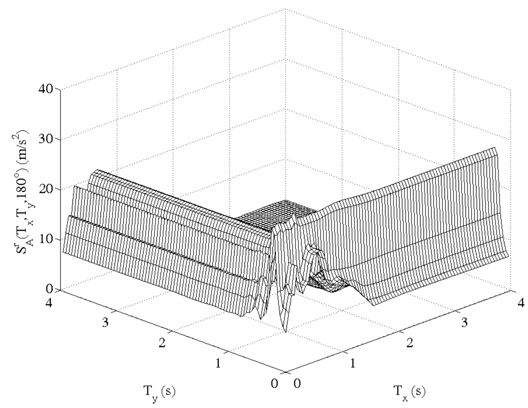

(d) 180 degrees

Figure 5-13 Bi-directional acceleration response spectra at various angles of incidence

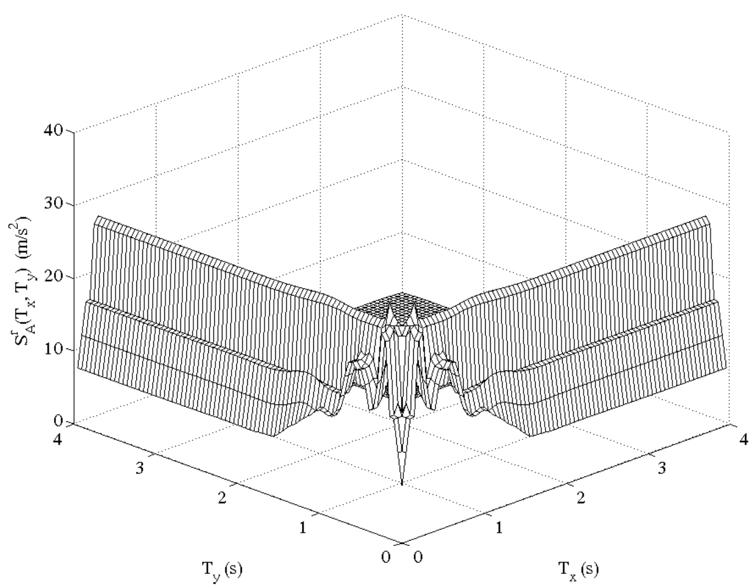

Figure 5-14 $\tilde{S}^r_A(T_x, T_y)$ for Newhall Fire Station record

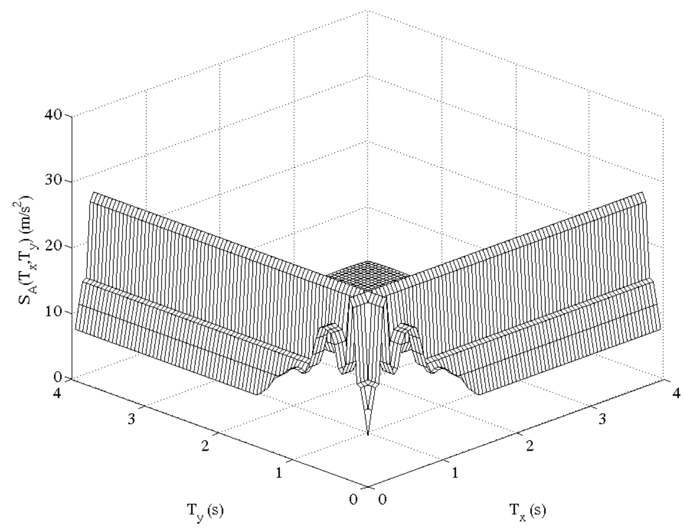

Figure 5-15 $S_A(T_x,T_y)$ for Newhall Fire Station record

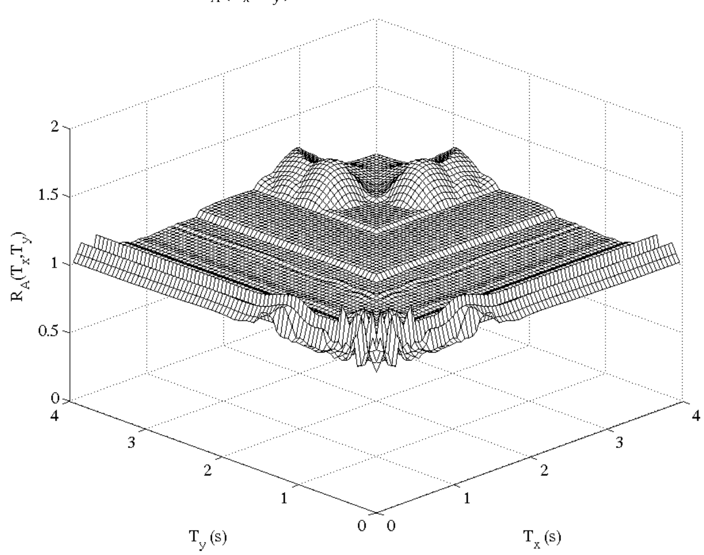

Figure 5-16 $R_A(T_x,T_y)$ for Newhall Fire Station record

The direction response spectra $\alpha(T_x,T_y,\theta)$ for different angles of incidence are illustrated in Figure 5-17. It is important to note that $\alpha(T_x,T_y,\theta=0^\circ)$ is equal to $\alpha(T_x,T_y,\theta=180^\circ)$. Figure 5-18 shows $\tilde{\alpha}(T_x,T_y)$ for this record. It is seen that when T_x is larger than T_y, $\tilde{\alpha}(T_x,T_y)$ is close to 90 degrees. And when T_y is larger than T_x, $\tilde{\alpha}(T_x,T_y)$ is close to 0 degree. It is known that as a natural period increases, a spectral pseudo-acceleration tends to decrease. The axis with a shorter natural period tends to have a larger acceleration. Hence the bi-directional response tends to bias to the direction with the shorter natural period.

Figure 5-19 shows $R_A(T_x, T_y)$ and $\tilde{\alpha}(T_x, T_y)$ of the ground motion recorded at the CHY025 Station during the 1999 Chi-Chi earthquake. The magnitude of the earthquake was 7.6 and the station was located about 19 km from the epicenter. It will be referred hereafter as the CHY025 record. Figure 5-20 shows $R_A(T_x, T_y)$ and $\tilde{\alpha}(T_x, T_y)$ of the ground motion recorded at the 16LGPC Station during the 1989 Loma-Prieta earthquake. The magnitude of the earthquake was 6.9 and the station was located about 4 km from the epicenter. It will be referred hereafter as the 16LGPC record. It is seen that different ground motion records yield the similar trends of response spectra. $R_A(T_x, T_y)$ is larger than one for all combinations of natural periods and the maximum value is about 1.5. As discussed above, the bi-directional response inclines to the direction of the shorter natural period. Figures 5-19 and 5-20 present the typical shapes of response spectra and typical ranges of values.

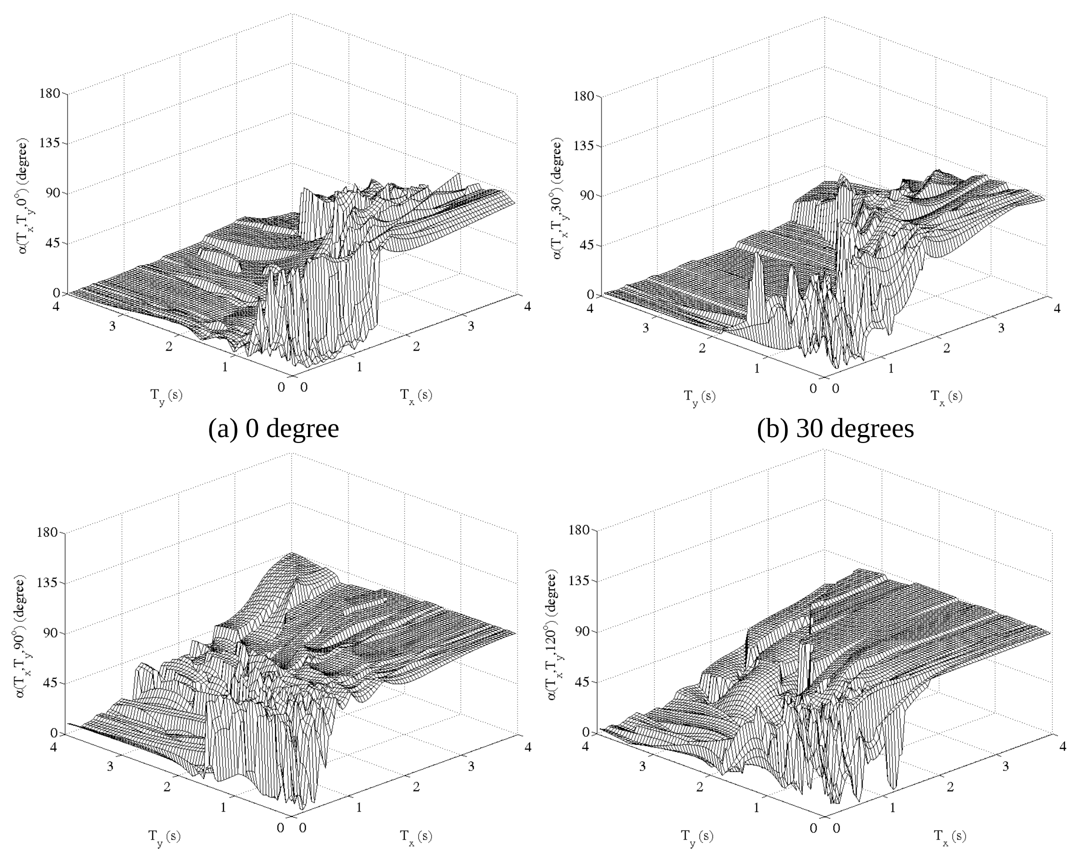

(a) 0 degree (b) 30 degrees

(c) 90 degrees (d) 120 degrees

Figure 5-17 $\alpha(T_x, T_y, \theta)$ for different angles of incidence

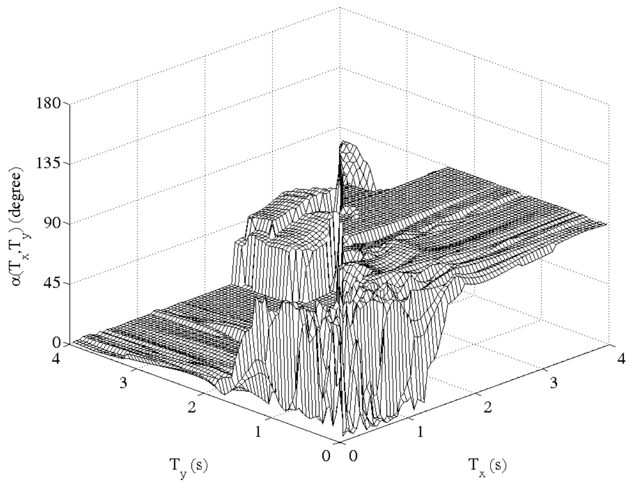

Figure 5-18 $\tilde{\alpha}(T_x, T_y)$ for Newhall Fire Station record

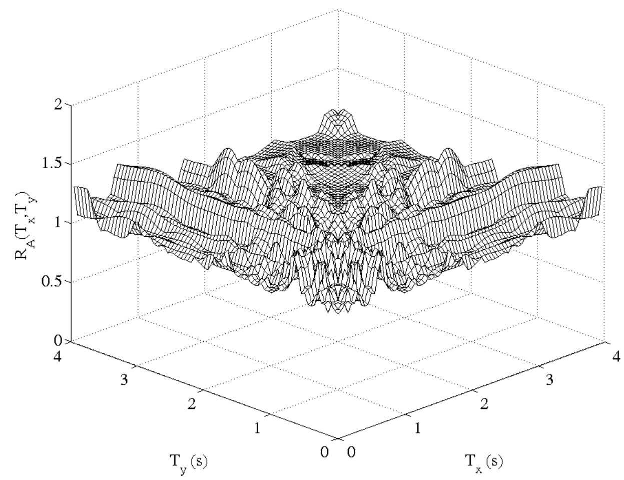

(a) $R_A(T_x, T_y)$

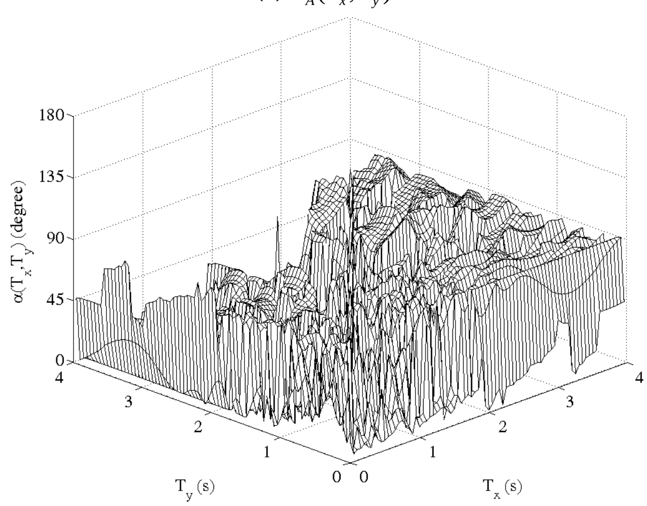

(b) $\tilde{\alpha}(T_x, T_y)$

Figure 5-19 $R_A(T_x, T_y)$ and $\tilde{\alpha}(T_x, T_y)$ of the CHY025 record

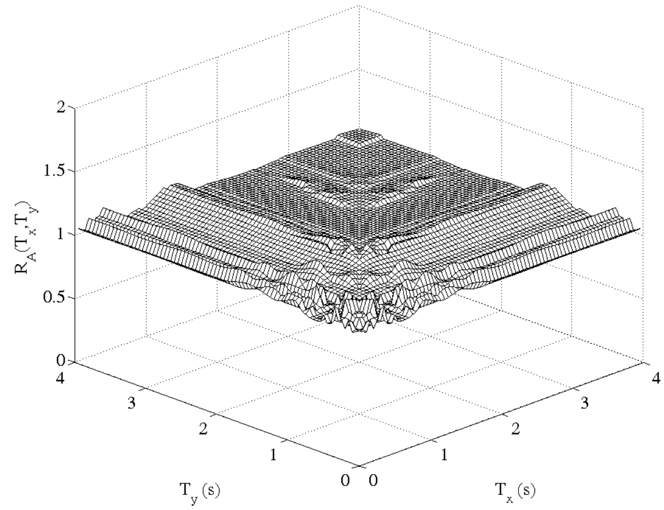

(a) $R_A(T_x, T_y)$

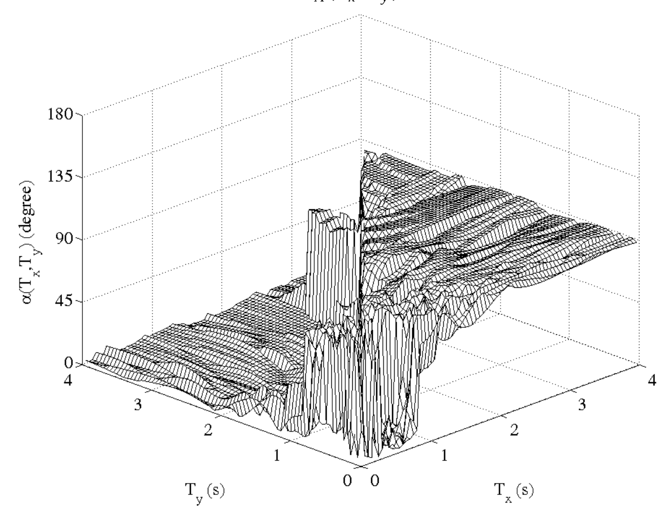

(b) $\tilde{\alpha}(T_x, T_y)$

Figure 5-20 $R_A(T_x, T_y)$ and $\tilde{\alpha}(T_x, T_y)$ of the 16LGPC record

5.7 Characteristics of Response Spectra

5.7.1 Acceleration ratio response spectra, direction response spectra, and their relations

Figure 5-21 shows the relations between $R_A(T_x,T_y)$ and $\tilde{\alpha}(T_x,T_y)$ at various combinations of natural periods in x- and y- axes for all ground motion records. For $T_x > T_y$, $\tilde{\alpha}(T_x,T_y)$ is biased to 90 degrees. But for $T_x < T_y$, $\tilde{\alpha}(T_x,T_y)$ is biased to 0 degree. The larger the difference between T_x and T_y is, the larger the bias is. For $T_x = T_y$, $\tilde{\alpha}(T_x,T_y)$ is well distributed in all angles, meaning that structures with the same natural periods in two orthogonal axes have random directions of maximum responses. The solid line in Figure 5-21 represents $\sec(\tilde{\alpha}(T_x,T_y))$ for $0° \le \tilde{\alpha}(T_x,T_y) \le 45°$ and $\mathrm{cosec}(\tilde{\alpha}(T_x,T_y))$ for $45° \le \tilde{\alpha}(T_x,T_y) \le 90°$. The value at $\tilde{\alpha}(T_x,T_y) = 45°$ is equal to 1.414 while the value at $\tilde{\alpha}(T_x,T_y) = 0° \text{ or } 90°$ is equal to 1. If $R_A(T_x,T_y)$ is on the solid line, the projection of the $R_A(T_x,T_y)$ on the principal axis is equal to one, meaning that there is no amplification of response under bi-directional excitations. If the value of $R_A(T_x,T_y)$ is above the solid line, the projection of $R_A(T_x,T_y)$ onto the principal axis will be greater than one. So, the response under bi-directional excitations is larger than that under uni-directional excitations. It is seen that $R_A(T_x,T_y)$ is above the solid line in most cases. For $T_x = T_y$, $\tilde{\alpha}(T_x,T_y)$ is below the solid line in the range of $30° \le \tilde{\alpha}(T_x,T_y) \le 60°$.

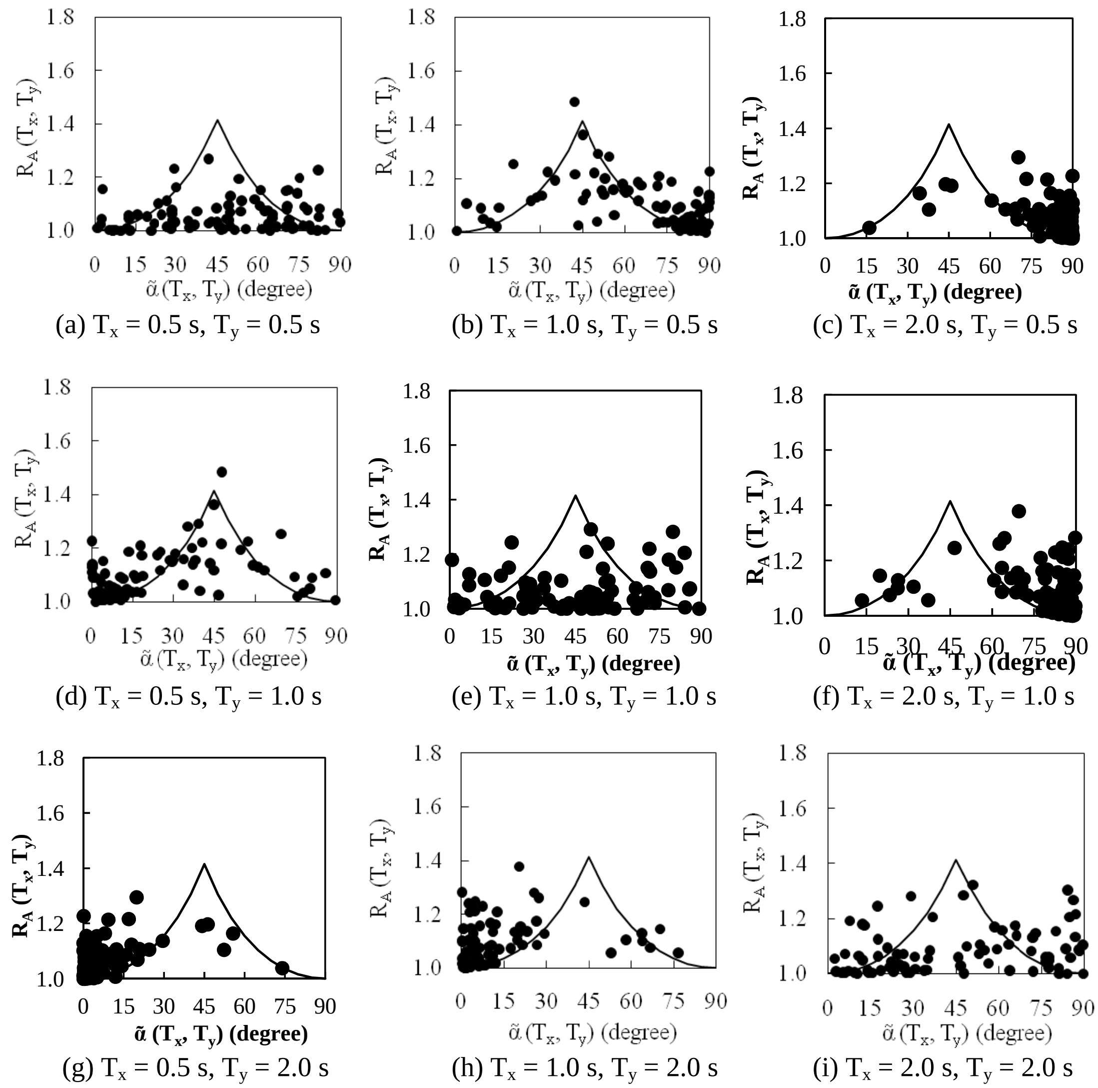

Figure 5-21 Relations between $R_A(T_x,T_y)$ and $\tilde{\alpha}(T_x,T_y)$ for all ground motion records

5.7.2 Effect of intensities of ground motions

Some inherit characteristics of ground motions may affect the trends of response spectra. In this study, the Arias intensity ratio R_I is defined as

$$R_I = \frac{I_{major}}{I_{\min or}} \tag{5-10}$$

where I_{major} is the Arias intensity in the major axis and I_{minor} is the Arias intensity in the minor axis. A ground motion record with accelerations well distributed in all directions tends to have R_I close to one but the ground motion record which has accelerations in one axis larger than those in the orthogonal axis tends to have a larger value of R_I.

Figure 5-22 shows the acceleration orbit and the Arias intensities in all directions for the CHY025 record and Figure 5-23 shows the acceleration orbit and the Arias intensities in all directions for the 16LGPC record. The CHY025 record has the acceleration orbit close to a circular shape. The Arias intensity is also quite uniform in all directions. The value of R_I is equal to 1.25. The 16LGPC record has the acceleration orbit elongated in the major axis. The Arias intensity is also elongated in the direction. The value of R_I is equal to 3.37. Each ground motion record is applied to structures with the same natural periods T_x and T_y. $\alpha(T_x, T_y, \theta = 0°)$ is plotted in Figure 5-24 for the two ground motion records. It is seen that the 16LGPC record causes the maximum response at angles close to 0 degree while the CHY025 record causes the maximum response at angles scattering in a wider range. The solid lines show the average angles of maximum responses. Figure 5-25 illustrates the relation between the average angles of the maximum accelerations and R_I for all ground motion records. It is obvious that the larger the Arias intensity ratio is biased to the major axis. Figure 5-26 shows the relation between $\tilde{\alpha}(T_x, T_y)$ and R_I for all ground motion records at various combinations of natural periods T_x and T_y (for $T_x = T_y$). It is interesting to note that the trend is not obvious when the angle of incidence is varied.

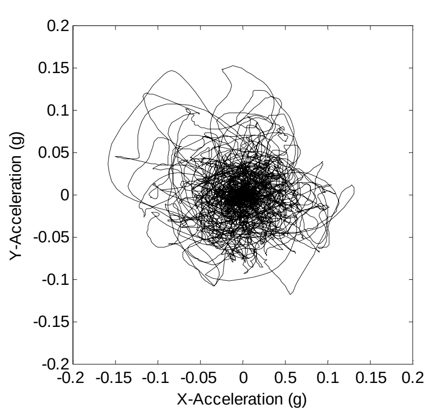

(a) Acceleration orbit

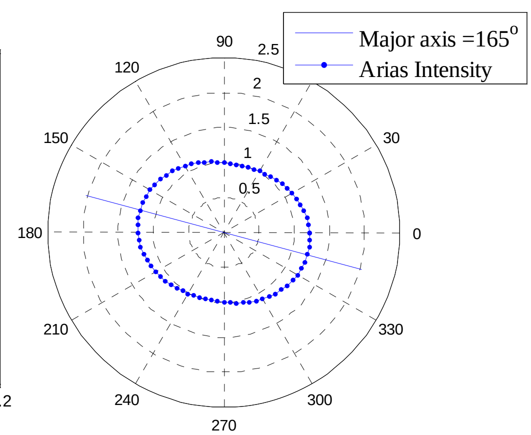

(b) Arias intensities

Figure 5-22 Acceleration orbit and the Arias intensities in all directions for CHY025 record

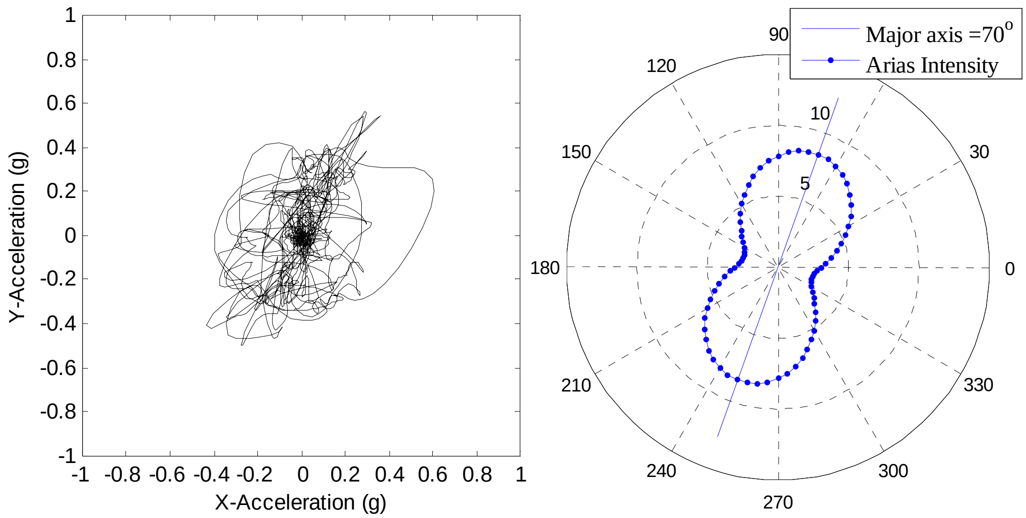

(a) Acceleration orbit (b) Arias intensities

Figure 5-23 Acceleration orbit and the Arias intensities in all directions for 16LGPC record

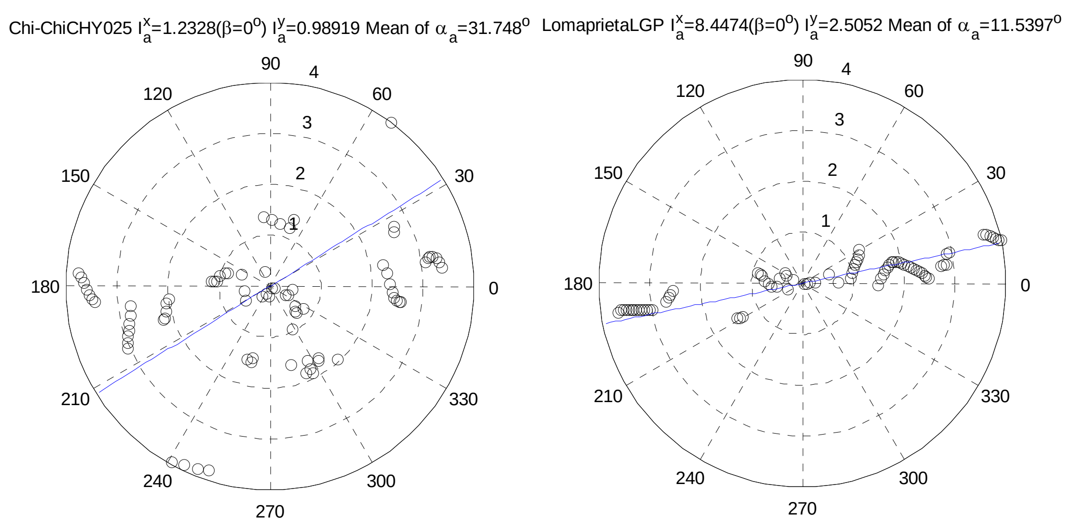

(a) CHY025 record (b) 16LGPC record

Figure 5-24 Directions of acceleration responses

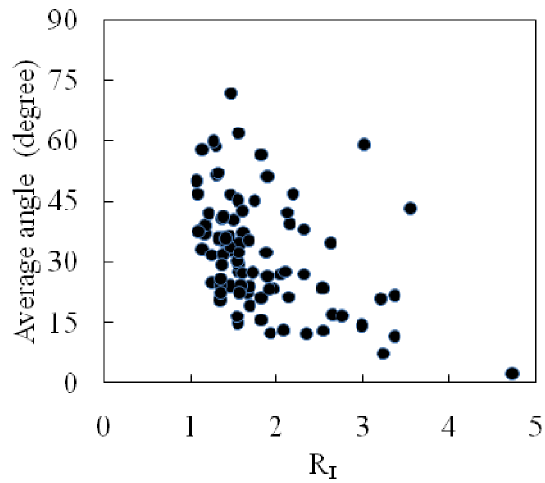

Figure 5-25 Average angles vs. R_I

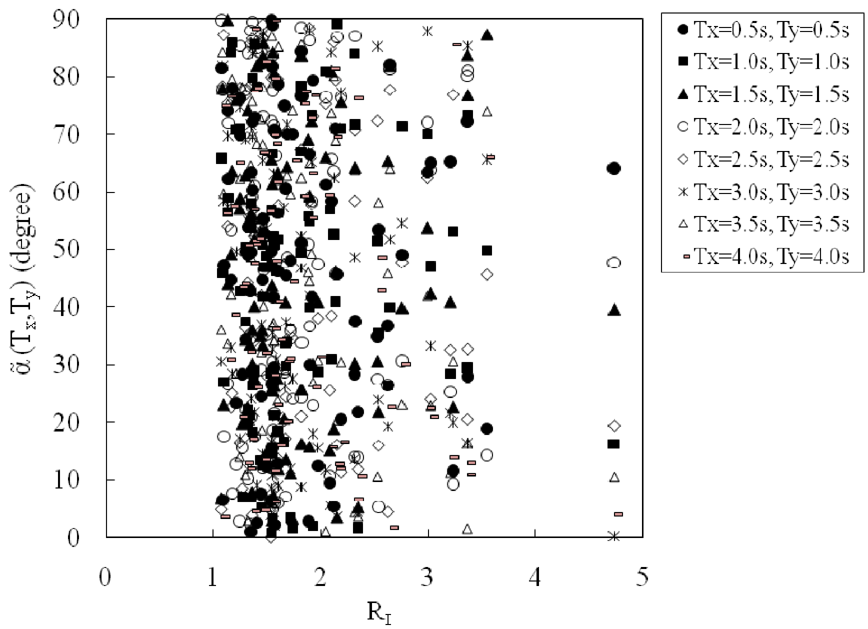

Figure 5-26 Relation between $\tilde{\alpha}(T_x,T_y)$ and R_I

Figure 5-27 shows the relation between $R_A(T_x,T_y)$ and R_I for all ground motion records at various combinations of natural periods T_x and T_y. It is found that ground motion records with the larger R_I result in $R_A(T_x,T_y)$ closes to one because the maximum acceleration inclines to the major axis of the ground motion which corresponds to the x-axis of the structure.

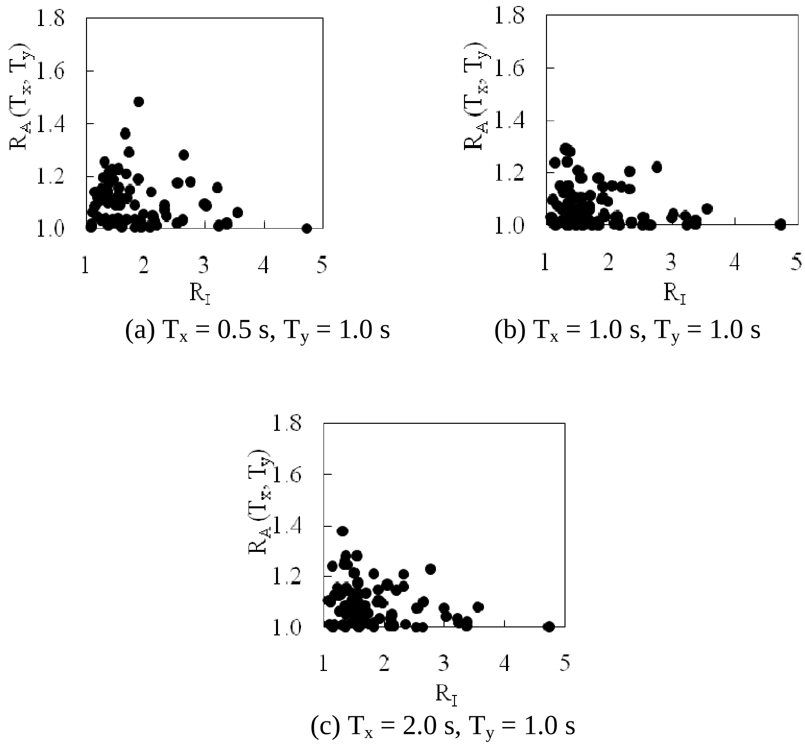

Figure 5-27 Relation between $R_A(T_x, T_y)$ and R_I for all ground motion records

5.7.3 <u>Effect of epicentral distances and earthquake magnitudes</u>

The effect of epicentral distances on $R_A(T_x, T_y)$ and $\tilde{\alpha}(T_x, T_y)$ is investigated as shown in Figure 5-28. There is no clear dependency of $R_A(T_x, T_y)$ and $\tilde{\alpha}(T_x, T_y)$ on epicentral distances. Figure 5-29 shows the effect of earthquake magnitudes on $R_A(T_x, T_y)$ and $\tilde{\alpha}(T_x, T_y)$. There is no clear dependency of $R_A(T_x, T_y)$ and $\tilde{\alpha}(T_x, T_y)$ on earthquake magnitudes.

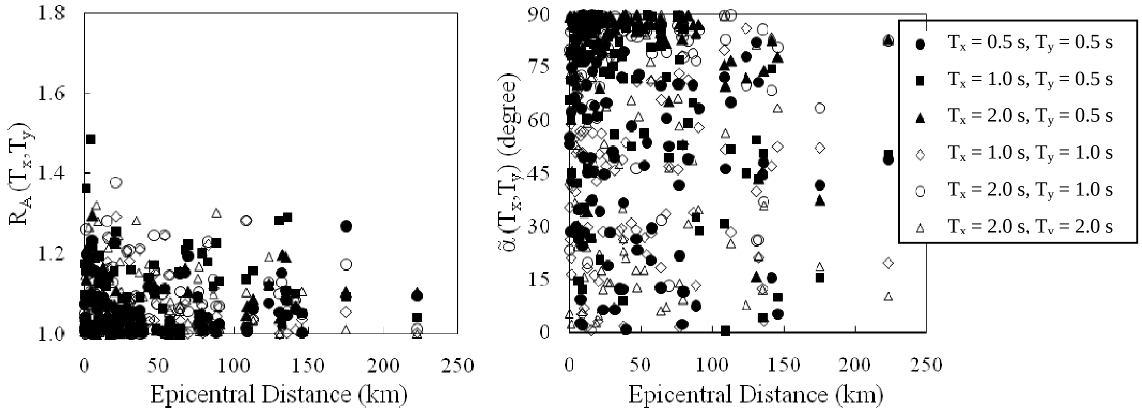

(a) $R_A(T_x,T_y)$ (b) $\tilde{\alpha}(T_x,T_y)$

Figure 5-28 Effect of epicentral distances on $R_A(T_x,T_y)$ and $\tilde{\alpha}(T_x,T_y)$

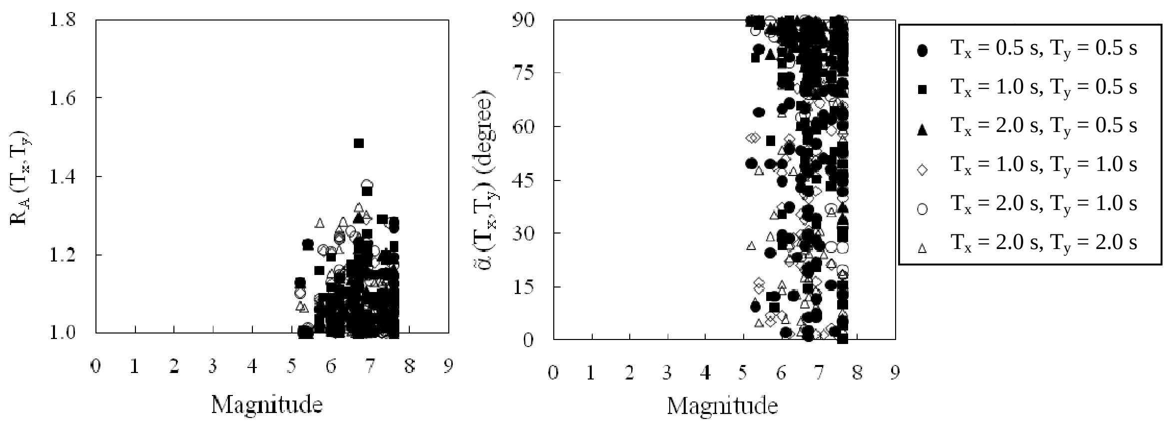

(a) $R_A(T_x,T_y)$ (b) $\tilde{\alpha}(T_x,T_y)$

Figure 5-29 Effect of magnitudes on $R_A(T_x,T_y)$ and $\tilde{\alpha}(T_x,T_y)$

5.7.4 Effect of site conditions

Site conditions are usually classified using shear wave velocities in top 30-m layers. The effect of shear wave velocities at recording stations on $R_A(T_x,T_y)$ and $\tilde{\alpha}(T_x,T_y)$ is shown in Figure 5-30. There is no clear relation between shear wave velocities and $R_A(T_x,T_y)$ as well as $\tilde{\alpha}(T_x,T_y)$.

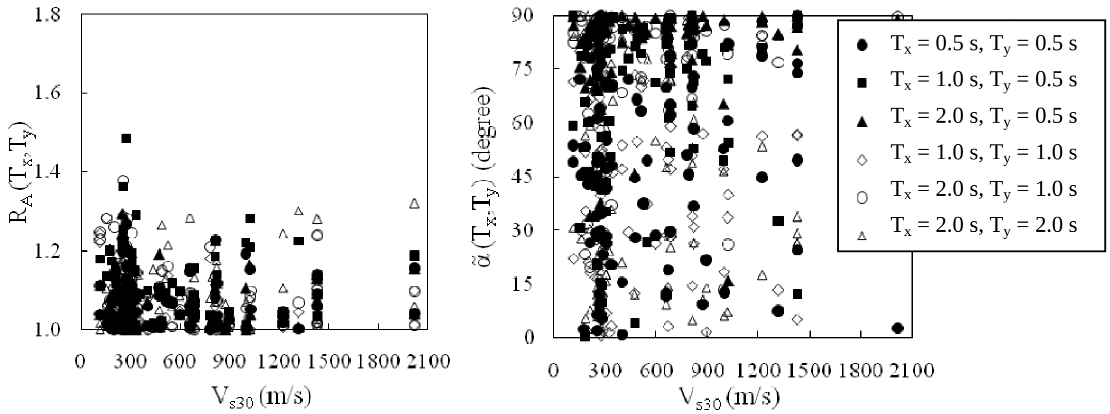

(a) $R_A(T_x, T_y)$ (b) $\tilde{\alpha}(T_x, T_y)$

Figure 5-30 Effect of Vs30 on $R_A(T_x, T_y)$ and $\tilde{\alpha}(T_x, T_y)$

5.8 Generalized Bi-directional Acceleration Response Spectra

Since there is no consistent trend of how earthquake magnitudes, epicentral distances, and soil conditions affect $R_A(T_x, T_y)$, $R_A(T_x, T_y)$ for 86 ground motion records is represented by statistical values which are mean and mean-plus-one-standard-deviation values. Figure 5-31 shows mean $R_A(T_x, T_y)$. It is seen that the mean value is 1.092 and it is quite uniform for all combinations of natural periods. For the design purpose, the mean $R_A(T_x, T_y)$ is proposed as 1.092. The mean-plus-one-standard-deviation value is overlaid in Figure 5-31. The mean-plus-one-standard-deviation value of $R_A(T_x, T_y)$ is proposed as 1.18. Figure 5-32 shows the maximum $R_A(T_x, T_y)$ from 86 ground motions. It is seen that the maximum value is generally less than 1.5.

The angles of maximum responses are averaged for all ground motion records. The mean $\tilde{\alpha}(T_x, T_y)$ is presented in Figure 5-33. When T_x is longer than T_y, the angle of the maximum response is larger than about 70 degrees, indicating that a structure is inclining to the direction with the shorter natural period as discussed in the previous section.

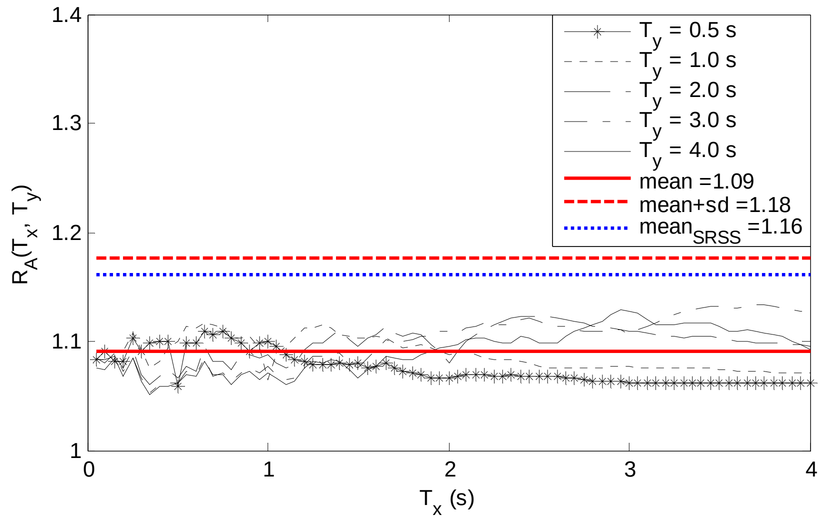

Figure 5-31 mean $R_A(T_x, T_y)$

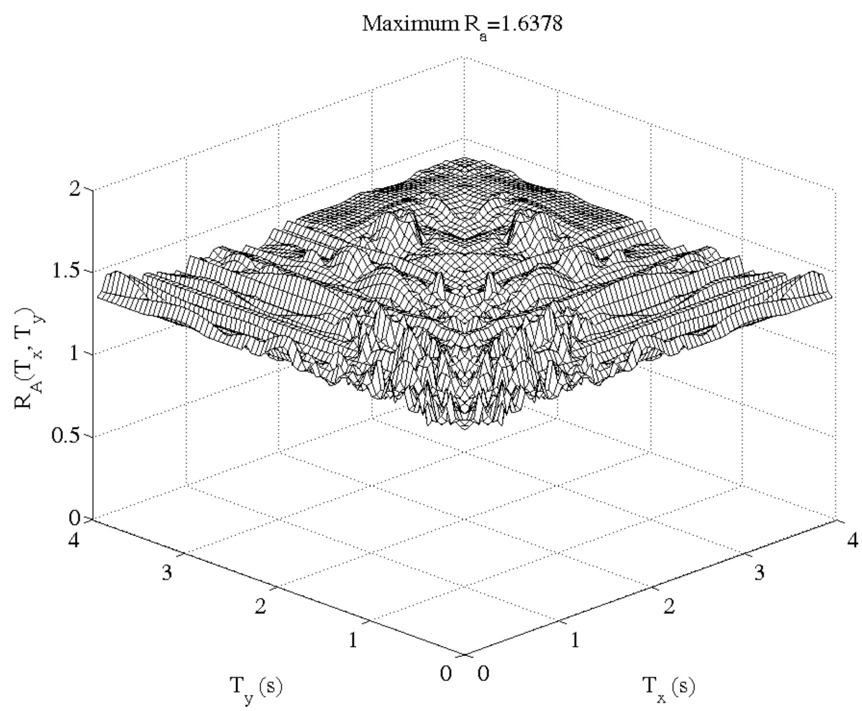

Figure 5-32 Maximum $R_A(T_x, T_y)$

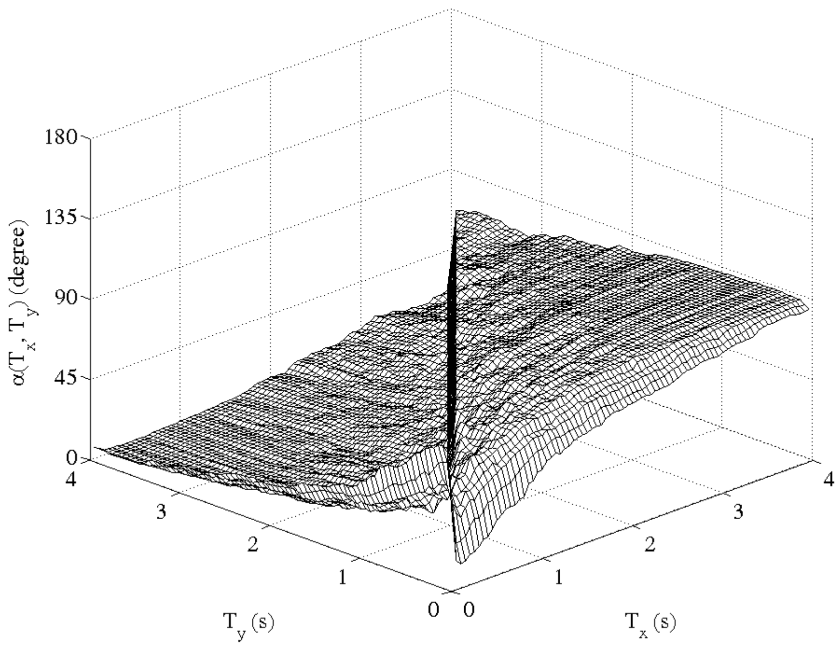

(a)

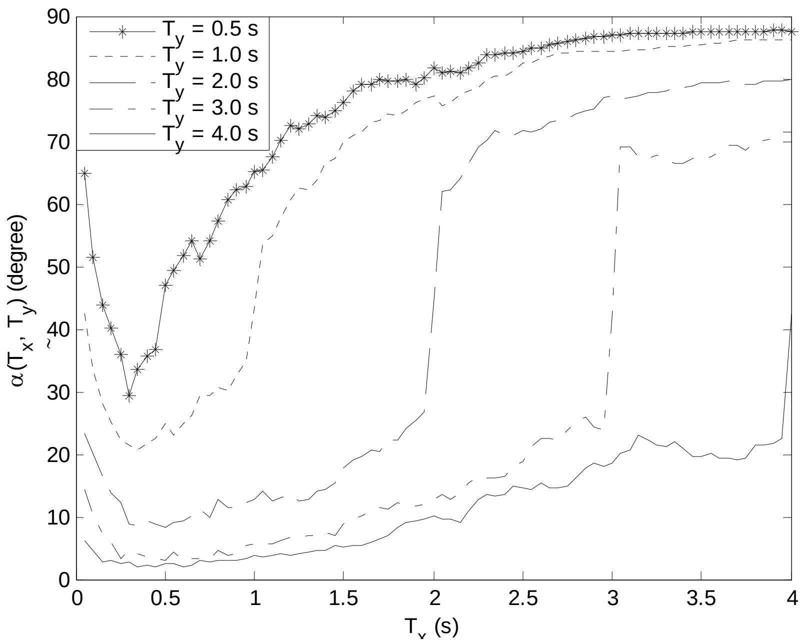

(b)

Figure 5-33 Mean $\tilde{\alpha}(T_x, T_y)$

(a) Plotting in 3D (b) Plotting in 2D

5.9 Direction of Structural Response

In this study, the direction of the maximum pseudo-acceleration responses is determined by using the time-histories analysis. The results can be shown that the direction of the maximum pseudo-acceleration responses correlate with the different predominant periods in the 2-horizontal axes of structures according to Figure 5-33. The trend of the relation among direction (α) and natural periods in x- and y- axes (T_x and T_y) is shown in Figure 5-34. The equation can be expressed as

$$\ln(\ln(90-\alpha)) = C_1 T_x/T_y + C_2 \tag{5-11}$$

where C_1 and C_2 are constants in the various T_y. The constants C_1 and C_2 in each T_y can be found in Table 5-2 and plotted as the functions of T_y in Figures 5-35 and 5-36. Those functions are expressed as

$$C_1=-0.0171T_y^5+0.0707T_y^4-0.0823T_y^3+0.1828T_y^2-0.4561T_y-0.0016 \tag{5-12}$$

$$C_2 = 0.0803T_y^4 - 0.4137T_y^3 + 0.633T_y^2 - 0.3421T_y + 1.5261 \tag{5-13}$$

C1 and C2 in Equation (5-11) can be substituted by Equations (5-12) and (5-13). Therefore, the Equation (5-11) becomes Equation (5-14) and plots in Figure 5-37

$$\begin{aligned}\ln(\ln(90-\alpha)) = {} & [-0.0171T_y^5+0.0707T_y^4-0.0823T_y^3+0.1828T_y^2-0.4561T_y-0.0016](T_x/T_y) \\ & +0.0803T_y^4-0.4137T_y^3+0.633T_y^2-0.3421T_y+1.5261\end{aligned} \tag{5-14}$$

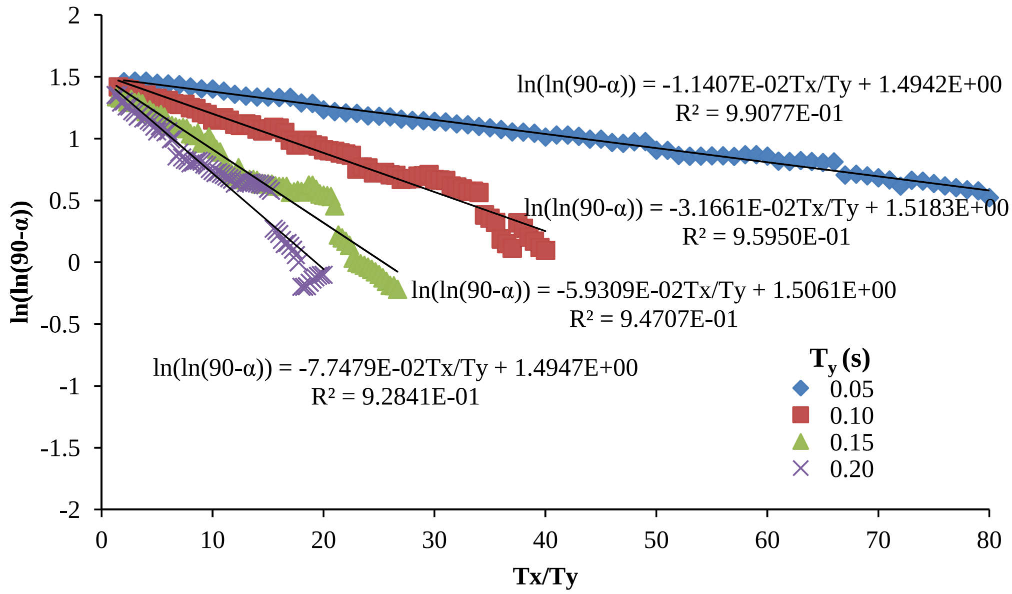

(a)

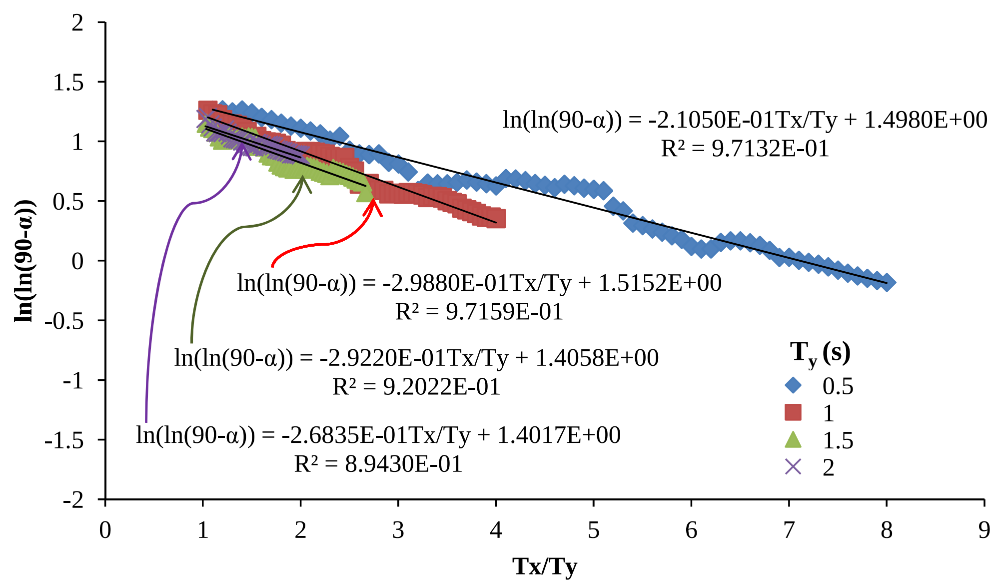

(b)

Figure 5-34 The relation among α, T_x and T_y by various T_y

(a) For T_y = 0.05 s, 0.10 s, 0.15 s and 0.20 s (b) For T_y = 0.5 s, 1 s, 1.5 s and 2 s

Table 5-2 C_1 and C_2 of the incident angle equation

T_y (s)	C_1	C_2	R^2	T_y (s)	C_1	C_2	R^2
0.05	-0.0114	1.4942	0.9908	1.95	-0.2371	1.3522	0.8466
0.10	-0.0317	1.5183	0.9595	2.00	-0.2684	1.4017	0.8943
0.15	-0.0593	1.5061	0.9471	2.05	-0.3095	1.4394	0.8668
0.20	-0.0775	1.4947	0.9284	2.10	-0.2753	1.3629	0.8440
0.25	-0.1168	1.5028	0.9412	2.15	-0.2414	1.2966	0.7964
0.30	-0.0930	1.2882	0.9434	2.20	-0.2314	1.2962	0.7926
0.35	-0.1283	1.3698	0.9552	2.25	-0.2449	1.3161	0.7705
0.40	-0.2168	1.6442	0.9203	2.30	-0.2121	1.2489	0.7481
0.45	-0.1985	1.5374	0.9713	2.35	-0.2525	1.3005	0.7530
0.50	-0.2105	1.4980	0.9713	2.40	-0.2575	1.3111	0.8412
0.55	-0.1751	1.4004	0.9617	2.45	-0.2926	1.3874	0.9095
0.60	-0.2545	1.5019	0.9754	2.50	-0.2382	1.3303	0.8941
0.65	-0.2515	1.4526	0.9617	2.55	-0.2144	1.3068	0.8652
0.70	-0.2588	1.4905	0.9142	2.60	-0.2479	1.3777	0.9059
0.75	-0.2855	1.5585	0.9529	2.65	-0.2421	1.3734	0.8571
0.80	-0.2529	1.4405	0.9649	2.70	-0.2397	1.3670	0.7483
0.85	-0.2673	1.4390	0.9713	2.75	-0.2218	1.3500	0.5619
0.90	-0.2892	1.4572	0.9671	2.80	-0.2936	1.4464	0.7376
0.95	-0.3053	1.4902	0.9581	2.85	-0.4139	1.5927	0.8726
1.00	-0.2988	1.5152	0.9716	2.90	-0.2931	1.4608	0.6934
1.05	-0.3215	1.5378	0.9753	2.95	-0.2722	1.4299	0.4438
1.10	-0.2805	1.4286	0.9567	3.00	-0.2865	1.4484	0.3891
1.15	-0.2978	1.4478	0.9565	3.05	-0.2591	1.4221	0.3850
1.20	-0.3576	1.5138	0.9617	3.10	-0.3329	1.5148	0.6663
1.25	-0.3575	1.5032	0.9287	3.15	-0.3056	1.4829	0.6285
1.30	-0.3423	1.4923	0.9412	3.20	-0.3698	1.5519	0.6576
1.35	-0.3113	1.4302	0.9387	3.25	-0.4391	1.6199	0.6645
1.40	-0.2656	1.3523	0.9377	3.30	-0.7042	1.9145	0.8330
1.45	-0.2977	1.4101	0.9625	3.35	-0.9154	2.1229	0.9392
1.50	-0.2922	1.4058	0.9202	3.40	-0.8550	2.0270	0.9579
1.55	-0.2876	1.4119	0.8867	3.45	-1.1888	2.3362	0.9733
1.60	-0.2835	1.4274	0.9187	3.50	-1.2154	2.3286	0.7889
1.65	-0.3080	1.4712	0.9342	3.55	-1.8522	3.0027	0.8356
1.70	-0.2826	1.4247	0.9145	3.60	-1.9844	3.1249	0.9536
1.75	-0.2570	1.3814	0.8999	3.65	-2.0085	3.1119	0.9519
1.80	-0.2412	1.3527	0.8575	3.70	-1.9369	2.9884	0.9980
1.85	-0.2627	1.3884	0.8366	3.75	-2.2940	3.3386	0.9393
1.90	-0.2637	1.3803	0.8658	3.80	-1.7619	2.7664	0.7066

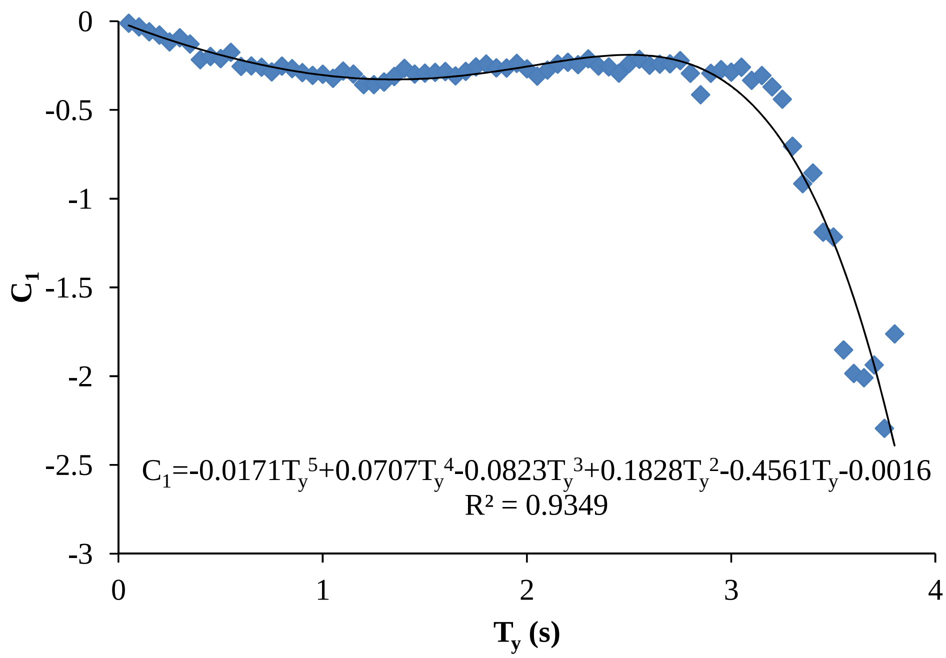

Figure 5-35 The relation between C_1 and T_y

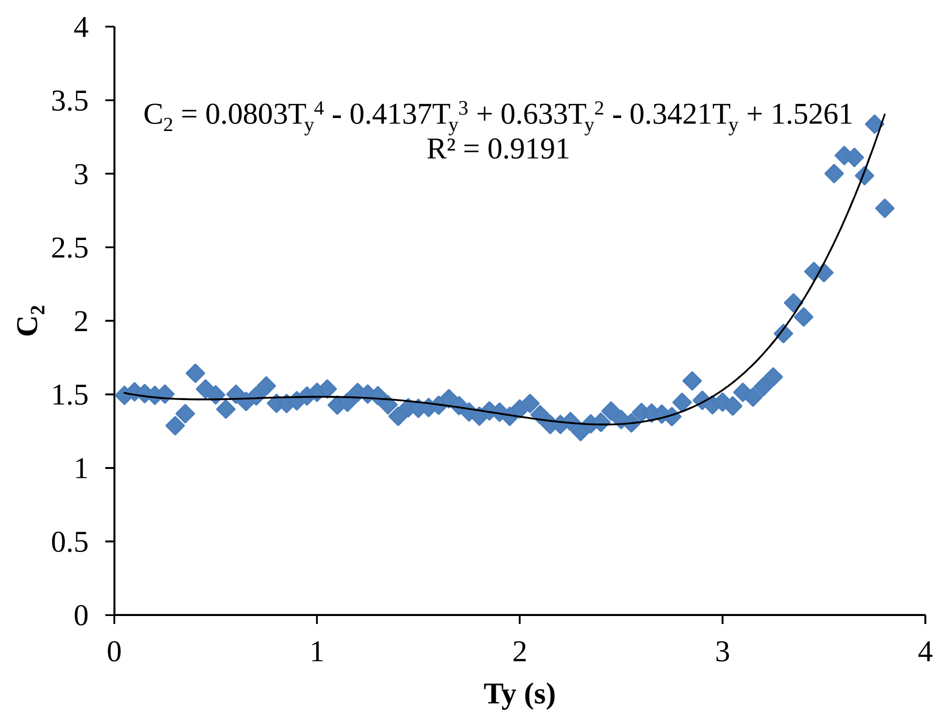

Figure 5-36 The relation between C_2 and T_y

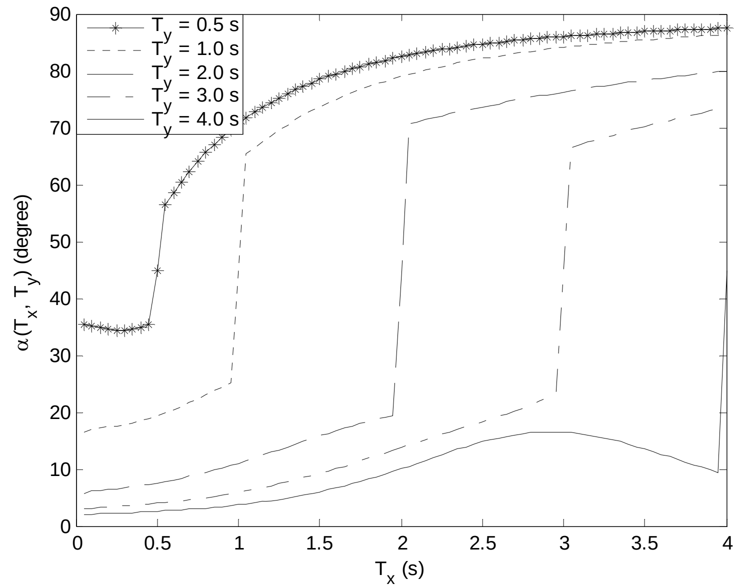

(a)

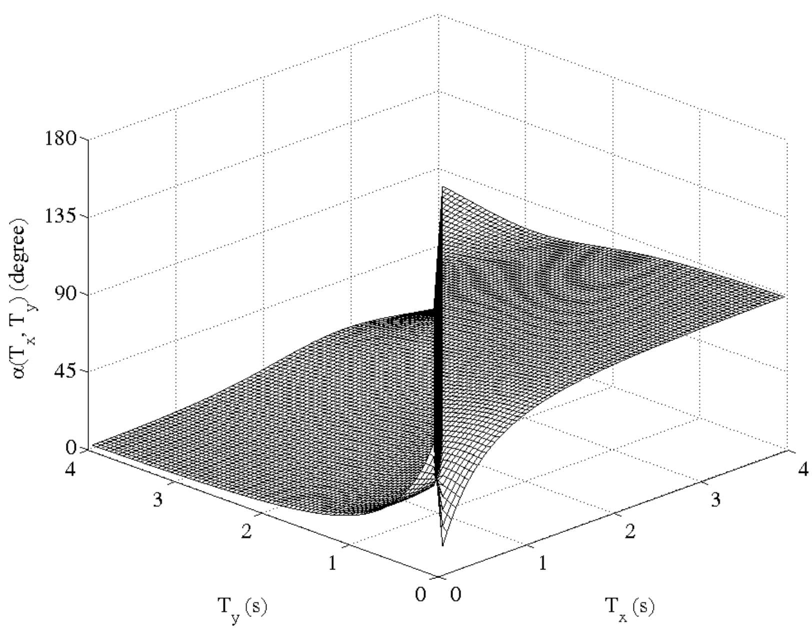

(b)

Figure 5-37 Incident angles $\alpha(T_x, T_y)$ from the proposed equation
(a) Plotting in 3D (b) Plotting in 2D

The proposed direction in Figure 5-37 is quite closes to the actual direction in Figure 5-33. So, the critical angle of a structure depends on the natural periods in x- and y- axes which can be determined by the Equation (5-14).

5.10 Applications and Comparison with Combination Rules

5.10.1 Application

Bi-directional excitation is taken into account in AASHTO (2002) by summing up seismic effects due to loading in one direction with 30% of seismic effects due to loading in the perpendicular direction. The seismic coefficient C_s is defined as:

$$C_s = \frac{1.2AS}{T^{2/3}} \leq 2.5A \qquad (5\text{-}15)$$

where A is a ground acceleration; S is a site coefficient equal to 1.0, 1.2, 1.5, and 2.0 for soil types I, II, III, and IV, respectively; and T is a natural period. Figure 5-38 depicts seismic coefficients normalized by ground accelerations for all soil types.

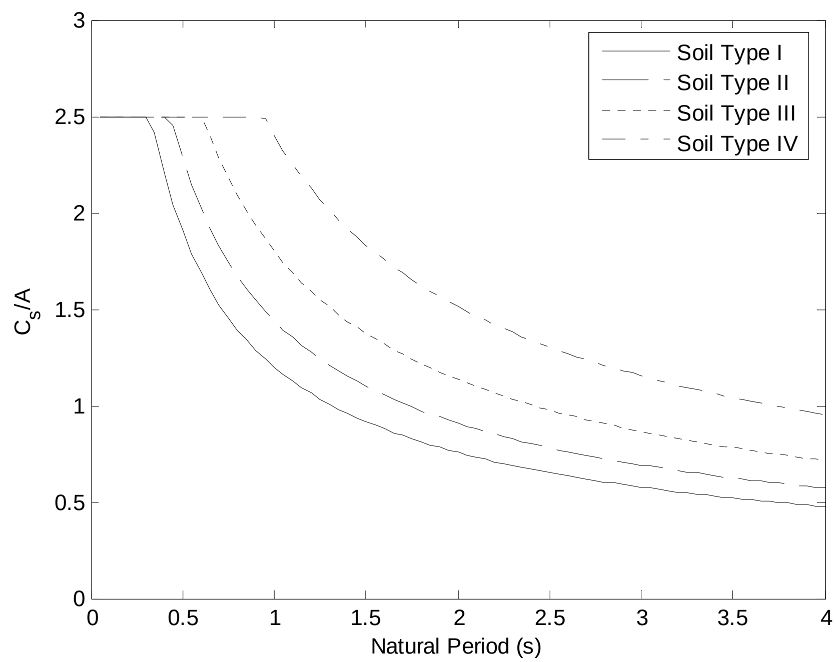

Figure 5-38 Seismic coefficient from the AASHTO (2002)

The acceleration response spectrum $S_A(T_x, T_y)$ can be determined from Equation (5-8) using the seismic coefficient in Equation (5-15). Then the bi-directional acceleration response spectrum $\tilde{S}_A^r(T_x, T_y)$ is obtained from Equation (5-7). The mean value of 1.092 for the acceleration ratio response spectrum $R_A(T_x, T_y)$ plus one standard deviation of 0.084 is used for this application. Figure 5-39 shows $S_A(T_x, T_y)$ and $\tilde{S}_A^r(T_x, T_y)$ for a type-I site condition.

The unit mass and ground acceleration are assumed for this computation. In seismic design, $\tilde{S}_A^r(T_x, T_y)$ in Figure 5-39 (b) which is proposed to the maximum response due to bidirectional excitation ($r_{proposed}$) can be determined by the equation as

$$r_{proposed} = 1.176\, S_A(T_x, T_y) \tag{5-16}$$

The proposed equation is developed from the average of bi-directional responses which calculated from the maximum resultant responses of the structural excitation due to 86 ground motions. This method can be used for the earthquake resistance designs of structure such as bridge columns or stanchions which are modeled as the 2DOF system.

Form Figure 5-40 which the responses are obtained from AASHTO (2002) in equation (5-15), $S_A(T_x, T_y)$ can be determined from the maximum values of $S_A(T_x) = \dfrac{1.2AS}{T_x^{\,2/3}}$ which is the acceleration response for a structure with the natural period in x-axis equal to T_x and $S_A(T_y) = \dfrac{1.2AS}{T_y^{\,2/3}}$ which is the acceleration response for a structure with the natural period in y-axis equal to T_y. If $S_A(T_x)$ or $S_A(T_y)$ are larger than 2.5A, $S_A(T_x, T_y)$ will be equal to 2.5A. For this method, the angle of structural movement from x-axis when the maximum acceleration response arises can be determined from the Equation (5-14).

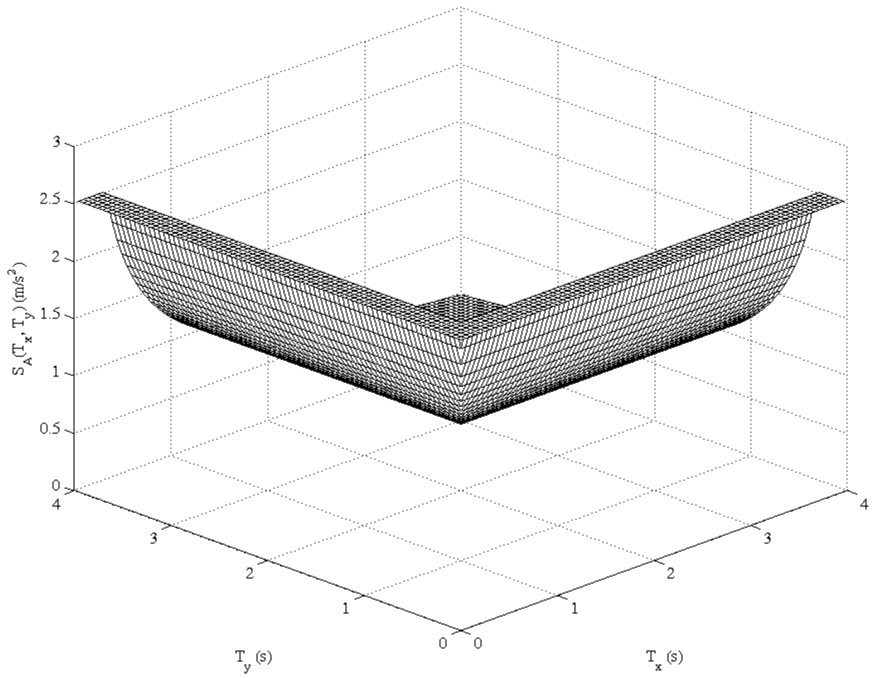

(a) $S_A(T_x, T_y)$

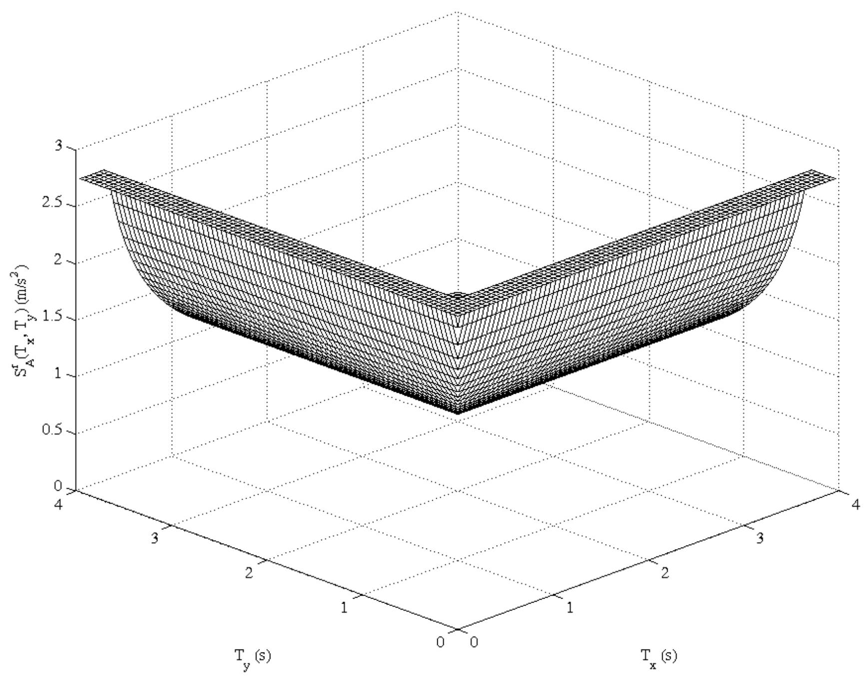

(b) $\tilde{S}_A^r(T_x, T_y)$

Figure 5-39 $S_A(T_x, T_y)$ and $\tilde{S}_A^r(T_x, T_y)$ for a type-I site condition

W

1. Find T_x and T_y of a structure

2. Determine responses from a design spectra
$S_A(T_x), S_A(T_y)$

y

3. Determine the combination of responses
$\tilde{S}_A^r(T_x, T_y) = 1.176\ \max[S_A(T_x), S_A(T_y)]$

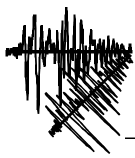

x

3D VIEW

y

$\tilde{S}_A^r(T_x, T_y)$

$\tilde{\alpha}(T_x, T_y)$

x

TOP VIEW

Figure 5-40 Maximum response of proposed method

5.10.2 Comparison with other combination rules

The 30%, 40%, SRSS and the critical response of CQC3 combination rules are considered for this comparison. They can be written as:

30%-rule (Rosenblueth and Contreras, 1977):

$$r_{30}=\text{larger of } \{r_x+0.3r_y;\ 0.3r_x+r_y\} \quad (5\text{-}17)$$

40%-rule (Newmark, 1975):

$$r_{40}=\text{larger of } \{r_x+0.4r_y;\ 0.4r_x+r_y\} \quad (5\text{-}18)$$

SRSS (Rosenbuleth's Ph.D. thesis, 1951):

$$r_{SRSS}=\text{larger of } \{[r_x^2+(\gamma r_y)^2]^{1/2};\ [(\gamma r_x)^2+r_y^2]^{1/2}\} \quad (5\text{-}19)$$

For the critical response of CQC3 combination rule, Lopez et al (2001) were determined from the maximum responses of all seismic incident angles. This equation can be expressed as:

$$r_{cr}=\left\{(1+\gamma^2)\left(\frac{r_x^2+r_y^2}{2}\right)+(1-\gamma^2)\sqrt{\left(\frac{r_x^2-r_y^2}{2}\right)^2+r_{xy}^2}\right\}^{1/2} \quad (5\text{-}20)$$

where γ is the ratio of the design spectra for the minor and major principal axes of ground motion. In this study, γ=1.0, 0.85 and 0.67 are considered. r_x and r_y are the peak values of responses in x- and y-axes respectively due to a single component of ground motion. In this comparison, the response can be defined by the spectrum from AASHTO (2002). From the CQC-rule, r_x and r_y can be given by

$$r_k=\left(\textstyle\sum_i\sum_j \rho_{ij} r_{ki} r_{kj}\right)^{1/2} \quad (5\text{-}21)$$

where k is x or y. r_{ki} is the peak response of k-axis due to the vibration mode i. ρ_{ij} is the modal correlation coefficient between modes i and j that can be calculated with the equation proposed by Wilson et al,(1981). r_{xy} is a cross-term of the modal responses which can be determined by

$$r_{xy} = \sum_i \sum_j \rho_{ij} r_{xi} r_{yj} \tag{5-22}$$

The responses from several combination rules calculated from the equations (5-17) to (5-22) by using r_x and r_y from Figure 5-38 for a type-I site condition can be shown in Figure 5-39.

For an example of a bridge column with the natural period T_x and T_y for x- and y-axes respectively, the weight of pier = W (assume =1 MN), the column height = H, the ground acceleration = A (assume = 1g) and the coefficient of soil type = S (type 1; S=1.0) as shown in Figure 5-41, the value of the elastic seismic response coefficient (C_s) from Equation (5-15). The base shears in x- and y-axes of the column can be summarized in Tables 5-3 and 5-4. It is seem that the combination responses of the elastic seismic shears in each axis from 30% rule, 40% rule, SRSS and CQC3 with γ =1.0 are equal for the symmetry column section. The comparison between responses from the proposed method and the other combination rules are displayed in Figures 5-42 and 5-43.

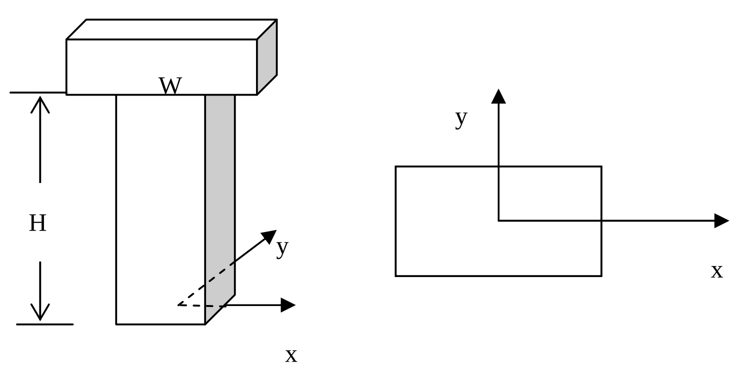

Figure 5-41 The example of a bridge column

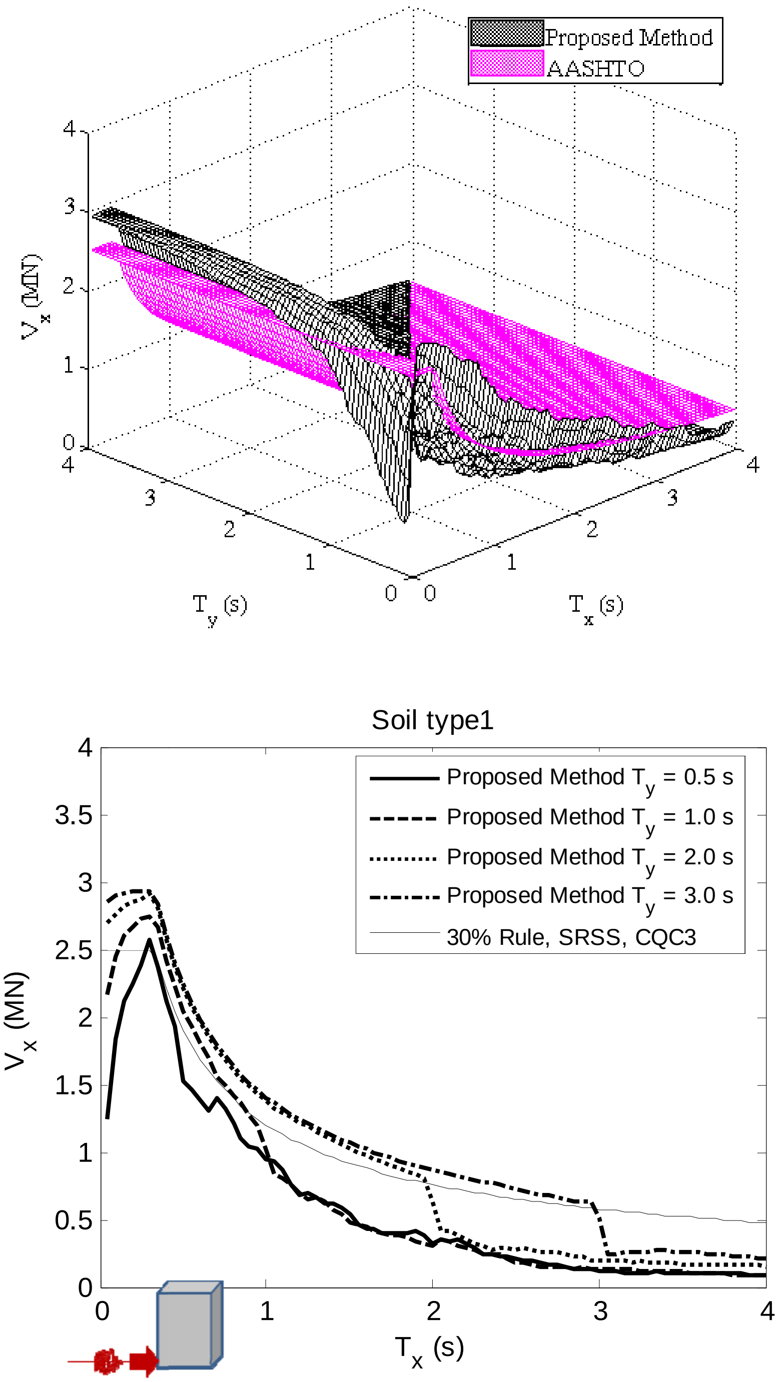

Figure 5-42 The comparison between the base shears in x-direction from the proposed method and the other combination rules

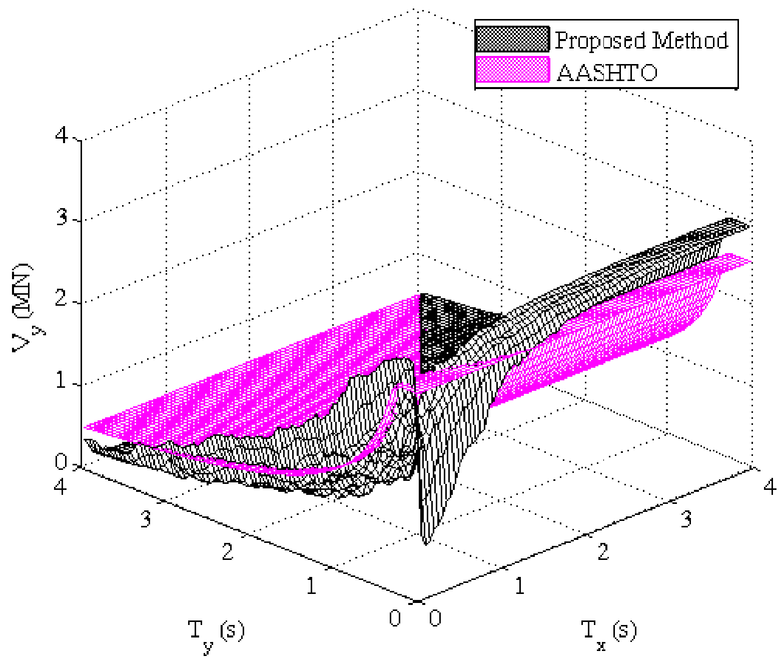

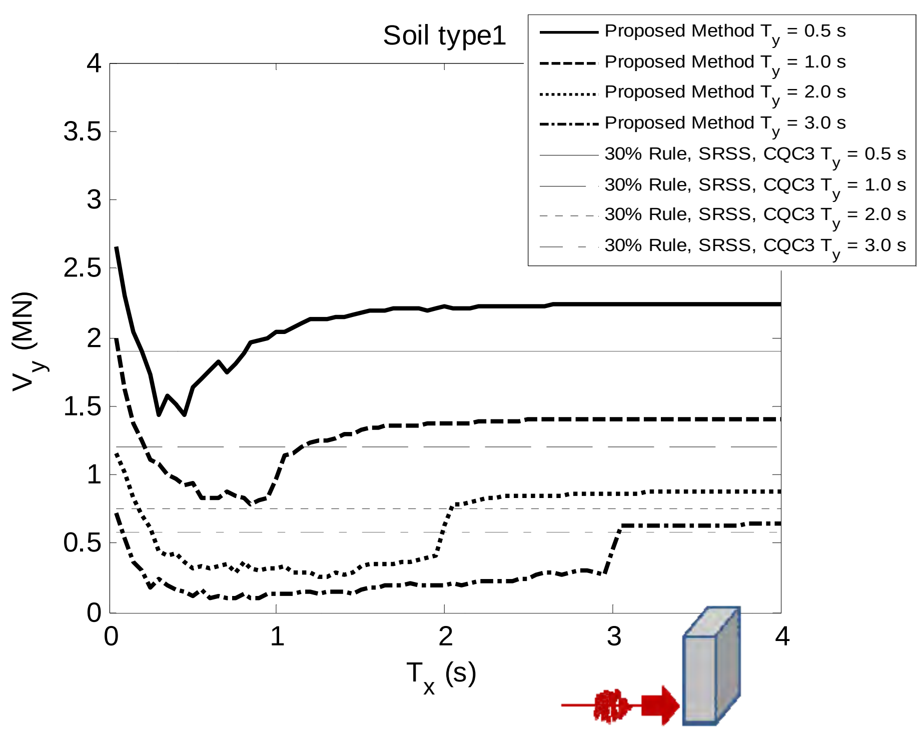

Figure 5-43 The comparison between the base shears in y-direction from the proposed method and the other combination rules

The comparison between the proposed method and other combination rules are shown in Figures 5-42 and 5-43. It is seen that the proposed method yields larger responses in both axes for certain combinations of natural periods. Base shears in the x-direction from the proposed method are larger than the responses from the other combination rules when T_x is shorter than T_y. And, the base shears in the y-direction from the proposed method are larger than the responses from the other combination rules when T_x is longer than T_y.

Table 5-3 Total base shears in x- and y-axes of the symmetry column (1)

Responses	**V_x (MN)**	**V_y (MN)**	**Angle**
r_x	C_s^x	0	
r_y	0	C_s^y	
30% rule			
(Case 1)	C_s^x	$0.3C_s^y$	$\tan^{-1}(0.3C_s^y/C_s^x)$
(Case 2)	$0.3C_s^x$	C_s^y	$\tan^{-1}(C_s^y/0.3C_s^x)$
40% rule			
(Case 1)	C_s^x	$0.4C_s^y$	$\tan^{-1}(0.4C_s^y/C_s^x)$
(Case 2)	$0.4C_s^x$	C_s^y	$\tan^{-1}(C_s^y/0.4C_s^x)$
SRSS and CQC3			
γ =1.0	C_s^x	C_s^y	$\tan^{-1}(C_s^y/C_s^x)$
Proposed method	$1.176\max(C_s^x,C_s^y)\cos\alpha$	$1.176\max(C_s^x,C_s^y)\sin\alpha$	$\alpha(T_x,T_y)$

T_x = 1 s, T_y = 2 s → α = 12.712°

r_x	$1.2x1x1/(1^{2/3}) = 1.2$	0	
r_y	0	$1.2x1x1/(2^{2/3}) = 0.756$	
30% rule			
(Case 1)	1.2	0.3x0.756 = 0.227	10.712°
(Case 2)	0.3x1.2 = 0.36	0.756	64.537°
40% rule			
(Case 1)	1.2	0.4x0.756 = 0.302	14.126°
(Case 2)	0.4x1.2 = 0.48	0.756	57.588°
SRSS and CQC3			
γ =1.0	1.2	0.756	32.211°
Proposed method	1.411cos12.712° = 1.377	1.411cos12.712° = 0.311	12.712°

Table 5-4 Total base shears in x- and y-axes of the symmetry column (2)

T_x = 1 s, T_y = 1 s → α = 43.382°			
r_x	$1.2x1x1/(1^{2/3}) = 1.2$	0	
r_y	0	$1.2x1x1/(1^{2/3}) = 1.2$	
30% rule			
(Case 1)	1.2	0.3x1.2 = 0.36	16.699°
(Case 2)	0.3x1.2 = 0.36	1.2	73.301°
40% rule			
(Case 1)	1.2	0.4x1.2 = 0.48	21.801°
(Case 2)	0.4x1.2 = 0.48	1.2	68.199°
SRSS and CQC3			
γ =1.0	1.2	1.2	45.000°
Proposed method	1.026	0.969	43.382°

T_x = 0.2 s, T_y = 0.5 s → α = 40.2004°			
r_x	$1.2x1x1/(.2^{2/3})=3.5 >2.5$	0	
r_y	0	$1.2x1x1/(.5^{2/3}) = 1.905$	
30% rule			
(Case 1)	2.5	0.3x1.905 = 0.571	12.866°
(Case 2)	0.3x2.5= 0.75	1.905	68.510°
40% rule			
(Case 1)	2.5	0.4x1.905 = 0.762	16.951°
(Case 2)	0.4x2.5= 1	1.905	62.303°
SRSS and CQC3			
γ =1.0	2.5	1.905	37.307°
Proposed method	2.246	1.898	40.200°

The 30%, SRSS, and CQC3 combination rule are considered for this comparison. Base shears in x- and y-axes of the structure can be summarized in Table 5-5. It is seen that the combined responses of base shears in each axis from the 30% rule, SRSS rule, and CQC3 rule are identical for this symmetrical structure. Those The responses of the base shear from the other combination rules are underestimated in the direction with a shorter period about 16%.

Table 5-5 Comparison between the maximum responses from proposed method and 30% rule, SRSS and CQC3

		Maximum Vx (MN)		Difference (%)	Maximum Vy (MN)		Difference (%)
		Proposed method	30% rule, SRSS, CQC3		Proposed method	30% rule, SRSS, CQC4	
Soil Type 1	Ty = 0.2 s	2.299	2.500	-8.36	2.937	2.500	16.08
	Ty = 0.5 s	2.566	2.500	2.62	2.239	1.905	16.11
	Ty = 1.0 s	2.739	2.500	9.12	1.408	1.200	15.98
	Ty = 1.5 s	2.860	2.500	13.43	1.073	0.916	15.78
	Ty = 2.0 s	2.907	2.500	15.04	0.876	0.756	14.66
	Ty = 2.5 s	2.922	2.500	15.57	0.743	0.651	13.17
	Ty = 3.0 s	2.935	2.500	16.01	0.643	0.577	10.87
	Ty = 4.0 s	2.938	2.500	16.10	0.378	0.476	-23.03
Soil Type 2	Ty = 0.2 s	2.299	2.500	-8.36	2.937	2.500	16.08
	Ty = 0.5 s	2.566	2.500	2.62	2.686	2.286	16.11
	Ty = 1.0 s	2.754	2.500	9.65	1.690	1.440	15.98
	Ty = 1.5 s	2.860	2.500	13.43	1.287	1.099	15.78
	Ty = 2.0 s	2.909	2.500	15.11	1.051	0.907	14.66
	Ty = 2.5 s	2.924	2.500	15.63	0.892	0.782	13.18
	Ty = 3.0 s	2.935	2.500	16.01	0.772	0.692	10.87
	Ty = 4.0 s	2.939	2.500	16.13	0.453	0.571	-23.03
Soil Type 3	Ty = 0.2 s	2.299	2.500	-8.36	2.937	2.500	16.08
	Ty = 0.5 s	2.566	2.500	2.62	2.938	2.500	16.11
	Ty = 1.0 s	2.754	2.500	9.65	2.113	1.800	15.98
	Ty = 1.5 s	2.880	2.500	14.12	1.609	1.374	15.78
	Ty = 2.0 s	2.910	2.500	15.16	1.313	1.134	14.66
	Ty = 2.5 s	2.929	2.500	15.80	1.115	0.977	13.17
	Ty = 3.0 s	2.936	2.500	16.05	0.965	0.865	10.87
	Ty = 4.0 s	2.939	2.500	16.13	0.567	0.714	-23.03
Soil Type 4	Ty = 0.2 s	2.299	2.500	-8.36	2.937	2.500	16.08
	Ty = 0.5 s	2.566	2.500	2.62	2.938	2.500	16.11
	Ty = 1.0 s	2.754	2.500	9.65	2.817	2.400	15.98
	Ty = 1.5 s	2.880	2.500	14.12	2.145	1.832	15.79
	Ty = 2.0 s	2.910	2.500	15.16	1.751	1.512	14.66
	Ty = 2.5 s	2.929	2.500	15.80	1.487	1.303	13.18
	Ty = 3.0 s	2.936	2.500	16.05	1.287	1.154	10.88
	Ty = 4.0 s	2.939	2.500	16.13	0.756	0.952	-23.03

CHAPTER VI
CONCLUSIONS

From the study, the following conclusions can be deduced:

1) For the seismic hazard analysis, probabilistic seismic hazard maps at rock sites in Thailand and neighboring areas are developed using up-to-date earthquake catalogs and attenuation models based on recent findings. Hazard deaggregation at key locations is investigated. Peak horizontal accelerations at Kanchanaburi and Bangkok are governed by the hazard of the source zone in western Thailand where the Three Pagodas fault and the Si Sawat fault are located. The seismic hazard maps for the 2% and 10% probability of exceedance in 50 years are proposed. For 10% probability of exceedance in 50 years, the maximum peak horizontal acceleration is about 0.25g in northern Thailand, about 0.15g in western Thailand, and about 0.03g in Bangkok. The spectral accelerations at the periods of 0.2s and 1.0s are about 2 and 0.5 times the peak horizontal accelerations respectively. For 2% probability of exceedance in 50 years, the peak horizontal accelerations and the spectral accelerations are about 1.6 to 2.0 times the peak horizontal accelerations and spectral accelerations with 10% probability of exceedance in 50 years.

2) For the effect of soil amplification study, the formulations for predicting shear wave velocity were developed. Seismic downhole tests were conducted at 6 sites to develop the relationship for predicting shear wave velocity in the areas. The relation between the shear wave velocity and the N-value of clay in Bangkok gives the shear wave velocity 12 % less than the shear wave velocity from equations developed by other researches. The relation between the shear wave velocity and the N-value of sand in the northern part gives the shear wave velocity 13 % less than the shear wave velocity from equations developed by other researches for N-values less than 14 blows/ft and 6 % more than of the shear wave velocity from equations developed by other researches for N-values more than 14 blows/ft.

3) Soil response analysis was done for 33 sites to obtain the acceleration response spectra at the ground and the amplification factors. It is found that the trend of soil amplification factors reduce along the increment of Vs30 and those factors are as large as 2.0 at locations where Vs30 is less than 200 m/s.

4) A simplified analytical model of a two-degree-of-freedom system was employed. 86 horizontal ground motion records from various site conditions were considered. The bi-directional pseudo-acceleration response spectra, acceleration ratio response spectra, and the direction of the maximum response were defined in order to generalize bi-directional responses of structures. Maximum radial pseudo-accelerations are generally larger than pseudo-accelerations in two orthogonal directions. The values of acceleration ratio response spectra are larger than 1.0 and generally less than about 1.5. The bi-directional response tends to bias to the direction of the shorter natural period.

5) Since there is no consistent trend of how earthquake magnitudes, epicentral distances, and soil conditions affect $R_A(T_x,T_y)$, $R_A(T_x,T_y)$ for 86 ground motion records is represented by statistical values which are mean and mean-plus-one-standard-deviation values. It is found that the mean value is 1.092 and the standard deviation is 0.084. The mean-plus-one-standard-deviation values of $R_A(T_x,T_y)$ is presented as a constant value of 1.18 for all combinations of natural periods. The angle of the maximum response is averaged for all ground motion records and presented as a direction response spectrum.

6) The proposed response spectra are applied to a simplified structure and compared with the 30%, SRSS and CQC3 combination rules. It is found that the proposed method yields larger responses in x- and y-directions for certain combinations of natural periods. Base shears in the x-direction from the proposed method are larger than the responses from the other combination rules when T_x is shorter than T_y. And, the base shears in the y-direction from the proposed method are larger than the responses from the other combination rules when T_x is longer than T_y. The responses from proposed method can reach about 16% larger than those from SRSS and CQC3-rules for the direction with a shorter period.

REFERENCES

Algermissen, S.T., Perkins, D.M., Thenhaus, P.C., Hanson, S.L., and Bender, B.L. (1982). Probabilistic Estimates of Maximum Acceleration and Velocity in Rock in the Contiguous United States, U.S. Geological Survey. Open-File Report 1982-1033.

American Association of State Highway and Transportation Officials. (2002). Standard Specifications for Highway Bridges, Seventeenth Edition: Division I-A: Seismic Design, Washington, DC.

Anastassiadis, K., Avramidis, I., and Panetsos, P. (2002). Concurrent design forces in structures under three-component orthotropic seismic excitation. Earthquake Spectra 18 : 1-17.

Arias, A. (1970). A measure of earthquake intensity. Seismic Design for Nuclear Power Plants MIT Press: Cambridge, MA : 438–483.

Ashford, S.A., Jakrapiyanun, W., and Lukkunaprasit, P. (2000). Amplification of earthquake ground motions in Bangkok. Proceedings, 12th World Conference on Earthquake Engineering, Auckland, New Zealand.

Athanatopoulou, A.M.. (2005). Critical orientation of three correlated seismic components. Engineering Structures 27 : 301-312.

BSSC. (1997). NEHRP Recommended Provisions for Seismic Regulations for New Buildings, Part 1 - Provisions, 1997 Edition: Building Seismic Safety Council, Washington, DC.

Chintanapakdee, C., Naguit, M.E., and Charoenyut, M. (2008). Suitable attenuation model for Thailand. Proceedings, 14th World Conference on Earthquake Engineering, Beijing, China.

Chopra, A., and Chintanapakdee, C. (2001). Comparing response of SDF systems to near-fault and far-fault earthquake motions in the context of spectra region. Earthquake Engineering and Structural Dynamics 30 : 1769-1789.

Clough, R.W., and Penzien, J. (1993). Dynamics of Structures, McGraw-Hill, New York.

Cornell, C.A. (1968). Engineering seismic risk analysis. Bulletin of the Seismological Society of America 58 : 1583–1606.

Dickenson, S.E. (1994). Dynamic Response of Soft and Deep Cohesive Soils During the Loma Prieta Earthquake of October 17, 1989. Dissertation presented to the Regents of the University of California at Berkeley in partial fulfillment of the requirements for the degree of Ph.D. in Engineering, Berkeley, California.

Dimova, S.L., and Elenas, A. (2002). Seismic intensity parameters for fragility analysis of structures with energy dissipating devices. Structural Safety 24 : 1-28.

Douglas, J. (2001). A Comprehensive Worldwide Summary of Strong-Motion Attenuation Relationships for Peak Ground Acceleration and Spectral Ordinates

(1969 to 2000), Engineering Seismology and Earthquake Engineering, ESEE Report No. 01-1.

EduPro Civil System, Inc. (2004). ProShake Ground Response Analysis Program, Version 1.1. User's Manual, Redmond, Washington.

Esteva, L., and Villaverde, R. (1973). Seismic risk, design spectra and structural reliability. Proceedings, the 5th World Conference on Earthquake Engineering, Rome, Italy : 2586–2597.

Fenton, C. H., Charusiri, P., and Wood, S.H. (2003). Recent paleoseismic investigations in Northern and Western Thailand. Annals of Geophysics 46(5) : 957-980.

Fujita, K., and Takewaki, I. (2010). Critical correlation of bi-directional horizontal ground motions. Engineering Structure 32 : 261-272.

Gardner, J. K., and Knopoff , L. (1974). Is the sequence of earthquakes in southern California, with aftershocks removed, Poissonian?. Bulletin of the Seismological Society of America 64(5) : 1363-1367.

Gutenberg, B., and Richter, C.F. (1954). Frequency of earthquakes in California. Bulletin of the Seismological Society of America 34(4) : 1985-1988.

Heaton, T.H., Tajima, F., and Mori, A.W. (1986). Estimating ground motions using recorded accelerograms. Survey in Geophysics 8 : 25-83.

Heredia-Zavoni, E., and Machicao-Barrionuevo, R. (2004). Response to orthogonal components of ground motion and assessment of percentage combination rules. Earthquake Engineering and Structural Dynamics 33(2) : 271-284.

Hernandez, J.J., and Lopez, O.A. (2003). Evaluation of combination rules for peak response calculation in three-component seismic analysis. Earthquake Engineering and Structural Dynamics 32(10) : 1585-1602.

Housner, G.V. (1952). Spectrum intensities of strong motion earthquakes. Proceedings of the Symposium on Earthquake and Blast Effects on Structures, EERI, Oakland, California : 20-36.

Idriss, I.M. (1993). Procedures for Selecting Earthquake Ground Motions at Rock Sites, Report No. NIST GCR 93-625, Report to National Institute of Standards and Technology, Gaithersburg, Maryland, Center for Geotechnical Modeling, Department of Civil and Environmental Engineering, University of California, Davis, California.

Imai, T., and Tonouchi, K. (1982). Correlation of N-value with S-wave velocity and shear modulus. Proceedings of the Second European Symposium on Penetration Testing, Amsterdam, The Netherlands : 67-72.

Kappos, A.J. (1990). Sensitivity of calculated inelastic seismic response to input motion characteristics. Proceedings of the 4th US National Conference on Earthquake Engineering, EERI, Oakland, California : 25-34.

Kramer, S.L. (1996). Geotechnical Earthquake Engineering, Prentice-Hall International Series in Civil Engineering and Engineering Mechanics.

Lopez, O.A., Chopra, A.K., and Hernandez, J.J. (2000). Critical response of structures to multicomponent earthquake excitation. Earthquake Engineering and Structural Dynamics 29(12) : 1759-1778.

Lopez, O.A., Chopra, A.K., and Hernandez, J.J. (2001). Evaluation of combination rules for maximum response calculation in multicomponent seismic analysis. Earthquake Engineering and Structural Dynamics 30(9) : 1379-1398.

Lopez, O.A., and Torres, R. (1997). The critical angle of seismic incidence and the maximum structural response. Earthquake Engineering and Structural Dynamics 26(9) : 881-894.

Lukkunaprasit, P. (1995). Lessons learned from damages in a low seismic risk country. Stop Disaster Magazine IDNDR, United Nations Publication : 18-19.

Magliulo, G., and Ramasco, R. (2007). Seismic response of three-dimensional R/C multi-storey frame building under uni- and bi-directional input ground motion. Earthquake Engineering and Structural Dynamics 36(12) : 1641-1657.

Malhotra. (1999). Response of buildings to near-field pulse-like ground motions. Earthquake Engineering and Structural Dynamics 28 : 1309-1326.

McGuire, R.K., and Arabasz, W. J. (1990). An introduction to probabilistic seismic hazard analysis. Geotechnical and Environmental Geophysics Vol. I, Review and Tutorial, SEG : 333-352.

Menun, C., and Der Kiureghian, A. (1998). A replacement for the 30%, 40%, ans SRSS rules for multicomponent seismic analysis. Earthquake Spectra 14(1) : 153-163.

Nau, J.M., and Hall, W.J. (1984). Scaling methods for earthquake response spectra. Journal of Structural Engineering, ASCE 110(7) : 1533-1548.

Newmark, N.M. (1975). Seismic design criteria for structures and facilities, Tran-Alaska pipeline system. Proceedings of the U.S. National Conference Earthquake Engineering: 94-103.

Nutalaya, P., Sodsri, S., and Arnold, E.P. (1985). Southeast Asia Association of Seismology and Earthquake Engineering, Series on Seismology-Volume II-Thailand.

Ohsaki, Y., and Iwasaki, R. (1973). On dynamic shear moduli and Poisson's ratio of soil deposits. Soil and Foundations 13(4) : 61-73.

Ohta, Y., and Goto, N. (1978). Empirical shear wave velocity equations in terms of characteristics soil indexes. Earthquake Engineering and Structural Dynamics 6 : 167-187.

Olivia, M., and Clough, R. (1987). Biaxial seismic response of R/C frames. Journal of Structural Engineering ASCE, 113(6) : 1264-1281.

PEER. (2010). Strong Motion Database [Online]. Available from : http://peer.berkeley.edu/smcat/index.html [2010,May]

Penzien, J., and Watabe, M. (1975). Characteristics of 3-dimensional earthquake ground motion. Earthquake Engineering and Structural Dynamics 3 : 365-374.

Perus, I., and Fajfar, P. (2005). On the inelastic torsional response of single-storey structures under bi-axial excitation. Earthquake Engineering and Structural Dynamics 34(8) : 931-941.

Petersen, M.D., Dewey, J., Hartzell, S., Mueller, C., Harmsen, S., Frankel, A.D., and Rukstales, K. (2004). Probabilistic seismic hazard analysis for Sumatra, Indonesia and Across the Southern Malaysian Peninsula. Tectonophysics 390 : 141-158.

Pitakwong, K., and Poovarodom, N. (2009). Estimation of shear wave velocity using microtremor simultaneously observed at two sites. Proceedings of the 14th National Convention on Civil Engineering, Nakorn Ratchasima, Thailand.

Riddell, R., and Santa-Maria, H. (1999). Inelastic response of one storey asymmetric-plan systems subjected to bi-directional earthquake motions. Earthquake Engineering and Structural Dynamics 28(3) : 273-285.

Rosenblueth, E., and Contreras, H. (1977). Approximate design for multicomponent earthquakes. Journal of Engineering Mechanics ASCE, 103 : 895-911.

Sadigh, K., Chang, C.-Y., Egan, J.A., Makdisi, F., and Youngs, R.R. (1997). Attenuation relationships for shallow crustal earthquakes based on California strong motion data. Seismological Research Letters 68(1) : 180-189.

Saithong, P., Kosuwan, S., Choowong, M., Won-in, K., Takashima, I., and Charusiri, P. (2004). Preliminary study on morphotectonic evidences along Moei-Mae Ping fault zone, Tak province, Northwestern Thailand. Asia Conference on Earthquake Engineering, Manila, Philippines.

Scordilis, E.M. (2006). Empirical global relations converting MS and mb to moment magnitude. Journal of Seismology 10 : 225-236.

Seed, H.B.,and Idriss, I.M. (1970). Soil Moduli and Damping Factors for Dynamic Response Analyses, Report No. EERC 70-10, Earthquake Engineering Research Center, University of California, Berkeley.

Seed, H.B., Idriss, I.M., and Arango, I. (1983). Evaluation of liquefaction potential using field performance data. Journal of Geotechnical Engineering, ASCE, 109(3) : 458-482.

Sipkin, S.A. (2003). A correction to body-wave magnitude mb based on moment magnitude Mw. Seismological Research Letters 74(6) : 739-742.

Smeby, W., and Der Kiureghian, A. (1985). Modal combination rules for multicomponent earthquake excitation. Earthquake Engineering and Structural Dynamics 13 : 1-12.

Stefano, M.D., Faella, G., and Ramasco, R. (1998). Inelastic seismic response of one-way plan-asymmetric systems under bi-directional ground motions. Earthquake Engineering and Structural Dynamics 27(4) : 363-376.

Stepp, J.C. (1972). Analysis of completeness in the earthquake sample in the Puget Sound area and its effect on statistical estimates of earthquake hazard. Proceedings, International Conference on Microzonation, Seattle, Washington, 2 : 897-910.

Sykora, D.W., and Stokoe, K.H. (1983). Correlations of In-Situ Measurements in Sands with Shear Wave Velocity, Geotechnical Engineering Report GR 83-33, The University of Texas at Austin, Texas.

Takizawa, H., and Aoyama, H. (1976). Biaxial effects in modelling earthquake response of R/C structures. Earthquake Engineering and Structural Dynamics 4 : 523-552.

Tuladhar, R., and Warnitchai, P. (2003). Classification of Soil Profile and Seismic Response Analysis (elastic) in The Greater Bangkok Area, Asian Institute of Technology, Thailand.

Tuladhar, R., Yamazaki, F., Warnitchai, P., and Saita, J. (2004). Seismic microzonation of the greater Bangkok area using microtremor observations. Earthquake Engineering and Structural Dynamics 33 : 211-225.

UBC. (1997). Uniform Building Code, International Conference of Building Officials, California.

Vucetic, M., and Dobry, R. (1991). Effect of soil plasticity on cyclic response. Journal of Geotechnical Engineering, ASCE, 117(1) : 89-107.

Warnitchai, P., and Lisantono, A. (1996). Probabilistic seismic risk mapping for Thailand. Proceedings, the 11th World Conference on Earthquake Engineering, Acapulco, Mexico.

Wilson, E. L., Der Kiureghian, A., and Bayo, E.P. (1981). A replacement for the SRSS method in seismic analysis. Earthquake Engineering and Structural Dynamics 9 : 187-194.

Wong, Y.L., Paulay, T., and Priestley, M.J.N. (1993). Response of circular reinforced concrete columns to multi-direction seismic attack. ACI Structural Journal 90(2) : 180–191.

Youngs, R.R., Chiou, S.J., Silva, W.J., and Humphrey, J.R. (1997). Strong ground motion attenuation relationships for subduction zone earthquakes. Seismological Research Letters 68(1) : 58-73.

Zeris, C.A., and Mahin, J.A. (1991). Behaviour of reinforced concrete structures subjected to biaxial excitation. Journal of Structural Engineering, ASCE, 117(9) : 2657-2673.

APPENDICES

Appendix A
Soil Profiles and Analytical results

A.1 Soil Profiles

Table A-1 Soil profile of Chulalongkorn University

Layer No.	Type of Sample	Depth, m	Thicknes s, m	Classification	Natural Water Content (%)	Su, t/m^2	SPT, N (Blow/ft)	Plastic Index (%)	Wet Unit Weight (t/m^3)	(Downhole) Vs (m/s)	(Downhole) Shear Modulus (MPa)
1	ST	0.3	1.05	CH	117.6				1.70	121	25
2	ST	1.8	1.50	CH	109.8	1.25			1.70	69	8
3	ST	3.3	1.50	CH	68.1	1.50			1.70	86	13
4	ST	4.8	1.50	CH	81.9	2.50			1.70	104	18
5	ST	6.3	1.50	CH	63.5	2.00			1.70	101	17
6	ST	7.8	1.50	CH	53.3	2.00			1.70	104	18
7	ST	9.3	1.50	CH	36	3.00			1.70	105	19
8	ST	10.8	1.50	CH	25.2	3.75			1.70	141	34
9	SS	12.3	1.00	CL	20	12.5			1.70	203	70
10	SS	12.8	0.75	CL	19.2		12		1.70	200	68
11	SS	13.8	1.25	CL	16.9		13		1.70	172	50
12	SS	15.3	1.50	CL	16.6		15		1.70	209	74
13	SS	16.8	1.50	CL	16.9		18		1.70	182	57
14	SS	18.3	1.50	CL	17.2		19		1.70	264	118
15	ST	19.8	1.50	CL	22.6		20		1.70	241	99
16	SS	21.3	1.50	CL	28.1		34		1.70	278	132
17	SS	22.8	1.50	CL	17.1		30		1.70	217	80
18	SS	24.3	1.50	CL	19.5		34		1.70	288	141
19	SS	25.8	1.50	CL	12.1		30		1.70	259	114
20	SS	27.3	1.50	SM	17.3		55		1.75	227	90
21	SS	28.8	1.50	SM	20.2		51		1.75	373	244
22	ST	30.3	1.50	SM	16		24		1.75	268	126
23	SS	31.8	1.50	SM	17.4		40		1.75		
24	SS	33.3	1.50	SM	19		60		1.75		
25	SS	34.8	1.50	SM	20.5		43		1.75		
26	SS	36.3	1.50	CH	18.4		42		1.80		
27	SS	37.8	1.50	CH	19		30		1.80		
28	SS	39.3	1.50	CH	14.8		36		1.80		
29	SS	40.8	1.50	CH	18		45		1.80		
30	SS	42.3	1.50	CH	15.6		37		1.80		
31	SS	43.8	1.50	CH	14		31		1.80		
32	SS	45.3	1.50	CH	17.2		37		1.80		
33	SS	46.8	1.50	CH	18.8		38		1.80		
34	SS	48.3	1.50	CH	16.3		49		1.80		
35	SS	49.8	1.50	SM	18.7		46		1.80		
36	SS	51.3	1.50	SM	20.7		75		1.80		
37	SS	52.8	1.50	CL	19.6		45		1.80		
38	SS	54.3	3.75	CL	21.4		56		1.80		
39	SS	60.3	3.00	SM	24.3		67		1.80		

Table A-2 Soil profile of Asian Institute Technology

Layer No.	Type of Sample	Depth, m	Thickness, m	Classification	Natural Water Content (%)	Su, t/m^2	SPT, N (Blow/ft)	Plastic Index (%)	Wet Unit Weight (t/m^3)	(Downhole) Vs (m/s)	(Downhole) Shear Modulus (MPa)
1	ST	1.8	2.55	CH	54.0	2.33		51.00	1.72	165	47
2	ST	3.3	1.50	CH	50.0	3.79			1.71	92	14
3	ST	4.8	1.50	CH	91.0	2.02		65.00	1.55	67	7
4	ST	6.3	1.50	CH	87.0	1.50			1.58	59	6
5	ST	7.8	1.50	CH/SC	58.0	0.65			1.63	123	25
6	ST	9.3	1.50	CH	30.0	3.82		29.00	1.88	192	69
7	ST	10.8	1.00	CL	25.0	6.70			2.01	263	139
8	SS	11.3	0.75	CL	21.0		18	32.00	2.09	196	81
9	SS	12.3	1.25	CL	27.0		17		1.97	179	63
10	SS	13.8	1.50	CL	28.0		18		1.96	195	74
11	SS	15.3	1.50	CL	27.0		13	17.00	2.18	292	186
12	SS	16.8	1.50	CL	27.0		25		2.00	463	429
13	SS	18.3	1.50	SM	15.0		44		2.13	385	316
14	SS	19.8	1.50	SM	9.0		83		2.11	329	229
15	SS	21.3	1.50	SP-SM	16.0		58		2.08	296	
16	SS	22.8	1.50	SP-SM	16.0		51		2.15	306	
17	SS	24.3	1.50	CL	30.0		24	43.00	1.99	313	
18	SS	25.8	1.50	CL	29.0		22		1.99	227	103
19	SS	27.3	1.50	CL/SC	32.0		25	24.00	2.17	481	502
20	SS	28.8	1.50	CL/SC	46.0		9		1.97	140	39
21	SS	30.3	0.75	SC/CL	41.0		17	15.00	1.95	163	52

Table A-3 Soil profile of the Department of Rural Road, Chiangrai

Layer No.	Type of Sampl e	Depth, m	Thickness, m	Classification	Natural Water Content (%)	Su, t/m^2	SPT, N (Blow/ft)	Plastic Index (%)	Wet Unit Weight (t/m^3)	(Downhole) Vs (m/s)	(Downhole) Shear Modulus (MPa)
1	SS	0.8	1.05	SM	12.0		14		1.94	111	24
2	SS	1.3	0.50	SM	16.0		13		2.04	88	16
3	SS	1.8	0.50	SP-SM	25.0		8		1.98	100	20
4	SS	2.3	0.50	SP-SM	20.0		11		1.84	134	33
5	SS	2.8	0.50	SP-SM	20.0		11		2.11	153	49
6	SS	3.3	1.00	SP-SM	21.0		7		2.01	160	52
7	SS	4.8	1.50	SP-SM	17.0		9		2.14	196	82
8	SS	6.3	1.50	CH	17.0		5	31.00	1.97	129	33
9	SS	7.8	1.50	SP-SM	18.0		21		2.07	279	161
10	SS	9.3	1.50	SP-SM	19.0		24		2.13	349	260
11	SS	10.8	1.50	SP-SM	10.0		29		1.96	224	99
12	SS	12.3	1.50	SP-SM	8.0		46		2.06	396	324
13	SS	13.8	1.50	GM			51				
14	SS	15.3	0.75	GM			52				

Table A-4 Soil profile of Chiangmai University

Layer No.	Type of Sample	Depth, m	Thickness, m	Classification	Natural Water Content (%)	Su, t/m^2	SPT, N (Blow/ft)	Plastic Index (%)	Wet Unit Weight (t/m^3)	(Downhole) Vs (m/s)	(Downhole) Shear Modulus (MPa)
1	SS	0.8	1.05	CL-ML	7.0		37	5.00	1.97	223	98
2	SS	1.3	0.50	SC/CL	7.0		16	13.00	2.00	294	173
3	SS	1.8	0.50	SC/CL	15.0		15	15.00	2.13	343	251
4	SS	2.3	0.50	CL	16.0		18		2.19	376	310
5	SS	2.8	0.50	CL	17.0		28	19.00	2.19	395	342
6	SS	3.3	1.00	CL	18.0		19		2.24	404	365
7	SS	4.8	1.50	SC/CL	14.0		12	11.00	2.24	432	418
8	SS	6.3	1.50	SC/CL	15.0		13		2.25	440	436
9	SS	7.8	1.50	CL	17.0		15	20.00	2.23	259	150
10	SS	9.3	1.50	CL	15.0		18	18.00	2.25	328	242
11	SS	10.8	1.50	CL	20.0		20		2.25	412	381
12	SS	12.3	1.50	CL	21.0		18	15.00	2.26	336	255
13	SS	13.8	1.50	SC/CL	19.0		12	15.00	2.06	420	363
14	SS	15.3	1.50	SC/CL	22.0		13		2.19	593	771
15	SS	16.8	1.50	SC	17.0		31	8.00	2.04	279	159
16	SS	18.3	1.50	SC	16.0		28		2.05	483	479
17	SS	19.8	1.50	SC	11.0		45	20.00	2.07	401	334
18	SS	21.3	1.50	GM						485	
19	SS	22.8	0.75	GM							

Table A-5 Soil profile of Wat Chedi Luang Woraviharn

Layer No.	Type of Sample	Depth, m	Thickness, m	Classification	Natural Water Content (%)	Su, t/m^2	SPT, N (Blow/ft)	Plastic Index (%)	Wet Unit Weight (t/m^3)	(Downhole) Vs (m/s)	(Downhole) Shear Modulus (MPa)
1	SS	0.8	1.05	SC-SM	12.0		28	6.00	2.04	349	249
2	SS	1.3	0.50	CL	18.0		24	10.00	2.06	311	199
3	SS	1.8	0.50	CL	14.0		10	8.00	2.12	328	229
4	SS	2.3	0.50	CL	18.0		5		2.06	383	302
5	SS	2.8	0.50	SC	14.0		21	14.00	2.13	452	436
6	SS	3.3	1.00	SC	12.0		22		2.10	531	592
7	SS	4.8	1.50	SC	12.0		31	17.00	2.00	541	584
8	SS	6.3	1.50	CL	20.0		20		2.00	205	84
9	SS	7.8	1.50	CL	21.0		22		1.97	448	395
10	SS	9.3	1.50	CL	25.0		33	24.00	1.87	233	102
11	SS	10.8	1.50	CL	20.0		22		1.98	309	189
12	SS	12.3	1.50	CL	24.0		30		1.96	367	264
13	SS	13.8	1.50	SM	20.0		47		1.97	255	127
14	SS	15.3	1.50	SM	16.0		79		1.97	568	637
15	SS	16.8	1.50	SM	14.0		60		1.98	537	571
16	SS	18.3	1.50	SM	13.0		63		2.16	675	983
17	SS	19.8	1.50	SM	13.0		47		2.06	292	176
18	SS	21.3	0.95	SM			75		2.06		
19	SS	21.7	0.20	SM							

Table A-6 Soil profile of CM01

Layer No.	Type of Sample	Depth, m	Thickness, m	Classification	Natural Water Content (%)	SPT, N (Blow/ft)	Plastic Index (%)	Wet Unit Weight (t/m^3)	Vs (m/s)
1	SS	1.8	2.55	SM	12.34	21		2.14	256
2	SS	3.3	1.50	SM	17.06	12		1.83	202
3	SS	4.8	1.50	CL	20.64	18	19.88	2.21	240
4	SS	6.3	1.50	CL	23.48	20	19.35	1.89	251
5	SS	7.8	1.50	CL	24.57	35	20.29	2.13	317
6	SS	9.3	1.50	CL	20.79	41	24.17	1.88	339
7	SS	10.8	1.50	CL	23.18	40	24.75	1.88	336
8	SS	12.3	1.50	CH	26.46	33	28.20	1.95	310
9	SS	13.8	1.50	SM	21.81	15		1.95	222
10	SS	15.3	1.50	ML-OL	25.01	22	20.01	1.99	261
11	SS	16.8	1.50	SM	30.00	23		1.94	266
12	SS	18.3	2.45	CH	29.59	37	26.64	2.02	325
13		20.0	5.00	SM				2.02	375
14		25.0	5.00	SM				2.02	387
15	Tested	30.0	10.00	SM				2.02	410
16	by	40.0	10.00	SM				2.02	442
17	2sSPAC	50.0	10.00	SM				2.02	471
18	method	60.0	10.00	SM				2.02	497
19		70.0	10.00	SM				2.02	517
20		80.0	infinite	SM				2.02	534

Table A-7 Soil profile of CM02

Layer No.	Type of Sample	Depth, m	Thickness, m	Classification	Natural Water Content (%)	SPT, N (Blow/ft)	Plastic Index (%)	Wet Unit Weight (t/m^3)	Vs (m/s)
1	SS	1.3	1.80	CL	8.09	6	10.04	1.66	151
2	SS	2.3	1.00	CL	16.92	37	9.46	2.23	325
3	SS	3.3	1.25	CL	20.41	34	12.33	2.13	314
4	SS	4.8	1.50	SC	8.41	52	9.70	2.15	375
5	SS	6.3	1.50	SP-SC	12.12	28	9.72	1.89	289
6	SS	7.8	1.50	SM	11.40	34		2.07	314
7	SS	9.3	1.50	SC	13.08	38	11.67	2.27	329
8	SS	10.8	1.50	SM	18.93	21		2.25	256
9	SS	12.3	1.50	SM	15.03	40		2.13	336
10	SS	13.8	1.50	CL	19.87	52	17.72	2.26	375
11	SS	15.3	1.50	SM	13.73	53		2.16	378
12	SS	16.8	1.50	SP-SM	15.17	75		2.20	438
13	SS	18.3	infinite	SP-SM	9.52	160		2.25	604

Table A-8 Soil profile of CM03

Layer No.	Type of Sample	Depth, m	Thickness , m	Classification	Natural Water Content (%)	SPT, N (Blow/ft)	Plastic Index (%)	Wet Unit Weight (t/m^3)	Vs (m/s)
1	SS	1.3	1.55	SC/CL	23.60	23		2.10	266
2	SS	1.8	0.50	CL	21.40	23	21.60	2.10	266
3	SS	2.3	0.75	CL	23.70	20		1.94	251
4	SS	3.3	1.25	CL	24.60	22		1.93	261
5	SS	4.8	1.50	CL	18.30	13		2.12	209
6	SS	6.3	1.50	CL	22.60	10	17.70	2.00	187
7	SS	7.8	1.50	SC	22.20	7		2.00	161
8	SS	9.3	1.50	SM	7.60	19		2.00	245
9	SS	10.8	1.50	SM	20.90	20		2.00	251
10	SS	12.3	1.50	GM-GP	21.30	44		2.00	350
11	SS	13.8	1.50	SM-SP	8.90	59		2.00	396
12	SS	15.3	infinite	SM	6.60	70		2.00	426

Table A-9 Soil profile of CM04

Layer No.	Type of Sample	Depth, m	Thickness, m	Classification	Natural Water Content (%)	SPT, N (Blow/ft)	Plastic Index (%)	Wet Unit Weight (t/m^3)	Vs (m/s)
1	SS	1.3	1.55	SC	8.50	5		2.06	139
2	SS	1.8	0.50	SC/CL	10.70	8		2.06	170
3	SS	2.3	0.75	SC	14.00	12		2.06	202
4	SS	3.3	1.25	SC	14.80	13		2.06	209
5	SS	4.8	1.50	SM-SP	15.00	12		2.06	202
6	SS	6.3	1.50	SM-SP	15.40	10		2.06	187
7	SS	7.8	1.50	SM-SP	20.20	13		2.06	209
8	SS	9.3	1.50	SM-SP	10.30	13		2.06	209
9	SS	10.8	1.50	GC	8.60	16		2.06	228
10	SS	12.3	1.50	SM	13.00	27		2.06	284
11	SS	13.8	1.50	SM	7.80	26		2.06	280
12	SS	15.3	1.50	SM	7.60	30		2.06	297
13	SS	16.8	1.50	SM	6.10	24		2.06	271
14	SS	18.3	1.50	CL/SC	13.70	27		2.06	284
15	SS	19.8	1.50	CL	18.20	27		2.08	284
16	SS	21.3	1.50	CL/SM	12.10	150		2.08	588
17	SS	22.8	1.50	SM	32.50	100		2.08	495
18	SS	24.3	infinite	SM	34.60	100		2.08	495

Table A-10 Soil profile of CM05

Layer No.	Type of Sample	Depth, m	Thickness, m	Classification	Natural Water Content (%)	SPT, N (Blow/ft)	Plastic Index (%)	Wet Unit Weight (t/m^3)	Vs (m/s)
1	SS	1.3	1.55	CH	14.90	31		2.16	302
2	SS	1.8	0.50	CL	13.90	43	18.80	2.16	346
3	SS	2.3	0.75	CH	15.60	42		2.14	343
4	SS	3.3	1.25	CH	19.20	26		2.14	280
5	SS	4.8	1.50	CH	23.10	18		2.08	240
6	SS	6.3	1.50	CL	31.30	15	26.10	1.96	222
7	SS	7.8	1.50	SM-SP	12.00	21		1.96	256
8	SS	9.3	1.50	SM-SP	7.40	21		1.96	256
9	SS	10.8	1.50	SM-SP	6.30	36		1.96	321
10	SS	12.3	1.50	CH/SC	39.40	12		1.96	202
11	SS	13.8	1.50	CH	14.80	53		1.96	378
12	SS	15.3	1.50	SC	13.30	60		1.96	399
13	SS	16.8	infinite	SC	13.00	55		1.96	384

Table A-11 Soil profile of CM06

Layer No.	Type of Sample	Depth, m	Thickness, m	Classification	Natural Water Content (%)	SPT, N (Blow/ft)	Plastic Index (%)	Wet Unit Weight (t/m^3)	Vs (m/s)
1	SS	1.8	2.55	CL	15.06	21	7.15	1.78	256
2	SS	3.3	1.50	CL	15.35	27	15.62	2.17	284
3	SS	4.8	1.50	CL	31.07	18	22.05	1.84	240
4	SS	6.3	1.50	OL-ML	26.35	22	13.81	1.99	261
5	SS	7.8	1.50	CL	17.92	27	18.92	2.19	284
6	SS	9.3	1.50	CL	19.53	22	18.98	2.11	261
7	SS	10.8	1.50	CL	25.84	20	14.30	1.99	251
8	SS	12.3	1.50	SM	16.96	44		2.11	350
9	SS	13.8	1.50	SM	12.60	36		2.13	321
10	SS	15.3	1.50	CL	15.68	48	15.26	2.16	363
11	SS	16.8	1.50	SM	10.13	45		2.24	353
12	SS	18.3	infinite	CL	19.13	43	14.44	2.13	346

Table A-12 Soil profile of CM07

Layer No.	Type of Sample	Depth, m	Thickness, m	Classification	Natural Water Content (%)	SPT, N (Blow/ft)	Plastic Index (%)	Wet Unit Weight (t/m^3)	Vs (m/s)
1	SS	1.3	1.55	CL	24.80	8		1.99	170
2	SS	1.8	0.50	SM	9.40	18		1.99	240
3	SS	2.3	0.75	SM	3.20	8		1.99	170
4	SS	3.3	1.25	SM	5.50	19		1.99	245
5	SS	4.8	1.50	SM-SP	18.10	13		1.99	209
6	SS	6.3	1.50	SM-SP	13.20	15		1.99	222
7	SS	7.8	1.50	SM-SP	10.90	20		1.99	251
8	SS	9.3	1.50	SM-SP	13.40	19		1.99	245
9	SS	10.8	1.50	GM-GP	13.60	12		1.99	202
10	SS	12.3	1.50	GM-GP	9.20	26		1.99	280
11	SS	13.8	1.50	SM	10.00	100		1.99	495
12	SS	15.3	infinite	SM		600		1.99	1056

Table A-13 Soil profile of CM08

Layer No.	Type of Sample	Depth, m	Thickness, m	Classification	Natural Water Content (%)	SPT, N (Blow/ft)	Plastic Index (%)	Wet Unit Weight (t/m^3)	Vs (m/s)
1	SS	1.3	1.80	SM	5.65	46		2.03	356
2	SS	2.3	1.00	SM	4.65	71		2.05	428
3	SS	3.3	infinite	SM	8.72	160		2.14	604

Table A-14 Soil profile of CM09

Layer No.	Type of Sample	Depth, m	Thickness , m	Classification	Natural Water Conten t (%)	SPT, N (Blow/ft)	Plastic Index (%)	Wet Unit Weight (t/m^3)	Vs (m/s)
1	SS	1.8	2.55	CL	16.15	46	15.27	2.06	356
2	SS	3.3	1.50	CL	13.95	15	15.41	2.17	222
3	SS	4.8	1.50	CL	15.23	17	14.56	2.10	234
4	SS	6.3	1.50	SM	15.04	22		1.93	261
5	SS	7.8	1.50	CL	13.07	35	21.10	2.17	317
6	SS	9.3	1.50	CL	17.78	32	17.61	2.12	306
7	SS	10.8	1.50	CL	17.31	34	18.81	2.09	314
8	SS	12.3	1.50	SC	21.21	57	19.75	1.98	390
9	SS	13.8	1.50	SW-SM	14.92	67		1.68	418
10	SS	15.3	infinite	SW-SM	13.25	55		2.22	384

Table A-15 Soil profile of CM10

Layer No.	Type of Sample	Depth, m	Thickness , m	Classification	Natural Water Content (%)	SPT, N (Blow/ft)	Plastic Index (%)	Wet Unit Weight (t/m^3)	Vs (m/s)
1	SS	1.3	1.80	CL	9.14	13		1.37	209
2	SS	2.3	1.00	SM	14.47	11		1.38	195
3	SS	3.3	1.25	SC	11.66	9		1.41	179
4	SS	4.8	1.50	SM	15.67	17		1.59	234
5	SS	6.3	1.50	SM	12.16	14		1.45	215
6	SS	7.8	1.50	SW-SM	18.02	10		1.70	187
7	SS	9.3	1.50	SW-SM	17.14	14		1.76	215
8	SS	10.8	1.50	SM	22.71	12		1.81	202
9	SS	12.3	1.50	SM	16.87	26		1.70	280
10	SS	13.8	1.50	SM	16.39	34		1.74	314
11	SS	15.3	1.50	SM	21.82	8		1.90	170
12	SS	16.8	1.50	SM	15.66	40		2.00	336
13	SS	18.3	1.50	SM	18.28	108		2.00	511
14	SS	19.8	1.50	SM	10.28	120		1.90	535
15	SS	21.3	infinite	SM	11.88	160		1.98	604

Table A-16 Soil profile of CR01

Layer No.	Type of Sample	Depth, m	Thickness, m	Classification	Natural Water Content (%)	SPT, N (Blow/ft)	Plastic Index (%)	Wet Unit Weight (t/m^3)	Vs (m/s)
1	SS	1.3	1.80	ML-OL	23.25	8	12.75	2.07	170
2	SS	2.3	1.00	ML-OL	24.36	15	2.52	2.05	222
3	SS	3.3	1.25	ML-OL	25.85	10	7.48	2.10	187
4	SS	4.8	1.50	CL	28.19	15	15.21	2.01	222
5	SS	6.3	1.50	CL	32.77	15	20.30	1.97	222
6	SS	7.8	1.50	MH-OH	30.46	11	18.51	2.12	195
7	SS	9.3	1.50	ML-OL	25.31	31	21.82	2.14	302
8	SS	10.8	1.50	CL	21.56	21	21.79	2.28	256
9	SS	12.3	1.50	CL	30.48	39		2.23	332
10	SS	13.8	1.50	SM	12.22	46		1.76	356
11	SS	15.3	infinite	SP-SM		65		1.76	412

Table A-17 Soil profile of CR02

Layer No.	Type of Sample	Depth, m	Thickness, m	Classification	Natural Water Content (%)	SPT, N (Blow/ft)	Plastic Index (%)	Wet Unit Weight (t/m^3)	Vs (m/s)
1	SS	1.3	1.55	CL	24.30	17		2.01	234
2	SS	1.8	0.50	CL	23.50	21	15.60	2.05	256
3	SS	2.3	0.75	CL	22.70	21		2.08	256
4	SS	3.3	1.25	CL	23.20	35		2.13	317
5	SS	4.8	1.50	CL	24.50	47		2.08	360
6	SS	6.3	1.50	CL	24.50	44		2.08	350
7	SS	7.8	1.50	CL	22.40	23		2.08	266
8	SS	9.3	1.50	SM	18.60	18		2.08	240
9	SS	10.8	1.50	SM	25.00	16		2.08	228
10	SS	12.3	1.50	SM	20.70	16		2.08	228
11	SS	13.8	1.50	SM	21.90	17		2.08	234
12	SS	15.3	infinite	GM	8.70	94		2.08	482

Table A-18 Soil profile of CR03

Layer No.	Type of Sample	Depth, m	Thickness, m	Classification	Natural Water Content (%)	SPT, N (Blow/ft)	Plastic Index (%)	Wet Unit Weight (t/m^3)	Vs (m/s)
1	SS	1.3	1.55	CL	21.90	6		2.07	151
2	SS	1.8	0.50	CL	24.20	8	15.10	2.07	170
3	SS	2.3	0.75	CL	22.50	9		2.03	179
4	SS	3.3	1.25	CL	27.50	11		1.98	195
5	SS	4.8	1.50	CL	25.90	14		1.99	215
6	SS	6.3	1.50	CL	25.60	18		1.94	240
7	SS	7.8	1.50	CL	25.70	22	15.40	2.07	261
8	SS	9.3	1.50	SM	25.90	5		2.07	139
9	SS	10.8	1.50	SM-SP	19.80	24		2.07	271
10	SS	12.3	1.50	SM	7.50	37		2.07	325
11	SS	13.8	1.50	SM	8.50	37		2.07	325
12	SS	15.3	infinite	SM	8.30	100		2.07	495

Table A-19 Soil profile of CR04

Layer No.	Type of Sample	Depth , m	Thickness , m	Classification	Natural Water Content (%)	SPT, N (Blow/ft)	Plastic Index (%)	Wet Unit Weight (t/m^3)	Vs (m/s)
1	SS	1.3	1.55	SC	0.60	32		2.07	306
2	SS	1.8	0.50	SC	4.60	31		2.07	302
3	SS	2.3	0.75	SM-SP	2.60	23		2.07	266
4	SS	3.3	1.25	SM-SP	4.40	11		2.07	195
5	SS	4.8	1.50	SM-SP	15.80	9		2.07	179
6	SS	6.3	1.50	SM-SP	12.40	17		2.07	234
7	SS	7.8	1.50	CH	12.00	2		2.07	95
8	SS	9.3	1.50	CH	32.90	3		2.07	112
9	SS	10.8	1.50	CL	17.90	25		2.07	275
10	SS	12.3	1.50	SM	11.00	45		2.07	353
11	SS	13.8	1.50	SM	10.80	61		2.07	402
12	SS	15.3	1.50	SM-SP	7.50	70		2.07	426
13	SS	16.8	infinite	SM-SP	5.90	81		2.07	453

Table A-20 Soil profile of CR05

Layer No.	Type of Sample	Depth , m	Thickness , m	Classificatio n	Natural Water Conten t (%)	SPT, N (Blow/ft)	Plastic Index (%)	Wet Unit Weight (t/m^3)	Vs (m/s)
1	SS	1.3	1.55	CL	23.30	10		2.04	187
2	SS	1.8	0.50	CL	22.50	14	15.10	1.99	215
3	SS	2.3	0.75	CL	23.90	13		2.03	209
4	SS	3.3	1.25	CL	21.90	16		2.08	228
5	SS	4.8	1.50	CL	24.30	15		2.13	222
6	SS	6.3	1.50	CL	26.20	7		2.13	161
7	SS	7.8	1.50	CL	27.20	8	8.10	2.13	170
8	SS	9.3	1.50	ML	25.40	9		2.13	179
9	SS	10.8	1.50	ML	30.70	7		2.13	161
10	SS	12.3	1.50	ML	29.40	7		2.13	161
11	SS	13.8	1.50	ML	28.80	10		2.13	187
12	SS	15.3	1.50	SM	14.00	61		2.13	402
13	SS	16.8	infinite	GM-GP	4.40	200		2.13	664

Table A-21 Soil profile of CR06

Layer No.	Type of Sample	Depth, m	Thickness , m	Classification	Natural Water Content (%)	SPT, N (Blow/ft)	Plastic Index (%)	Wet Unit Weight (t/m^3)	Vs (m/s)
1	SS	1.8	2.55	SW-SM	15.34	2		1.53	95
2	SS	3.3	1.50	CL	56.31	5	11.18	1.46	139
3	SS	4.8	1.50	SM	17.39	10		1.94	187
4	SS	6.3	1.50	SP-SM	14.63	11		2.16	195
5	SS	7.8	1.50	SP-SM	12.94	28		2.13	289
6	SS	9.3	1.50	SM	10.17	35		1.92	317
7	SS	10.8	1.50	SM	10.61	38		1.98	329
8	SS	12.3	1.50	SM	11.63	51		2.10	372
9	SS	13.8	infinite	SM	12.23	49		2.01	366

Table A-22 Soil profile of KN01

Layer No.	Type of Sample	Depth, m	Thickness, m	Classification	Natural Water Content (%)	SPT, N (Blow/ft)	Plastic Index (%)	Wet Unit Weight (t/m^3)	Vs (m/s)
1	SS	1.3	1.80	CL	16.66	2	22.48	2.21	95
2	SS	2.3	1.00	CL	21.05	5	17.33	2.35	139
3	SS	3.3	1.25	CL	23.55	4	17.66	2.22	127
4	SS	4.8	1.50	SM-SC	25.21	8	17.86	1.81	170
5	SS	6.3	1.50	SW-SM	24.64	17		1.66	234
6	SS	7.8	1.50	SM	22.45	25		1.66	275
7	SS	9.3	1.50	SW-SM	21.27	17		1.63	234
8	SS	10.8	1.50	SM	17.34	15		1.75	222
9	SS	12.3	1.50	SW-SM	8.55	19		1.73	245
10	SS	13.8	1.50	SM	8.19	20		1.86	251
11	SS	15.3	1.50	SM	9.27	33		1.91	310
12	SS	16.8	1.50	SM	9.53	33		1.87	310
13	SS	18.3	1.50	SM	10.93	51		1.85	372
14	SS	19.8	1.50	SM	8.95	55		1.87	384
15	SS	21.3	infinite	SM	9.35	58		1.87	393

Table A-23 Soil profile of KN02

Layer No.	Type of Sample	Depth, m	Thickness, m	Classification	Natural Water Content (%)	SPT, N (Blow/ft)	Plastic Index (%)	Wet Unit Weight (t/m^3)	Vs (m/s)
1	SS	1.8	2.55	SM	5.62	13		1.59	209
2	SS	3.3	1.50	SM	4.44	9		1.66	179
3	SS	4.8	1.50	SM	6.25	9		1.72	179
4	SS	6.3	1.50	SP-SM	12.91	20		1.94	251
5	SS	7.8	1.50	SP-SM		21		1.87	256
6	SS	9.3	1.50	SP-SM	15.14	25		1.81	275
7	SS	10.8	1.50	SP-SM		28		1.93	289
8	SS	12.3	1.50	GW-GC	7.33	69		2.06	423
9	SS	13.8	1.50	SP-SM	8.84	65		2.20	412
10	SS	15.3	infinite	SP-SM		89		2.20	471

Table A-24 Soil profile of KN03

Layer No.	Type of Sample	Depth, m	Thickness, m	Classification	Natural Water Content (%)	SPT, N (Blow/ft)	Plastic Index (%)	Wet Unit Weight (t/m^3)	Vs (m/s)
1	SS	1.3	1.55	SM	5.94	6		1.75	151
2	SS	1.8	0.50	SM	6.59	12		1.90	202
3	SS	2.3	0.75	SC	10.72	17	3.19	1.95	234
4	SS	3.3	1.25	SC	4.33	12	6.53	1.78	202
5	SS	4.8	1.50	SC	12.28	92	7.82	2.09	478
6	SS	6.3	1.50	SM	11.29	120		2.11	535
7	SS	7.8	infinite	SM	10.87	90		2.02	473

Table A-25 Soil profile of KN04

Layer No.	Type of Sample	Depth, m	Thickness, m	Classification	Natural Water Content (%)	SPT, N (Blow/ft)	Plastic Index (%)	Wet Unit Weight (t/m^3)	Vs (m/s)
1	SS	1.8	2.55	SM	3.49	27		1.29	284
2	SS	3.3	1.50	SM	4.37	34		1.35	314
3	SS	4.8	1.50	SW	13.40	27		1.89	284
4	SS	6.3	1.50	SW	8.11	27		1.92	284
5	SS	7.8	1.50	SP	10.96	29		1.82	293
6	SS	9.3	1.50	SW	8.90	33		1.74	310
7	SS	10.8	1.50	SP	14.52	128		1.84	549
8	SS	12.3	infinite	SP	14.18	130		1.64	553

Table A-26 Soil profile of KN05

Layer No.	Type of Sample	Depth, m	Thickness, m	Classification	Natural Water Content (%)	SPT, N (Blow/ft)	Plastic Index (%)	Wet Unit Weight (t/m^3)	Vs (m/s)
1	SS	1.8	2.55	ML-OL	12.54	39	6.52	1.42	332
2	SS	3.3	1.50	ML-OL	17.24	37	4.93	2.15	325
3	SS	4.8	1.50	ML-OL	14.80	84	5.27	1.61	460
4	SS	6.3	1.50	SM	5.69	69		1.52	423
5	SS	7.8	1.50	SM	9.71	87		1.62	467
6	SS	9.3	1.50	SM	8.70	44		1.58	350
7	SS	10.8	1.50	SM-SP	11.72	18		2.08	240
8	SS	12.3	1.50	SM	13.85	22		1.90	261
9	SS	13.8	1.50	CL	22.29	28	13.14	2.12	289
10	SS	15.3	1.50	ML-OL	21.38	37	11.04	2.10	325
11	SS	16.8	1.50	CL	21.03	32	8.86	2.25	306
12	SS	18.3	infinite	CL	20.81	33	9.72	2.21	310

Table A-27 Soil profile of KN06

Layer No.	Type of Sample	Depth, m	Thickness, m	Classification	Natural Water Content (%)	SPT, N (Blow/ft)	Plastic Index (%)	Wet Unit Weight (t/m^3)	Vs (m/s)
1	SS	1.3	1.80	GM-GC	3.00	82	10.66	1.67	455
2	SS	2.3	1.00	SC	4.02	60	25.79	1.83	399
3	SS	3.3	1.25	SC	3.73	75	23.57	1.90	438
4	SS	4.8	1.50	GM	3.84	80	18.27	1.90	450
5	SS	6.3	infinite	SM	3.34	100	16.77	2.00	495

Table A-28 Soil profile of KN07

Layer No.	Type of Sample	Depth, m	Thickness, m	Classification	Natural Water Content (%)	SPT, N (Blow/ft)	Plastic Index (%)	Wet Unit Weight (t/m^3)	Vs (m/s)
1	SS	1.3	1.80	CL-ML	21.41	3	4.90	1.53	112
2	SS	2.3	1.00	CL-ML	19.36	4	5.25	1.54	127
3	SS	3.3	1.25	SC	12.04	6		1.62	151
4	SS	4.8	1.50	SC	9.18	19		1.54	245
5	SS	6.3	1.50	SC	8.92	20	6.52	1.59	251
6	SS	7.8	1.50	CL-ML	12.13	27	5.02	1.76	284
7	SS	9.3	1.50	SM	13.43	19		1.68	245
8	SS	10.8	1.50	SM	7.90	38		2.01	329
9	SS	12.3	1.50	GM	10.48	26		1.98	280
10	SS	13.8	1.50	GW-GM	10.20	28		1.98	289
11	SS	15.3	1.50	GW-GM	7.80	35		2.03	317
12	SS	16.8	1.50	GW-GM	9.72	21		1.98	256
13	SS	18.3	1.50	GW-GM	6.55	22		1.96	261
14	SS	19.8	1.50	GW-GM	6.76	61		2.13	402
15	SS	21.3	1.50	GM	7.74	68		2.09	420
16	SS	22.8	infinite	GW-GM	7.80	72		2.08	431

Table A-29 Soil profile of KN08

Layer No.	Type of Sample	Depth, m	Thickness, m	Classification	Natural Water Content (%)	SPT, N (Blow/ft)	Plastic Index (%)	Wet Unit Weight (t/m^3)	Vs (m/s)
1	SS	1.3	1.80	CL	17.18	14	12.34	1.84	215
2	SS	2.3	1.00	CL	12.31	28	17.32	1.95	289
3	SS	3.3	1.25	SC	7.34	29	5.75	1.88	293
4	SS	4.8	1.50	SC	11.12	28	1.38	1.85	289
5	SS	6.3	1.50	CL-ML	9.01	58	5.22	2.16	393
6	SS	7.8	1.50	SM	7.29	60		1.93	399
7	SS	9.3	1.50	SM	8.49	62		1.91	404
8	SS	10.8	infinite	SM	5.18	70		1.99	426

Table A-30 Soil profile of BK01

Layer No.	Type of Sample	Depth, m	Thickness, m	Classification	Natural Water Content (%)	Su, t/m^2	SPT, N (Blow/ft)	Plastic Index (%)	Wet Unit Weight (t/m^3)	Vs (m/s)
1	SS	1.8	2.55	CL	23.95	3.20		21.19	1.67	109
2	SS	3.3	2.25	CL	89.30	2.00		18.35	1.47	85
3	SS	6.3	3.00	CL	79.51	1.90		19.68	1.47	83
4	SS	9.3	3.00	OL-ML	55.83	2.30		11.52	1.66	92
5	SS	12.3	3.00	CH	63.55	1.30		24.63	1.66	68
6	SS	15.3	2.25	CH	26.10	16.60		27.85	2.05	259
7	SS	16.8	1.50	CL	34.51	15.90	19	14.13	1.81	253
8	SS	18.3	1.50	CL	22.27	32.50	43	16.18	2.23	368
9	SS	19.8	1.50	CL	22.13		29	15.15	1.84	269
10	SS	21.3	1.50	CH	22.89	17.40	19	32.91	2.10	219
11	SS	22.8	1.50	CL	22.51	22.30	36	23.10	1.94	298
12	SS	24.3	1.50	CH	19.03		28	34.78	2.26	264
13	SS	25.8	1.50	CL	23.16		53	13.29	1.95	359
14	SS	27.3	1.50	SM	25.53		55		1.78	366
15	SS	28.8	1.50	SM	18.43		63		1.97	390
16	SS	30.3	30.45	SM	18.12		67		1.79	402
17		60.0	60.00	CL					2.16	450
18		120.0	280.00	CL			Tuladhar et al. (2004)		2.16	550
19		400.0	infinite	SM					2.16	2000

Table A-31 Soil profile of BK02

Layer No.	Type of Sample	Depth, m	Thickness, m	Classification	Natural Water Content (%)	Su, t/m^2	SPT, N (Blow/ft)	Plastic Index (%)	Wet Unit Weight (t/m^3)	Vs (m/s)
1	SS	1.8	4.05	OL-ML	52.18	1.10		11.20	1.59	62
2	SS	6.3	3.75	OL-ML	60.20	1.10		11.30	1.56	62
3	SS	9.3	3.75	OL-ML	52.12	1.00		11.65	1.65	59
4	SS	13.8	3.00	SC	27.03		60	12.68	1.72	381
5	SS	15.3	1.50	SM	18.57		60		1.79	381
6	SS	16.8	1.50	SW-SM	22.23		60		1.78	381
7	SS	18.3	1.50	SW-SM	17.80		113		1.99	517
8	SS	19.8	1.50	SW-SM	22.07		85		1.98	451
9	SS	21.3	4.45	SW-SM	25.45		90		1.95	463
10		25.0	5.00	SM					2.08	400
11		30.0	30.00	CL					2.16	400
12		60.0	60.00	CL			Tuladhar et al. (2004)		2.16	450
13		120.0	280.00	CL					2.16	550
14		400.0	infinite	SM					2.16	2000

Table A-32 Soil profile of BK03

Layer No.	Type of Sample	Depth, m	Thickness, m	Classification	Natural Water Content	Su, t/m^2	SPT, N (Blow/ft)	Plastic Index (%)	Wet Unit Weight (t/m^3)	Vs (m/s)
1	SS	1.8	4.05	CL	35.05	3.50		17.12	1.79	114
2	SS	6.3	3.75	OH-MH	100.05	2.50		25.35	1.36	96
3	SS	9.3	3.00	OH-MH	99.26	0.60		19.06	1.38	45
4	SS	12.3	3.00	CL	65.49	5.00		20.60	1.54	138
5	SS	15.3	2.25	CH	31.10	13.70		43.82	1.85	234
6	SS	16.8	1.50	CH	24.35	28.70	25	40.44	1.90	250
7	SS	18.3	1.50	SC	21.62		24	13.07	1.65	245
8	SS	19.8	1.50	SM	22.34		55		2.01	366
9	SS	21.3	1.50	SM	22.56		23		1.70	240
10	SS	22.8	1.50	SM	22.09		40		2.02	314
11	SS	24.3	1.50	SM	22.41		45		2.03	332
12	SS	25.8	1.50	SM	11.31		25		1.73	250
13	SS	27.3	1.50	CL	26.71		51	20.33	2.10	353
14	SS	28.8	1.50	CL	26.84		53	19.84	2.14	359
15	SS	30.3	5.45	CL	25.27		60	18.70	2.13	381
16		35.0	25.00	CL					2.16	400
17		60.0	60.00	CL					2.16	450
18		120.0	480.00	CL			Tuladhar et al. (2004)		2.16	550
19		600.0	infinite	SM					2.16	2000

Table A-33 Soil profile of BK04

Layer No.	Type of Sample	Depth, m	Thickness, m	Classification	Natural Water Content	Su, t/m^2	SPT, N (Blow/ft)	Plastic Index (%)	Wet Unit Weight (t/m^3)	Vs (m/s)
1	ST	1.8	2.55	OH-MH	37.73	4.70		24.03	1.72	133
2	ST	3.3	2.25	OH-MH	75.93	0.80		24.27	1.54	53
3	ST	6.3	3.00	OH-MH	81.43	0.80		21.44	1.44	53
4	ST	9.3	3.00	OH-MH	60.76	2.20		37.73	1.50	90
5	ST	12.3	3.00	OH-MH	72.06	2.50		39.46	1.51	96
6	ST	15.3	2.25	CH	25.72	12.40		32.30	1.87	222
7	SS	16.8	1.50	CL	28.80	21.70	16	17.32	1.85	298
8	SS	18.3	1.50	CL	12.04		37	14.71	1.88	302
9	SS	19.8	1.50	CL	22.15	45.30	23	16.08	1.97	240
10	SS	21.3	1.50	CL	19.11		15	17.34	1.80	196
11	SS	22.8	1.50	CL	20.48	43.70	25	17.34	1.92	250
12	SS	24.3	1.50	CL	23.61	23.40	31	15.82	1.98	278
13	SS	25.8	1.50	CL	18.64		58	10.26	2.03	375
14	SS	27.3	1.50	SC	13.00		39	17.77	1.90	310
15	SS	28.8	1.50	SM	13.28		43		1.92	325
16	SS	30.3	5.45	SM	14.36		75		2.10	425
17		35.0	25.00	CL					2.16	425
18		60.0	60.00	CL					2.16	450
19		120.0	480.00	CL	Tuladhar et al. (2004)				2.16	550
20		600.0	infinite	SM					2.16	2000

Table A-34 Soil profile of BK05

Layer No.	Type of Sample	Depth, m	Thickness, m	Classification	Natural Water Content	Su, t/m^2	SPT, N (Blow/ft)	Plastic Index (%)	Wet Unit Weight (t/m^3)	Vs (m/s)
1	ST	1.8	2.55	CH	38.74	2.90		33.02	1.82	104
2	ST	3.3	2.25	OL-ML	33.07	2.90		7.35	1.79	104
3	ST	6.3	3.00	CL	89.51	3.10		16.51	1.50	107
4	ST	9.3	3.00	OH-MH	81.95	2.10		25.02	1.47	87
5	ST	12.3	3.00	OH-MH	74.52	2.90		29.54	1.62	104
6	ST	15.3	2.25	CL	21.01	10.10		22.35	1.90	199
7	SS	16.8	1.50	CL	30.15	12.00	22	19.79	1.80	218
8	SS	18.3	1.50	CL	37.15	19.60	23	19.51	1.82	282
9	SS	19.8	1.50	CL	21.95	27.80	47	22.35	2.21	339
10	SS	21.3	1.50	CL	24.67	20.20	28	20.52	2.10	264
11	SS	22.8	1.50	OL-ML	24.04	11.00	23	16.14	2.03	240
12	SS	24.3	1.50	CL	24.92		27	17.84	1.93	260
13	SS	25.8	1.50	CL	20.97		51	18.29	1.95	353
14	SS	27.3	1.50	SM	21.25		66		1.98	399
15	SS	28.8	1.50	SM	23.82		59		1.98	378
16	SS	30.3	5.45	SM	25.96		84		1.99	448
17		35.0	25.00	CL					2.16	448
18		60.0	60.00	CL	Tuladhar et al. (2004)				2.16	450
19		120.0	480.00	CL					2.16	550
20		600.0	infinite	SM					2.16	2000

Table A-35 Soil profile of BK06

Layer No.	Type of Sample	Depth, m	Thickness, m	Classification	Natural Water Content	Su, t/m^2	SPT, N (Blow/ft)	Plastic Index (%)	Wet Unit Weight (t/m^3)	Vs (m/s)
1	ST	1.8	2.55	OH-MH	34.49	5.10		26.47	1.62	139
2	ST	3.3	2.25	CH	30.37	2.50		30.38	1.57	96
3	ST	6.3	3.00	OH-MH	78.56	1.50		32.41	1.34	73
4	ST	9.3	3.00	OH-MH	94.04	3.50		32.66	1.45	114
5	ST	12.3	3.00	OH-MH	53.18	5.40		33.34	1.57	144
6	ST	15.3	2.25	OH-MH	27.42	11.30		25.94	1.83	212
7	SS	16.8	1.50	OH-MH	35.00	15.90	17	21.07	1.88	208
8	SS	18.3	1.50	OH-MH	38.52		16	22.28	1.85	202
9	SS	19.8	1.50	CL	25.49	25.50	24	12.26	1.89	245
10	SS	21.3	1.50	CH	20.97		12	25.41	1.83	176
11	SS	22.8	1.50	CL	20.35	33.30	48	10.97	2.11	343
12	SS	24.3	1.50	CL	18.17	34.60	52	15.96	2.12	356
13	SS	25.8	1.50	SW-SM	14.23		58		2.00	375
14	SS	27.3	1.50	SM	14.67		63		2.03	390
15	SS	28.8	1.50	SW-SM	13.07		80		2.01	438
16	SS	30.3	5.45	SM	15.32		85		2.05	451
17		35.0	25.00	CL					2.16	451
18		60.0	60.00	CL					2.16	451
19		120.0	480.00	CL	Tuladhar et al. (2004)				2.16	550
20		600.0	infinite	SM					2.16	2000

Table A-36 Soil profile of BK07

Layer No.	Type of Sample	Depth, m	Thickness, m	Classification	Natural Water Content	Su, t/m^2	SPT, N (Blow/ft)	Plastic Index (%)	Wet Unit Weight (t/m^3)	Vs (m/s)
1	ST	1.8	2.55	OH-MH	39.19	4.90		25.78	1.56	136
2	ST	3.3	2.25	CL	82.25	3.50		24.12	1.40	114
3	ST	6.3	3.00	OL-ML	64.26	3.80		19.37	1.50	119
4	ST	9.3	3.00	CH	69.85	4.00		30.18	1.49	123
5	ST	12.3	3.00	CH	62.64	4.20		27.95	1.49	126
6	ST	15.3	2.25	CH	37.93	10.10		27.52	1.62	199
7	SS	16.8	1.50	OH-MH	37.22	16.90	21	26.30	1.81	261
8	SS	18.3	1.50	OH-MH	31.17	24.10	26	25.97	1.85	315
9	SS	19.8	1.50	SM	22.01		40		1.73	314
10	SS	21.3	1.50	CH	22.22	38.90	35	27.07	1.92	294
11	SS	22.8	1.50	CL	24.25	22.00	38	19.15	1.92	306
12	SS	24.3	1.50	CL	16.24	54.00	68	17.75	2.06	405
13	SS	25.8	1.50	CL	24.00	45.40	62	17.33	2.01	387
14	SS	27.3	1.50	SC	12.18		75	18.12	2.16	425
15	SS	28.8	1.50	SM	13.02		82		2.15	443
16	SS	30.3	30.45	SM	10.85		65		2.09	443
17		60.0	60.00	CL					2.16	450
18		120.0	280.00	CL	Tuladhar et al. (2004)				2.16	550
19		400.0	infinite	SM					2.16	2000

Table A-37 Soil profile of BK08

Layer No.	Type of Sample	Depth, m	Thickness, m	Classification	Natural Water Content	Su, t/m^2	SPT, N (Blow/ft)	Plastic Index (%)	Wet Unit Weight (t/m^3)	Vs (m/s)
1	ST	1.8	2.55	OL-ML	45.65	2.70		14.26	1.75	100
2	ST	3.3	2.25	OL-ML	89.47	0.70		12.68	1.36	49
3	ST	6.3	3.00	OL-ML	58.92	1.00		14.86	1.57	59
4	ST	9.3	3.00	OL-ML	61.30	3.00		11.36	1.57	105
5	ST	12.3	3.00	OL-ML	84.53	5.70		11.68	1.52	148
6	ST	15.3	2.25	OL-ML	49.97	8.40		10.36	1.66	181
7	SS	16.8	1.50	OH-MH	35.72	16.60	16	30.46	1.93	202
8	SS	18.3	1.50	OH-MH	34.11	19.40	16	29.76	1.89	202
9	SS	19.8	1.50	OH-MH	31.03	21.70	16	20.95	1.96	202
10	SS	21.3	1.50	CL	25.58	22.20	14	16.55	2.05	189
11	SS	22.8	1.50	CL	27.70		10	15.46	1.97	161
12	SS	24.3	1.50	SM	16.30		53		2.02	359
13	SS	25.8	1.50	SM	17.09		59		2.09	378
14	SS	27.3	1.50	SM	15.94		52		2.18	356
15	SS	28.8	1.50	SW-SM	12.82		56		2.22	369
16	SS	30.3	1.50	SW-SM	14.90		63		2.13	390
17	SS	31.8	1.50	SM	15.47		67		2.17	402
18	SS	33.3	27.45	SW-SM	17.90		75		2.19	425
19		60.0	60.00	CL					2.16	450
20		120.0	280.00	CL	Tuladhar et al. (2004)				2.16	550
21		400.0	infinite	SM					2.16	2000

Table A-38 Soil profile of BK09

Layer No.	Type of Sample	Depth, m	Thickness, m	Classification	Natural Water Content	Su, t/m^2	SPT, N (Blow/ft)	Plastic Index (%)	Wet Unit Weight (t/m^3)	Vs (m/s)
1	ST	1.8	2.55	CH	33.74	3.80		38.06	1.73	119
2	ST	3.3	2.25	CH	30.82	4.60		37.13	1.74	132
3	ST	6.3	3.00	CH	102.76	3.00		32.30	1.35	105
4	ST	9.3	3.00	OH-MH	87.01	3.00		23.89	1.39	105
5	ST	12.3	3.00	OH-MH	72.30	1.10		24.09	1.39	62
6	ST	15.3	2.25	OH-MH	19.71	15.50		18.09	1.87	250
7	SS	16.8	1.50	OH-MH	38.24	18.30	14	25.99	1.90	272
8	SS	18.3	1.50	OH-MH	27.37		42	28.30	1.74	321
9	SS	19.8	1.50	OH-MH	34.61		15	29.93	1.80	196
10	SS	21.3	1.50	CL	26.76	21.40	13	19.42	2.07	183
11	SS	22.8	1.50	CL	24.40	25.30	30	22.59	2.07	273
12	SS	24.3	1.50	SM	20.45		70		1.90	411
13	SS	25.8	1.50	SM	20.94		74		1.89	422
14	SS	27.3	1.50	SM	22.17		55		1.88	366
15	SS	28.8	1.50	SM	19.69		58		1.95	375
16	SS	30.3	30.45	SW-SM	18.73		62		1.95	387
17		60.0	60.00	CL					2.16	450
18		120.0	280.00	CL	Tuladhar et al. (2004)				2.16	550
19		400.0	infinite	SM					2.16	2000

A.2 Analytical results

The analytical results are presented as the soil amplification factors which are the ratio between the spectral accelerations of output ground motions and input outcrop motions. The soil amplification factors in Chiangmai, Chiangrai, Kanchanaburi and Bangkok can be expressed in Tables A-39 to A-71

Table A-39 Soil amplification factors of CM01 due to input motions 0.05g

T (s)	SOY	KTX	LDX	KSX	BIX	HAX	SIX	LGX	HPX	SCX	Av.	Max.
0.0	1.089	1.131	1.170	1.133	1.227	1.022	1.119	1.069	1.118	1.075	**1.115**	**1.227**
0.2	1.070	1.056	1.109	1.096	1.151	1.005	1.027	0.956	0.997	1.086	**1.055**	**1.151**
0.5	1.223	1.201	1.195	1.139	1.365	1.151	1.237	1.048	1.144	1.151	**1.185**	**1.365**
1.0	1.247	1.224	1.204	1.188	1.171	1.125	1.183	1.124	1.177	1.142	**1.178**	**1.247**
1.5	1.180	1.145	1.093	1.094	1.216	1.099	1.080	1.086	1.084	1.051	**1.113**	**1.216**
2.0	1.166	1.090	1.051	1.071	1.208	1.041	1.059	1.049	1.050	1.041	**1.083**	**1.208**
2.5	1.176	1.042	1.056	1.079	1.271	1.029	1.047	1.016	1.032	1.022	**1.077**	**1.271**
3.0	1.197	1.049	1.023	1.032	1.282	1.016	1.009	1.017	1.008	1.017	**1.065**	**1.282**

Table A-40 Soil amplification factors of CM02 due to input motions 0.05g

T (s)	SOY	KTX	LDX	KSX	BIX	HAX	SIX	LGX	HPX	SCX	Av.	Max.
0.0	1.478	1.240	1.337	1.135	1.477	1.547	1.553	1.147	1.351	1.178	**1.344**	**1.553**
0.2	1.966	1.893	1.523	1.173	1.730	1.975	1.831	1.743	1.660	1.684	**1.718**	**1.975**
0.5	1.124	1.175	1.171	1.149	1.154	1.178	1.195	1.154	1.157	1.140	**1.160**	**1.195**
1.0	1.058	1.056	1.071	1.037	1.054	1.038	1.034	1.045	1.039	1.040	**1.047**	**1.071**
1.5	1.058	1.041	1.016	1.017	1.091	1.020	1.029	1.021	1.016	1.016	**1.033**	**1.091**
2.0	1.030	1.034	1.002	1.010	1.099	1.011	1.011	1.012	1.009	1.011	**1.023**	**1.099**
2.5	1.013	1.021	1.012	1.006	1.129	1.007	1.019	1.005	1.006	1.008	**1.023**	**1.129**
3.0	1.012	1.022	1.003	1.010	1.154	1.001	1.006	1.006	1.003	1.006	**1.022**	**1.154**

Table A-41 Soil amplification factors of CM03 due to input motions 0.05g

T (s)	SOY	KTX	LDX	KSX	BIX	HAX	SIX	LGX	HPX	SCX	Av.	Max.
0.0	1.300	1.278	1.300	1.164	1.338	1.172	1.487	1.123	1.341	1.201	**1.270**	**1.487**
0.2	1.703	1.634	1.487	1.162	1.600	1.584	1.508	1.364	1.491	1.501	**1.503**	**1.703**
0.5	1.198	1.261	1.267	1.244	1.310	1.236	1.282	1.213	1.245	1.206	**1.246**	**1.310**
1.0	1.074	1.101	1.109	1.055	1.073	1.040	1.044	1.064	1.058	1.055	**1.067**	**1.109**
1.5	1.075	1.060	1.023	1.024	1.122	1.024	1.034	1.029	1.022	1.022	**1.043**	**1.122**
2.0	1.052	1.046	1.000	1.014	1.116	1.015	1.018	1.017	1.013	1.015	**1.030**	**1.116**
2.5	1.031	1.025	1.018	1.009	1.153	1.009	1.035	1.006	1.008	1.011	**1.030**	**1.153**
3.0	1.025	1.026	1.005	1.015	1.172	1.003	1.003	1.008	1.005	1.009	**1.027**	**1.172**

Table A-42 Soil amplification factors of CM04 due to input motions 0.05g

T (s)	SOY	KTX	LDX	KSX	BIX	HAX	SIX	LGX	HPX	SCX	Av.	Max.
0.0	1.563	1.432	1.484	1.263	1.680	1.503	1.576	1.359	1.471	1.289	**1.462**	**1.680**
0.2	1.564	1.533	1.489	1.339	1.574	1.403	1.431	1.319	1.480	1.468	**1.460**	**1.574**
0.5	1.434	1.580	1.605	1.575	1.696	1.454	1.600	1.482	1.535	1.465	**1.543**	**1.696**
1.0	1.172	1.228	1.229	1.120	1.107	1.088	1.112	1.133	1.126	1.109	**1.142**	**1.229**
1.5	1.139	1.101	1.063	1.047	1.254	1.058	1.041	1.064	1.042	1.045	**1.085**	**1.254**
2.0	1.145	1.078	1.011	1.029	1.195	1.031	1.045	1.035	1.027	1.031	**1.063**	**1.195**
2.5	1.130	1.029	1.045	1.036	1.352	1.025	1.062	1.014	1.018	1.023	**1.073**	**1.352**
3.0	1.139	1.042	1.015	1.038	1.420	1.011	1.002	1.017	1.014	1.019	**1.071**	**1.420**

Table A-43 Soil amplification factors of CM05 due to input motions 0.05g

T (s)	SOY	KTX	LDX	KSX	BIX	HAX	SIX	LGX	HPX	SCX	Av.	Max.
0.0	1.141	1.088	1.143	1.082	1.163	1.100	1.226	1.063	1.171	1.096	**1.127**	**1.226**
0.2	1.354	1.320	1.140	1.088	1.300	1.302	1.258	1.181	1.244	1.199	**1.239**	**1.354**
0.5	1.104	1.131	1.137	1.128	1.116	1.126	1.142	1.121	1.110	1.115	**1.123**	**1.142**
1.0	1.046	1.051	1.058	1.031	1.039	1.027	1.028	1.035	1.033	1.032	**1.038**	**1.058**
1.5	1.042	1.031	1.013	1.013	1.064	1.016	1.018	1.017	1.012	1.013	**1.024**	**1.064**
2.0	1.026	1.024	1.000	1.008	1.065	1.008	1.009	1.009	1.007	1.009	**1.016**	**1.065**
2.5	1.017	1.012	1.010	1.004	1.086	1.006	1.014	1.003	1.004	1.006	**1.016**	**1.086**
3.0	1.016	1.013	1.002	1.008	1.100	1.000	1.001	1.004	1.002	1.005	**1.015**	**1.100**

Table A-44 Soil amplification factors of CM06 due to input motions 0.05g

T (s)	SOY	KTX	LDX	KSX	BIX	HAX	SIX	LGX	HPX	SCX	Av.	Max.
0.0	1.121	1.038	1.102	1.032	1.119	1.161	1.158	1.037	1.108	1.027	**1.090**	**1.161**
0.2	1.260	1.239	1.079	1.047	1.194	1.275	1.234	1.133	1.189	1.132	**1.178**	**1.275**
0.5	1.032	1.050	1.045	1.039	1.041	1.050	1.056	1.042	1.025	1.040	**1.042**	**1.056**
1.0	1.016	1.011	1.017	1.006	1.013	1.010	1.006	1.008	1.006	1.008	**1.010**	**1.017**
1.5	1.015	1.008	1.001	1.001	1.024	1.004	1.004	1.000	1.000	1.001	**1.006**	**1.024**
2.0	1.002	1.006	0.997	0.999	1.026	1.000	0.999	1.000	0.999	1.001	**1.003**	**1.026**
2.5	1.001	1.003	1.001	0.998	1.033	1.001	1.000	0.998	0.999	1.000	**1.003**	**1.033**
3.0	1.001	1.002	0.998	1.000	1.046	0.998	0.999	0.999	0.998	1.000	**1.004**	**1.046**

Table A-45 Soil amplification factors of CM07 due to input motions 0.05g

T (s)	SOY	KTX	LDX	KSX	BIX	HAX	SIX	LGX	HPX	SCX	Av.	Max.
0.0	1.793	1.910	1.663	1.326	1.996	1.809	2.608	1.221	1.669	1.506	**1.750**	**2.608**
0.2	2.763	2.597	2.471	1.638	2.670	2.524	2.302	2.088	2.193	2.464	**2.371**	**2.763**
0.5	1.305	1.447	1.408	1.353	1.703	1.387	1.642	1.304	1.418	1.291	**1.426**	**1.703**
1.0	1.086	1.170	1.166	1.073	1.150	1.046	1.076	1.086	1.079	1.079	**1.101**	**1.170**
1.5	1.119	1.101	1.028	1.033	1.212	1.026	1.062	1.039	1.028	1.033	**1.068**	**1.212**
2.0	1.068	1.078	1.002	1.018	1.239	1.024	1.020	1.023	1.019	1.020	**1.051**	**1.239**
2.5	1.043	1.054	1.024	1.017	1.478	1.017	1.072	1.009	1.010	1.014	**1.074**	**1.478**
3.0	1.038	1.044	1.008	1.020	1.624	1.019	1.010	1.011	1.005	1.014	**1.079**	**1.624**

Table A-46 Soil amplification factors of CM08 due to input motions 0.05g

T (s)	SOY	KTX	LDX	KSX	BIX	HAX	SIX	LGX	HPX	SCX	Av.	Max.
0.0	1.015	1.011	1.008	1.003	0.992	1.021	1.012	1.006	1.007	1.009	**1.008**	**1.021**
0.2	1.023	1.018	1.006	1.001	1.013	1.013	1.011	1.008	1.008	1.004	**1.010**	**1.023**
0.5	1.001	1.004	1.002	1.003	0.999	1.003	1.003	0.999	1.002	1.003	**1.002**	**1.004**
1.0	1.001	1.001	1.001	1.001	0.999	1.001	1.000	0.999	1.000	1.001	**1.001**	**1.001**
1.5	1.001	1.000	1.000	1.000	0.999	1.001	1.000	1.000	1.000	1.001	**1.000**	**1.001**
2.0	1.000	1.000	1.000	1.000	1.001	1.001	1.000	1.000	1.000	1.001	**1.000**	**1.001**
2.5	1.000	1.000	1.000	1.000	1.000	1.001	1.000	1.000	1.000	1.001	**1.000**	**1.001**
3.0	1.000	1.000	1.000	1.000	1.003	1.001	1.000	1.000	1.000	1.001	**1.001**	**1.003**

Table A-47 Soil amplification factors of CM09 due to input motions 0.05g

T (s)	SOY	KTX	LDX	KSX	BIX	HAX	SIX	LGX	HPX	SCX	Av.	Max.
0.0	1.172	1.080	1.156	1.058	1.193	1.276	1.246	1.057	1.165	1.061	**1.146**	**1.276**
0.2	1.374	1.350	1.129	1.073	1.275	1.388	1.333	1.266	1.276	1.223	**1.269**	**1.388**
0.5	1.053	1.078	1.074	1.066	1.066	1.076	1.086	1.069	1.050	1.064	**1.068**	**1.086**
1.0	1.028	1.024	1.031	1.017	1.024	1.020	1.017	1.021	1.017	1.018	**1.022**	**1.031**
1.5	1.026	1.017	1.008	1.007	1.038	1.011	1.011	1.009	1.007	1.007	**1.014**	**1.038**
2.0	1.008	1.014	1.000	1.004	1.040	1.004	1.003	1.005	1.004	1.005	**1.009**	**1.040**
2.5	1.007	1.008	1.006	1.002	1.052	1.004	1.004	1.002	1.002	1.004	**1.009**	**1.052**
3.0	1.008	1.007	1.001	1.004	1.065	1.001	1.002	1.002	1.001	1.003	**1.009**	**1.065**

Table A-48 Soil amplification factors of CM10 due to input motions 0.05g

T (s)	SOY	KTX	LDX	KSX	BIX	HAX	SIX	LGX	HPX	SCX	Av.	Max.
0.0	1.801	1.717	1.747	1.341	2.048	1.756	1.879	1.529	1.658	1.375	**1.685**	**2.048**
0.2	1.744	1.689	1.820	1.635	1.867	1.488	1.545	1.359	1.609	1.748	**1.650**	**1.867**
0.5	1.578	1.838	1.849	1.762	2.058	1.569	1.844	1.582	1.740	1.540	**1.736**	**2.058**
1.0	1.193	1.301	1.288	1.136	1.117	1.089	1.139	1.147	1.147	1.116	**1.167**	**1.301**
1.5	1.170	1.126	1.088	1.048	1.371	1.061	1.031	1.070	1.044	1.050	**1.106**	**1.371**
2.0	1.176	1.095	1.007	1.030	1.390	1.032	1.057	1.040	1.032	1.033	**1.089**	**1.390**
2.5	1.161	1.030	1.055	1.044	1.630	1.029	1.084	1.015	1.021	1.026	**1.110**	**1.630**
3.0	1.173	1.060	1.019	1.051	1.742	1.012	1.003	1.018	1.019	1.023	**1.112**	**1.742**

Table A-49 Soil amplification factors of CR01 due to input motions 0.05g

T (s)	SOY	KTX	LDX	KSX	BIX	HAX	SIX	LGX	HPX	SCX	Av.	Max.
0.0	1.231	1.106	1.213	1.089	1.277	1.315	1.321	1.088	1.221	1.095	**1.196**	**1.321**
0.2	1.535	1.491	1.237	1.108	1.408	1.534	1.456	1.358	1.375	1.350	**1.385**	**1.535**
0.5	1.089	1.123	1.122	1.110	1.103	1.122	1.135	1.108	1.101	1.103	**1.112**	**1.135**
1.0	1.044	1.041	1.052	1.027	1.036	1.028	1.026	1.031	1.028	1.029	**1.034**	**1.052**
1.5	1.041	1.029	1.012	1.012	1.059	1.016	1.018	1.015	1.011	1.011	**1.022**	**1.059**
2.0	1.019	1.023	1.000	1.006	1.069	1.007	1.007	1.008	1.006	1.008	**1.015**	**1.069**
2.5	1.012	1.013	1.009	1.003	1.089	1.006	1.012	1.003	1.004	1.006	**1.016**	**1.089**
3.0	1.011	1.013	1.002	1.007	1.103	1.001	1.003	1.003	1.001	1.004	**1.015**	**1.103**

Table A-50 Soil amplification factors of CR02 due to input motions 0.05g

T (s)	SOY	KTX	LDX	KSX	BIX	HAX	SIX	LGX	HPX	SCX	Av.	Max.
0.0	1.270	1.220	1.250	1.149	1.297	1.088	1.385	1.108	1.286	1.181	**1.223**	**1.385**
0.2	1.509	1.460	1.343	1.145	1.446	1.396	1.338	1.258	1.372	1.343	**1.361**	**1.509**
0.5	1.191	1.247	1.257	1.240	1.267	1.221	1.268	1.215	1.231	1.202	**1.234**	**1.268**
1.0	1.074	1.099	1.106	1.055	1.066	1.041	1.046	1.064	1.058	1.055	**1.066**	**1.106**
1.5	1.071	1.055	1.024	1.024	1.106	1.026	1.030	1.030	1.022	1.022	**1.041**	**1.106**
2.0	1.051	1.042	1.000	1.014	1.109	1.014	1.018	1.018	1.013	1.015	**1.029**	**1.109**
2.5	1.032	1.022	1.019	1.009	1.144	1.010	1.031	1.006	1.008	1.011	**1.029**	**1.144**
3.0	1.028	1.024	1.005	1.016	1.158	1.002	1.002	1.008	1.005	1.009	**1.026**	**1.158**

Table A-51 Soil amplification factors of CR03 due to input motions 0.05g

T (s)	SOY	KTX	LDX	KSX	BIX	HAX	SIX	LGX	HPX	SCX	Av.	Max.
0.0	1.574	1.403	1.343	1.246	1.604	1.379	1.687	1.175	1.462	1.283	**1.415**	**1.687**
0.2	1.708	1.584	1.597	1.369	1.702	1.516	1.424	1.303	1.502	1.526	**1.523**	**1.708**
0.5	1.330	1.442	1.453	1.423	1.599	1.352	1.517	1.341	1.425	1.325	**1.421**	**1.599**
1.0	1.114	1.179	1.175	1.086	1.100	1.056	1.080	1.096	1.092	1.081	**1.106**	**1.179**
1.5	1.113	1.088	1.041	1.034	1.219	1.039	1.035	1.045	1.032	1.035	**1.068**	**1.219**
2.0	1.093	1.067	1.002	1.021	1.149	1.022	1.031	1.026	1.021	1.022	**1.045**	**1.149**
2.5	1.071	1.029	1.031	1.022	1.309	1.017	1.058	1.010	1.013	1.016	**1.058**	**1.309**
3.0	1.072	1.039	1.010	1.028	1.391	1.010	1.001	1.012	1.009	1.014	**1.059**	**1.391**

Table A-52 Soil amplification factors of CR04 due to input motions 0.05g

T (s)	SOY	KTX	LDX	KSX	BIX	HAX	SIX	LGX	HPX	SCX	Av.	Max.
0.0	1.295	1.401	1.406	1.282	1.043	1.259	1.040	1.436	1.223	1.204	**1.259**	**1.436**
0.2	0.683	0.722	1.209	1.206	0.932	0.622	0.640	1.056	0.816	1.153	**0.904**	**1.209**
0.5	1.877	2.049	2.063	2.149	2.073	1.647	1.991	2.241	1.917	2.114	**2.012**	**2.241**
1.0	1.337	1.405	1.393	1.261	1.202	1.159	1.223	1.312	1.263	1.198	**1.275**	**1.405**
1.5	1.182	1.130	1.148	1.114	1.313	1.135	1.084	1.160	1.104	1.075	**1.144**	**1.313**
2.0	1.328	1.089	1.134	1.070	1.314	1.063	1.074	1.072	1.048	1.060	**1.125**	**1.328**
2.5	1.347	1.033	1.072	1.086	1.519	1.055	1.074	1.034	1.042	1.039	**1.130**	**1.519**
3.0	1.389	1.010	1.035	1.056	1.580	1.025	1.025	1.040	1.033	1.026	**1.122**	**1.580**

Table A-53 Soil amplification factors of CR05 due to input motions 0.05g

T (s)	SOY	KTX	LDX	KSX	BIX	HAX	SIX	LGX	HPX	SCX	Av.	Max.
0.0	1.542	1.546	1.629	1.349	1.481	1.441	1.207	1.575	1.301	1.491	**1.456**	**1.629**
0.2	0.915	0.943	1.547	1.276	1.244	0.851	0.890	1.213	1.041	1.287	**1.121**	**1.547**
0.5	2.083	2.396	2.380	2.343	2.399	1.878	2.245	2.366	2.138	2.248	**2.248**	**2.399**
1.0	1.369	1.437	1.427	1.250	1.205	1.179	1.219	1.298	1.259	1.193	**1.284**	**1.437**
1.5	1.211	1.134	1.177	1.104	1.337	1.131	1.082	1.150	1.093	1.076	**1.150**	**1.337**
2.0	1.352	1.114	1.135	1.068	1.452	1.066	1.085	1.069	1.047	1.060	**1.145**	**1.452**
2.5	1.366	1.038	1.095	1.079	1.699	1.056	1.081	1.034	1.041	1.039	**1.153**	**1.699**
3.0	1.413	1.030	1.035	1.061	1.780	1.027	1.029	1.040	1.034	1.026	**1.147**	**1.780**

Table A-54 Soil amplification factors of CR06 due to input motions 0.05g

T (s)	SOY	KTX	LDX	KSX	BIX	HAX	SIX	LGX	HPX	SCX	Av.	Max.
0.0	1.935	1.579	1.487	1.146	1.578	2.098	2.069	1.230	1.540	1.230	**1.589**	**2.098**
0.2	2.788	2.630	1.892	1.270	2.218	2.971	2.700	2.540	2.160	2.211	**2.338**	**2.971**
0.5	1.131	1.187	1.180	1.144	1.201	1.214	1.228	1.160	1.187	1.147	**1.178**	**1.228**
1.0	1.069	1.051	1.076	1.037	1.054	1.050	1.038	1.048	1.040	1.042	**1.050**	**1.076**
1.5	1.065	1.046	1.016	1.018	1.118	1.025	1.036	1.020	1.016	1.016	**1.038**	**1.118**
2.0	1.037	1.041	1.003	1.009	1.135	1.014	1.015	1.013	1.009	1.012	**1.029**	**1.135**
2.5	1.013	1.024	1.013	1.005	1.175	1.008	1.023	1.005	1.006	1.008	**1.028**	**1.175**
3.0	1.008	1.032	1.002	1.009	1.215	1.003	1.009	1.006	1.002	1.005	**1.029**	**1.215**

Table A-55 Soil amplification factors of KN01 due to input motions 0.05g

T (s)	SOY	KTX	LDX	KSX	BIX	HAX	SIX	LGX	HPX	SCX	Av.	Max.
0.0	1.576	1.433	1.490	1.242	1.701	1.612	1.645	1.277	1.485	1.244	**1.471**	**1.701**
0.2	1.721	1.649	1.527	1.300	1.690	1.568	1.541	1.421	1.564	1.509	**1.549**	**1.721**
0.5	1.346	1.439	1.476	1.447	1.576	1.382	1.497	1.382	1.428	1.367	**1.434**	**1.576**
1.0	1.137	1.180	1.186	1.097	1.105	1.074	1.090	1.107	1.101	1.091	**1.117**	**1.186**
1.5	1.119	1.088	1.046	1.038	1.215	1.047	1.040	1.050	1.035	1.037	**1.071**	**1.215**
2.0	1.112	1.067	1.005	1.023	1.177	1.026	1.035	1.028	1.022	1.025	**1.052**	**1.177**
2.5	1.094	1.028	1.035	1.026	1.257	1.020	1.054	1.010	1.014	1.018	**1.056**	**1.257**
3.0	1.098	1.037	1.011	1.029	1.322	1.010	1.004	1.013	1.009	1.015	**1.055**	**1.322**

Table A-56 Soil amplification factors of KN02 due to input motions 0.05g

T (s)	SOY	KTX	LDX	KSX	BIX	HAX	SIX	LGX	HPX	SCX	Av.	Max.
0.0	1.616	1.342	1.393	1.142	1.579	1.819	1.792	1.168	1.446	1.171	**1.447**	**1.819**
0.2	2.334	2.230	1.706	1.216	1.989	2.421	2.217	2.111	1.898	1.948	**2.007**	**2.421**
0.5	1.123	1.179	1.173	1.146	1.170	1.191	1.207	1.155	1.167	1.142	**1.165**	**1.207**
1.0	1.062	1.051	1.073	1.037	1.054	1.043	1.035	1.046	1.039	1.040	**1.048**	**1.073**
1.5	1.060	1.044	1.016	1.018	1.100	1.022	1.032	1.020	1.016	1.016	**1.034**	**1.100**
2.0	1.032	1.037	1.003	1.009	1.119	1.012	1.013	1.012	1.009	1.012	**1.026**	**1.119**
2.5	1.009	1.023	1.012	1.006	1.156	1.008	1.020	1.005	1.006	1.008	**1.025**	**1.156**
3.0	1.008	1.026	1.003	1.010	1.183	1.002	1.007	1.006	1.003	1.006	**1.025**	**1.183**

Table A-57 Soil amplification factors of KN03 due to input motions 0.05g

T (s)	SOY	KTX	LDX	KSX	BIX	HAX	SIX	LGX	HPX	SCX	Av.	Max.
0.0	1.244	1.084	1.076	1.037	1.309	1.387	1.169	1.032	1.078	1.040	**1.146**	**1.387**
0.2	1.183	1.144	1.093	1.034	1.103	1.172	1.147	1.074	1.125	1.101	**1.117**	**1.183**
0.5	1.022	1.030	1.024	1.023	1.020	1.028	1.033	1.028	1.015	1.022	**1.024**	**1.033**
1.0	1.010	1.008	1.010	1.006	1.008	1.008	1.007	1.008	1.006	1.006	**1.008**	**1.010**
1.5	1.012	1.005	1.004	1.003	1.010	1.005	1.005	1.003	1.003	1.003	**1.005**	**1.012**
2.0	1.004	1.004	1.001	1.001	1.006	1.001	1.001	1.002	1.001	1.002	**1.002**	**1.006**
2.5	1.009	1.003	1.002	1.001	1.007	1.003	1.002	1.001	1.001	1.002	**1.003**	**1.009**
3.0	1.012	1.001	1.001	1.001	1.011	1.003	1.002	1.001	1.000	1.001	**1.003**	**1.012**

Table A-58 Soil amplification factors of KN04 due to input motions 0.05g

T (s)	SOY	KTX	LDX	KSX	BIX	HAX	SIX	LGX	HPX	SCX	Av.	Max.
0.0	1.191	1.110	1.176	1.051	1.283	1.399	1.244	1.054	1.160	1.082	**1.175**	**1.399**
0.2	1.305	1.292	1.146	1.060	1.201	1.336	1.291	1.237	1.249	1.182	**1.230**	**1.336**
0.5	1.033	1.057	1.048	1.043	1.042	1.053	1.063	1.044	1.029	1.043	**1.045**	**1.063**
1.0	1.021	1.015	1.020	1.011	1.019	1.017	1.013	1.014	1.011	1.012	**1.015**	**1.021**
1.5	1.020	1.011	1.007	1.005	1.024	1.009	1.008	1.007	1.005	1.005	**1.010**	**1.024**
2.0	1.003	1.010	1.001	1.003	1.026	1.002	1.002	1.004	1.003	1.004	**1.006**	**1.026**
2.5	1.007	1.006	1.004	1.001	1.031	1.004	1.002	1.002	1.002	1.003	**1.006**	**1.031**
3.0	1.009	1.004	1.001	1.003	1.045	1.003	1.004	1.002	1.001	1.002	**1.007**	**1.045**

Table A-59 Soil amplification factors of KN05 due to input motions 0.05g

T (s)	SOY	KTX	LDX	KSX	BIX	HAX	SIX	LGX	HPX	SCX	Av.	Max.
0.0	1.028	0.997	1.021	1.006	0.999	0.982	1.022	1.004	1.035	1.010	**1.010**	**1.035**
0.2	1.082	1.075	1.009	1.006	1.037	1.072	1.060	1.008	1.048	1.026	**1.042**	**1.082**
0.5	1.012	1.017	1.016	1.013	1.015	1.018	1.019	1.014	1.006	1.016	**1.015**	**1.019**
1.0	1.004	1.003	1.004	0.998	1.002	1.001	0.999	0.999	0.999	1.001	**1.001**	**1.004**
1.5	1.003	1.001	0.997	0.997	1.009	0.999	0.998	0.996	0.997	0.999	**1.000**	**1.009**
2.0	0.999	1.000	0.996	0.997	1.009	0.998	0.997	0.997	0.997	0.998	**0.999**	**1.009**
2.5	0.998	0.999	0.998	0.997	1.012	0.999	0.996	0.996	0.997	0.998	**0.999**	**1.012**
3.0	0.997	0.998	0.997	0.997	1.021	0.998	0.997	0.997	0.997	0.998	**1.000**	**1.021**

Table A-60 Soil amplification factors of KN06 due to input motions 0.05g

T (s)	SOY	KTX	LDX	KSX	BIX	HAX	SIX	LGX	HPX	SCX	Av.	Max.
0.0	1.014	1.008	1.012	1.003	1.008	1.030	1.016	1.001	1.007	1.010	**1.011**	**1.030**
0.2	1.020	1.017	1.010	1.004	1.001	1.020	1.017	0.998	1.013	1.005	**1.010**	**1.020**
0.5	1.002	1.003	1.003	1.002	1.000	1.004	1.004	1.005	1.001	1.003	**1.003**	**1.005**
1.0	1.001	1.001	1.001	1.000	1.000	1.001	1.001	1.000	1.000	1.001	**1.001**	**1.001**
1.5	1.001	1.000	1.000	1.000	1.002	1.001	1.000	1.000	1.000	1.001	**1.001**	**1.002**
2.0	1.000	1.000	1.000	1.000	0.999	1.001	1.000	1.000	1.000	1.001	**1.000**	**1.001**
2.5	1.001	1.000	1.000	1.000	0.999	1.001	1.000	1.000	1.000	1.001	**1.000**	**1.001**
3.0	1.001	1.000	1.000	1.000	1.004	1.001	1.000	1.000	1.000	1.001	**1.001**	**1.004**

Table A-61 Soil amplification factors of KN07 due to input motions 0.05g

T (s)	SOY	KTX	LDX	KSX	BIX	HAX	SIX	LGX	HPX	SCX	Av.	Max.
0.0	1.794	1.417	1.584	1.230	1.870	2.135	2.042	1.260	1.669	1.295	**1.629**	**2.135**
0.2	2.195	2.078	1.840	1.302	2.077	2.166	2.027	1.890	1.951	1.936	**1.946**	**2.195**
0.5	1.285	1.377	1.388	1.350	1.482	1.351	1.415	1.314	1.366	1.300	**1.363**	**1.482**
1.0	1.112	1.141	1.157	1.079	1.104	1.070	1.077	1.092	1.083	1.080	**1.099**	**1.157**
1.5	1.109	1.081	1.033	1.033	1.200	1.037	1.045	1.042	1.030	1.031	**1.064**	**1.200**
2.0	1.084	1.062	0.999	1.019	1.184	1.023	1.028	1.024	1.018	1.022	**1.047**	**1.184**
2.5	1.064	1.033	1.027	1.020	1.243	1.016	1.048	1.009	1.012	1.015	**1.049**	**1.243**
3.0	1.063	1.038	1.007	1.023	1.286	1.011	1.009	1.011	1.007	1.013	**1.047**	**1.286**

Table A-62 Soil amplification factors of KN08 due to input motions 0.05g

T (s)	SOY	KTX	LDX	KSX	BIX	HAX	SIX	LGX	HPX	SCX	Av.	Max.
0.0	1.110	1.058	1.070	1.025	1.104	1.199	1.096	1.010	1.059	1.027	**1.076**	**1.199**
0.2	1.133	1.115	1.063	1.023	1.085	1.128	1.110	1.060	1.093	1.065	**1.088**	**1.133**
0.5	1.014	1.023	1.019	1.018	1.015	1.022	1.025	1.015	1.012	1.018	**1.018**	**1.025**
1.0	1.008	1.006	1.008	1.004	1.006	1.006	1.005	1.005	1.004	1.005	**1.006**	**1.008**
1.5	1.008	1.004	1.003	1.002	1.007	1.004	1.003	1.002	1.001	1.002	**1.004**	**1.008**
2.0	1.002	1.003	1.000	1.001	1.009	1.001	1.000	1.001	1.001	1.002	**1.002**	**1.009**
2.5	1.004	1.002	1.002	1.000	1.009	1.002	1.001	1.000	1.000	1.001	**1.002**	**1.009**
3.0	1.005	1.000	1.000	1.001	1.012	1.001	1.001	1.000	1.000	1.001	**1.002**	**1.012**

Table A-63 Soil amplification factors of BK01 due to input motions 0.05g

T (s)	SOY	KTX	LDX	KSX	BIX	HAX	SIX	LGX	HPX	SCX	Av.	Max.
0.0	1.552	1.763	1.930	1.830	1.179	1.570	1.574	1.981	1.715	1.763	**1.686**	**1.981**
0.2	0.849	0.844	1.578	1.626	1.012	0.663	0.710	1.350	0.919	1.457	**1.101**	**1.626**
0.5	1.729	1.516	1.215	1.323	1.572	1.601	1.687	1.156	1.622	1.007	**1.443**	**1.729**
1.0	4.028	4.031	2.744	2.842	5.477	3.173	3.855	1.948	2.674	2.293	**3.307**	**5.477**
1.5	3.636	2.794	3.837	3.836	4.388	3.733	3.177	3.209	3.741	3.375	**3.573**	**4.388**
2.0	2.922	2.172	3.181	2.718	3.479	2.349	2.424	2.886	2.499	2.744	**2.737**	**3.479**
2.5	3.051	2.402	2.666	3.054	3.730	2.978	2.915	2.741	2.619	2.706	**2.886**	**3.730**
3.0	3.291	3.285	3.361	2.746	3.718	2.784	2.907	2.876	2.707	2.607	**3.028**	**3.718**

Table A-64 Soil amplification factors of BK02 due to input motions 0.05g

T (s)	SOY	KTX	LDX	KSX	BIX	HAX	SIX	LGX	HPX	SCX	Av.	Max.
0.0	1.100	1.194	0.933	1.130	1.123	0.954	1.000	1.271	1.318	1.094	**1.112**	**1.318**
0.2	0.577	0.594	0.745	0.997	1.037	0.373	0.415	0.808	0.692	0.873	**0.711**	**1.037**
0.5	1.206	1.140	0.920	0.974	1.585	1.005	1.268	0.707	1.023	0.581	**1.041**	**1.585**
1.0	2.229	2.074	1.620	1.462	4.380	1.647	1.543	0.786	0.916	0.968	**1.762**	**4.380**
1.5	2.904	3.754	2.967	2.497	3.728	2.219	3.011	0.921	1.705	1.479	**2.519**	**3.754**
2.0	2.474	2.907	3.242	3.862	2.907	3.200	3.154	1.481	2.875	1.923	**2.803**	**3.862**
2.5	2.709	3.109	3.449	4.089	3.027	3.794	3.302	3.066	3.780	3.383	**3.371**	**4.089**
3.0	2.925	3.852	4.043	3.735	2.964	3.774	3.556	3.934	3.725	3.672	**3.618**	**4.043**

Table A-65 Soil amplification factors of BK03 due to input motions 0.05g

T (s)	SOY	KTX	LDX	KSX	BIX	HAX	SIX	LGX	HPX	SCX	Av.	Max.
0.0	1.268	1.317	1.048	1.133	1.438	1.195	1.420	1.259	1.161	1.200	**1.244**	**1.438**
0.2	0.976	0.779	1.028	1.086	1.686	0.599	0.702	0.800	0.637	1.011	**0.930**	**1.686**
0.5	1.127	1.274	0.849	0.748	1.525	1.034	1.096	0.601	0.817	0.696	**0.977**	**1.525**
1.0	2.202	1.904	1.764	1.441	3.594	2.017	1.511	0.810	0.933	0.931	**1.711**	**3.594**
1.5	3.024	5.511	4.899	3.230	3.648	3.153	3.854	1.438	2.655	2.402	**3.381**	**5.511**
2.0	2.547	3.949	3.252	3.524	2.809	3.202	2.818	2.674	2.832	3.010	**3.062**	**3.949**
2.5	2.589	2.411	2.656	3.066	2.944	2.723	2.475	2.304	2.545	2.300	**2.601**	**3.066**
3.0	2.806	2.715	2.119	2.638	2.901	2.277	2.163	2.299	2.024	2.575	**2.452**	**2.901**

Table A-66 Soil amplification factors of BK04 due to input motions 0.05g

T (s)	SOY	KTX	LDX	KSX	BIX	HAX	SIX	LGX	HPX	SCX	Av.	Max.
0.0	1.483	1.571	1.782	1.745	1.238	1.469	1.515	1.868	1.623	1.683	**1.598**	**1.868**
0.2	0.755	0.801	1.436	1.499	1.106	0.576	0.574	1.196	0.872	1.374	**1.019**	**1.499**
0.5	1.663	1.665	1.354	1.319	1.791	1.595	1.724	0.962	1.312	0.918	**1.430**	**1.791**
1.0	3.606	2.716	2.728	2.172	5.310	2.858	3.320	1.273	1.932	1.523	**2.744**	**5.310**
1.5	3.983	5.561	5.377	4.619	4.473	4.326	4.470	2.241	4.537	3.973	**4.356**	**5.561**
2.0	3.169	3.585	2.954	3.342	3.674	3.024	2.346	4.105	3.427	3.392	**3.302**	**4.105**
2.5	3.007	2.001	2.435	3.537	3.899	2.560	2.073	2.270	2.226	2.118	**2.612**	**3.899**
3.0	3.248	2.410	2.283	2.550	3.870	2.161	1.743	2.173	1.831	2.524	**2.479**	**3.870**

Table A-67 Soil amplification factors of BK05 due to input motions 0.05g

T (s)	SOY	KTX	LDX	KSX	BIX	HAX	SIX	LGX	HPX	SCX	Av.	Max.
0.0	1.909	1.615	1.951	2.279	1.105	1.376	1.832	1.824	2.535	1.946	**1.837**	**2.535**
0.2	0.939	0.933	1.583	1.994	1.268	0.606	0.785	1.186	1.343	1.623	**1.226**	**1.994**
0.5	1.811	1.624	1.294	1.713	2.347	1.168	1.821	1.199	1.989	1.396	**1.636**	**2.347**
1.0	4.364	4.158	2.727	4.452	4.360	2.927	4.402	2.641	3.652	3.782	**3.746**	**4.452**
1.5	3.339	3.620	3.123	3.481	3.596	2.439	3.026	2.197	2.979	2.263	**3.006**	**3.620**
2.0	2.602	2.409	1.968	2.073	3.095	1.685	1.658	2.323	2.181	1.998	**2.199**	**3.095**
2.5	2.765	1.780	1.904	2.642	3.529	1.578	1.602	1.464	1.511	1.433	**2.021**	**3.529**
3.0	2.977	1.938	1.901	2.041	3.591	1.553	1.573	1.337	1.410	1.775	**2.010**	**3.591**

Table A-68 Soil amplification factors of BK06 due to input motions 0.05g

T (s)	SOY	KTX	LDX	KSX	BIX	HAX	SIX	LGX	HPX	SCX	Av.	Max.
0.0	2.058	1.801	2.150	2.274	1.103	1.323	1.763	2.153	2.923	2.002	**1.955**	**2.923**
0.2	0.941	0.944	1.771	2.034	1.035	0.536	0.658	1.429	1.523	1.738	**1.261**	**2.034**
0.5	2.342	2.113	1.826	2.116	3.221	1.498	2.251	1.487	2.354	1.525	**2.073**	**3.221**
1.0	4.037	3.699	2.802	4.256	3.624	2.501	3.824	2.565	3.988	3.107	**3.440**	**4.256**
1.5	3.218	3.345	2.882	3.006	3.270	2.137	2.700	1.876	2.668	1.993	**2.710**	**3.345**
2.0	2.628	2.222	1.748	1.904	3.017	1.570	1.564	2.135	2.033	1.841	**2.066**	**3.017**
2.5	2.830	1.836	1.858	2.397	3.345	1.457	1.536	1.367	1.469	1.376	**1.947**	**3.345**
3.0	3.043	1.886	1.837	1.790	3.412	1.484	1.546	1.277	1.277	1.629	**1.918**	**3.412**

Table A-69 Soil amplification factors of BK07 due to input motions 0.05g

T (s)	SOY	KTX	LDX	KSX	BIX	HAX	SIX	LGX	HPX	SCX	Av.	Max.
0.0	2.114	1.899	2.163	2.235	1.550	1.738	1.651	2.662	2.070	1.605	**1.969**	**2.662**
0.2	1.534	1.587	1.712	2.020	1.983	1.277	1.230	1.861	1.338	1.576	**1.612**	**2.020**
0.5	2.909	2.747	2.870	2.354	4.179	2.260	2.560	2.235	2.142	2.373	**2.663**	**4.179**
1.0	3.088	2.845	2.547	2.628	3.143	2.270	2.373	2.770	2.339	2.362	**2.636**	**3.143**
1.5	2.506	1.619	2.032	1.709	2.894	1.866	1.821	1.852	1.797	1.783	**1.988**	**2.894**
2.0	2.577	1.661	1.985	1.680	2.564	1.422	1.630	1.462	1.472	1.447	**1.790**	**2.577**
2.5	2.724	2.067	2.082	2.034	2.867	2.144	2.575	1.875	1.980	1.812	**2.216**	**2.867**
3.0	2.902	2.691	2.906	2.367	2.942	2.256	2.571	2.216	2.103	1.953	**2.491**	**2.942**

Table A-70 Soil amplification factors of BK08 due to input motions 0.05g

T (s)	**SOY**	**KTX**	**LDX**	**KSX**	**BIX**	**HAX**	**SIX**	**LGX**	**HPX**	**SCX**	**Av.**	**Max.**
0.0	1.297	1.457	1.662	1.636	1.110	1.486	1.507	1.642	1.558	1.483	**1.484**	**1.662**
0.2	0.647	0.709	1.320	1.434	0.943	0.565	0.565	1.063	0.829	1.204	**0.928**	**1.434**
0.5	1.701	1.474	1.327	1.169	2.187	1.587	1.794	1.021	1.316	0.918	**1.449**	**2.187**
1.0	3.089	2.818	2.626	2.097	6.184	2.730	2.900	1.547	1.738	1.872	**2.760**	**6.184**
1.5	3.448	3.746	4.011	3.074	4.634	3.581	3.766	2.172	3.002	2.753	**3.419**	**4.634**
2.0	2.883	2.714	3.517	3.380	3.731	2.875	2.751	3.041	3.116	3.506	**3.151**	**3.731**
2.5	3.153	2.940	3.227	3.616	3.992	3.374	3.017	3.393	3.305	3.260	**3.328**	**3.992**
3.0	3.408	3.798	3.705	3.192	3.963	3.281	3.170	3.706	3.177	3.138	**3.454**	**3.963**

Table A-71 Soil amplification factors of BK09 due to input motions 0.05g

T (s)	**SOY**	**KTX**	**LDX**	**KSX**	**BIX**	**HAX**	**SIX**	**LGX**	**HPX**	**SCX**	**Av.**	**Max.**
0.0	1.023	1.132	1.003	1.257	0.874	1.198	1.306	1.322	1.192	1.187	**1.149**	**1.322**
0.2	0.659	0.743	0.871	1.089	0.951	0.550	0.662	0.880	0.665	0.981	**0.805**	**1.089**
0.5	0.943	0.920	0.721	0.855	1.018	0.967	1.181	0.612	1.000	0.660	**0.888**	**1.181**
1.0	2.766	2.864	1.893	1.815	4.461	2.221	2.222	1.161	1.264	1.306	**2.197**	**4.461**
1.5	3.010	3.066	3.583	2.978	3.818	2.981	3.478	1.689	2.624	2.223	**2.945**	**3.818**
2.0	2.567	2.273	3.196	3.067	2.937	2.714	2.730	2.736	2.998	3.345	**2.856**	**3.345**
2.5	2.737	2.553	3.114	3.388	3.096	3.285	2.918	3.248	3.213	3.198	**3.075**	**3.388**
3.0	2.980	3.465	3.620	2.886	3.161	3.169	3.185	3.578	3.106	3.074	**3.222**	**3.620**

Appendix B
Bi-directional Responses of 86 Ground Motions

B.1 Major axes of ground motions

From the Chapter V, the largest Arias Intensity in the horizontal plane of a ground motion is defined as the major axis. The major axes of 86 ground motions can be expressed in Figure B-1 to B-8.

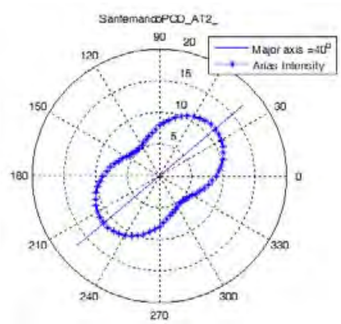

(a) San Fernando
279 Pacoima Dam

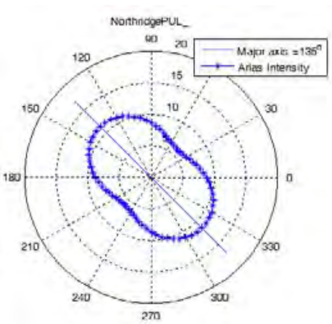

(b) Northridge
24207 Pacoima Dam (upper left)

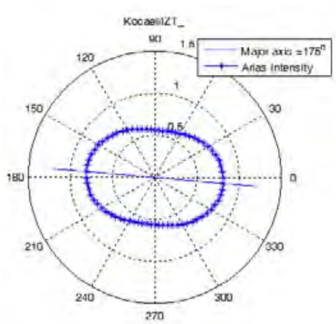

(c) Kocaeli, Turkey
Izmit

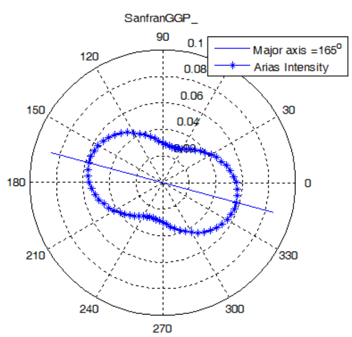

(d) San Francisco
1117 Golden Gate Park

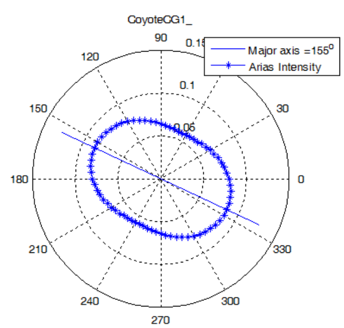

(e) Coyote Lake
47379 Gilroy Array #1

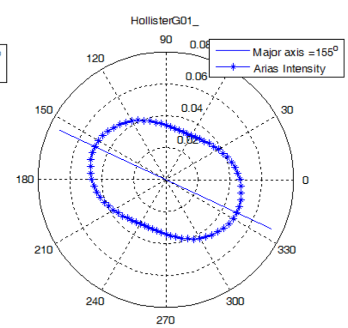

(f) Hollister
47379 Gilroy Array #1

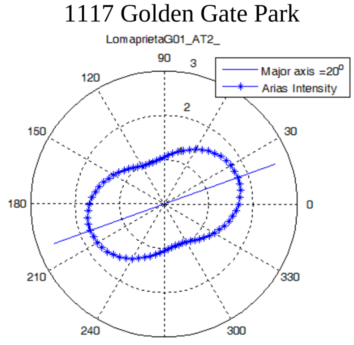

(g) Loma Prieta
47379 Gilroy Array #1

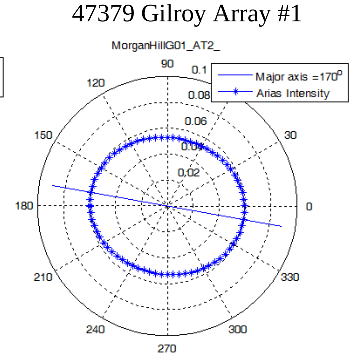

(h) Morgan Hill
47379 Gilroy Array #1

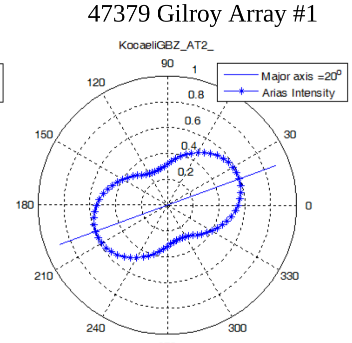

(i) Kocaeli, Turkey
Gebze

Figure B-1 Major axes of ground motions (1)

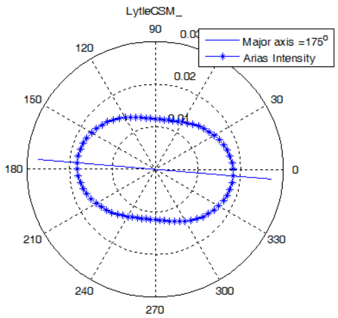

(a) Lytle Creek
111 Cedar Springs, Allen Ranch

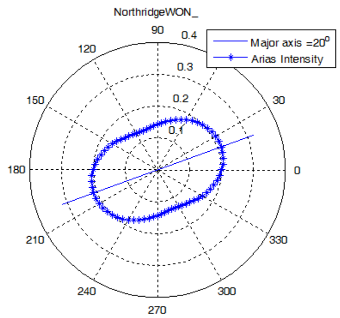

(b) Northridge
90017 LA - Wonderland Ave

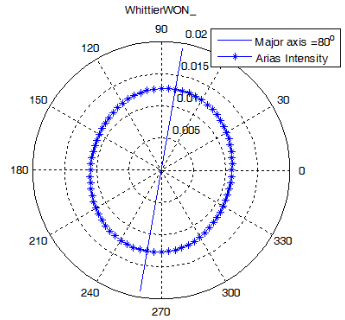

(c) Whittier Narrows
90017 LA - Wonderland Ave

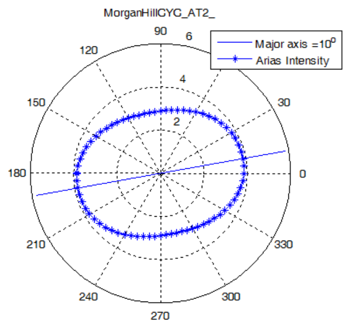

(d) Morgan Hill
57217 Coyote Lake Dam

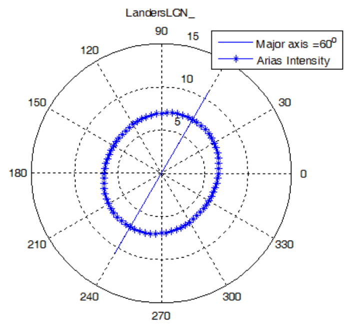

(e) Landers
24 Lucerne

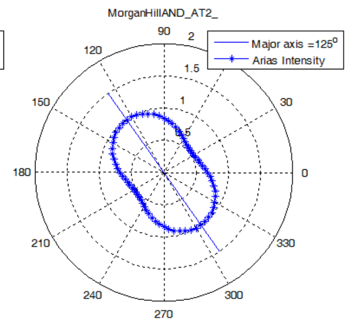

(f) Morgan Hill
1652 Anderson Dam

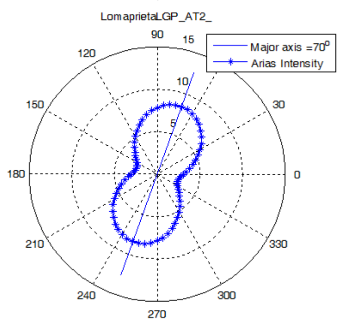

(g) Loma Prieta
16 LGPC

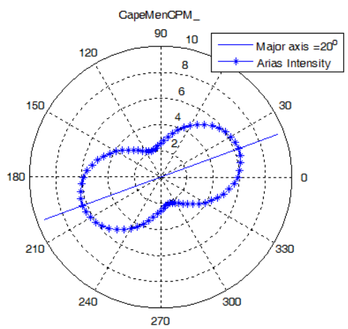

(h) Cape Mendocino
89005 Cape Mendocino

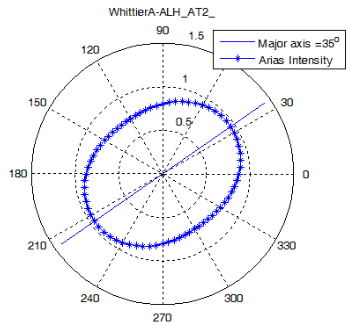

(i) Whittier Narrows
24461 Alhambra, Fremont Sch

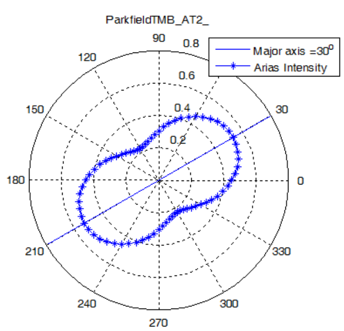

(j) Parkfield
1438 Temblor pre-1969

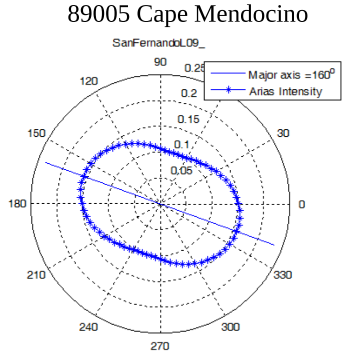

(k) San Fernando
127 Lake Hughes #9

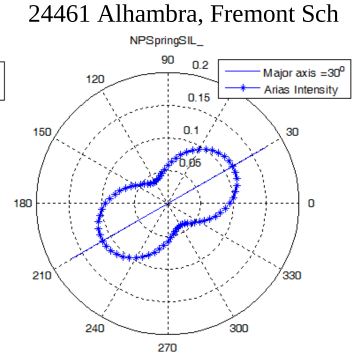

(l) N. Palm Springs
12206 Silent Valley - Poppet F

Figure B-2 Major axes of ground motions (2)

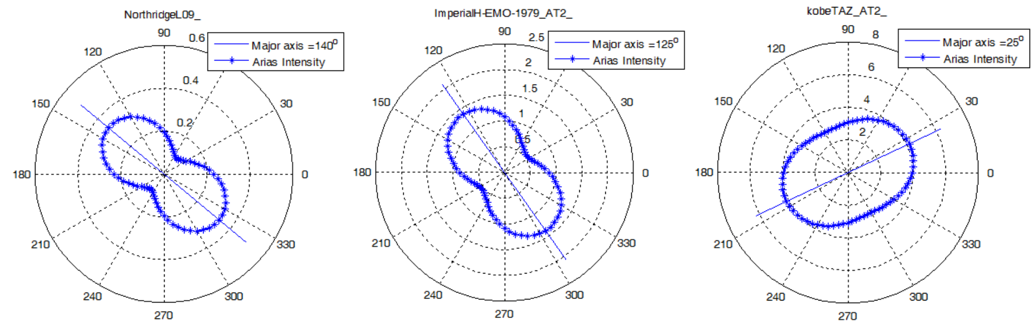

(a) Northridge
127 Lake Hughes #9

(b) Imperial Valley
5155 EC Meloland Overpass FF

(c) Kobe
0 Takarazuka

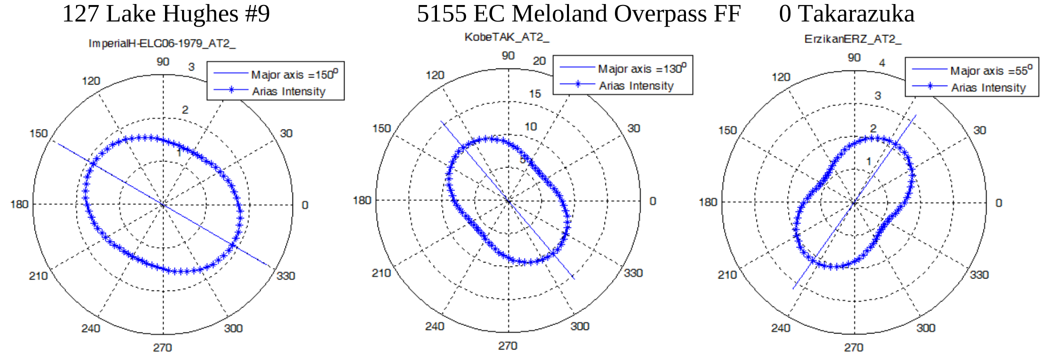

(d) Imperial Valley
942 El Centro Array #6

(e) Kobe
0 Takatori

(f) Erzincan, Turkey
95 Erzincan

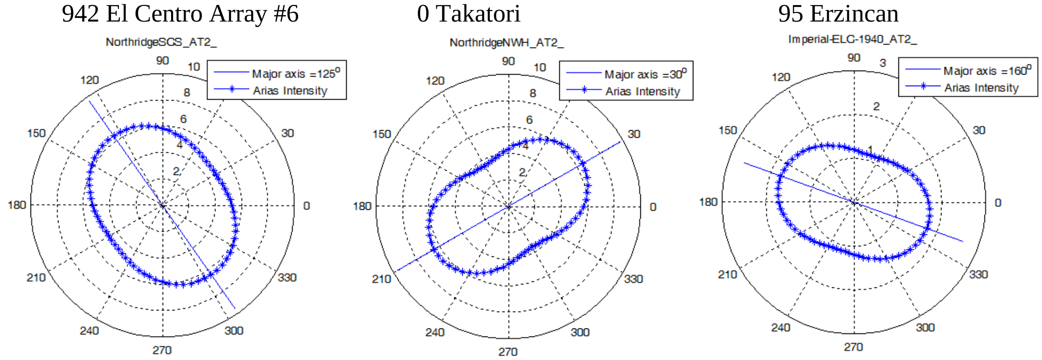

(g) Northridge
74 Sylmar - Converter Sta

(h) Northridge
24279 Newhall - Fire Sta

(i) Imperial Valley
117 El Centro Array #9

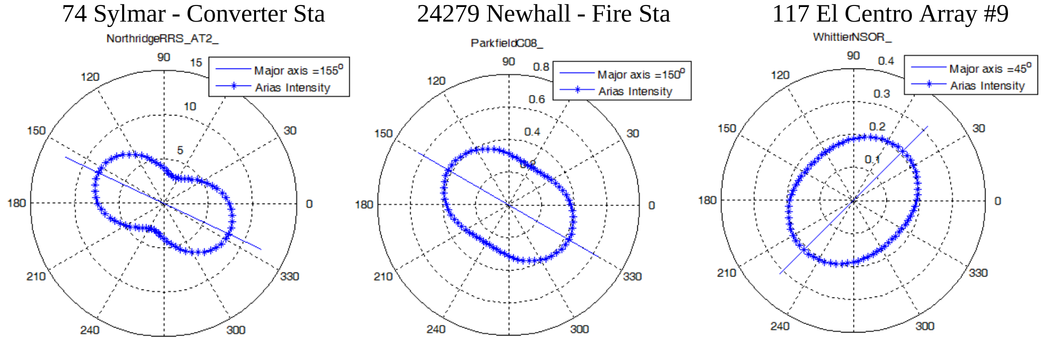

(j) Northridge
77 Rinaldi Receiving Sta

(k) Parkfield
1015 Cholame #8

(l) Whittier Narrows
90071 West Covina - S Orange

Figure B-3 Major axes of ground motions (3)

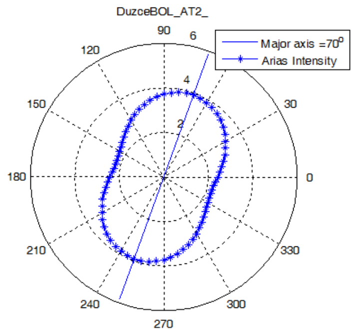

(a) Duzce, Turkey
Bolu

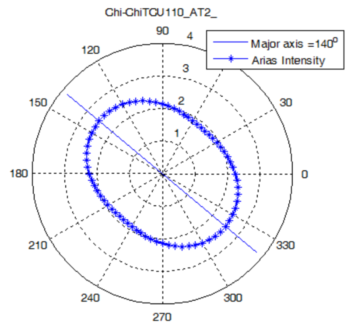

(b) Chi-Chi, Taiwan
TCU110

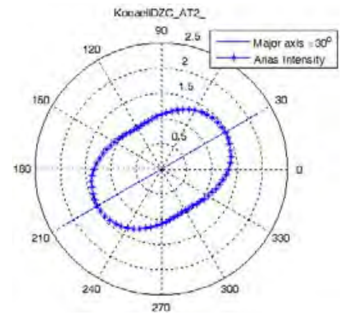

(c) Kocaeli, Turkey
Duzce

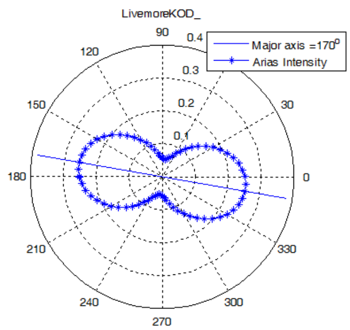

(d) Livermore
57187 San Ramon - Eastman Kodak

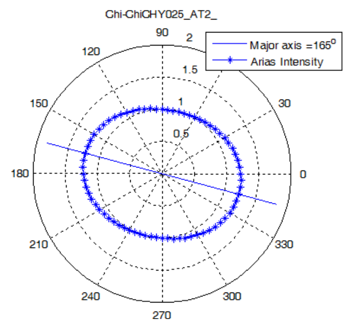

(e) Chi-Chi, Taiwan
CHY025

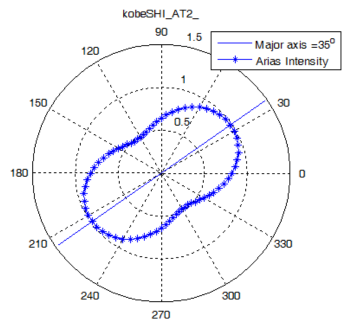

(f) Kobe
0 Shin-Osaka

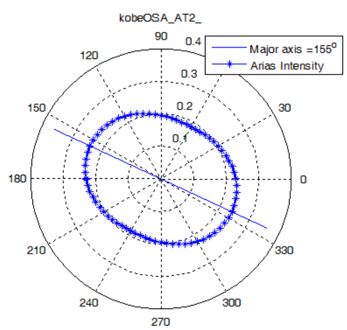

(g) Kobe
0 OSAJ

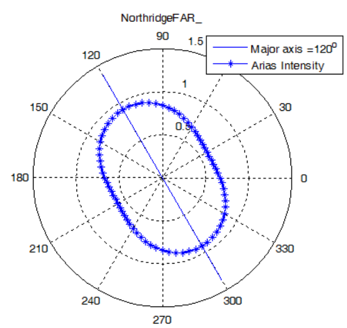

(h) Northridge
90016 LA - N Faring Rd

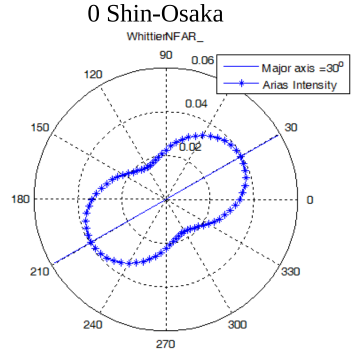

(i) Whittier Narrows
90016 LA - N Faring Rd

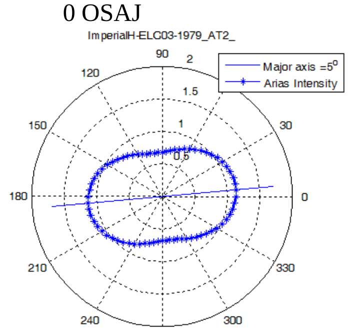

(j) Imperial Valley
5057 El Centro Array #3

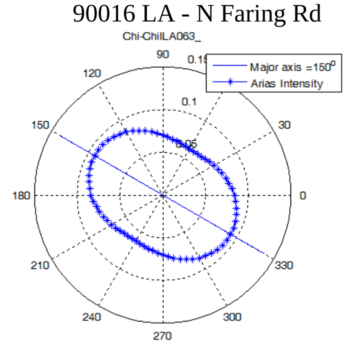

(k) Chi-Chi, Taiwan
ILA063

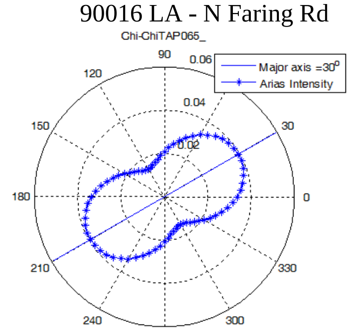

(l) Chi-Chi, Taiwan
TAP065

Figure B-4 Major axes of ground motions (4)

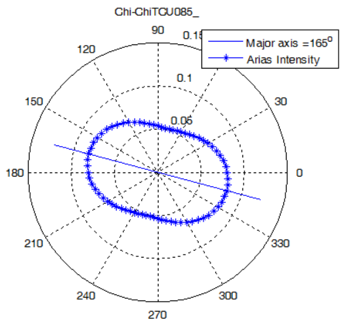

(a) Chi-Chi, Taiwan
TCU085

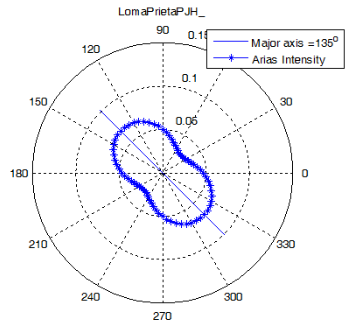

(b) Loma Prieta
58338 Piedmont Jr High

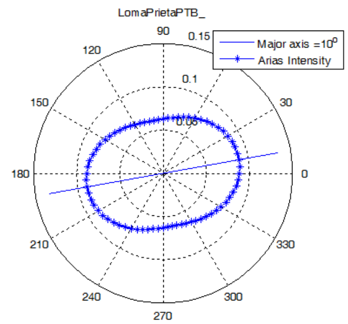

(c) Loma Prieta
58043 Point Bonita

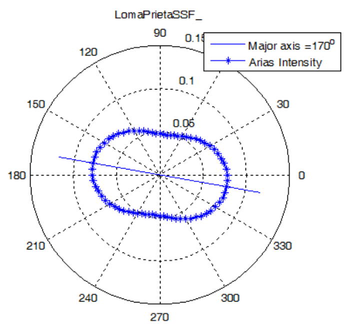

(d) Loma Prieta
58539 So. San Francisco, Sierra Pt.

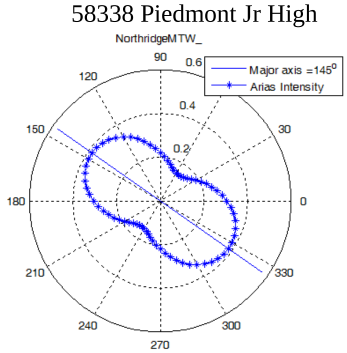

(e) Northridge
24399 Mt Wilson - CIT Seis Sta

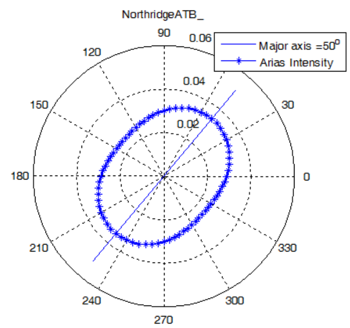

(f) Northridge
24310 Antelope Buttes

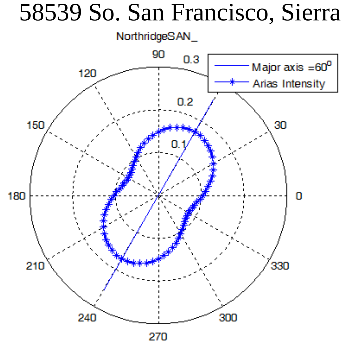

(g) Northridge
24644 Sandberg - Bald Mtn

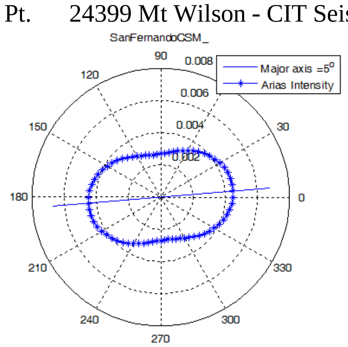

(h) San Fernando
111 Cedar Springs, Allen Ranch

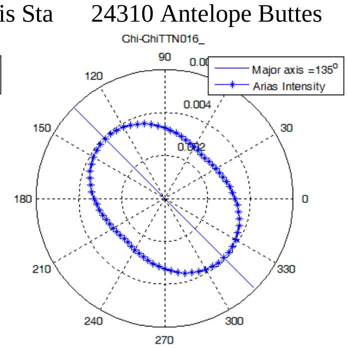

(i) Chi-Chi, Taiwan
TTN016

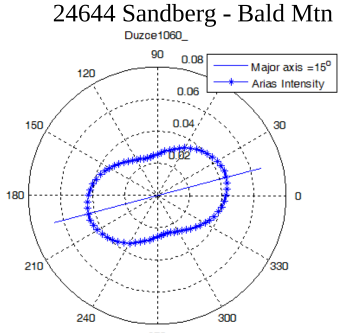

(j) Duzce, Turkey
1060 Lamont 1060

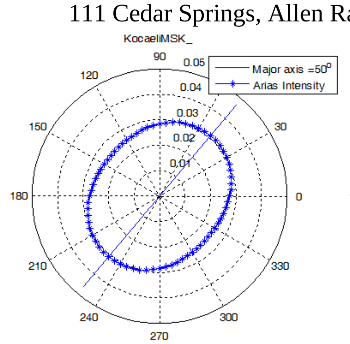

(k) Kocaeli, Turkey
Maslak

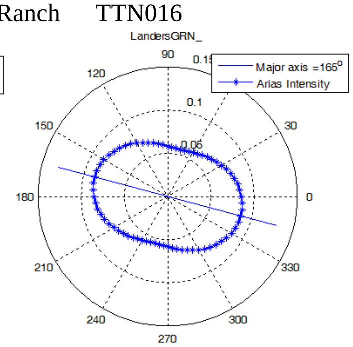

(l) Landers
90019 San Gabriel - E Grand Av

Figure B-5 Major axes of ground motions (5)

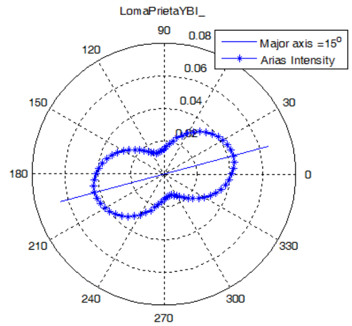

(a) Loma Prieta
58163 Yerba Buena Island

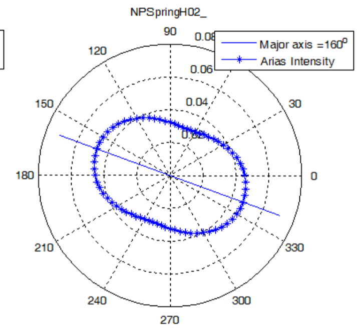

(b) N. Palm Springs
13199 Winchester Bergman Ran

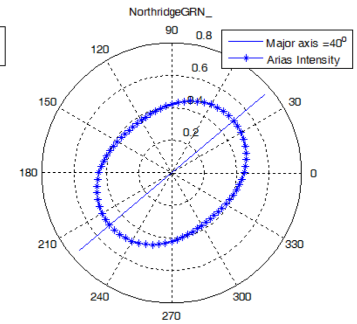

(c) Northridge
90019 San Gabriel - E. Grand

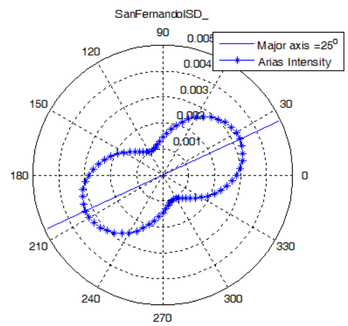

(d) San Fernando
1035 Isabella Dam (Aux Abut)

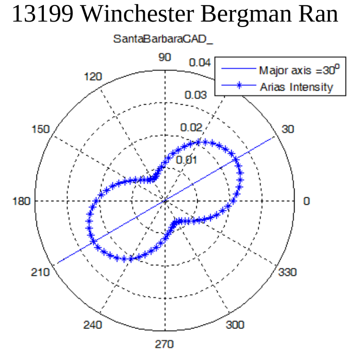

(e) Santa Barbara
106 Cachuma Dam Toe

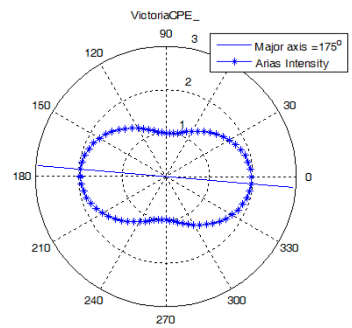

(f) Victoria, Mexico
6604 Cerro Prieto

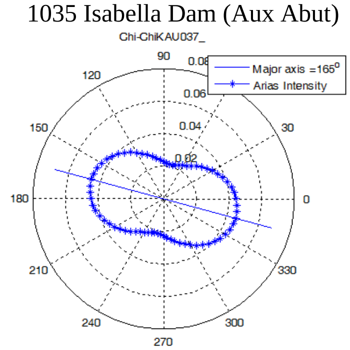

(g) Chi-Chi, Taiwan
KAU037

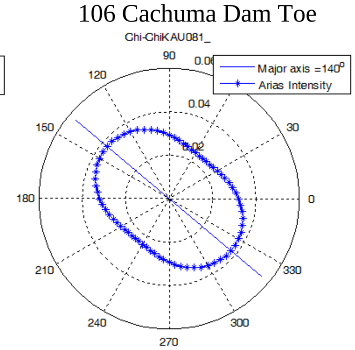

(h) Chi-Chi, Taiwan
KAU081

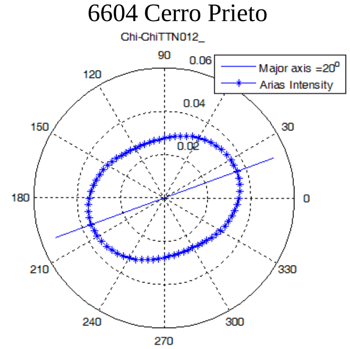

(i) Chi-Chi, Taiwan
TTN012

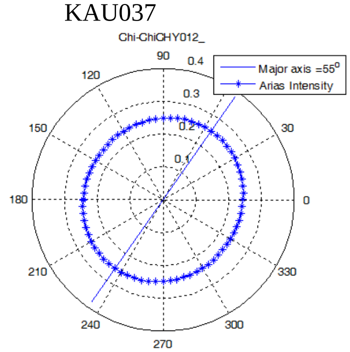

(j) Chi-Chi, Taiwan
CHY012

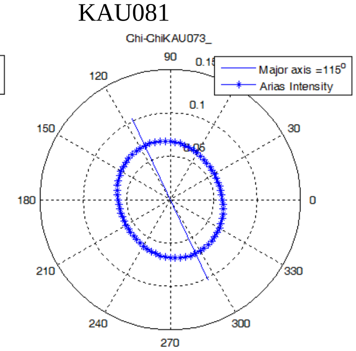

(k) Chi-Chi, Taiwan
KAU073

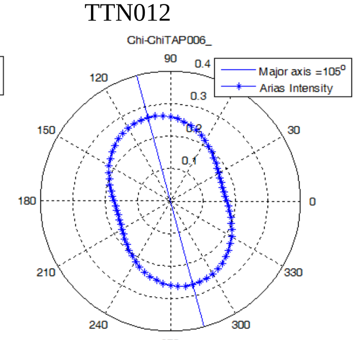

(l) Chi-Chi, Taiwan
TAP006

Figure B-6 Major axes of ground motions (6)

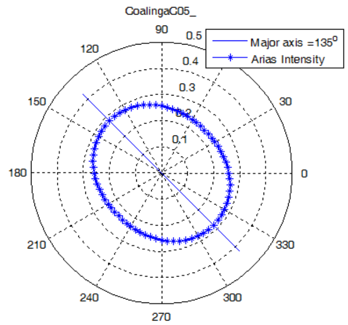

(a) Coalinga
36227 Parkfield - Cholame 5W

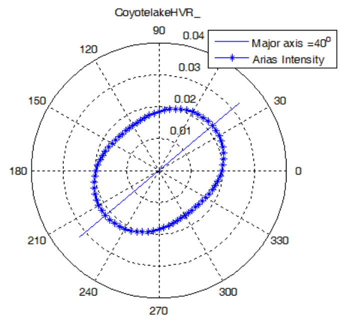

(b) Coyote Lake
57191 Halls Valley

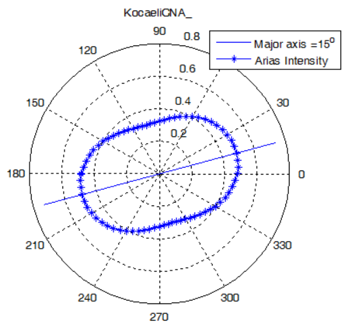

(c) Kocaeli, Turkey
Cekmece

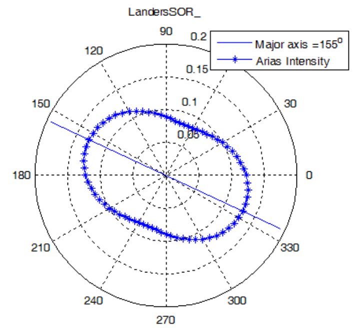

(d) Landers
90071 West Covina - S Orange

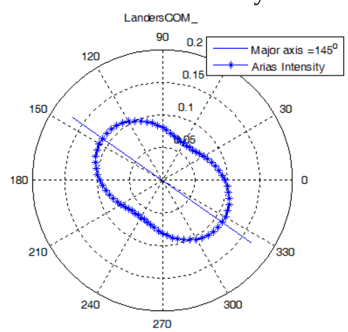

(e) Landers
90073 Hacienda Heights - Colima

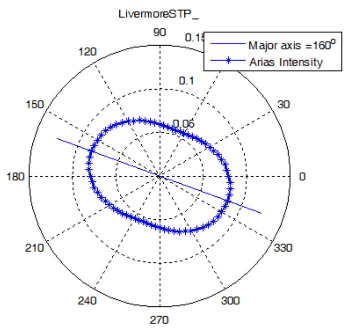

(f) Livermore
57063 Tracy - Sewage Treatm

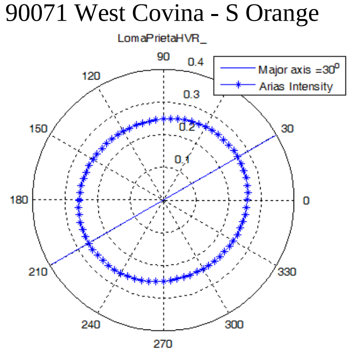

(g) Loma Prieta
57191 Halls Valley

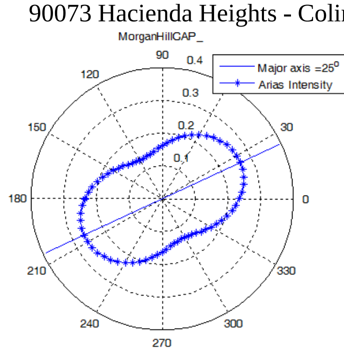

(h) Morgan Hill
47125 Capitola

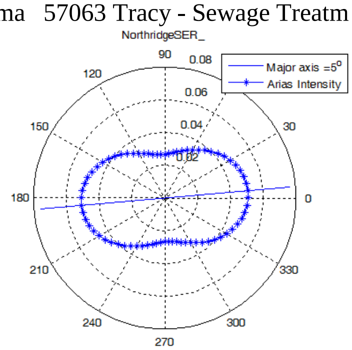

(i) Northridge
90090 Villa Park-Serrano Ave

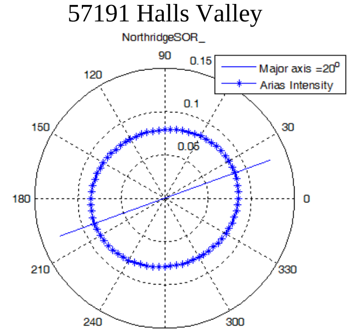

(j) Northridge
90071 West Covina - S. Orange Ave

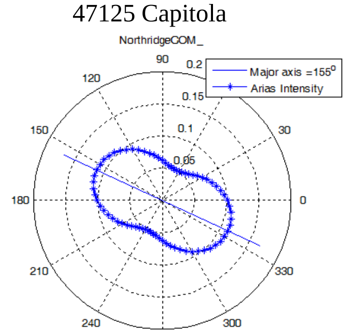

(k) Northridge
90073 Hacienda Hts - Colima Rd

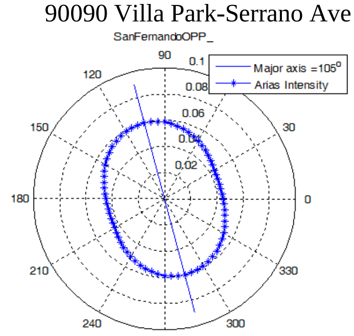

(l) San Fernando
994 Gormon - Oso Pump Plant

Figure B-7 Major axes of ground motions (7)

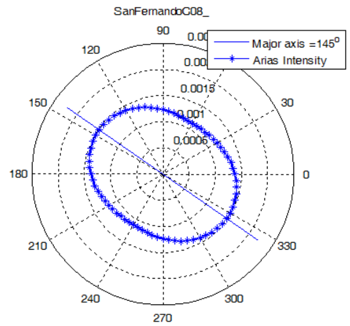

(a) San Fernando
1015 Cholame-Shandon Array #8

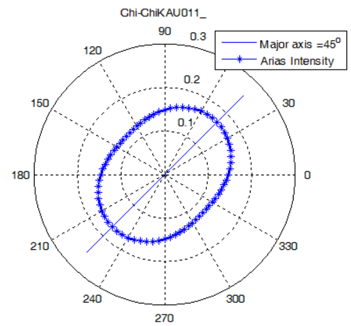

(b) Chi-Chi, Taiwan
KAU011

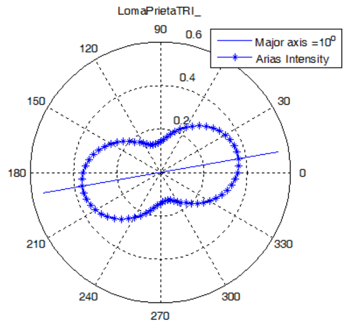

(c) Loma Prieta
58117 Treasure Island

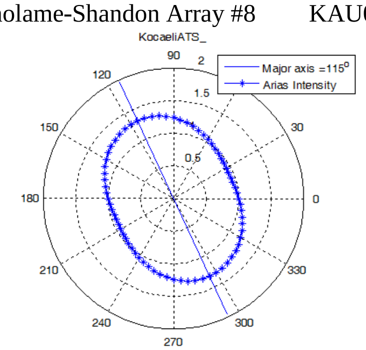

(d) Kocaeli, Turkey
Ambarli

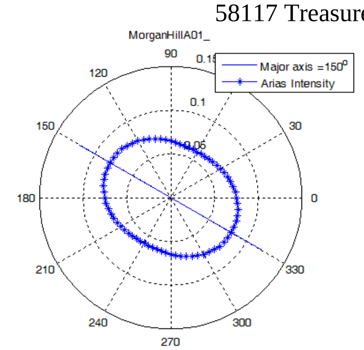

(e) Morgan Hill
58375 APEEL 1 - Redwood City

Figure B-8 Major axes of ground motions (8)

B.2 Bi-directional responses

The 86 ground motions were analyzed in this study. The bi-directional responses which are exemplified in Chapter V can be plotted all responses of 86 ground motions in Figures B-9 to B-180. For an example in Figure B-9 and B-10, the maximum resultant pseudo-acceleration at θ = 0 degree ($S_A^r(T_x,T_y,0^\circ)$) is shown in Figure B-9(a). The direction response spectrum for θ = 0 degree ($\alpha(T_x,T_y,0^\circ)$) is shown in Figure B-9(b). The maximum resultant pseudo-acceleration considering all angles of horizontal motions ($\widetilde{S}_A^r(T_x,T_y)$) is shown in Figure B-9(c). The direction response spectrum considering all angles of horizontal motions ($\widetilde{\alpha}(T_x,T_y)$) is shown in Figure B-9(d). $S_A(T_x,T_y)$ is the maximum value of the uni-directional pseudo-acceleration in x-axis ($S_A(T_x)$) or y-axis ($S_A(T_y)$) that can be shown in Figure B-9(e). $R_A(T_x,T_y)$ which represents the amplification of the maximum resultant pseudo-acceleration is presented in Figure B-9(e). $S_A^r(T_x,T_y,\theta)$ is computed for various angles of 30°, 60°, and 90° as shown in Figure B-10(a), (c), and (e) respectively. $\alpha(T_x,T_y,\theta)$ is computed for various angles of 30°, 60°, and 90° as shown in Figure B-10(b), (d), and (f) respectively.

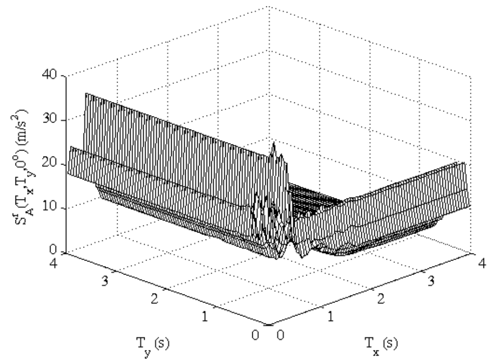

(a) $S_A^r(T_x, T_y, 0^\circ)$

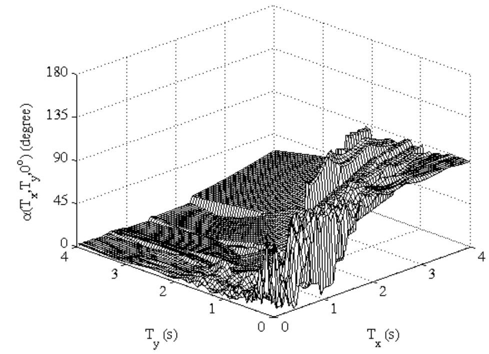

(b) $\alpha(T_x, T_y, 0^\circ)$

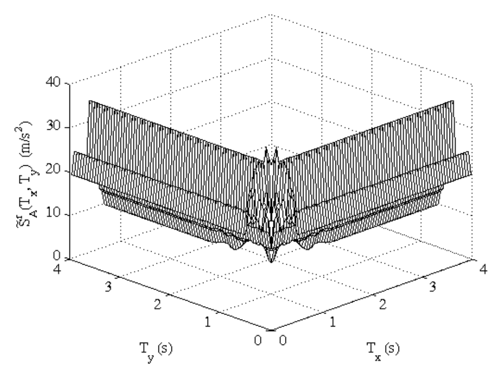

(c) $\tilde{S}_A^r(T_x, T_y)$

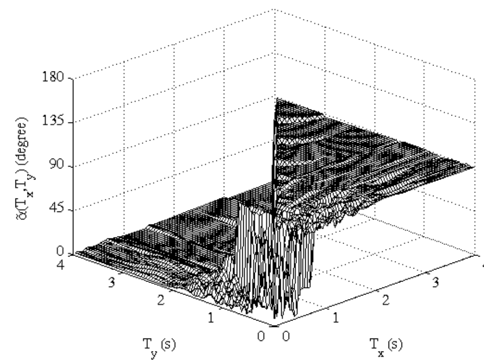

(d) $\tilde{\alpha}(T_x, T_y)$

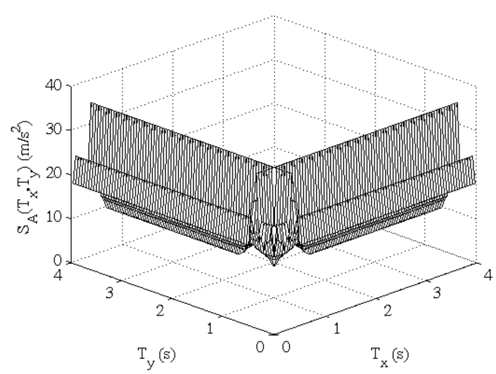

(e) $S_A(T_x, T_y)$

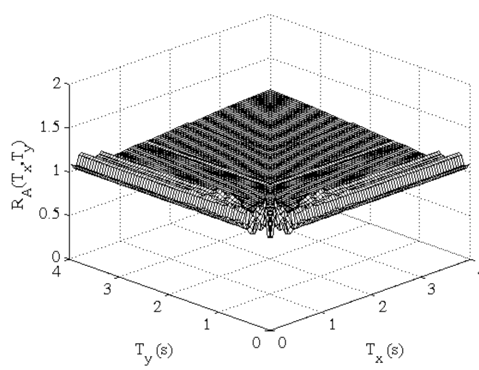

(f) $R_A(T_x, T_y)$

Figure B-9 Bi-directional responses of San Fernando earthquake, 279 Pacoima Dam station

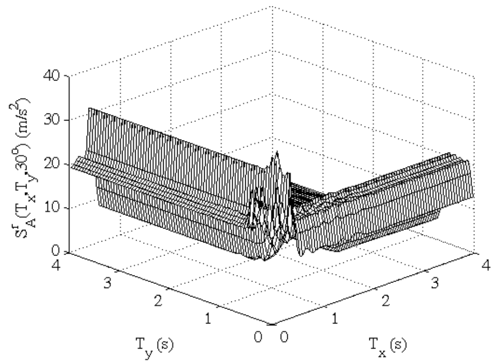

(a) $S_A^r(T_x, T_y, 30^\circ)$

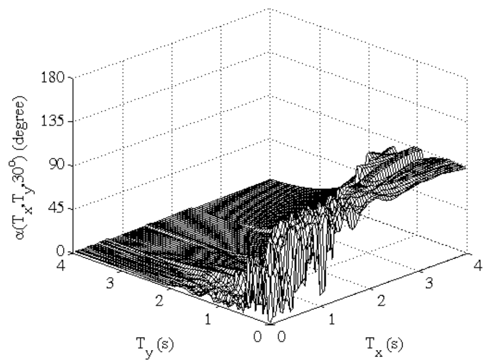

(b) $\alpha(T_x, T_y, 30^\circ)$

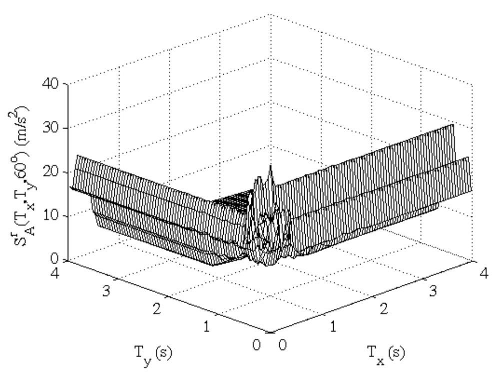

(c) $S_A^r(T_x, T_y, 60^\circ)$

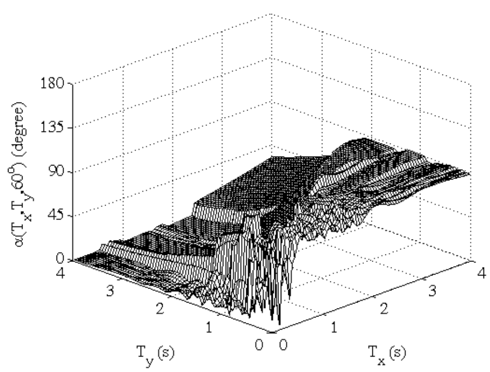

(d) $\alpha(T_x, T_y, 60^\circ)$

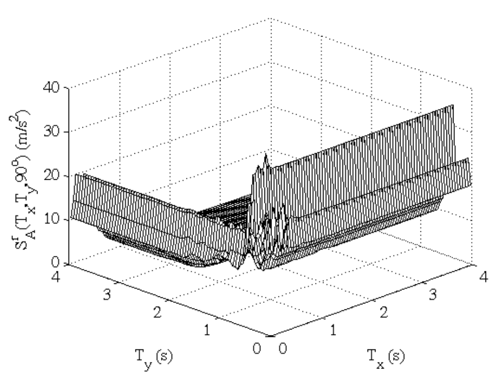

(e) $S_A^r(T_x, T_y, 90^\circ)$

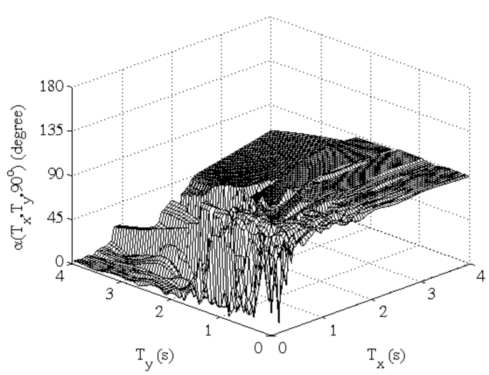

(f) $\alpha(T_x, T_y, 90^\circ)$

Figure B-10 Pseudo acceleration spectra and incident angles in various directions of San Fernando earthquake, 279 Pacoima Dam station

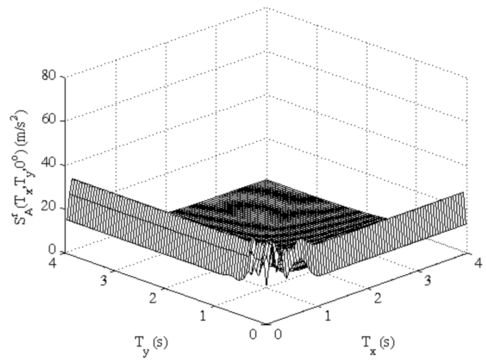

(a) $S_A^r(T_x, T_y, 0^\circ)$

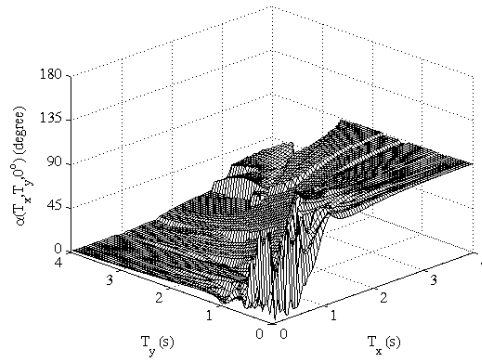

(b) $\alpha(T_x, T_y, 0^\circ)$

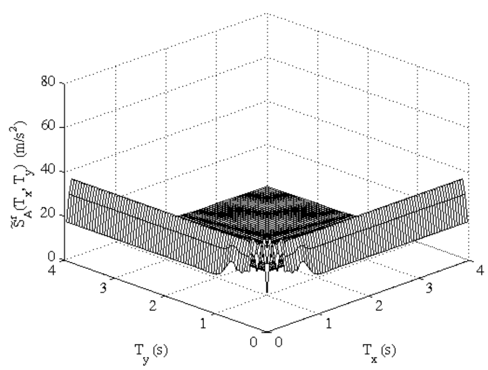

(c) $\widetilde{S}_A^r(T_x, T_y)$

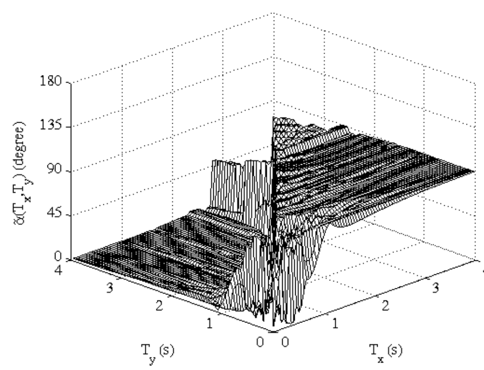

(d) $\widetilde{\alpha}(T_x, T_y)$

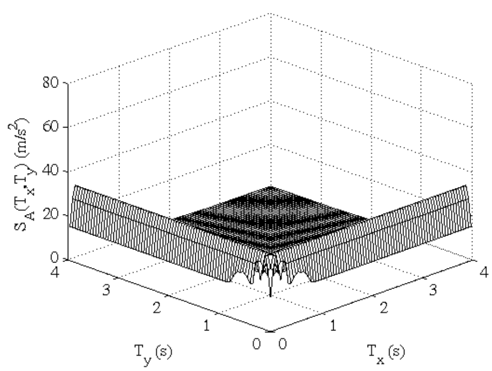

(e) $S_A(T_x, T_y)$

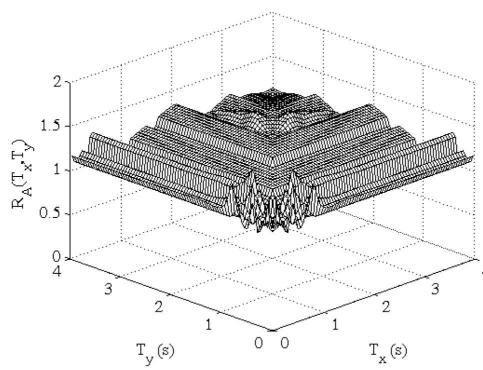

(f) $R_A(T_x, T_y)$

Figure B-11 Bi-directional responses of Northridge earthquake, 24207 Pacoima Dam (upper left) station

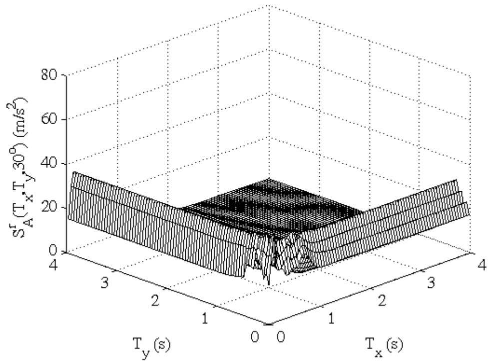

(a) $S_A^r(T_x, T_y, 30^{\circ})$

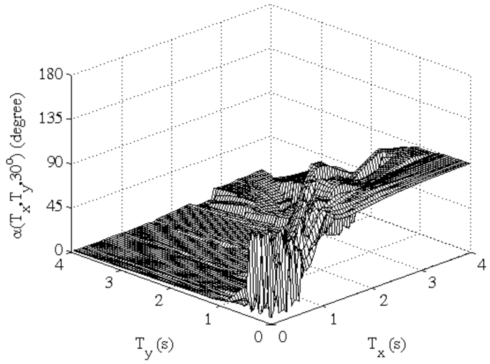

(b) $\alpha(T_x, T_y, 30^{\circ})$

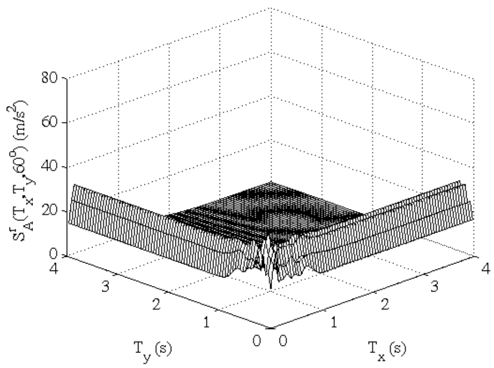

(c) $S_A^r(T_x, T_y, 60^{\circ})$

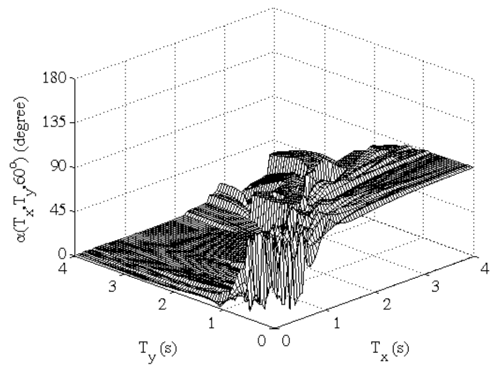

(d) $\alpha(T_x, T_y, 60^{\circ})$

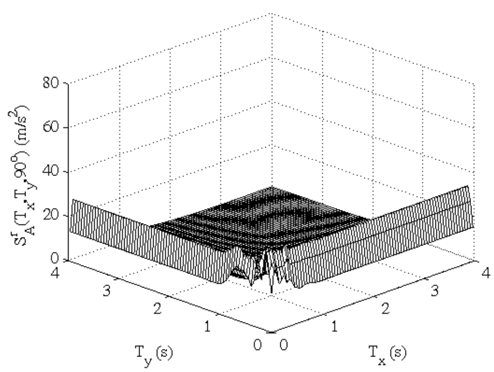

(e) $S_A^r(T_x, T_y, 90^{\circ})$

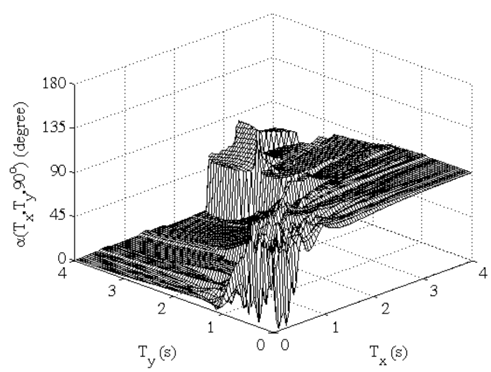

(f) $\alpha(T_x, T_y, 90^{\circ})$

Figure B-12 Pseudo acceleration spectra and incident angles in various directions of Northridge earthquake, 24207 Pacoima Dam (upper left) station

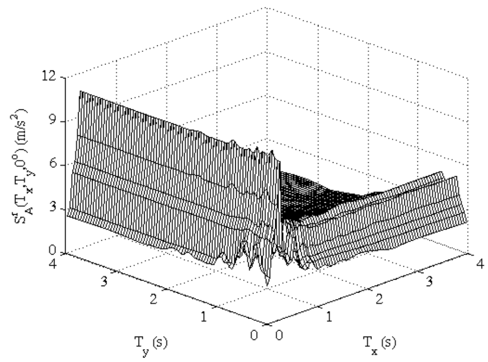

(a) $S_A^r(T_x,T_y,0^\circ)$

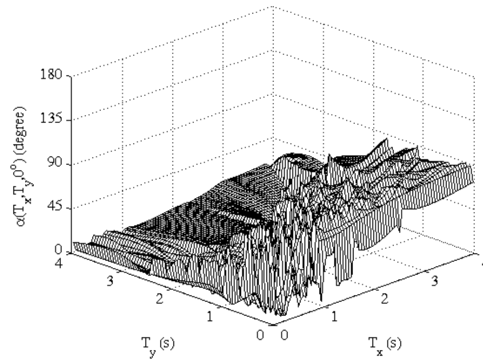

(b) $\alpha(T_x,T_y,0^\circ)$

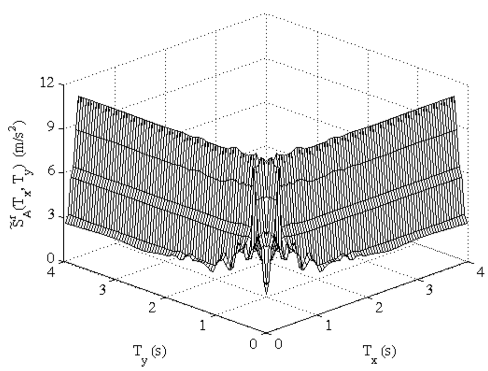

(c) $\widetilde{S}_A^r(T_x,T_y)$

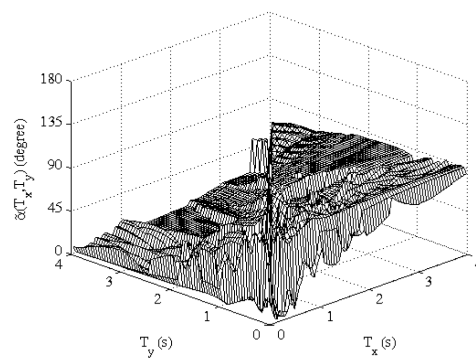

(d) $\widetilde{\alpha}(T_x,T_y)$

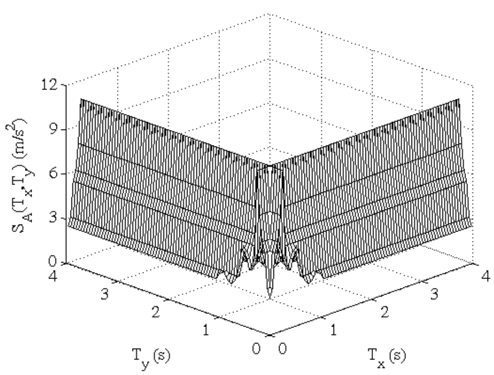

(e) $S_A(T_x,T_y)$

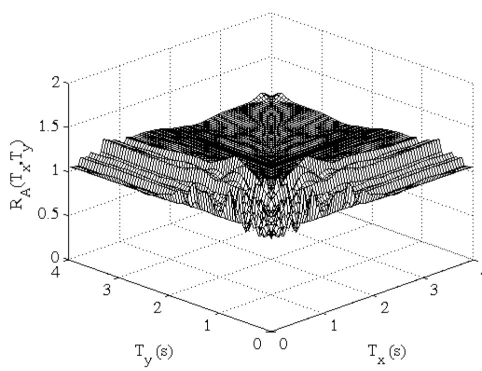

(f) $R_A(T_x,T_y)$

Figure B-13 Bi-directional responses of Kocaeli, Turkey earthquake, Izmit station

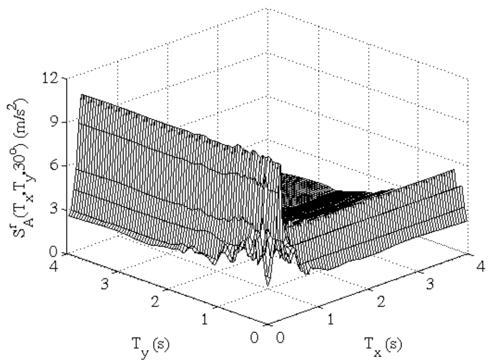

(a) $S_A^r(T_x, T_y, 30^\circ)$

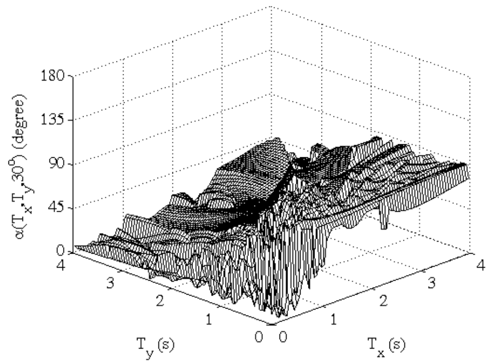

(b) $\alpha(T_x, T_y, 30^\circ)$

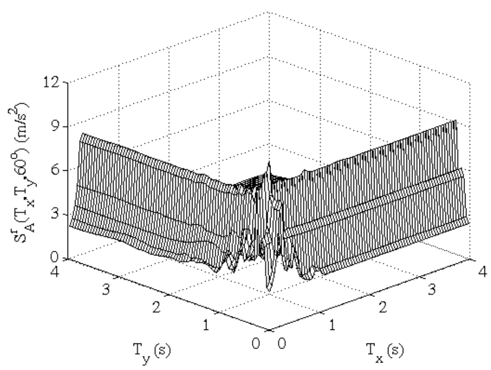

(c) $S_A^r(T_x, T_y, 60^\circ)$

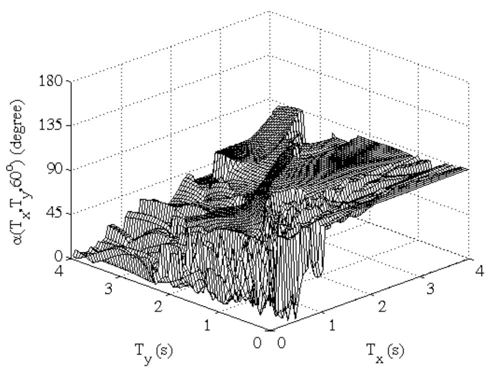

(d) $\alpha(T_x, T_y, 60^\circ)$

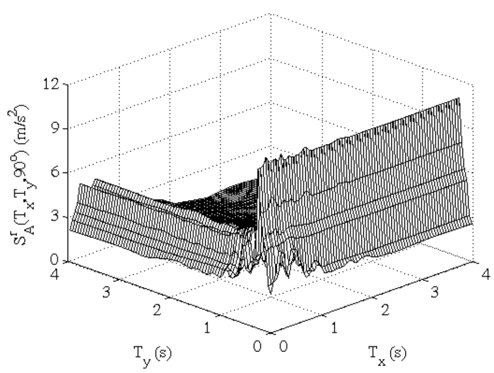

(e) $S_A^r(T_x, T_y, 90^\circ)$

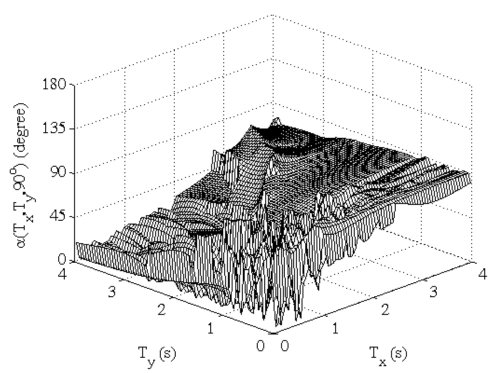

(f) $\alpha(T_x, T_y, 90^\circ)$

Figure B-14 Pseudo acceleration spectra and incident angles in various directions of Kocaeli, Turkey earthquake, Izmit station

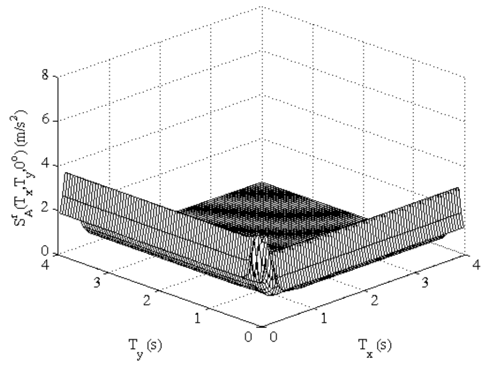

(a) $S_A^r(T_x, T_y, 0^\circ)$

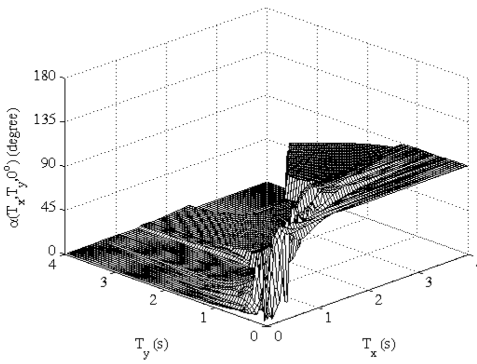

(b) $\alpha(T_x, T_y, 0^\circ)$

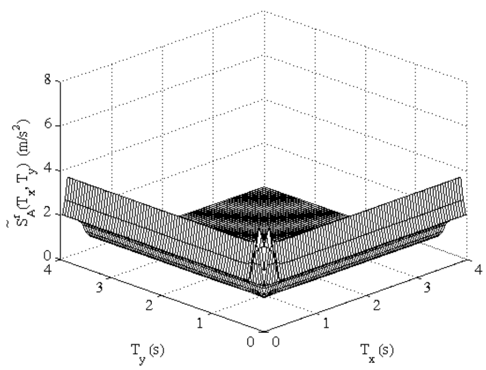

(c) $\tilde{S}_A^r(T_x, T_y)$

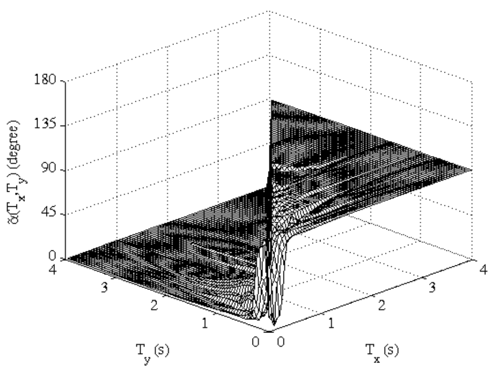

(d) $\tilde{\alpha}(T_x, T_y)$

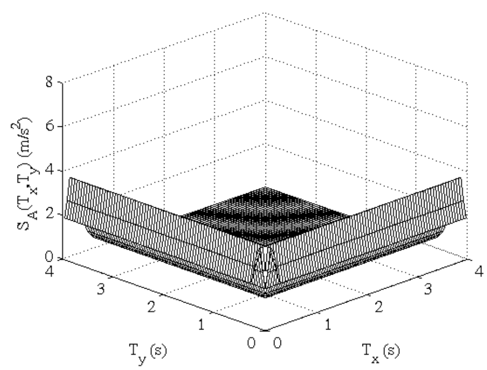

(e) $S_A(T_x, T_y)$

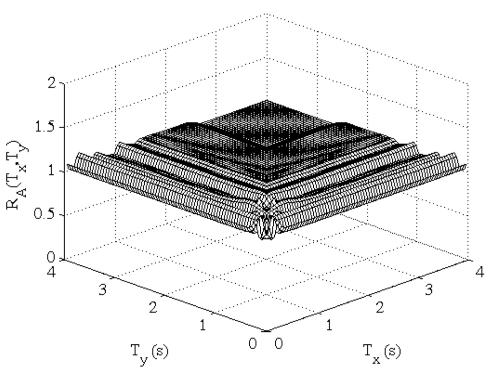

(f) $R_A(T_x, T_y)$

Figure B-15 Bi-directional responses of San Francisco earthquake, 1117 Golden Gate Park station

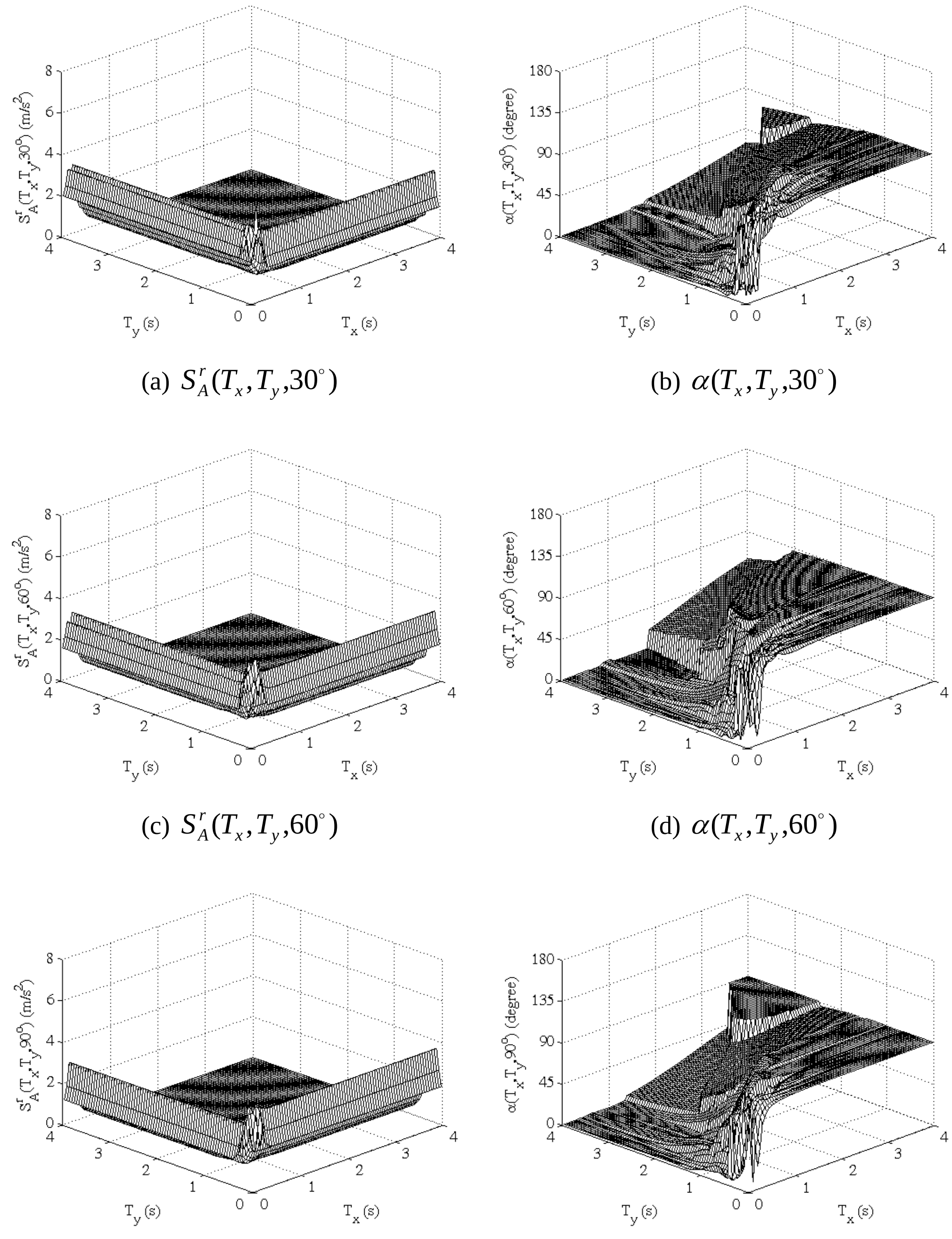

(a) $S_A^r(T_x, T_y, 30^\circ)$ (b) $\alpha(T_x, T_y, 30^\circ)$

(c) $S_A^r(T_x, T_y, 60^\circ)$ (d) $\alpha(T_x, T_y, 60^\circ)$

(e) $S_A^r(T_x, T_y, 90^\circ)$ (f) $\alpha(T_x, T_y, 90^\circ)$

Figure B-16 Pseudo acceleration spectra and incident angles in various directions of San Francisco earthquake, 1117 Golden Gate Park station

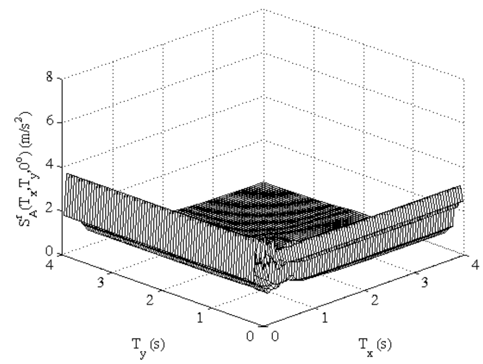

(a) $S_A^r(T_x, T_y, 0^\circ)$

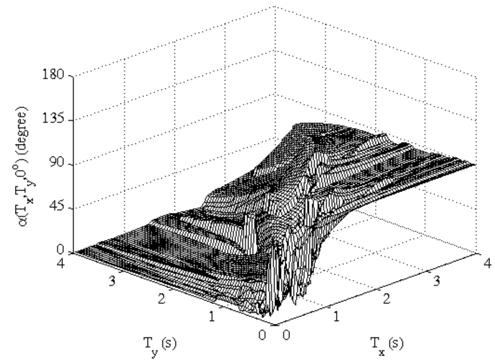

(b) $\alpha(T_x, T_y, 0^\circ)$

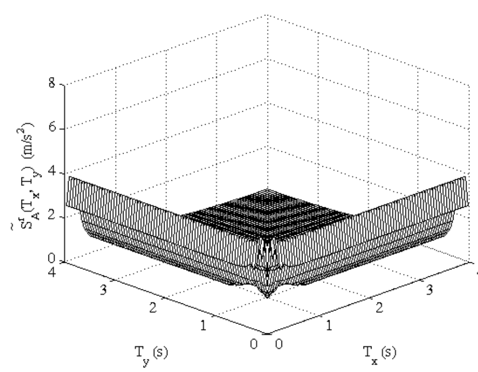

(c) $\tilde{S}_A^r(T_x, T_y)$

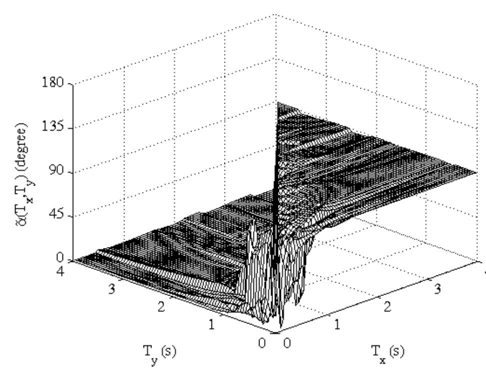

(d) $\tilde{\alpha}(T_x, T_y)$

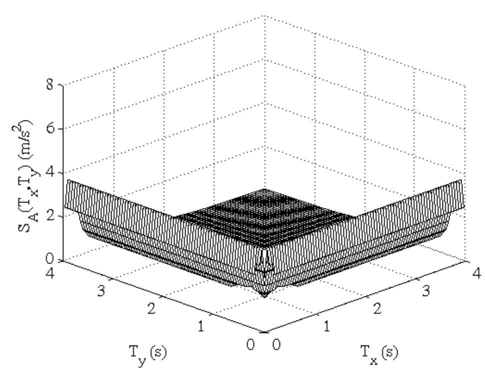

(e) $S_A(T_x, T_y)$

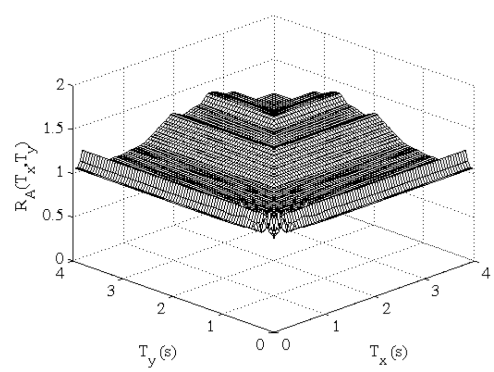

(f) $R_A(T_x, T_y)$

Figure B-17 Bi-directional responses of Coyote Lake earthquake, 47379 Gilroy Array #1 station

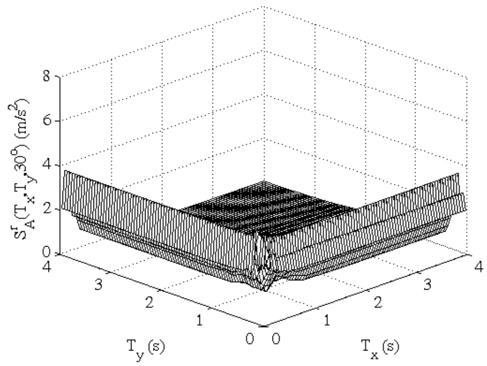

(a) $S_A^r(T_x, T_y, 30^\circ)$

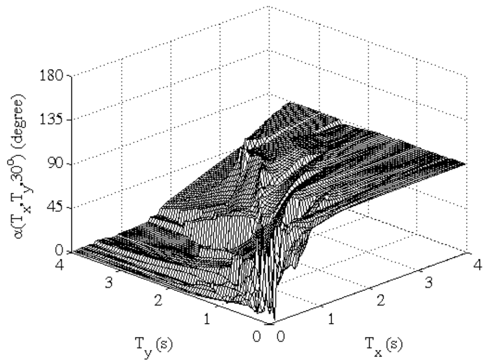

(b) $\alpha(T_x, T_y, 30^\circ)$

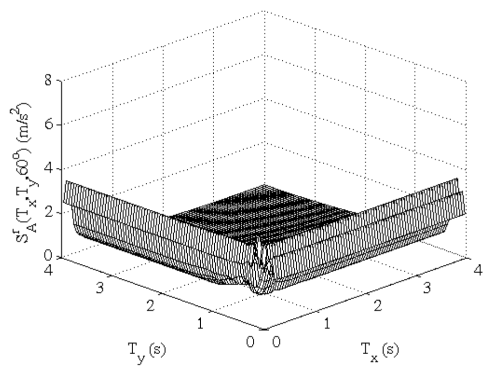

(c) $S_A^r(T_x, T_y, 60^\circ)$

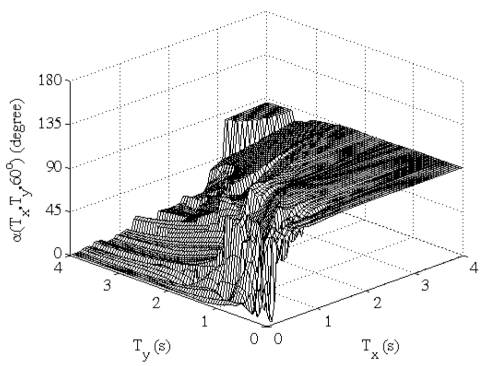

(d) $\alpha(T_x, T_y, 60^\circ)$

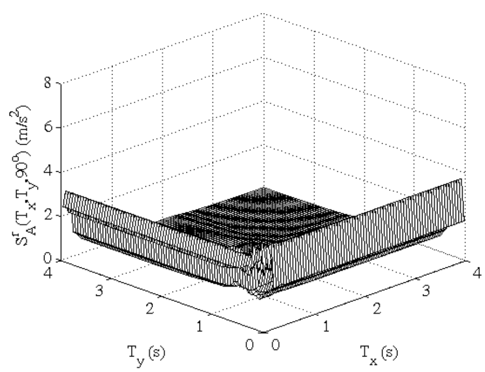

(e) $S_A^r(T_x, T_y, 90^\circ)$

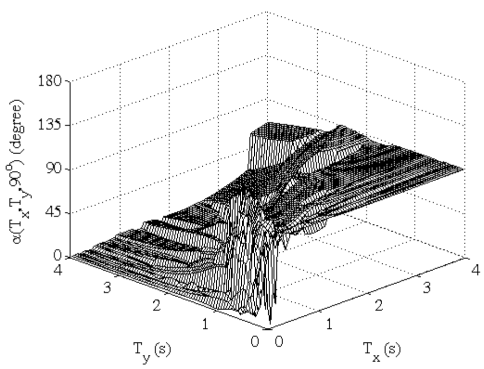

(f) $\alpha(T_x, T_y, 90^\circ)$

Figure B-18 Pseudo acceleration spectra and incident angles in various directions of Coyote Lake earthquake, 47379 Gilroy Array #1 station

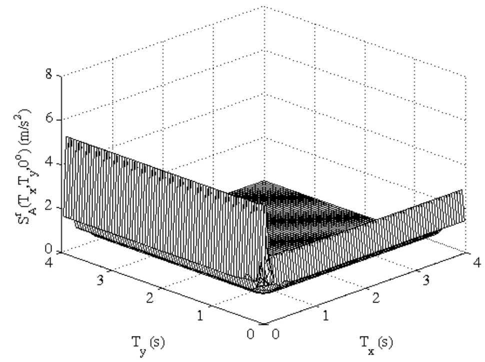

(a) $S_A^r(T_x,T_y,0^\circ)$

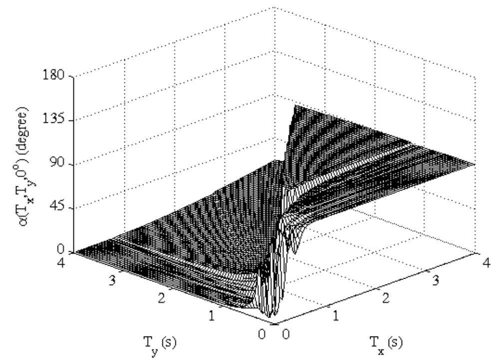

(b) $\alpha(T_x,T_y,0^\circ)$

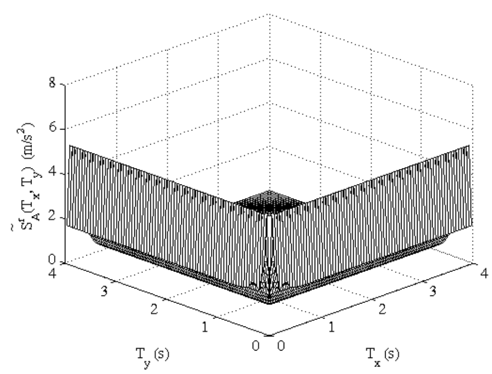

(c) $\widetilde{S}_A^r(T_x,T_y)$

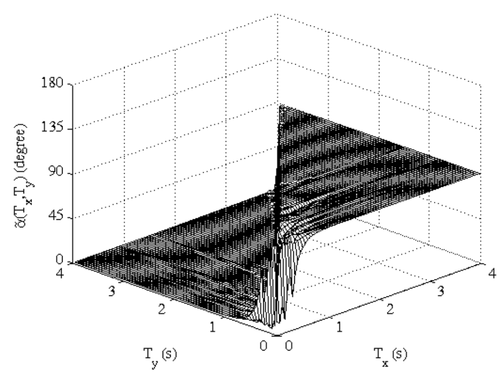

(d) $\widetilde{\alpha}(T_x,T_y)$

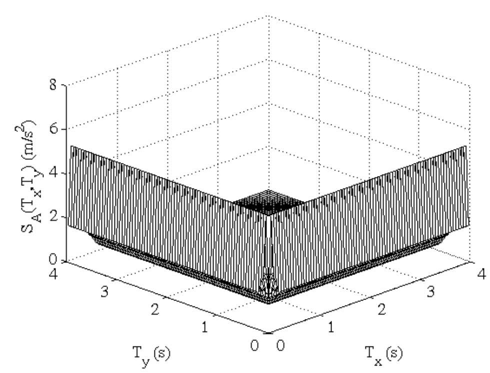

(e) $S_A(T_x,T_y)$

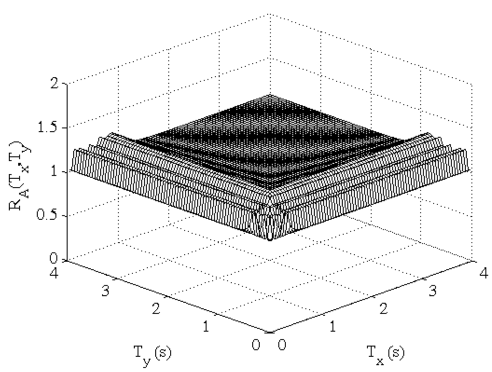

(f) $R_A(T_x,T_y)$

Figure B-19 Bi-directional responses of Hollister earthquake, 47379 Gilroy Array #1 station

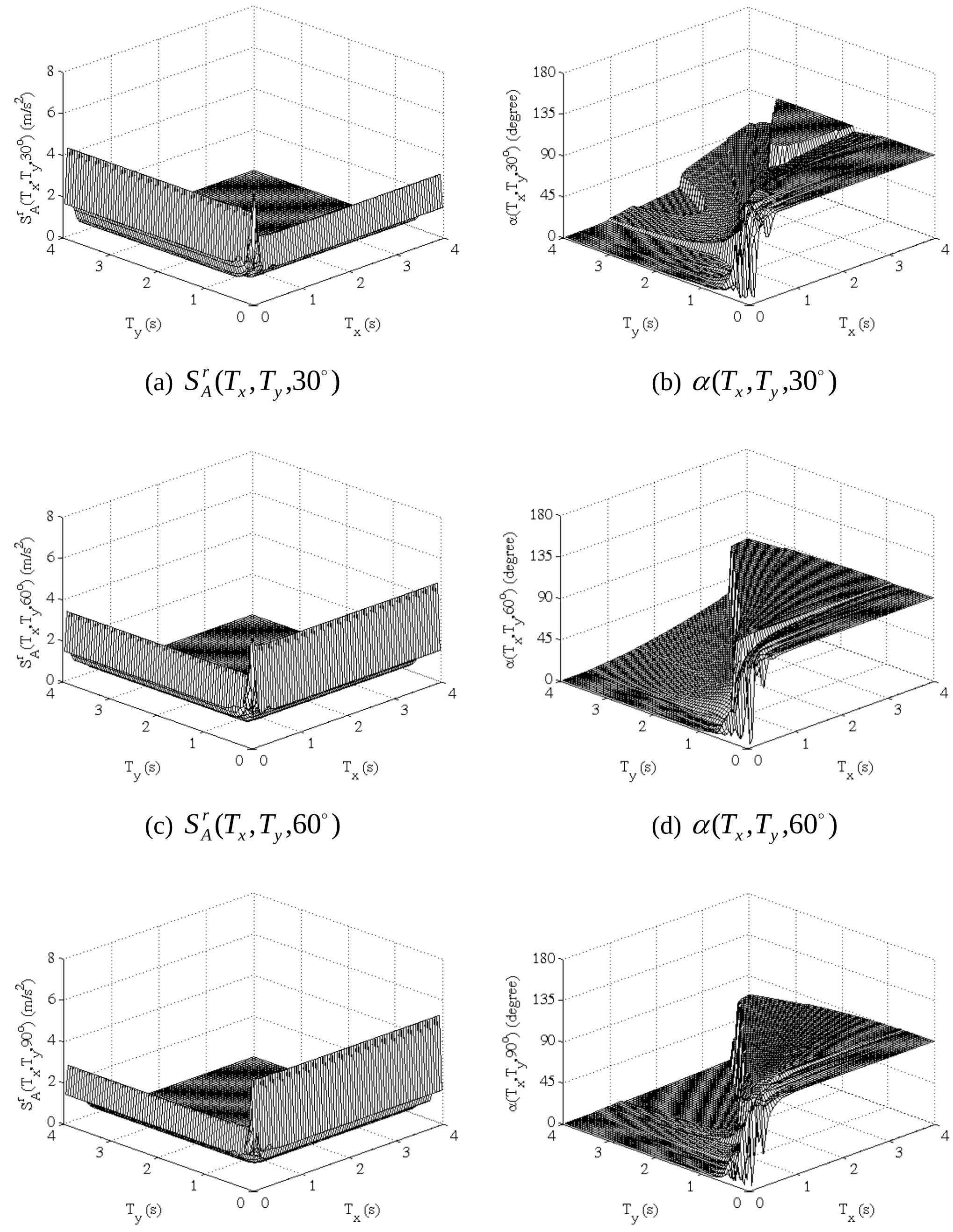

(a) $S_A^r(T_x, T_y, 30^\circ)$

(b) $\alpha(T_x, T_y, 30^\circ)$

(c) $S_A^r(T_x, T_y, 60^\circ)$

(d) $\alpha(T_x, T_y, 60^\circ)$

(e) $S_A^r(T_x, T_y, 90^\circ)$

(f) $\alpha(T_x, T_y, 90^\circ)$

Figure B-20 Pseudo acceleration spectra and incident angles in various directions of Hollister earthquake, 47379 Gilroy Array #1 station

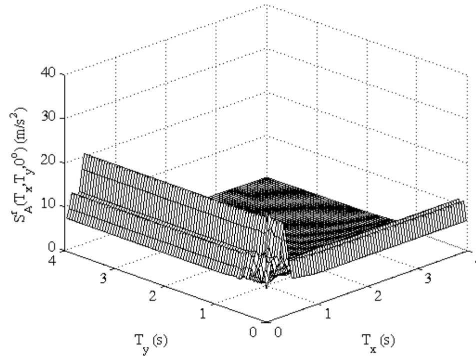

(a) $S_A^r(T_x, T_y, 0^\circ)$

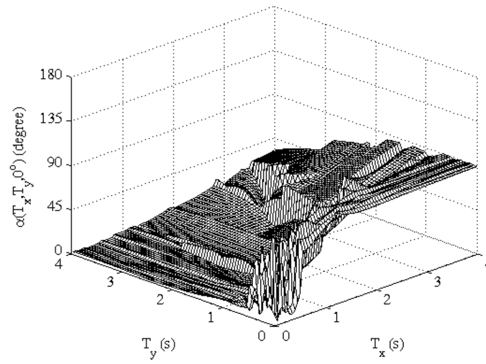

(b) $\alpha(T_x, T_y, 0^\circ)$

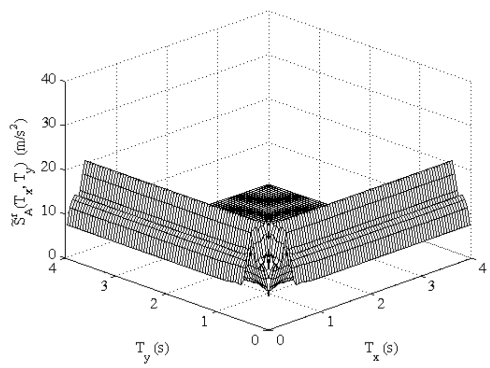

(c) $\tilde{S}_A^r(T_x, T_y)$

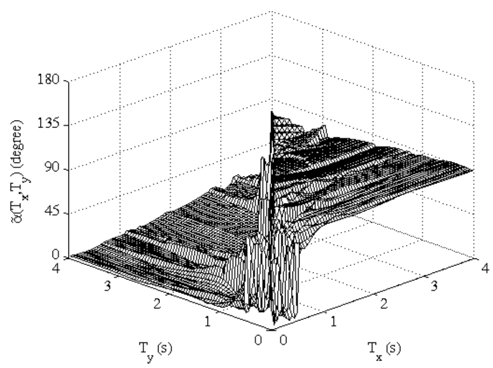

(d) $\tilde{\alpha}(T_x, T_y)$

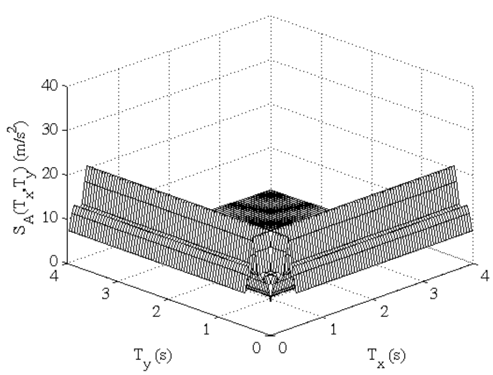

(e) $S_A(T_x, T_y)$

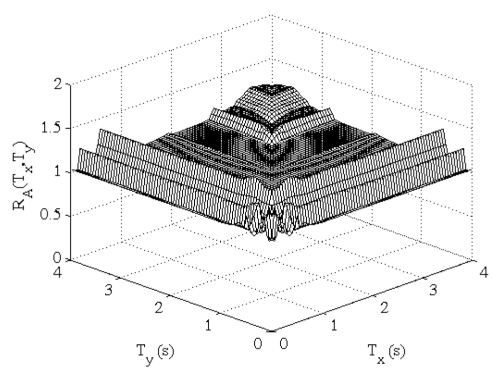

(f) $R_A(T_x, T_y)$

Figure B-21 Bi-directional responses of Loma Prieta earthquake, 47379 Gilroy Array #1 station

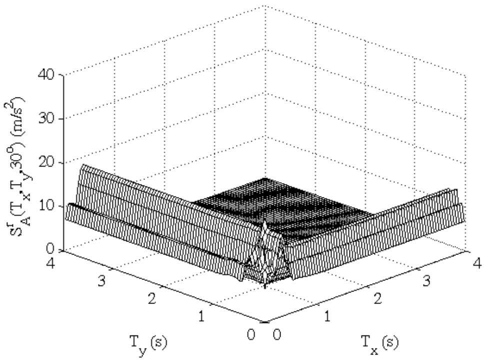

(a) $S_A^r(T_x, T_y, 30^\circ)$

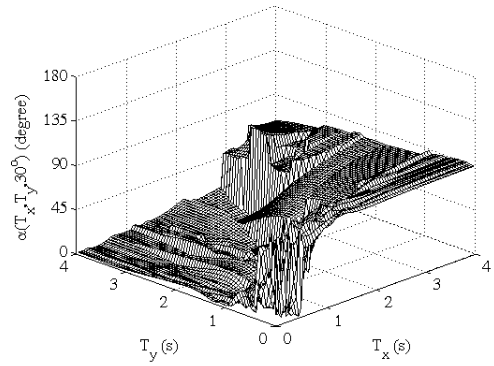

(b) $\alpha(T_x, T_y, 30^\circ)$

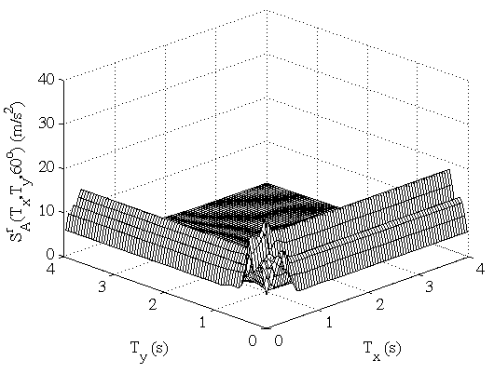

(c) $S_A^r(T_x, T_y, 60^\circ)$

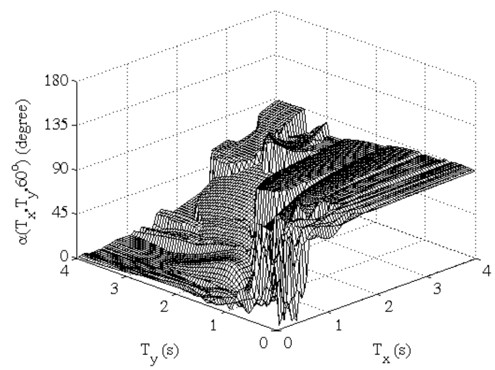

(d) $\alpha(T_x, T_y, 60^\circ)$

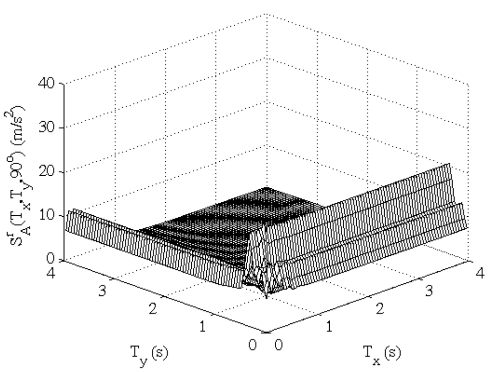

(e) $S_A^r(T_x, T_y, 90^\circ)$

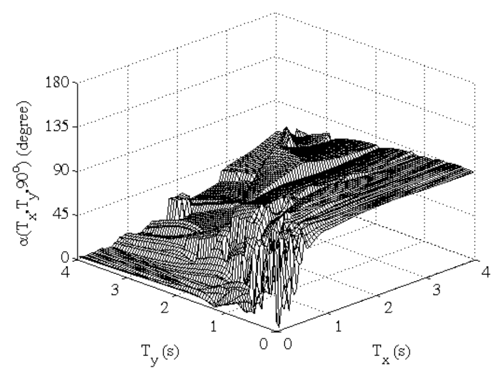

(f) $\alpha(T_x, T_y, 90^\circ)$

Figure B-22 Pseudo acceleration spectra and incident angles in various directions of Loma Prieta earthquake, 47379 Gilroy Array #1 station

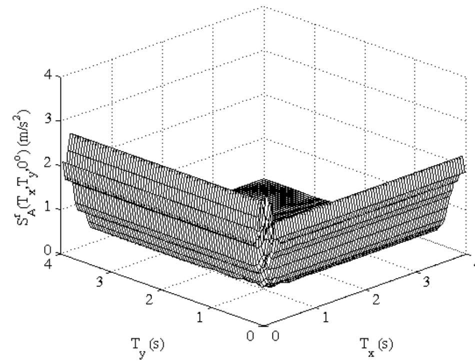

(a) $S_A^r(T_x,T_y,0^\circ)$

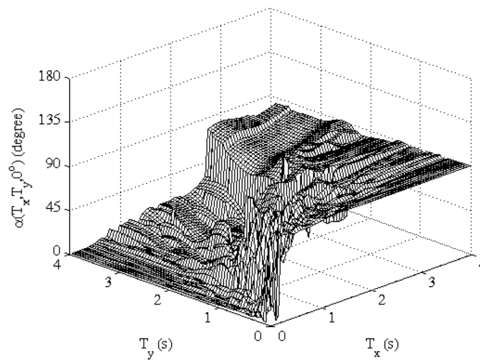

(b) $\alpha(T_x,T_y,0^\circ)$

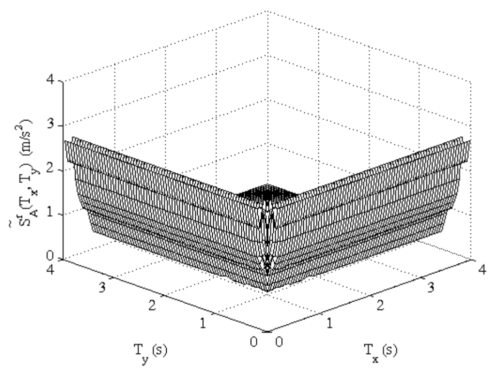

(c) $\widetilde{S}_A^r(T_x,T_y)$

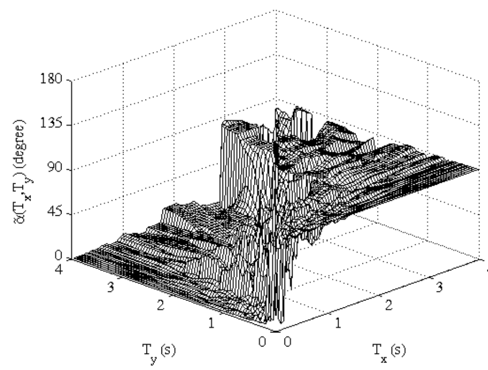

(d) $\widetilde{\alpha}(T_x,T_y)$

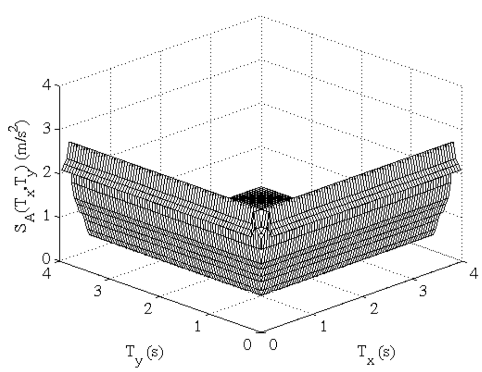

(e) $S_A(T_x,T_y)$

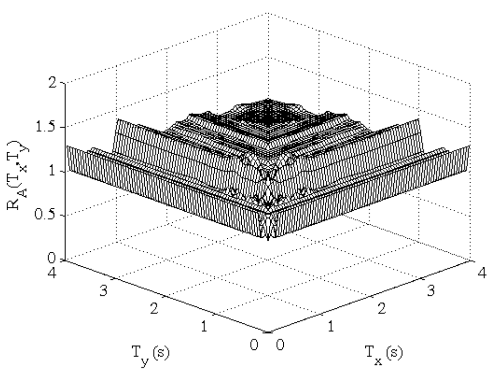

(f) $R_A(T_x,T_y)$

Figure B-23 Bi-directional responses of Morgan Hill earthquake, 47379 Gilroy Array #1 station

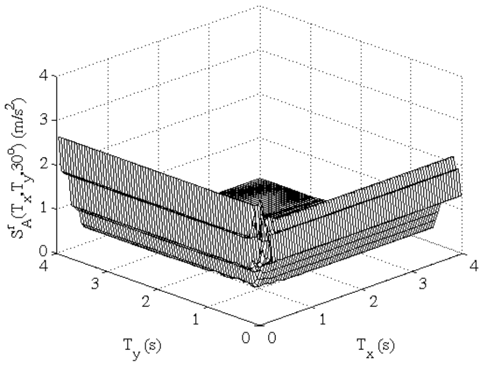

(a) $S_A^r(T_x, T_y, 30^{\circ})$

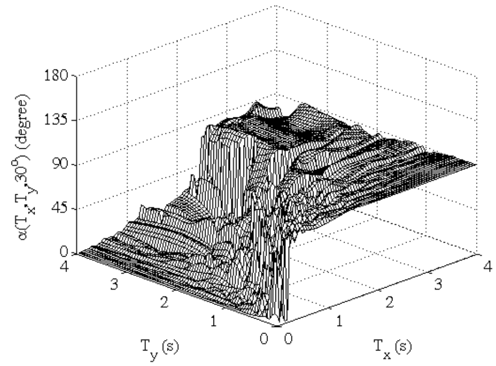

(b) $\alpha(T_x, T_y, 30^{\circ})$

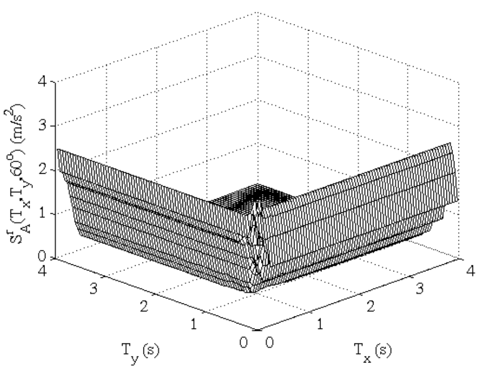

(c) $S_A^r(T_x, T_y, 60^{\circ})$

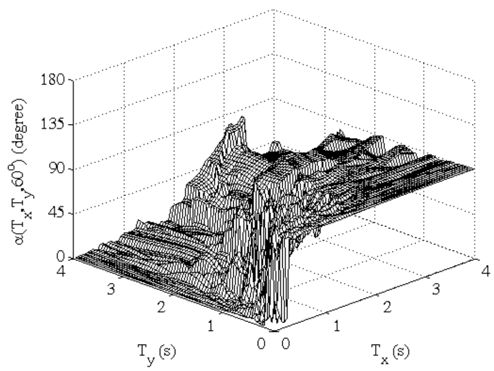

(d) $\alpha(T_x, T_y, 60^{\circ})$

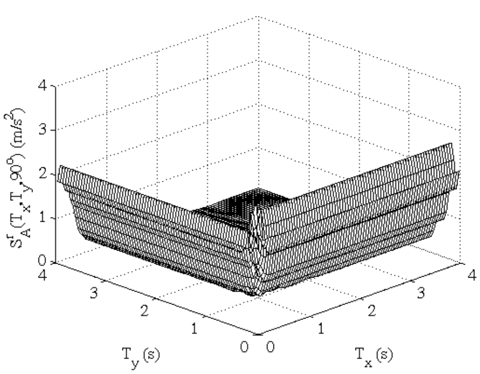

(e) $S_A^r(T_x, T_y, 90^{\circ})$

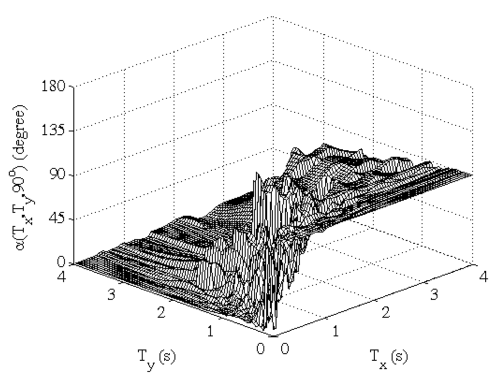

(f) $\alpha(T_x, T_y, 90^{\circ})$

Figure B-24 Pseudo acceleration spectra and incident angles in various directions of Morgan Hill earthquake, 47379 Gilroy Array #1 station

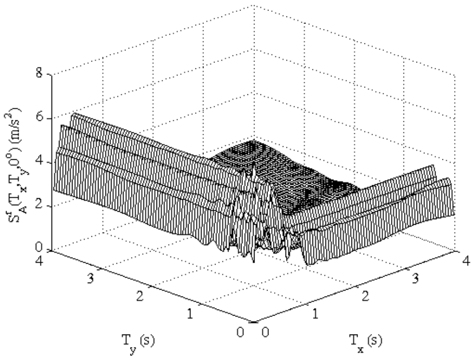

(a) $S_A^r(T_x, T_y, 0^\circ)$

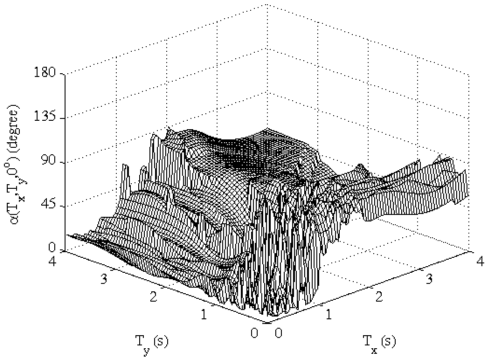

(b) $\alpha(T_x, T_y, 0^\circ)$

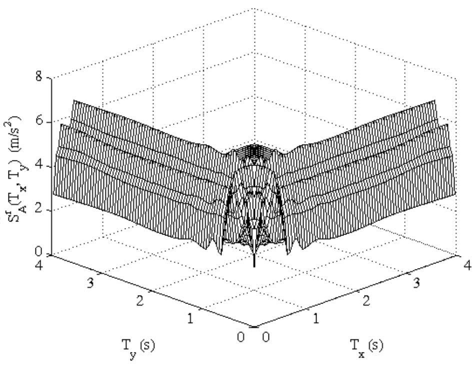

(c) $\tilde{S}_A^r(T_x, T_y)$

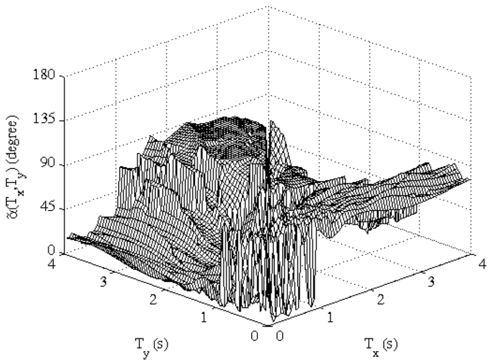

(d) $\tilde{\alpha}(T_x, T_y)$

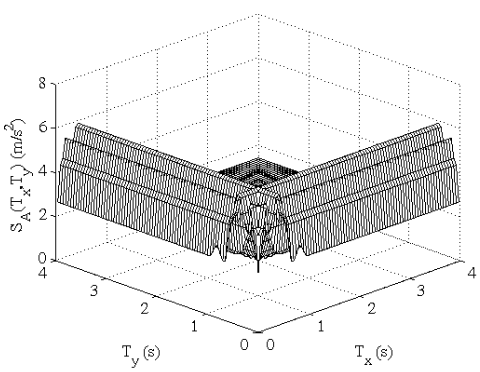

(e) $S_A(T_x, T_y)$

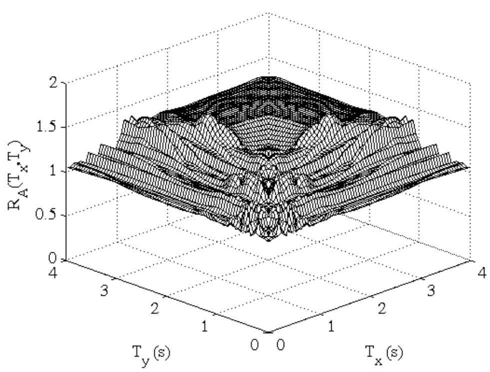

(f) $R_A(T_x, T_y)$

Figure B-25 Bi-directional responses of Kocaeli, Turkey earthquake, Gebze station

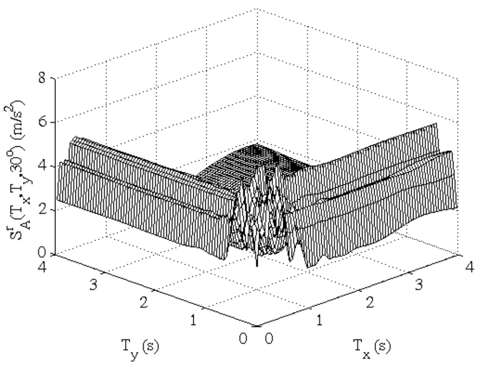

(a) $S_A^r(T_x, T_y, 30^\circ)$

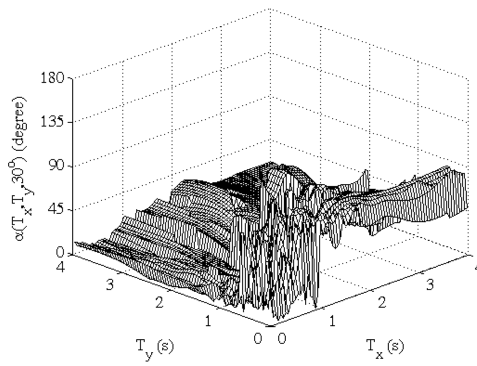

(b) $\alpha(T_x, T_y, 30^\circ)$

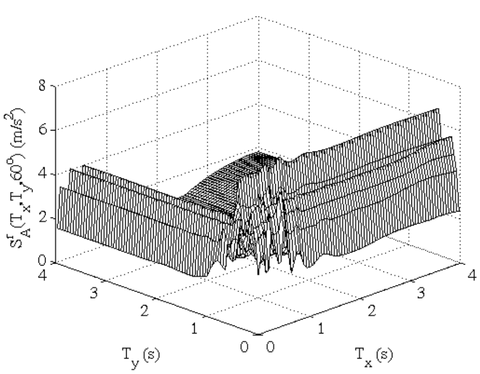

(c) $S_A^r(T_x, T_y, 60^\circ)$

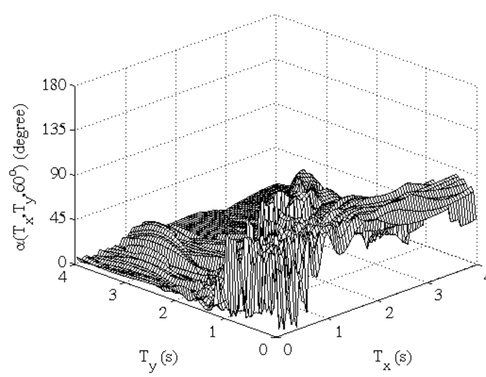

(d) $\alpha(T_x, T_y, 60^\circ)$

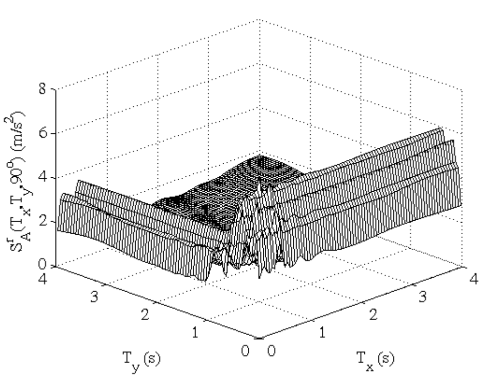

(e) $S_A^r(T_x, T_y, 90^\circ)$

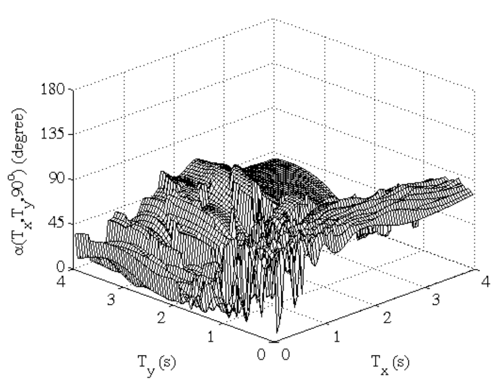

(f) $\alpha(T_x, T_y, 90^\circ)$

Figure B-26 Pseudo acceleration spectra and incident angles in various directions of Kocaeli, Turkey earthquake, Gebze station

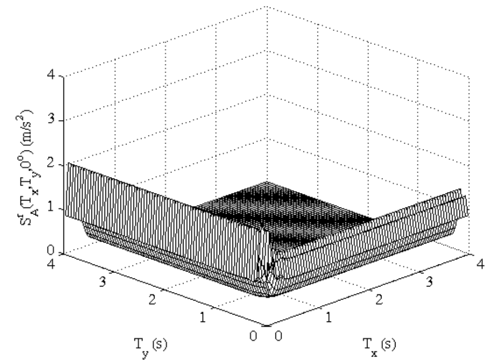

(a) $S_A^r(T_x,T_y,0^\circ)$

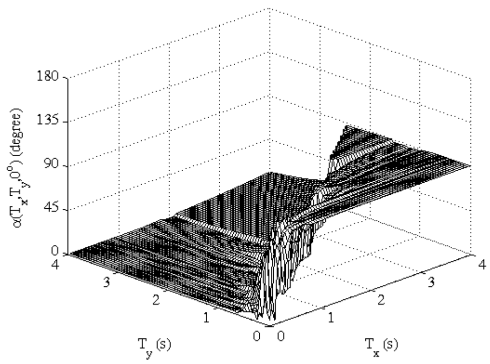

(b) $\alpha(T_x,T_y,0^\circ)$

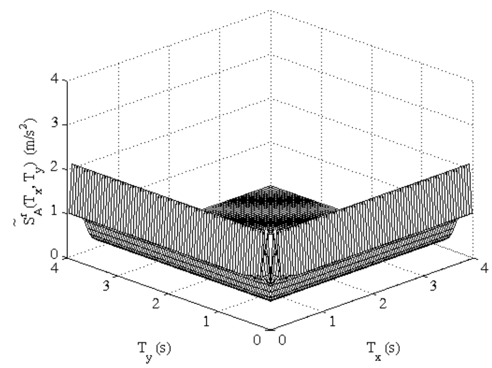

(c) $\tilde{S}_A^r(T_x,T_y)$

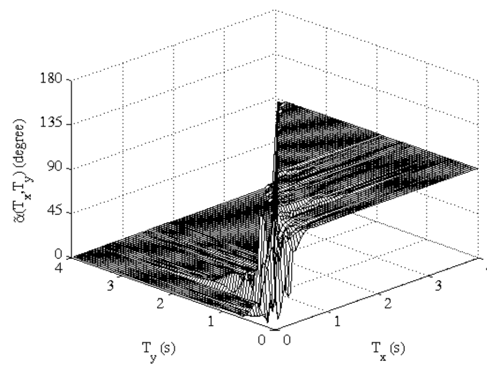

(d) $\tilde{\alpha}(T_x,T_y)$

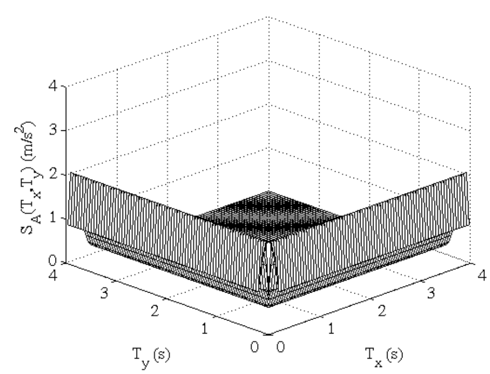

(e) $S_A(T_x,T_y)$

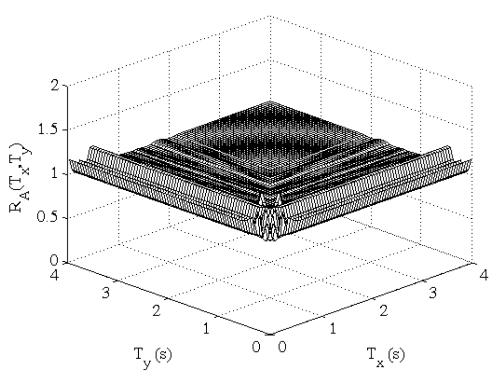

(f) $R_A(T_x,T_y)$

Figure B-27 Bi-directional responses of Lytle Creek earthquake, 111 Cedar Springs, Allen Ranch station

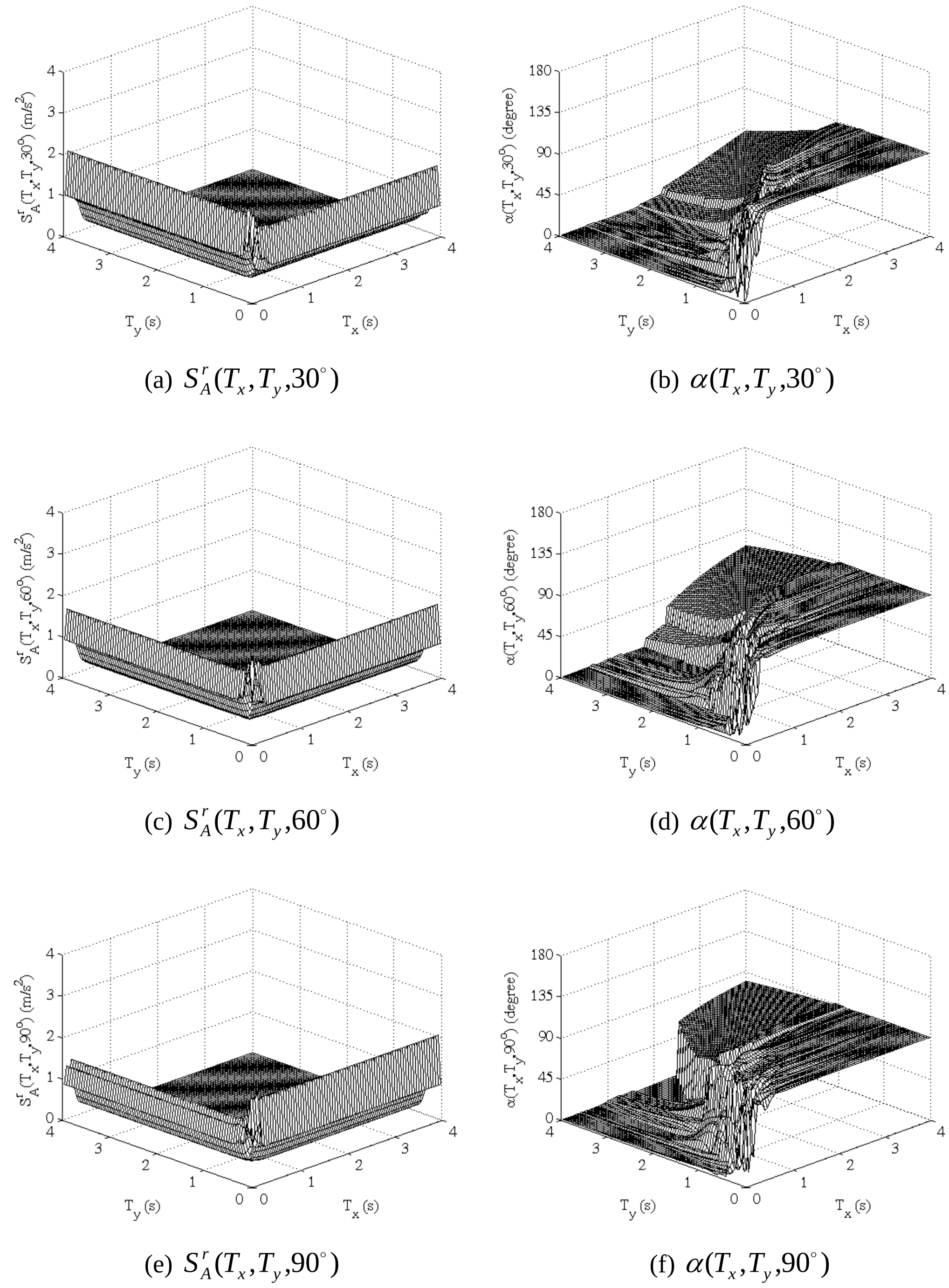

(a) $S_A^r(T_x, T_y, 30^\circ)$ (b) $\alpha(T_x, T_y, 30^\circ)$

(c) $S_A^r(T_x, T_y, 60^\circ)$ (d) $\alpha(T_x, T_y, 60^\circ)$

(e) $S_A^r(T_x, T_y, 90^\circ)$ (f) $\alpha(T_x, T_y, 90^\circ)$

Figure B-28 Pseudo acceleration spectra and incident angles in various directions of Lytle Creek earthquake, 111 Cedar Springs, Allen Ranch station

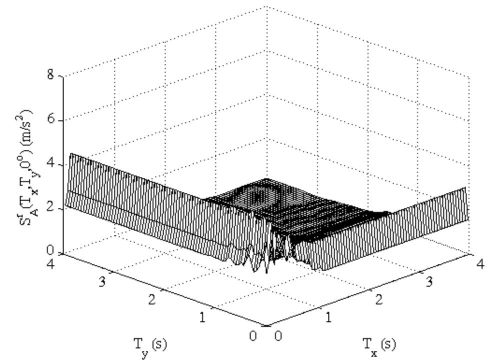

(a) $S^r_A(T_x,T_y,0^\circ)$

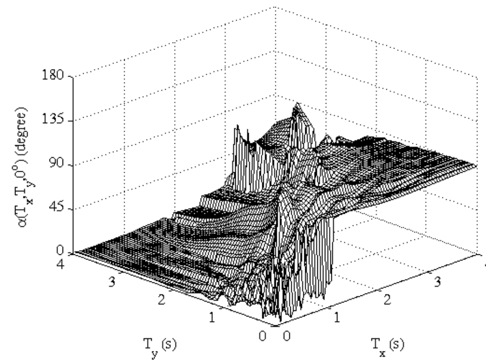

(b) $\alpha(T_x,T_y,0^\circ)$

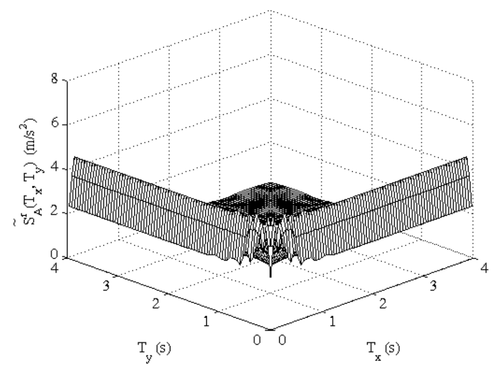

(c) $\tilde{S}^r_A(T_x,T_y)$

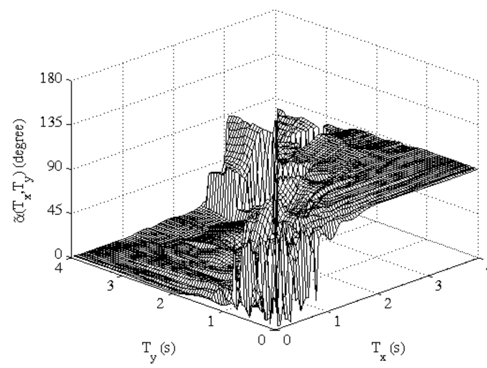

(d) $\tilde{\alpha}(T_x,T_y)$

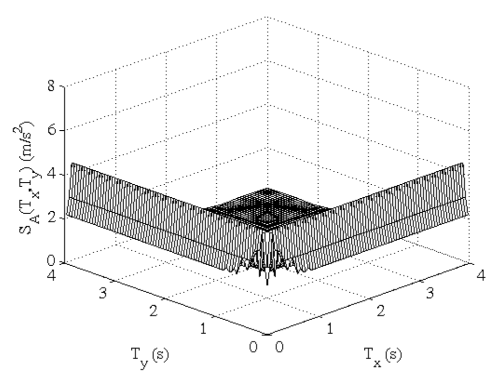

(e) $S_A(T_x,T_y)$

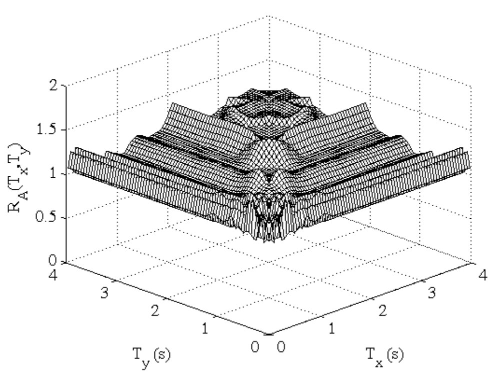

(f) $R_A(T_x,T_y)$

Figure B-29 Bi-directional responses of Northridge earthquake, 90017 LA - Wonderland Ave station

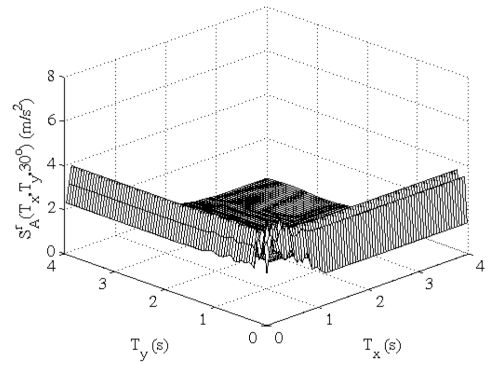

(a) $S_A^r(T_x,T_y,30^\circ)$

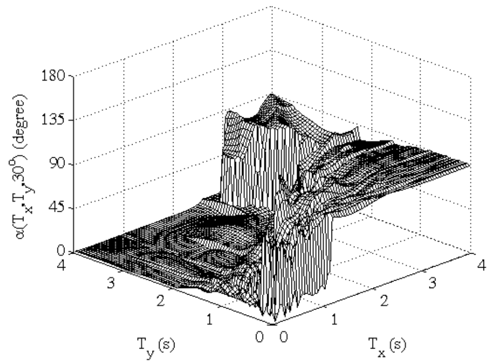

(b) $\alpha(T_x,T_y,30^\circ)$

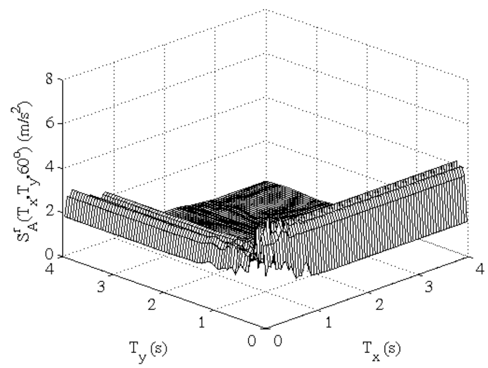

(c) $S_A^r(T_x,T_y,60^\circ)$

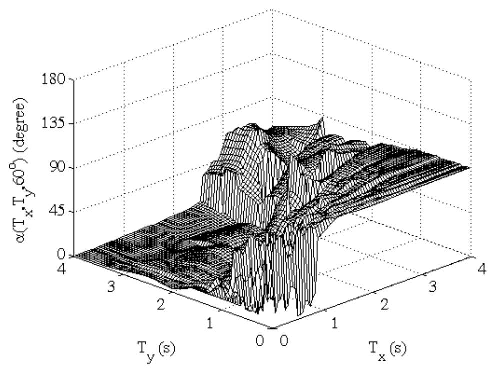

(d) $\alpha(T_x,T_y,60^\circ)$

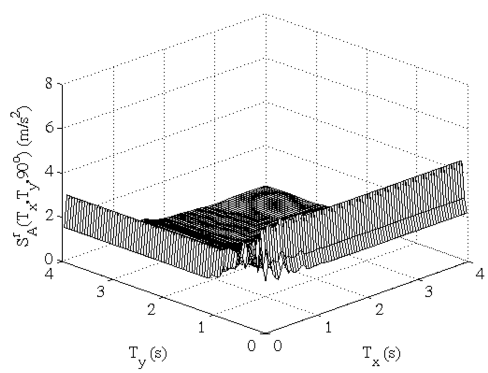

(e) $S_A^r(T_x,T_y,90^\circ)$

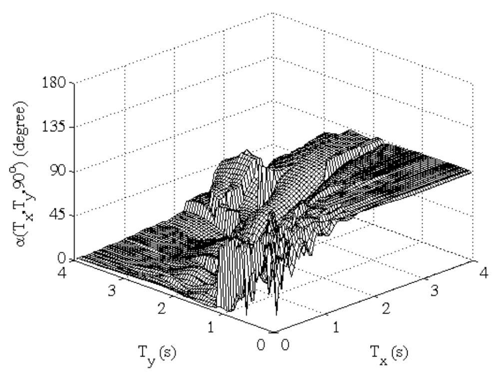

(f) $\alpha(T_x,T_y,90^\circ)$

Figure B-30 Pseudo acceleration spectra and incident angles in various directions of Northridge earthquake, 90017 LA - Wonderland Ave station

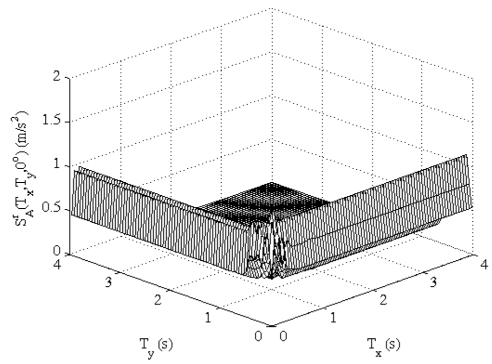

(a) $S^r_A(T_x,T_y,0^\circ)$

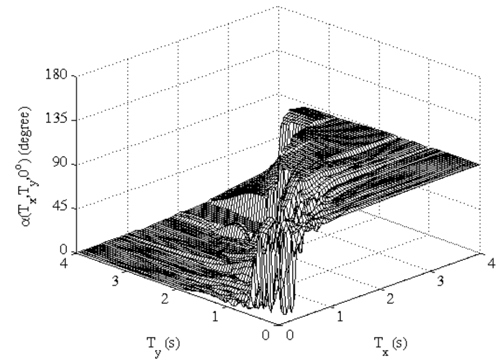

(b) $\alpha(T_x,T_y,0^\circ)$

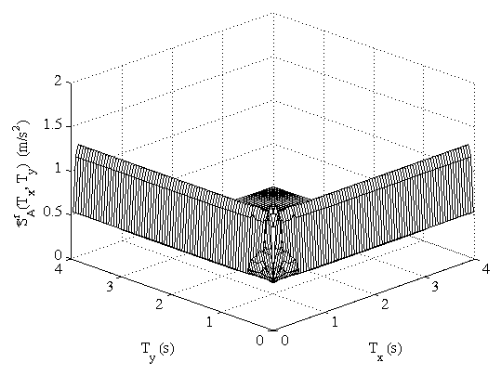

(c) $\tilde{S}^r_A(T_x,T_y)$

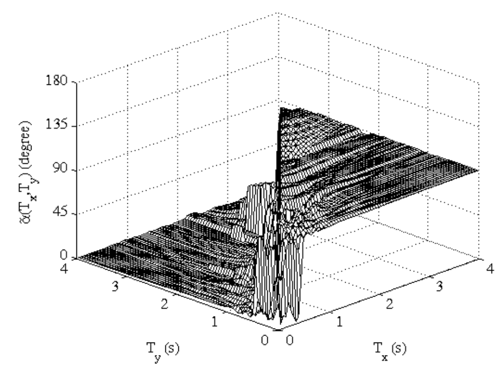

(d) $\tilde{\alpha}(T_x,T_y)$

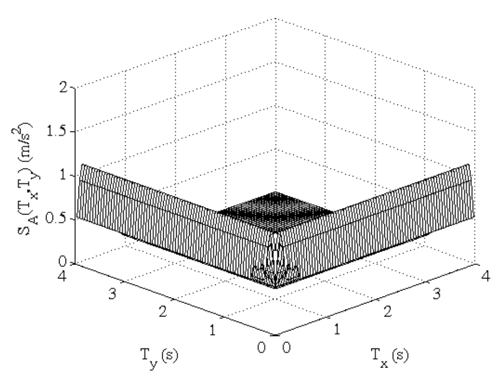

(e) $S_A(T_x,T_y)$

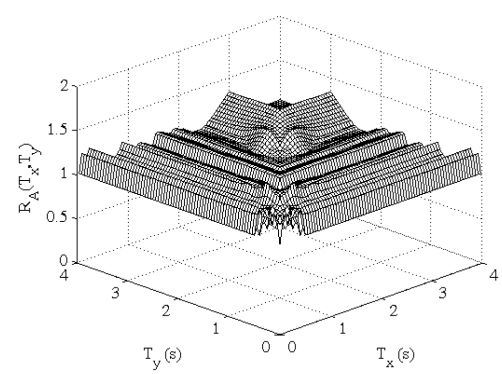

(f) $R_A(T_x,T_y)$

Figure B-31 Bi-directional responses of Whittier Narrows earthquake, 90017 LA - Wonderland Ave station

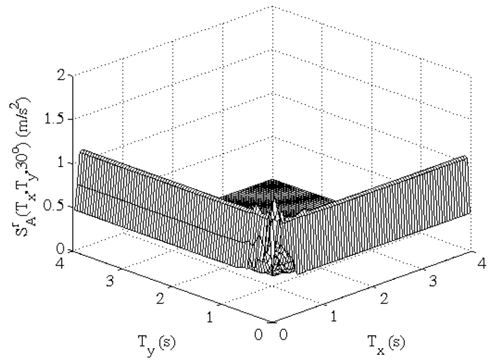

(a) $S_A^r(T_x, T_y, 30^\circ)$

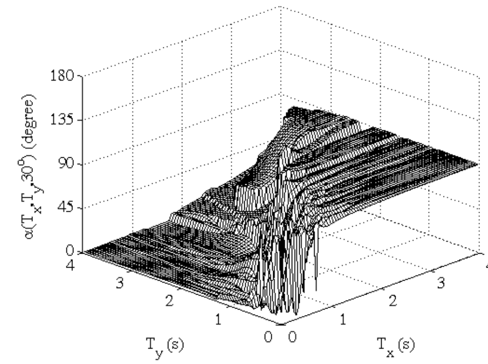

(b) $\alpha(T_x, T_y, 30^\circ)$

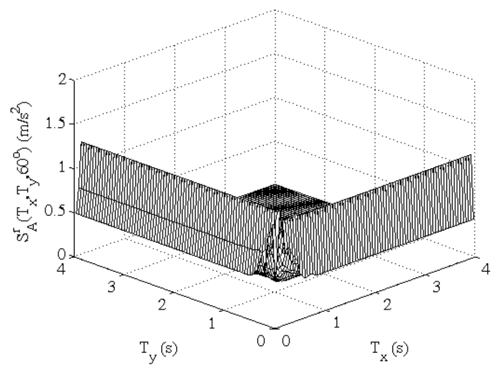

(c) $S_A^r(T_x, T_y, 60^\circ)$

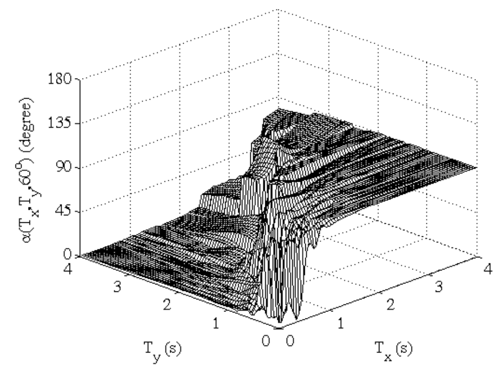

(d) $\alpha(T_x, T_y, 60^\circ)$

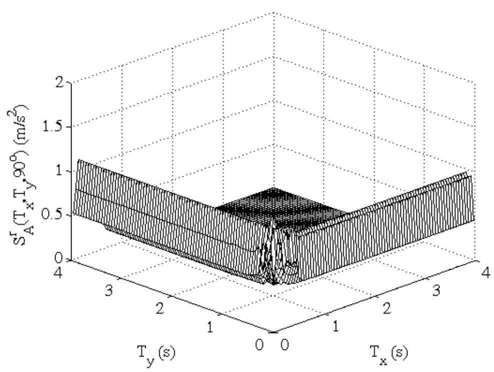

(e) $S_A^r(T_x, T_y, 90^\circ)$

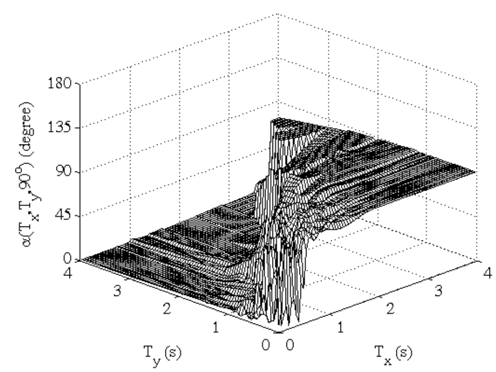

(f) $\alpha(T_x, T_y, 90^\circ)$

Figure B-32 Pseudo acceleration spectra and incident angles in various directions of Whittier Narrows earthquake, 90017 LA - Wonderland Ave station

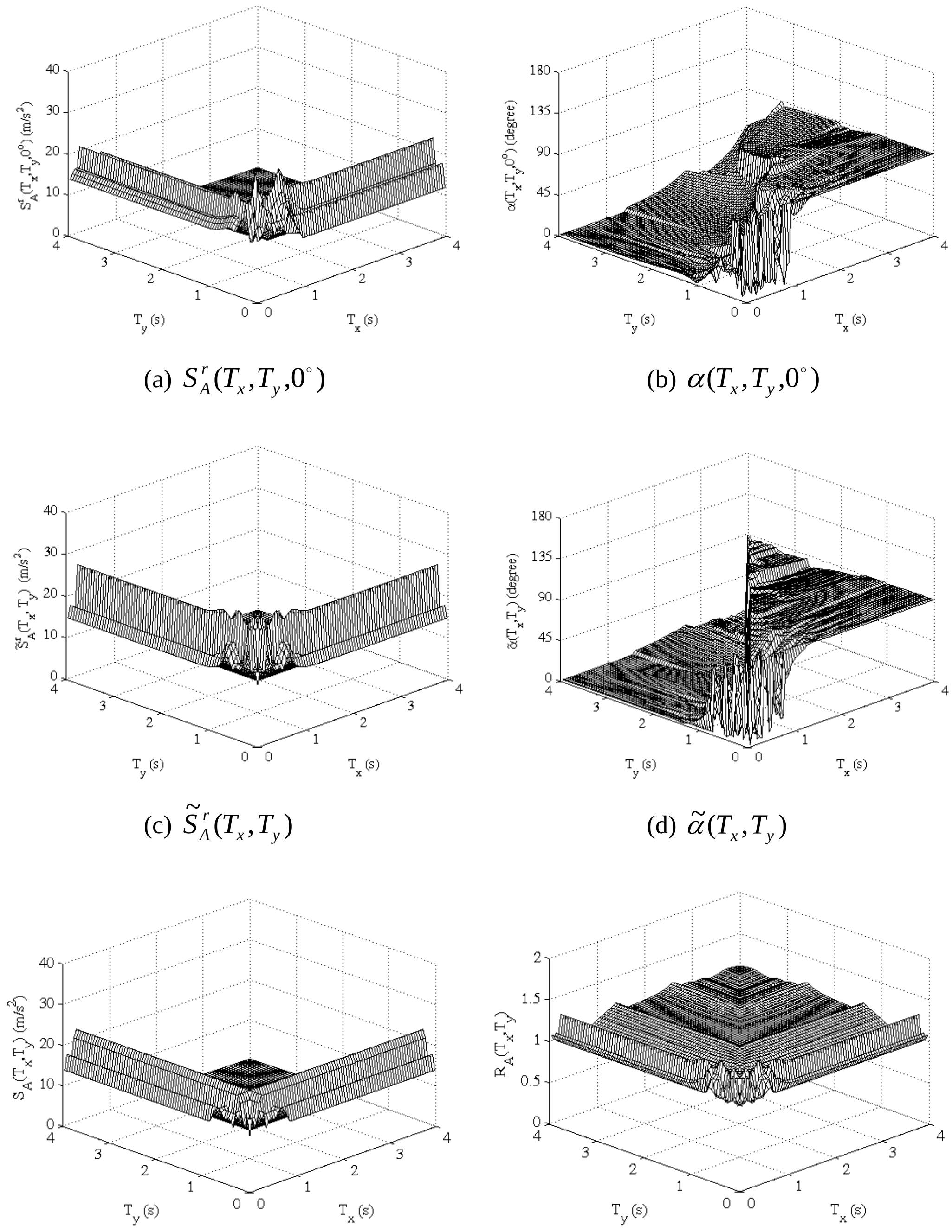

(a) $S_A^r(T_x, T_y, 0^\circ)$ (b) $\alpha(T_x, T_y, 0^\circ)$

(c) $\tilde{S}_A^r(T_x, T_y)$ (d) $\tilde{\alpha}(T_x, T_y)$

(e) $S_A(T_x, T_y)$ (f) $R_A(T_x, T_y)$

Figure B-33 Bi-directional responses of Morgan Hill earthquake, 57217 Coyote Lake Dam (SW Abut) station

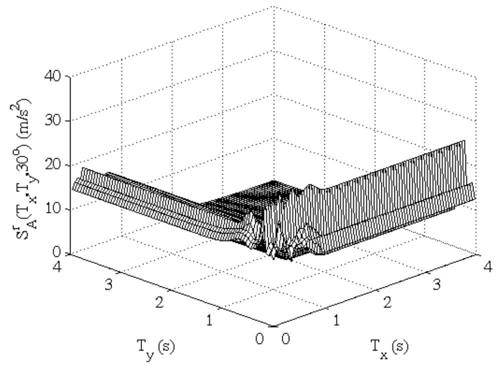

(a) $S^r_A(T_x,T_y,30^\circ)$

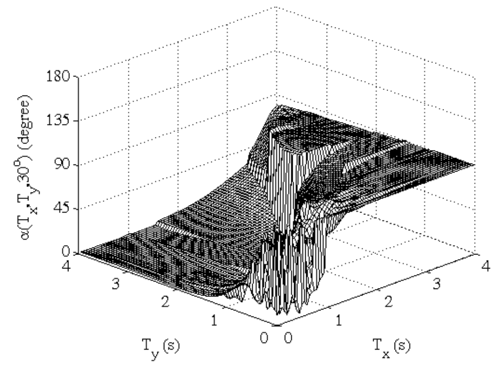

(b) $\alpha(T_x,T_y,30^\circ)$

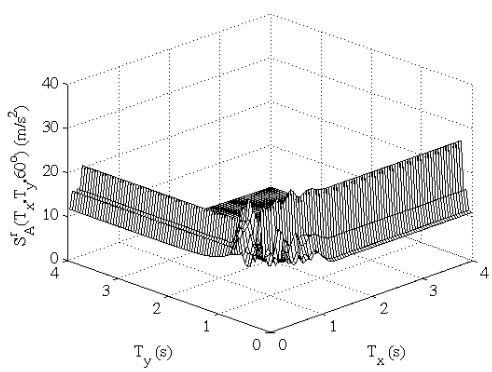

(c) $S^r_A(T_x,T_y,60^\circ)$

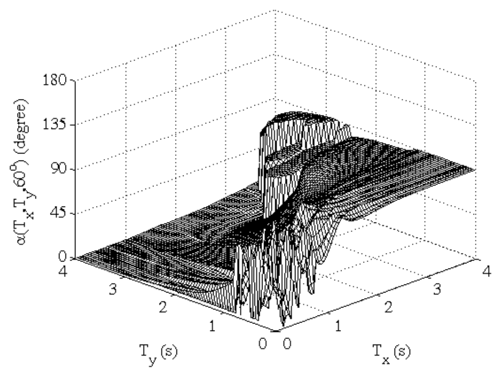

(d) $\alpha(T_x,T_y,60^\circ)$

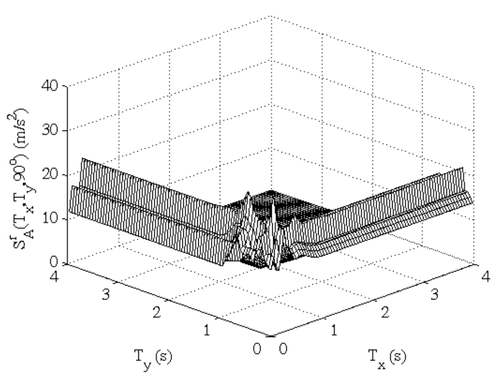

(e) $S^r_A(T_x,T_y,90^\circ)$

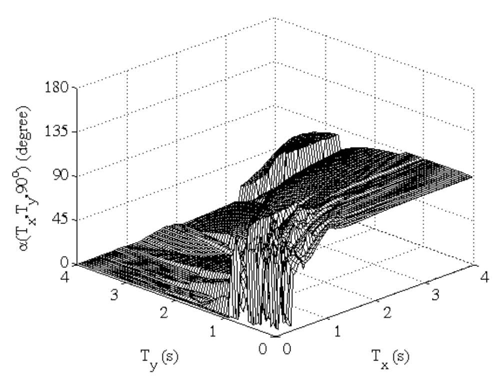

(f) $\alpha(T_x,T_y,90^\circ)$

Figure B-34 Pseudo acceleration spectra and incident angles in various directions of Morgan Hill earthquake, 57217 Coyote Lake Dam (SW Abut) station

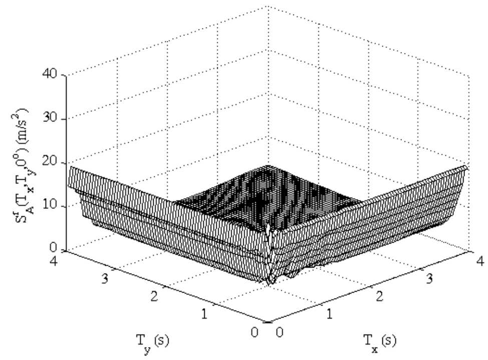

(a) $S_A^r(T_x, T_y, 0^\circ)$

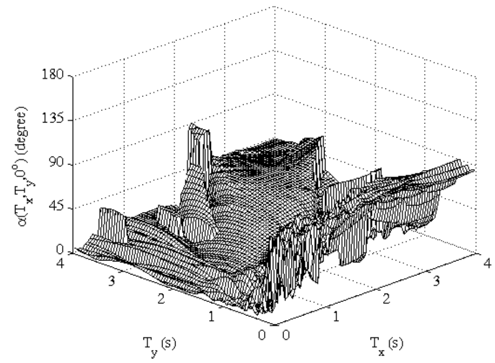

(b) $\alpha(T_x, T_y, 0^\circ)$

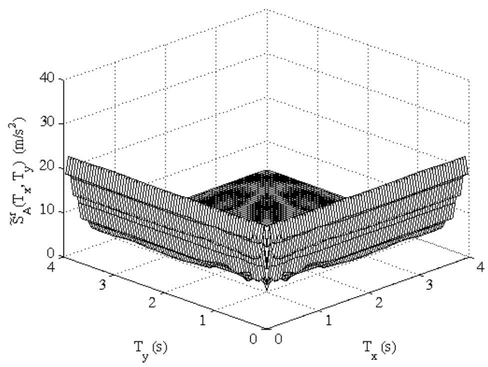

(c) $\tilde{S}_A^r(T_x, T_y)$

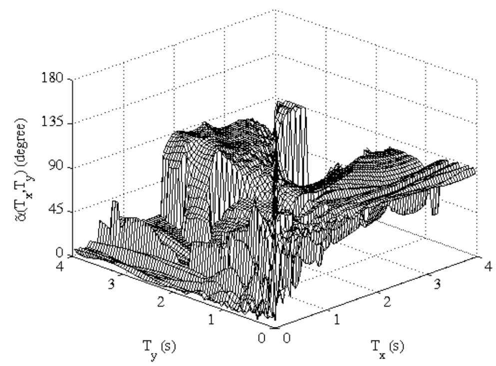

(d) $\tilde{\alpha}(T_x, T_y)$

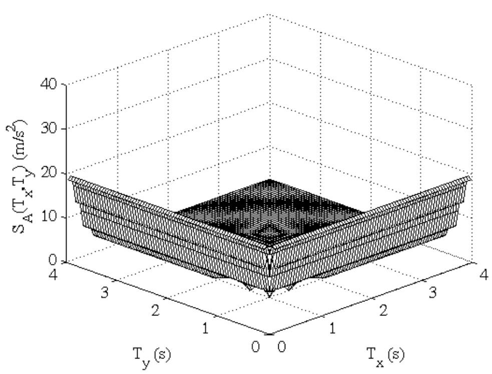

(e) $S_A(T_x, T_y)$

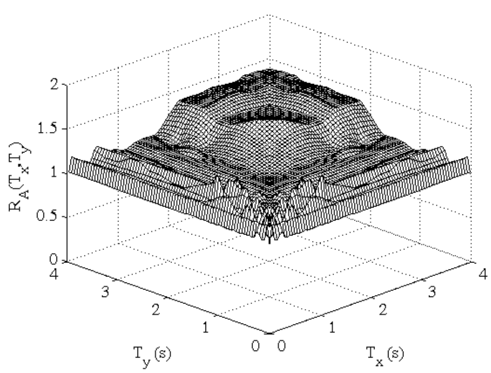

(f) $R_A(T_x, T_y)$

Figure B-35 Bi-directional responses of Landers earthquake, 24 Lucerne station

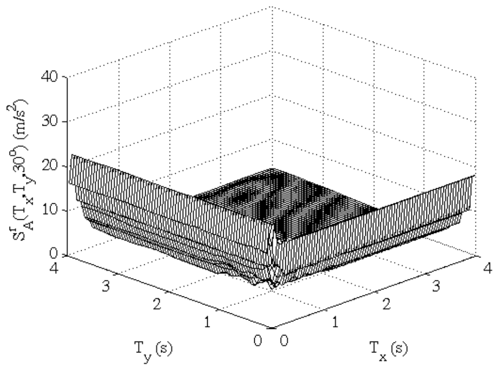

(a) $S_A^r(T_x, T_y, 30^\circ)$

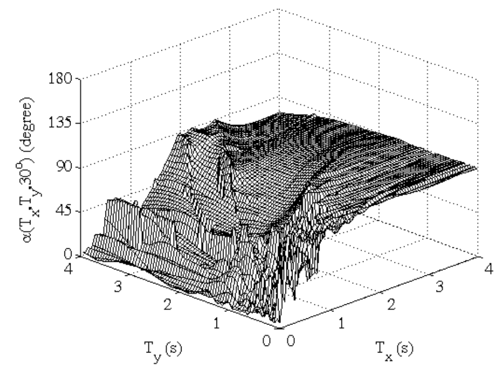

(b) $\alpha(T_x, T_y, 30^\circ)$

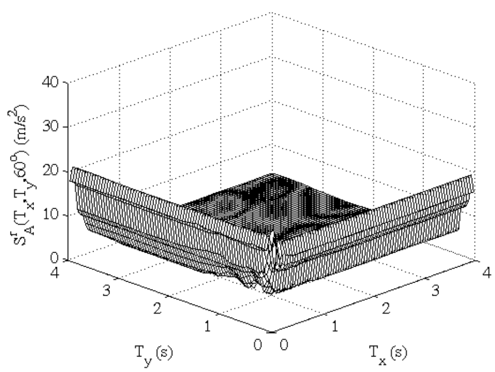

(c) $S_A^r(T_x, T_y, 60^\circ)$

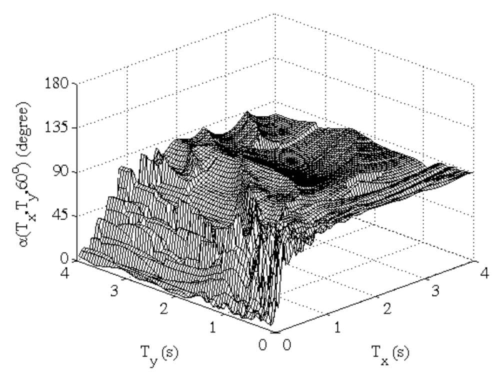

(d) $\alpha(T_x, T_y, 60^\circ)$

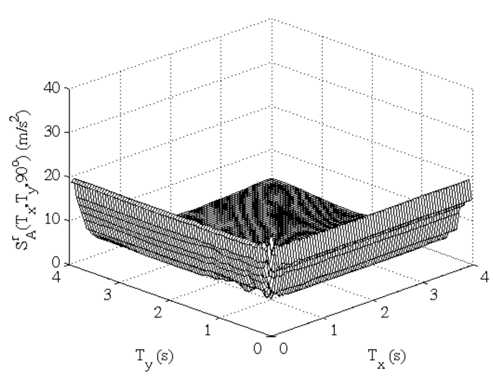

(e) $S_A^r(T_x, T_y, 90^\circ)$

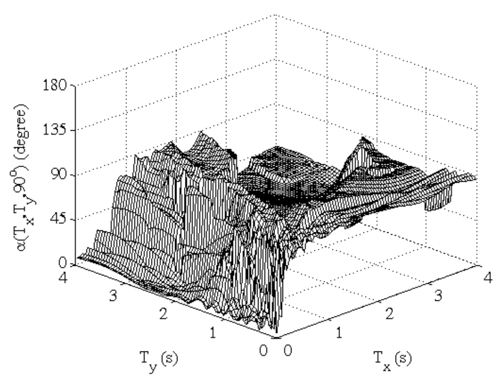

(f) $\alpha(T_x, T_y, 90^\circ)$

Figure B-36 Pseudo acceleration spectra and incident angles in various directions of Landers earthquake, 24 Lucerne station

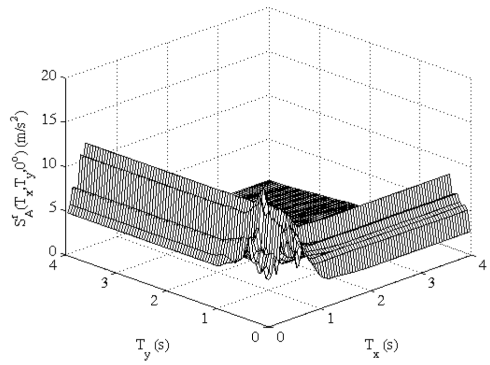

(a) $S^r_A(T_x,T_y,0^\circ)$

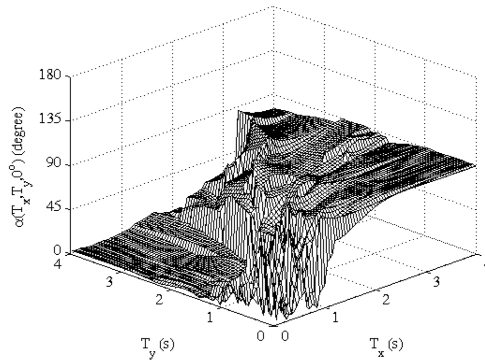

(b) $\alpha(T_x,T_y,0^\circ)$

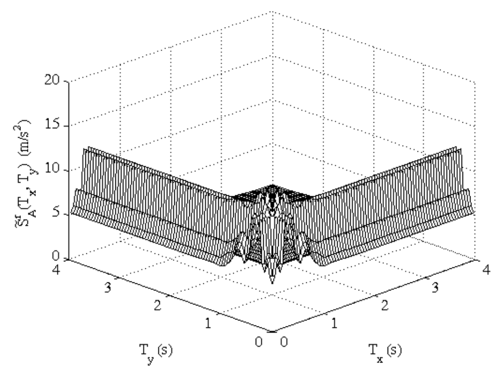

(c) $\tilde{S}^r_A(T_x,T_y)$

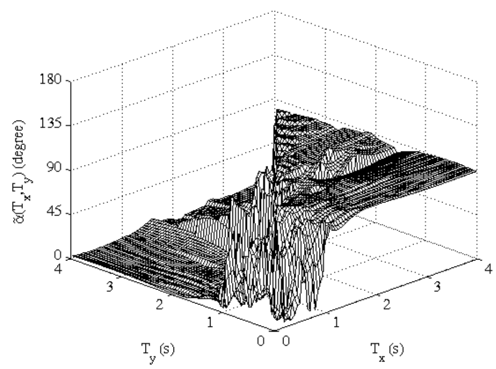

(d) $\tilde{\alpha}(T_x,T_y)$

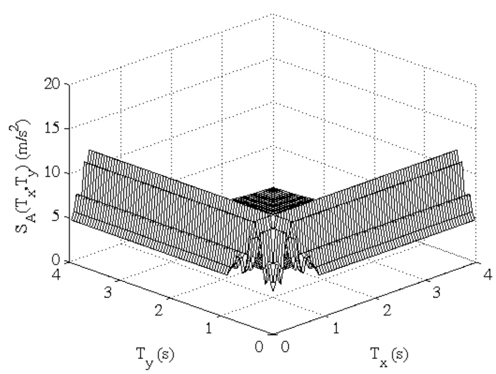

(e) $S_A(T_x,T_y)$

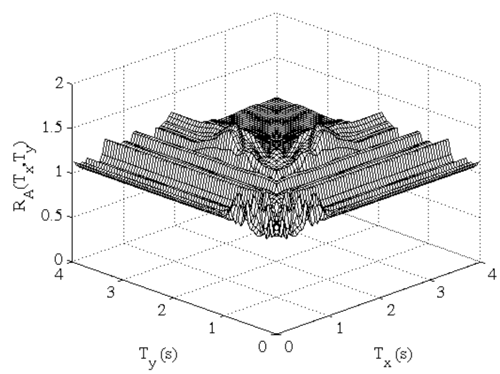

(f) $R_A(T_x,T_y)$

Figure B-37 Bi-directional responses of Morgan Hill earthquake, 1652 Anderson Dam (Downstream) station

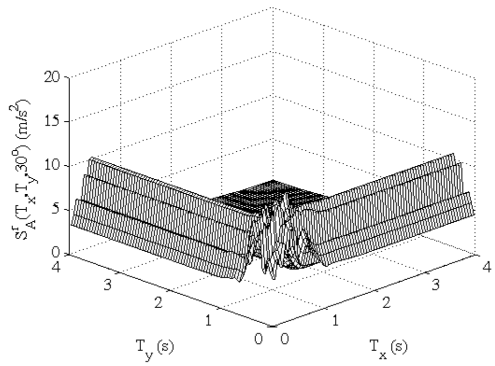

(a) $S_A^r(T_x,T_y,30^\circ)$

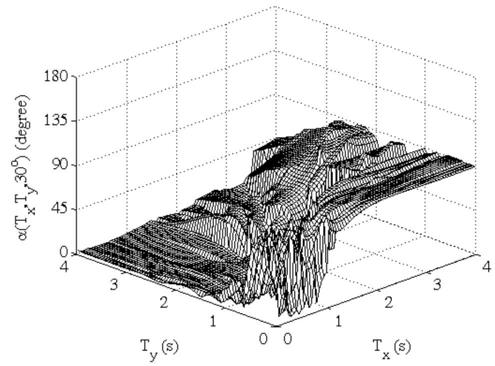

(b) $\alpha(T_x,T_y,30^\circ)$

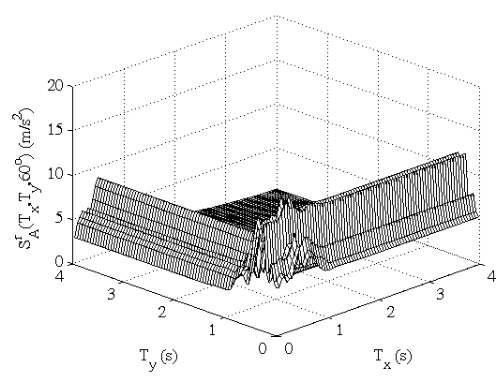

(c) $S_A^r(T_x,T_y,60^\circ)$

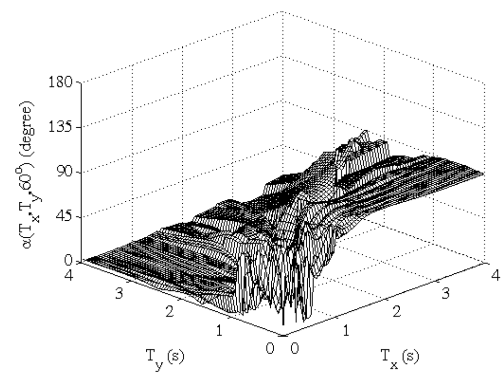

(d) $\alpha(T_x,T_y,60^\circ)$

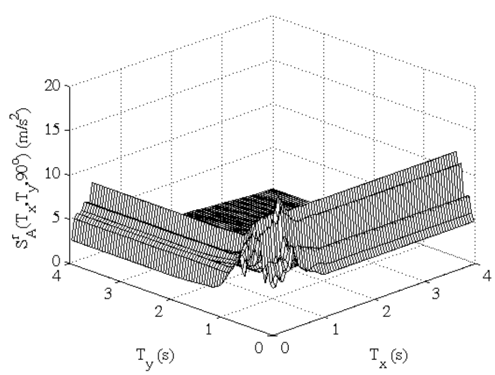

(e) $S_A^r(T_x,T_y,90^\circ)$

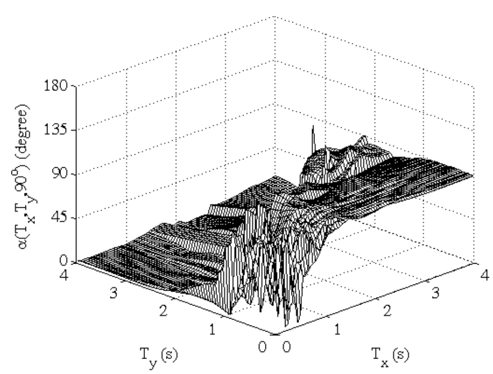

(f) $\alpha(T_x,T_y,90^\circ)$

Figure B-38 Pseudo acceleration spectra and incident angles in various directions of Morgan Hill earthquake, 1652 Anderson Dam (Downstream) station

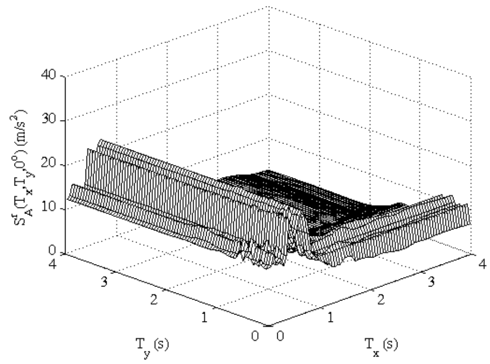

(a) $S_A^r(T_x,T_y,0^\circ)$

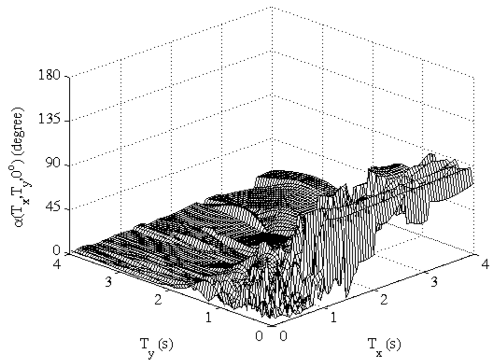

(b) $\alpha(T_x,T_y,0^\circ)$

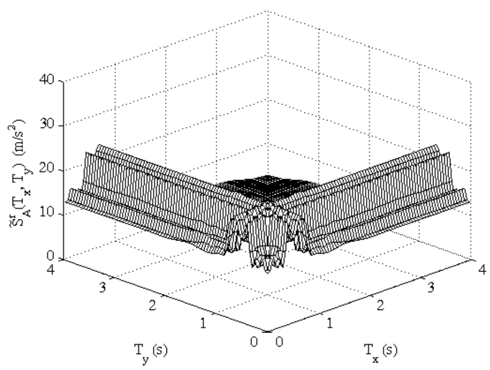

(c) $\tilde{S}_A^r(T_x,T_y)$

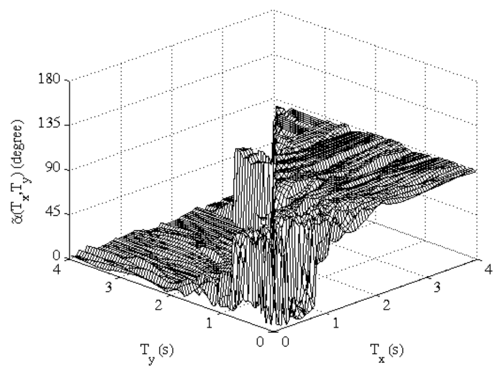

(d) $\tilde{\alpha}(T_x,T_y)$

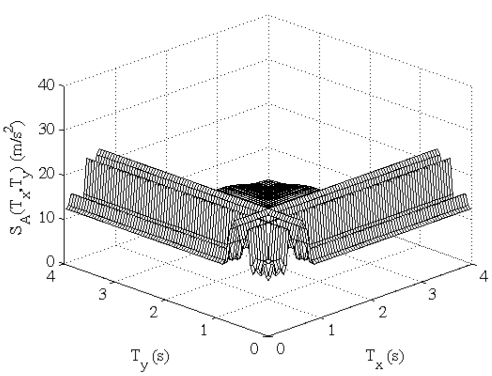

(e) $S_A(T_x,T_y)$

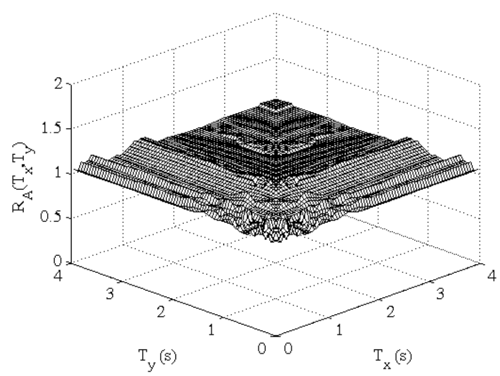

(f) $R_A(T_x,T_y)$

Figure B-39 Bi-directional responses of Loma Prieta earthquake, 16 LGPC station

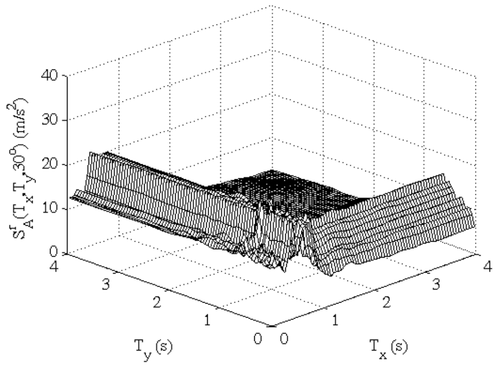

(a) $S_A^r(T_x,T_y,30^\circ)$

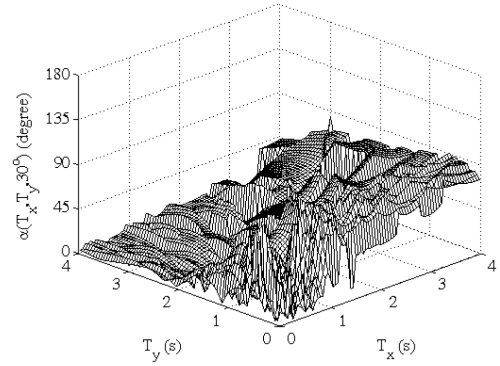

(b) $\alpha(T_x,T_y,30^\circ)$

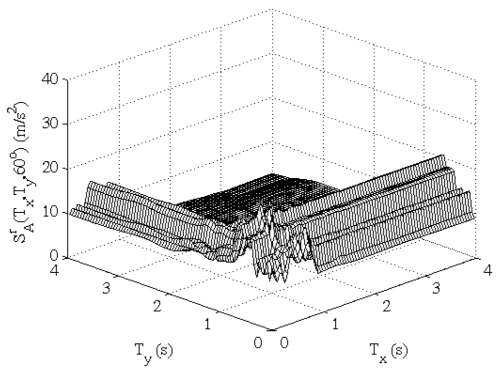

(c) $S_A^r(T_x,T_y,60^\circ)$

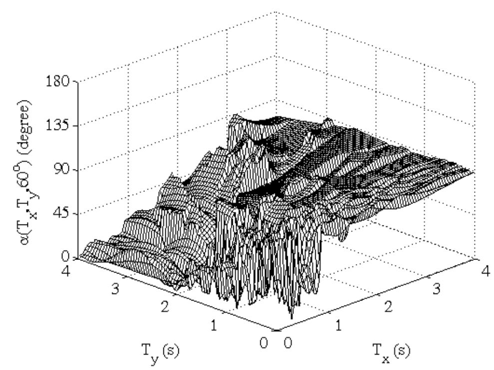

(d) $\alpha(T_x,T_y,60^\circ)$

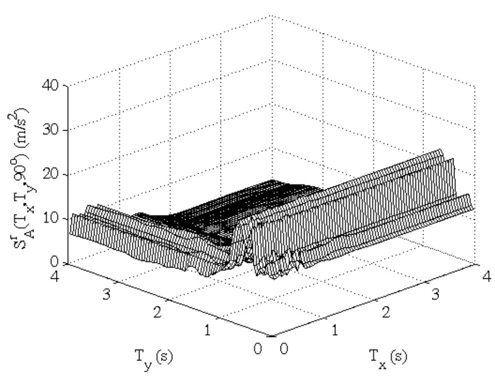

(e) $S_A^r(T_x,T_y,90^\circ)$

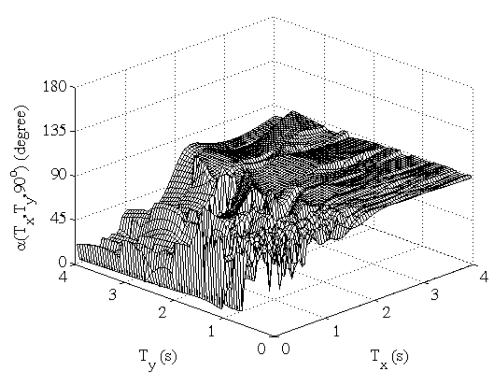

(f) $\alpha(T_x,T_y,90^\circ)$

Figure B-40 Pseudo acceleration spectra and incident angles in various directions of Loma Prieta earthquake, 16 LGPC station

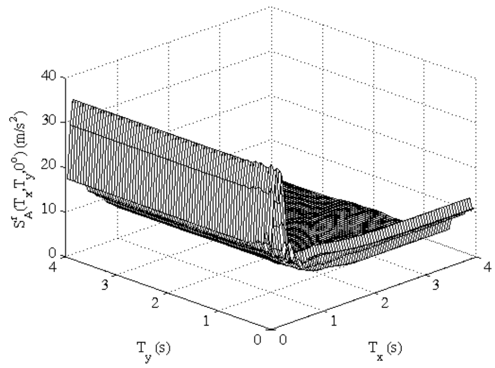

(a) $S_A^r(T_x,T_y,0^\circ)$

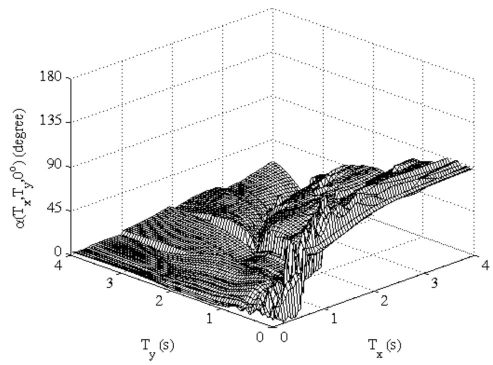

(b) $\alpha(T_x,T_y,0^\circ)$

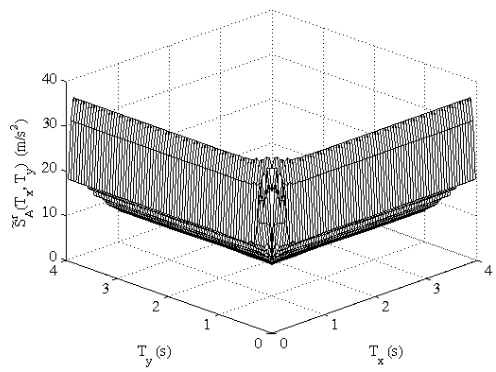

(c) $\widetilde{S}_A^r(T_x,T_y)$

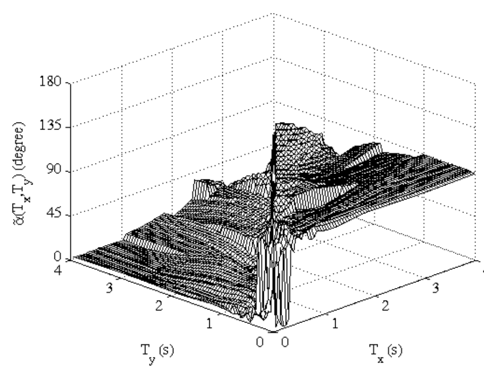

(d) $\widetilde{\alpha}(T_x,T_y)$

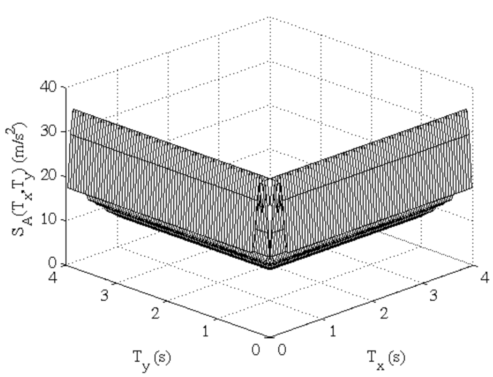

(e) $S_A(T_x,T_y)$

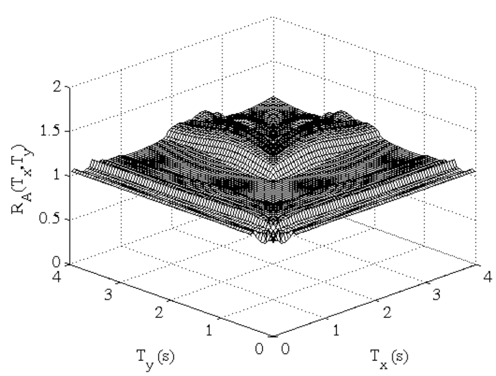

(f) $R_A(T_x,T_y)$

Figure B-41 Bi-directional responses of Cape Mendocino earthquake, 89005 Cape Mendocino station

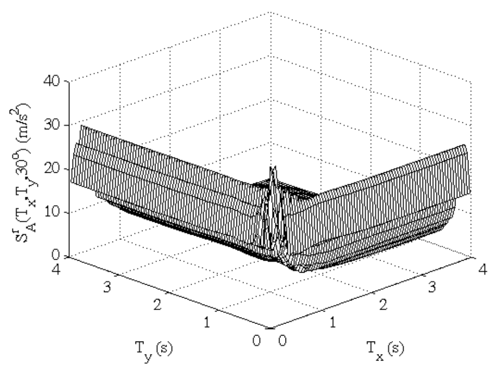

(a) $S_A^r(T_x, T_y, 30^\circ)$

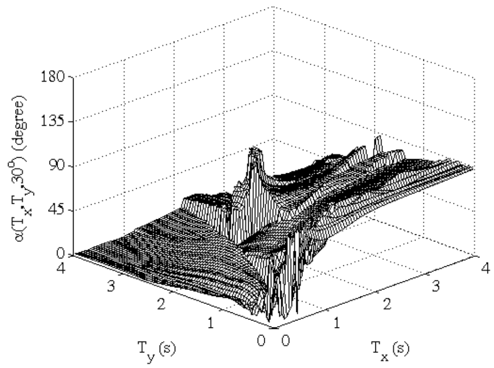

(b) $\alpha(T_x, T_y, 30^\circ)$

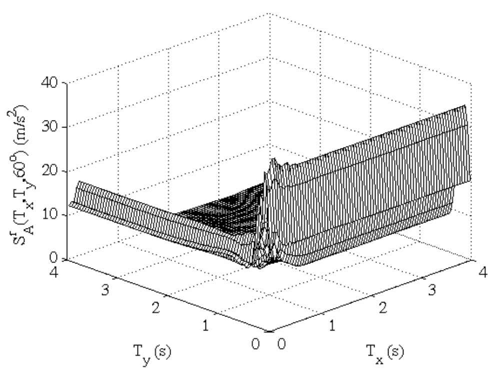

(c) $S_A^r(T_x, T_y, 60^\circ)$

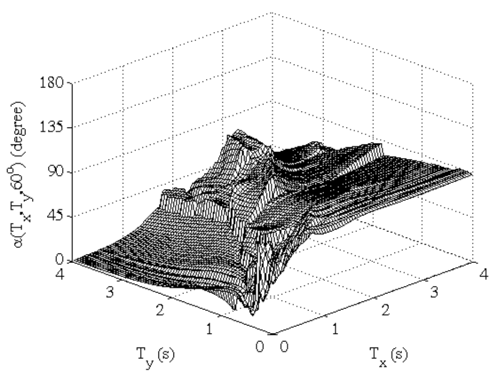

(d) $\alpha(T_x, T_y, 60^\circ)$

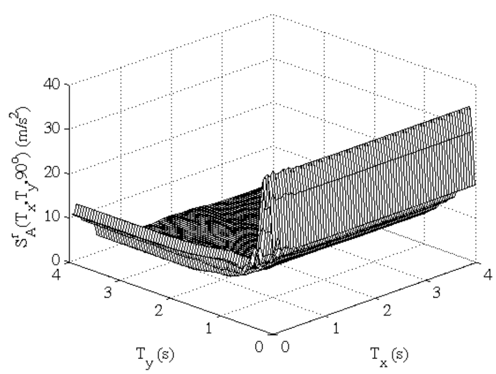

(e) $S_A^r(T_x, T_y, 90^\circ)$

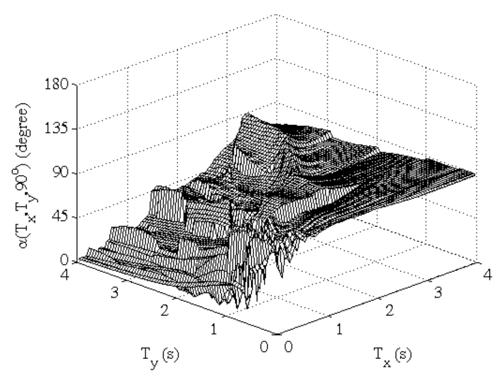

(f) $\alpha(T_x, T_y, 90^\circ)$

Figure B-42 Pseudo acceleration spectra and incident angles in various directions of Cape Mendocino earthquake, 89005 Cape Mendocino station

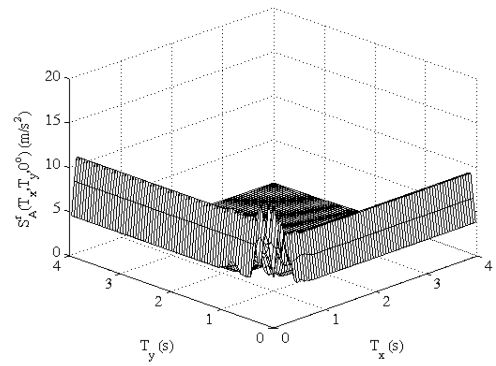

(a) $S^r_A(T_x,T_y,0^\circ)$

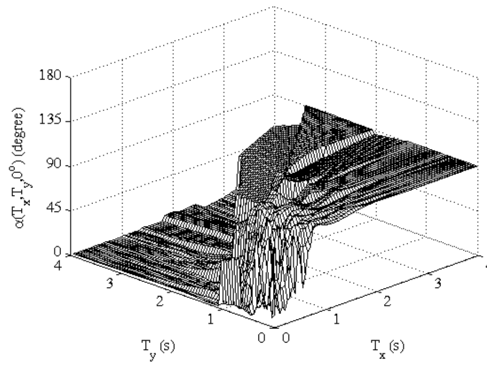

(b) $\alpha(T_x,T_y,0^\circ)$

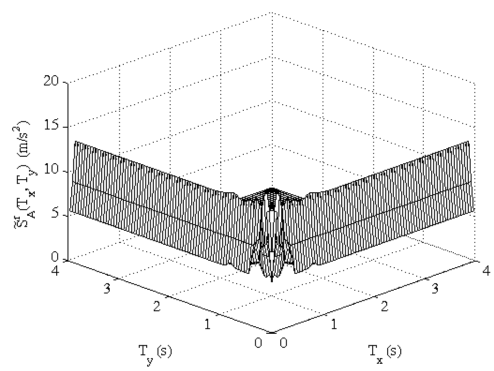

(c) $\widetilde{S}^r_A(T_x,T_y)$

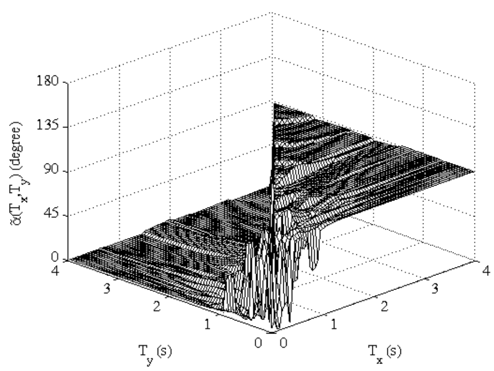

(d) $\widetilde{\alpha}(T_x,T_y)$

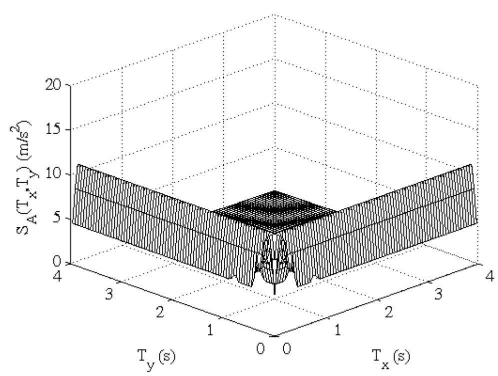

(e) $S_A(T_x,T_y)$

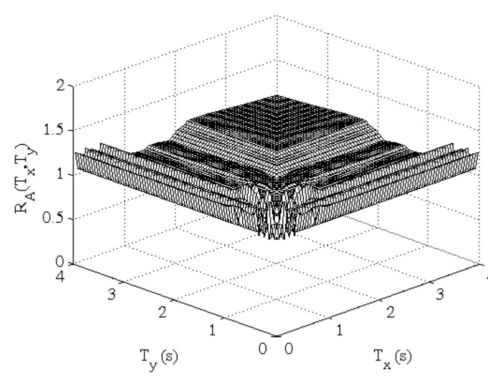

(f) $R_A(T_x,T_y)$

Figure B-43 Bi-directional responses of Whittier Narrows earthquake, 24461 Alhambra, Fremont Sch station

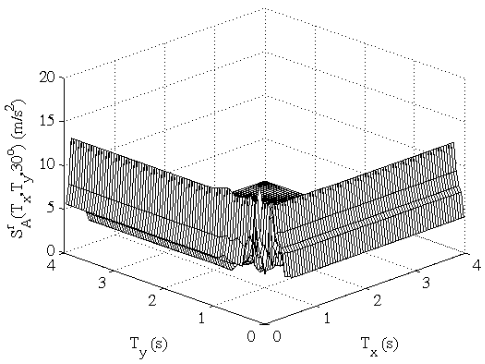

(a) $S_A^r(T_x,T_y,30^\circ)$

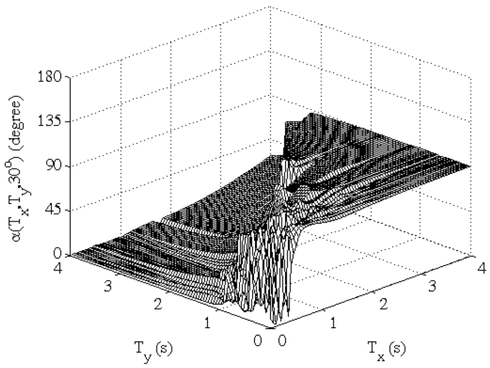

(b) $\alpha(T_x,T_y,30^\circ)$

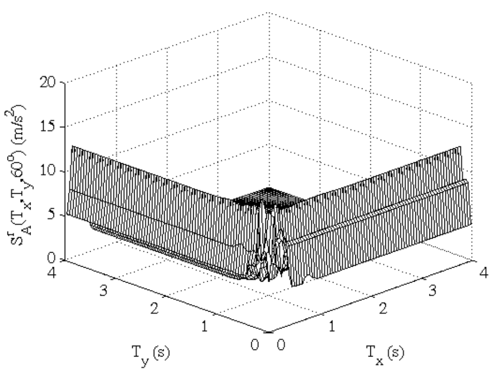

(c) $S_A^r(T_x,T_y,60^\circ)$

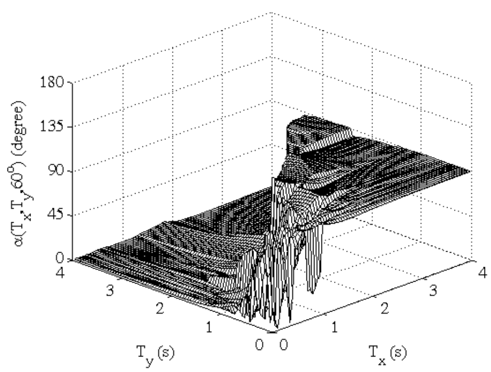

(d) $\alpha(T_x,T_y,60^\circ)$

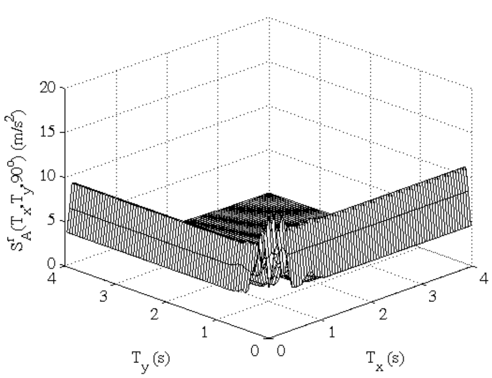

(e) $S_A^r(T_x,T_y,90^\circ)$

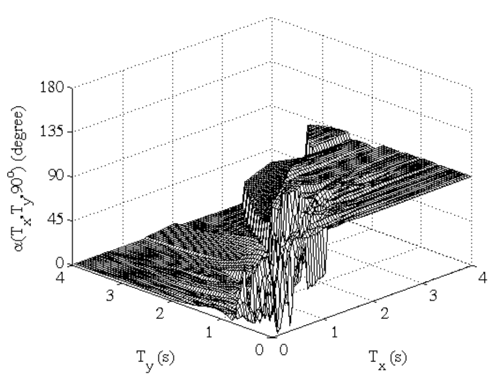

(f) $\alpha(T_x,T_y,90^\circ)$

Figure B-44 Pseudo acceleration spectra and incident angles in various directions of Whittier Narrows earthquake, 24461 Alhambra, Fremont Sch station

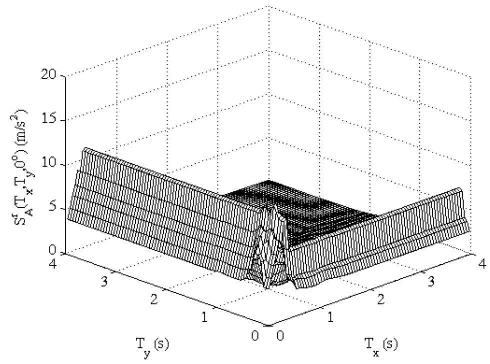

(a) $S_A^r(T_x, T_y, 0^\circ)$

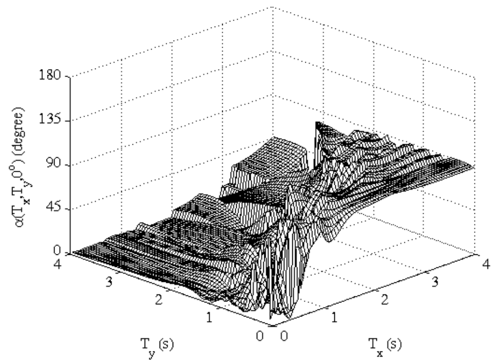

(b) $\alpha(T_x, T_y, 0^\circ)$

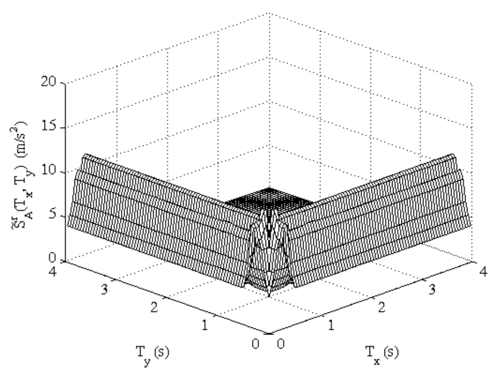

(c) $\widetilde{S}_A^r(T_x, T_y)$

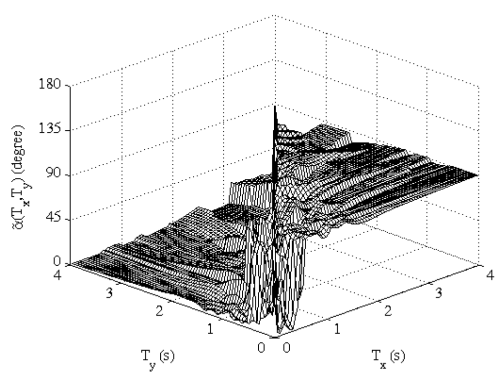

(d) $\widetilde{\alpha}(T_x, T_y)$

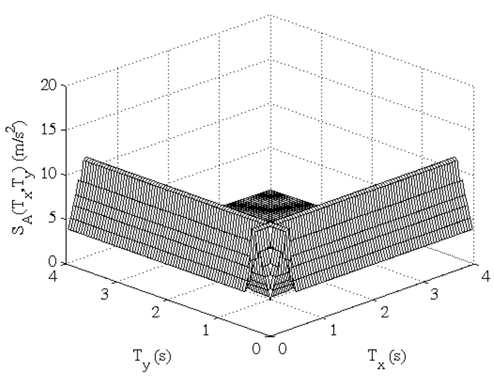

(e) $S_A(T_x, T_y)$

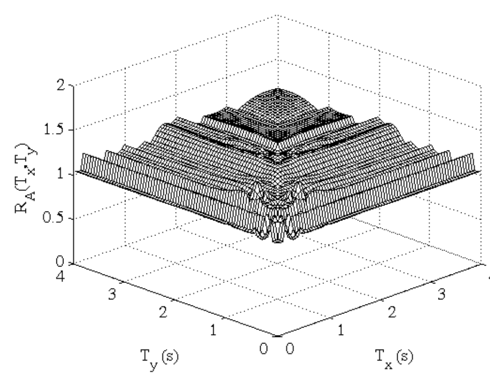

(f) $R_A(T_x, T_y)$

Figure B-45 Bi-directional responses of Parkfield earthquake, 1438 Temblor pre-1969 station

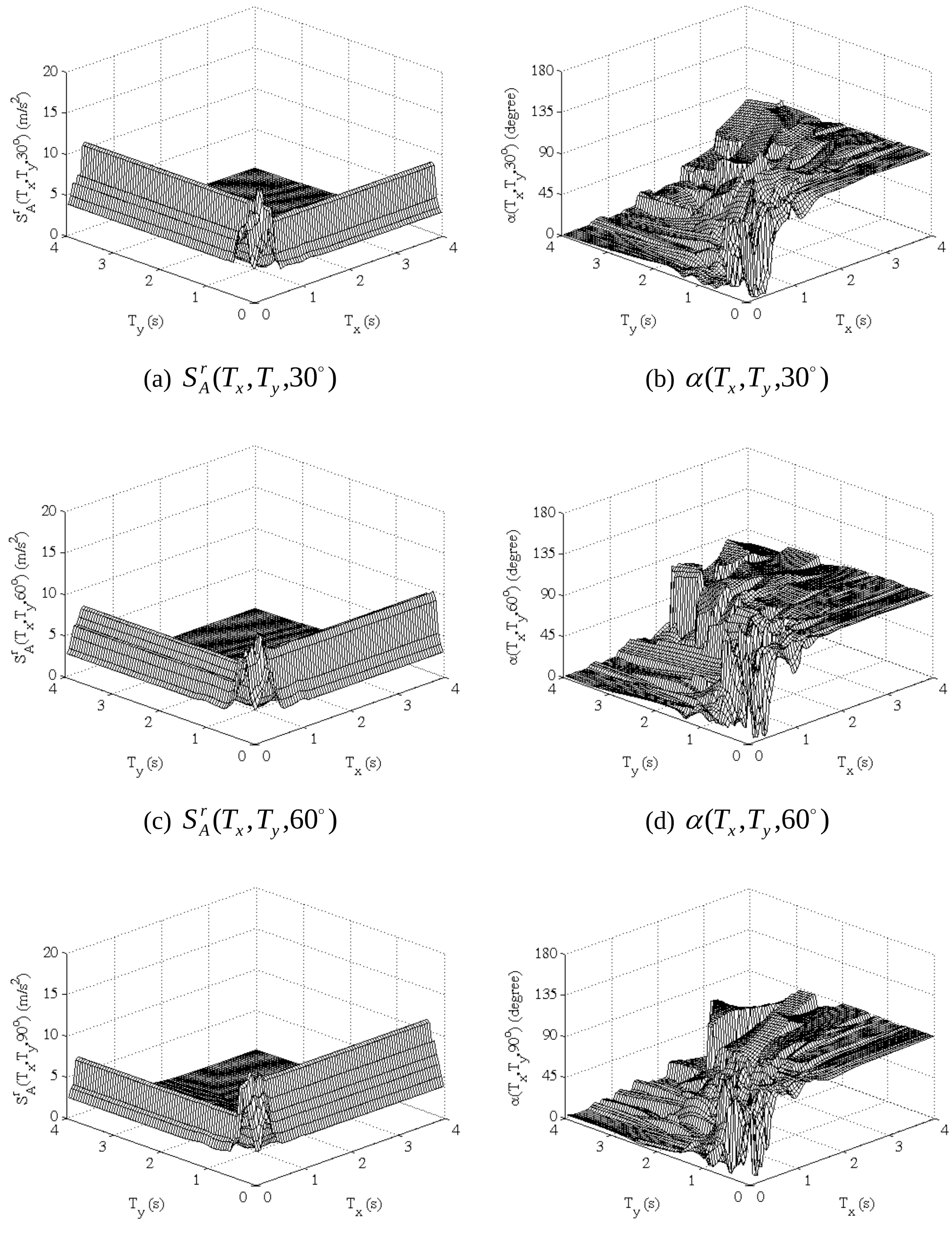

(a) $S_A^r(T_x, T_y, 30^\circ)$ (b) $\alpha(T_x, T_y, 30^\circ)$

(c) $S_A^r(T_x, T_y, 60^\circ)$ (d) $\alpha(T_x, T_y, 60^\circ)$

(e) $S_A^r(T_x, T_y, 90^\circ)$ (f) $\alpha(T_x, T_y, 90^\circ)$

Figure B-46 Pseudo acceleration spectra and incident angles in various directions of Parkfield earthquake, 1438 Temblor pre-1969 station

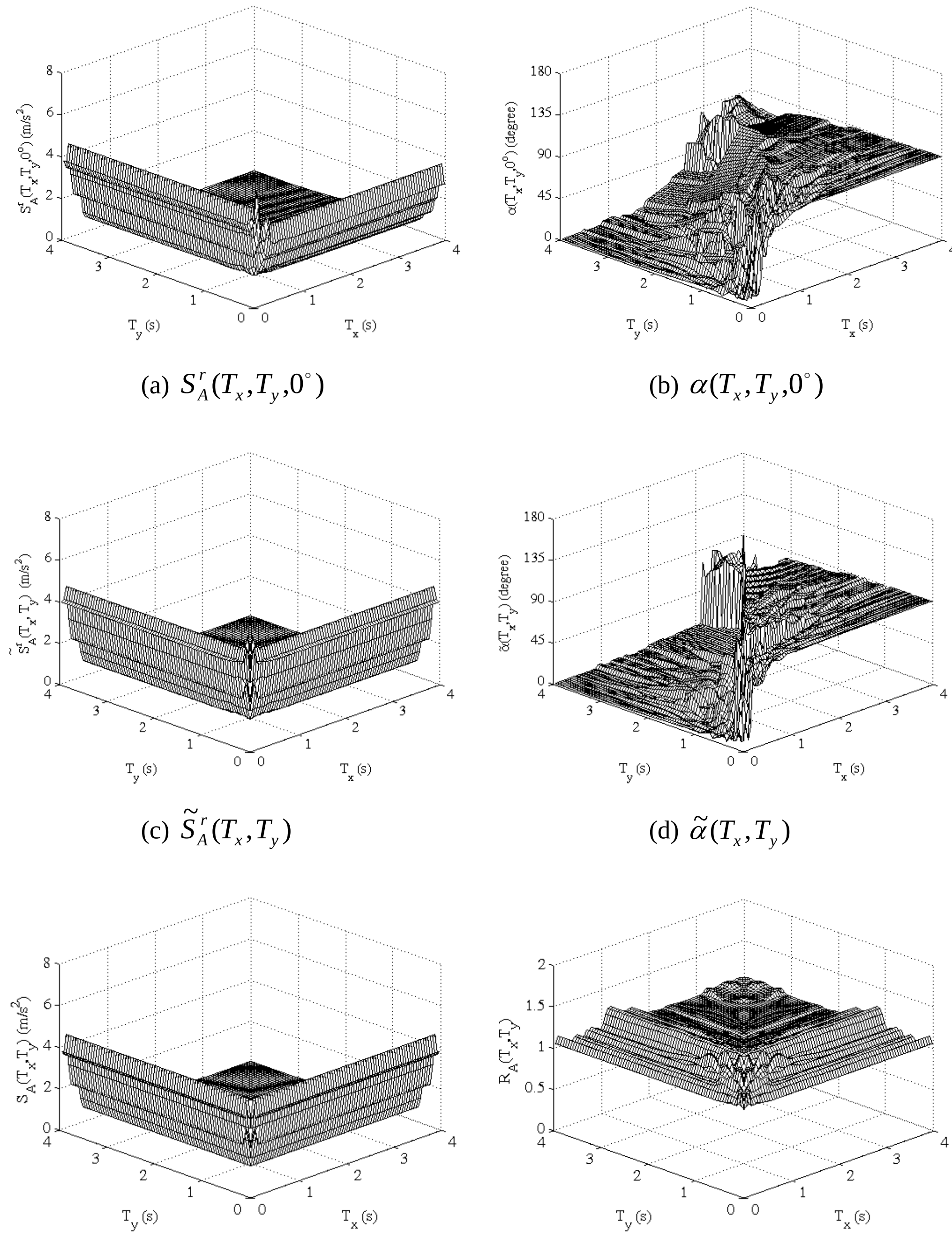

(a) $S_A^r(T_x,T_y,0^\circ)$

(b) $\alpha(T_x,T_y,0^\circ)$

(c) $\tilde{S}_A^r(T_x,T_y)$

(d) $\tilde{\alpha}(T_x,T_y)$

(e) $S_A(T_x,T_y)$

(f) $R_A(T_x,T_y)$

Figure B-47 Bi-directional responses of San Fernando earthquake, 127 Lake Hughes #9 station

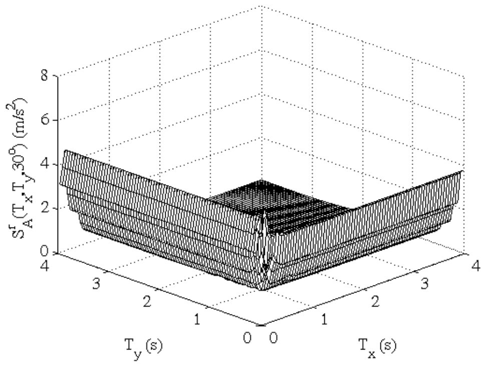

(a) $S_A^r(T_x, T_y, 30^\circ)$

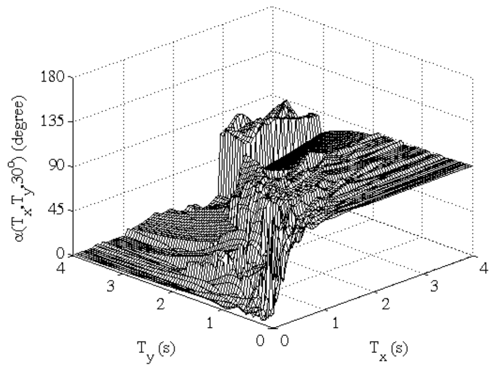

(b) $\alpha(T_x, T_y, 30^\circ)$

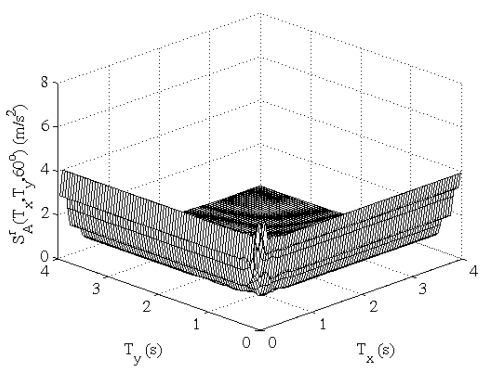

(c) $S_A^r(T_x, T_y, 60^\circ)$

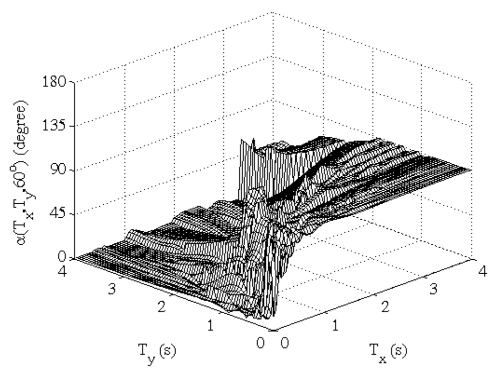

(d) $\alpha(T_x, T_y, 60^\circ)$

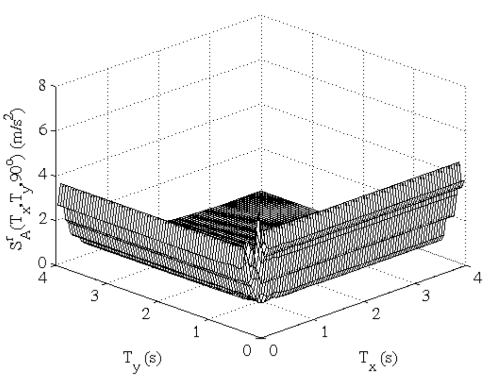

(e) $S_A^r(T_x, T_y, 90^\circ)$

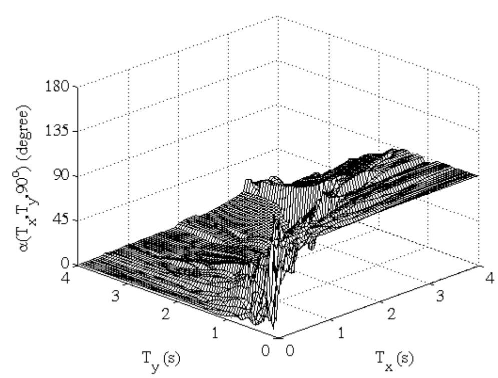

(f) $\alpha(T_x, T_y, 90^\circ)$

Figure B-48 Pseudo acceleration spectra and incident angles in various directions of San Fernando earthquake, 127 Lake Hughes #9 station

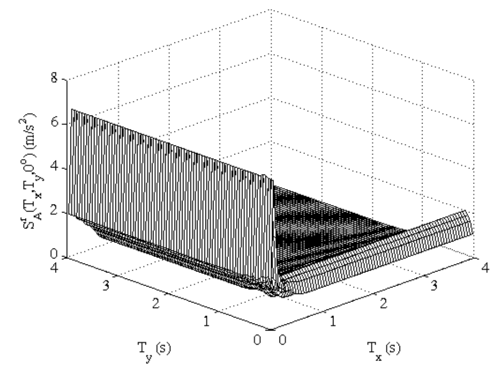

(a) $S_A^r(T_x,T_y,0^\circ)$

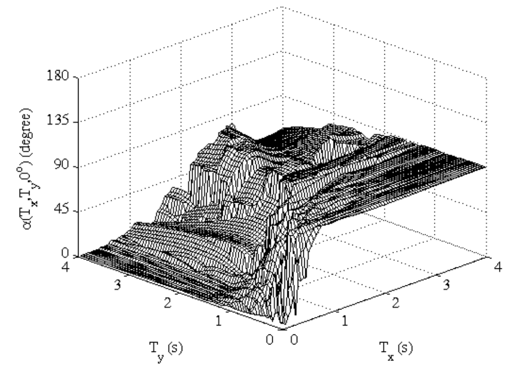

(b) $\alpha(T_x,T_y,0^\circ)$

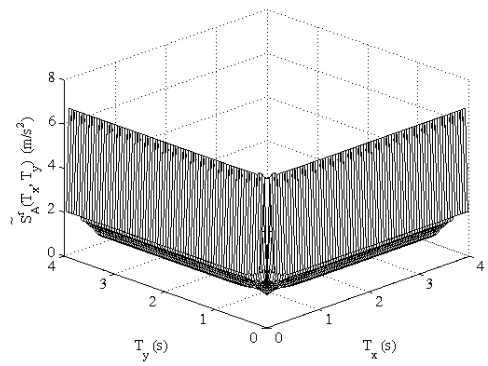

(c) $\tilde{S}_A^r(T_x,T_y)$

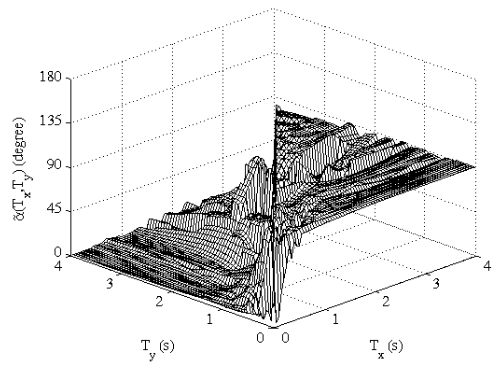

(d) $\tilde{\alpha}(T_x,T_y)$

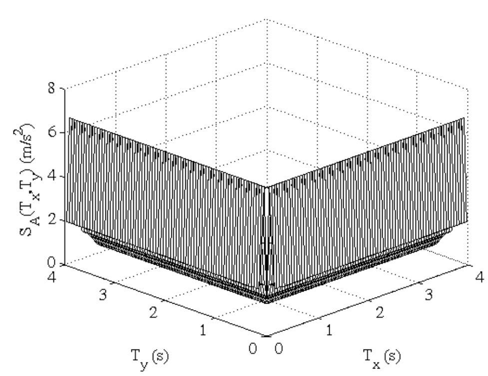

(e) $S_A(T_x,T_y)$

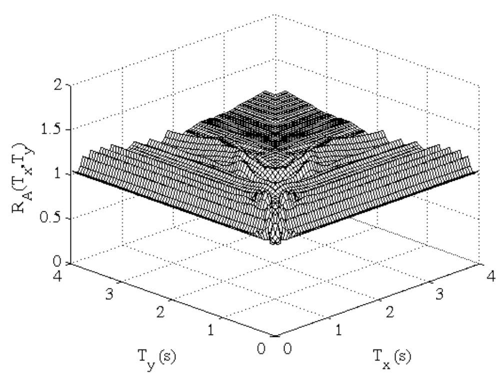

(f) $R_A(T_x,T_y)$

Figure B-49 Bi-directional responses of N. Palm Springs earthquake, 12206 Silent Valley - Poppet F station

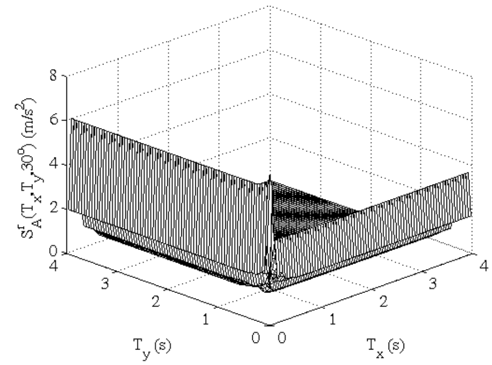

(a) $S^r_A(T_x, T_y, 30^\circ)$

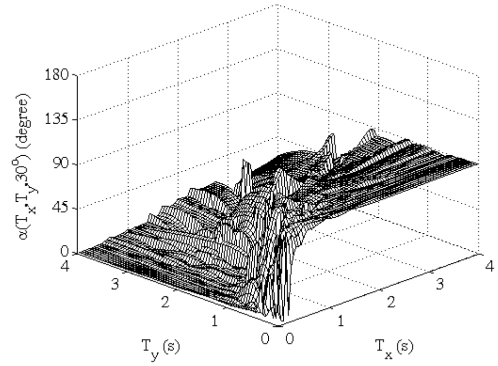

(b) $\alpha(T_x, T_y, 30^\circ)$

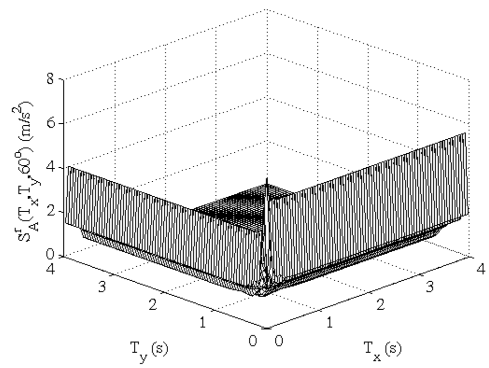

(c) $S^r_A(T_x, T_y, 60^\circ)$

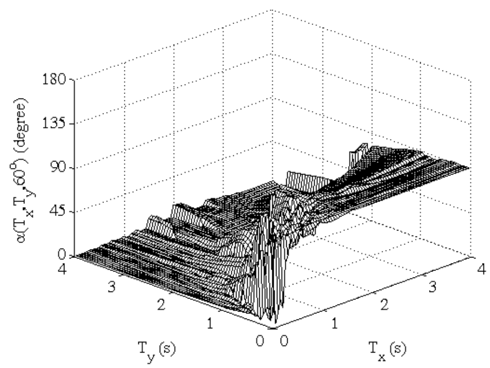

(d) $\alpha(T_x, T_y, 60^\circ)$

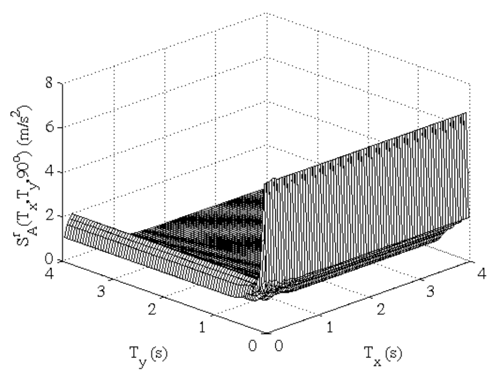

(e) $S^r_A(T_x, T_y, 90^\circ)$

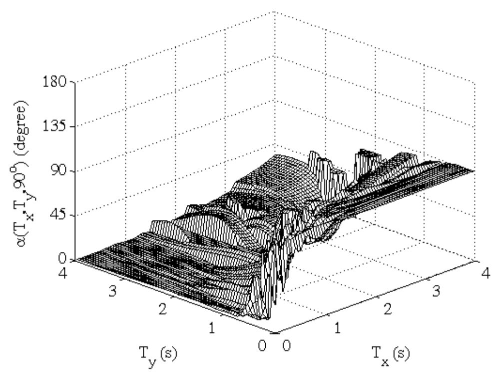

(f) $\alpha(T_x, T_y, 90^\circ)$

Figure B-50 Pseudo acceleration spectra and incident angles in various directions of N. Palm Springs earthquake, 12206 Silent Valley - Poppet F station

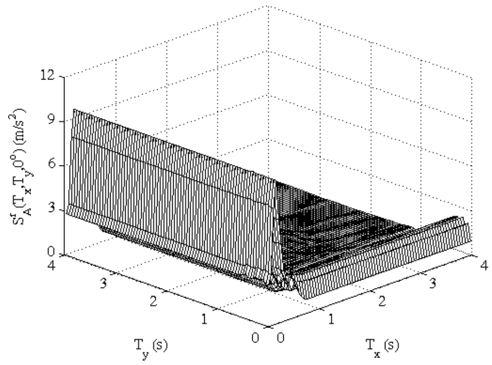

(a) $S_A^r(T_x,T_y,0^\circ)$

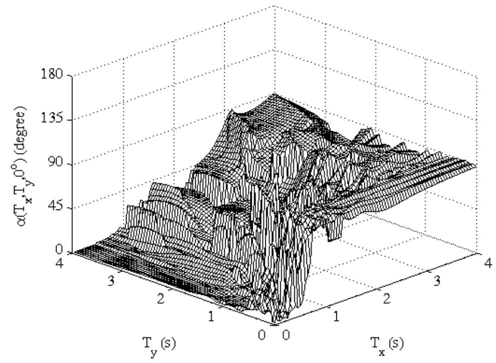

(b) $\alpha(T_x,T_y,0^\circ)$

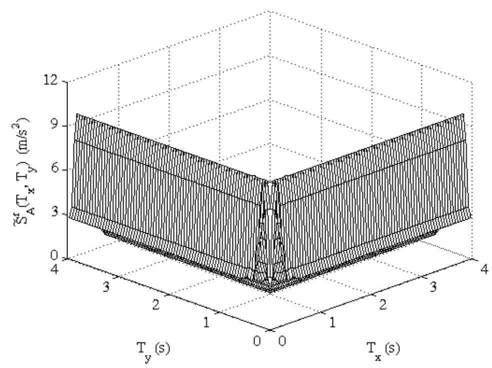

(c) $\tilde{S}_A^r(T_x,T_y)$

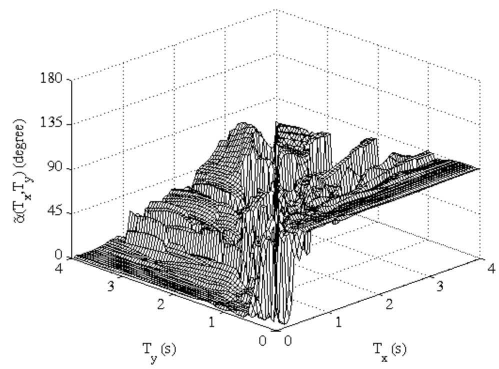

(d) $\tilde{\alpha}(T_x,T_y)$

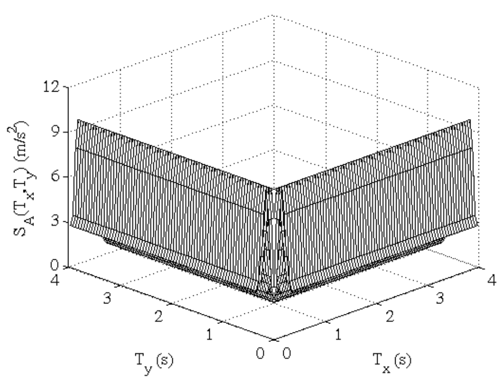

(e) $S_A(T_x,T_y)$

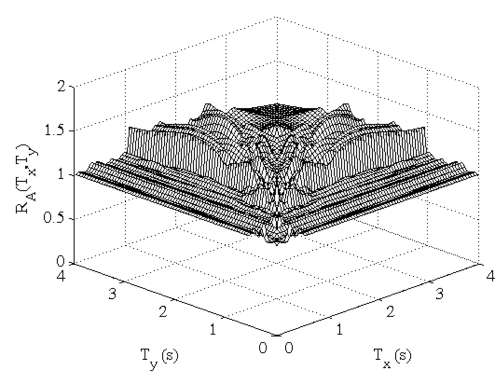

(f) $R_A(T_x,T_y)$

Figure B-51 Bi-directional responses of Northridge earthquake, 127 Lake Hughes #9 station

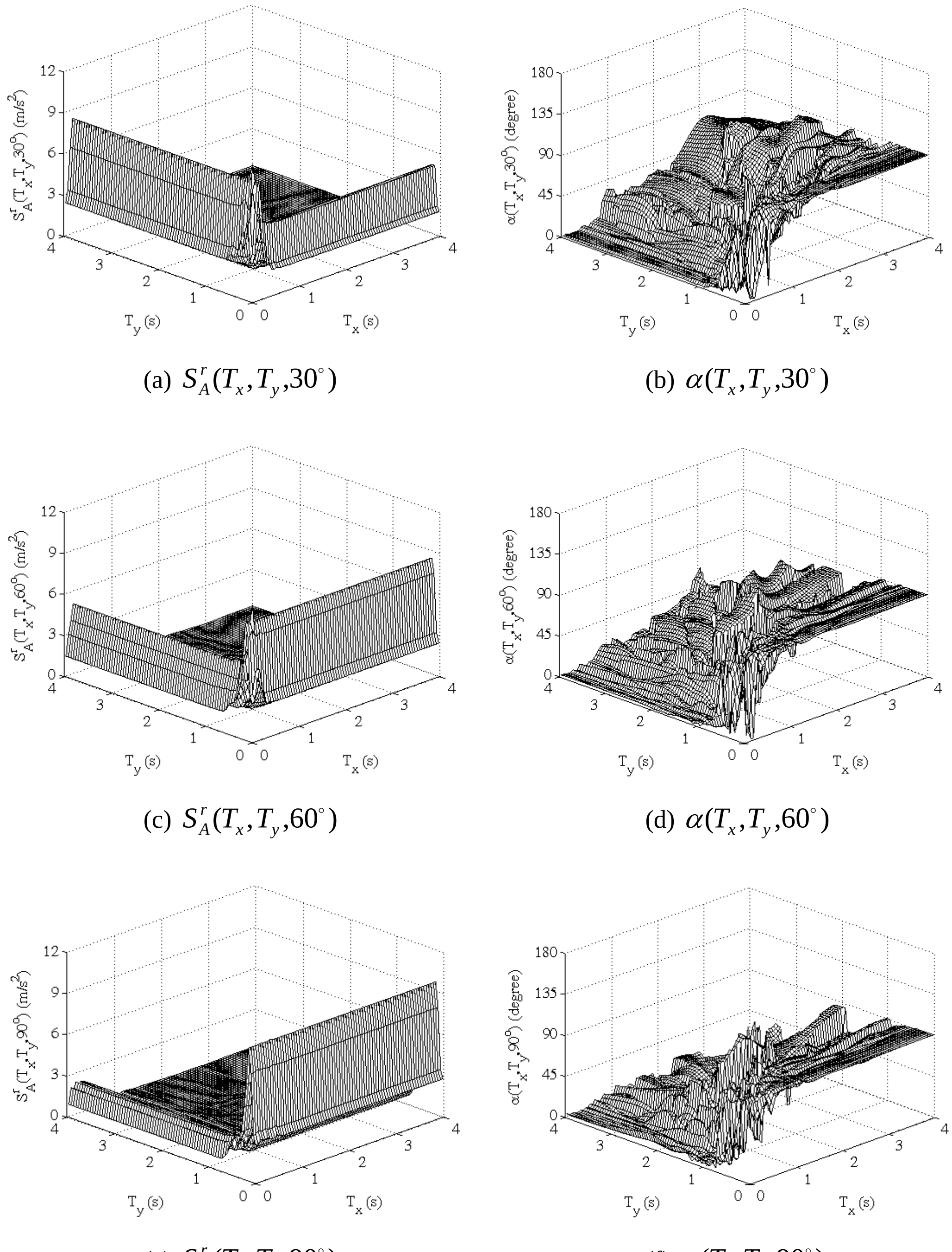

(a) $S_A^r(T_x, T_y, 30^\circ)$ (b) $\alpha(T_x, T_y, 30^\circ)$

(c) $S_A^r(T_x, T_y, 60^\circ)$ (d) $\alpha(T_x, T_y, 60^\circ)$

(e) $S_A^r(T_x, T_y, 90^\circ)$ (f) $\alpha(T_x, T_y, 90^\circ)$

Figure B-52 Pseudo acceleration spectra and incident angles in various directions of Northridge earthquake, 127 Lake Hughes #9 station

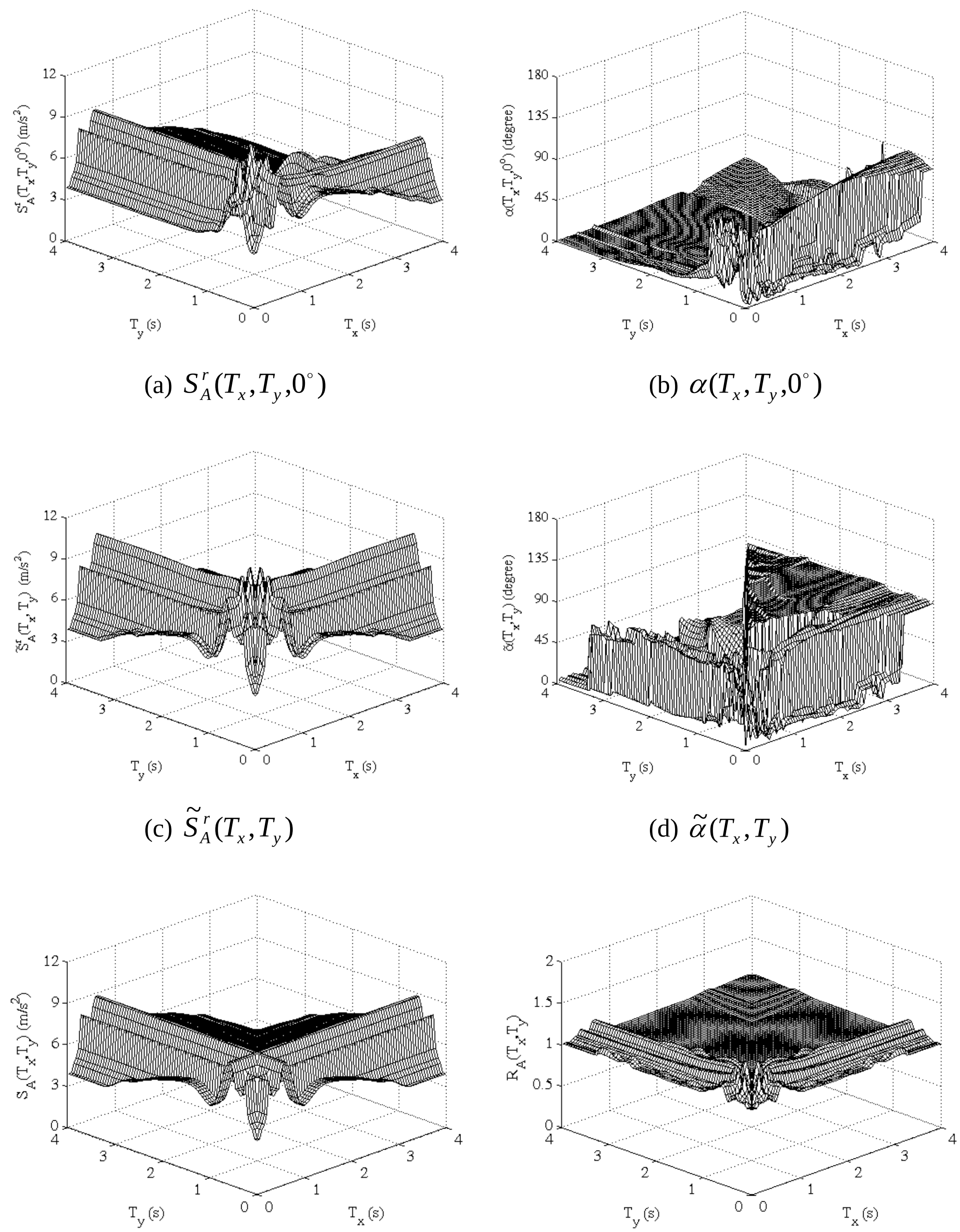

(a) $S_A^r(T_x, T_y, 0^\circ)$ (b) $\alpha(T_x, T_y, 0^\circ)$

(c) $\tilde{S}_A^r(T_x, T_y)$ (d) $\tilde{\alpha}(T_x, T_y)$

(e) $S_A(T_x, T_y)$ (f) $R_A(T_x, T_y)$

Figure B-53 Bi-directional responses of Imperial Valley earthquake, 5155 EC Meloland Overpass FF station

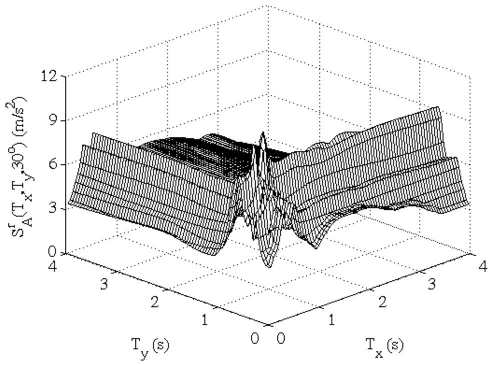

(a) $S_A^r(T_x, T_y, 30^\circ)$

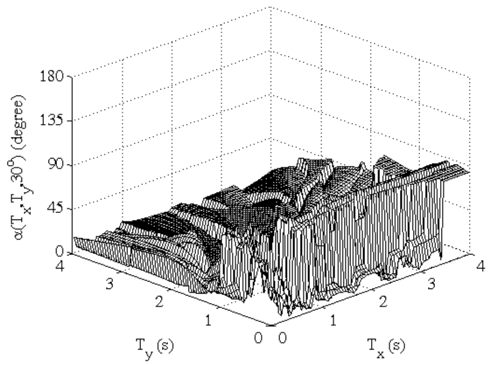

(b) $\alpha(T_x, T_y, 30^\circ)$

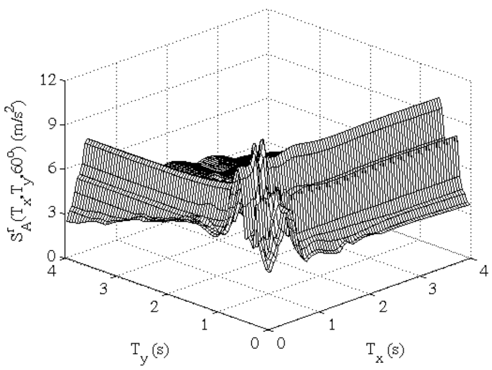

(c) $S_A^r(T_x, T_y, 60^\circ)$

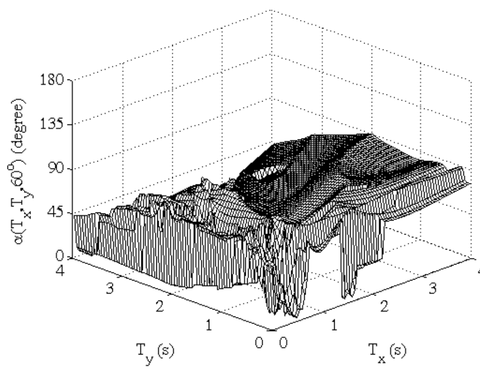

(d) $\alpha(T_x, T_y, 60^\circ)$

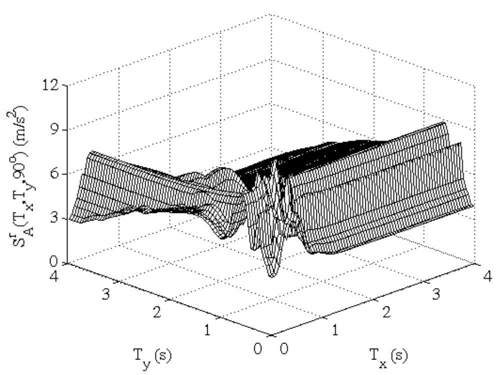

(e) $S_A^r(T_x, T_y, 90^\circ)$

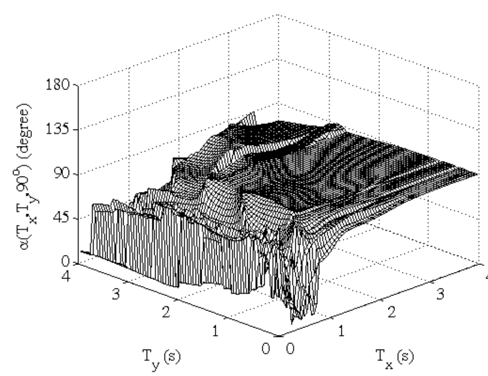

(f) $\alpha(T_x, T_y, 90^\circ)$

Figure B-54 Pseudo acceleration spectra and incident angles in various directions of Imperial Valley earthquake, 5155 EC Meloland Overpass FF station

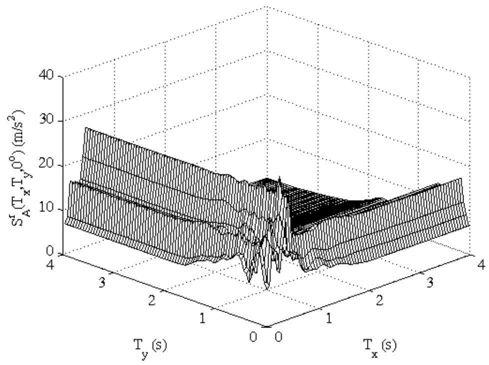

(a) $S_A^r(T_x,T_y,0^\circ)$

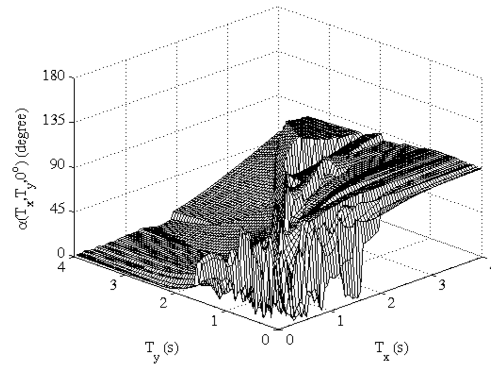

(b) $\alpha(T_x,T_y,0^\circ)$

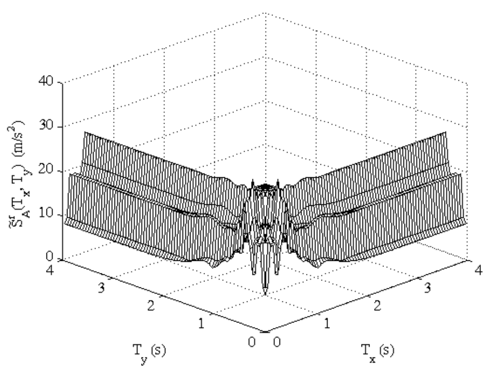

(c) $\widetilde{S}_A^r(T_x,T_y)$

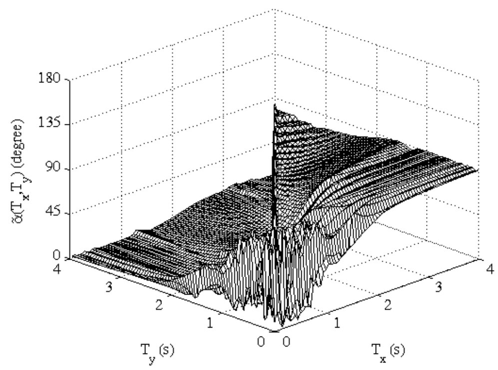

(d) $\widetilde{\alpha}(T_x,T_y)$

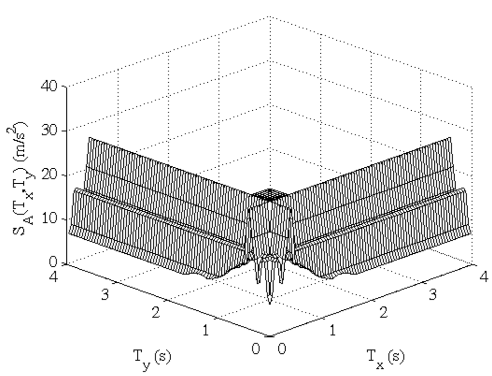

(e) $S_A(T_x,T_y)$

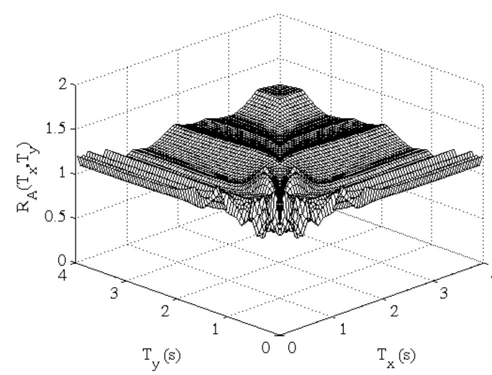

(f) $R_A(T_x,T_y)$

Figure B-55 Bi-directional responses of Kobe earthquake, 0 Takarazuka station

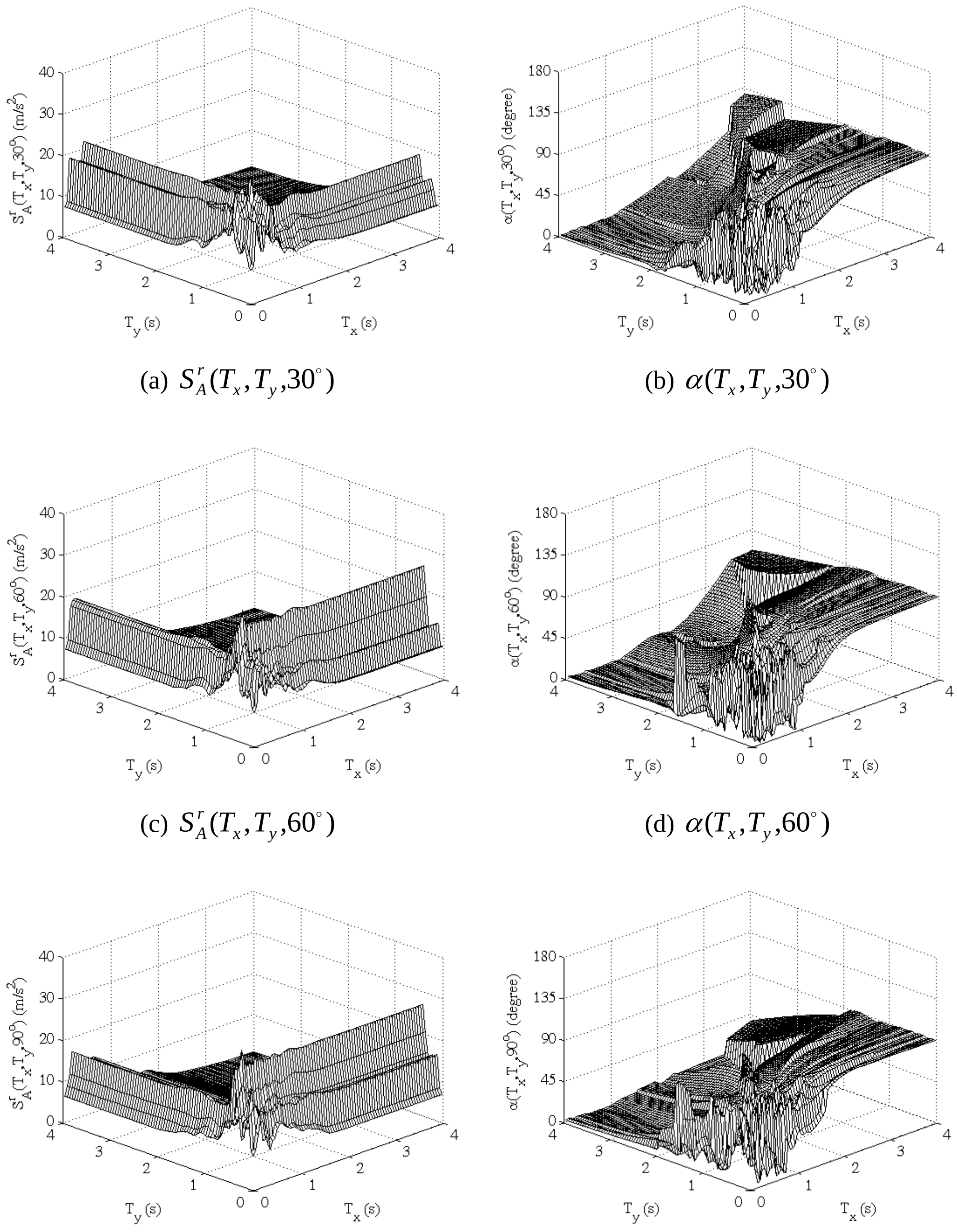

(a) $S_A^r(T_x, T_y, 30^\circ)$

(b) $\alpha(T_x, T_y, 30^\circ)$

(c) $S_A^r(T_x, T_y, 60^\circ)$

(d) $\alpha(T_x, T_y, 60^\circ)$

(e) $S_A^r(T_x, T_y, 90^\circ)$

(f) $\alpha(T_x, T_y, 90^\circ)$

Figure B-56 Pseudo acceleration spectra and incident angles in various directions of Kobe earthquake, 0 Takarazuka station

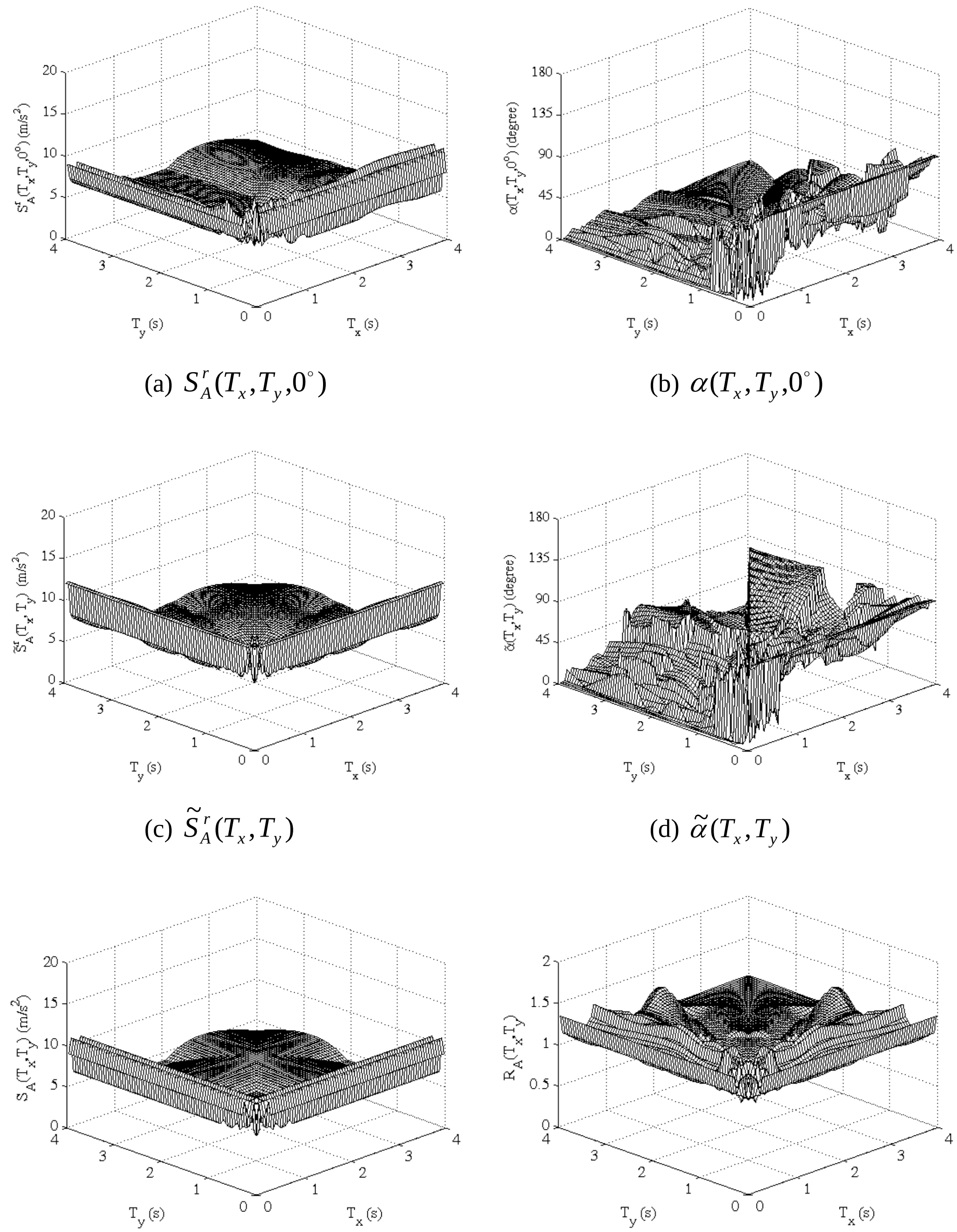

(a) $S_A^r(T_x, T_y, 0^\circ)$ (b) $\alpha(T_x, T_y, 0^\circ)$

(c) $\tilde{S}_A^r(T_x, T_y)$ (d) $\tilde{\alpha}(T_x, T_y)$

(e) $S_A(T_x, T_y)$ (f) $R_A(T_x, T_y)$

Figure B-57 Bi-directional responses of Imperial Valley earthquake, 942 El Centro Array #6 station

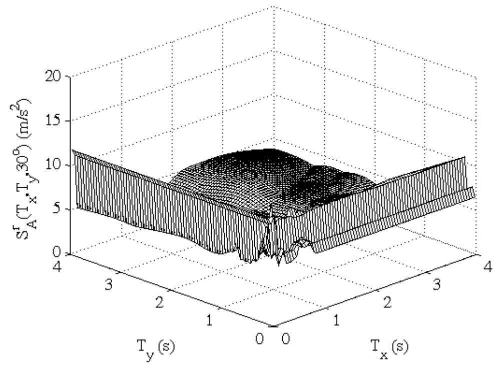

(a) $S_A^r(T_x,T_y,30^\circ)$

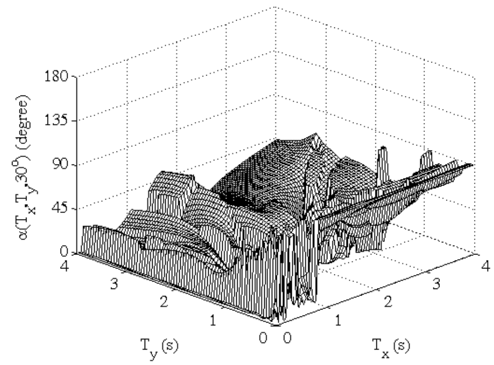

(b) $\alpha(T_x,T_y,30^\circ)$

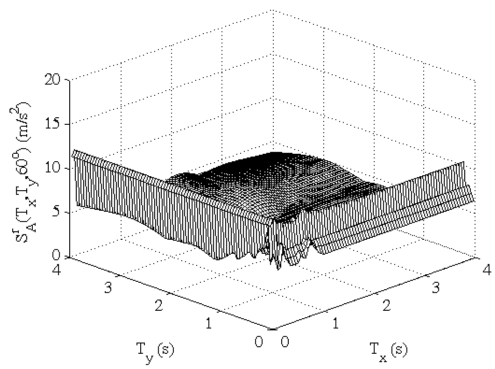

(c) $S_A^r(T_x,T_y,60^\circ)$

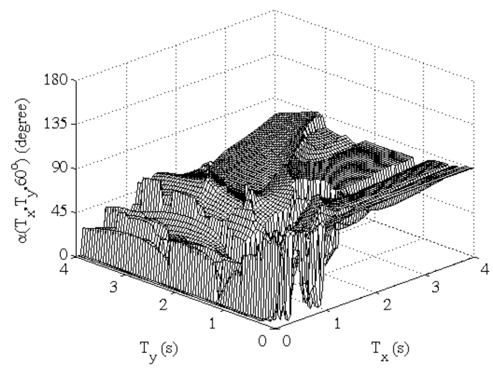

(d) $\alpha(T_x,T_y,60^\circ)$

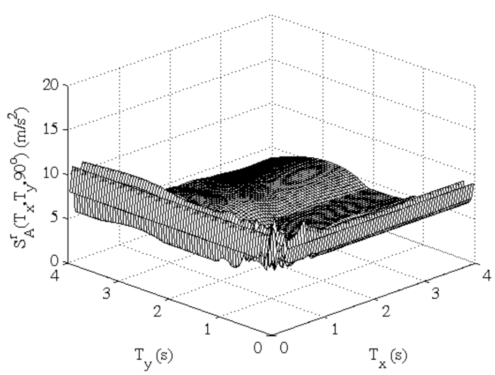

(e) $S_A^r(T_x,T_y,90^\circ)$

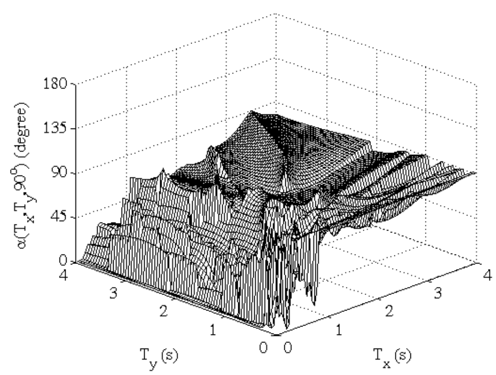

(f) $\alpha(T_x,T_y,90^\circ)$

Figure B-58 Pseudo acceleration spectra and incident angles in various directions of Imperial Valley earthquake, 942 El Centro Array #6 station

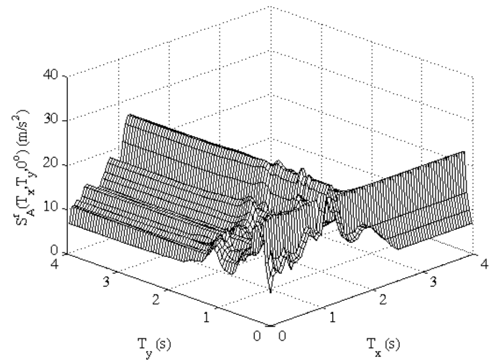

(a) $S^r_A(T_x,T_y,0^\circ)$

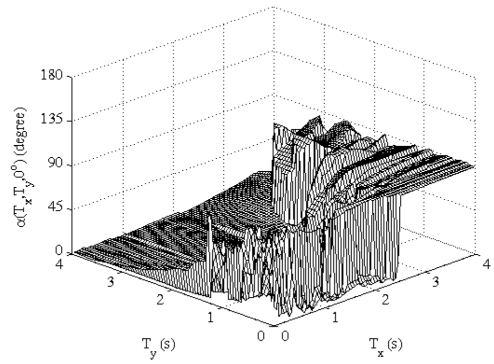

(b) $\alpha(T_x,T_y,0^\circ)$

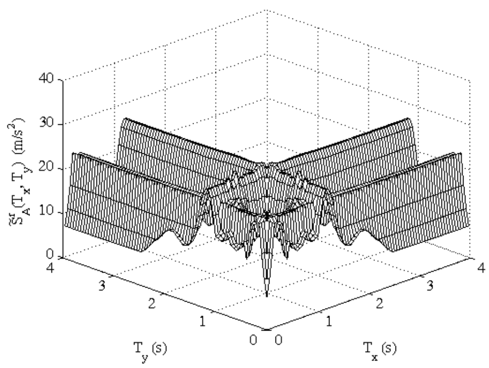

(c) $\tilde{S}^r_A(T_x,T_y)$

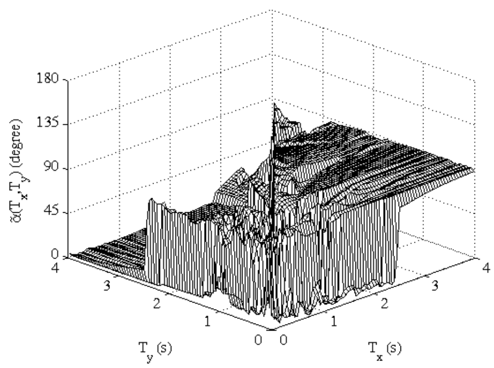

(d) $\tilde{\alpha}(T_x,T_y)$

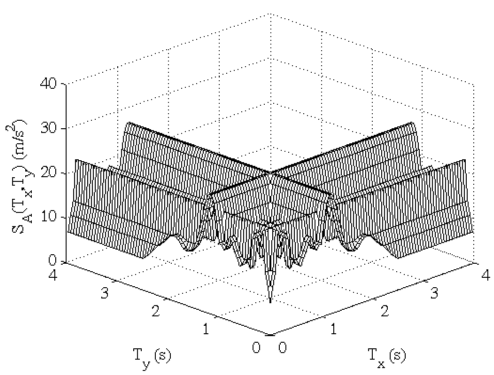

(e) $S_A(T_x,T_y)$

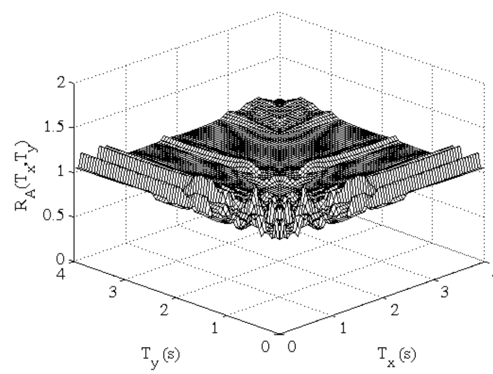

(f) $R_A(T_x,T_y)$

Figure B-59 Bi-directional responses of Kobe earthquake, 0 Takatori station

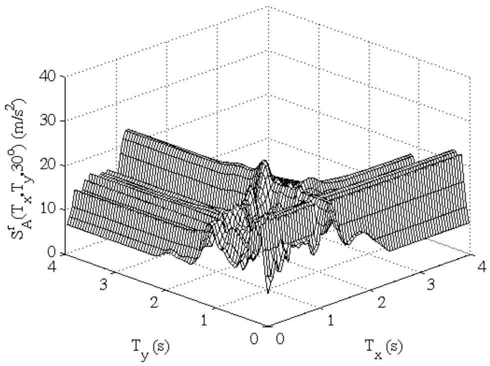

(a) $S_A^r(T_x, T_y, 30^\circ)$

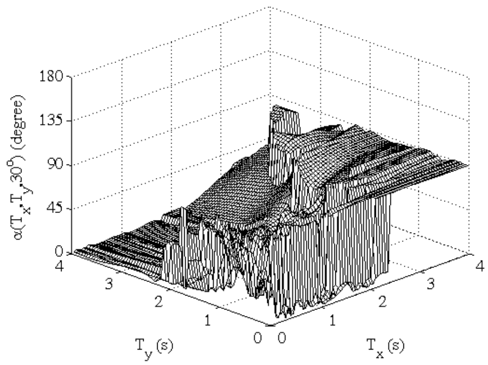

(b) $\alpha(T_x, T_y, 30^\circ)$

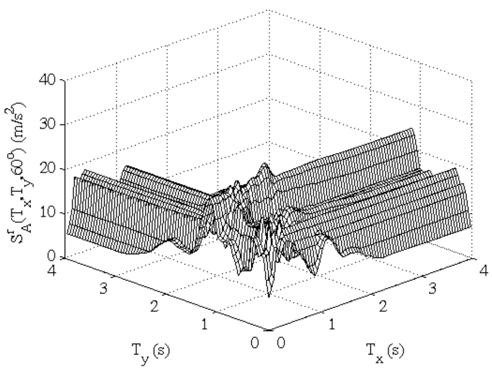

(c) $S_A^r(T_x, T_y, 60^\circ)$

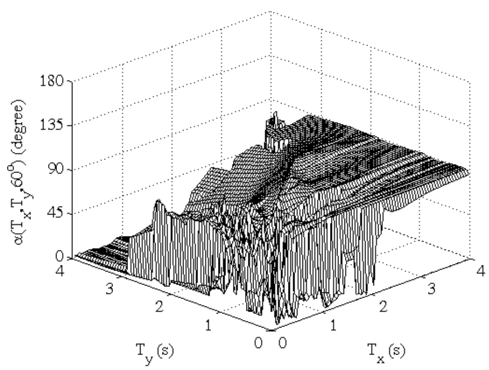

(d) $\alpha(T_x, T_y, 60^\circ)$

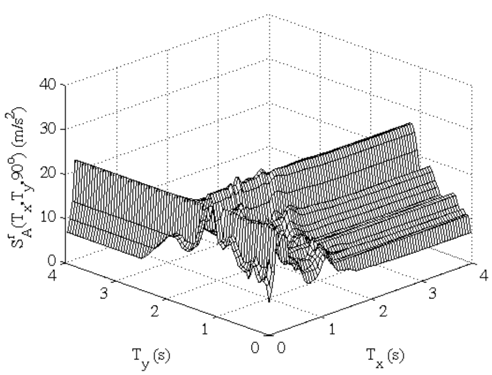

(e) $S_A^r(T_x, T_y, 90^\circ)$

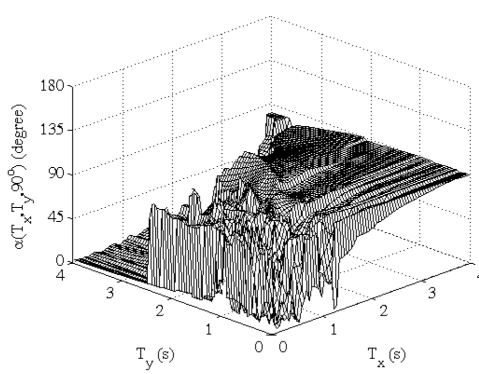

(f) $\alpha(T_x, T_y, 90^\circ)$

Figure B-60 Pseudo acceleration spectra and incident angles in various directions of Kobe earthquake, 0 Takatori station

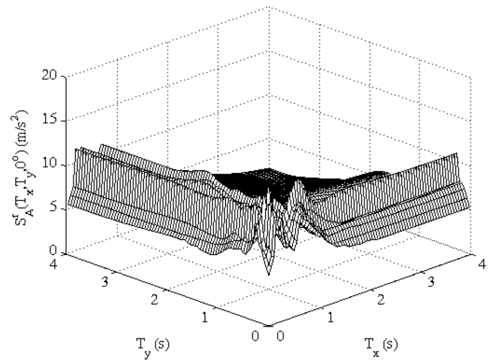

(a) $S_A^r(T_x,T_y,0^\circ)$

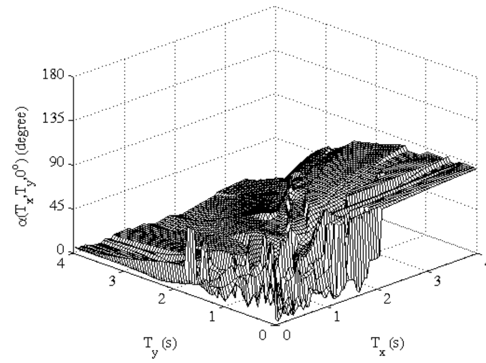

(b) $\alpha(T_x,T_y,0^\circ)$

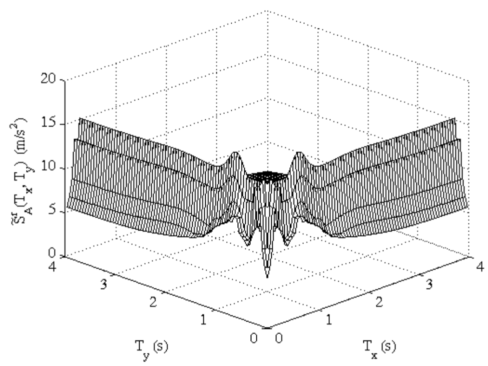

(c) $\widetilde{S}_A^r(T_x,T_y)$

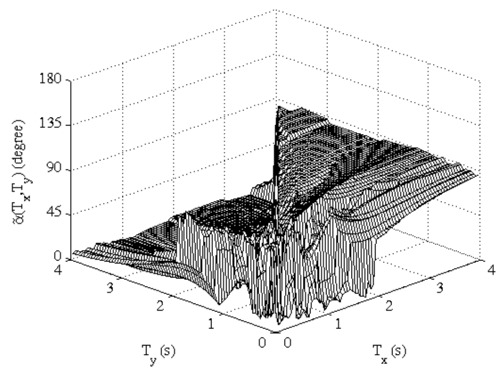

(d) $\widetilde{\alpha}(T_x,T_y)$

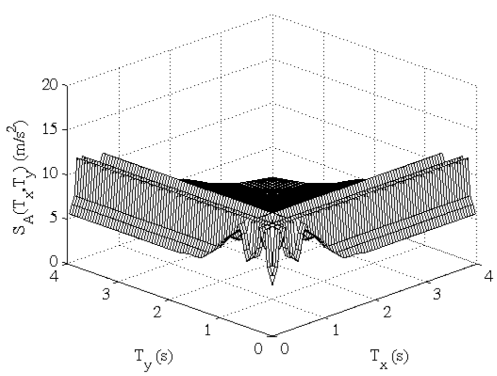

(e) $S_A(T_x,T_y)$

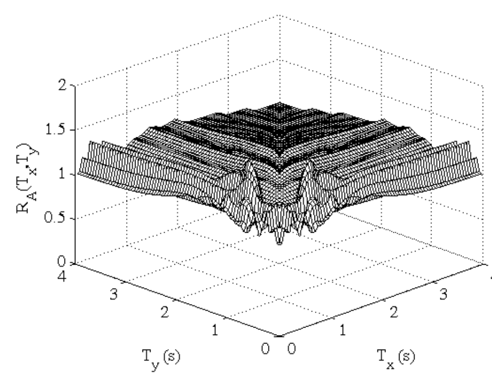

(f) $R_A(T_x,T_y)$

Figure B-61 Bi-directional responses of Erzincan, Turkey earthquake, 95 Erzincan station

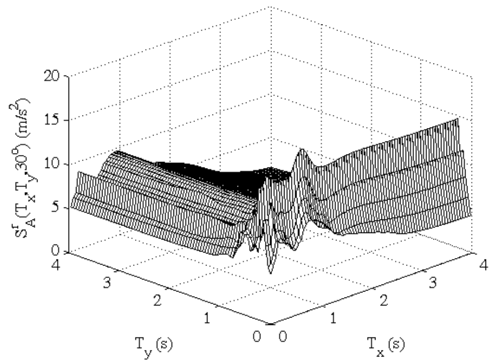

(a) $S_A^r(T_x,T_y,30^\circ)$

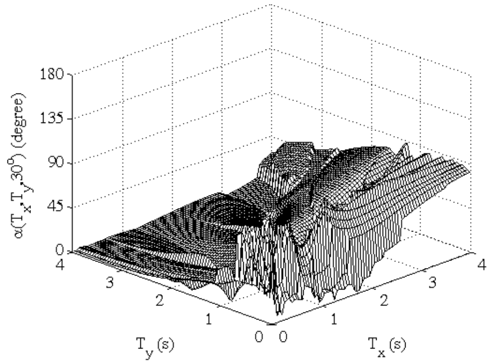

(b) $\alpha(T_x,T_y,30^\circ)$

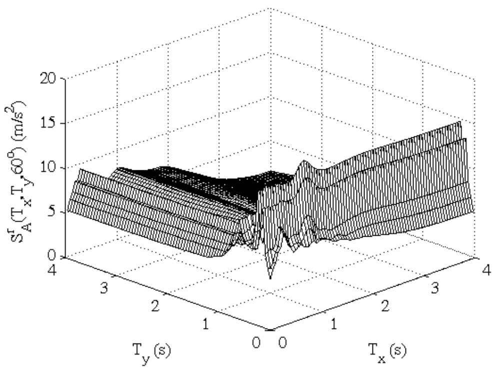

(c) $S_A^r(T_x,T_y,60^\circ)$

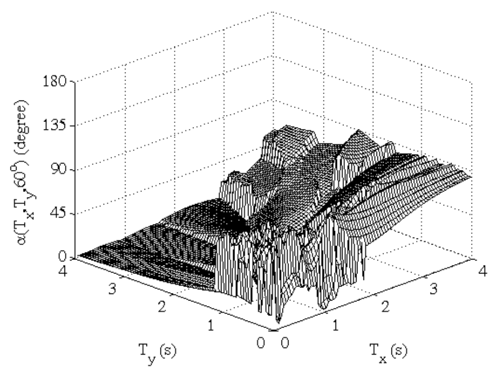

(d) $\alpha(T_x,T_y,60^\circ)$

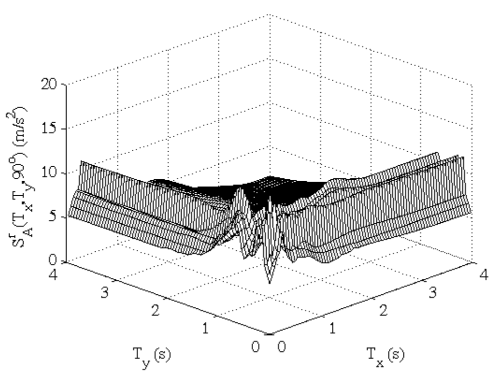

(e) $S_A^r(T_x,T_y,90^\circ)$

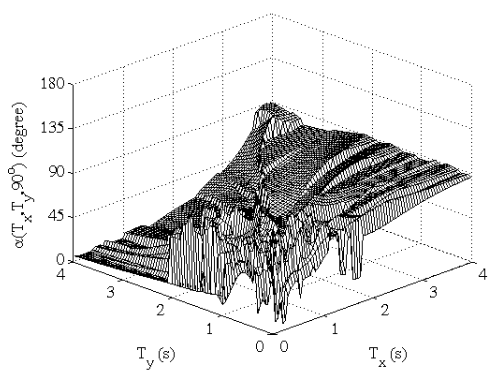

(f) $\alpha(T_x,T_y,90^\circ)$

Figure B-62 Pseudo acceleration spectra and incident angles in various directions of Erzincan, Turkey earthquake, 95 Erzincan station

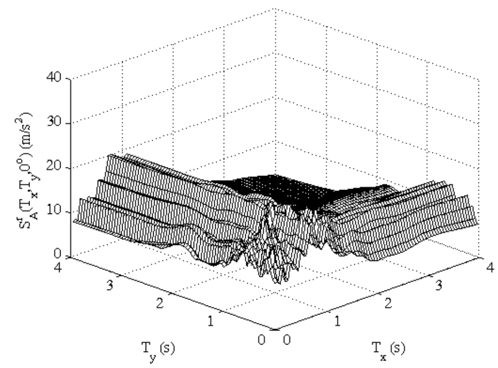

(a) $S_A^r(T_x, T_y, 0^\circ)$

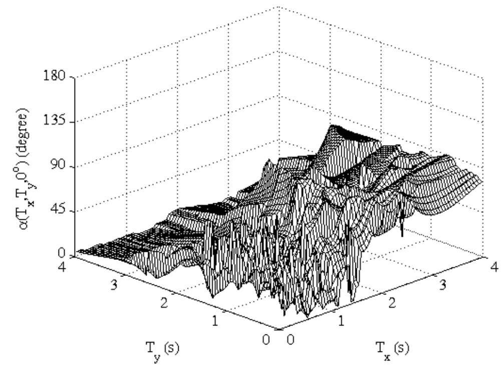

(b) $\alpha(T_x, T_y, 0^\circ)$

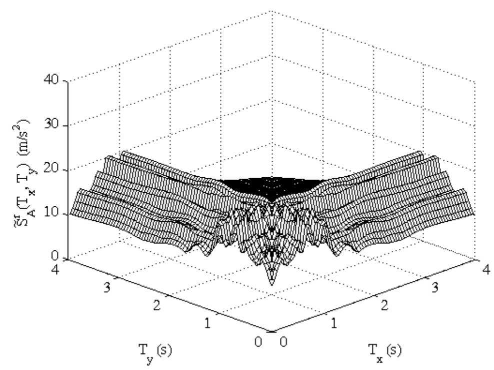

(c) $\widetilde{S}_A^r(T_x, T_y)$

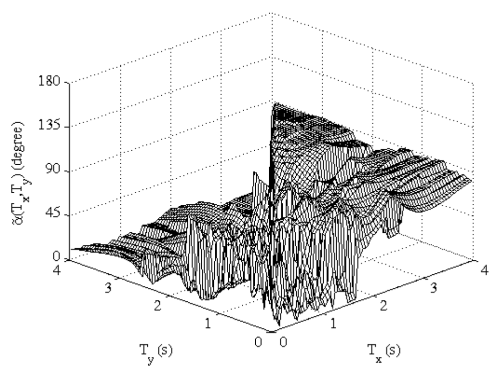

(d) $\widetilde{\alpha}(T_x, T_y)$

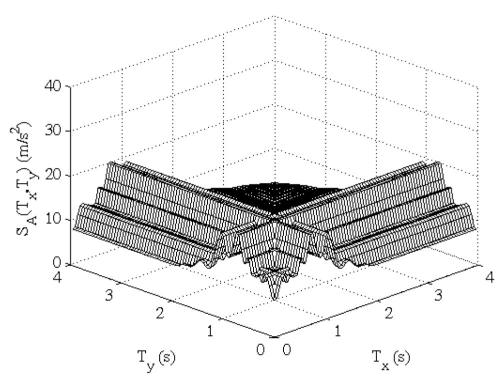

(e) $S_A(T_x, T_y)$

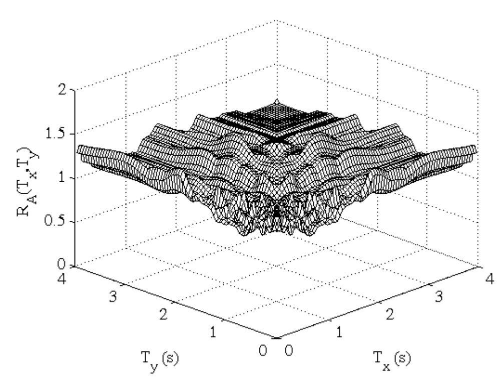

(f) $R_A(T_x, T_y)$

Figure B-63 Bi-directional responses of Northridge earthquake, 74 Sylmar - Converter station

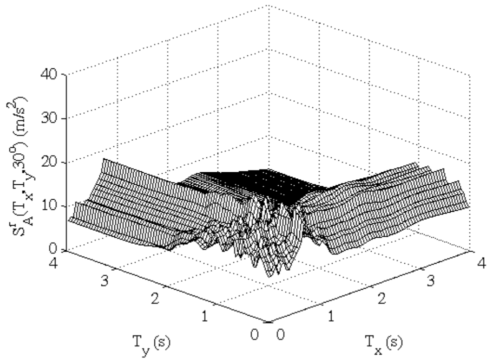

(a) $S_A^r(T_x, T_y, 30^\circ)$

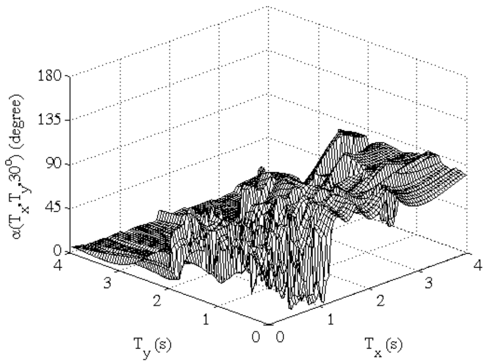

(b) $\alpha(T_x, T_y, 30^\circ)$

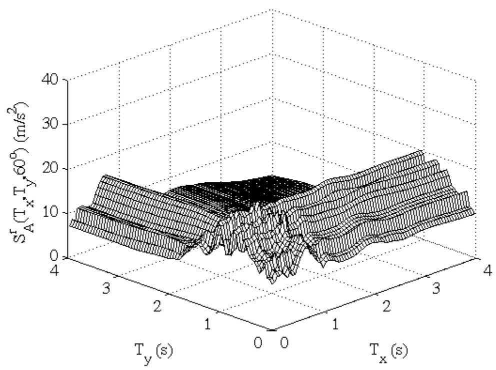

(c) $S_A^r(T_x, T_y, 60^\circ)$

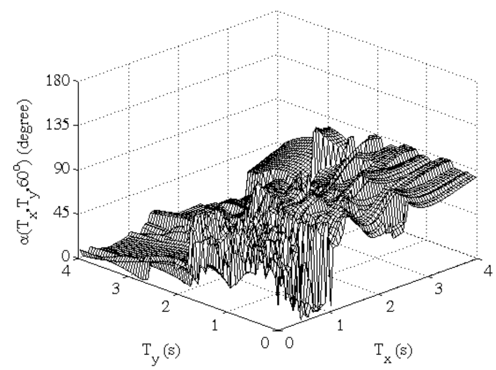

(d) $\alpha(T_x, T_y, 60^\circ)$

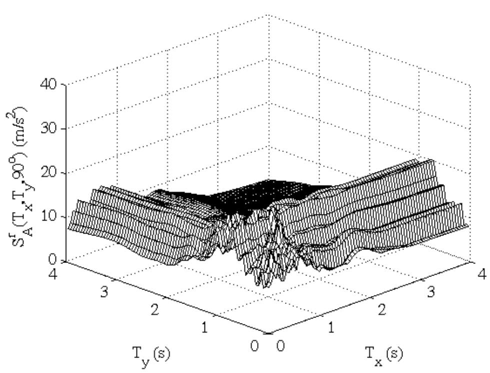

(e) $S_A^r(T_x, T_y, 90^\circ)$

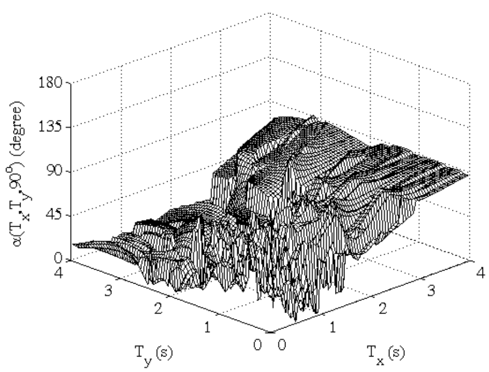

(f) $\alpha(T_x, T_y, 90^\circ)$

Figure B-64 Pseudo acceleration spectra and incident angles in various directions of Northridge earthquake, 74 Sylmar - Converter station

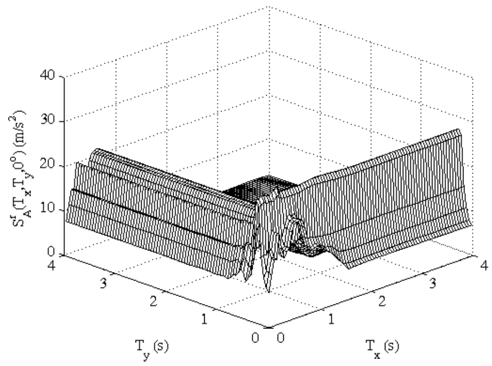

(a) $S_A^r(T_x,T_y,0^\circ)$

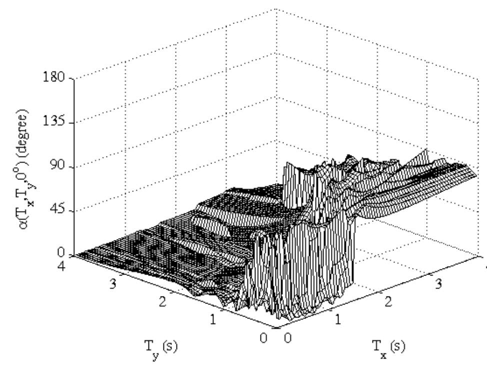

(b) $\alpha(T_x,T_y,0^\circ)$

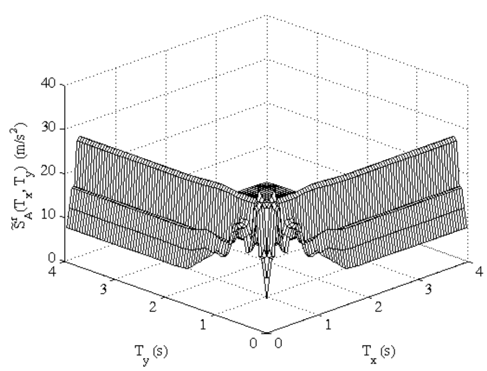

(c) $\widetilde{S}_A^r(T_x,T_y)$

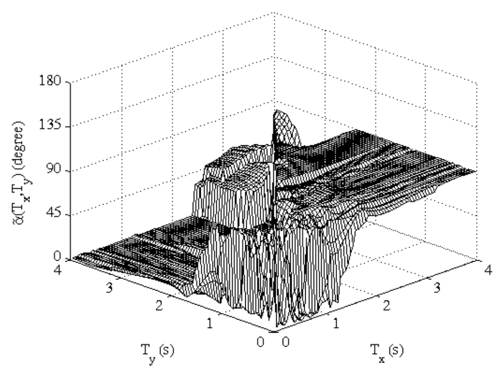

(d) $\widetilde{\alpha}(T_x,T_y)$

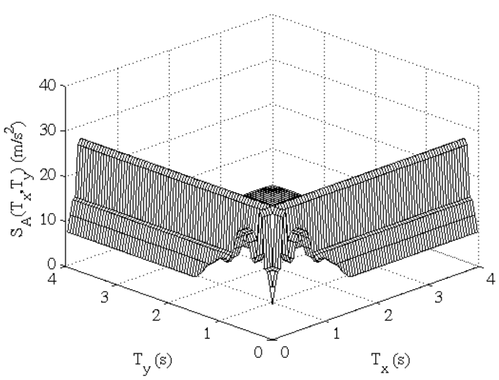

(e) $S_A(T_x,T_y)$

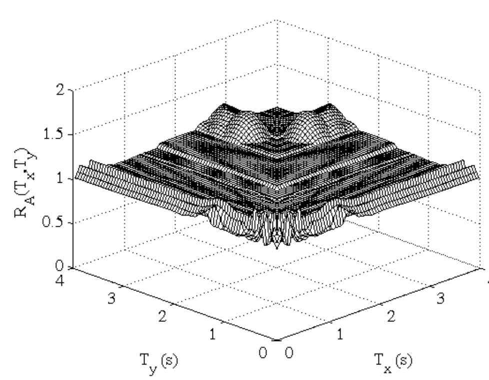

(f) $R_A(T_x,T_y)$

Figure B-65 Bi-directional responses of Northridge earthquake, 24279 Newhall - Fire station

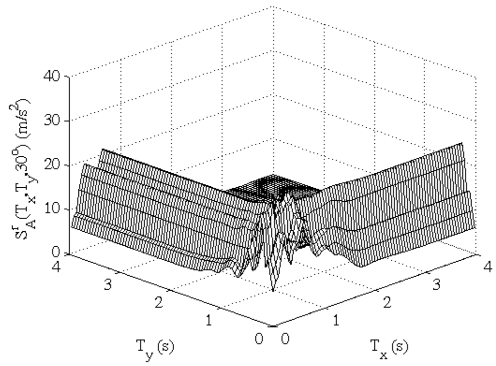

(a) $S^r_A(T_x, T_y, 30^\circ)$

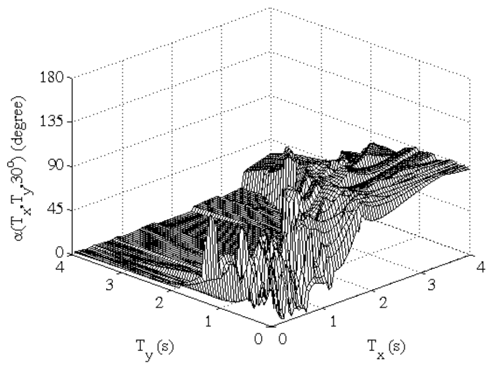

(b) $\alpha(T_x, T_y, 30^\circ)$

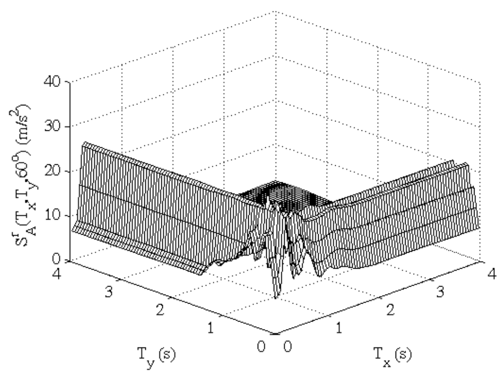

(c) $S^r_A(T_x, T_y, 60^\circ)$

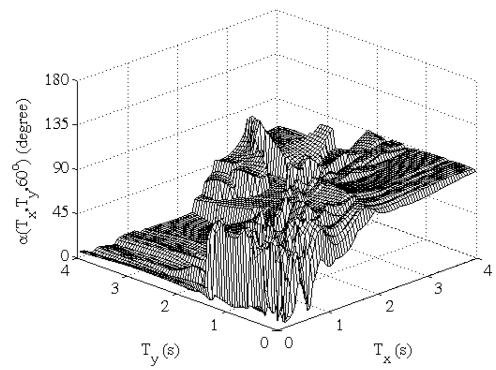

(d) $\alpha(T_x, T_y, 60^\circ)$

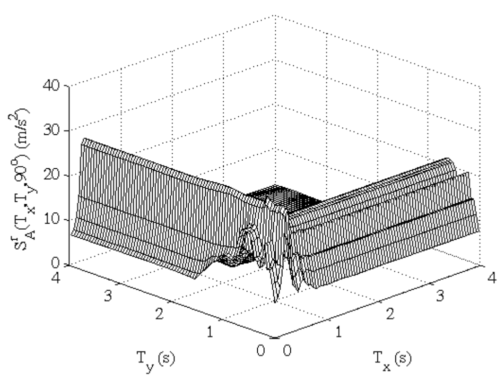

(e) $S^r_A(T_x, T_y, 90^\circ)$

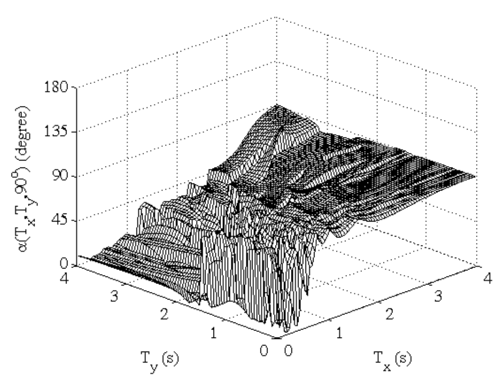

(f) $\alpha(T_x, T_y, 90^\circ)$

Figure B-66 Pseudo acceleration spectra and incident angles in various directions of Northridge earthquake, 24279 Newhall - Fire station

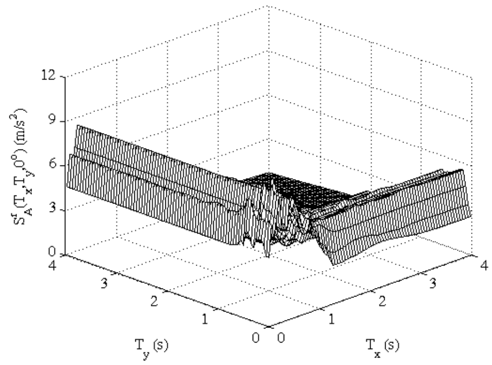

(a) $S_A^r(T_x,T_y,0^\circ)$

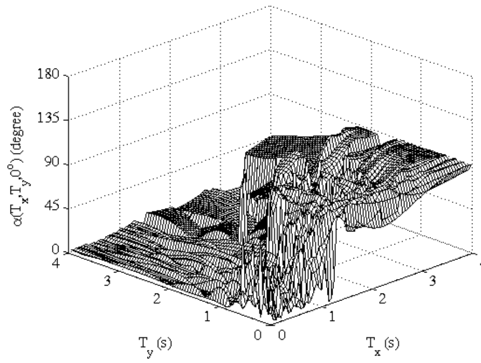

(b) $\alpha(T_x,T_y,0^\circ)$

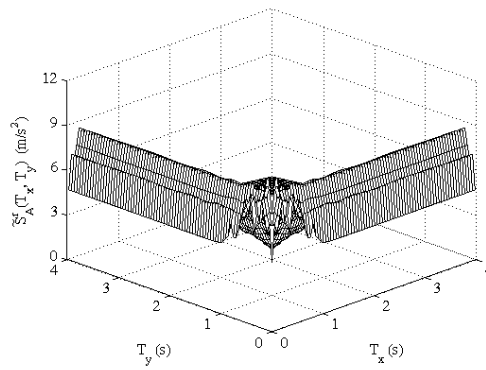

(c) $\widetilde{S}_A^r(T_x,T_y)$

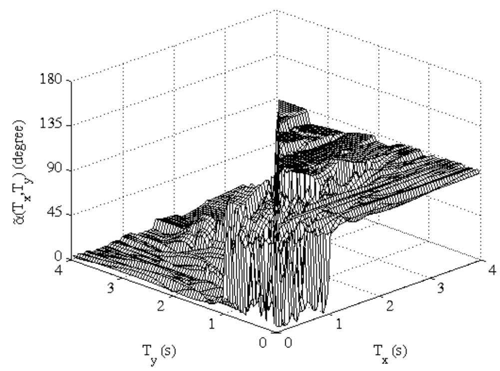

(d) $\widetilde{\alpha}(T_x,T_y)$

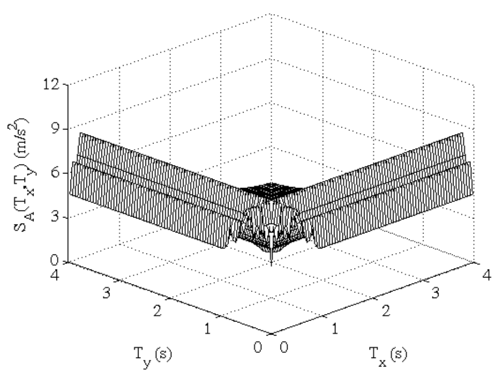

(e) $S_A(T_x,T_y)$

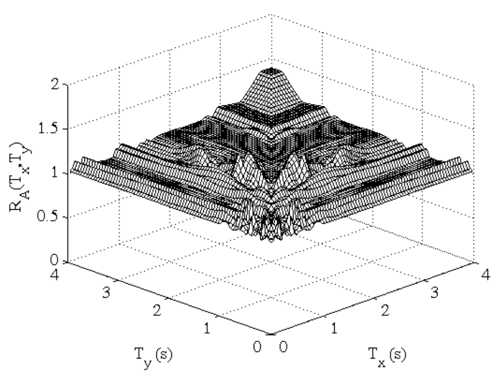

(f) $R_A(T_x,T_y)$

Figure B-67 Bi-directional responses of Imperial Valley earthquake, 117 El Centro Array #9 station

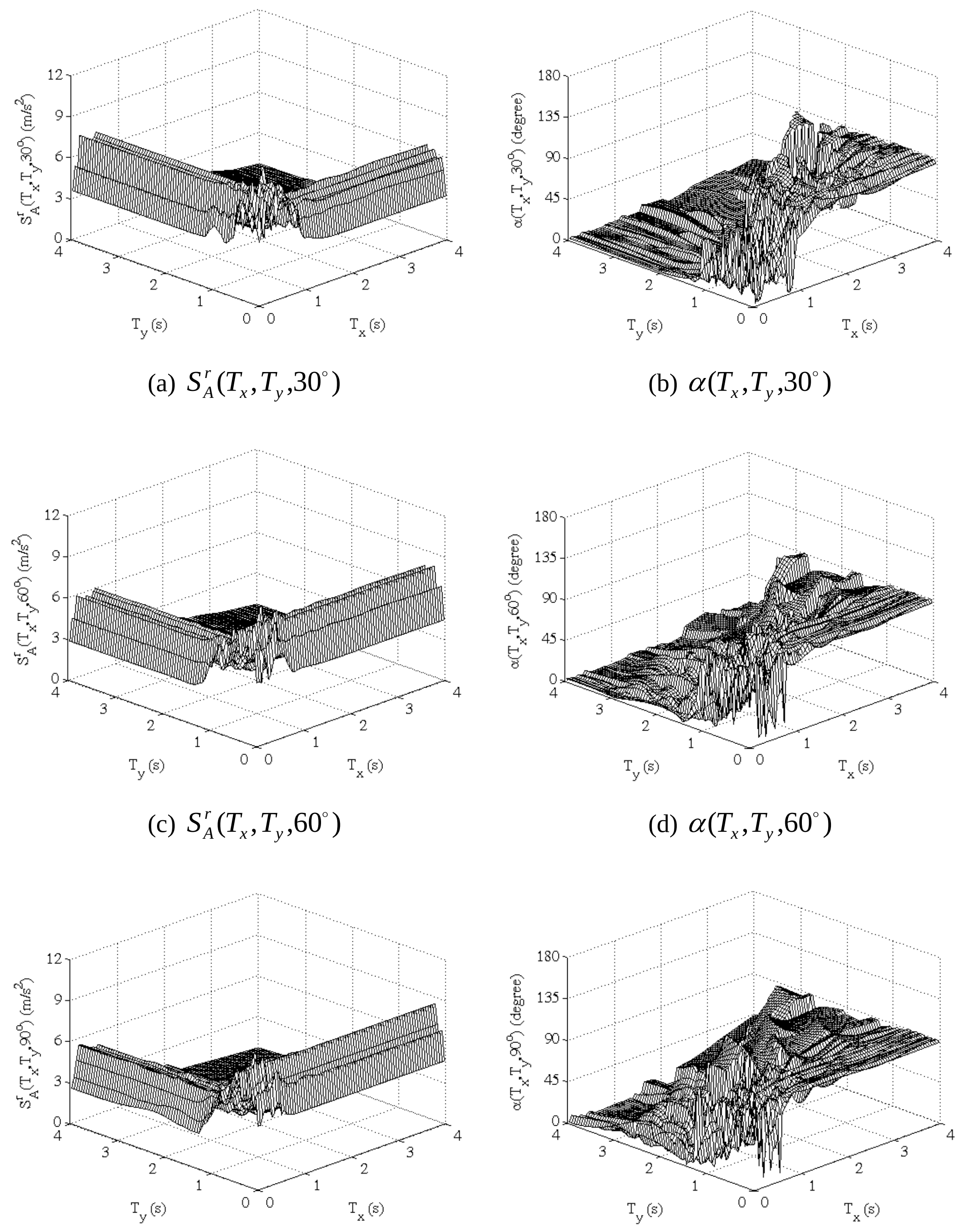

(a) $S_A^r(T_x, T_y, 30^\circ)$ (b) $\alpha(T_x, T_y, 30^\circ)$

(c) $S_A^r(T_x, T_y, 60^\circ)$ (d) $\alpha(T_x, T_y, 60^\circ)$

(e) $S_A^r(T_x, T_y, 90^\circ)$ (f) $\alpha(T_x, T_y, 90^\circ)$

Figure B-68 Pseudo acceleration spectra and incident angles in various directions of Imperial Valley earthquake, 117 El Centro Array #9 station

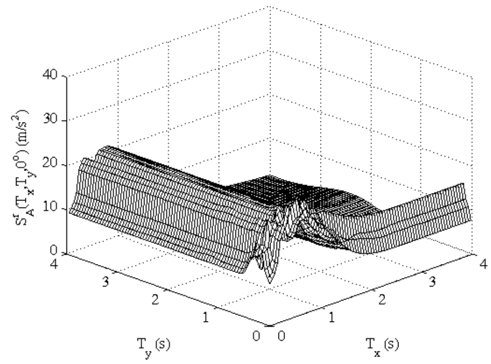

(a) $S^r_A(T_x,T_y,0^\circ)$

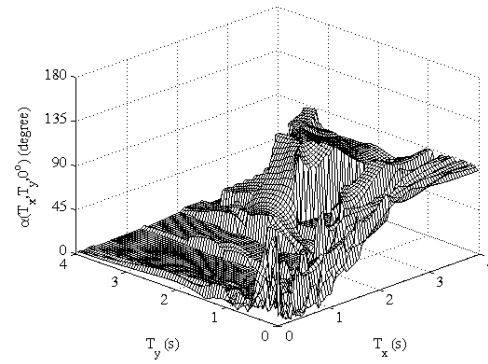

(b) $\alpha(T_x,T_y,0^\circ)$

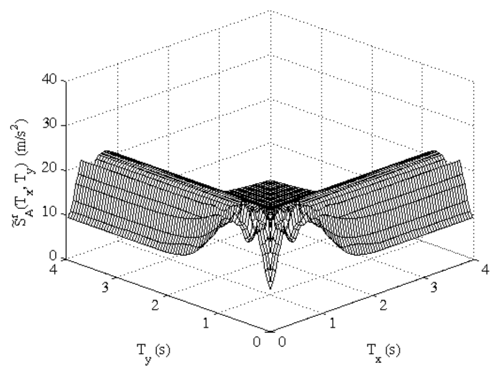

(c) $\tilde{S}^r_A(T_x,T_y)$

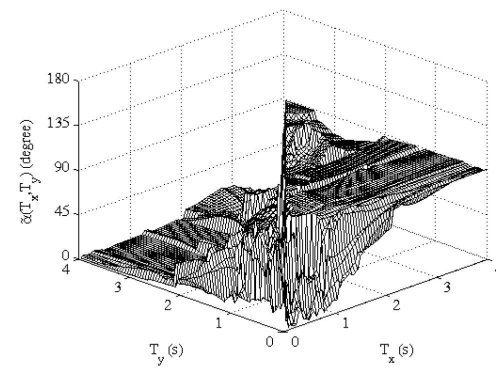

(d) $\tilde{\alpha}(T_x,T_y)$

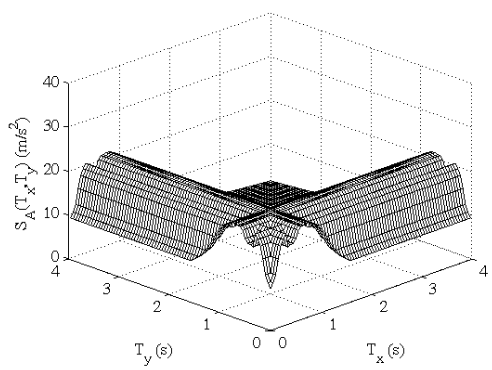

(e) $S_A(T_x,T_y)$

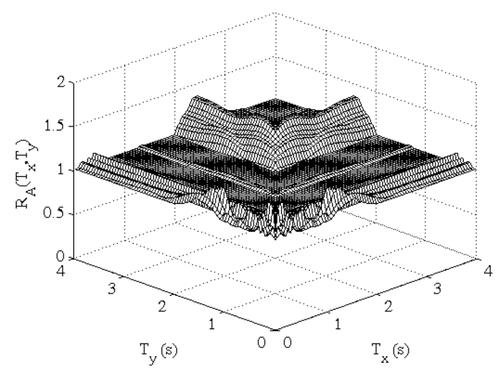

(f) $R_A(T_x,T_y)$

Figure B-69 Bi-directional responses of Northridge earthquake, 77 Rinaldi Receiving station

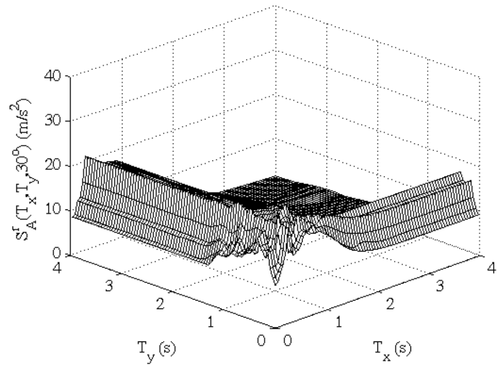

(a) $S_A^r(T_x, T_y, 30^\circ)$

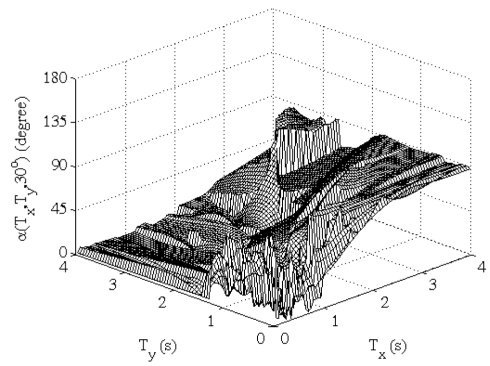

(b) $\alpha(T_x, T_y, 30^\circ)$

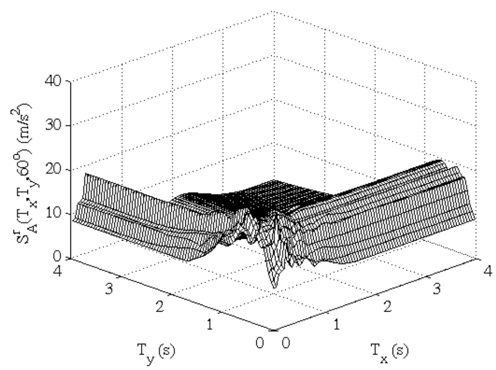

(c) $S_A^r(T_x, T_y, 60^\circ)$

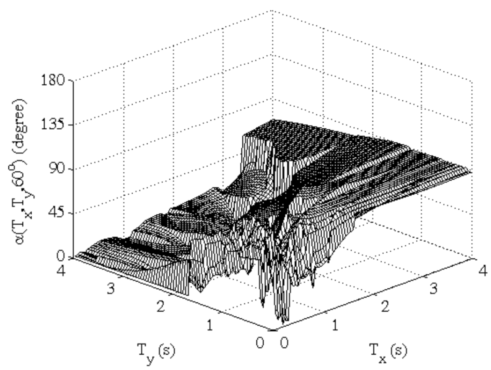

(d) $\alpha(T_x, T_y, 60^\circ)$

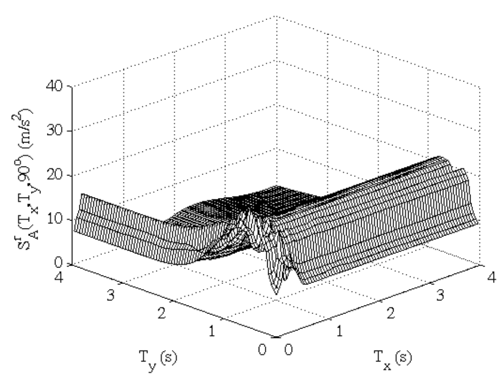

(e) $S_A^r(T_x, T_y, 90^\circ)$

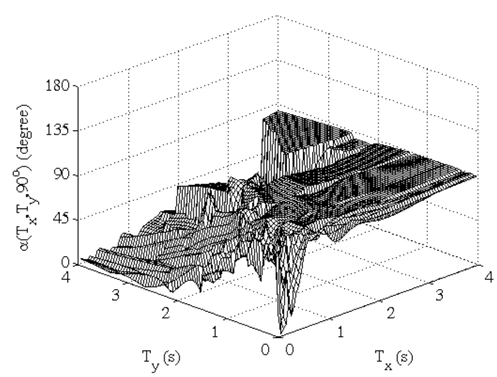

(f) $\alpha(T_x, T_y, 90^\circ)$

Figure B-70 Pseudo acceleration spectra and incident angles in various directions of Northridge earthquake, 77 Rinaldi Receiving station

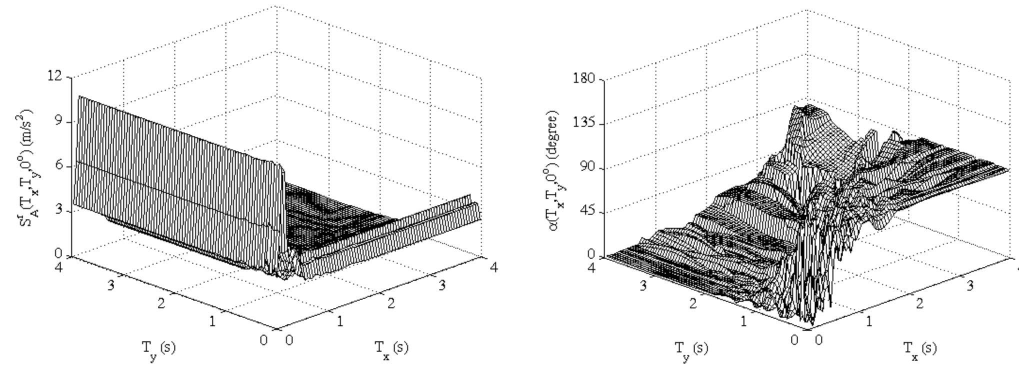

(a) $S_A^r(T_x, T_y, 0^\circ)$

(b) $\alpha(T_x, T_y, 0^\circ)$

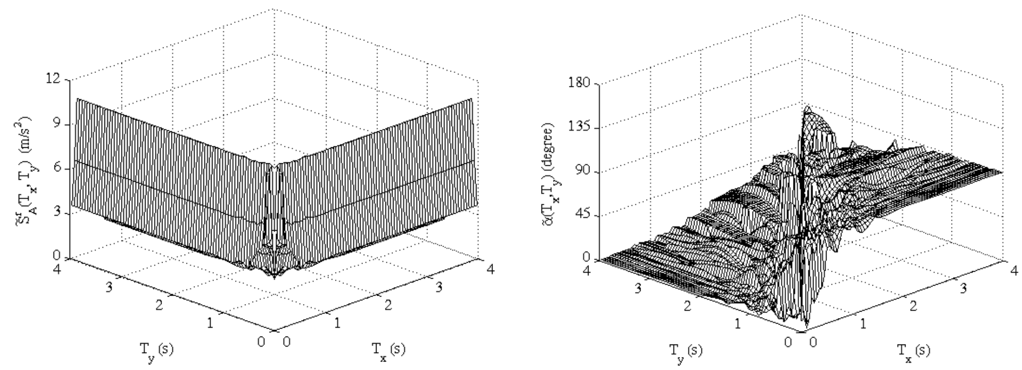

(c) $\tilde{S}_A^r(T_x, T_y)$

(d) $\tilde{\alpha}(T_x, T_y)$

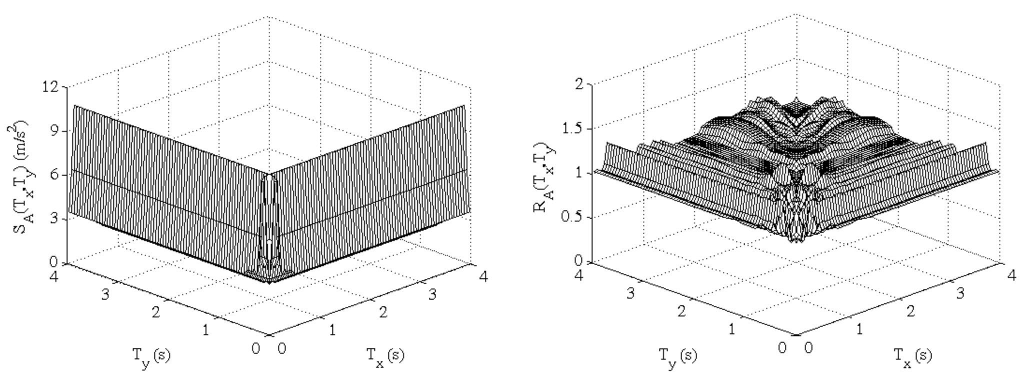

(e) $S_A(T_x, T_y)$

(f) $R_A(T_x, T_y)$

Figure B-71 Bi-directional responses of Parkfield earthquake, 1015 Cholame #8 station

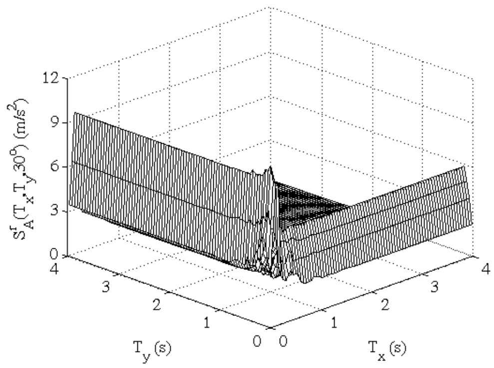

(a) $S_A^r(T_x, T_y, 30^\circ)$

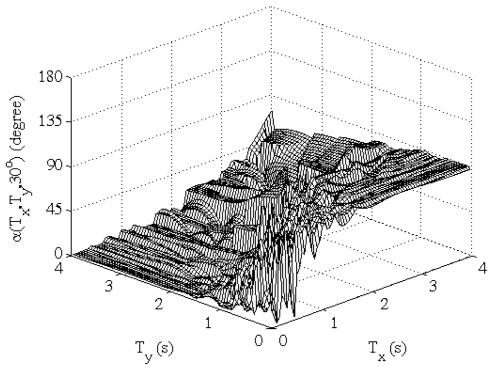

(b) $\alpha(T_x, T_y, 30^\circ)$

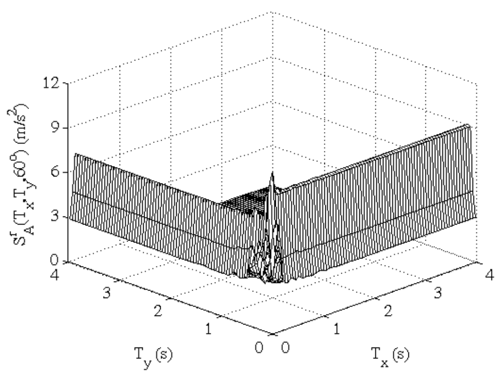

(c) $S_A^r(T_x, T_y, 60^\circ)$

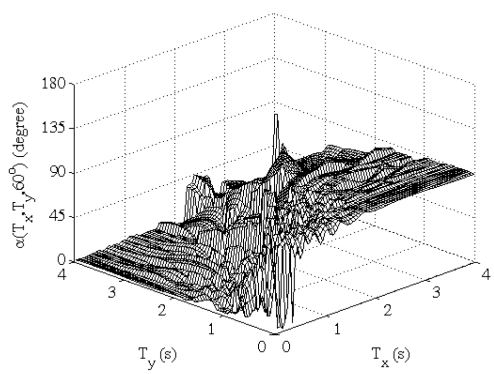

(d) $\alpha(T_x, T_y, 60^\circ)$

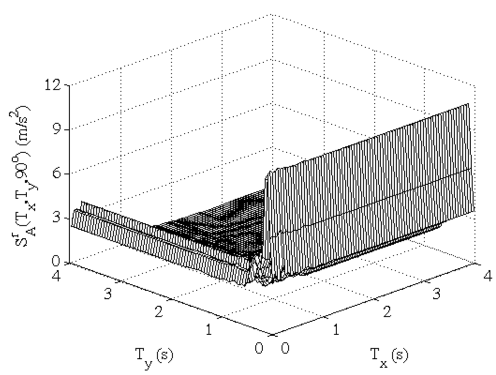

(e) $S_A^r(T_x, T_y, 90^\circ)$

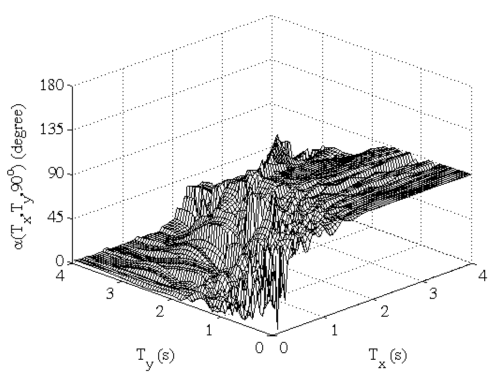

(f) $\alpha(T_x, T_y, 90^\circ)$

Figure B-72 Pseudo acceleration spectra and incident angles in various directions of Parkfield earthquake, 1015 Cholame #8 station

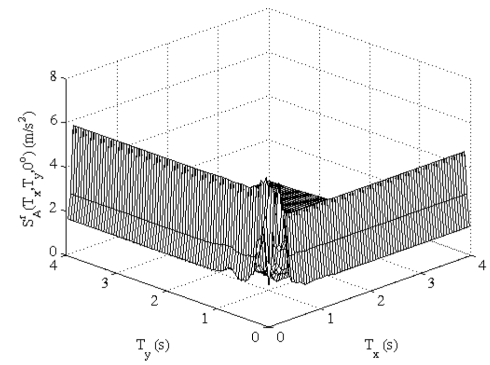

(a) $S_A^r(T_x,T_y,0^\circ)$

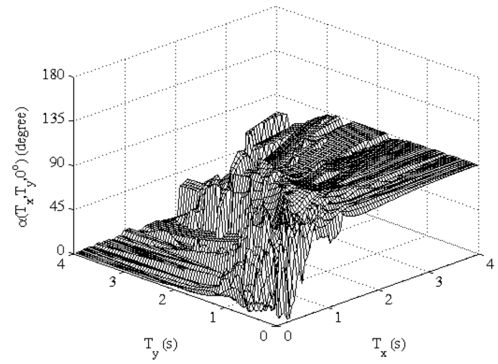

(b) $\alpha(T_x,T_y,0^\circ)$

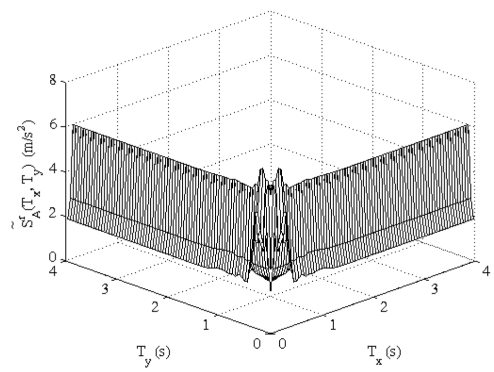

(c) $\widetilde{S}_A^r(T_x,T_y)$

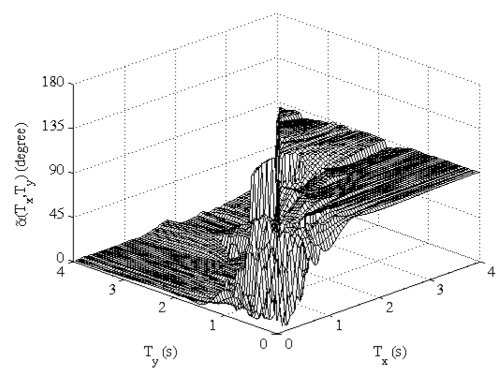

(d) $\widetilde{\alpha}(T_x,T_y)$

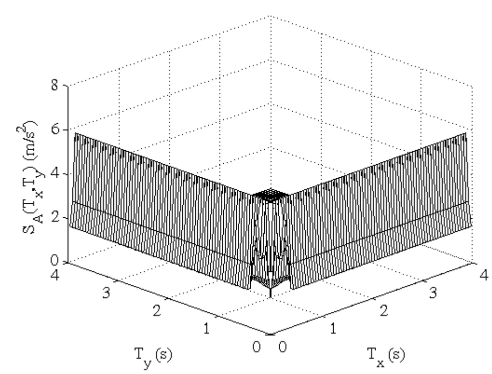

(e) $S_A(T_x,T_y)$

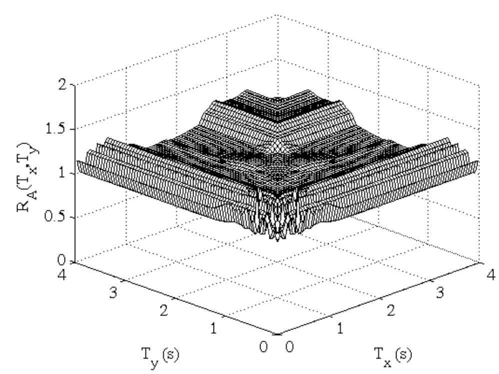

(f) $R_A(T_x,T_y)$

Figure B-73 Bi-directional responses of Whittier Narrows earthquake, 90071 West Covina - S Orange station

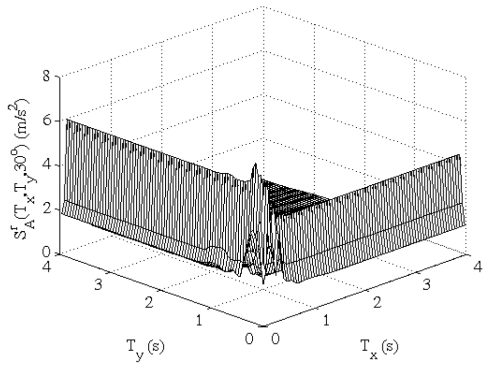

(a) $S_A^r(T_x, T_y, 30^\circ)$

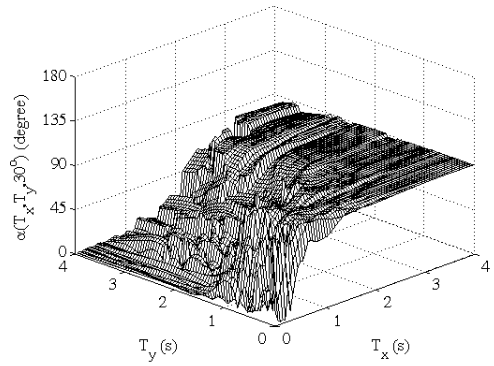

(b) $\alpha(T_x, T_y, 30^\circ)$

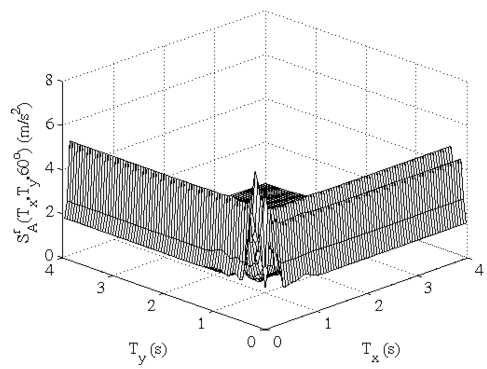

(c) $S_A^r(T_x, T_y, 60^\circ)$

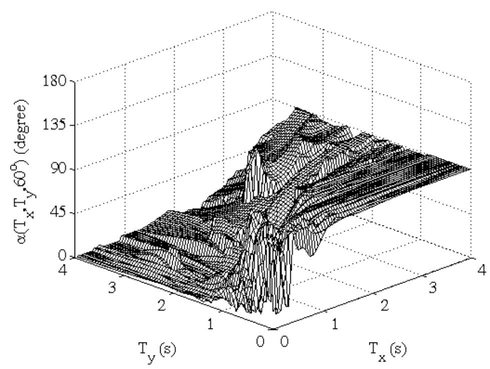

(d) $\alpha(T_x, T_y, 60^\circ)$

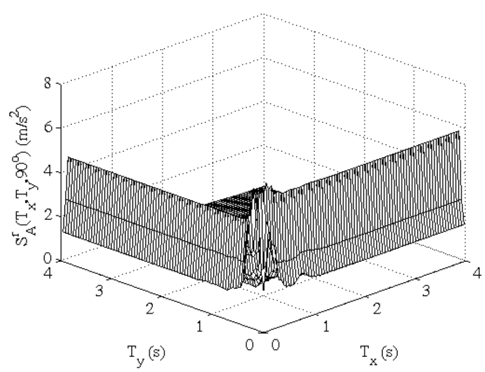

(e) $S_A^r(T_x, T_y, 90^\circ)$

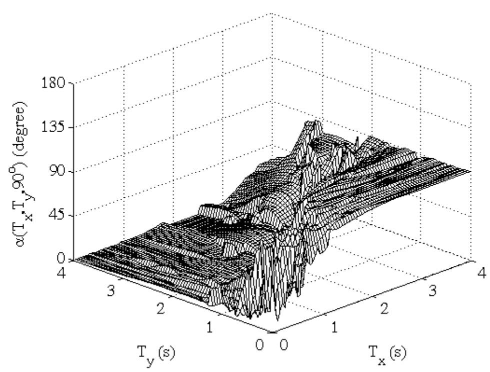

(f) $\alpha(T_x, T_y, 90^\circ)$

Figure B-74 Pseudo acceleration spectra and incident angles in various directions of Whittier Narrows earthquake, 90071 West Covina - S Orange station

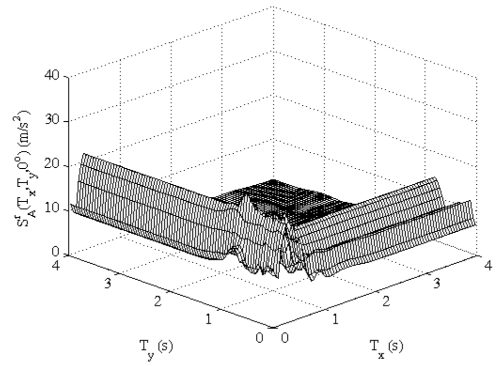

(a) $S_A^r(T_x, T_y, 0^\circ)$

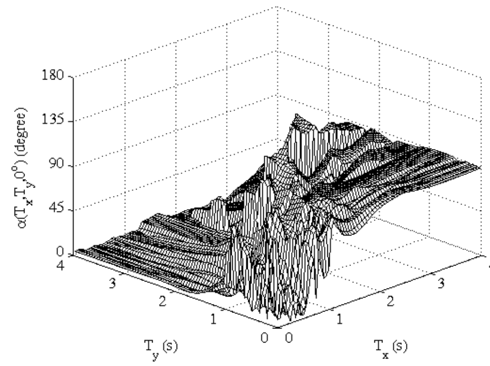

(b) $\alpha(T_x, T_y, 0^\circ)$

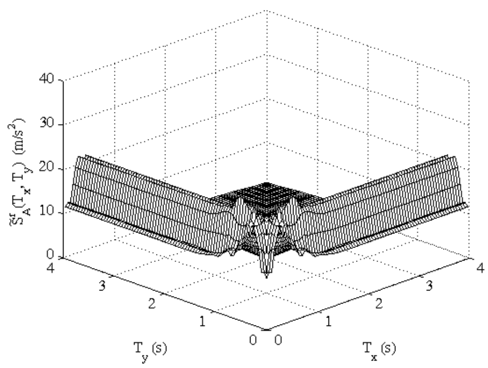

(c) $\widetilde{S}_A^r(T_x, T_y)$

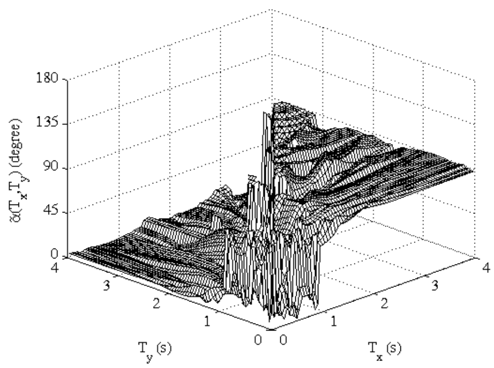

(d) $\widetilde{\alpha}(T_x, T_y)$

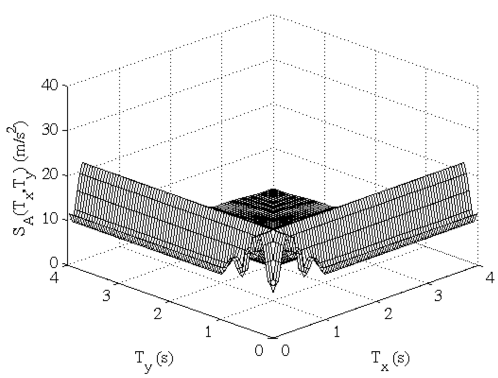

(e) $S_A(T_x, T_y)$

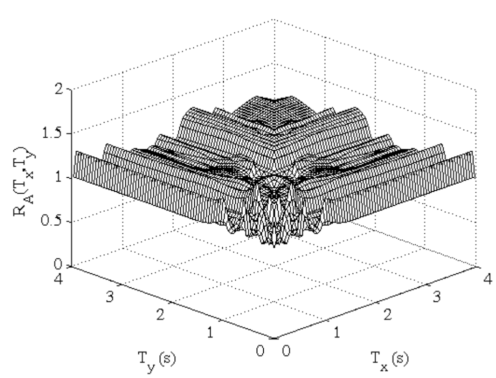

(f) $R_A(T_x, T_y)$

Figure B-75 Bi-directional responses of Duzce, Turkey earthquake, Bolu station

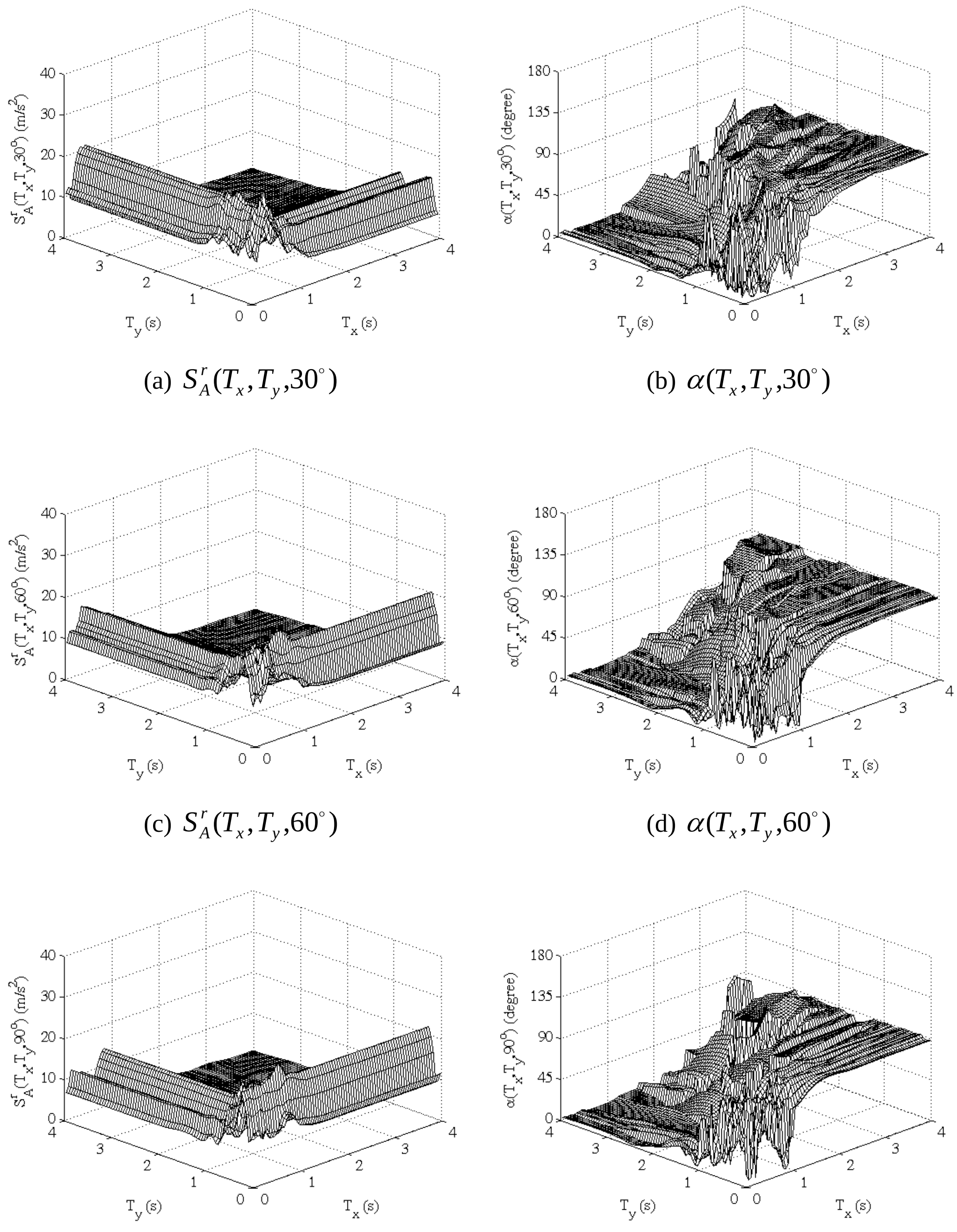

(a) $S_A^r(T_x,T_y,30^\circ)$ (b) $\alpha(T_x,T_y,30^\circ)$

(c) $S_A^r(T_x,T_y,60^\circ)$ (d) $\alpha(T_x,T_y,60^\circ)$

(e) $S_A^r(T_x,T_y,90^\circ)$ (f) $\alpha(T_x,T_y,90^\circ)$

Figure B-76 Pseudo acceleration spectra and incident angles in various directions of Duzce, Turkey earthquake, Bolu station

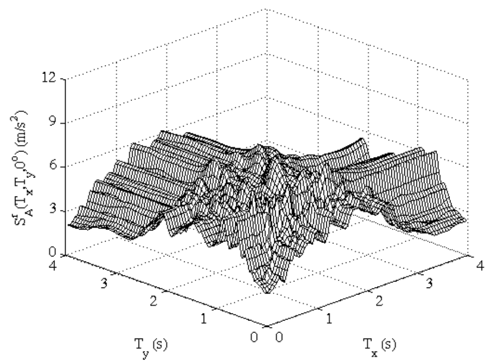

(a) $S_A^r(T_x,T_y,0^\circ)$

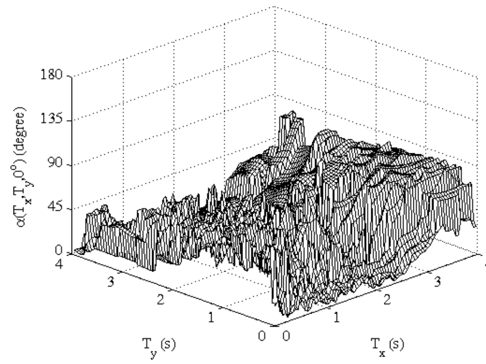

(b) $\alpha(T_x,T_y,0^\circ)$

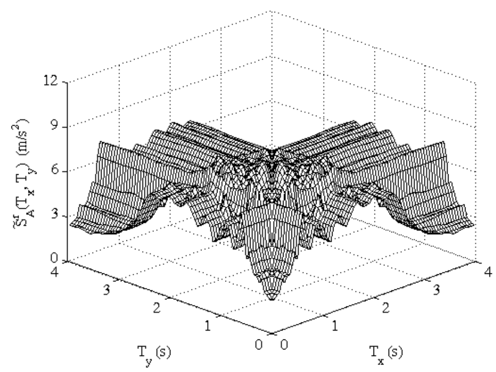

(c) $\widetilde{S}_A^r(T_x,T_y)$

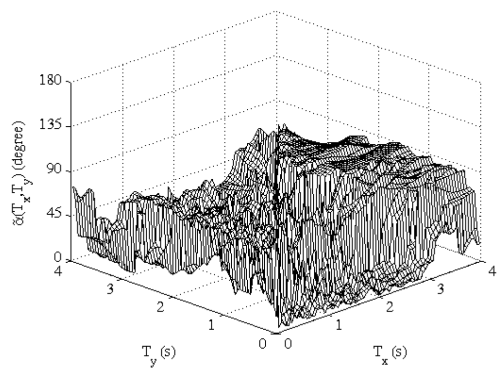

(d) $\widetilde{\alpha}(T_x,T_y)$

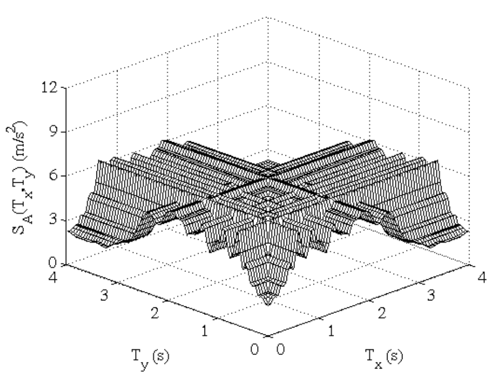

(e) $S_A(T_x,T_y)$

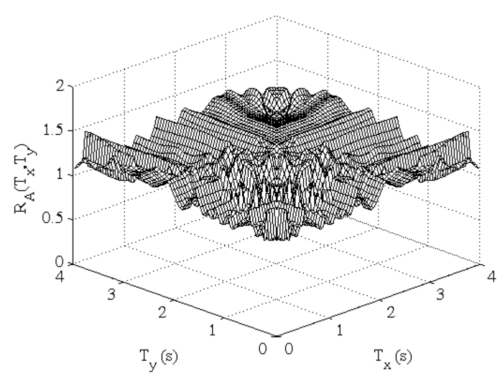

(f) $R_A(T_x,T_y)$

Figure B-77 Bi-directional responses of Chi-Chi, Taiwan earthquake, TCU110 station

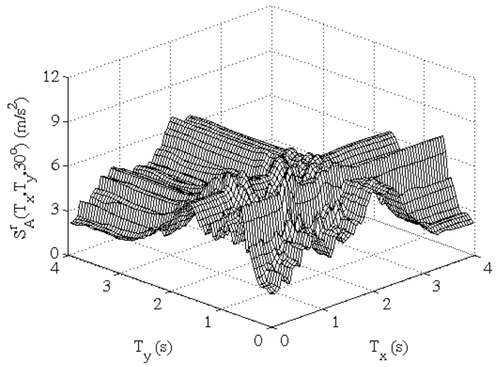

(a) $S_A^r(T_x, T_y, 30^\circ)$

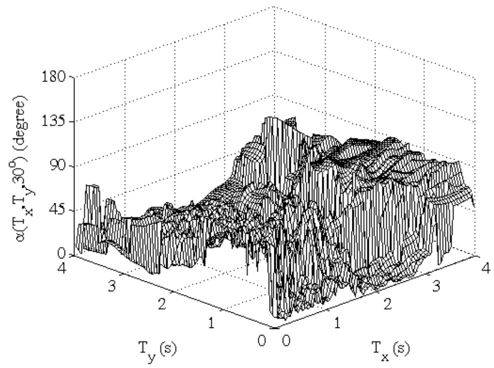

(b) $\alpha(T_x, T_y, 30^\circ)$

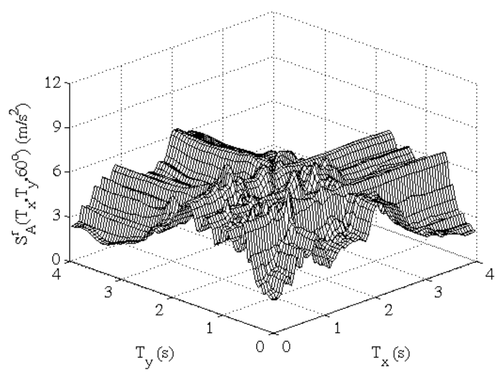

(c) $S_A^r(T_x, T_y, 60^\circ)$

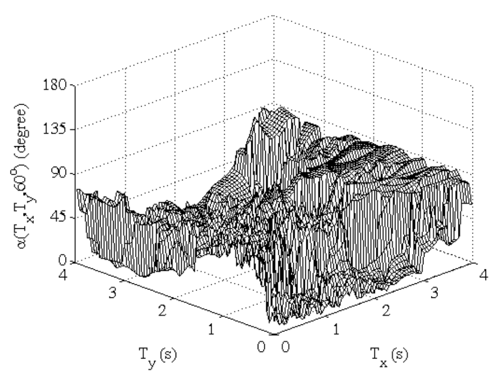

(d) $\alpha(T_x, T_y, 60^\circ)$

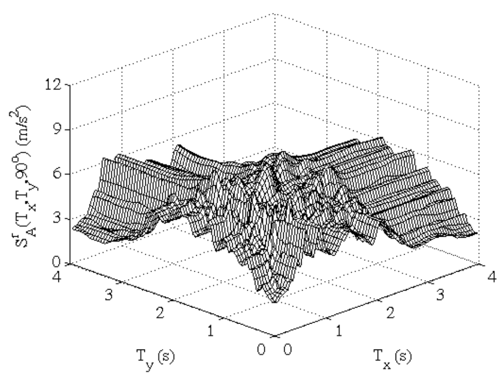

(e) $S_A^r(T_x, T_y, 90^\circ)$

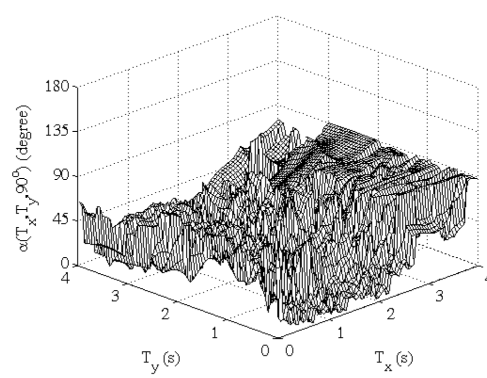

(f) $\alpha(T_x, T_y, 90^\circ)$

Figure B-78 Pseudo acceleration spectra and incident angles in various directions of Chi-Chi, Taiwan earthquake, TCU110 station

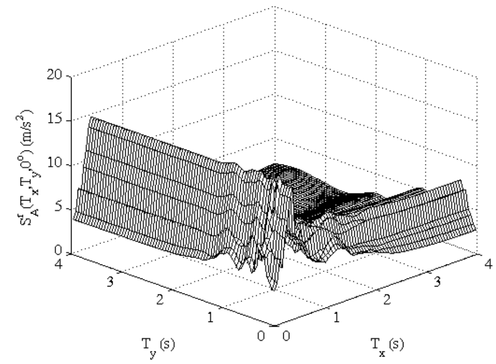

(a) $S_A^r(T_x, T_y, 0^\circ)$

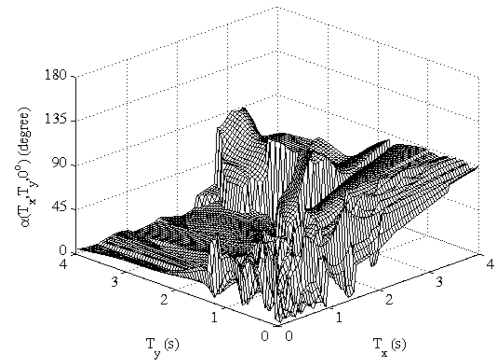

(b) $\alpha(T_x, T_y, 0^\circ)$

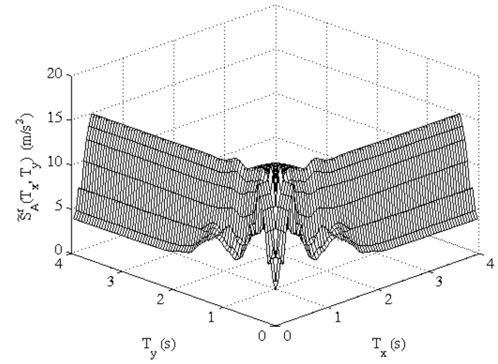

(c) $\tilde{S}_A^r(T_x, T_y)$

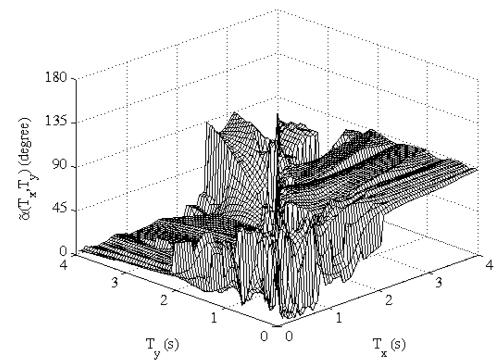

(d) $\tilde{\alpha}(T_x, T_y)$

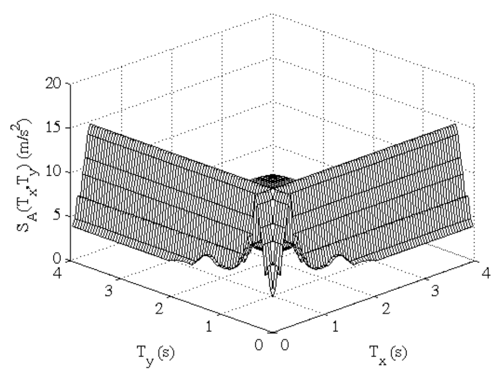

(e) $S_A(T_x, T_y)$

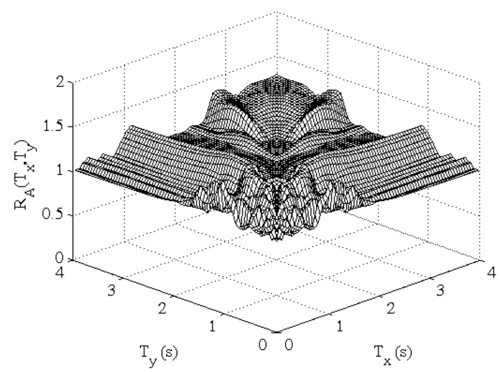

(f) $R_A(T_x, T_y)$

Figure B-79 Bi-directional responses of Kocaeli, Turkey earthquake, Duzce station

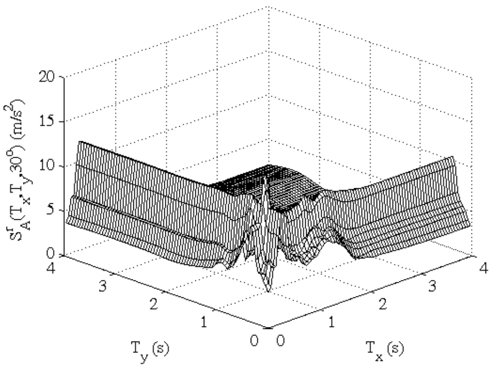

(a) $S_A^r(T_x, T_y, 30^\circ)$

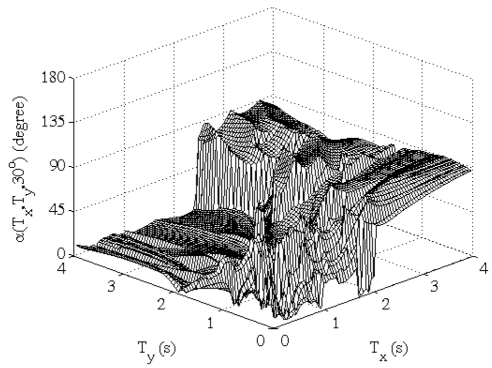

(b) $\alpha(T_x, T_y, 30^\circ)$

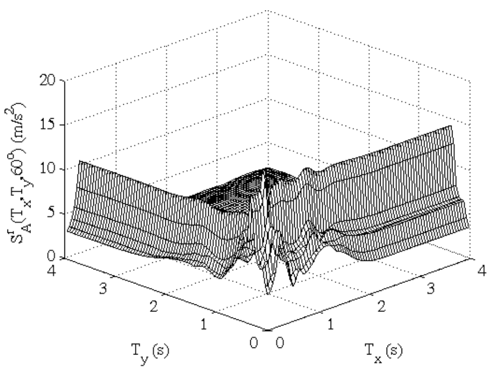

(c) $S_A^r(T_x, T_y, 60^\circ)$

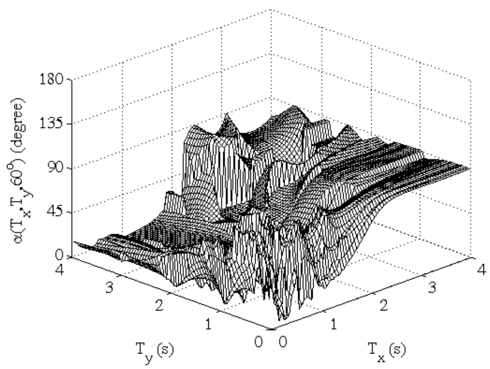

(d) $\alpha(T_x, T_y, 60^\circ)$

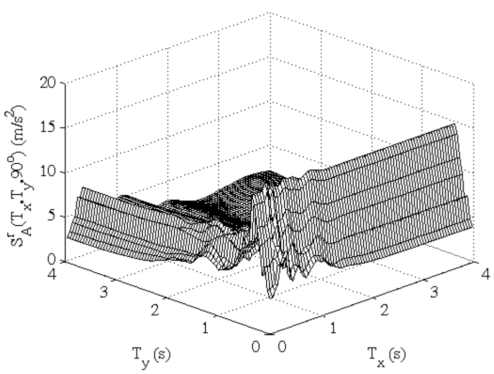

(e) $S_A^r(T_x, T_y, 90^\circ)$

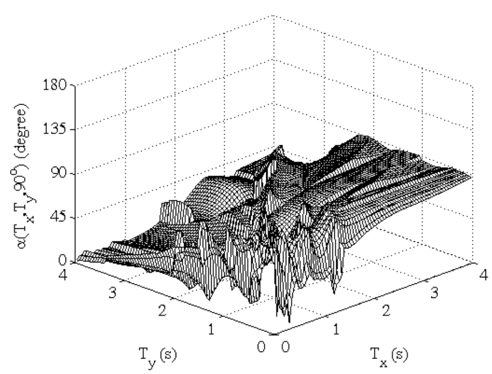

(f) $\alpha(T_x, T_y, 90^\circ)$

Figure B-80 Pseudo acceleration spectra and incident angles in various directions of Kocaeli, Turkey earthquake, Duzce station

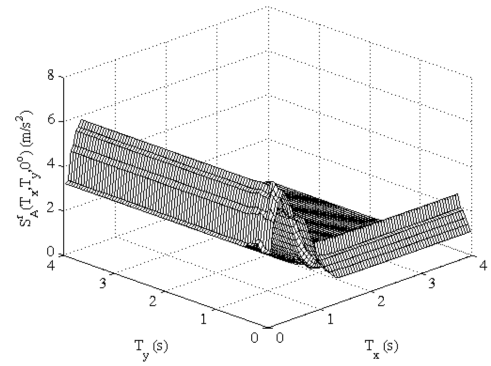

(a) $S_A^r(T_x, T_y, 0^\circ)$

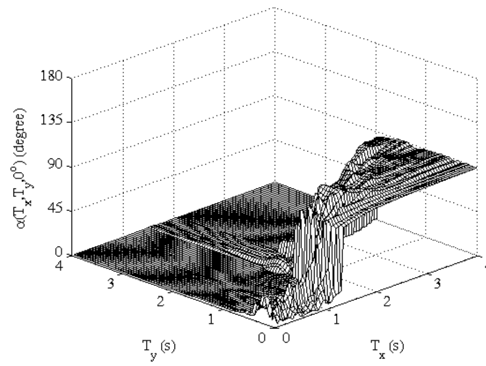

(b) $\alpha(T_x, T_y, 0^\circ)$

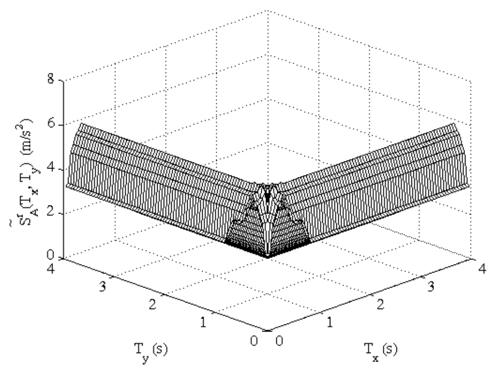

(c) $\tilde{S}_A^r(T_x, T_y)$

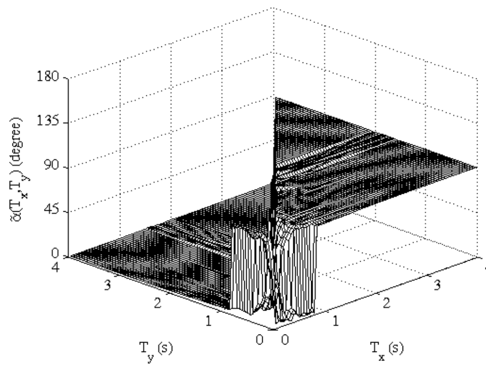

(d) $\tilde{\alpha}(T_x, T_y)$

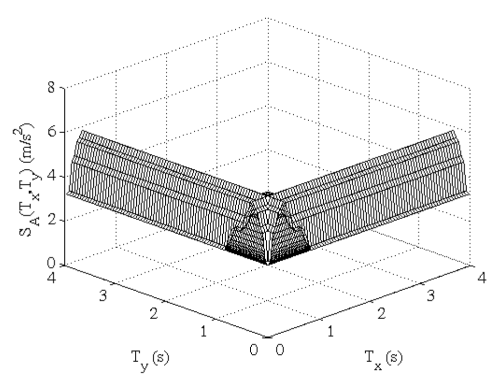

(e) $S_A(T_x, T_y)$

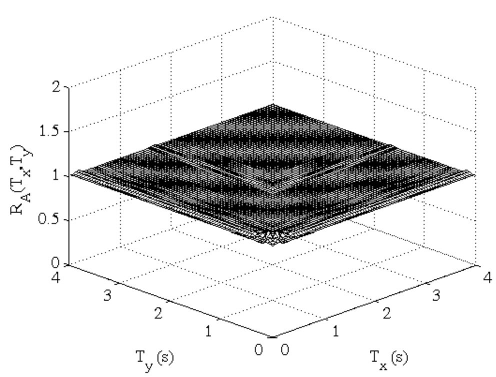

(f) $R_A(T_x, T_y)$

Figure B-81 Bi-directional responses of Livermore earthquake, 57187 San Ramon - Eastman Kodak station

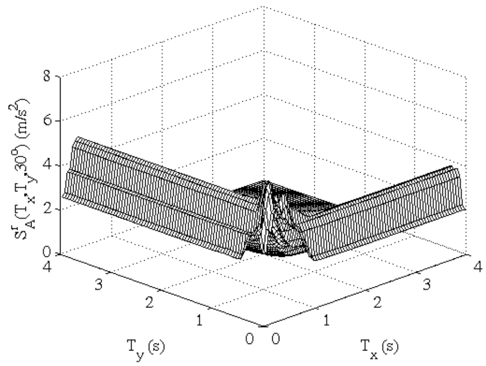

(a) $S_A^r(T_x, T_y, 30^\circ)$

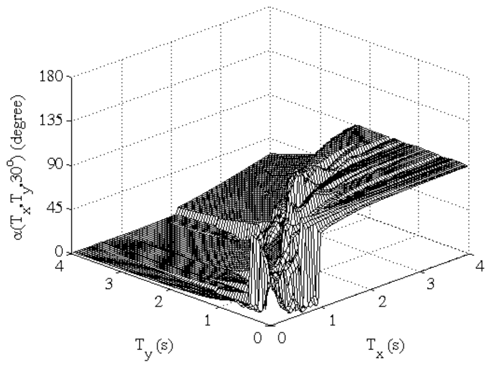

(b) $\alpha(T_x, T_y, 30^\circ)$

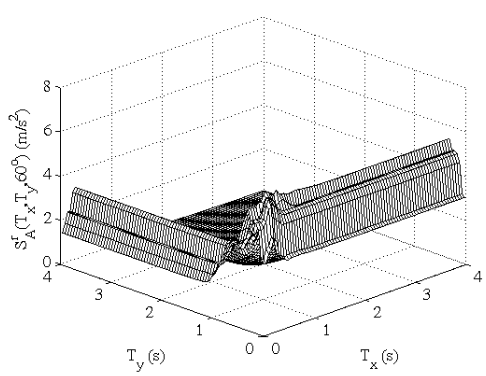

(c) $S_A^r(T_x, T_y, 60^\circ)$

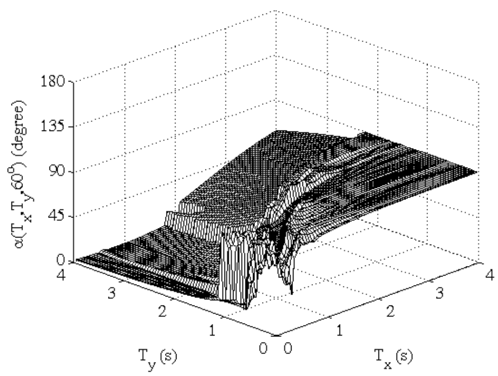

(d) $\alpha(T_x, T_y, 60^\circ)$

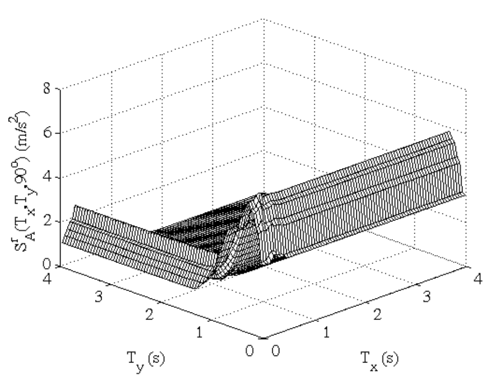

(e) $S_A^r(T_x, T_y, 90^\circ)$

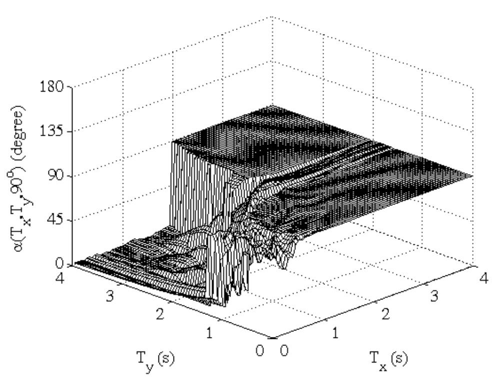

(f) $\alpha(T_x, T_y, 90^\circ)$

Figure B-82 Pseudo acceleration spectra and incident angles in various directions of Livermore earthquake, 57187 San Ramon - Eastman Kodak station

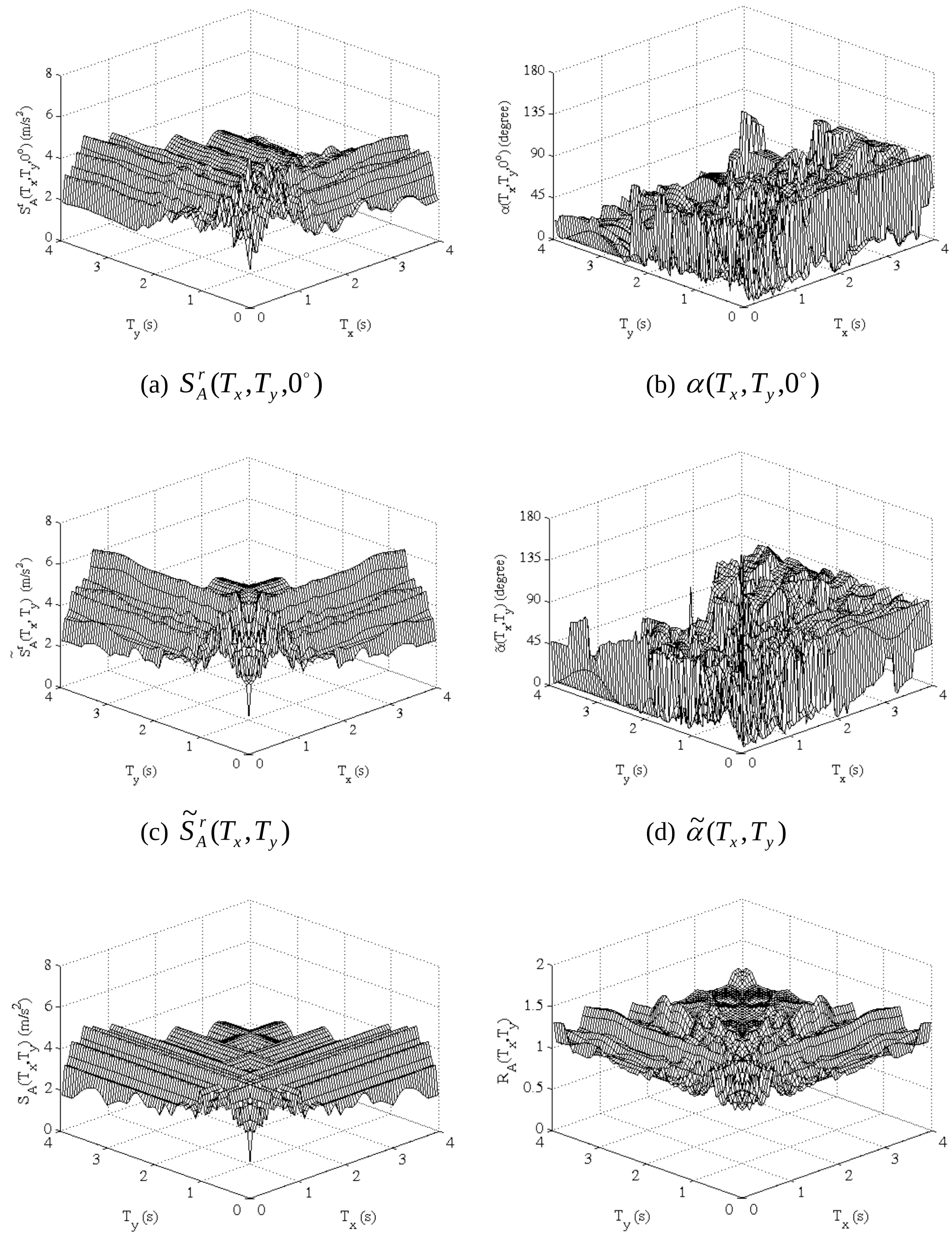

(a) $S_A^r(T_x,T_y,0^\circ)$ (b) $\alpha(T_x,T_y,0^\circ)$

(c) $\widetilde{S}_A^r(T_x,T_y)$ (d) $\widetilde{\alpha}(T_x,T_y)$

(e) $S_A(T_x,T_y)$ (f) $R_A(T_x,T_y)$

Figure B-83 Bi-directional responses of Chi-Chi, Taiwan earthquake, CHY025 station

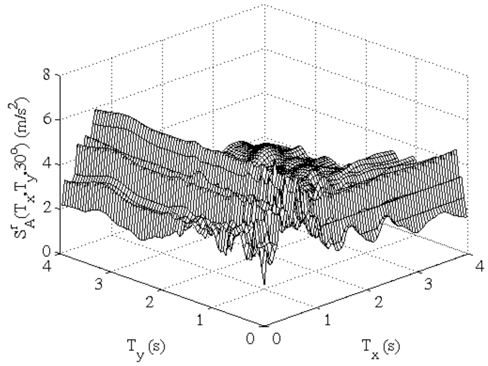

(a) $S_A^r(T_x, T_y, 30^\circ)$

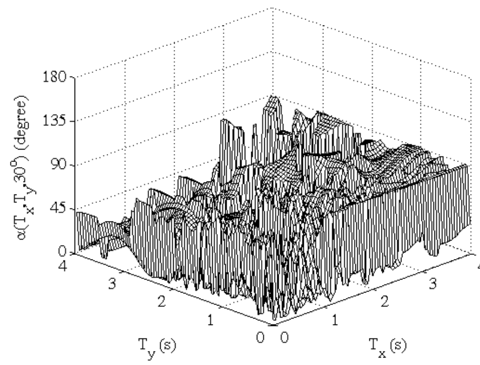

(b) $\alpha(T_x, T_y, 30^\circ)$

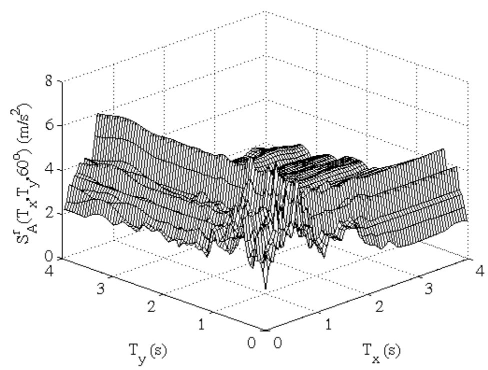

(c) $S_A^r(T_x, T_y, 60^\circ)$

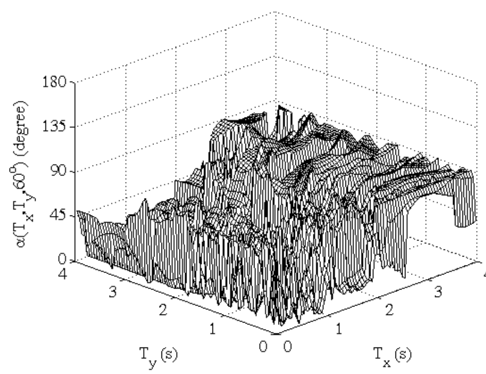

(d) $\alpha(T_x, T_y, 60^\circ)$

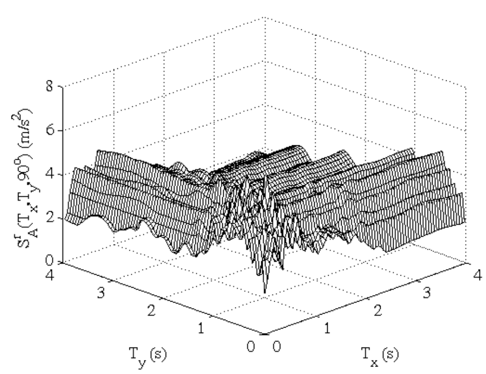

(e) $S_A^r(T_x, T_y, 90^\circ)$

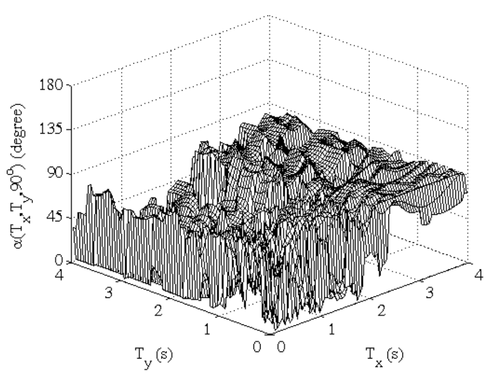

(f) $\alpha(T_x, T_y, 90^\circ)$

Figure B-84 Pseudo acceleration spectra and incident angles in various directions of Chi-Chi, Taiwan earthquake, CHY025 station

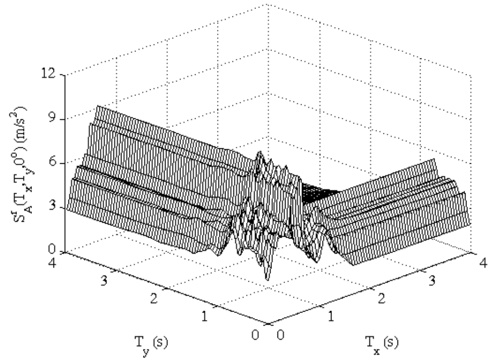

(a) $S_A^r(T_x, T_y, 0^\circ)$

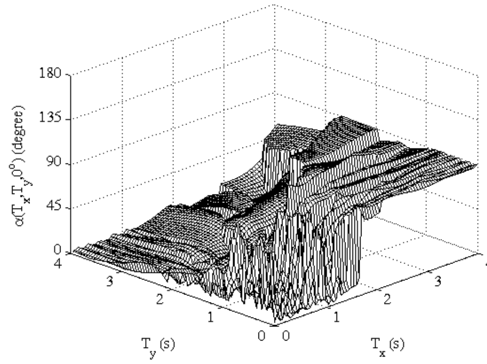

(b) $\alpha(T_x, T_y, 0^\circ)$

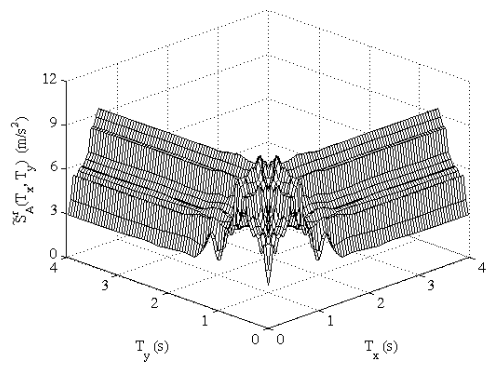

(c) $\widetilde{S}_A^r(T_x, T_y)$

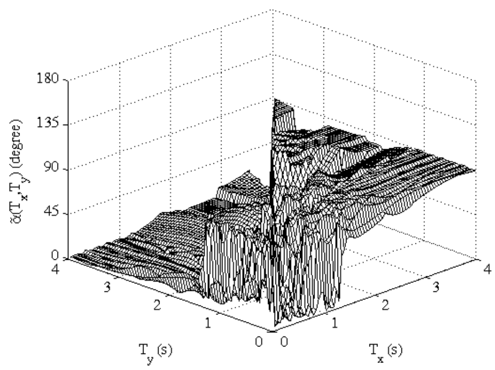

(d) $\widetilde{\alpha}(T_x, T_y)$

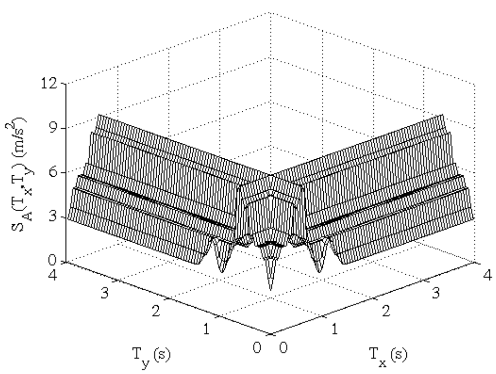

(e) $S_A(T_x, T_y)$

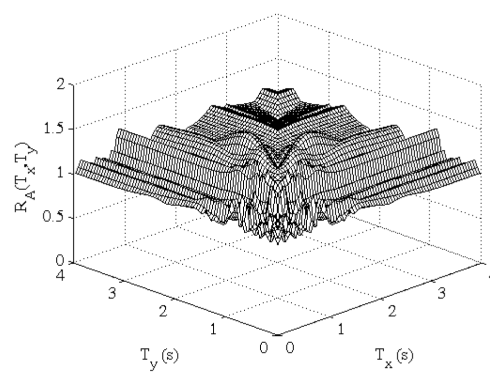

(f) $R_A(T_x, T_y)$

Figure B-85 Bi-directional responses of Kobe earthquake, 0 Shin-Osaka station

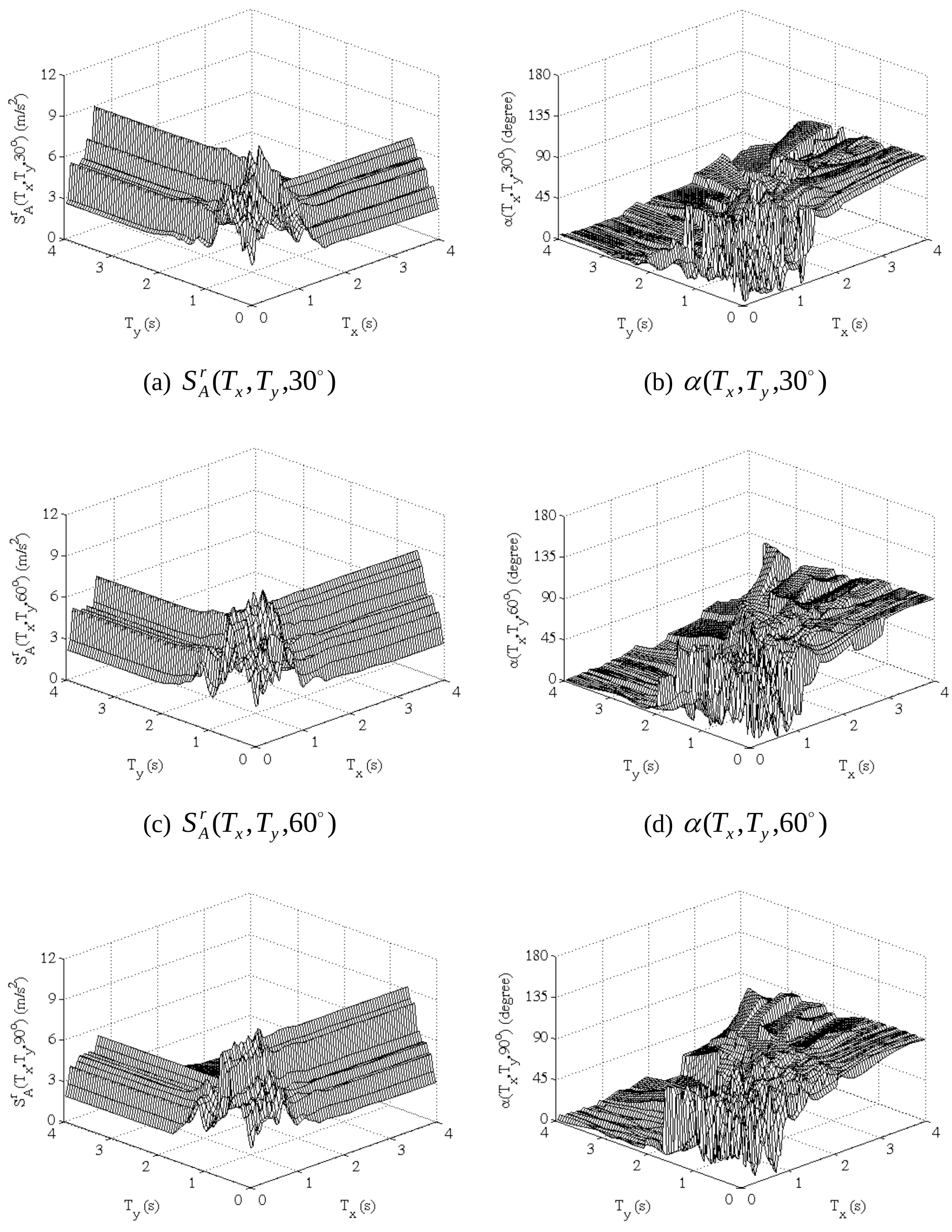

(a) $S_A^r(T_x, T_y, 30^\circ)$ (b) $\alpha(T_x, T_y, 30^\circ)$

(c) $S_A^r(T_x, T_y, 60^\circ)$ (d) $\alpha(T_x, T_y, 60^\circ)$

(e) $S_A^r(T_x, T_y, 90^\circ)$ (f) $\alpha(T_x, T_y, 90^\circ)$

Figure B-86 Pseudo acceleration spectra and incident angles in various directions of Kobe earthquake, 0 Shin-Osaka station

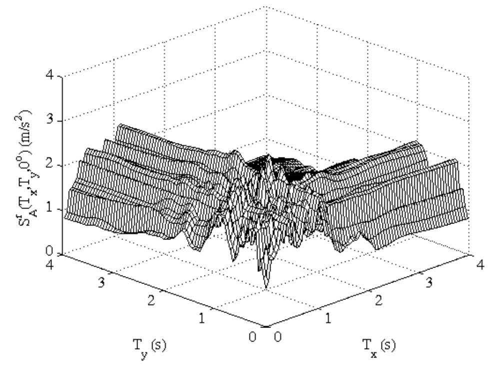

(a) $S_A^r(T_x, T_y, 0^\circ)$

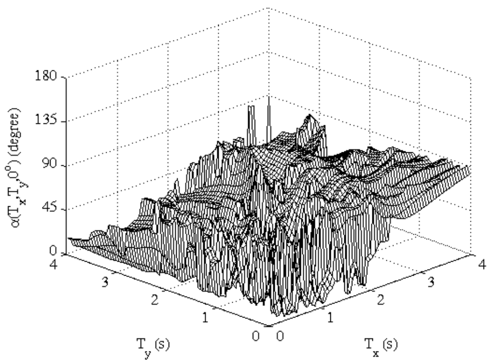

(b) $\alpha(T_x, T_y, 0^\circ)$

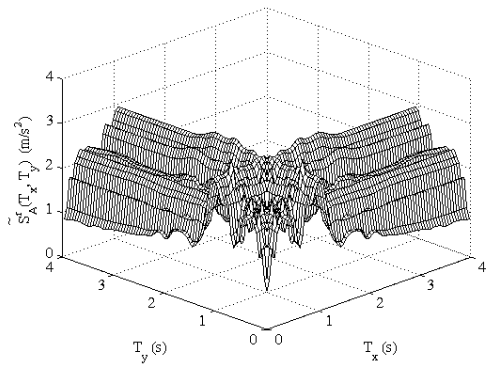

(c) $\tilde{S}_A^r(T_x, T_y)$

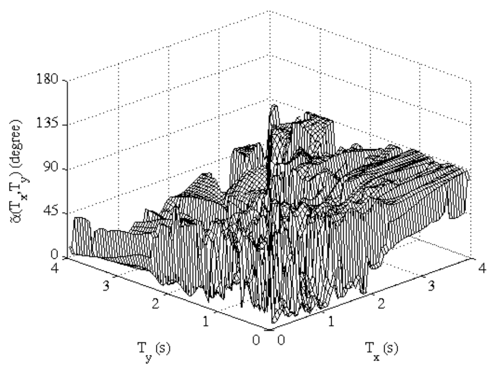

(d) $\tilde{\alpha}(T_x, T_y)$

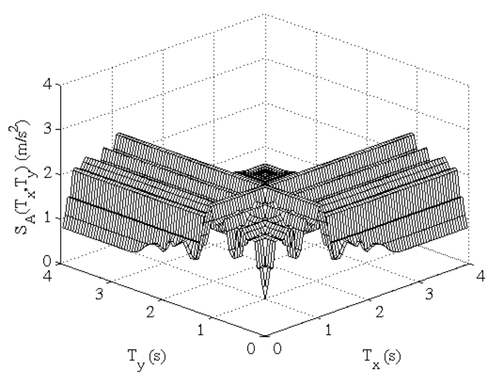

(e) $S_A(T_x, T_y)$

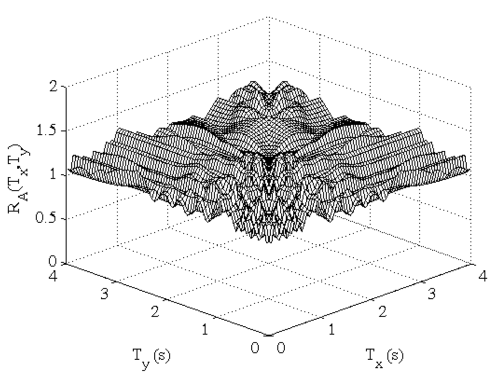

(f) $R_A(T_x, T_y)$

Figure B-87 Bi-directional responses of Kobe earthquake, 0 OSAJ station

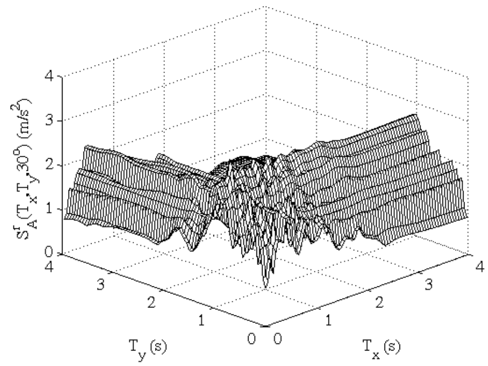

(a) $S_A^r(T_x,T_y,30^\circ)$

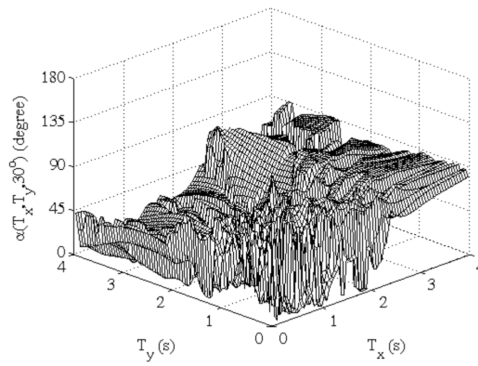

(b) $\alpha(T_x,T_y,30^\circ)$

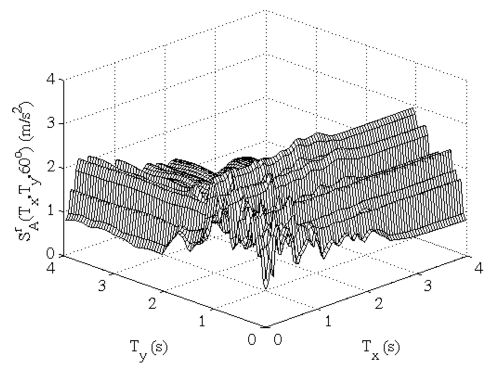

(c) $S_A^r(T_x,T_y,60^\circ)$

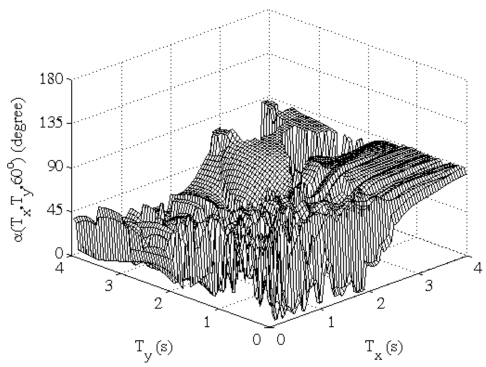

(d) $\alpha(T_x,T_y,60^\circ)$

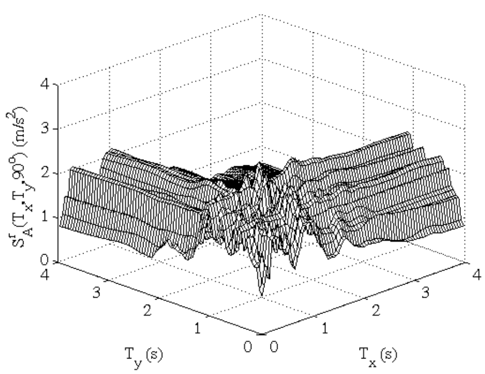

(e) $S_A^r(T_x,T_y,90^\circ)$

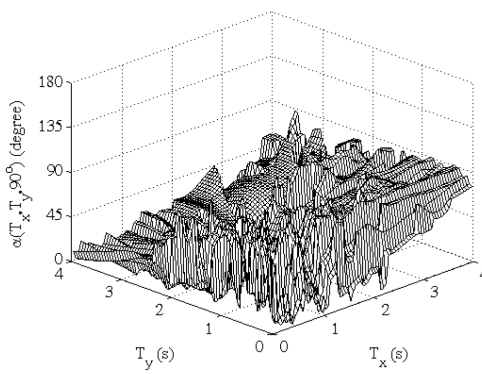

(f) $\alpha(T_x,T_y,90^\circ)$

Figure B-88 Pseudo acceleration spectra and incident angles in various directions of Kobe earthquake, 0 OSAJ station

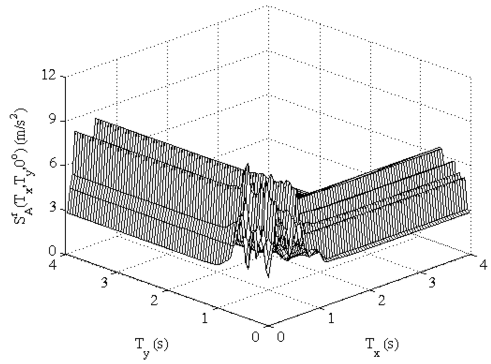

(a) $S_A^r(T_x,T_y,0^\circ)$

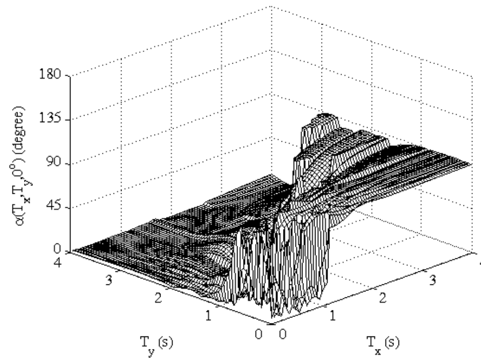

(b) $\alpha(T_x,T_y,0^\circ)$

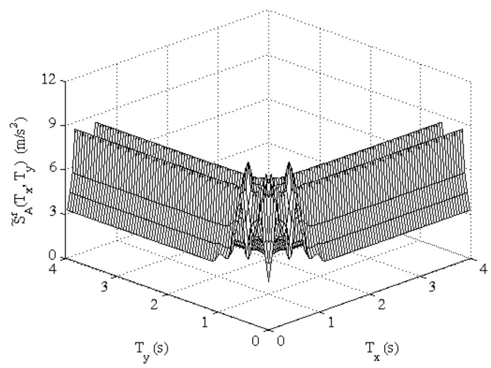

(c) $\tilde{S}_A^r(T_x,T_y)$

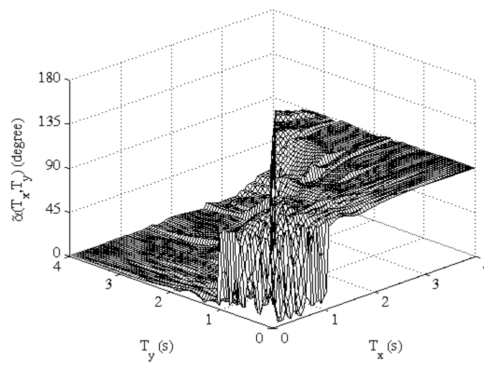

(d) $\tilde{\alpha}(T_x,T_y)$

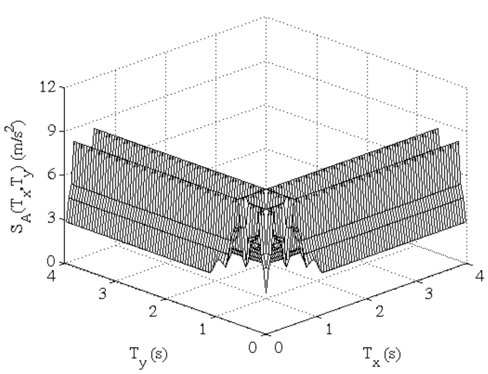

(e) $S_A(T_x,T_y)$

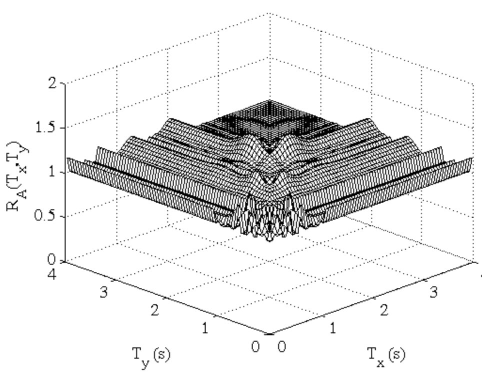

(f) $R_A(T_x,T_y)$

Figure B-89 Bi-directional responses of Northridge earthquake, 90016 LA - N Faring Rd station

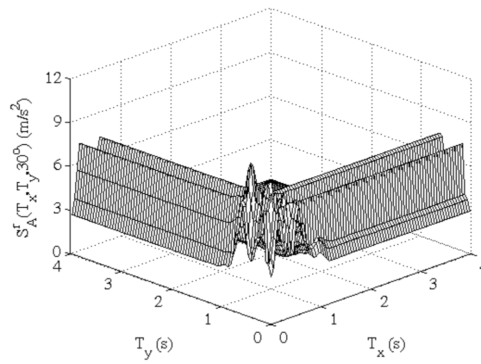

(a) $S_A^r(T_x,T_y,30^\circ)$

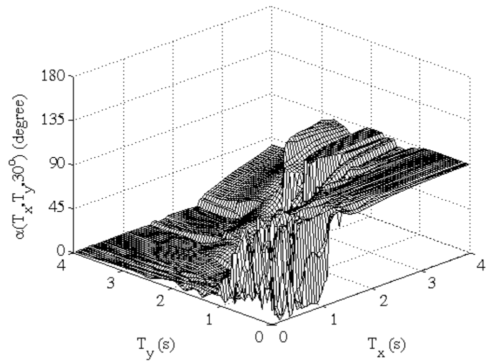

(b) $\alpha(T_x,T_y,30^\circ)$

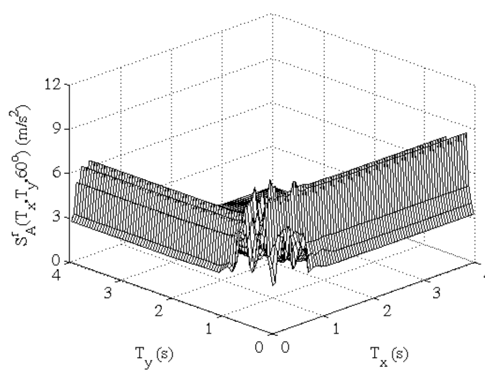

(c) $S_A^r(T_x,T_y,60^\circ)$

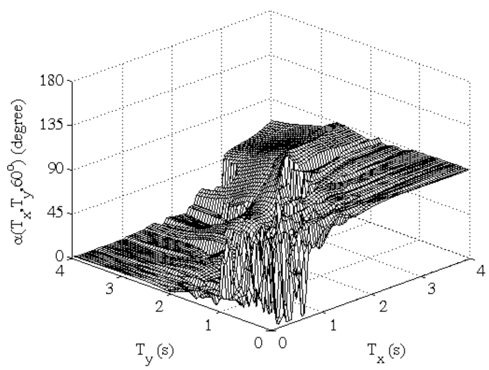

(d) $\alpha(T_x,T_y,60^\circ)$

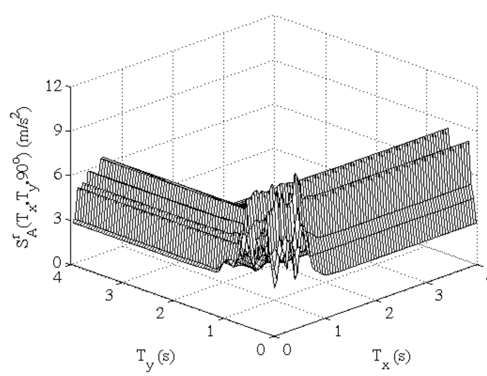

(e) $S_A^r(T_x,T_y,90^\circ)$

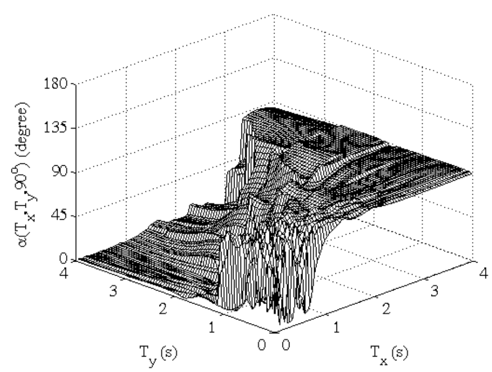

(f) $\alpha(T_x,T_y,90^\circ)$

Figure B-90 Pseudo acceleration spectra and incident angles in various directions of Northridge earthquake, 90016 LA - N Faring Rd station

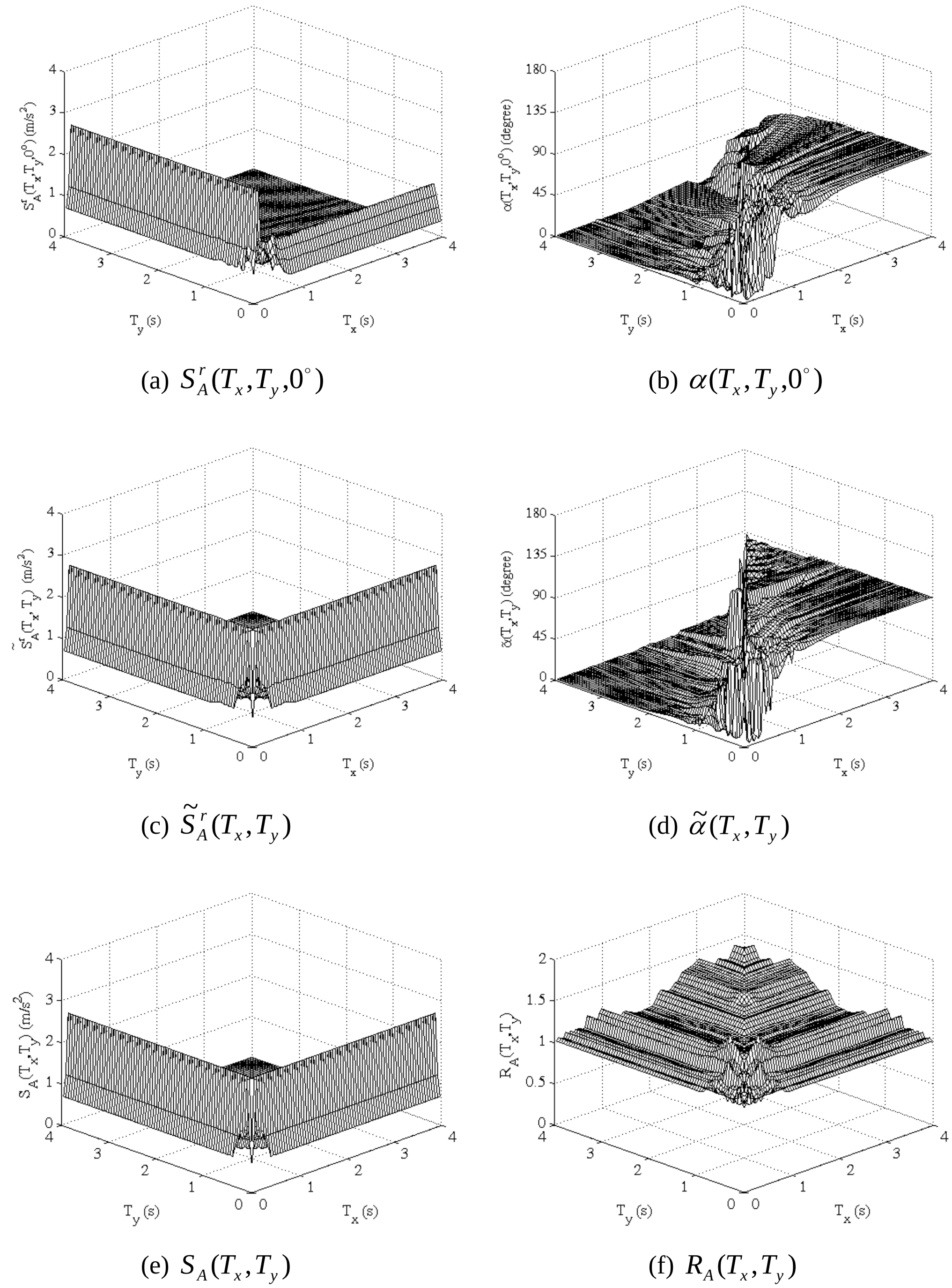

(a) $S_A^r(T_x,T_y,0^\circ)$ (b) $\alpha(T_x,T_y,0^\circ)$

(c) $\tilde{S}_A^r(T_x,T_y)$ (d) $\tilde{\alpha}(T_x,T_y)$

(e) $S_A(T_x,T_y)$ (f) $R_A(T_x,T_y)$

Figure B-91 Bi-directional responses of Whittier Narrows earthquake, 90016 LA - N Faring Rd station

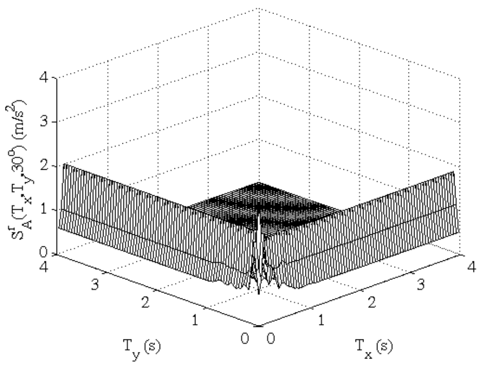

(a) $S_A^r(T_x, T_y, 30^\circ)$

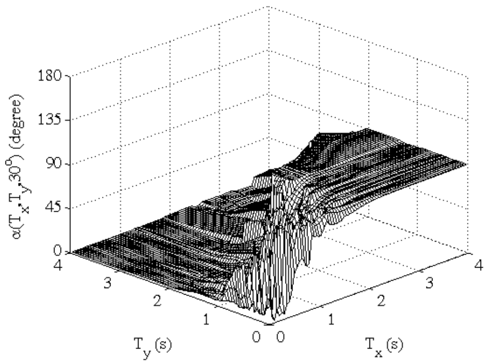

(b) $\alpha(T_x, T_y, 30^\circ)$

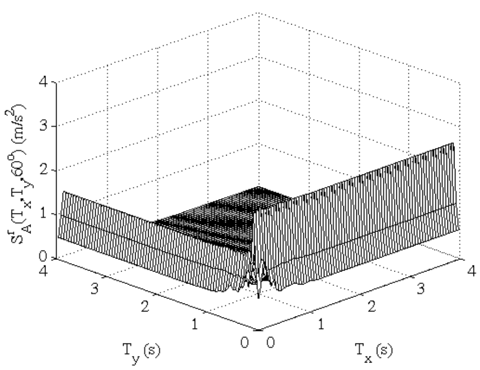

(c) $S_A^r(T_x, T_y, 60^\circ)$

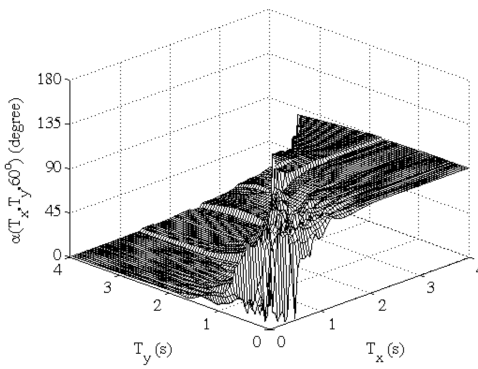

(d) $\alpha(T_x, T_y, 60^\circ)$

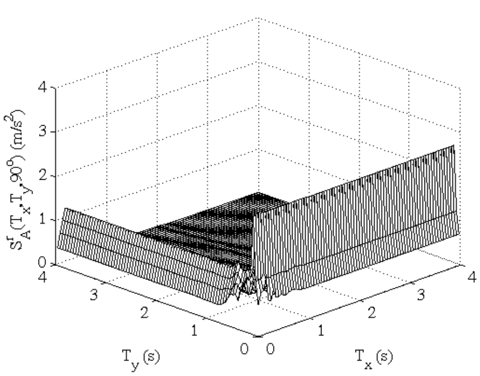

(e) $S_A^r(T_x, T_y, 90^\circ)$

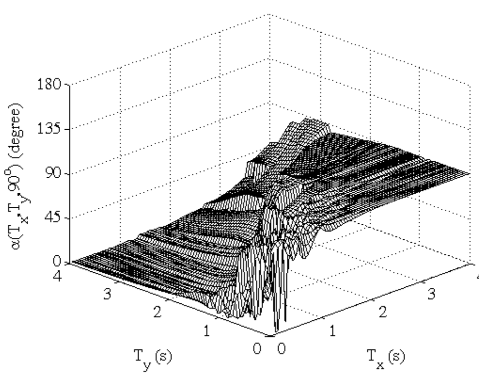

(f) $\alpha(T_x, T_y, 90^\circ)$

Figure B-92 Pseudo acceleration spectra and incident angles in various directions of Whittier Narrows earthquake, 90016 LA - N Faring Rd station

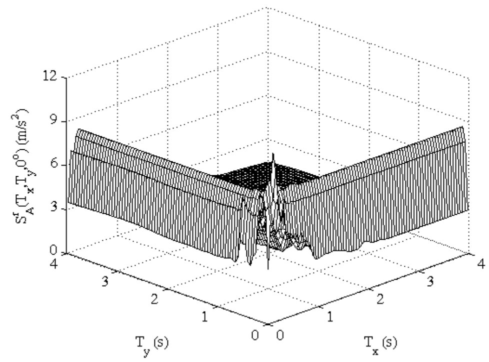
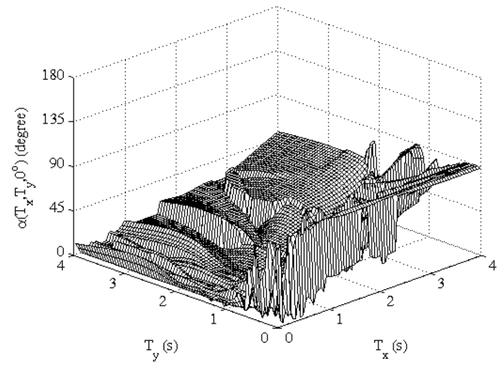

(a) $S_A^r(T_x,T_y,0^\circ)$ (b) $\alpha(T_x,T_y,0^\circ)$

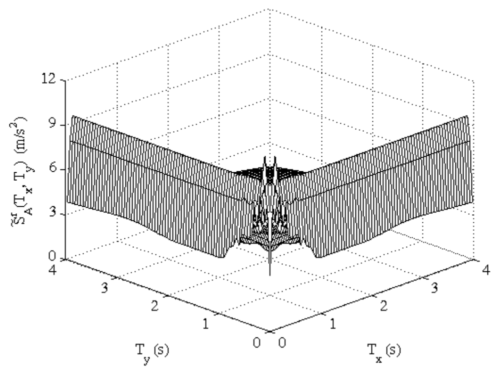
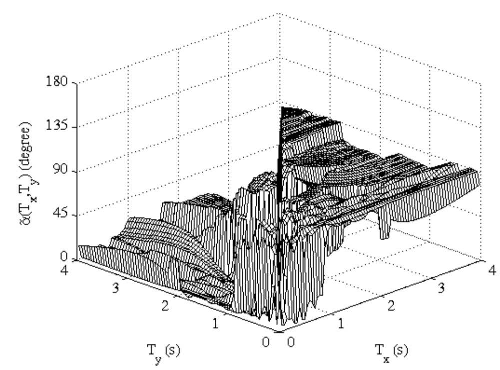

(c) $\widetilde{S}_A^r(T_x,T_y)$ (d) $\widetilde{\alpha}(T_x,T_y)$

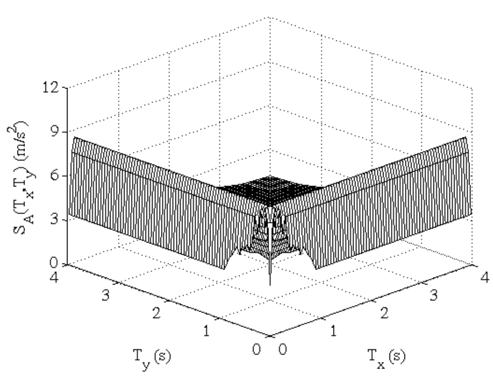
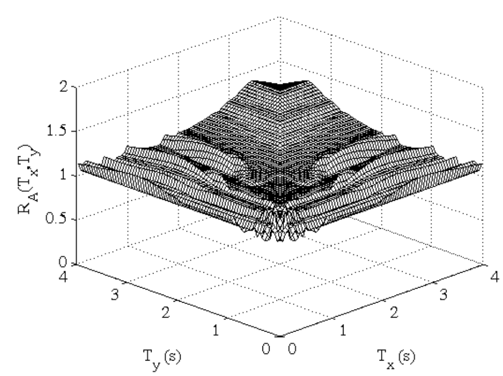

(e) $S_A(T_x,T_y)$ (f) $R_A(T_x,T_y)$

Figure B-93 Bi-directional responses of Imperial Valley earthquake, 5057 El Centro Array #3 station

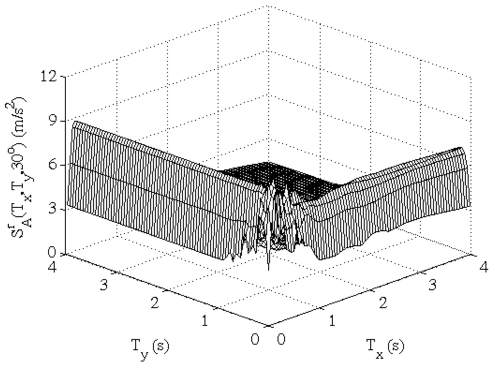

(a) $S_A^r(T_x, T_y, 30^\circ)$

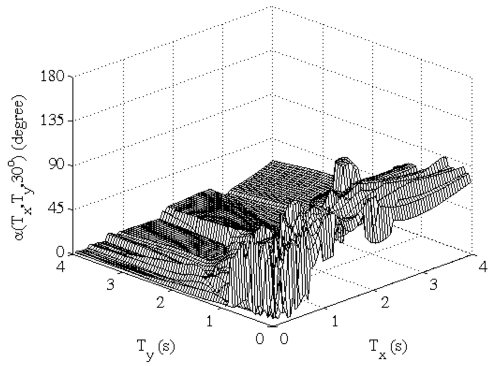

(b) $\alpha(T_x, T_y, 30^\circ)$

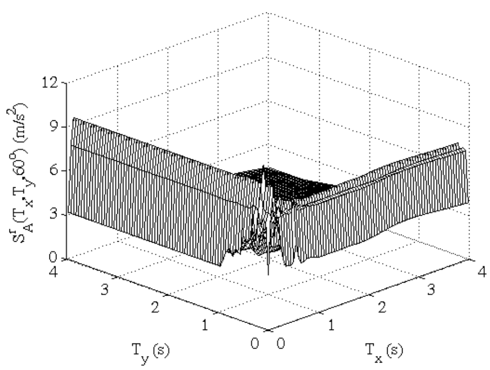

(c) $S_A^r(T_x, T_y, 60^\circ)$

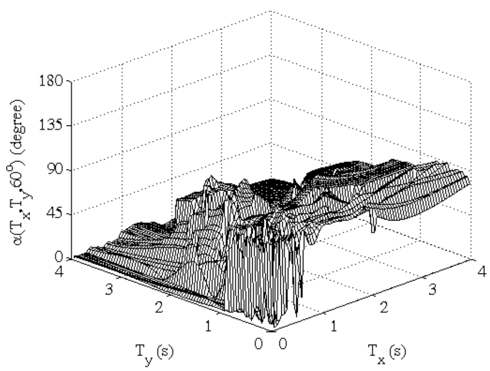

(d) $\alpha(T_x, T_y, 60^\circ)$

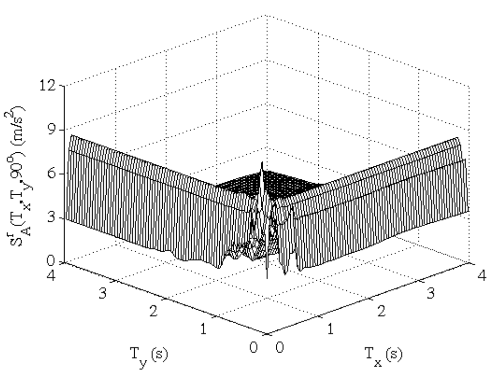

(e) $S_A^r(T_x, T_y, 90^\circ)$

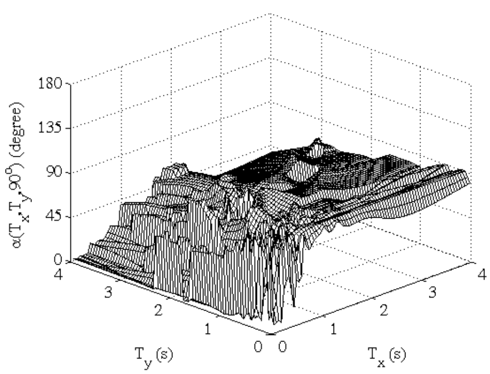

(f) $\alpha(T_x, T_y, 90^\circ)$

Figure B-94 Pseudo acceleration spectra and incident angles in various directions of Imperial Valley earthquake, 5057 El Centro Array #3 station

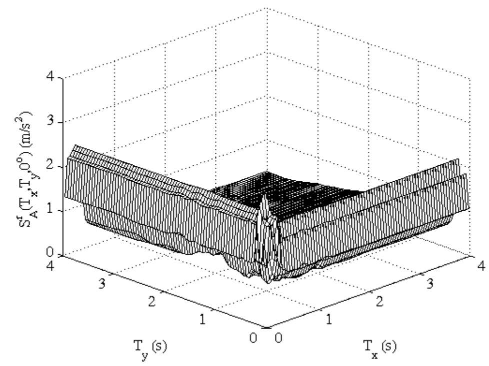

(a) $S_A^r(T_x, T_y, 0^\circ)$

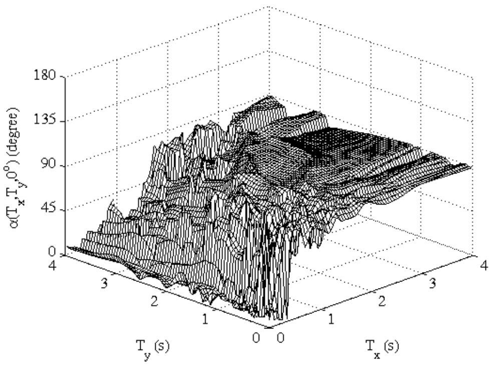

(b) $\alpha(T_x, T_y, 0^\circ)$

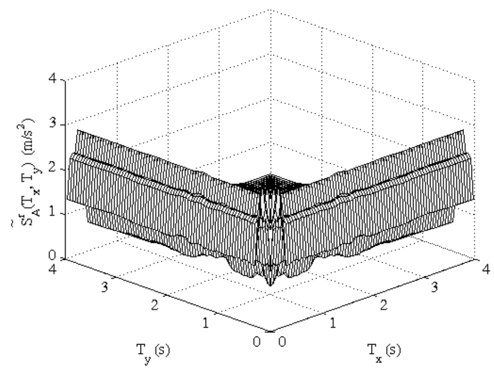

(c) $\tilde{S}_A^r(T_x, T_y)$

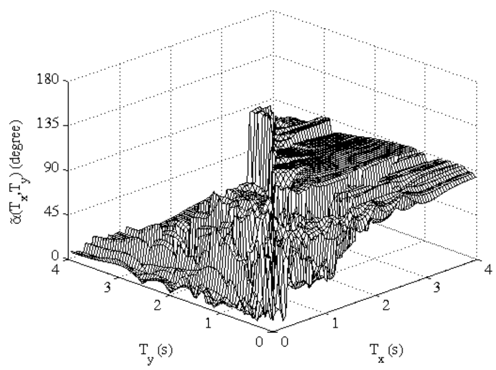

(d) $\tilde{\alpha}(T_x, T_y)$

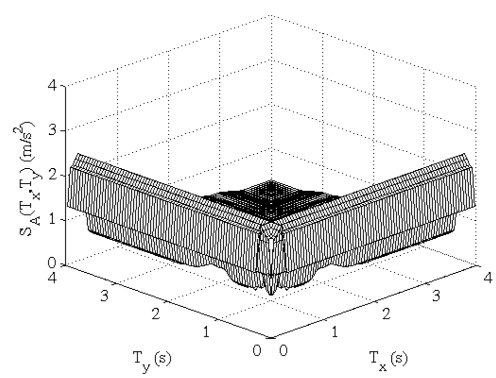

(e) $S_A(T_x, T_y)$

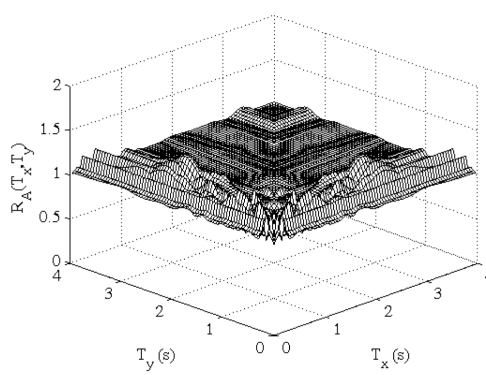

(f) $R_A(T_x, T_y)$

Figure B-95 Bi-directional responses of Chi-Chi, Taiwan earthquake, ILA063 station

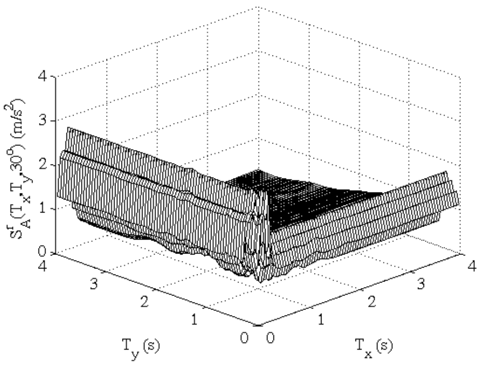

(a) $S^r_A(T_x,T_y,30^\circ)$

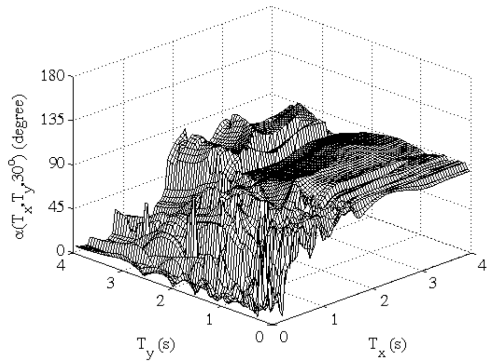

(b) $\alpha(T_x,T_y,30^\circ)$

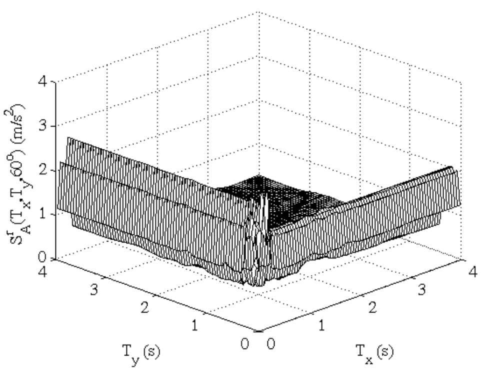

(c) $S^r_A(T_x,T_y,60^\circ)$

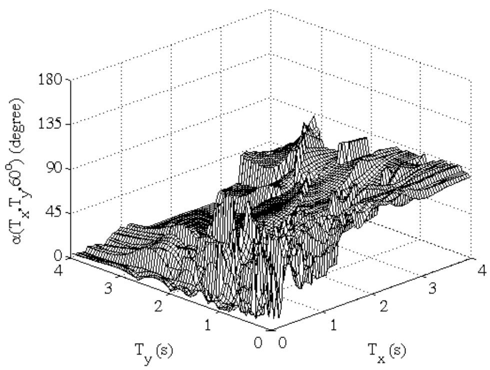

(d) $\alpha(T_x,T_y,60^\circ)$

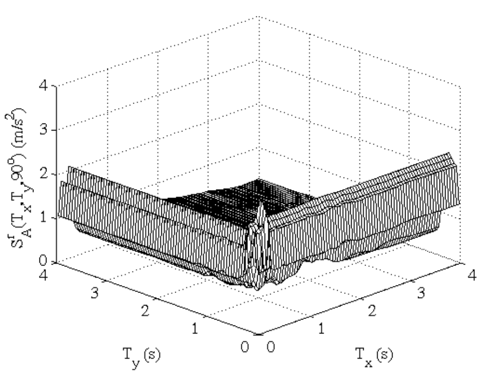

(e) $S^r_A(T_x,T_y,90^\circ)$

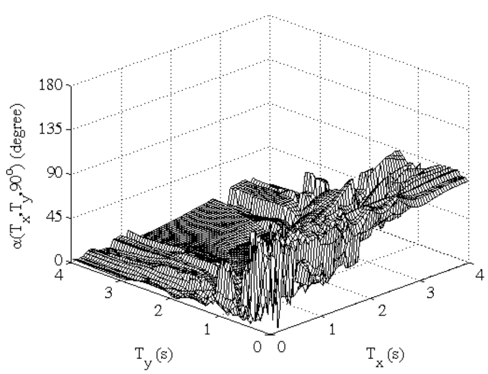

(f) $\alpha(T_x,T_y,90^\circ)$

Figure B-96 Pseudo acceleration spectra and incident angles in various directions of Chi-Chi, Taiwan earthquake, ILA063 station

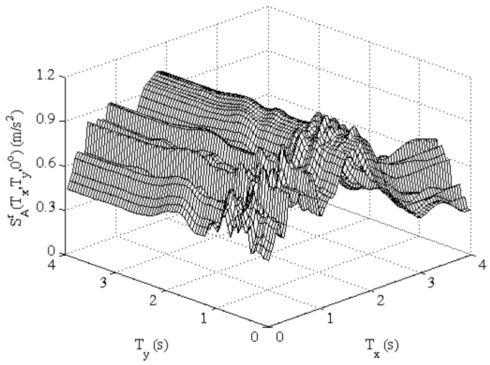

(a) $S_A^r(T_x, T_y, 0^\circ)$

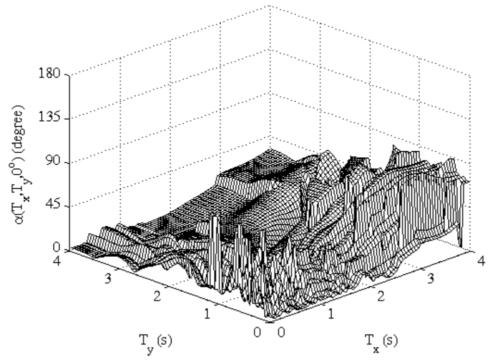

(b) $\alpha(T_x, T_y, 0^\circ)$

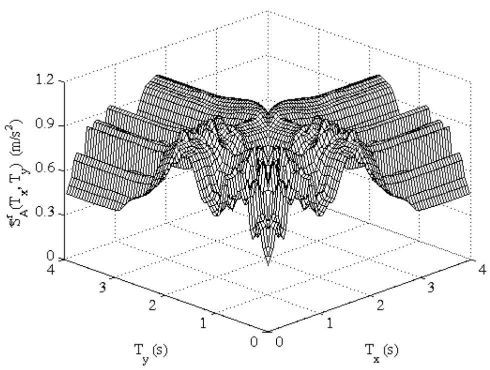

(c) $\widetilde{S}_A^r(T_x, T_y)$

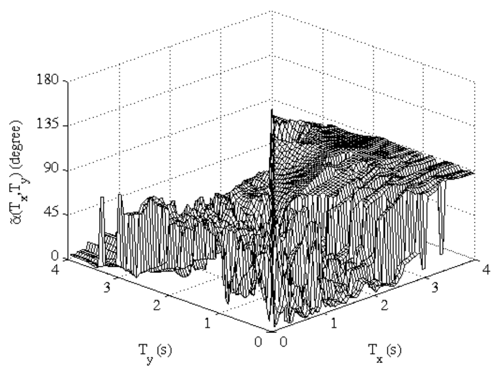

(d) $\widetilde{\alpha}(T_x, T_y)$

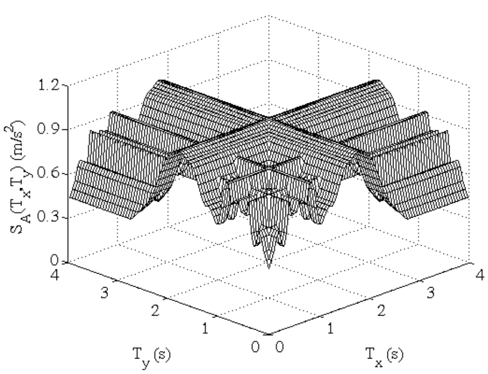

(e) $S_A(T_x, T_y)$

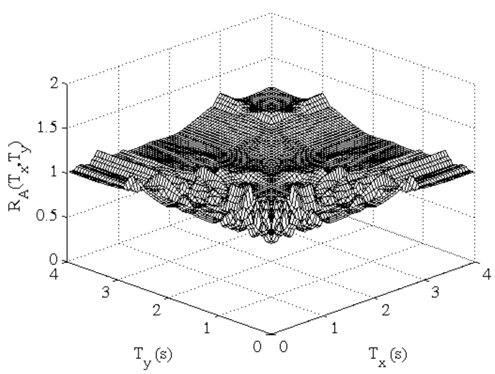

(f) $R_A(T_x, T_y)$

Figure B-97 Bi-directional responses of Chi-Chi, Taiwan earthquake, TAP065 station

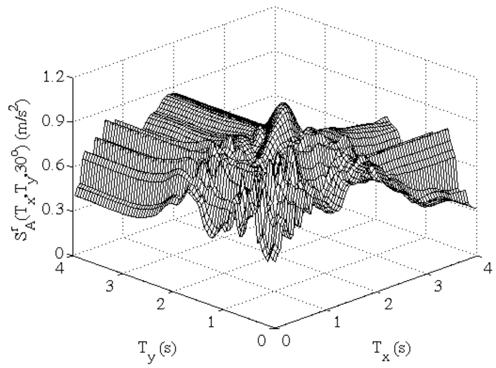

(a) $S_A^r(T_x, T_y, 30^\circ)$

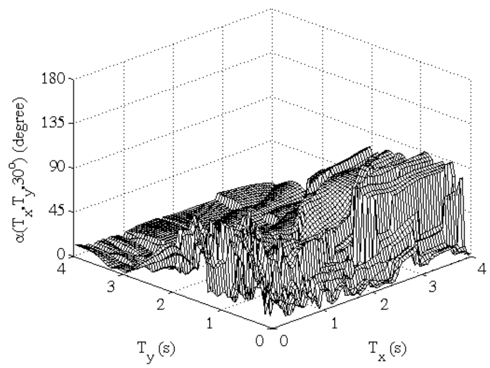

(b) $\alpha(T_x, T_y, 30^\circ)$

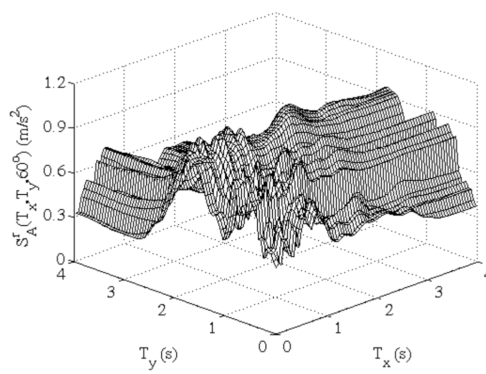

(c) $S_A^r(T_x, T_y, 60^\circ)$

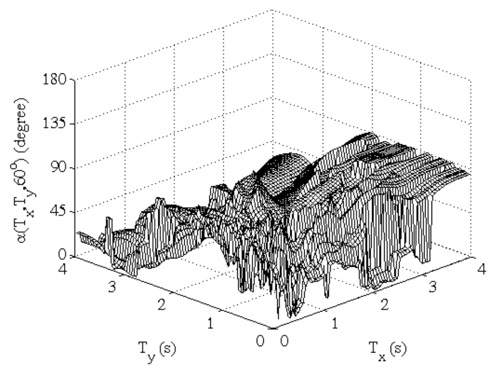

(d) $\alpha(T_x, T_y, 60^\circ)$

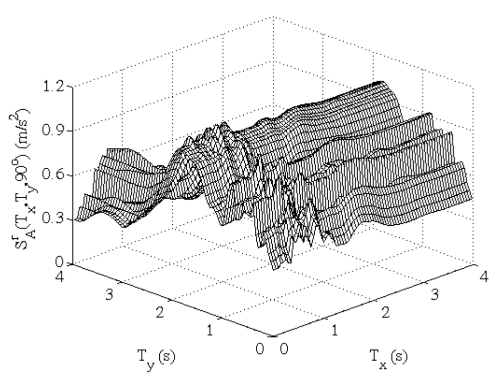

(e) $S_A^r(T_x, T_y, 90^\circ)$

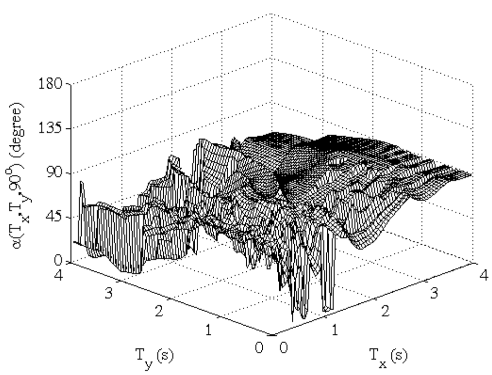

(f) $\alpha(T_x, T_y, 90^\circ)$

Figure B-98 Pseudo acceleration spectra and incident angles in various directions of Chi-Chi, Taiwan earthquake, TAP065 station

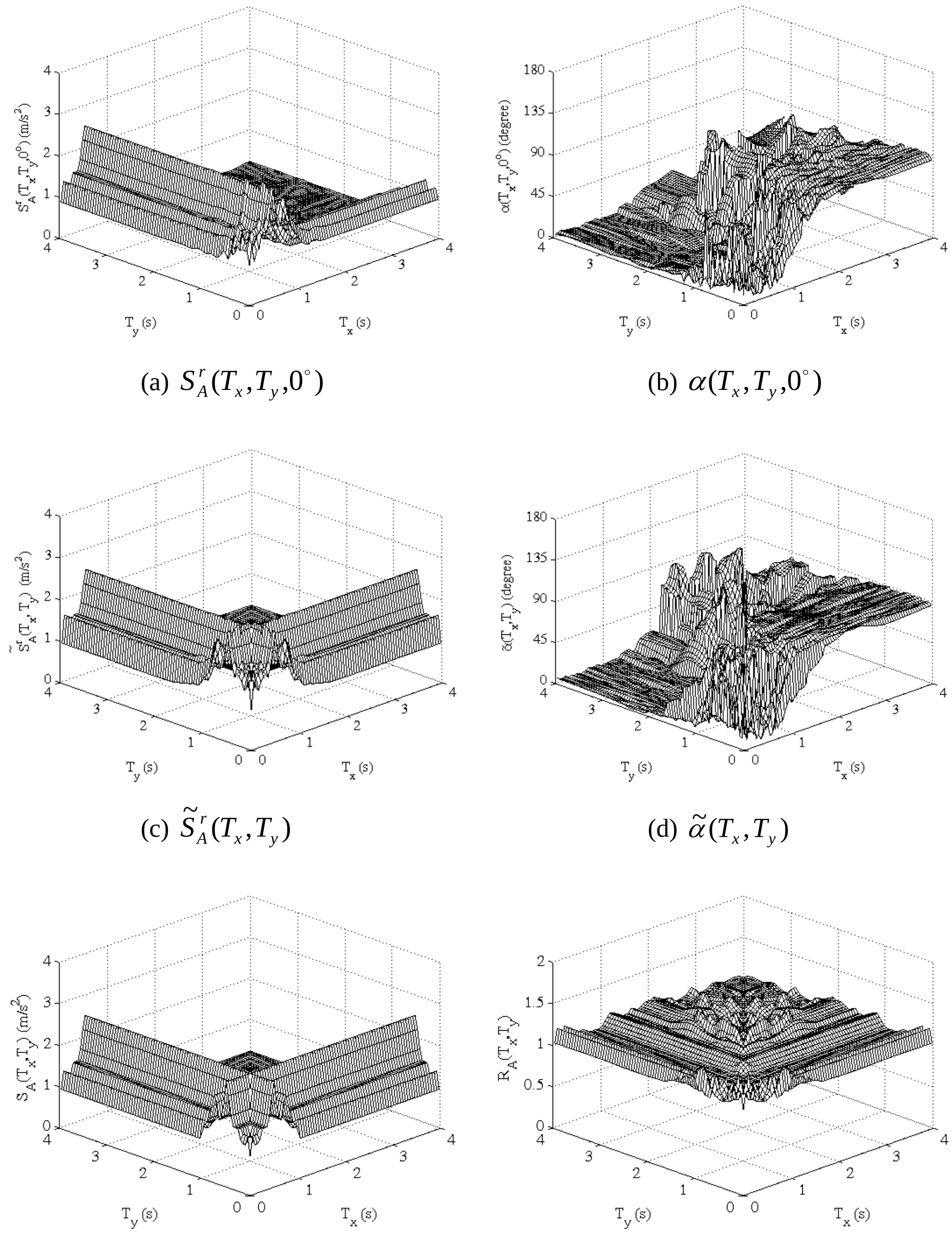

(a) $S_A^r(T_x, T_y, 0^\circ)$ (b) $\alpha(T_x, T_y, 0^\circ)$

(c) $\tilde{S}_A^r(T_x, T_y)$ (d) $\tilde{\alpha}(T_x, T_y)$

(e) $S_A(T_x, T_y)$ (f) $R_A(T_x, T_y)$

Figure B-99 Bi-directional responses of Chi-Chi, Taiwan earthquake, TCU085 station

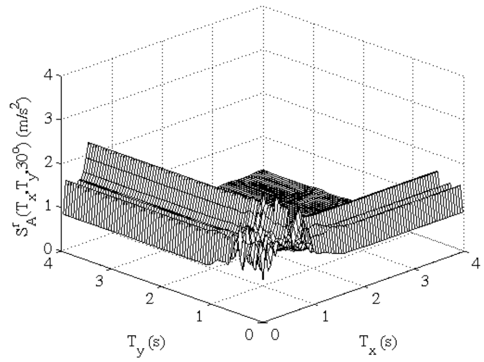

(a) $S_A^r(T_x, T_y, 30^\circ)$

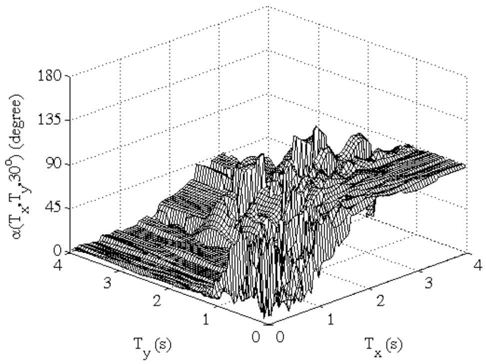

(b) $\alpha(T_x, T_y, 30^\circ)$

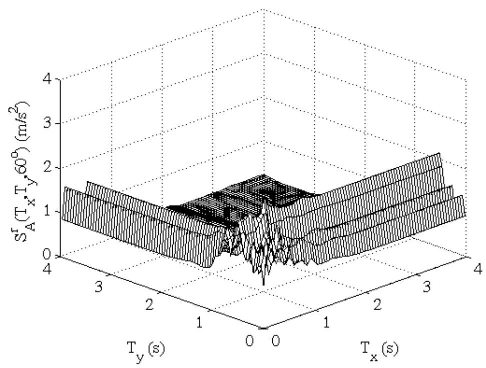

(c) $S_A^r(T_x, T_y, 60^\circ)$

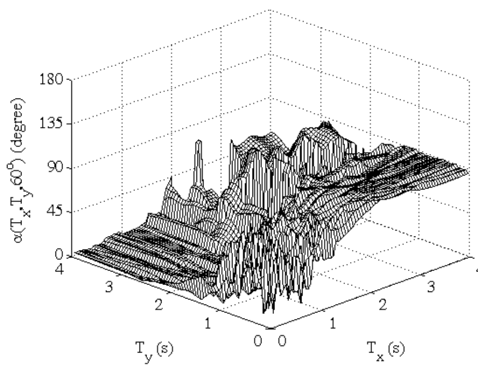

(d) $\alpha(T_x, T_y, 60^\circ)$

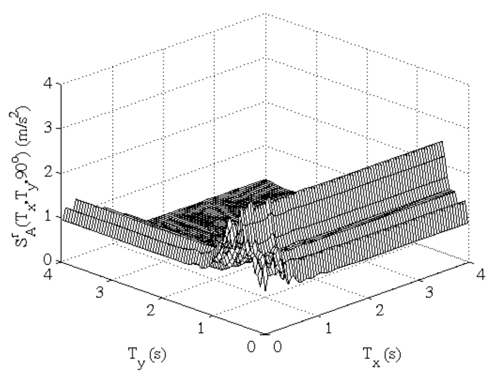

(e) $S_A^r(T_x, T_y, 90^\circ)$

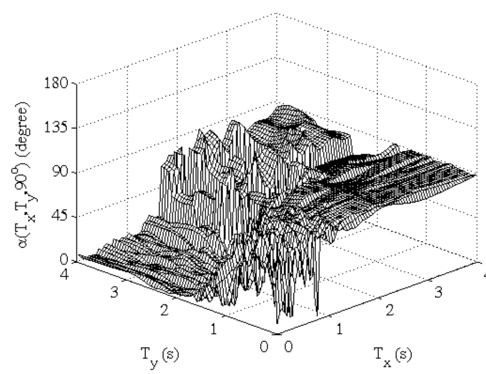

(f) $\alpha(T_x, T_y, 90^\circ)$

Figure B-100 Pseudo acceleration spectra and incident angles in various directions of Chi-Chi, Taiwan earthquake, TCU085 station

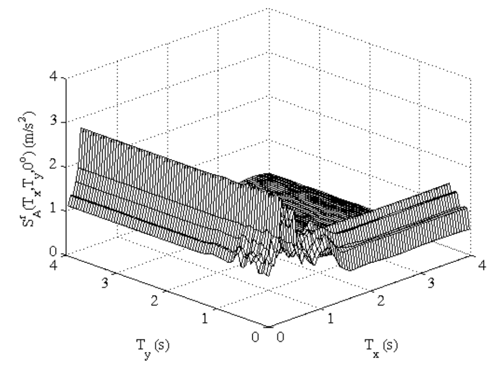

(a) $S_A^r(T_x, T_y, 0^\circ)$

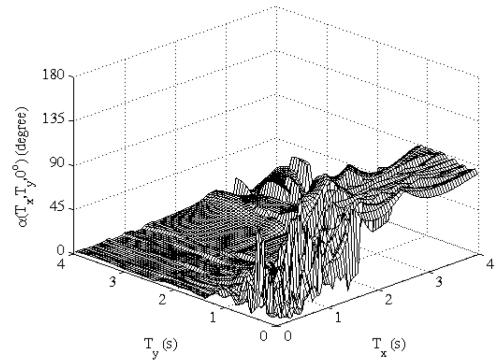

(b) $\alpha(T_x, T_y, 0^\circ)$

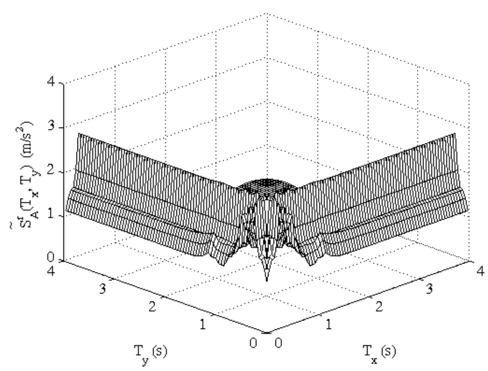

(c) $\tilde{S}_A^r(T_x, T_y)$

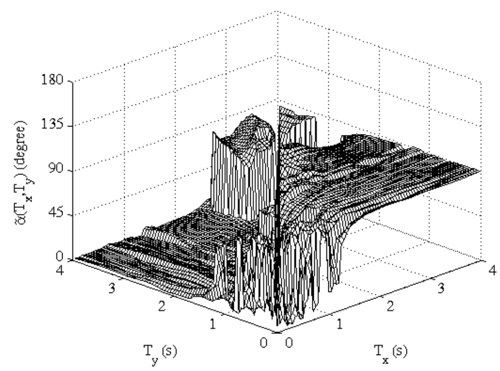

(d) $\tilde{\alpha}(T_x, T_y)$

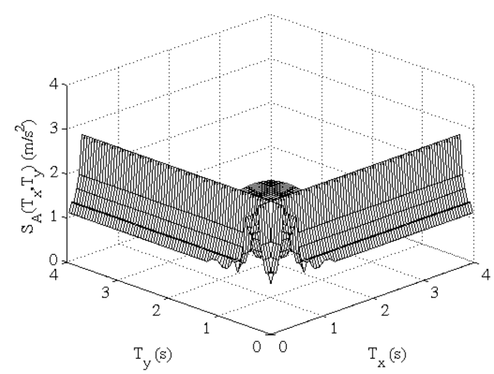

(e) $S_A(T_x, T_y)$

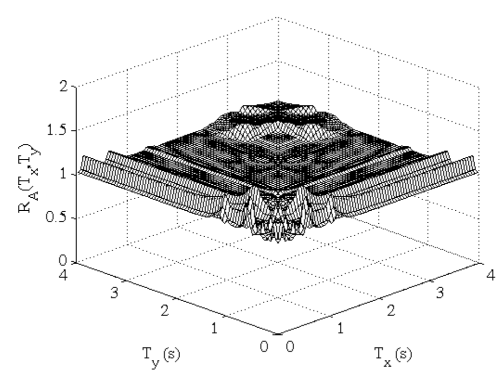

(f) $R_A(T_x, T_y)$

Figure B-101 Bi-directional responses of Loma Prieta earthquake, 58338 Piedmont Jr High station

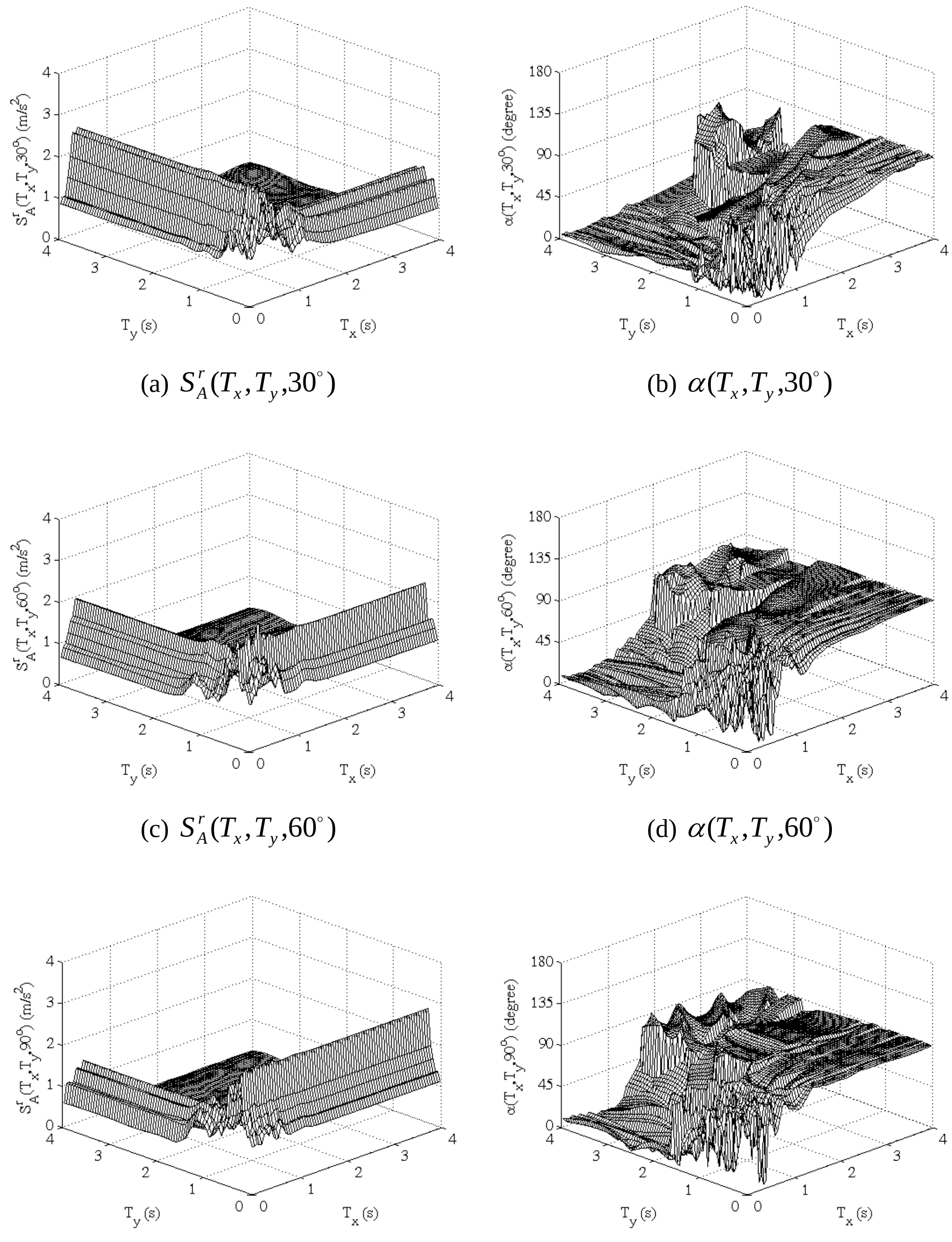

(a) $S_A^r(T_x,T_y,30^{\circ})$ (b) $\alpha(T_x,T_y,30^{\circ})$

(c) $S_A^r(T_x,T_y,60^{\circ})$ (d) $\alpha(T_x,T_y,60^{\circ})$

(e) $S_A^r(T_x,T_y,90^{\circ})$ (f) $\alpha(T_x,T_y,90^{\circ})$

Figure B-102 Pseudo acceleration spectra and incident angles in various directions of Loma Prieta earthquake, 58338 Piedmont Jr High station

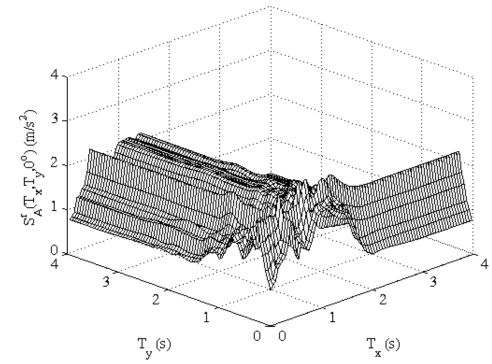

(a) $S_A^r(T_x,T_y,0^\circ)$

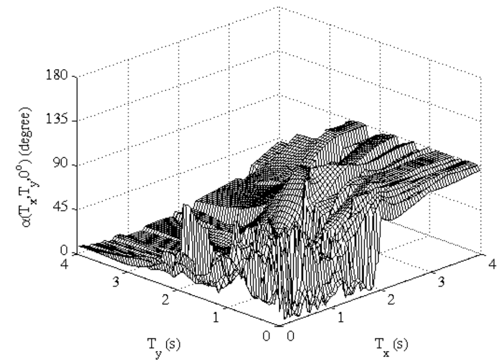

(b) $\alpha(T_x,T_y,0^\circ)$

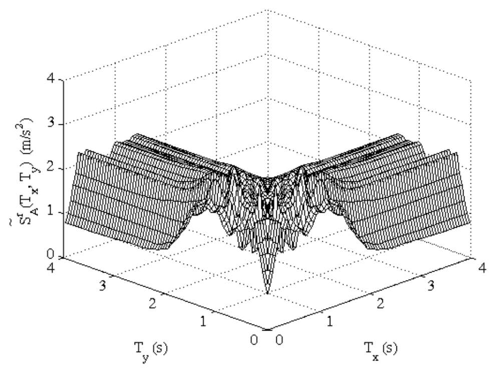

(c) $\widetilde{S}_A^r(T_x,T_y)$

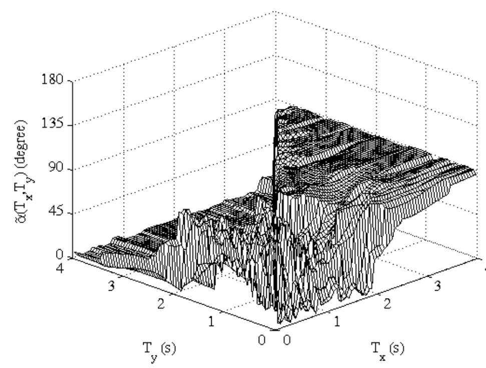

(d) $\widetilde{\alpha}(T_x,T_y)$

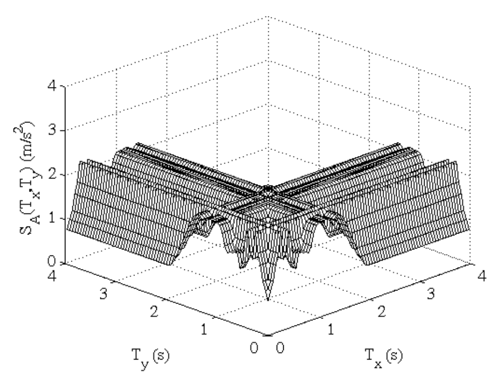

(e) $S_A(T_x,T_y)$

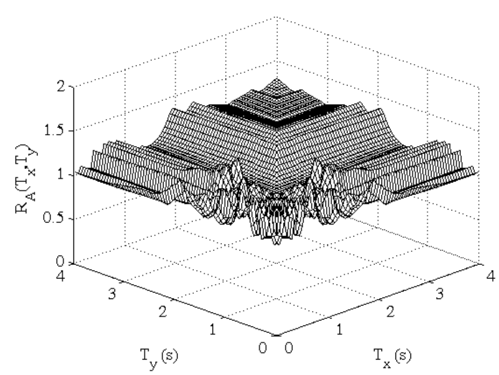

(f) $R_A(T_x,T_y)$

Figure B-103 Bi-directional responses of Loma Prieta earthquake, 58043 Point Bonita station

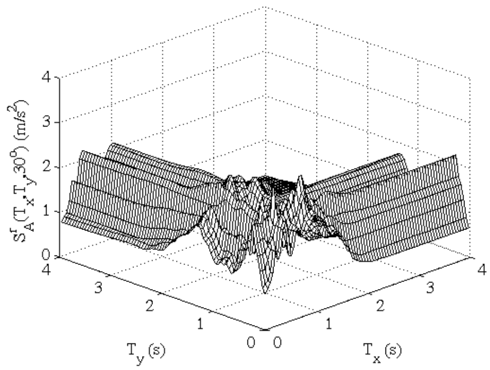

(a) $S_A^r(T_x, T_y, 30^\circ)$

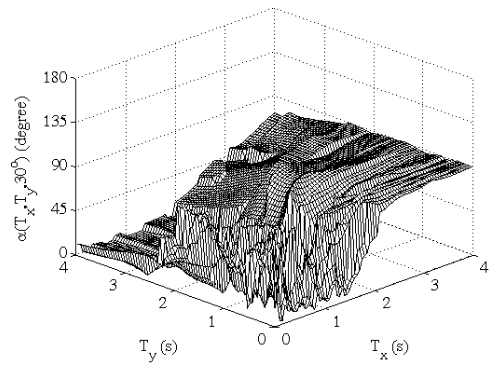

(b) $\alpha(T_x, T_y, 30^\circ)$

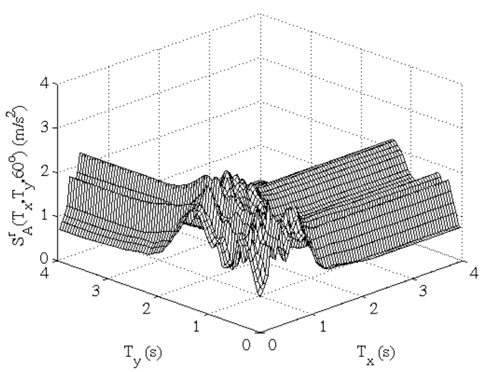

(c) $S_A^r(T_x, T_y, 60^\circ)$

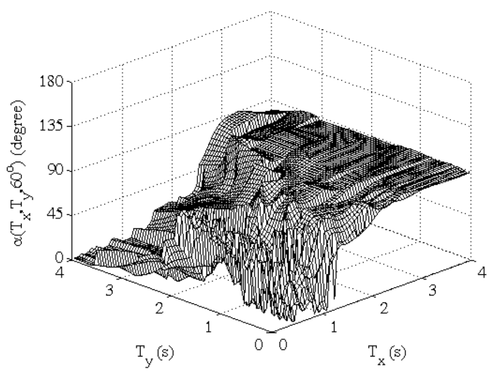

(d) $\alpha(T_x, T_y, 60^\circ)$

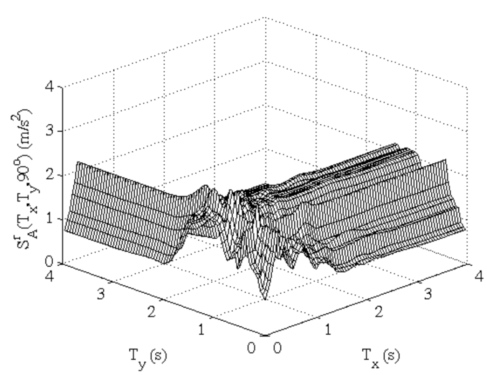

(e) $S_A^r(T_x, T_y, 90^\circ)$

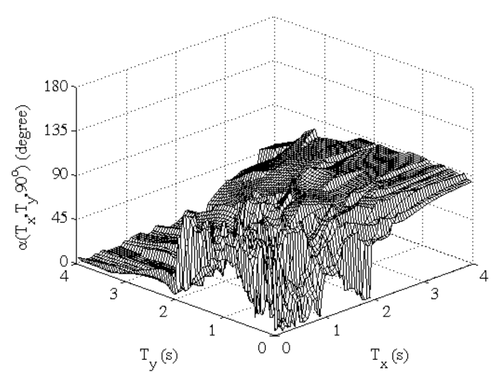

(f) $\alpha(T_x, T_y, 90^\circ)$

Figure B-104 Pseudo acceleration spectra and incident angles in various directions of Loma Prieta earthquake, 58043 Point Bonita station

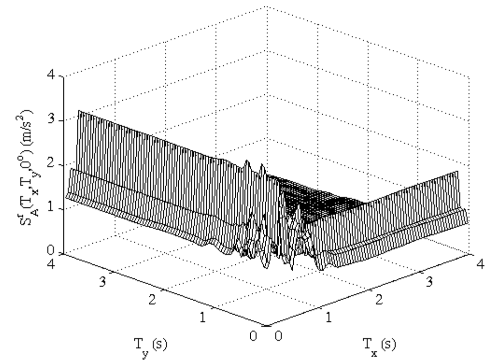

(a) $S_A^r(T_x, T_y, 0^\circ)$

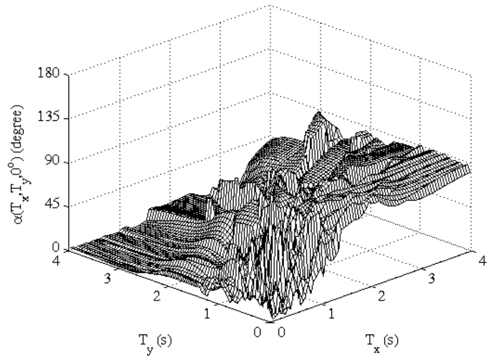

(b) $\alpha(T_x, T_y, 0^\circ)$

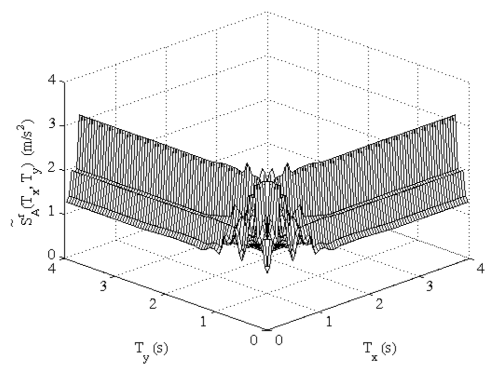

(c) $\tilde{S}_A^r(T_x, T_y)$

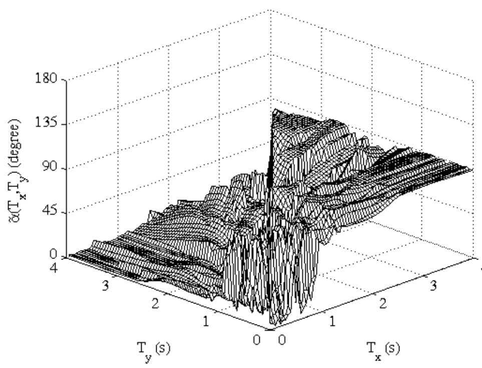

(d) $\tilde{\alpha}(T_x, T_y)$

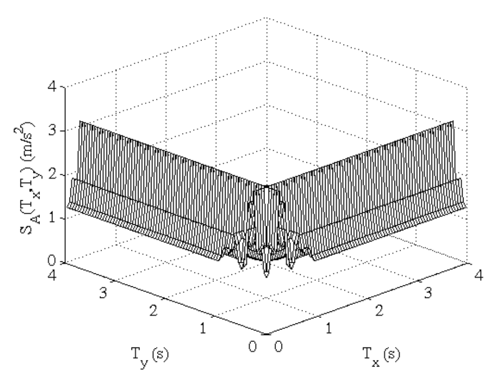

(e) $S_A(T_x, T_y)$

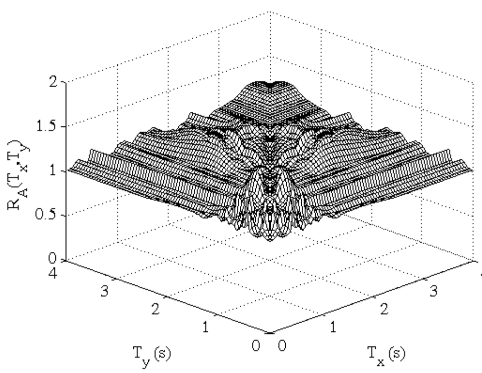

(f) $R_A(T_x, T_y)$

Figure B-105 Bi-directional responses of Loma Prieta earthquake, 58539 So San Francisco, Sierra Pt station

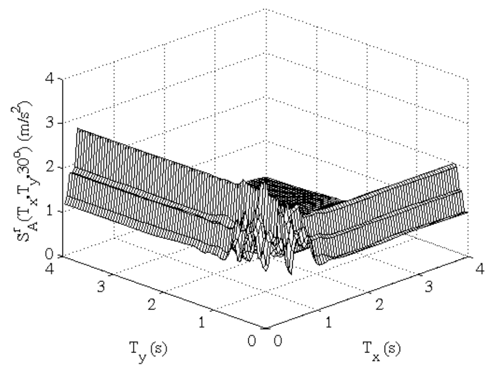

(a) $S^r_A(T_x,T_y,30^\circ)$

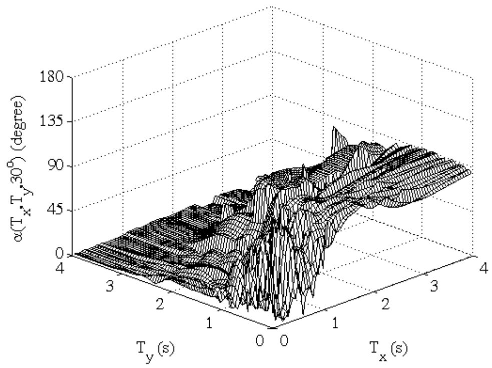

(b) $\alpha(T_x,T_y,30^\circ)$

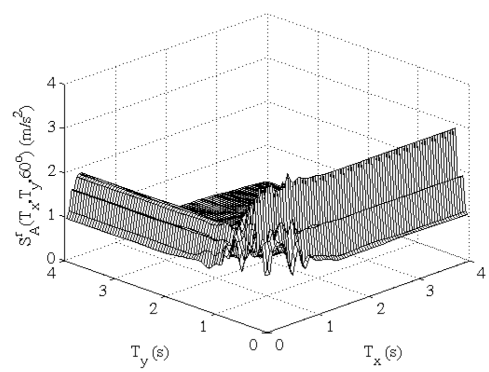

(c) $S^r_A(T_x,T_y,60^\circ)$

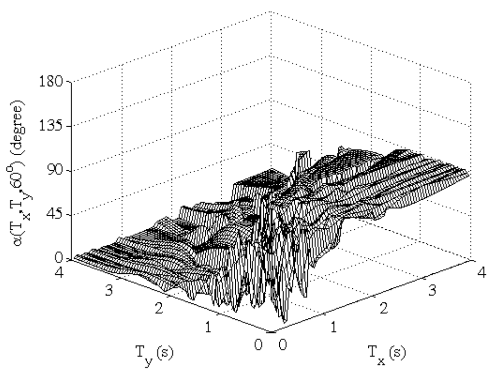

(d) $\alpha(T_x,T_y,60^\circ)$

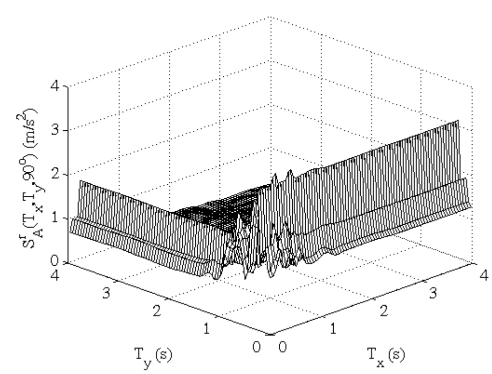

(e) $S^r_A(T_x,T_y,90^\circ)$

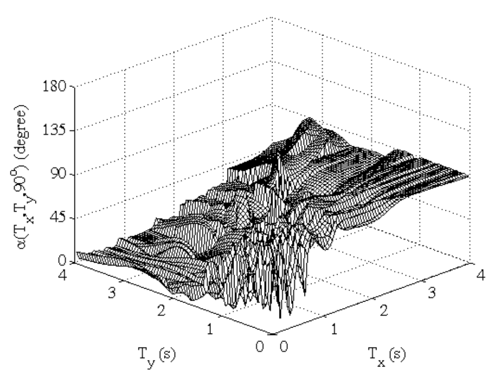

(f) $\alpha(T_x,T_y,90^\circ)$

Figure B-106 Pseudo acceleration spectra and incident angles in various directions of Loma Prieta earthquake, 58539 So San Francisco, Sierra Pt station

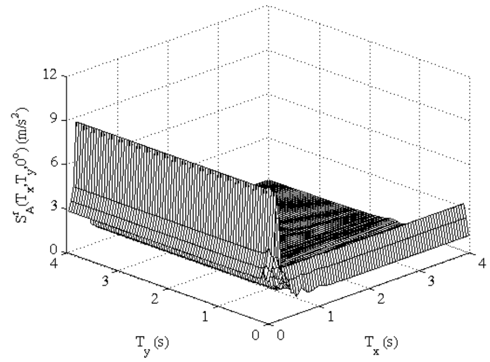

(a) $S_A^r(T_x, T_y, 0^\circ)$

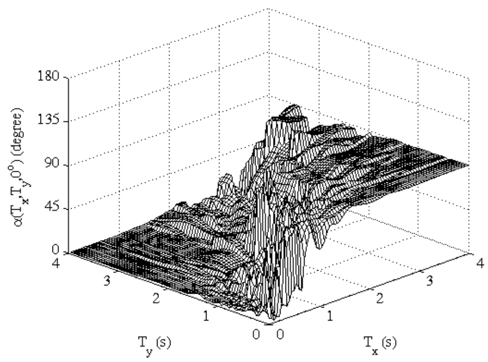

(b) $\alpha(T_x, T_y, 0^\circ)$

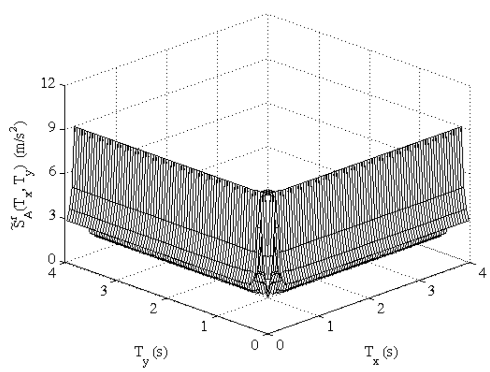

(c) $\widetilde{S}_A^r(T_x, T_y)$

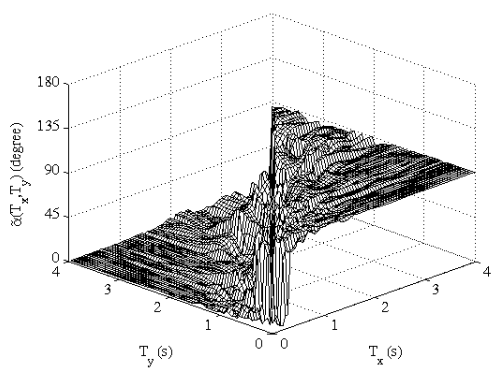

(d) $\widetilde{\alpha}(T_x, T_y)$

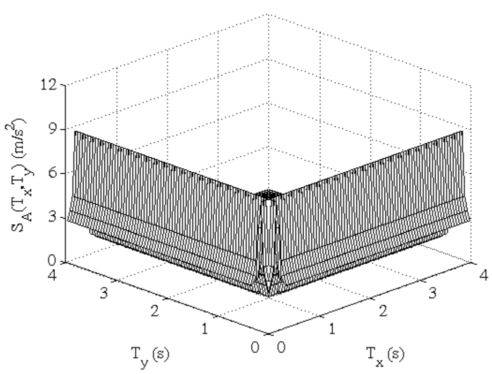

(e) $S_A(T_x, T_y)$

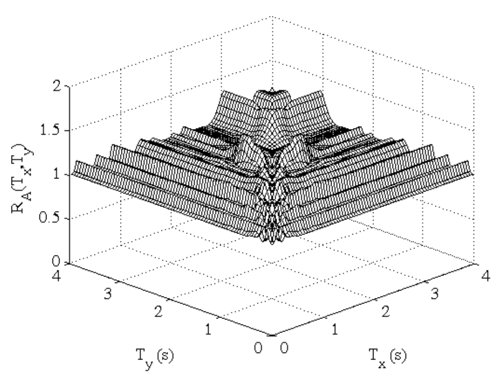

(f) $R_A(T_x, T_y)$

Figure B-107 Bi-directional responses of Northridge earthquake, 24399 Mt Wilson - CIT Seismic station

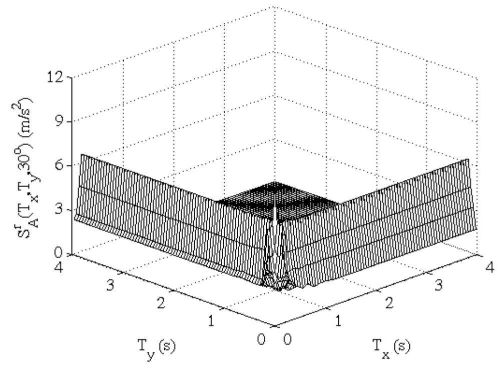

(a) $S^r_A(T_x, T_y, 30^\circ)$

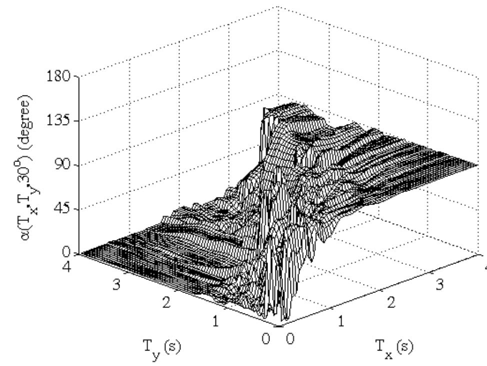

(b) $\alpha(T_x, T_y, 30^\circ)$

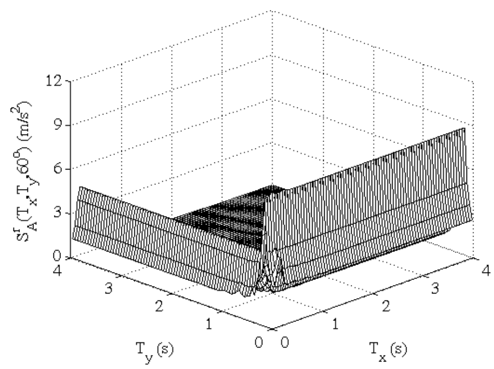

(c) $S^r_A(T_x, T_y, 60^\circ)$

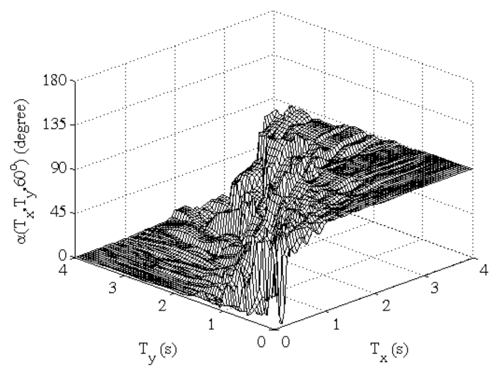

(d) $\alpha(T_x, T_y, 60^\circ)$

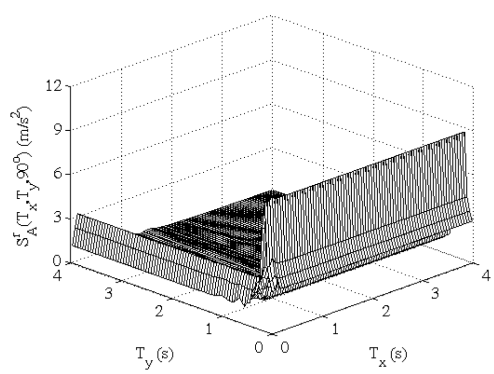

(e) $S^r_A(T_x, T_y, 90^\circ)$

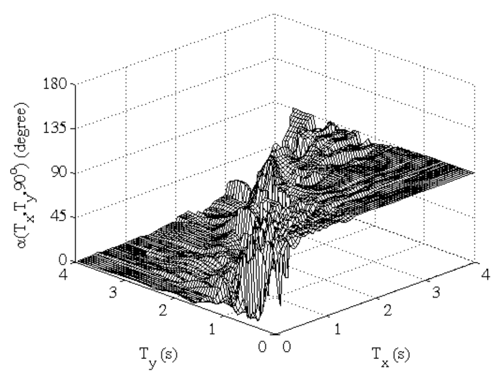

(f) $\alpha(T_x, T_y, 90^\circ)$

Figure B-108 Pseudo acceleration spectra and incident angles in various directions of Northridge earthquake, 24399 Mt Wilson - CIT Seismic station

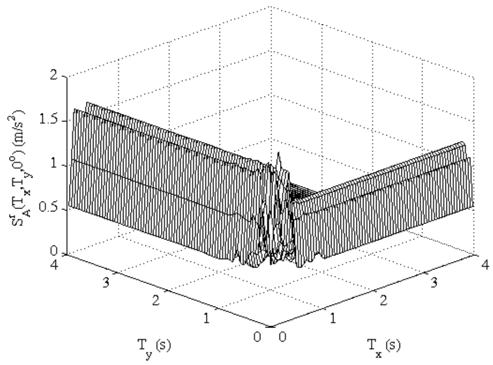

(a) $S_A^r(T_x, T_y, 0^\circ)$

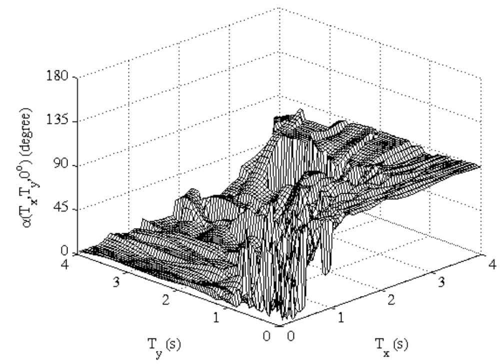

(b) $\alpha(T_x, T_y, 0^\circ)$

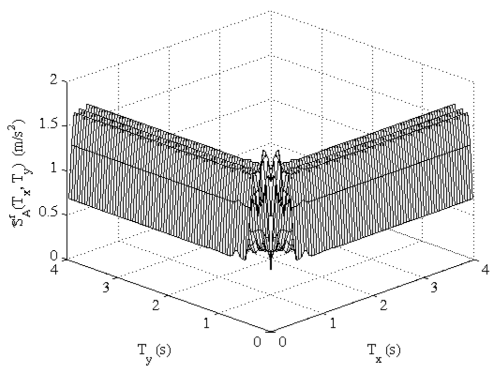

(c) $\widetilde{S}_A^r(T_x, T_y)$

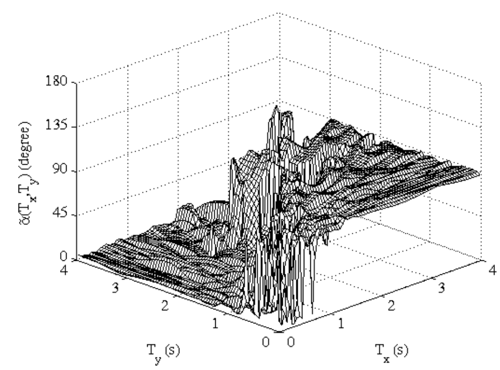

(d) $\widetilde{\alpha}(T_x, T_y)$

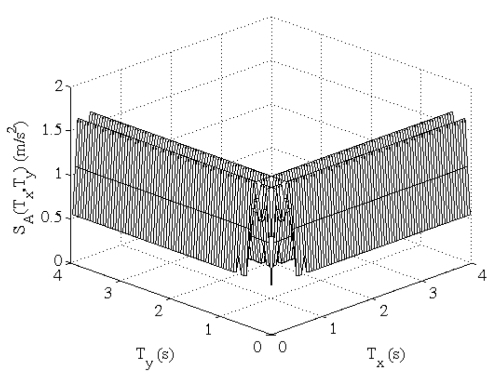

(e) $S_A(T_x, T_y)$

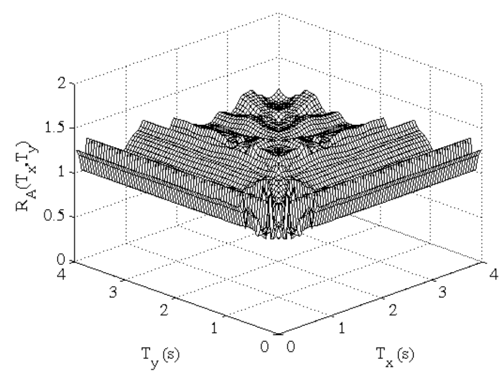

(f) $R_A(T_x, T_y)$

Figure B-109 Bi-directional responses of Northridge earthquake, 24310 Antelope Buttes station

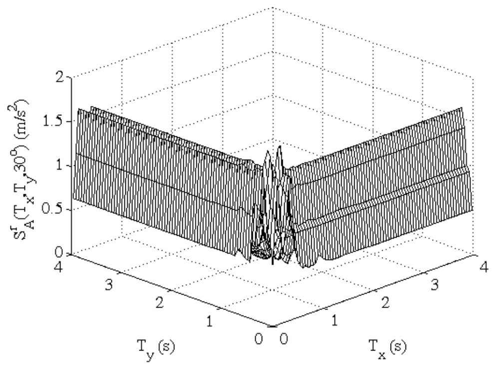

(a) $S_A^r(T_x, T_y, 30^\circ)$

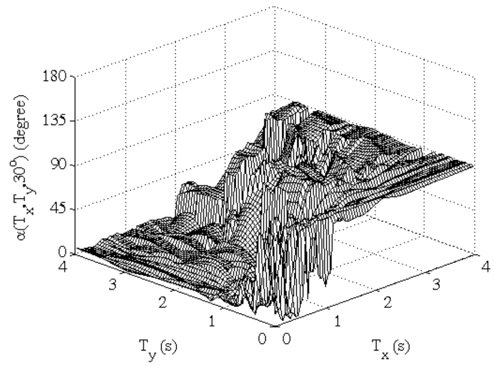

(b) $\alpha(T_x, T_y, 30^\circ)$

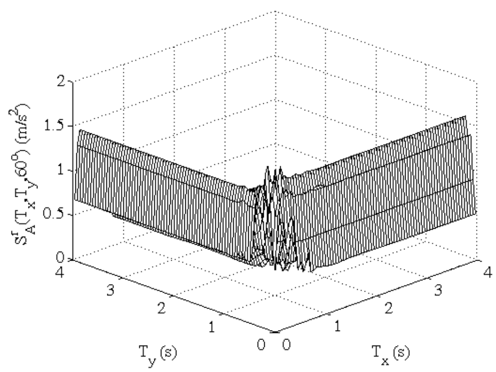

(c) $S_A^r(T_x, T_y, 60^\circ)$

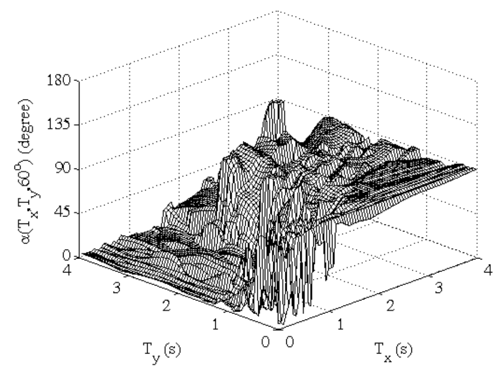

(d) $\alpha(T_x, T_y, 60^\circ)$

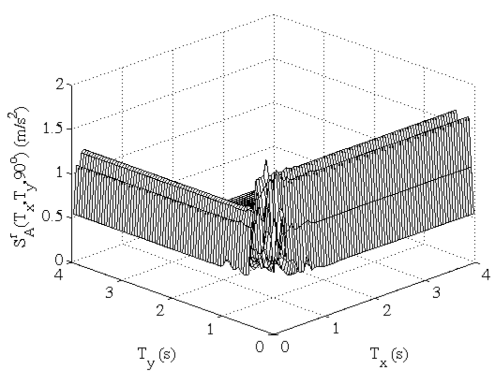

(e) $S_A^r(T_x, T_y, 90^\circ)$

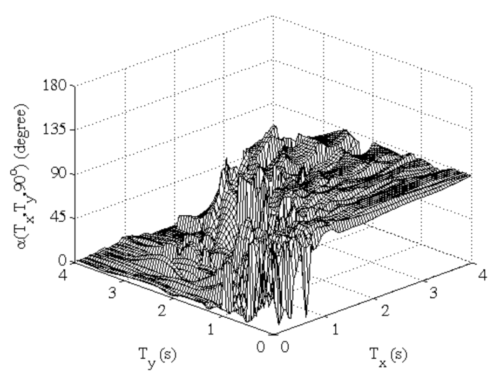

(f) $\alpha(T_x, T_y, 90^\circ)$

Figure B-110 Pseudo acceleration spectra and incident angles in various directions of Northridge earthquake, 24310 Antelope Buttes station

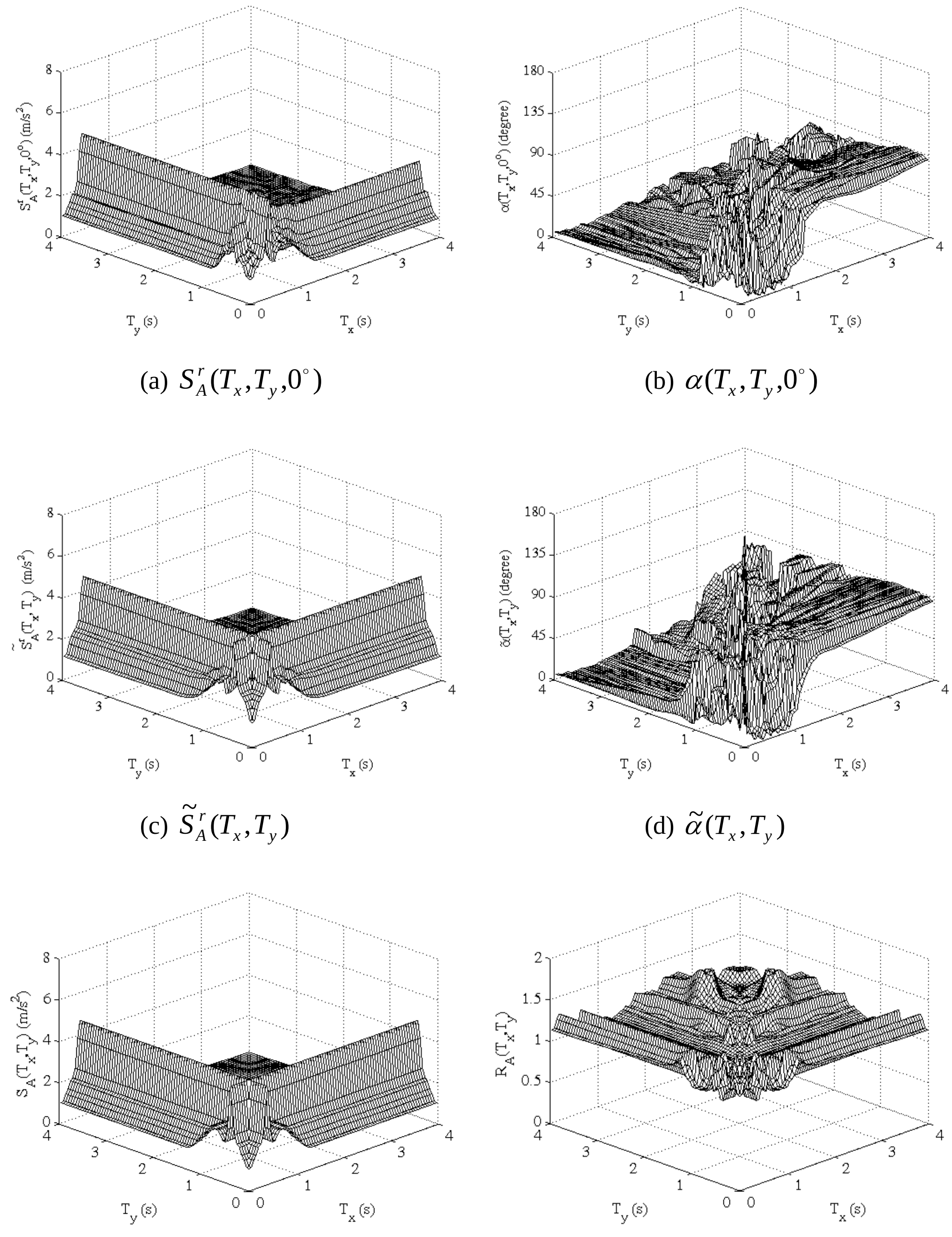

(a) $S_A^r(T_x, T_y, 0^\circ)$ (b) $\alpha(T_x, T_y, 0^\circ)$

(c) $\tilde{S}_A^r(T_x, T_y)$ (d) $\tilde{\alpha}(T_x, T_y)$

(e) $S_A(T_x, T_y)$ (f) $R_A(T_x, T_y)$

Figure B-111 Bi-directional responses of Northridge earthquake, 24644 Sandberg - Bald Mtn station

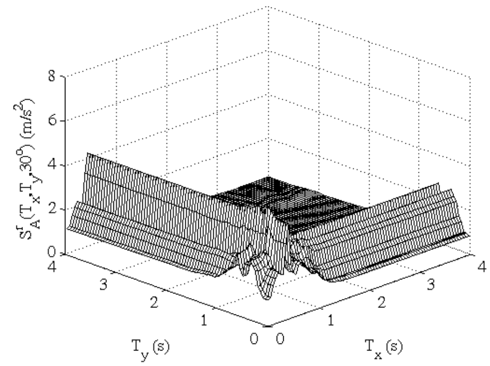

(a) $S_A^r(T_x, T_y, 30^\circ)$

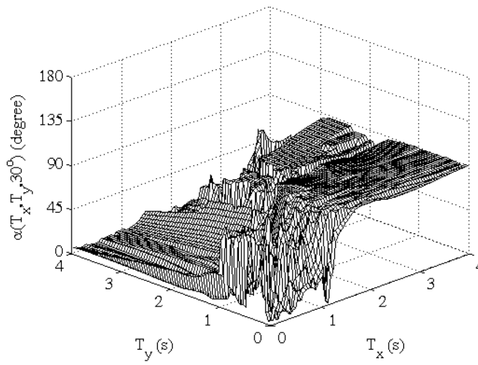

(b) $\alpha(T_x, T_y, 30^\circ)$

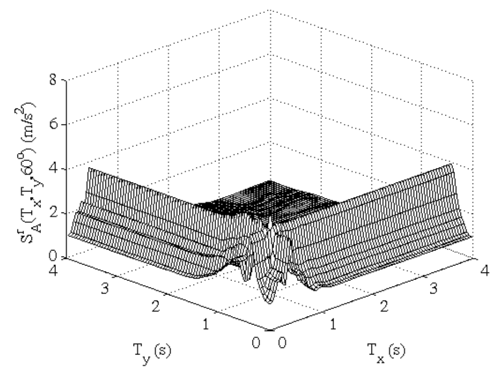

(c) $S_A^r(T_x, T_y, 60^\circ)$

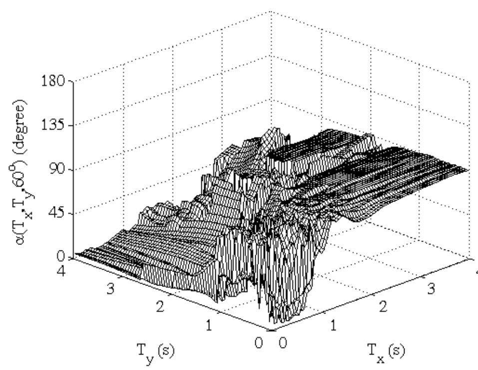

(d) $\alpha(T_x, T_y, 60^\circ)$

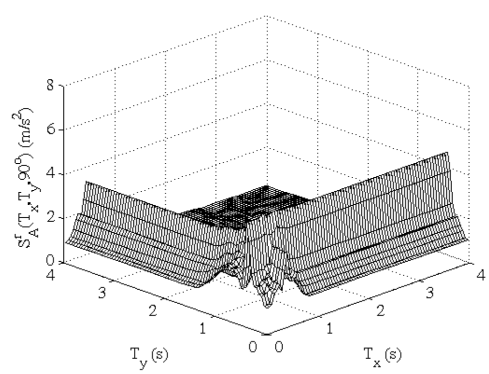

(e) $S_A^r(T_x, T_y, 90^\circ)$

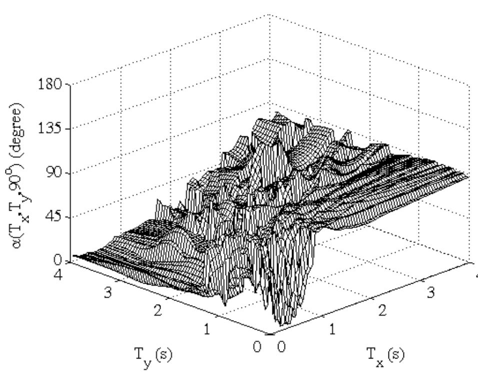

(f) $\alpha(T_x, T_y, 90^\circ)$

Figure B-112 Pseudo acceleration spectra and incident angles in various directions of Northridge earthquake, 24644 Sandberg - Bald Mtn station

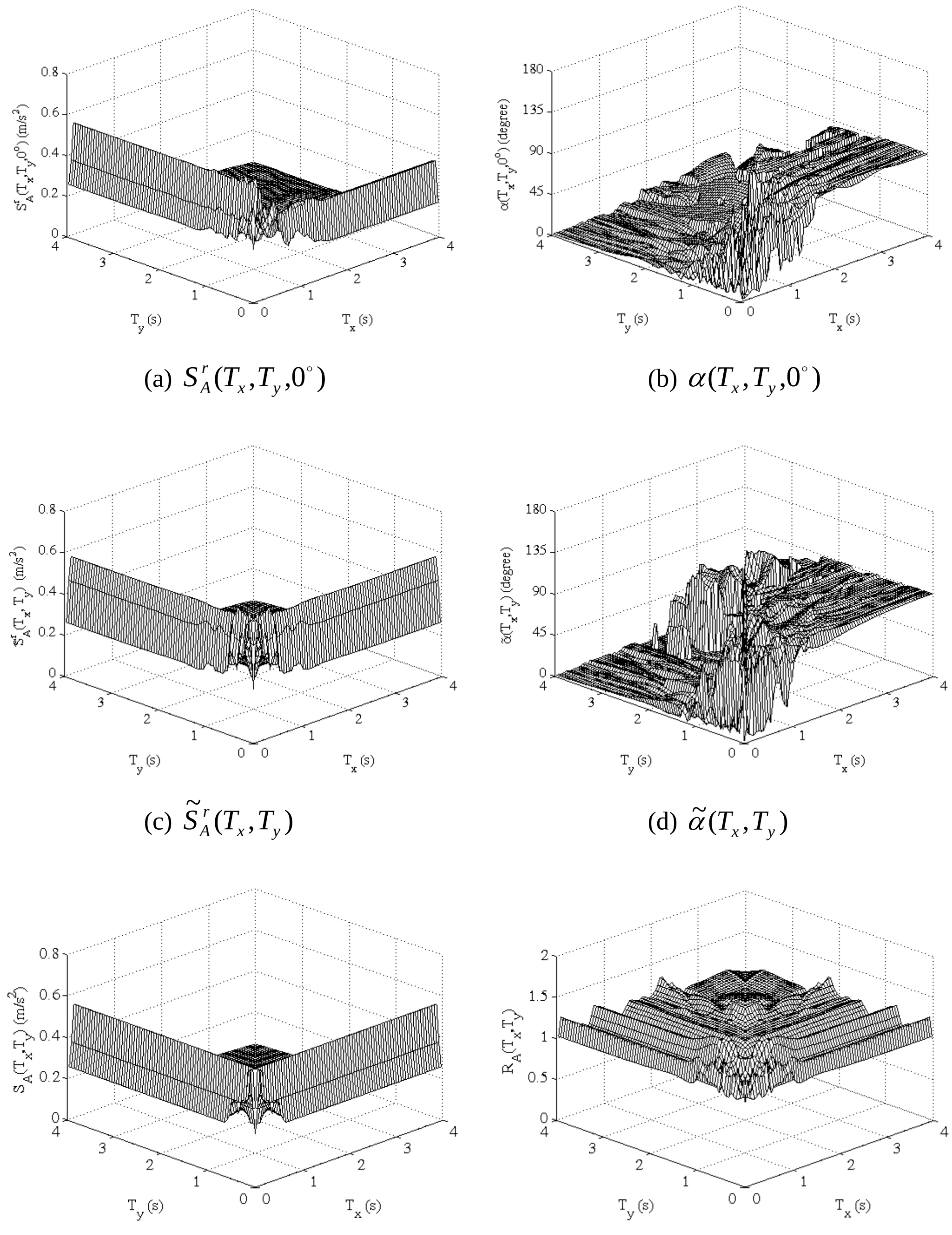

(a) $S_A^r(T_x, T_y, 0^\circ)$ (b) $\alpha(T_x, T_y, 0^\circ)$

(c) $\tilde{S}_A^r(T_x, T_y)$ (d) $\tilde{\alpha}(T_x, T_y)$

(e) $S_A(T_x, T_y)$ (f) $R_A(T_x, T_y)$

Figure B-113 Bi-directional responses of San Fernando earthquake, 111 Cedar Springs, Allen Ranch station

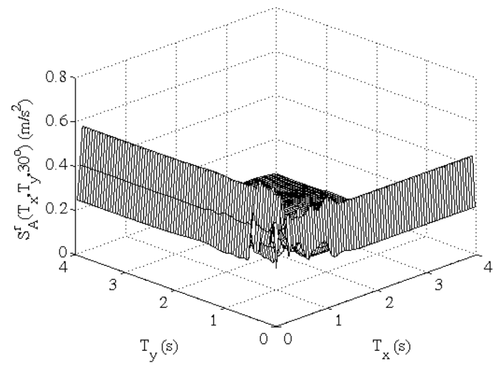

(a) $S^r_A(T_x, T_y, 30^\circ)$

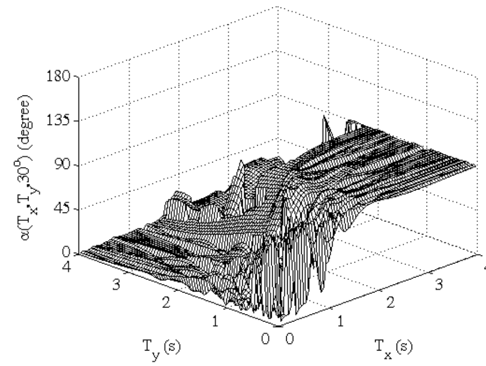

(b) $\alpha(T_x, T_y, 30^\circ)$

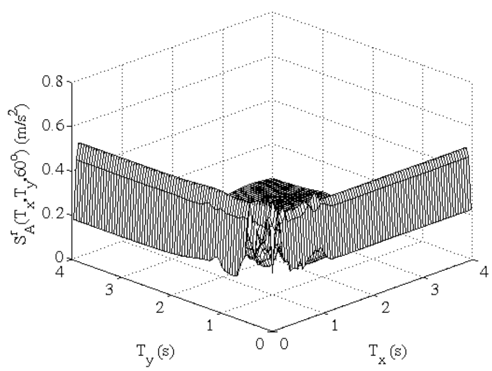

(c) $S^r_A(T_x, T_y, 60^\circ)$

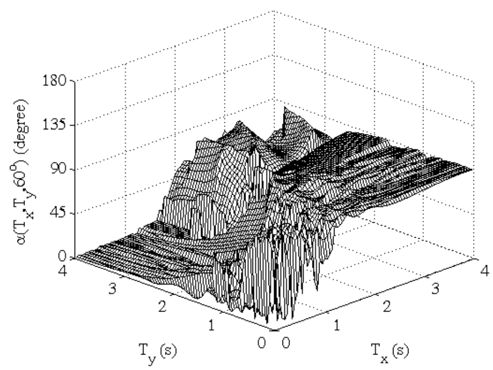

(d) $\alpha(T_x, T_y, 60^\circ)$

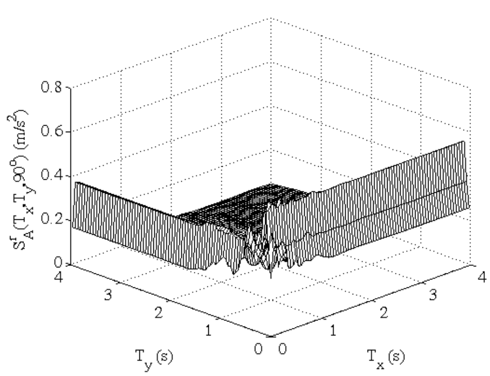

(e) $S^r_A(T_x, T_y, 90^\circ)$

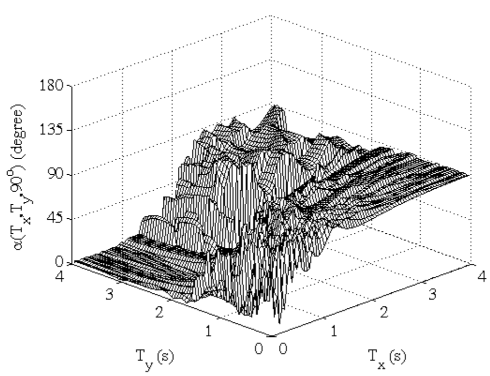

(f) $\alpha(T_x, T_y, 90^\circ)$

Figure B-114 Pseudo acceleration spectra and incident angles in various directions of San Fernando earthquake, 111 Cedar Springs, Allen Ranch station

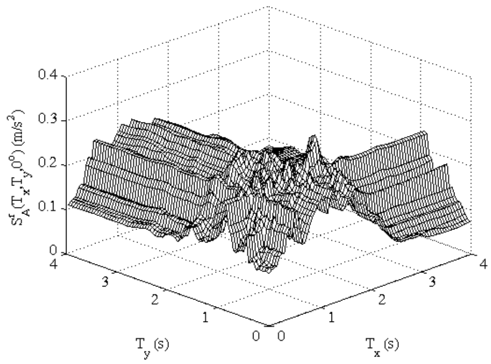

(a) $S_A^r(T_x,T_y,0^\circ)$

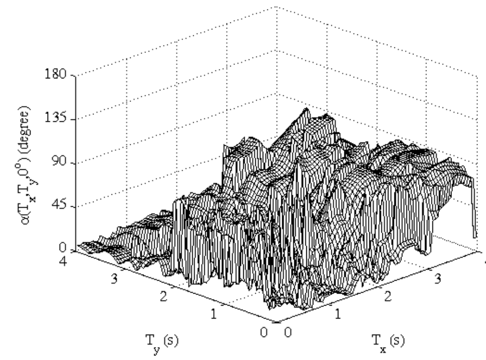

(b) $\alpha(T_x,T_y,0^\circ)$

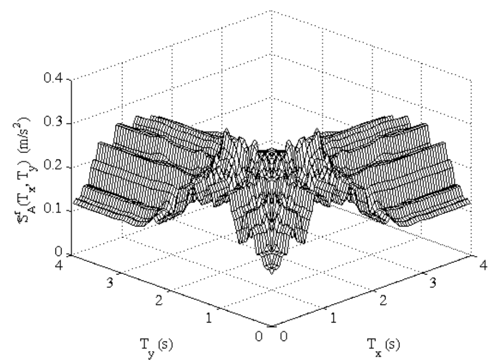

(c) $\widetilde{S}_A^r(T_x,T_y)$

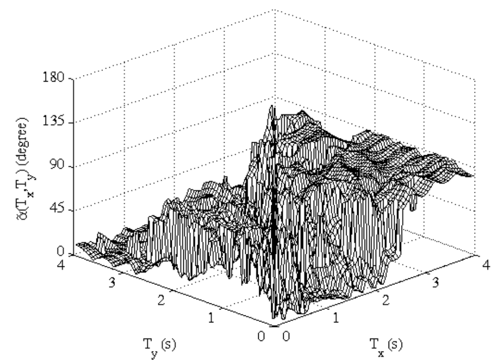

(d) $\widetilde{\alpha}(T_x,T_y)$

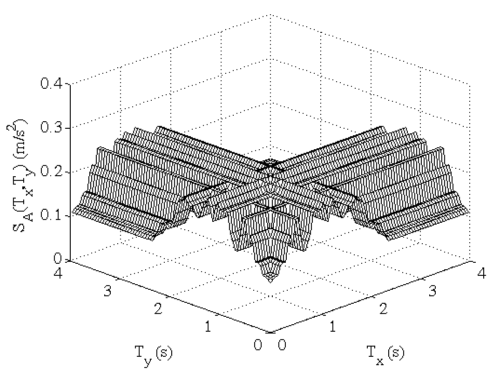

(e) $S_A(T_x,T_y)$

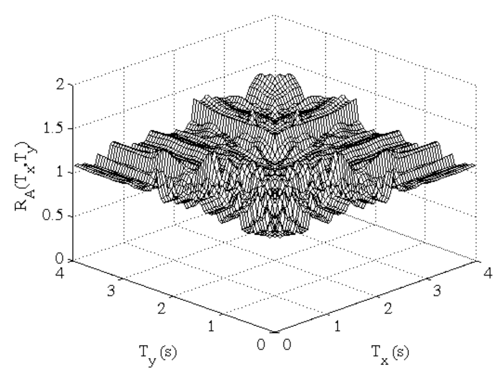

(f) $R_A(T_x,T_y)$

Figure B-115 Bi-directional responses of Chi-Chi, Taiwan earthquake, TTN016 station

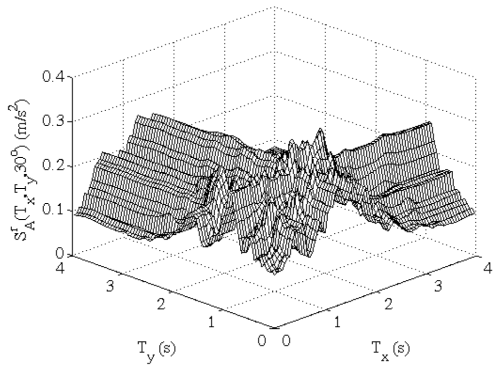

(a) $S_A^r(T_x,T_y,30^\circ)$

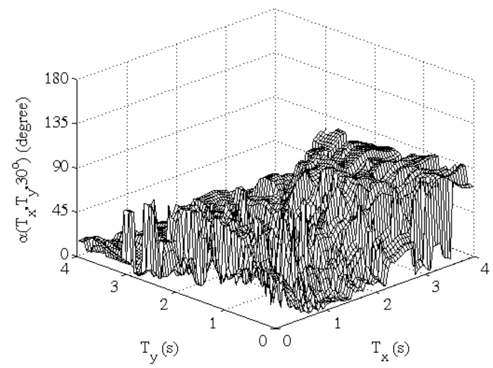

(b) $\alpha(T_x,T_y,30^\circ)$

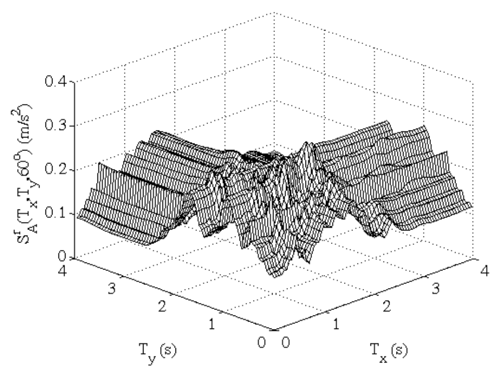

(c) $S_A^r(T_x,T_y,60^\circ)$

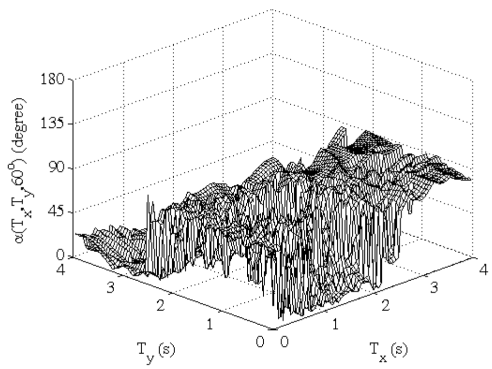

(d) $\alpha(T_x,T_y,60^\circ)$

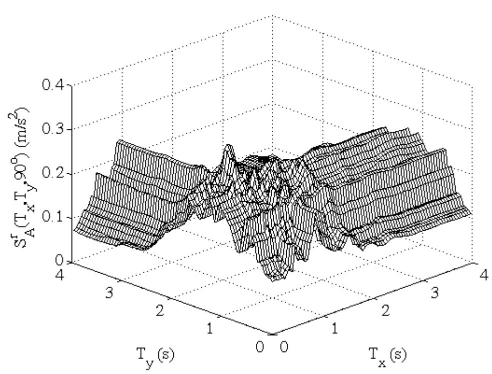

(e) $S_A^r(T_x,T_y,90^\circ)$

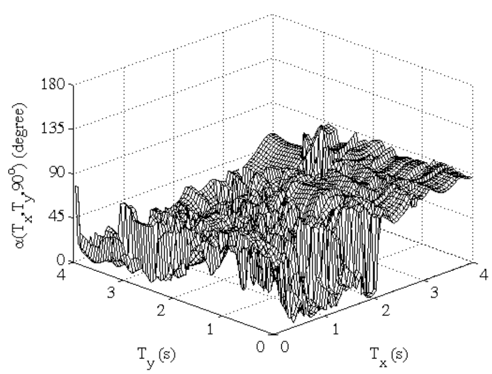

(f) $\alpha(T_x,T_y,90^\circ)$

Figure B-116 Pseudo acceleration spectra and incident angles in various directions of Chi-Chi, Taiwan earthquake, TTN016 station

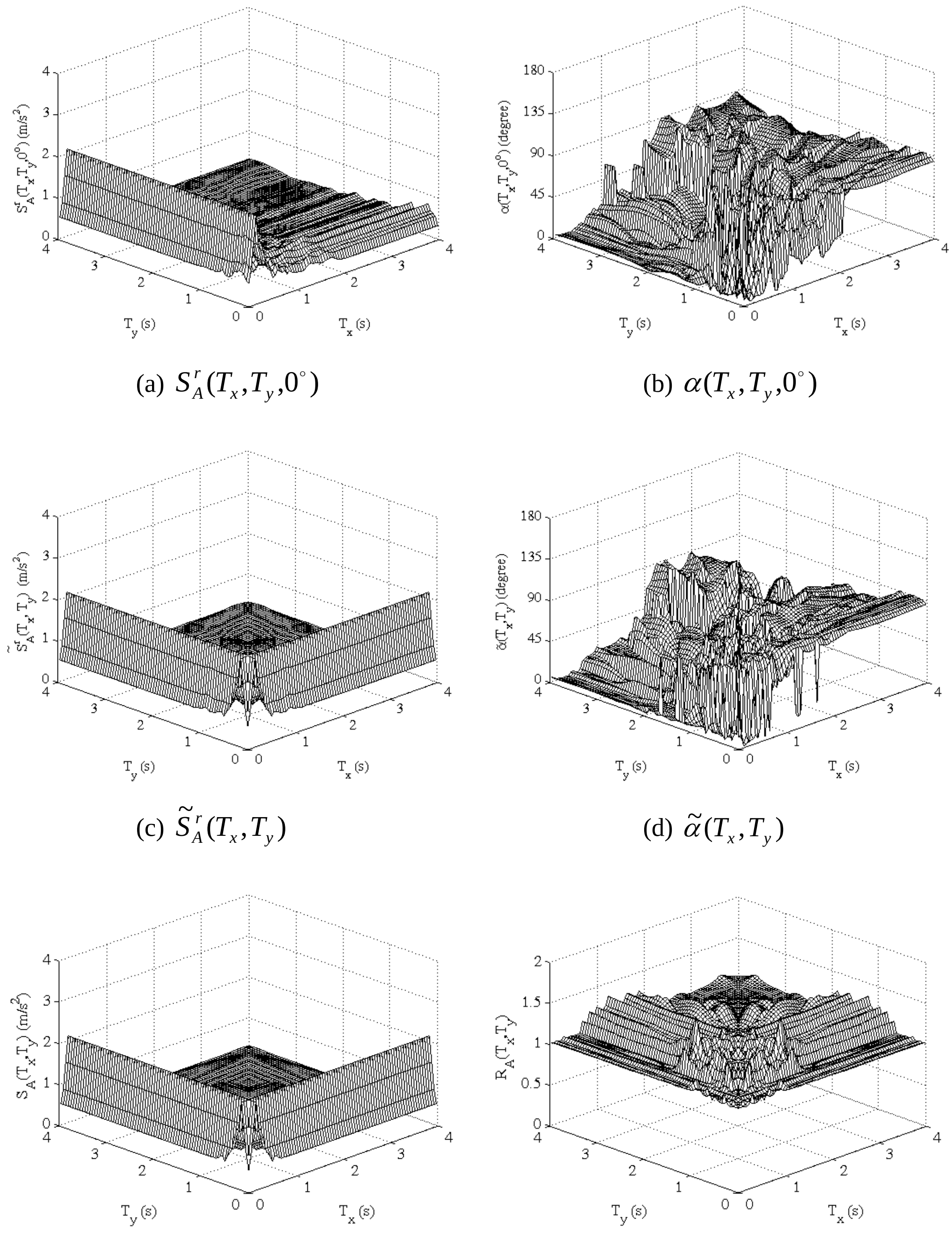

(a) $S_A^r(T_x, T_y, 0^{\circ})$ (b) $\alpha(T_x, T_y, 0^{\circ})$

(c) $\tilde{S}_A^r(T_x, T_y)$ (d) $\tilde{\alpha}(T_x, T_y)$

(e) $S_A(T_x, T_y)$ (f) $R_A(T_x, T_y)$

Figure B-117 Bi-directional responses of Duzce, Turkey earthquake, 1060 Lamont 1060 station

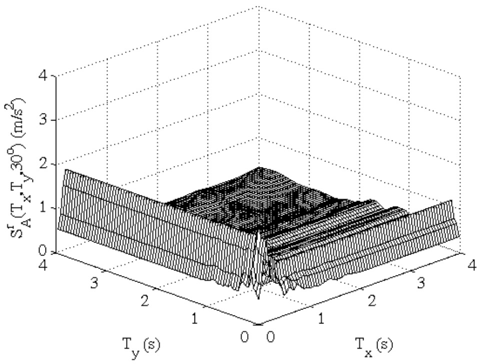

(a) $S_A^r(T_x,T_y,30^\circ)$

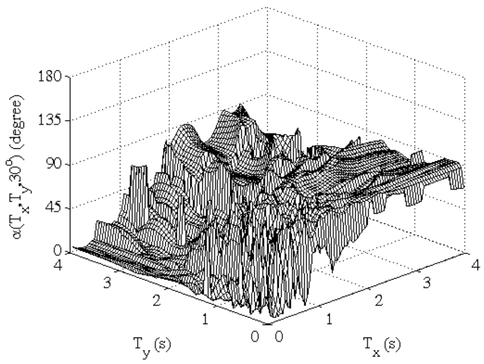

(b) $\alpha(T_x,T_y,30^\circ)$

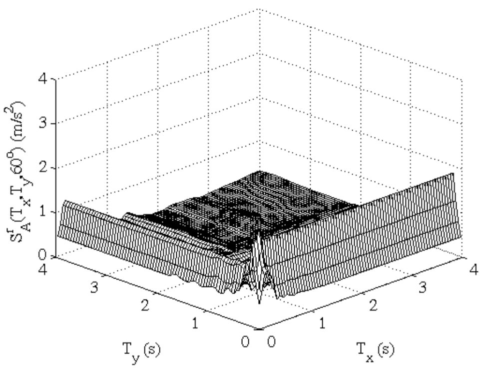

(c) $S_A^r(T_x,T_y,60^\circ)$

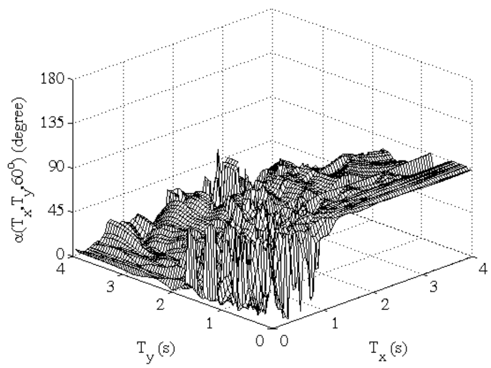

(d) $\alpha(T_x,T_y,60^\circ)$

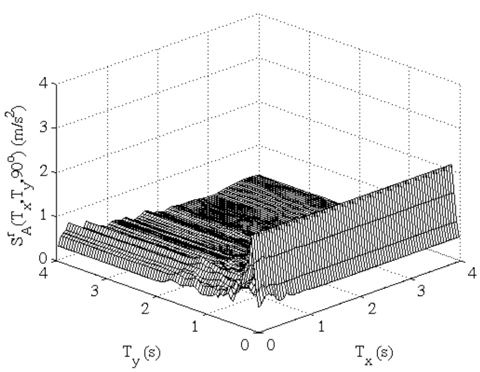

(e) $S_A^r(T_x,T_y,90^\circ)$

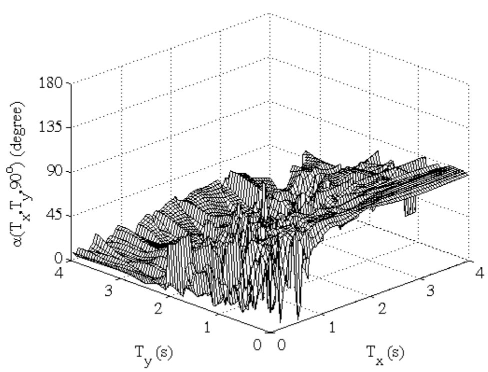

(f) $\alpha(T_x,T_y,90^\circ)$

Figure B-118 Pseudo acceleration spectra and incident angles in various directions of Duzce, Turkey earthquake, 1060 Lamont 1060 station

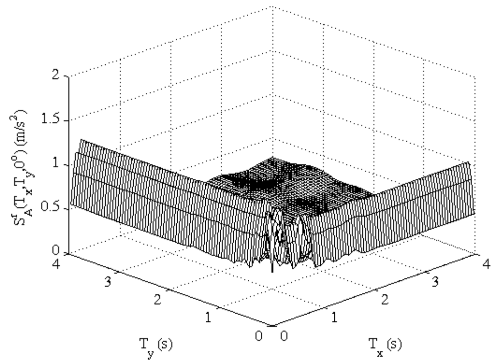

(a) $S_A^r(T_x, T_y, 0^\circ)$

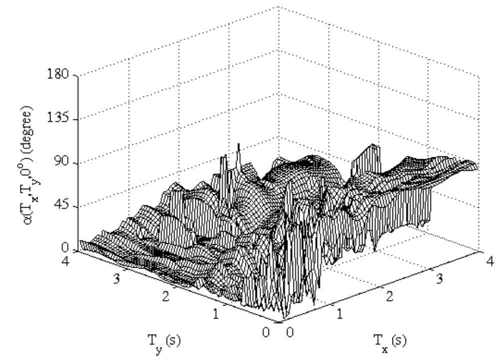

(b) $\alpha(T_x, T_y, 0^\circ)$

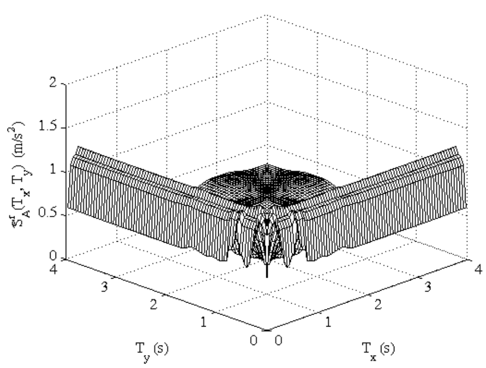

(c) $\tilde{S}_A^r(T_x, T_y)$

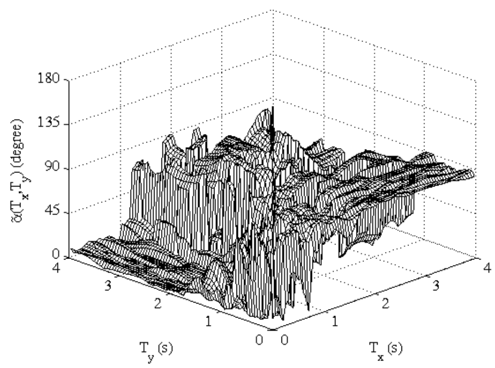

(d) $\tilde{\alpha}(T_x, T_y)$

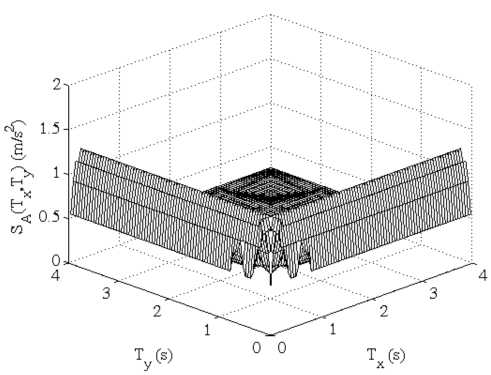

(e) $S_A(T_x, T_y)$

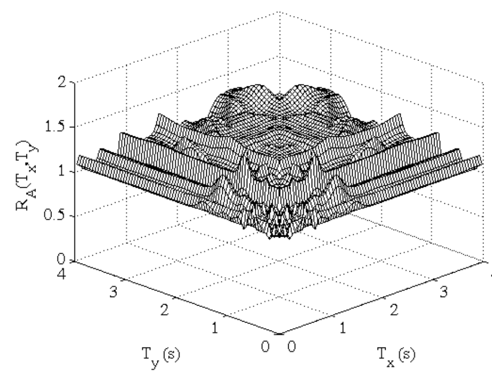

(f) $R_A(T_x, T_y)$

Figure B-119 Bi-directional responses of Kocaeli, Turkey earthquake, Maslak station

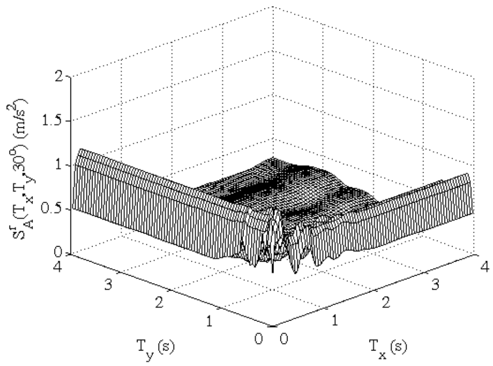

(a) $S_A^r(T_x,T_y,30^\circ)$

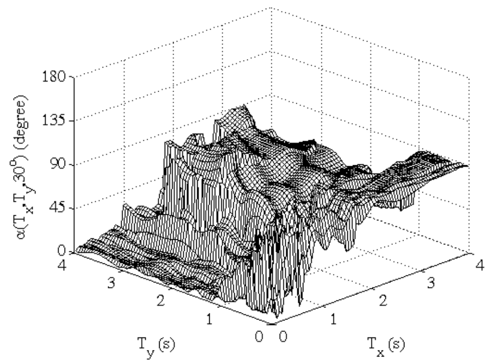

(b) $\alpha(T_x,T_y,30^\circ)$

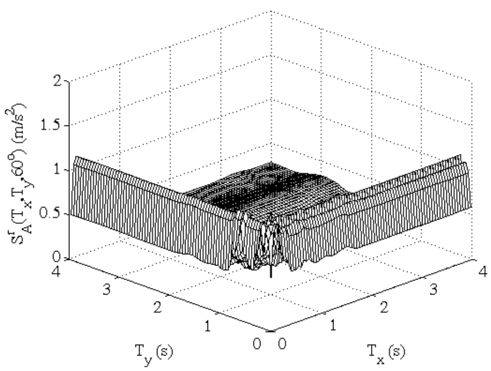

(c) $S_A^r(T_x,T_y,60^\circ)$

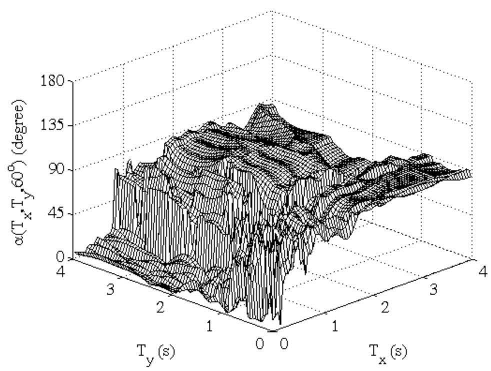

(d) $\alpha(T_x,T_y,60^\circ)$

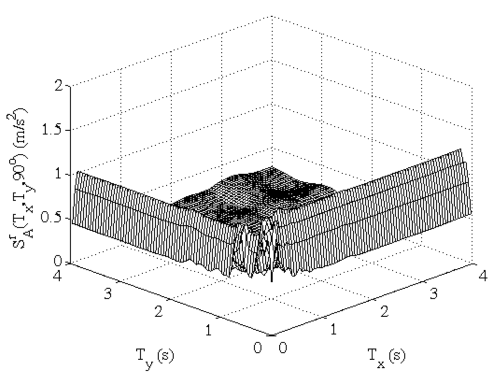

(e) $S_A^r(T_x,T_y,90^\circ)$

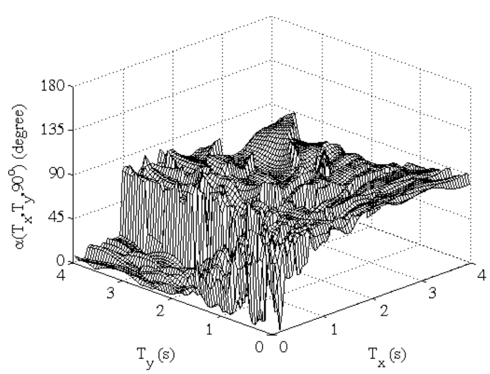

(f) $\alpha(T_x,T_y,90^\circ)$

Figure B-120 Pseudo acceleration spectra and incident angles in various directions of Kocaeli, Turkey earthquake, Maslak station

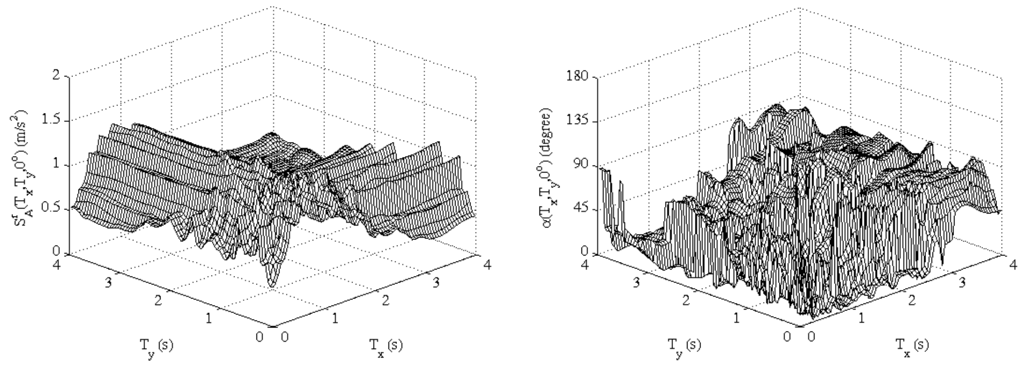

(a) $S_A^r(T_x, T_y, 0^\circ)$ (b) $\alpha(T_x, T_y, 0^\circ)$

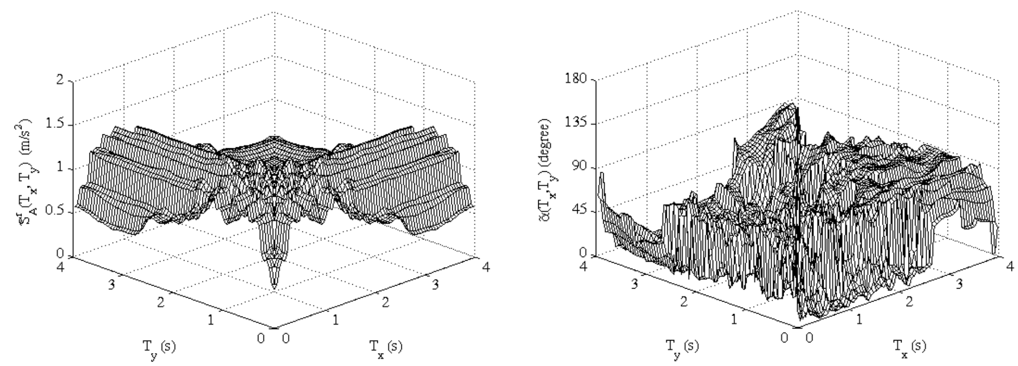

(c) $\widetilde{S}_A^r(T_x, T_y)$ (d) $\widetilde{\alpha}(T_x, T_y)$

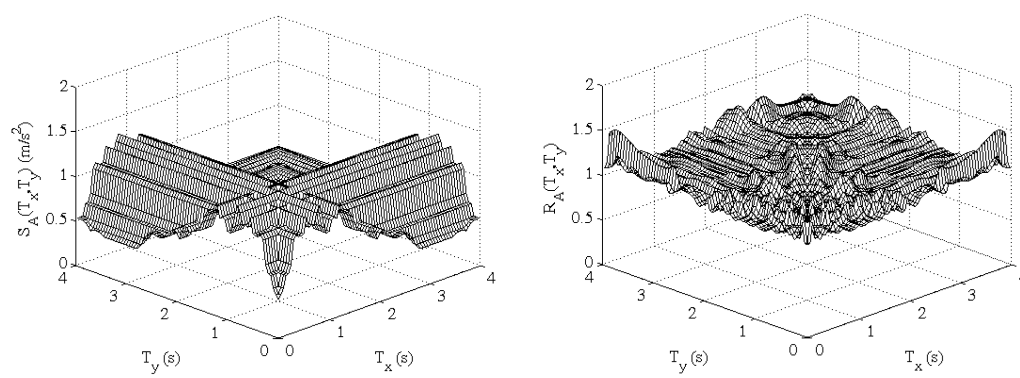

(e) $S_A(T_x, T_y)$ (f) $R_A(T_x, T_y)$

Figure B-121 Bi-directional responses of Landers earthquake, 90019 San Gabriel - E Grand Av station

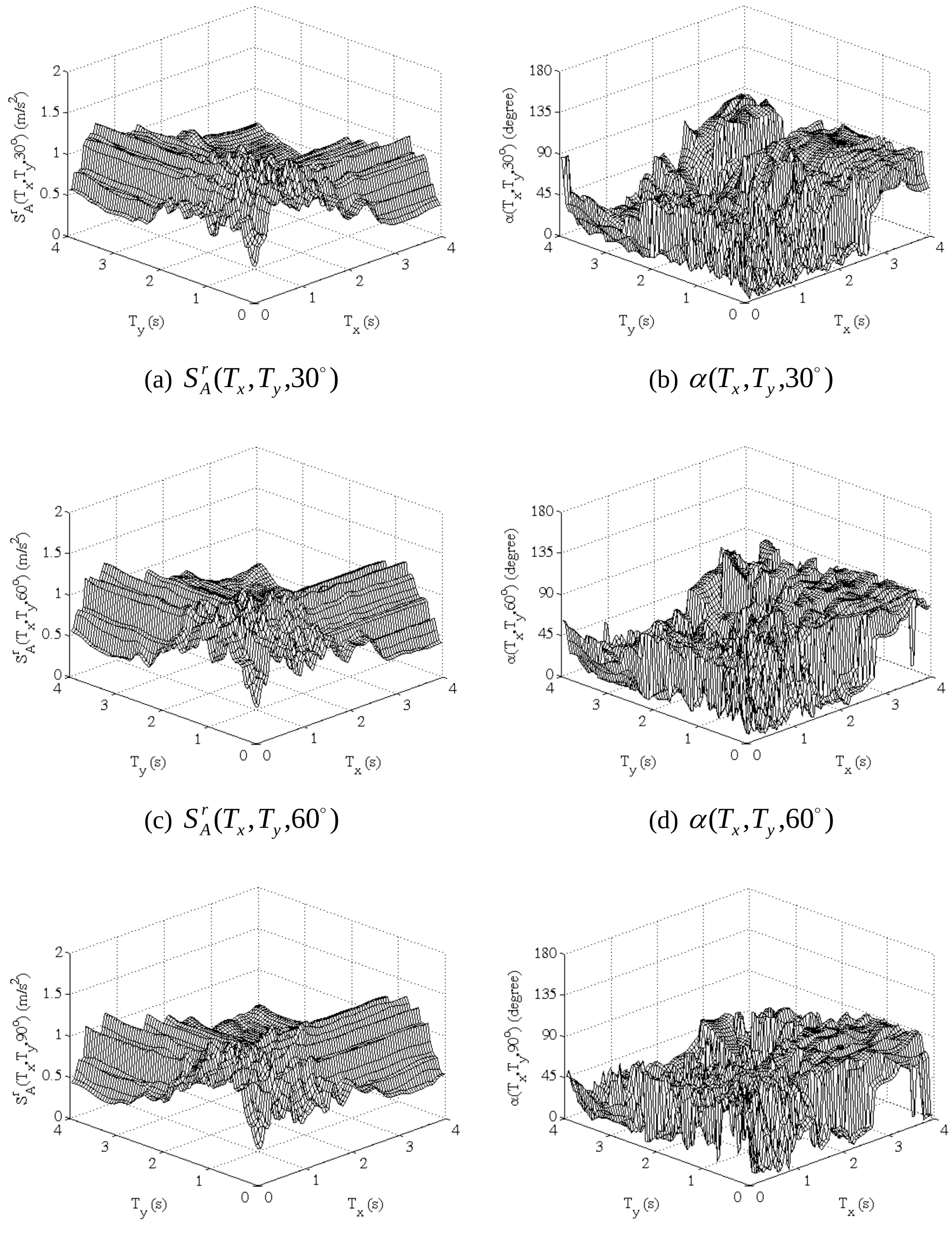

(a) $S_A^r(T_x, T_y, 30^{\circ})$ (b) $\alpha(T_x, T_y, 30^{\circ})$

(c) $S_A^r(T_x, T_y, 60^{\circ})$ (d) $\alpha(T_x, T_y, 60^{\circ})$

(e) $S_A^r(T_x, T_y, 90^{\circ})$ (f) $\alpha(T_x, T_y, 90^{\circ})$

Figure B-122 Pseudo acceleration spectra and incident angles in various directions of Landers earthquake, 90019 San Gabriel - E Grand Av station

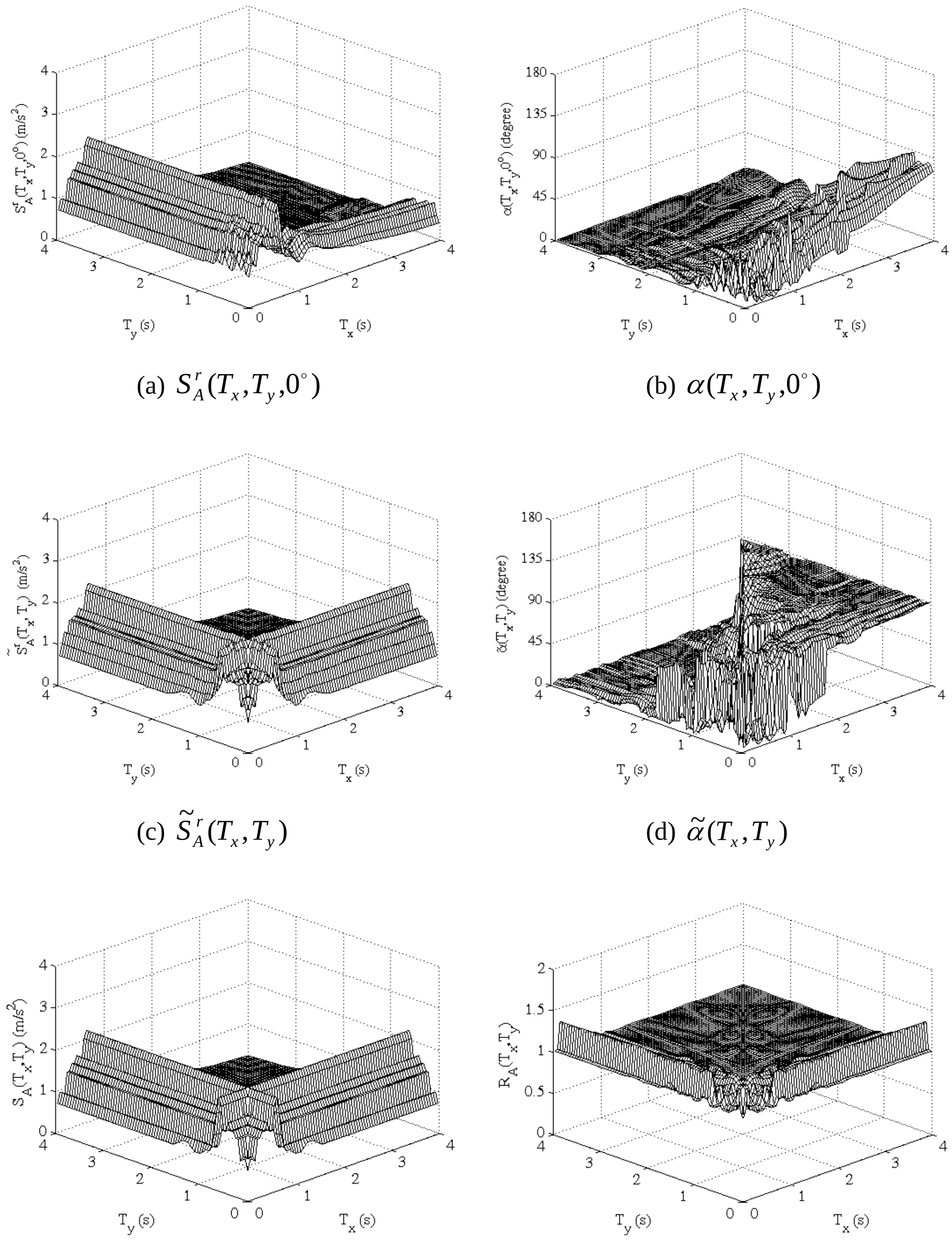

(a) $S_A^r(T_x,T_y,0^\circ)$ (b) $\alpha(T_x,T_y,0^\circ)$

(c) $\tilde{S}_A^r(T_x,T_y)$ (d) $\tilde{\alpha}(T_x,T_y)$

(e) $S_A(T_x,T_y)$ (f) $R_A(T_x,T_y)$

Figure B-123 Bi-directional responses of Loma Prieta earthquake, 58163 Yerba Buena Island station

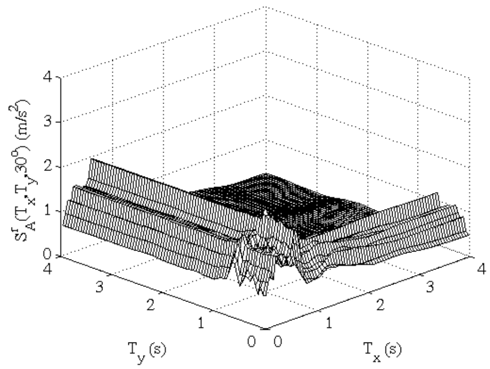

(a) $S_A^r(T_x, T_y, 30^\circ)$

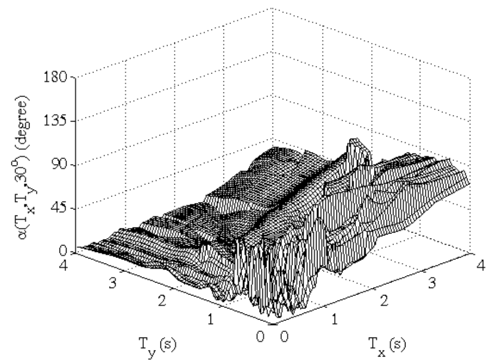

(b) $\alpha(T_x, T_y, 30^\circ)$

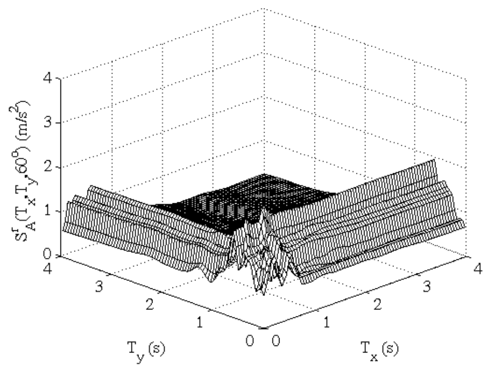

(c) $S_A^r(T_x, T_y, 60^\circ)$

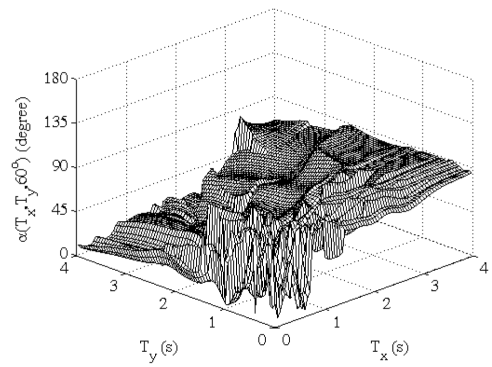

(d) $\alpha(T_x, T_y, 60^\circ)$

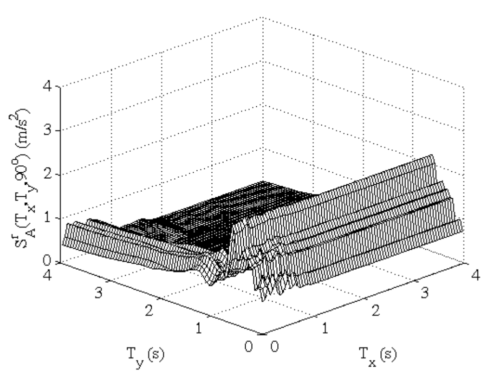

(e) $S_A^r(T_x, T_y, 90^\circ)$

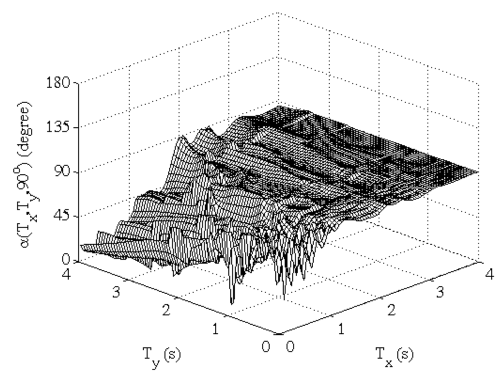

(f) $\alpha(T_x, T_y, 90^\circ)$

Figure B-124 Pseudo acceleration spectra and incident angles in various directions of Loma Prieta earthquake, 58163 Yerba Buena Island station

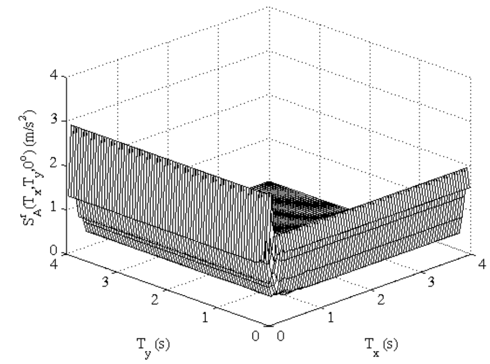

(a) $S^r_A(T_x, T_y, 0^\circ)$

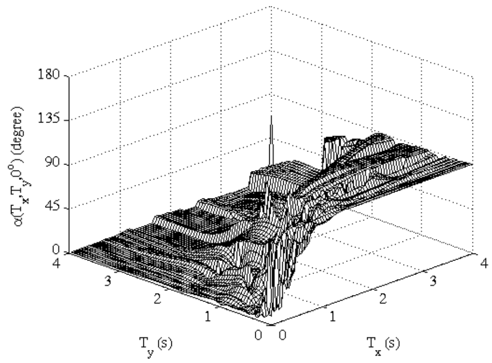

(b) $\alpha(T_x, T_y, 0^\circ)$

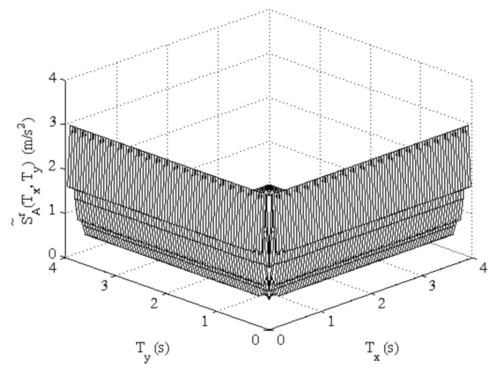

(c) $\tilde{S}^r_A(T_x, T_y)$

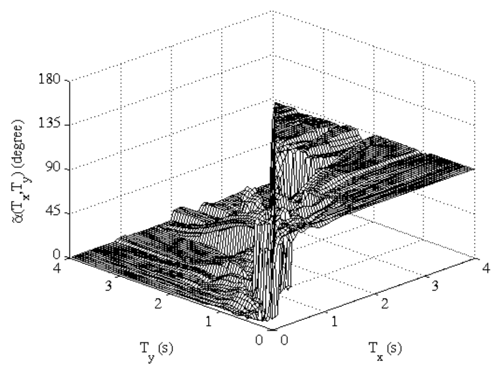

(d) $\tilde{\alpha}(T_x, T_y)$

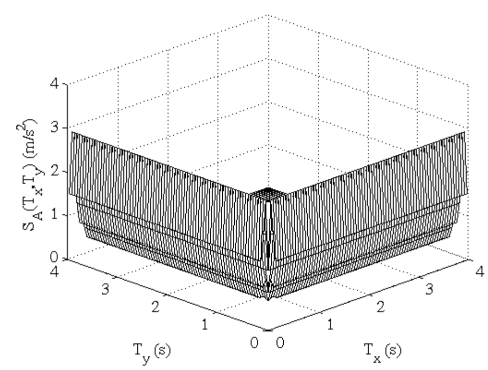

(e) $S_A(T_x, T_y)$

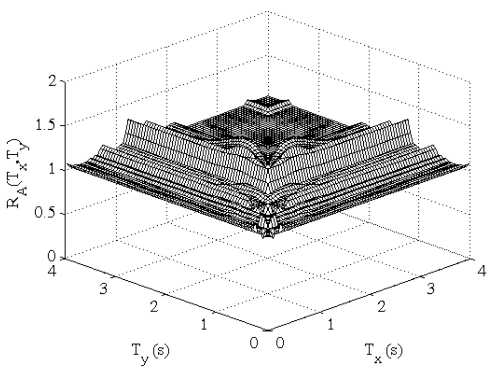

(f) $R_A(T_x, T_y)$

Figure B-125 Bi-directional responses of N. Palm Springs earthquake, 13199 Winchester Bergman Ran station

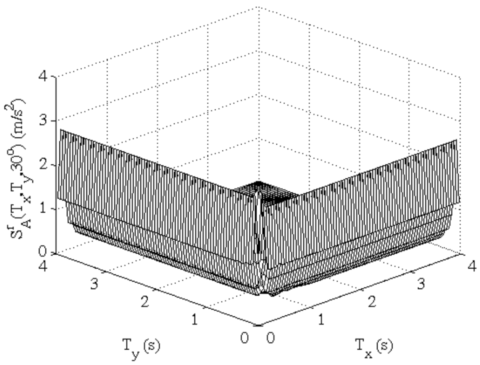

(a) $S^r_A(T_x,T_y,30^\circ)$

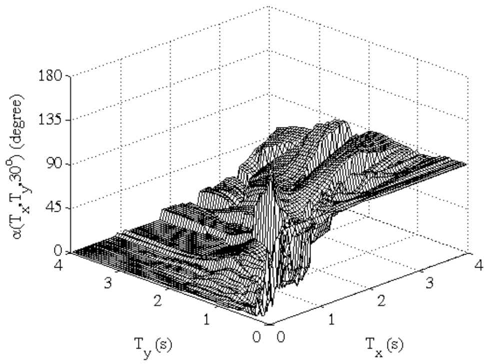

(b) $\alpha(T_x,T_y,30^\circ)$

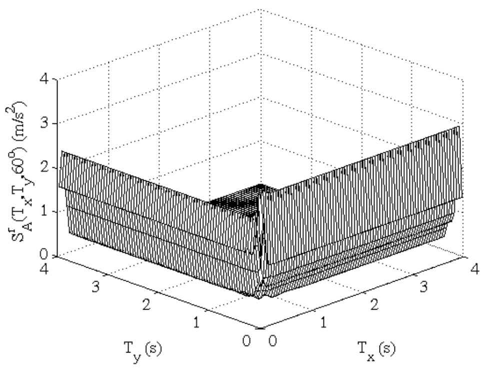

(c) $S^r_A(T_x,T_y,60^\circ)$

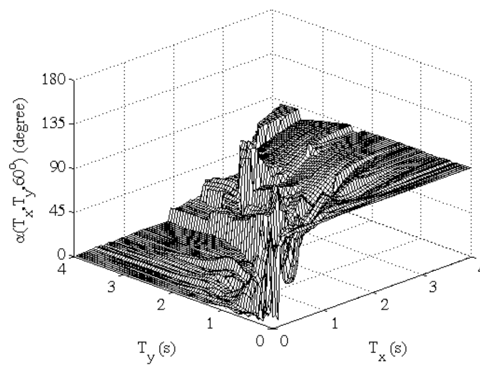

(d) $\alpha(T_x,T_y,60^\circ)$

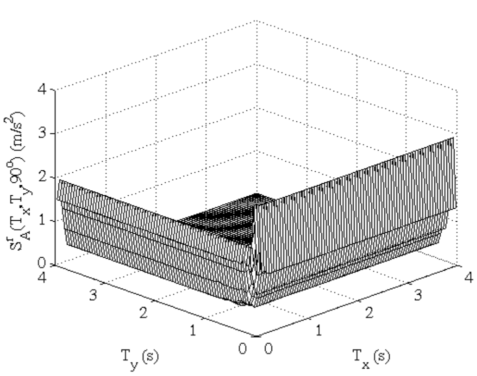

(e) $S^r_A(T_x,T_y,90^\circ)$

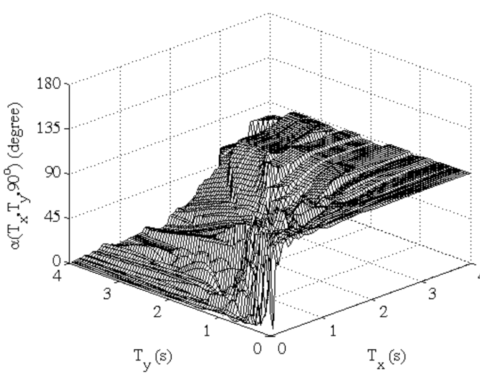

(f) $\alpha(T_x,T_y,90^\circ)$

Figure B-126 Pseudo acceleration spectra and incident angles in various directions of N. Palm Springs earthquake, 13199 Winchester Bergman Ran station

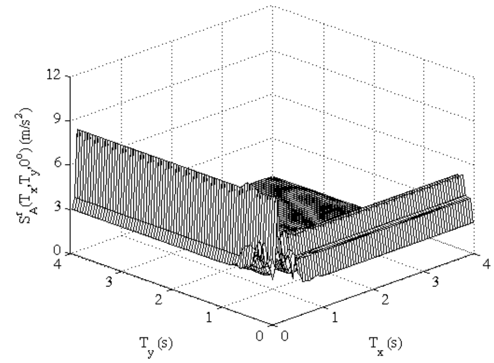

(a) $S_A^r(T_x, T_y, 0^\circ)$

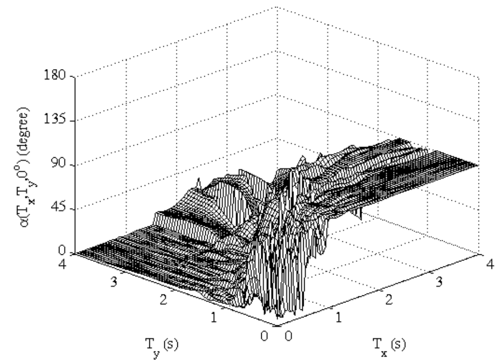

(b) $\alpha(T_x, T_y, 0^\circ)$

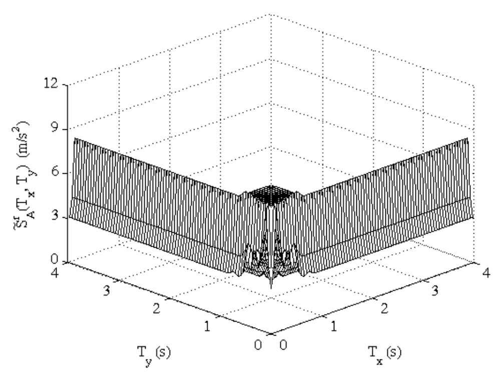

(c) $\tilde{S}_A^r(T_x, T_y)$

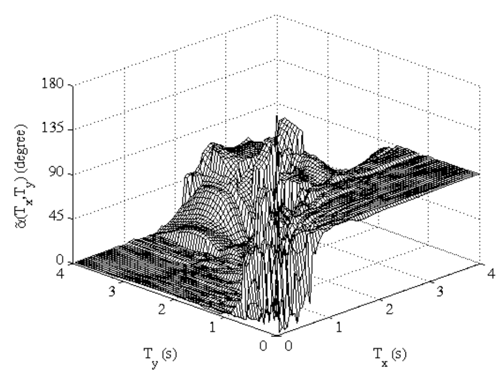

(d) $\tilde{\alpha}(T_x, T_y)$

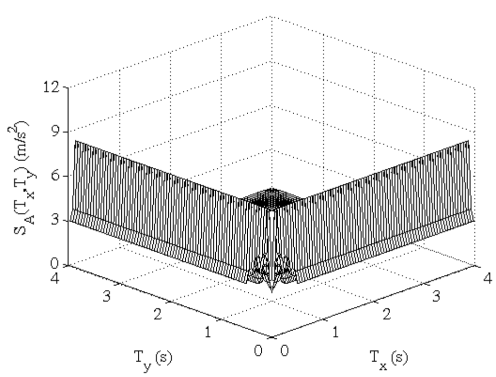

(e) $S_A(T_x, T_y)$

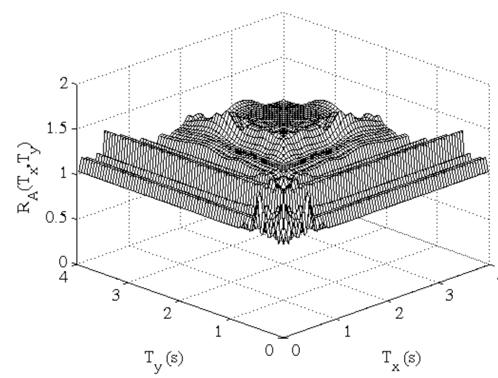

(f) $R_A(T_x, T_y)$

Figure B-127 Bi-directional responses of Northridge earthquake, 90019 San Gabriel - E. Grand Ave station

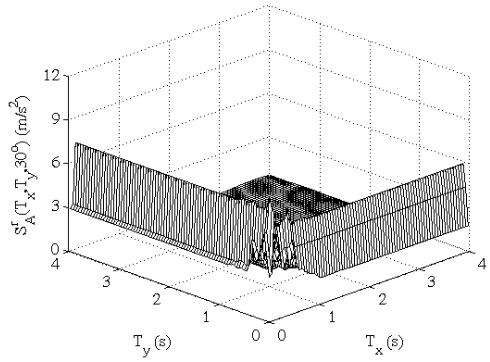

(a) $S_A^r(T_x, T_y, 30^\circ)$

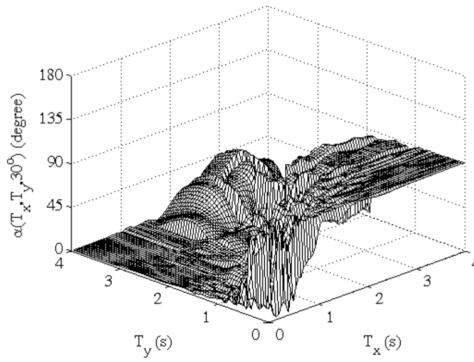

(b) $\alpha(T_x, T_y, 30^\circ)$

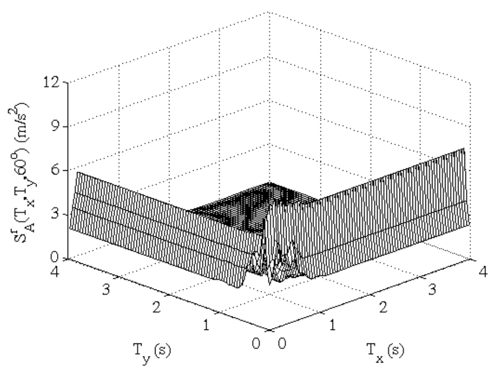

(c) $S_A^r(T_x, T_y, 60^\circ)$

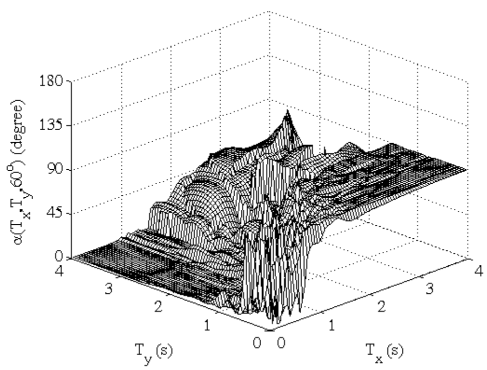

(d) $\alpha(T_x, T_y, 60^\circ)$

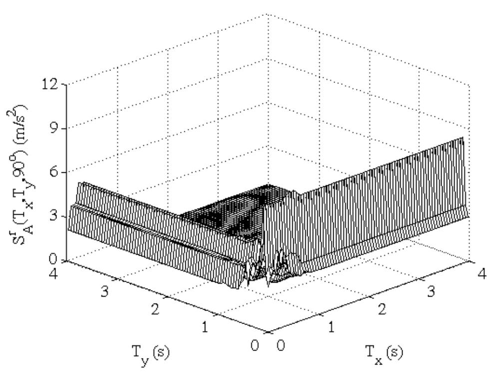

(e) $S_A^r(T_x, T_y, 90^\circ)$

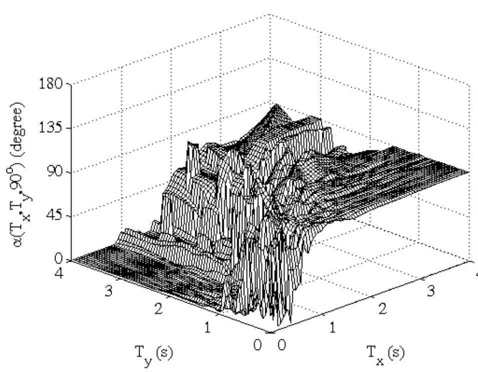

(f) $\alpha(T_x, T_y, 90^\circ)$

Figure B-128 Pseudo acceleration spectra and incident angles in various directions of Northridge earthquake, 90019 San Gabriel - E. Grand Ave station

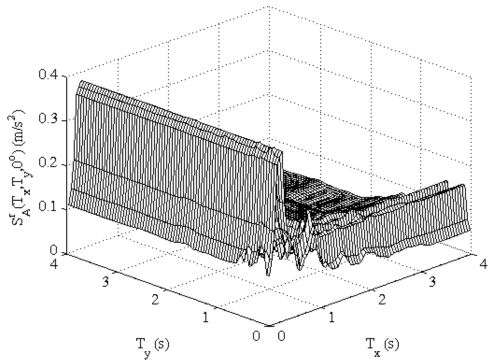

(a) $S^r_A(T_x, T_y, 0^\circ)$

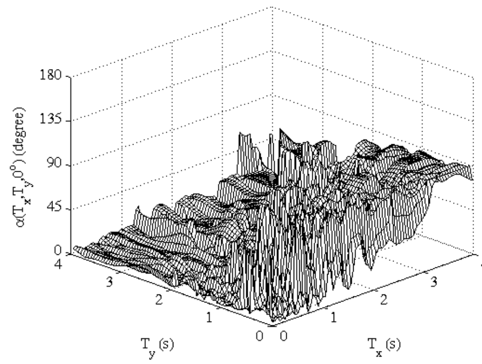

(b) $\alpha(T_x, T_y, 0^\circ)$

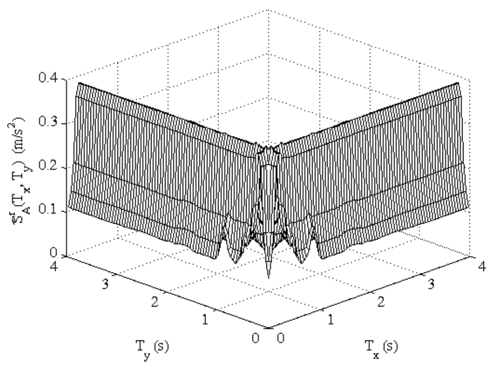

(c) $\widetilde{S}^r_A(T_x, T_y)$

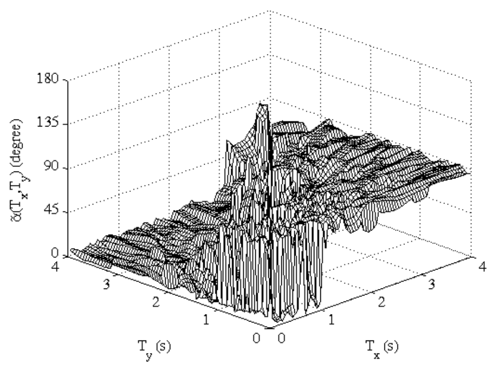

(d) $\widetilde{\alpha}(T_x, T_y)$

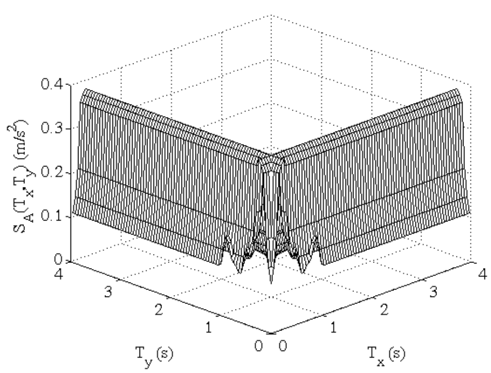

(e) $S_A(T_x, T_y)$

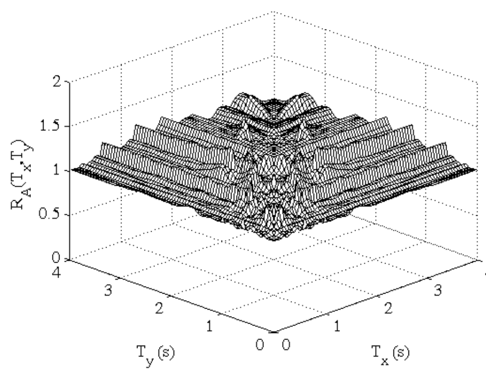

(f) $R_A(T_x, T_y)$

Figure B-129 Bi-directional responses of San Fernando earthquake, 1035 Isabella Dam (Aux Abut) station

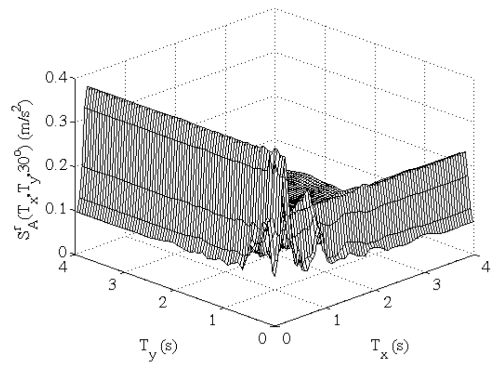

(a) $S_A^r(T_x, T_y, 30^\circ)$

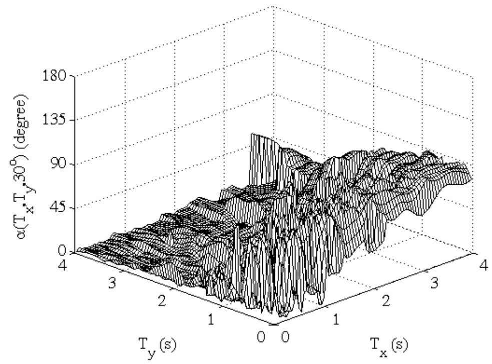

(b) $\alpha(T_x, T_y, 30^\circ)$

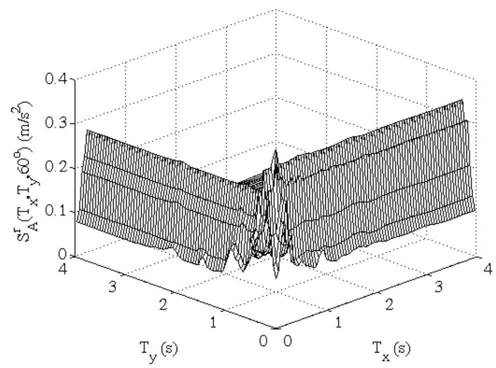

(c) $S_A^r(T_x, T_y, 60^\circ)$

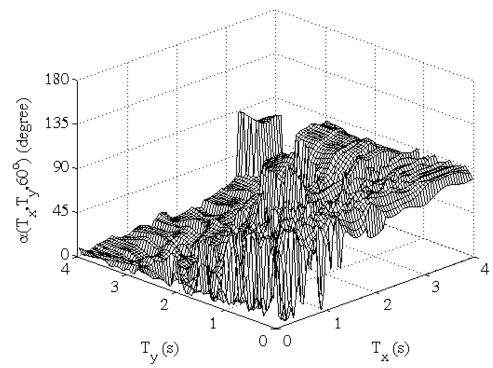

(d) $\alpha(T_x, T_y, 60^\circ)$

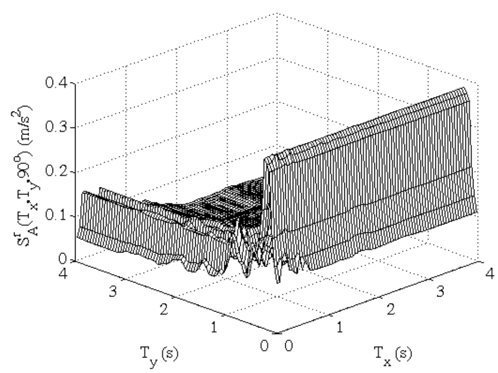

(e) $S_A^r(T_x, T_y, 90^\circ)$

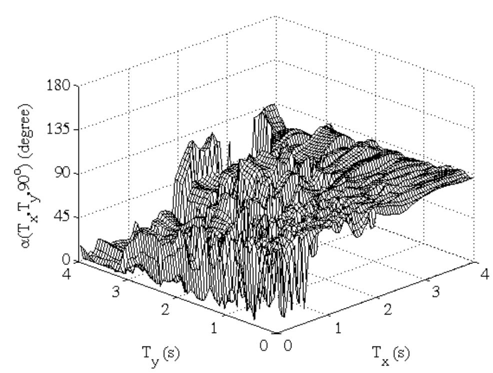

(f) $\alpha(T_x, T_y, 90^\circ)$

Figure B-130 Pseudo acceleration spectra and incident angles in various directions of San Fernando earthquake, 1035 Isabella Dam (Aux Abut) station

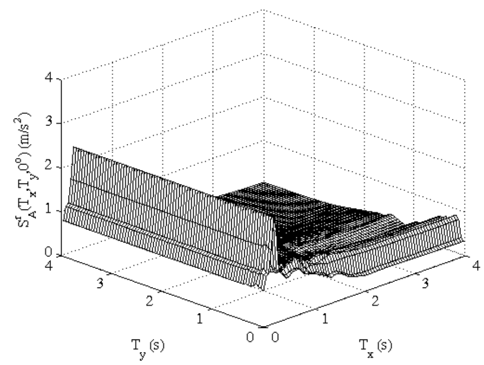

(a) $S_A^r(T_x, T_y, 0^\circ)$

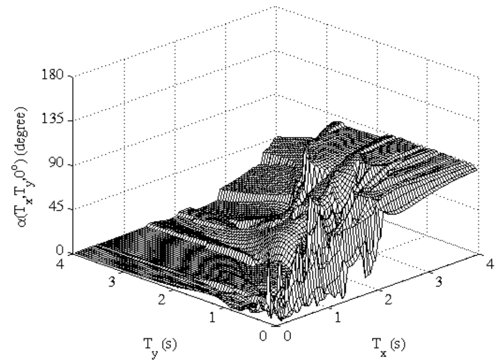

(b) $\alpha(T_x, T_y, 0^\circ)$

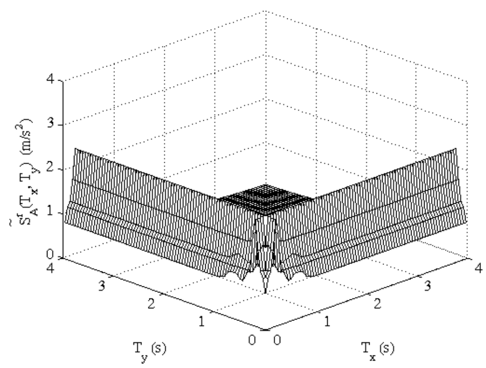

(c) $\tilde{S}_A^r(T_x, T_y)$

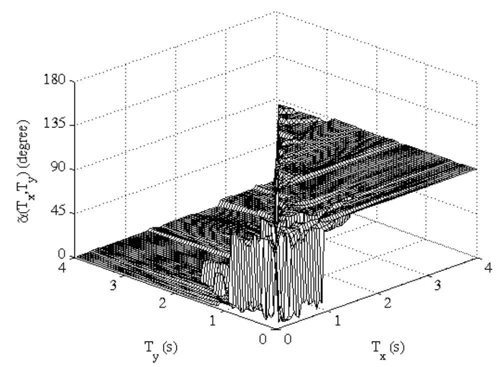

(d) $\tilde{\alpha}(T_x, T_y)$

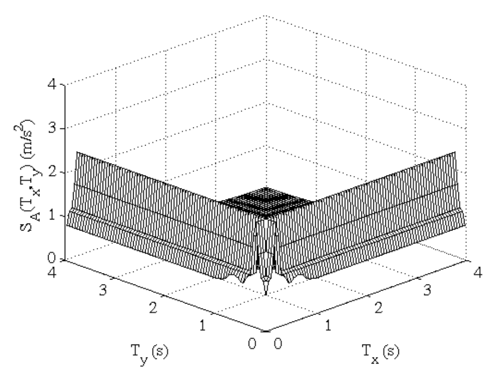

(e) $S_A(T_x, T_y)$

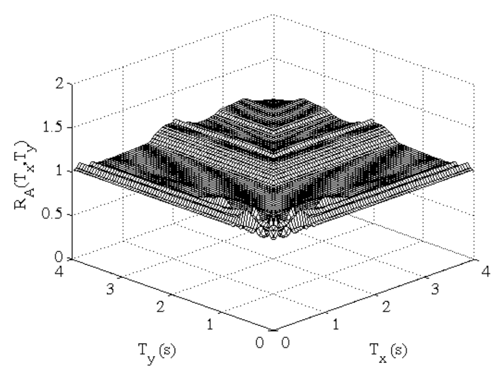

(f) $R_A(T_x, T_y)$

Figure B-131 Bi-directional responses of Santa Barbara earthquake, 106 Cachuma Dam Toe station

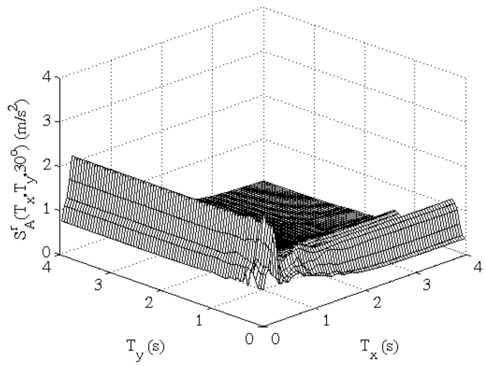

(a) $S_A^r(T_x,T_y,30^\circ)$

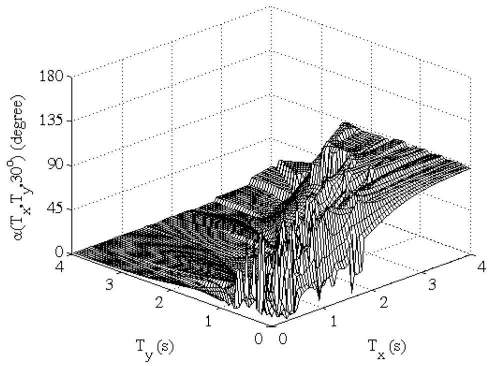

(b) $\alpha(T_x,T_y,30^\circ)$

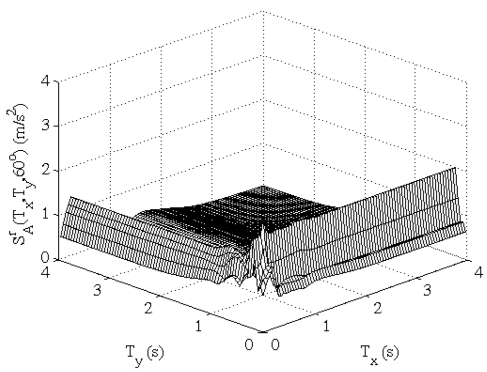

(c) $S_A^r(T_x,T_y,60^\circ)$

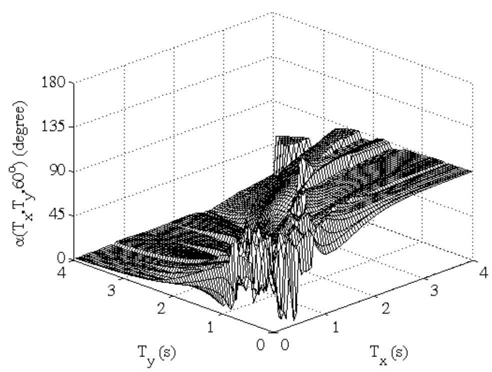

(d) $\alpha(T_x,T_y,60^\circ)$

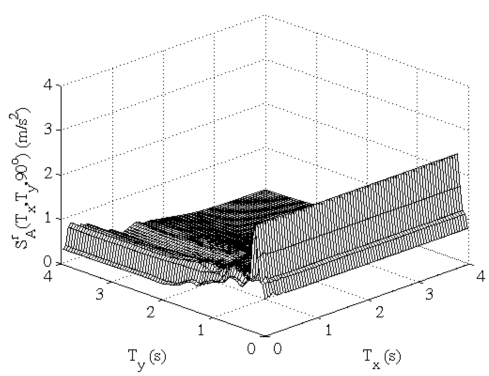

(e) $S_A^r(T_x,T_y,90^\circ)$

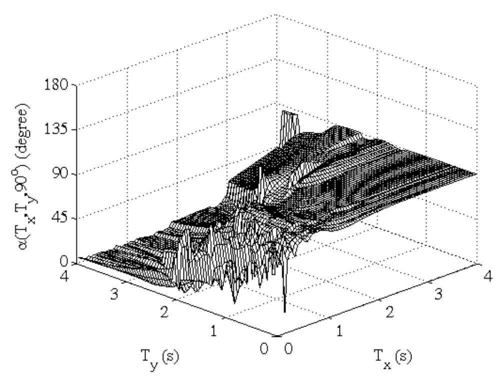

(f) $\alpha(T_x,T_y,90^\circ)$

Figure B-132 Pseudo acceleration spectra and incident angles in various directions of Santa Barbara earthquake, 106 Cachuma Dam Toe station

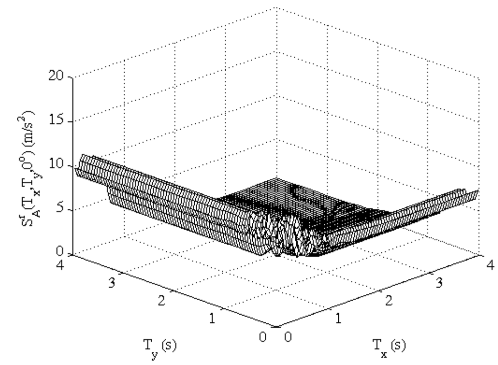

(a) $S^r_A(T_x, T_y, 0^\circ)$

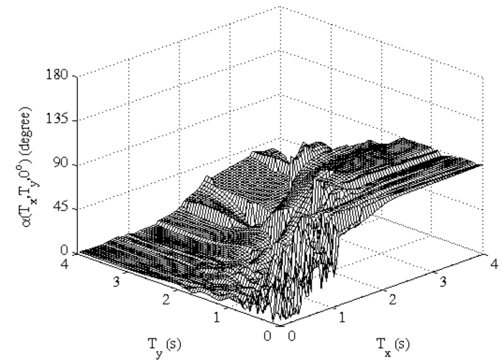

(b) $\alpha(T_x, T_y, 0^\circ)$

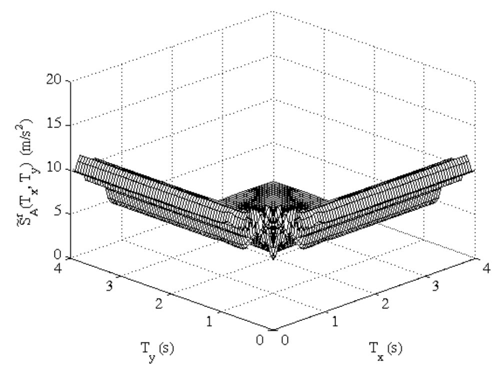

(c) $\tilde{S}^r_A(T_x, T_y)$

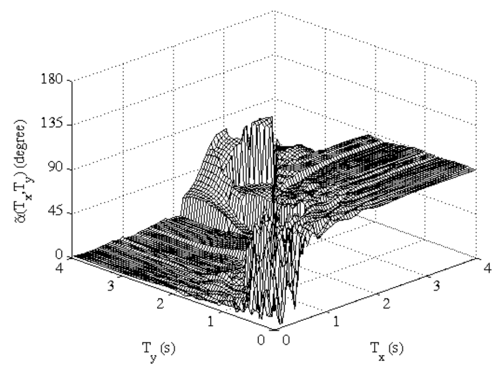

(d) $\tilde{\alpha}(T_x, T_y)$

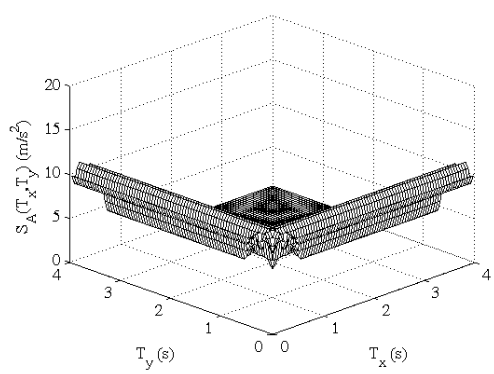

(e) $S_A(T_x, T_y)$

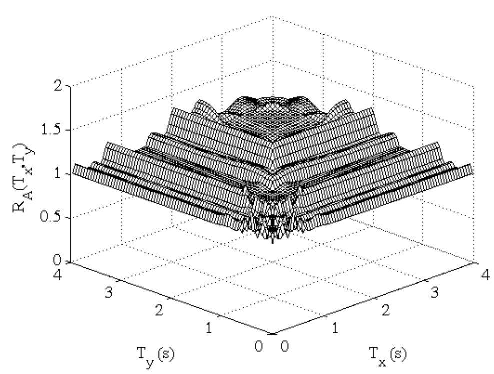

(f) $R_A(T_x, T_y)$

Figure B-133 Bi-directional responses of Victoria, Mexico earthquake, 6604 Cerro Prieto station

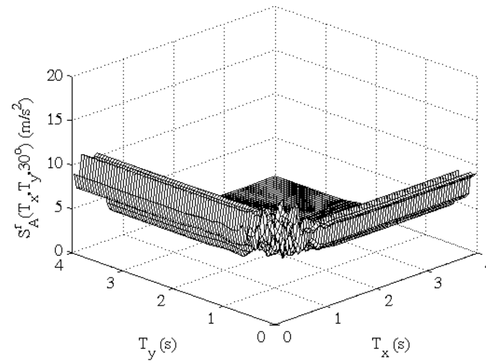

(a) $S_A^r(T_x, T_y, 30^\circ)$

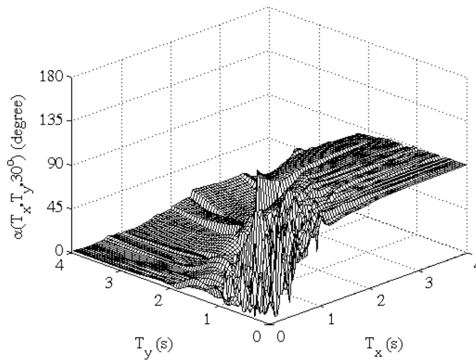

(b) $\alpha(T_x, T_y, 30^\circ)$

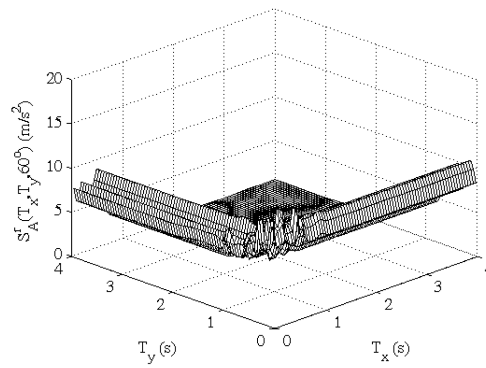

(c) $S_A^r(T_x, T_y, 60^\circ)$

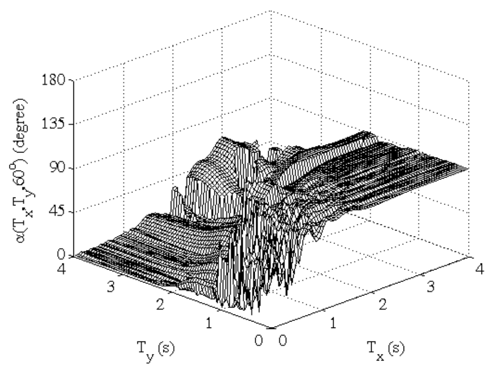

(d) $\alpha(T_x, T_y, 60^\circ)$

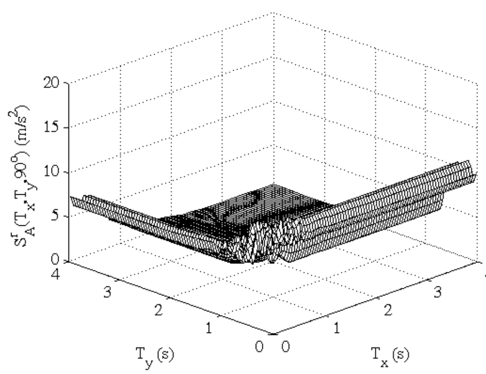

(e) $S_A^r(T_x, T_y, 90^\circ)$

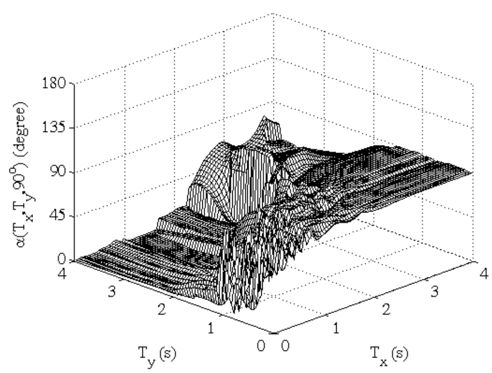

(f) $\alpha(T_x, T_y, 90^\circ)$

Figure B-134 Pseudo acceleration spectra and incident angles in various directions of Victoria, Mexico earthquake, 6604 Cerro Prieto station

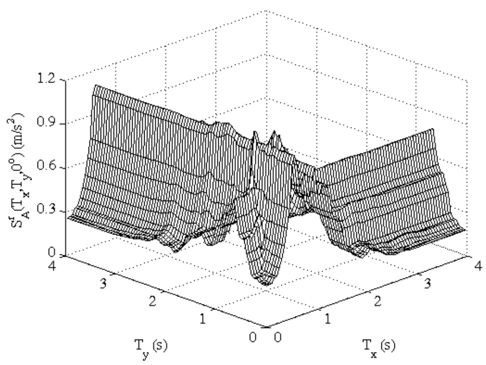

(a) $S^r_A(T_x,T_y,0^\circ)$

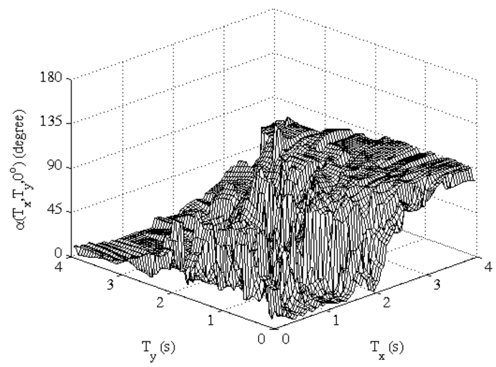

(b) $\alpha(T_x,T_y,0^\circ)$

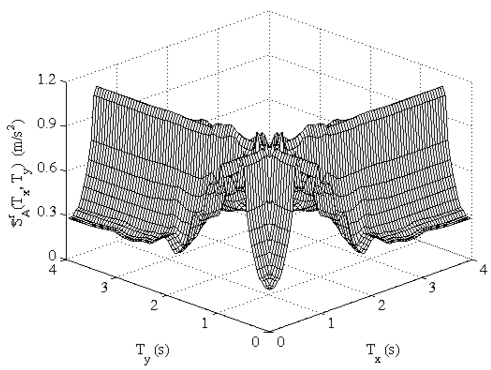

(c) $\tilde{S}^r_A(T_x,T_y)$

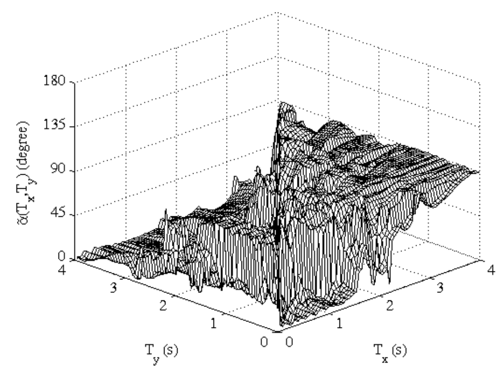

(d) $\tilde{\alpha}(T_x,T_y)$

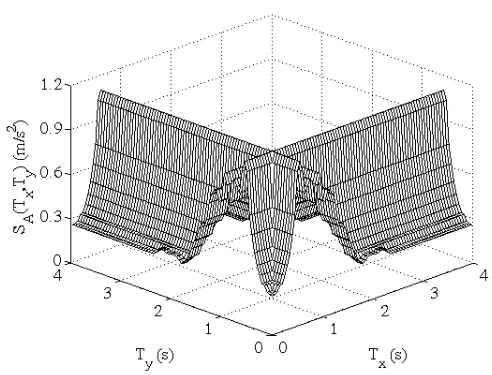

(e) $S_A(T_x,T_y)$

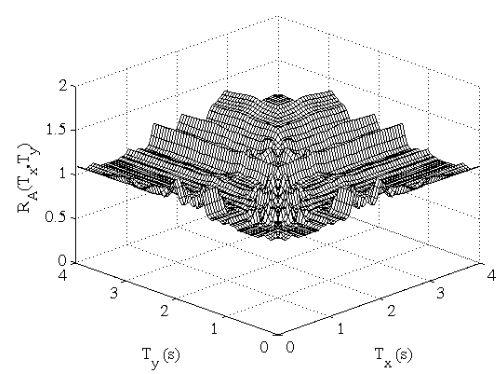

(f) $R_A(T_x,T_y)$

Figure B-135 Bi-directional responses of Chi-Chi, Taiwan earthquake, KAU037 station

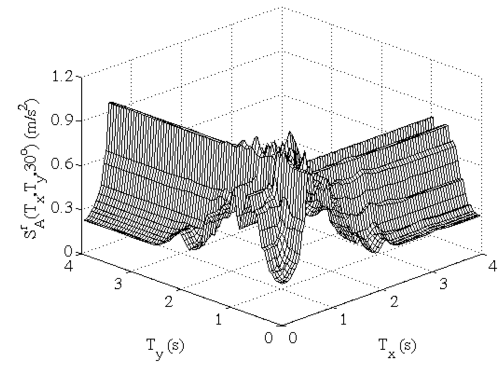

(a) $S_A^r(T_x,T_y,30^\circ)$

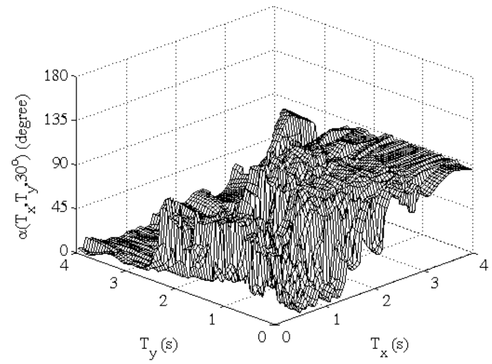

(b) $\alpha(T_x,T_y,30^\circ)$

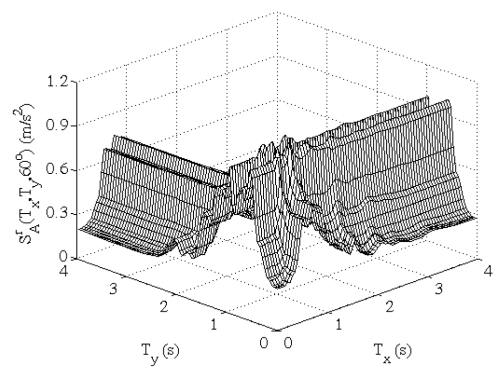

(c) $S_A^r(T_x,T_y,60^\circ)$

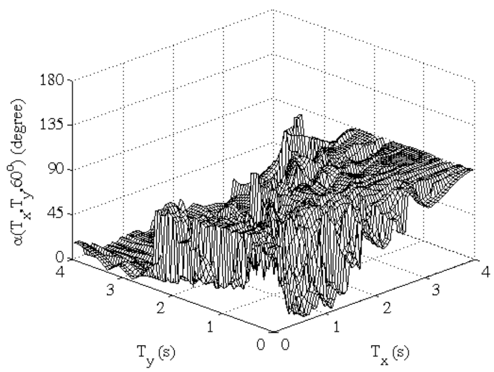

(d) $\alpha(T_x,T_y,60^\circ)$

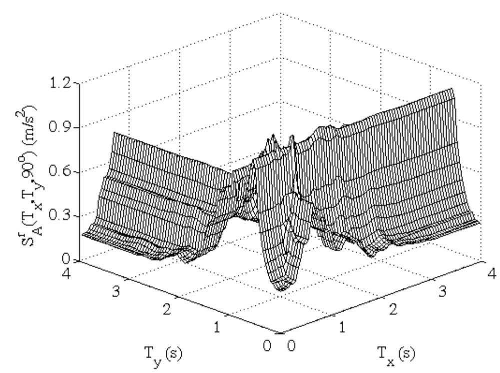

(e) $S_A^r(T_x,T_y,90^\circ)$

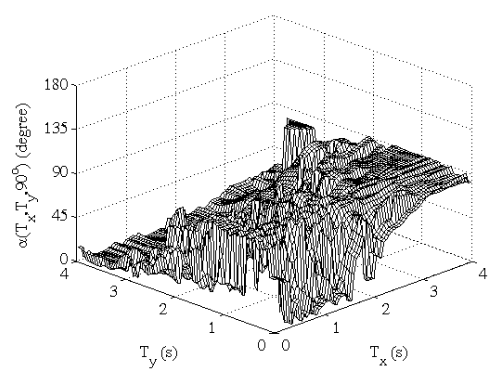

(f) $\alpha(T_x,T_y,90^\circ)$

Figure B-136 Pseudo acceleration spectra and incident angles in various directions of Chi-Chi, Taiwan earthquake, KAU037 station

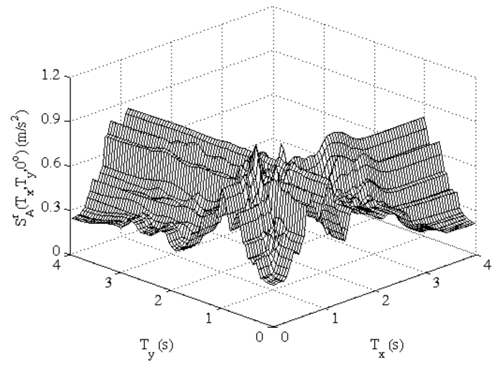

(a) $S_A^r(T_x,T_y,0^\circ)$

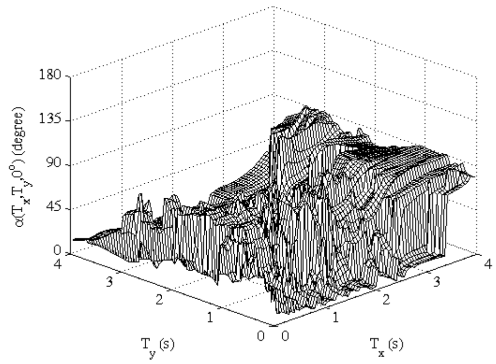

(b) $\alpha(T_x,T_y,0^\circ)$

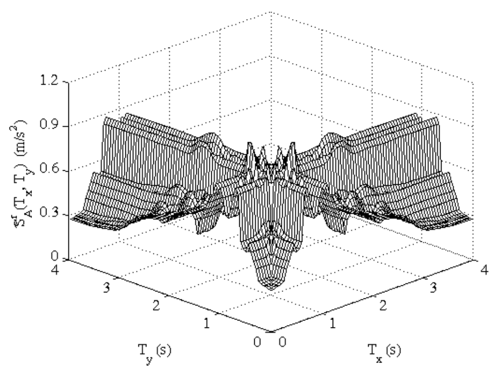

(c) $\tilde{S}_A^r(T_x,T_y)$

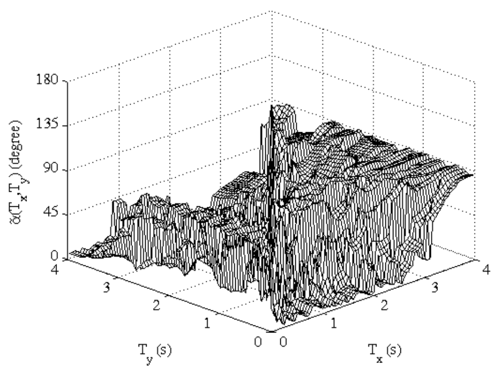

(d) $\tilde{\alpha}(T_x,T_y)$

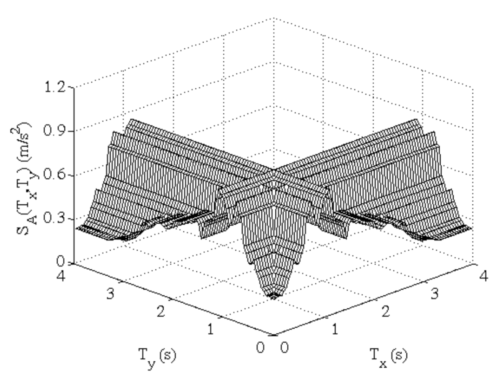

(e) $S_A(T_x,T_y)$

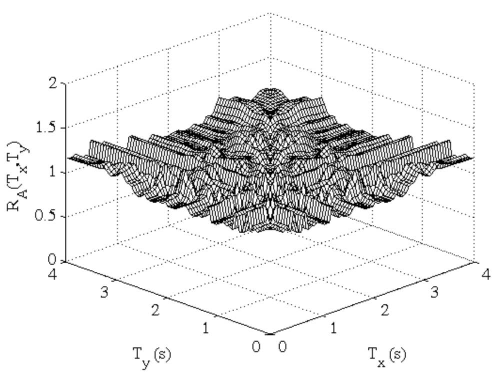

(f) $R_A(T_x,T_y)$

Figure B-137 Bi-directional responses of Chi-Chi, Taiwan earthquake, KAU081 station

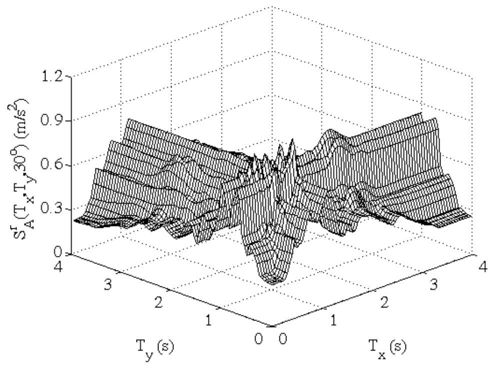

(a) $S^r_A(T_x, T_y, 30^\circ)$

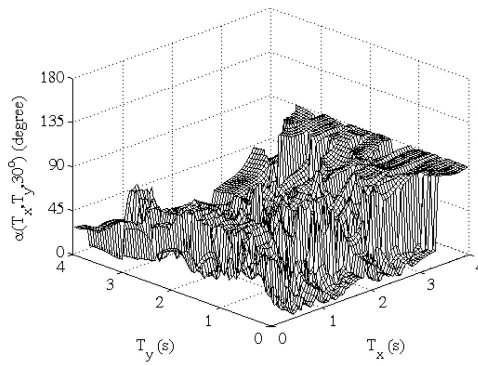

(b) $\alpha(T_x, T_y, 30^\circ)$

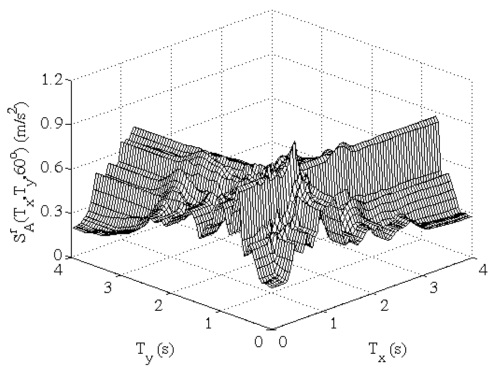

(c) $S^r_A(T_x, T_y, 60^\circ)$

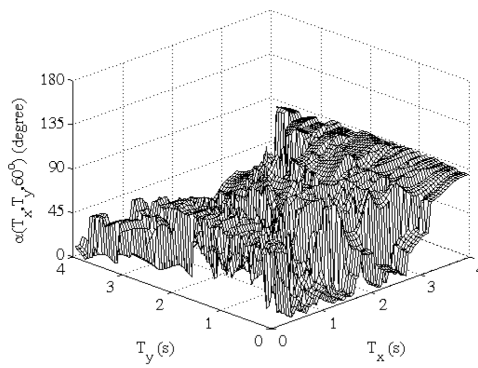

(d) $\alpha(T_x, T_y, 60^\circ)$

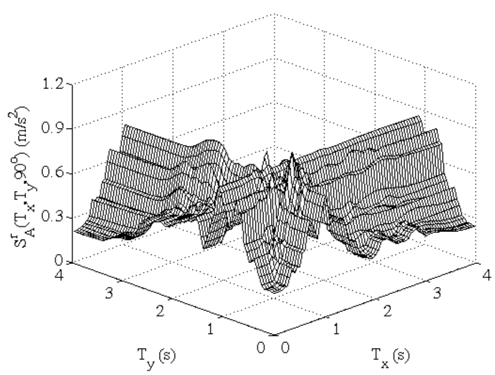

(e) $S^r_A(T_x, T_y, 90^\circ)$

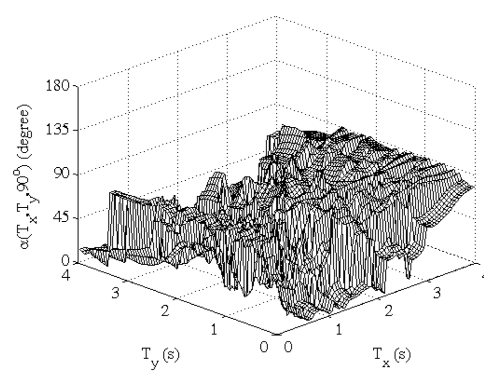

(f) $\alpha(T_x, T_y, 90^\circ)$

Figure B-138 Pseudo acceleration spectra and incident angles in various directions of Chi-Chi, Taiwan earthquake, KAU081 station

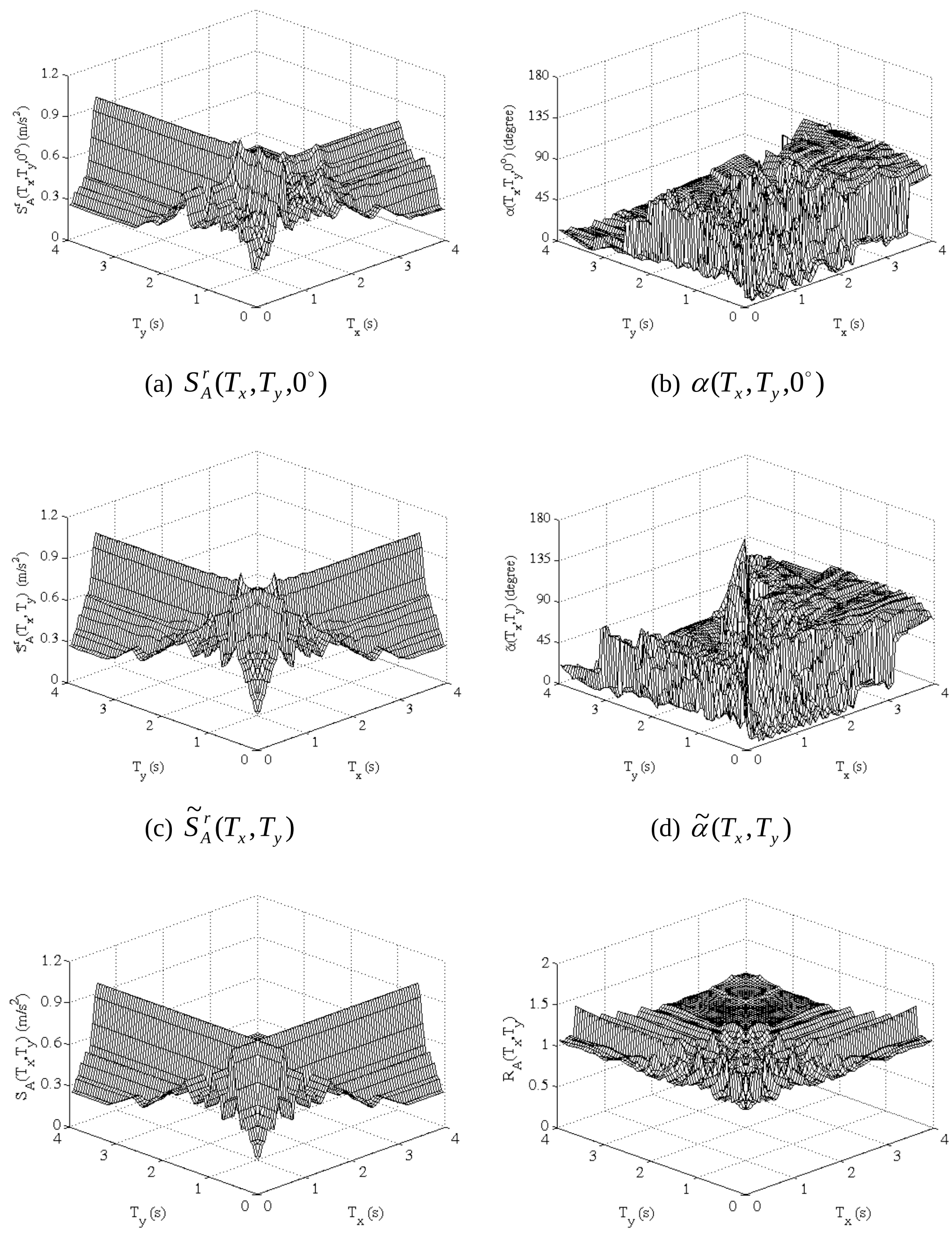

(a) $S_A^r(T_x,T_y,0^\circ)$ (b) $\alpha(T_x,T_y,0^\circ)$

(c) $\tilde{S}_A^r(T_x,T_y)$ (d) $\tilde{\alpha}(T_x,T_y)$

(e) $S_A(T_x,T_y)$ (f) $R_A(T_x,T_y)$

Figure B-139 Bi-directional responses of Chi-Chi, Taiwan earthquake, TTN012 station

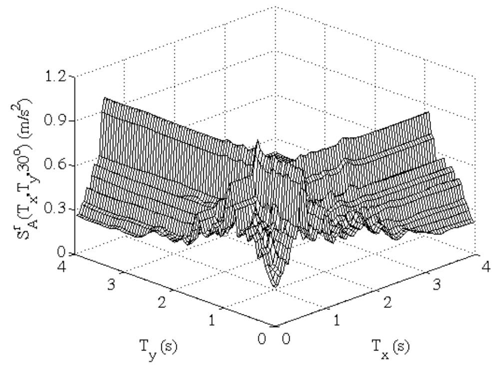

(a) $S_A^r(T_x, T_y, 30^{\circ})$

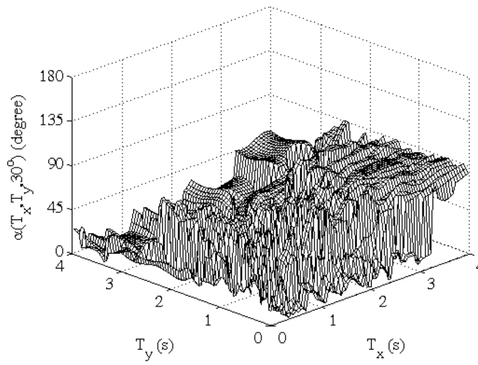

(b) $\alpha(T_x, T_y, 30^{\circ})$

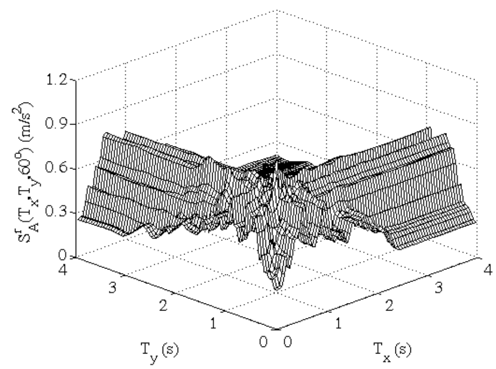

(c) $S_A^r(T_x, T_y, 60^{\circ})$

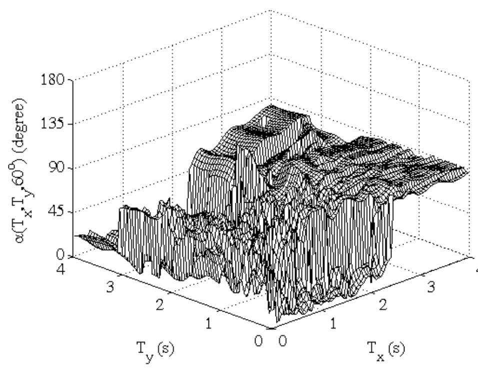

(d) $\alpha(T_x, T_y, 60^{\circ})$

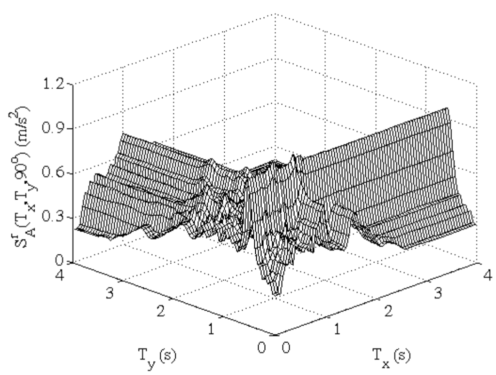

(e) $S_A^r(T_x, T_y, 90^{\circ})$

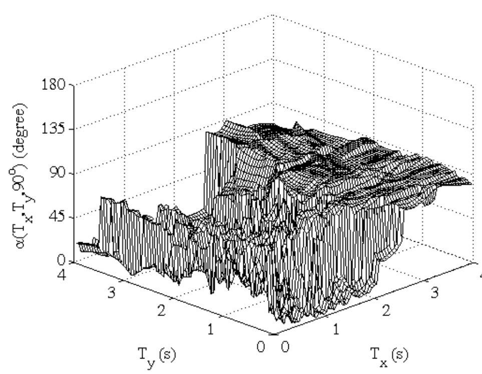

(f) $\alpha(T_x, T_y, 90^{\circ})$

Figure B-140 Pseudo acceleration spectra and incident angles in various directions of Chi-Chi, Taiwan earthquake, TTN012 station

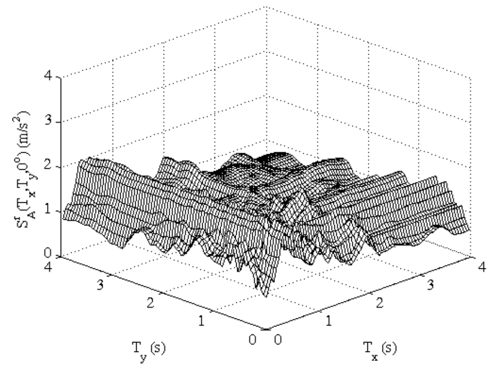

(a) $S_A^r(T_x, T_y, 0^\circ)$

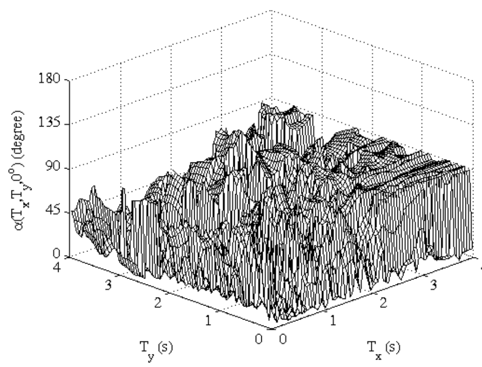

(b) $\alpha(T_x, T_y, 0^\circ)$

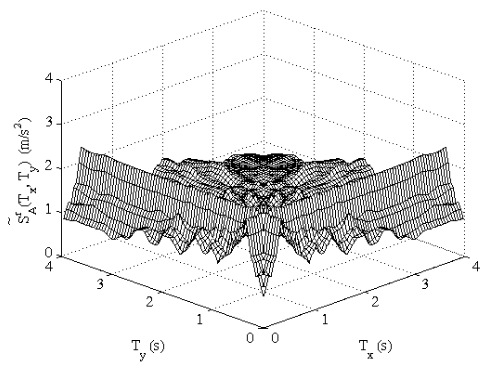

(c) $\tilde{S}_A^r(T_x, T_y)$

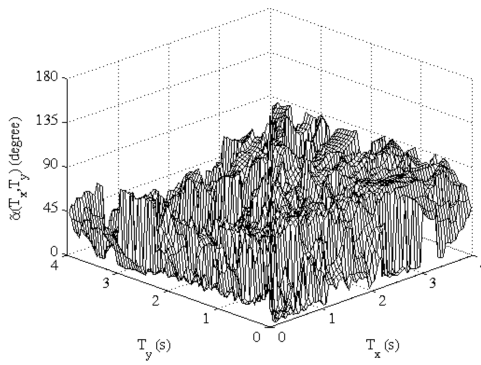

(d) $\tilde{\alpha}(T_x, T_y)$

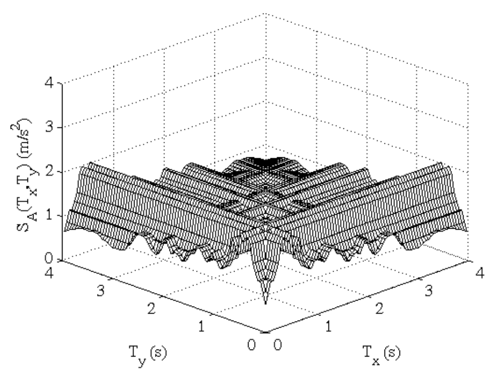

(e) $S_A(T_x, T_y)$

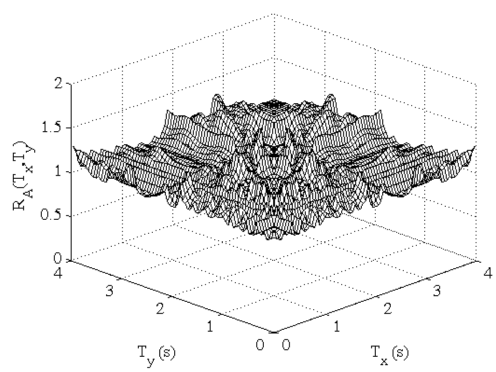

(f) $R_A(T_x, T_y)$

Figure B-141 Bi-directional responses of Chi-Chi, Taiwan earthquake, CHY012 station

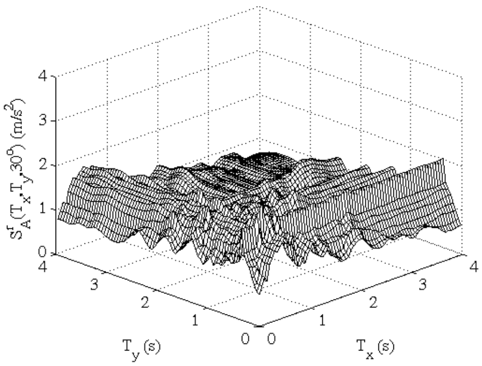

(a) $S_A^r(T_x, T_y, 30^{\circ})$

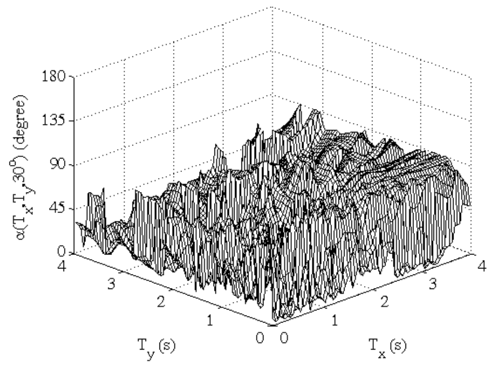

(b) $\alpha(T_x, T_y, 30^{\circ})$

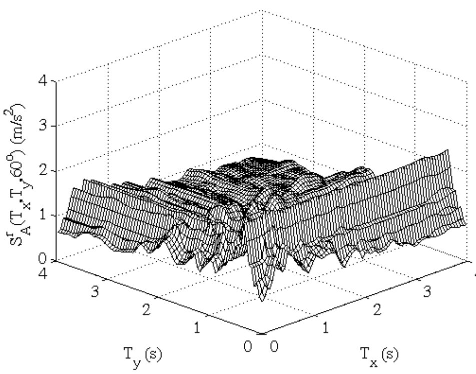

(c) $S_A^r(T_x, T_y, 60^{\circ})$

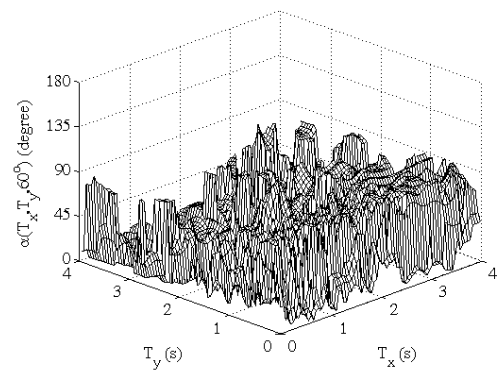

(d) $\alpha(T_x, T_y, 60^{\circ})$

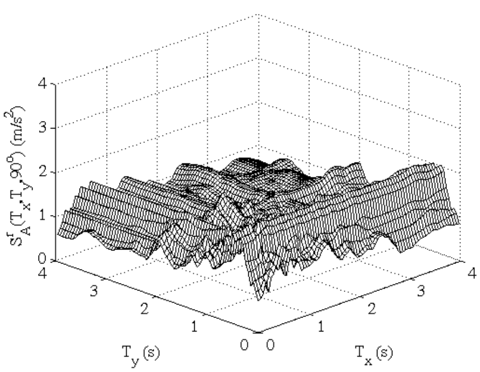

(e) $S_A^r(T_x, T_y, 90^{\circ})$

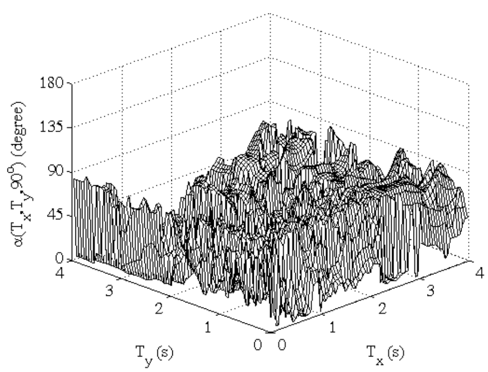

(f) $\alpha(T_x, T_y, 90^{\circ})$

Figure B-142 Pseudo acceleration spectra and incident angles in various directions of Chi-Chi, Taiwan earthquake, CHY012 station

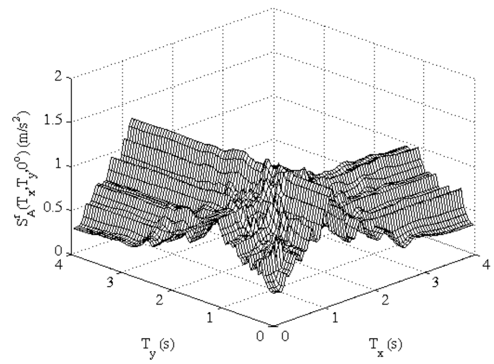

(a) $S_A^r(T_x, T_y, 0^\circ)$

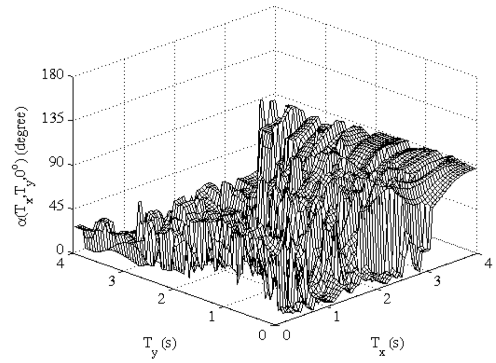

(b) $\alpha(T_x, T_y, 0^\circ)$

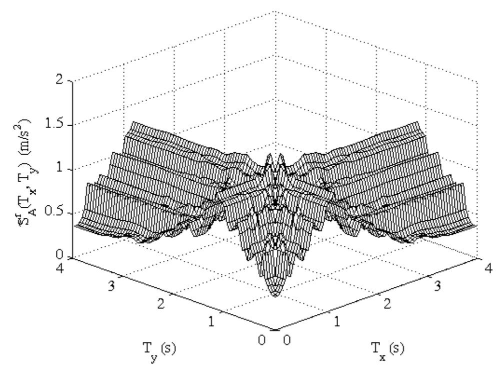

(c) $\tilde{S}_A^r(T_x, T_y)$

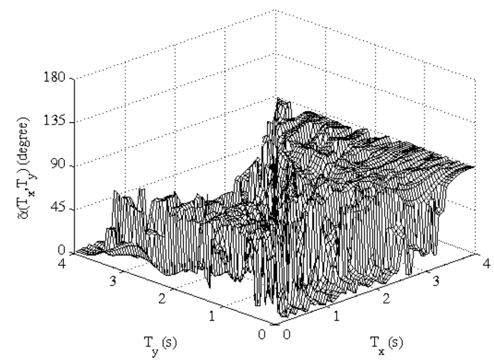

(d) $\tilde{\alpha}(T_x, T_y)$

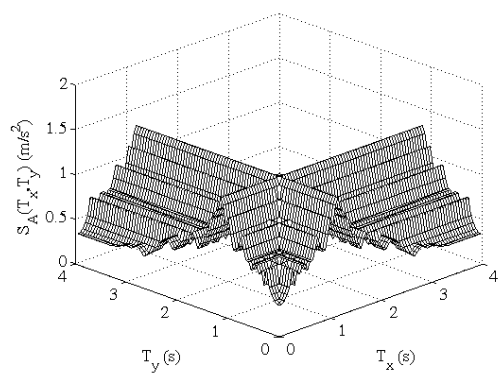

(e) $S_A(T_x, T_y)$

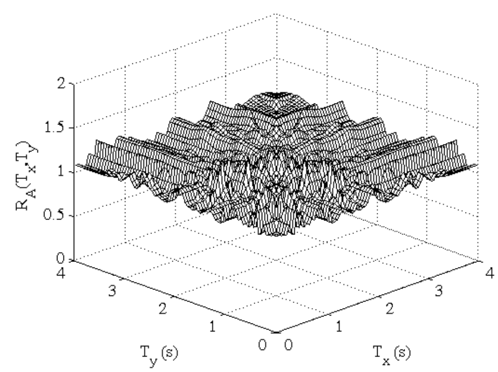

(f) $R_A(T_x, T_y)$

Figure B-143 Bi-directional responses of Chi-Chi, Taiwan earthquake, KAU073 station

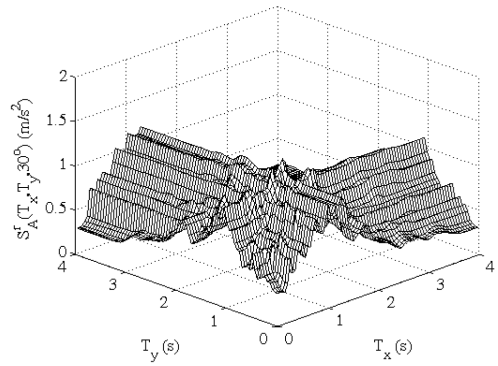

(a) $S_A^r(T_x, T_y, 30^\circ)$

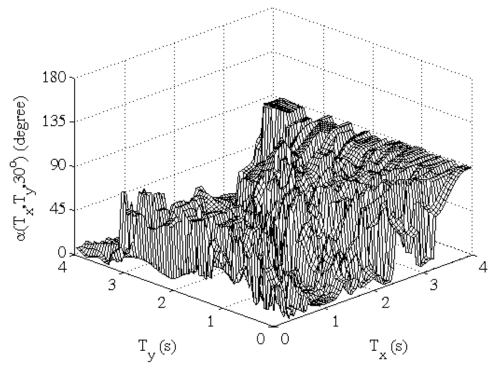

(b) $\alpha(T_x, T_y, 30^\circ)$

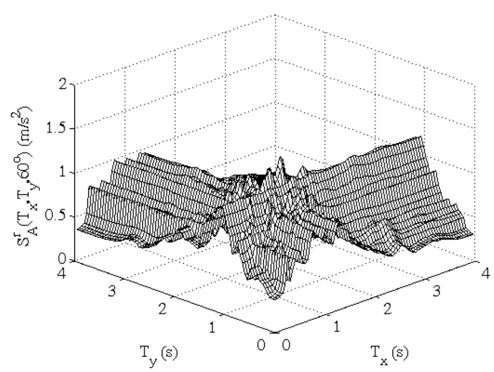

(c) $S_A^r(T_x, T_y, 60^\circ)$

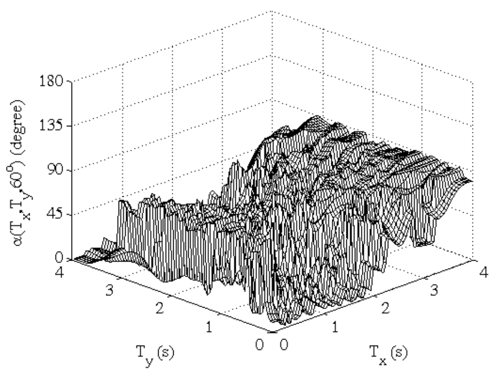

(d) $\alpha(T_x, T_y, 60^\circ)$

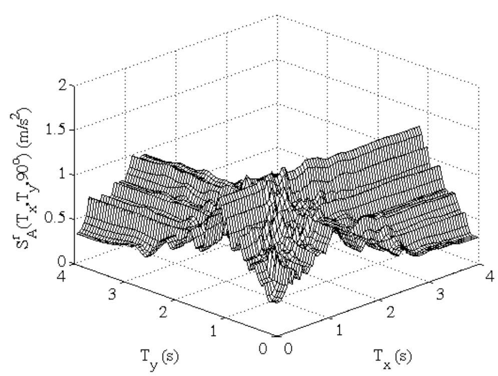

(e) $S_A^r(T_x, T_y, 90^\circ)$

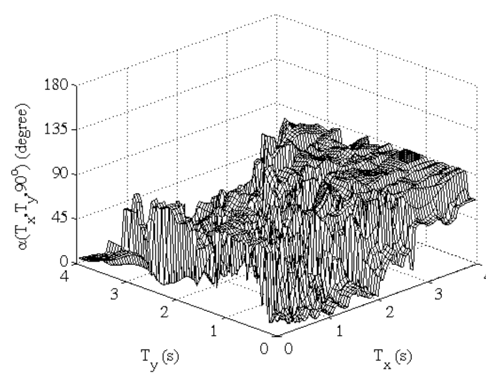

(f) $\alpha(T_x, T_y, 90^\circ)$

Figure B-144 Pseudo acceleration spectra and incident angles in various directions of Chi-Chi, Taiwan earthquake, KAU073 station

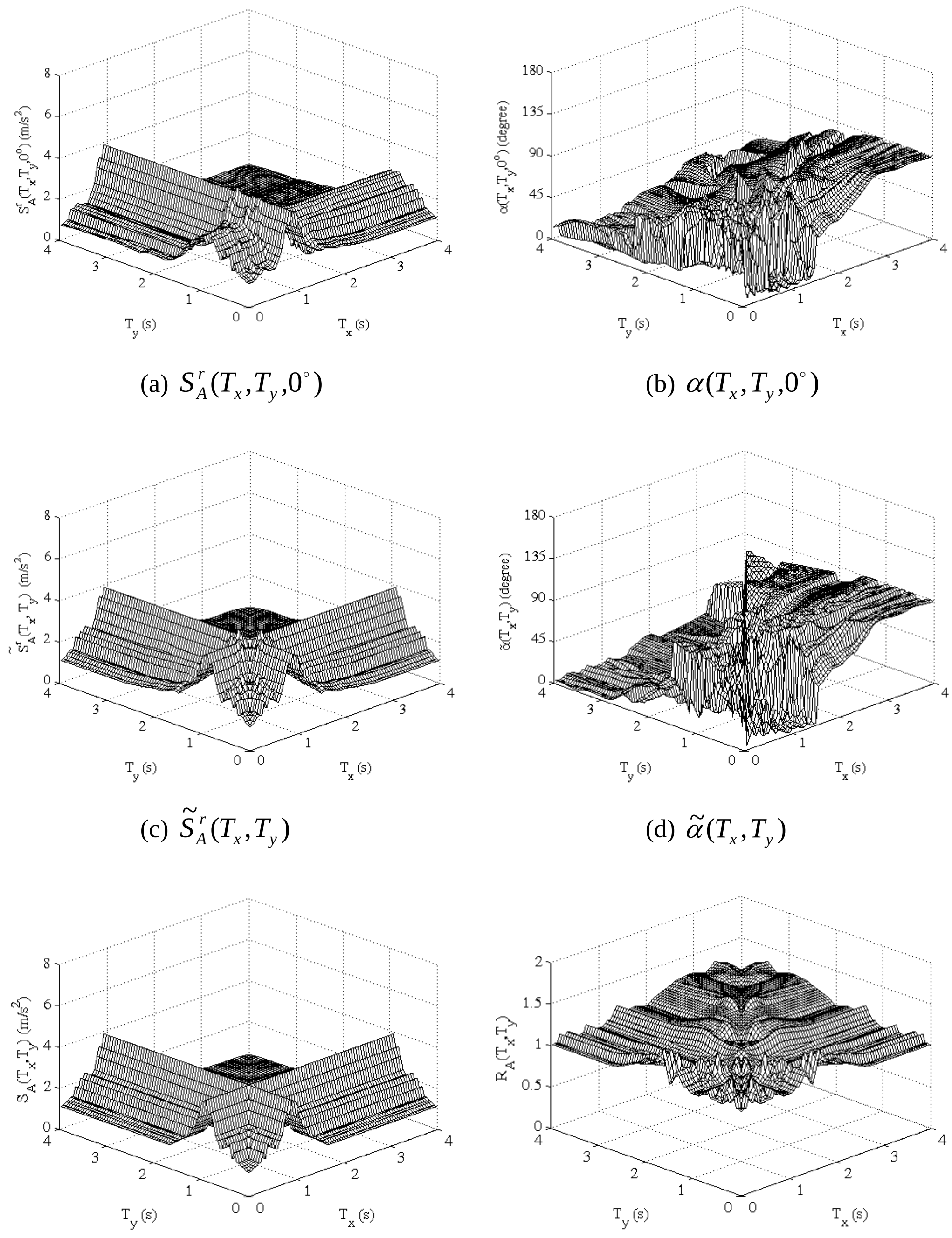

(a) $S_A^r(T_x, T_y, 0^\circ)$

(b) $\alpha(T_x, T_y, 0^\circ)$

(c) $\widetilde{S}_A^r(T_x, T_y)$

(d) $\widetilde{\alpha}(T_x, T_y)$

(e) $S_A(T_x, T_y)$

(f) $R_A(T_x, T_y)$

Figure B-145 Bi-directional responses of Chi-Chi, Taiwan earthquake, TAP006 station

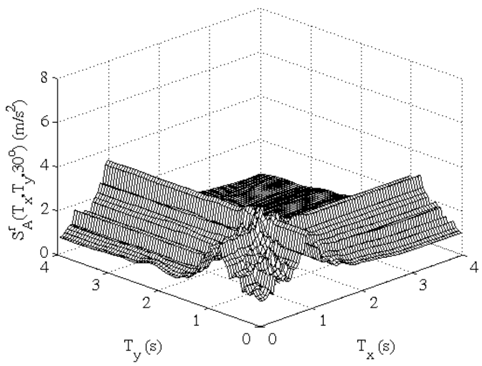

(a) $S_A^r(T_x, T_y, 30^\circ)$

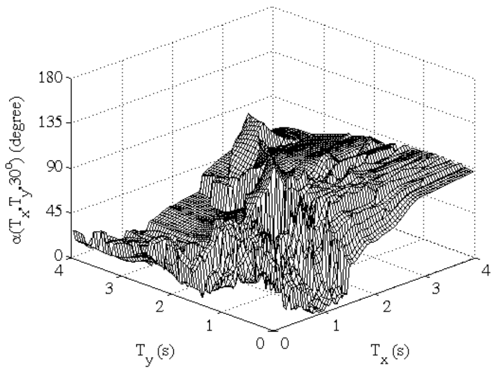

(b) $\alpha(T_x, T_y, 30^\circ)$

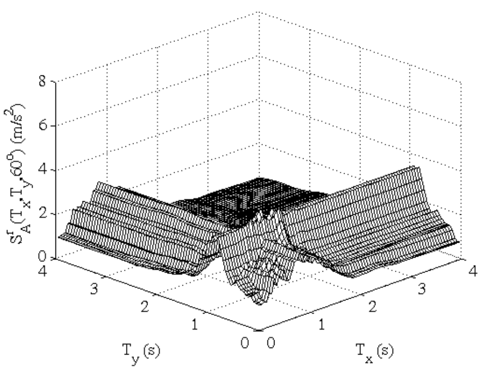

(c) $S_A^r(T_x, T_y, 60^\circ)$

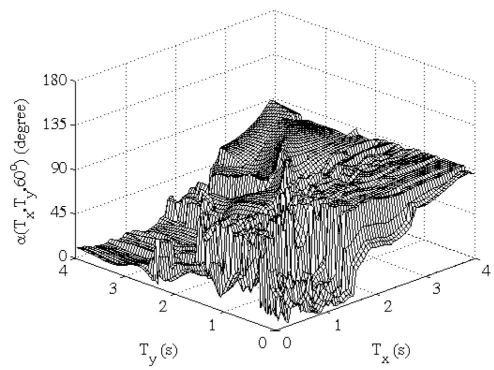

(d) $\alpha(T_x, T_y, 60^\circ)$

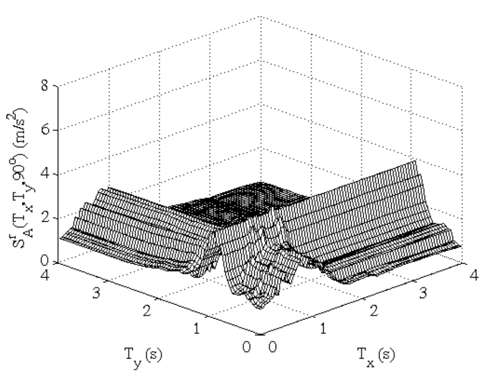

(e) $S_A^r(T_x, T_y, 90^\circ)$

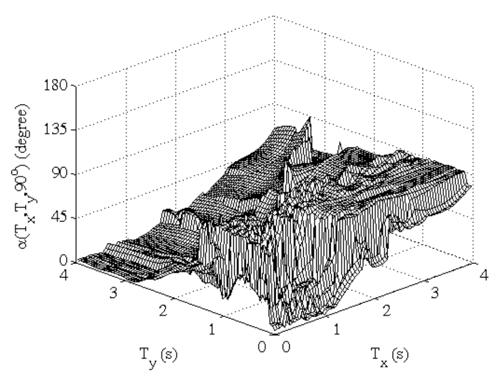

(f) $\alpha(T_x, T_y, 90^\circ)$

Figure B-146 Pseudo acceleration spectra and incident angles in various directions of Chi-Chi, Taiwan earthquake, TAP006 station

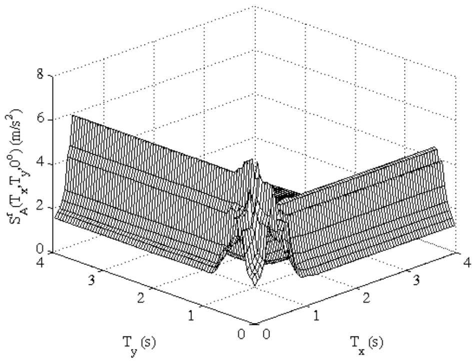

(a) $S_A^r(T_x,T_y,0^\circ)$

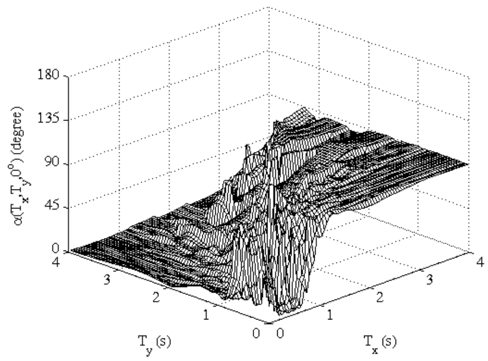

(b) $\alpha(T_x,T_y,0^\circ)$

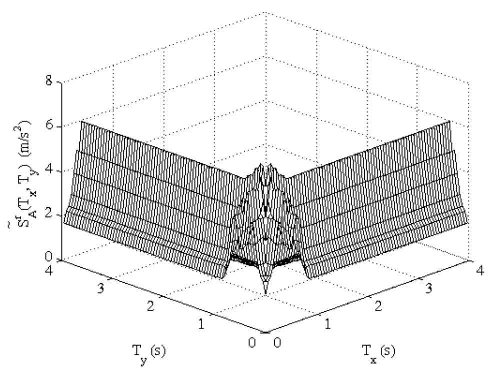

(c) $\widetilde{S}_A^r(T_x,T_y)$

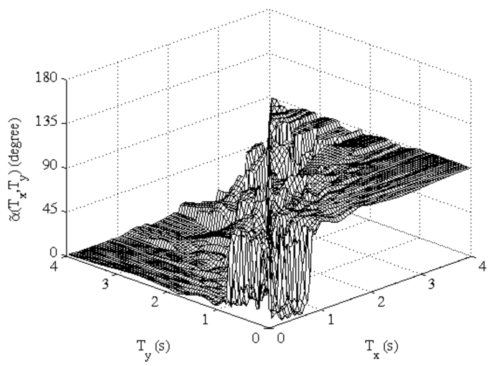

(d) $\widetilde{\alpha}(T_x,T_y)$

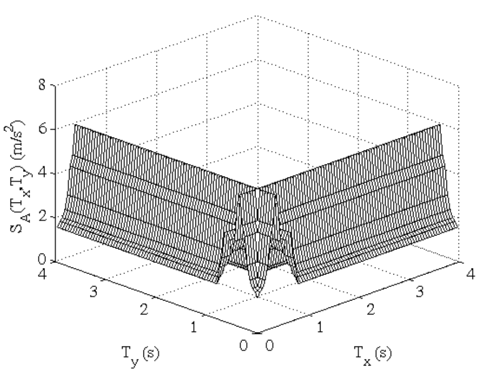

(e) $S_A(T_x,T_y)$

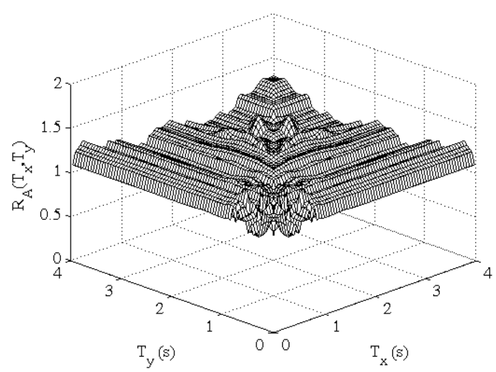

(f) $R_A(T_x,T_y)$

Figure B-147 Bi-directional responses of Coalinga earthquake, 36227 Parkfield - Cholame 5W station

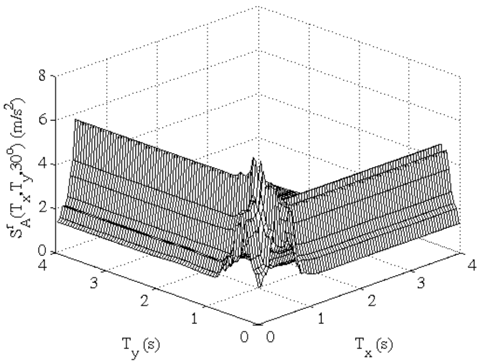

(a) $S_A^r(T_x, T_y, 30^\circ)$

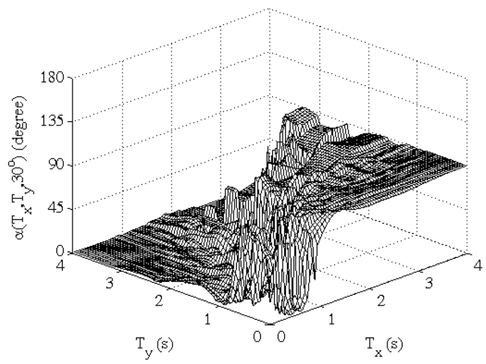

(b) $\alpha(T_x, T_y, 30^\circ)$

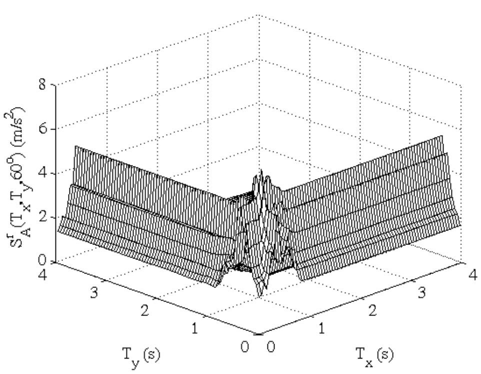

(c) $S_A^r(T_x, T_y, 60^\circ)$

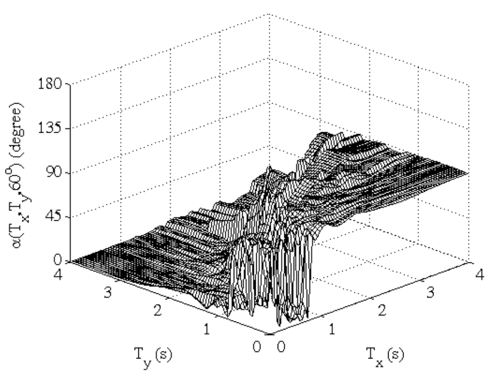

(d) $\alpha(T_x, T_y, 60^\circ)$

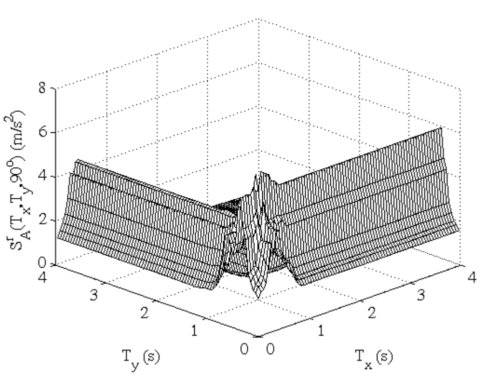

(e) $S_A^r(T_x, T_y, 90^\circ)$

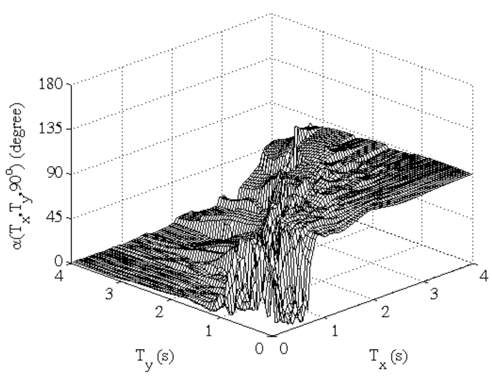

(f) $\alpha(T_x, T_y, 90^\circ)$

Figure B-148 Pseudo acceleration spectra and incident angles in various directions of Coalinga earthquake, 36227 Parkfield - Cholame 5W station

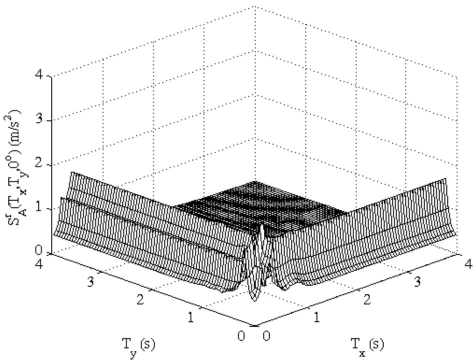

(a) $S_A^r(T_x, T_y, 0^\circ)$

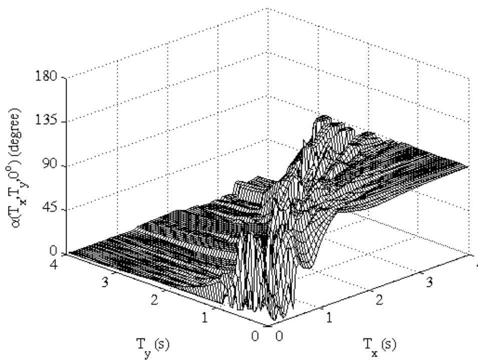

(b) $\alpha(T_x, T_y, 0^\circ)$

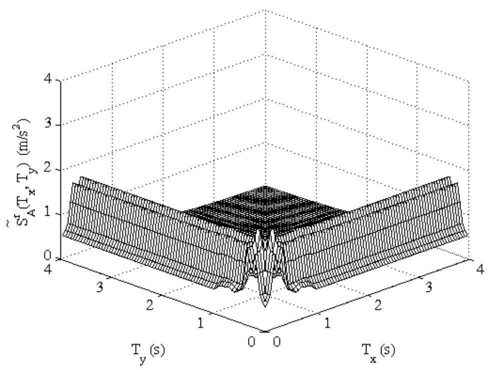

(c) $\tilde{S}_A^r(T_x, T_y)$

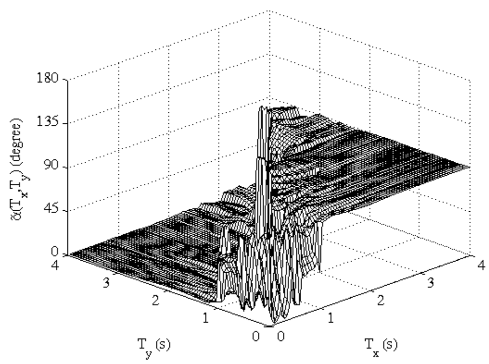

(d) $\tilde{\alpha}(T_x, T_y)$

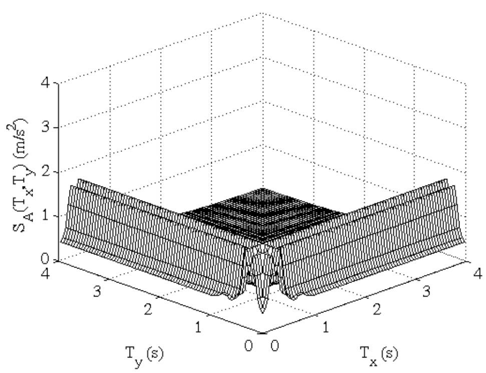

(e) $S_A(T_x, T_y)$

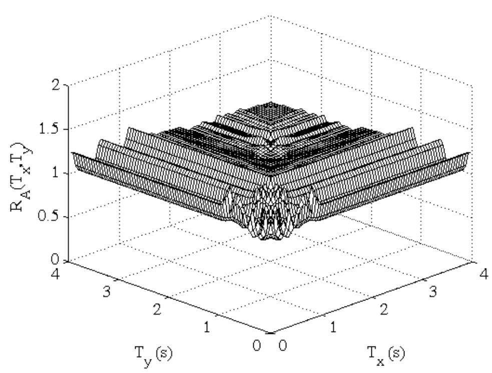

(f) $R_A(T_x, T_y)$

Figure B-149 Bi-directional responses of Coyote Lake earthquake, 57191 Halls Valley station

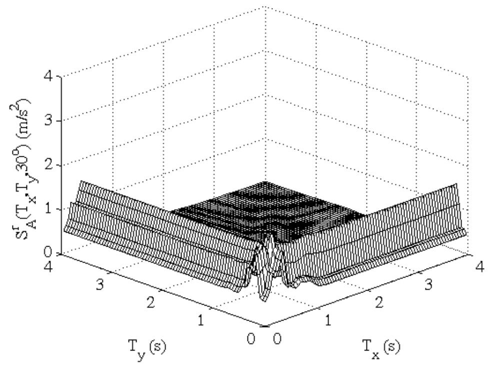

(a) $S_A^r(T_x, T_y, 30^{\circ})$

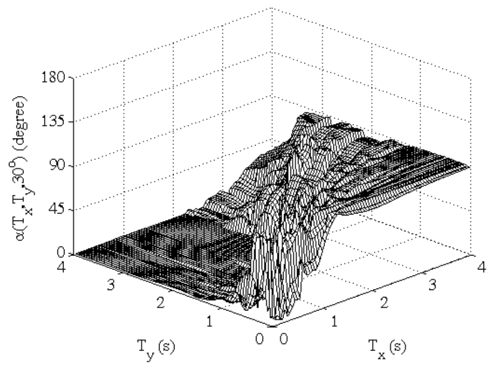

(b) $\alpha(T_x, T_y, 30^{\circ})$

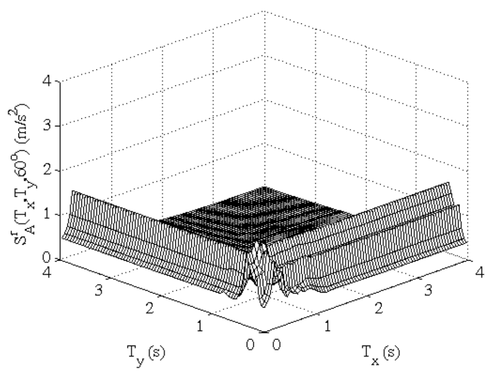

(c) $S_A^r(T_x, T_y, 60^{\circ})$

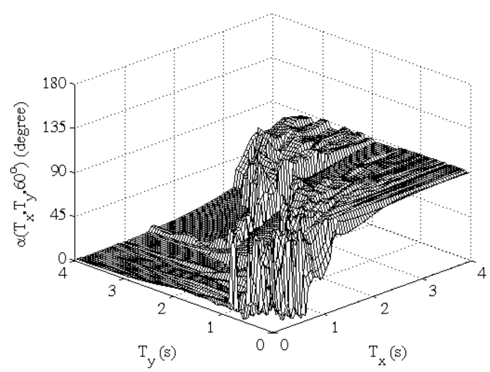

(d) $\alpha(T_x, T_y, 60^{\circ})$

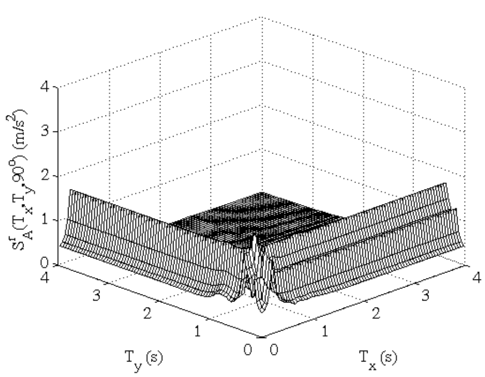

(e) $S_A^r(T_x, T_y, 90^{\circ})$

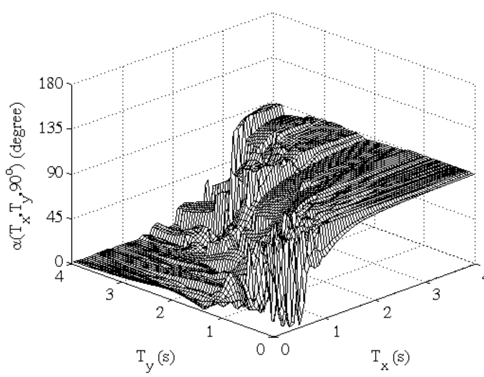

(f) $\alpha(T_x, T_y, 90^{\circ})$

Figure B-150 Pseudo acceleration spectra and incident angles in various directions of Coyote Lake earthquake, 57191 Halls Valley station

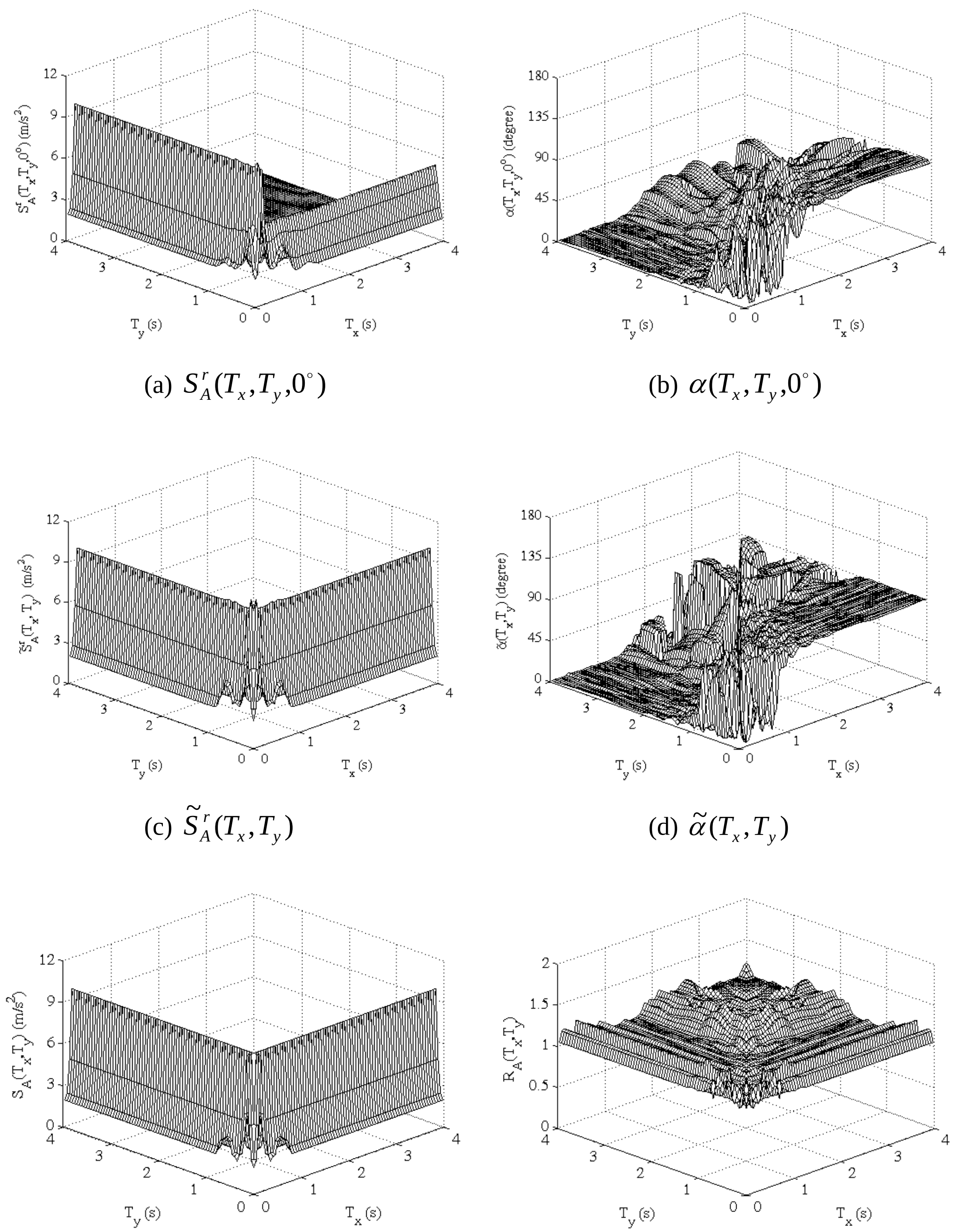

(a) $S_A^r(T_x, T_y, 0^\circ)$ (b) $\alpha(T_x, T_y, 0^\circ)$

(c) $\tilde{S}_A^r(T_x, T_y)$ (d) $\tilde{\alpha}(T_x, T_y)$

(e) $S_A(T_x, T_y)$ (f) $R_A(T_x, T_y)$

Figure B-151 Bi-directional responses of Kocaeli, Turkey earthquake, Cekmece station

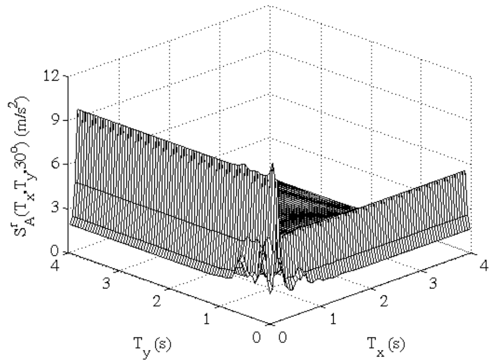

(a) $S_A^r(T_x, T_y, 30^\circ)$

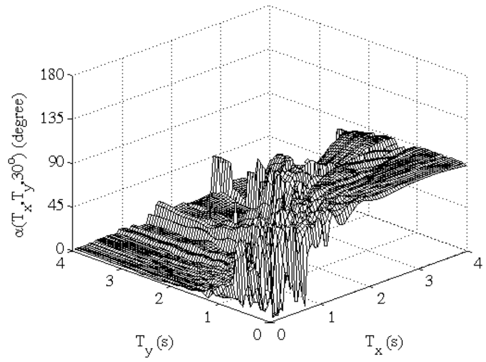

(b) $\alpha(T_x, T_y, 30^\circ)$

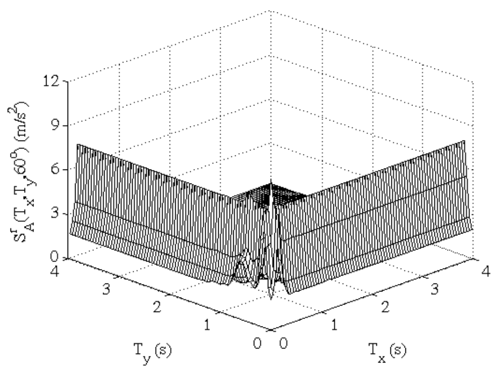

(c) $S_A^r(T_x, T_y, 60^\circ)$

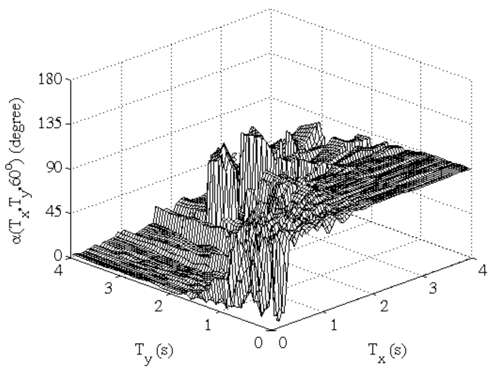

(d) $\alpha(T_x, T_y, 60^\circ)$

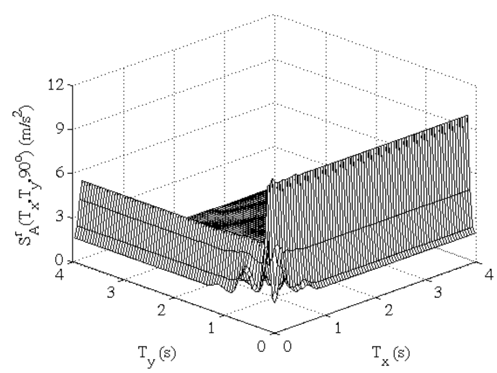

(e) $S_A^r(T_x, T_y, 90^\circ)$

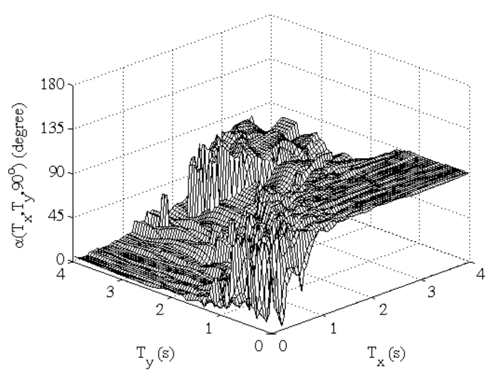

(f) $\alpha(T_x, T_y, 90^\circ)$

Figure B-152 Pseudo acceleration spectra and incident angles in various directions of Kocaeli, Turkey earthquake, Cekmece station

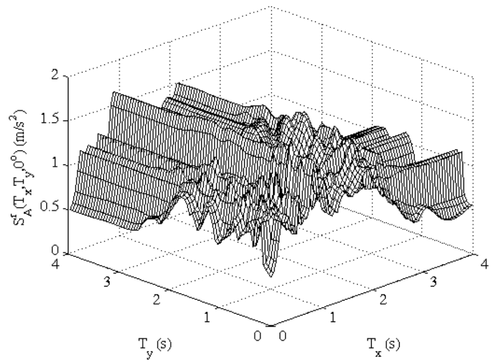

(a) $S_A^r(T_x,T_y,0^\circ)$

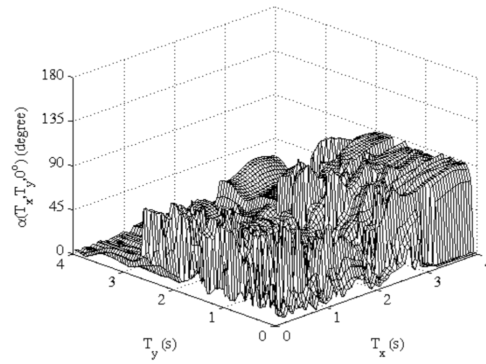

(b) $\alpha(T_x,T_y,0^\circ)$

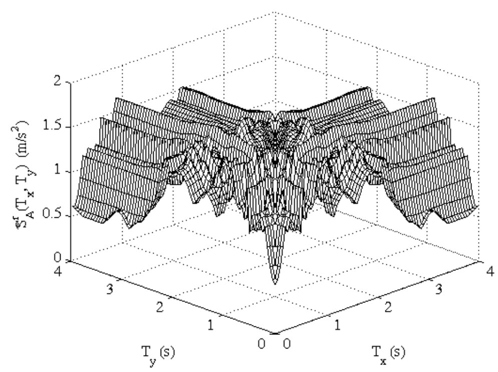

(c) $\tilde{S}_A^r(T_x,T_y)$

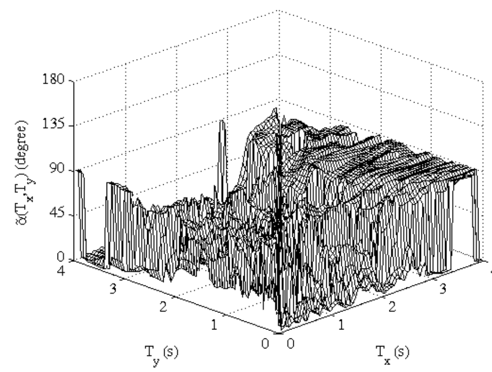

(d) $\tilde{\alpha}(T_x,T_y)$

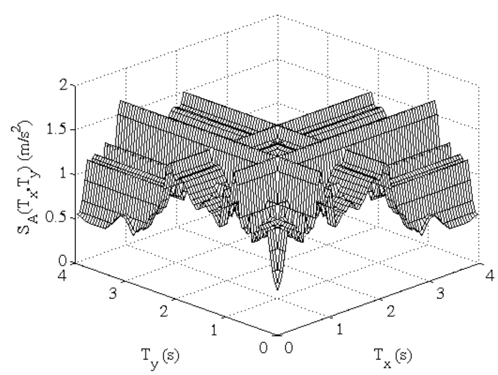

(e) $S_A(T_x,T_y)$

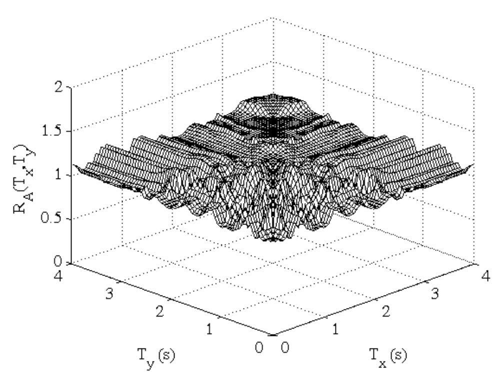

(f) $R_A(T_x,T_y)$

Figure B-153 Bi-directional responses of Landers earthquake, 90071 West Covina - S Orange station

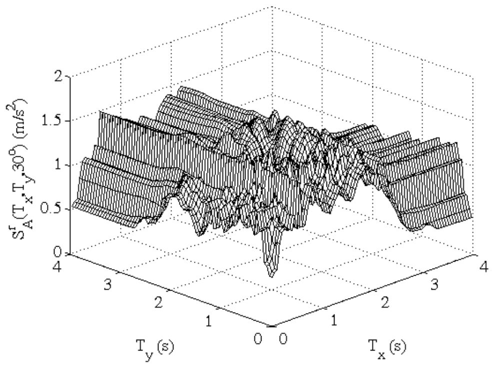

(a) $S_A^r(T_x, T_y, 30^\circ)$

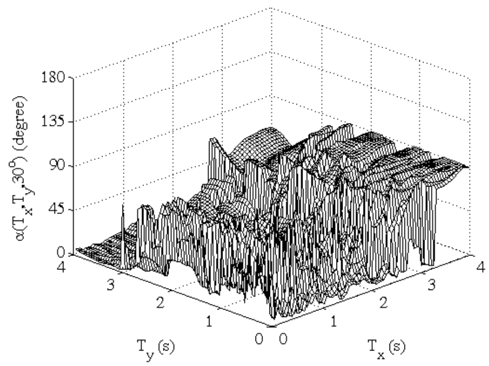

(b) $\alpha(T_x, T_y, 30^\circ)$

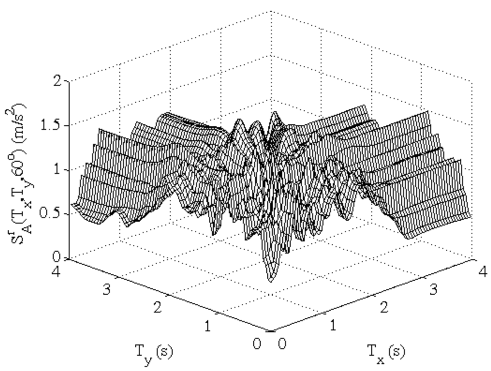

(c) $S_A^r(T_x, T_y, 60^\circ)$

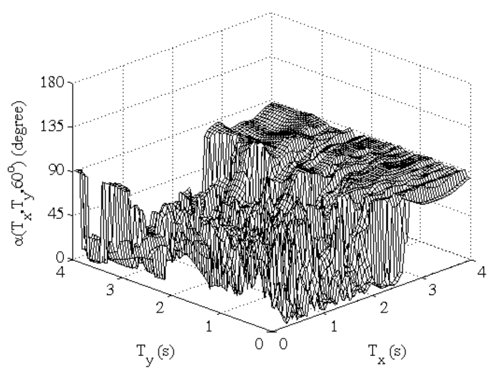

(d) $\alpha(T_x, T_y, 60^\circ)$

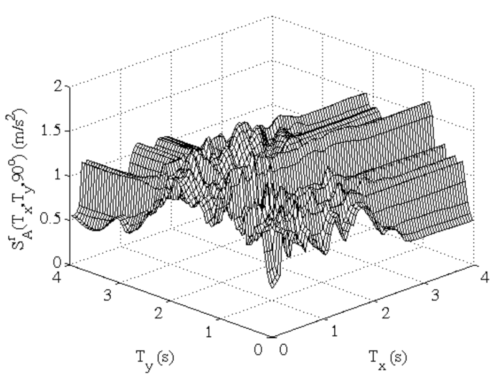

(e) $S_A^r(T_x, T_y, 90^\circ)$

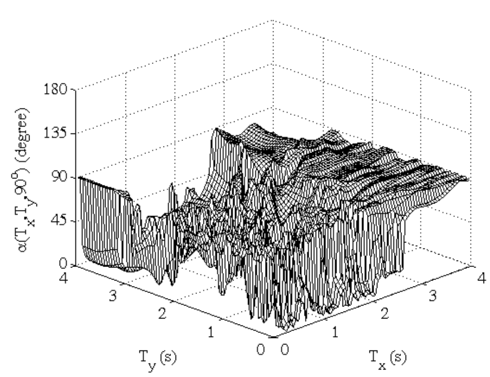

(f) $\alpha(T_x, T_y, 90^\circ)$

Figure B-154 Pseudo acceleration spectra and incident angles in various directions of Landers earthquake, 90071 West Covina - S Orange station

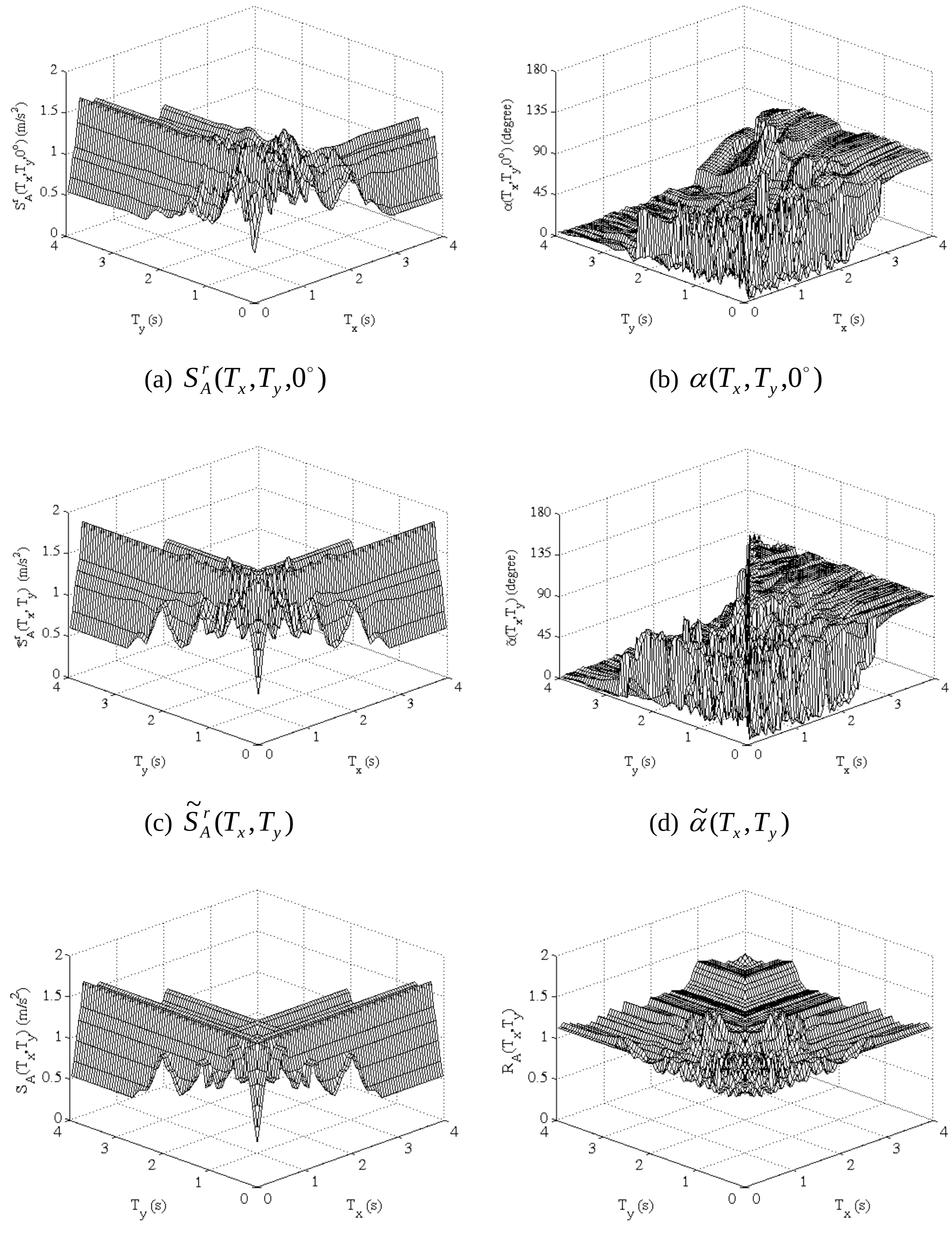

(a) $S_A^r(T_x, T_y, 0^\circ)$ (b) $\alpha(T_x, T_y, 0^\circ)$

(c) $\tilde{S}_A^r(T_x, T_y)$ (d) $\tilde{\alpha}(T_x, T_y)$

(e) $S_A(T_x, T_y)$ (f) $R_A(T_x, T_y)$

Figure B-155 Bi-directional responses of Landers earthquake, 90073 Hacienda Heights - Colima station

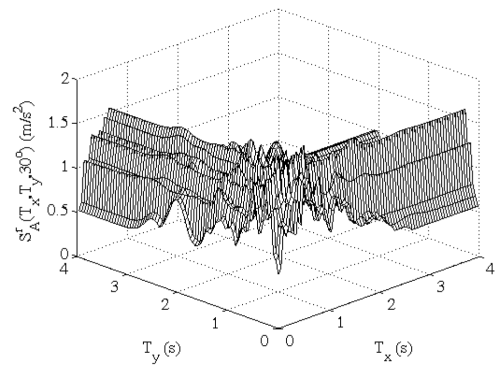

(a) $S_A^r(T_x,T_y,30^\circ)$

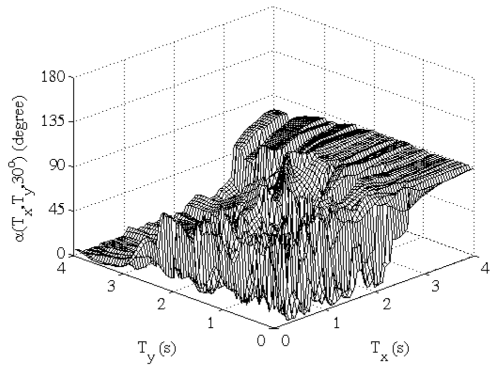

(b) $\alpha(T_x,T_y,30^\circ)$

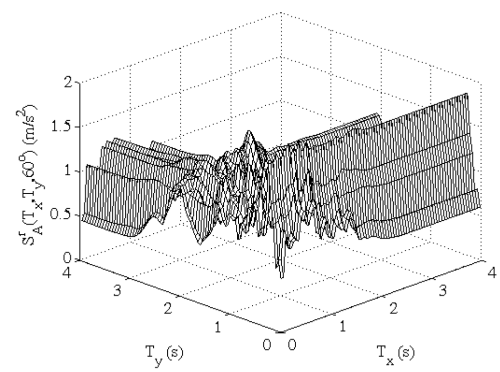

(c) $S_A^r(T_x,T_y,60^\circ)$

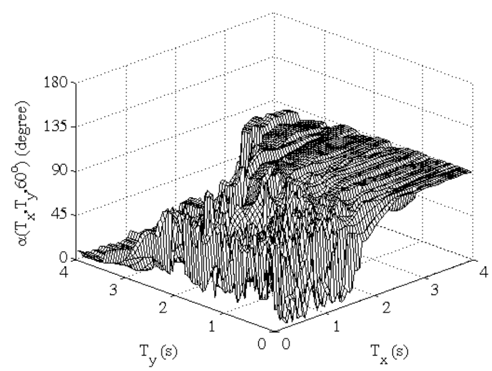

(d) $\alpha(T_x,T_y,60^\circ)$

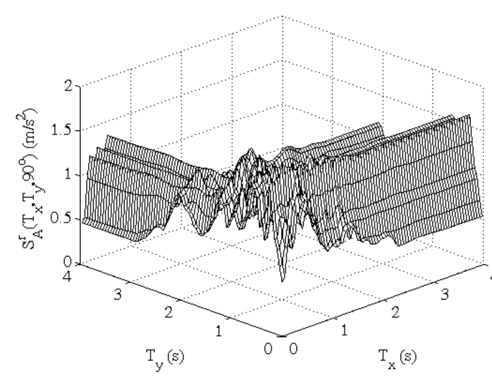

(e) $S_A^r(T_x,T_y,90^\circ)$

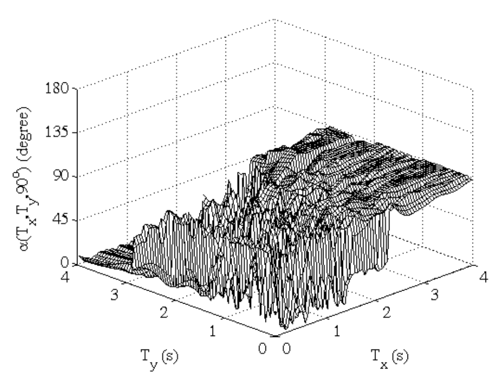

(f) $\alpha(T_x,T_y,90^\circ)$

Figure B-156 Pseudo acceleration spectra and incident angles in various directions of Landers earthquake, 90073 Hacienda Heights - Colima station

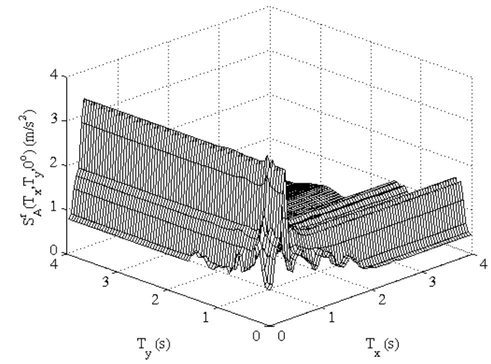

(a) $S^r_A(T_x,T_y,0^\circ)$

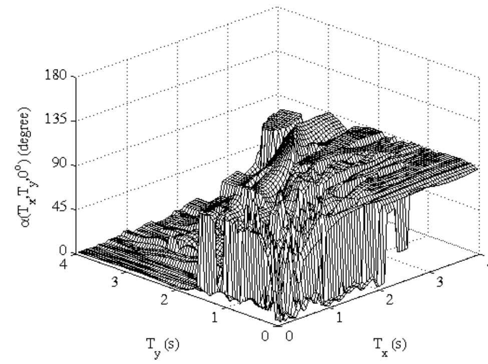

(b) $\alpha(T_x,T_y,0^\circ)$

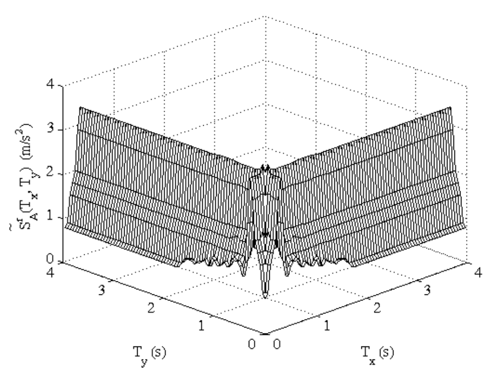

(c) $\tilde{S}^r_A(T_x,T_y)$

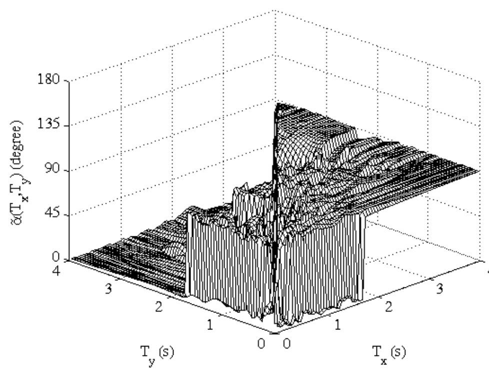

(d) $\tilde{\alpha}(T_x,T_y)$

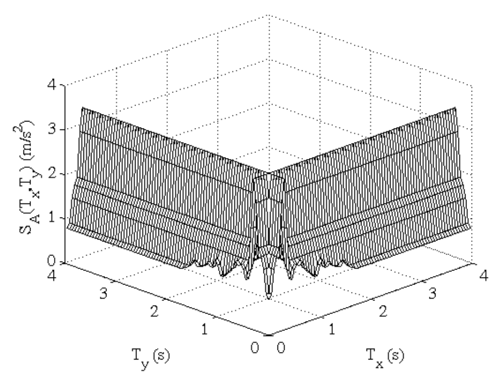

(e) $S_A(T_x,T_y)$

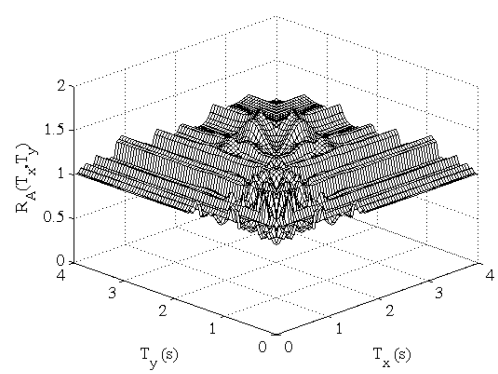

(f) $R_A(T_x,T_y)$

Figure B-157 Bi-directional responses of Livermore earthquake, 57063 Tracy - Sewage Treatm Plant station

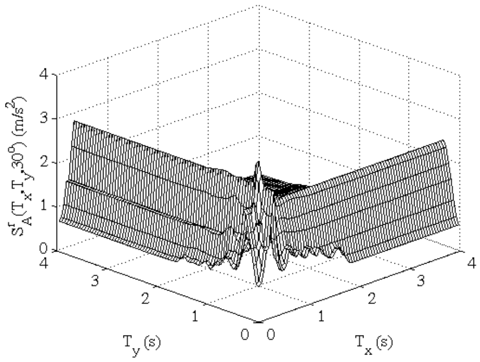

(a) $S_A^r(T_x, T_y, 30^\circ)$

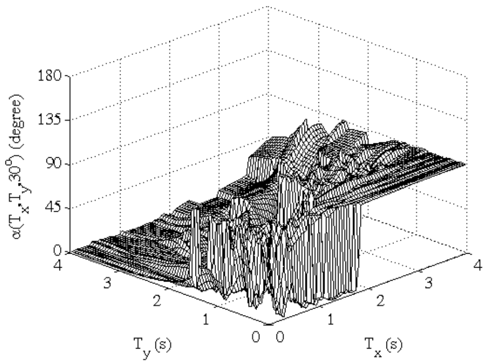

(b) $\alpha(T_x, T_y, 30^\circ)$

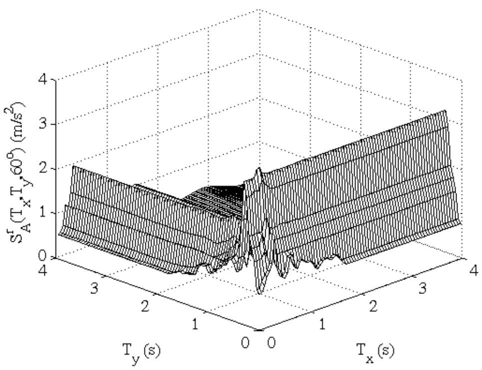

(c) $S_A^r(T_x, T_y, 60^\circ)$

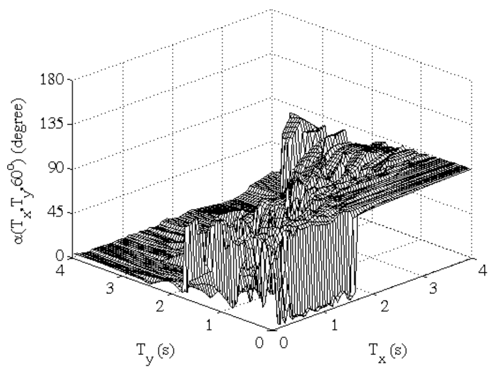

(d) $\alpha(T_x, T_y, 60^\circ)$

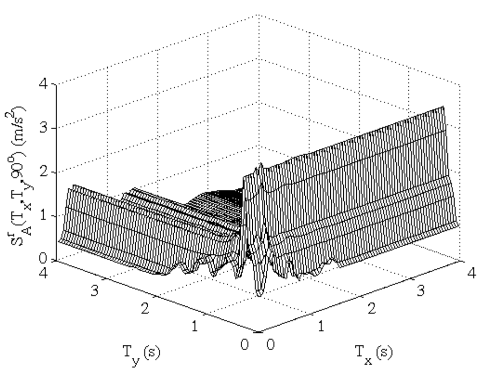

(e) $S_A^r(T_x, T_y, 90^\circ)$

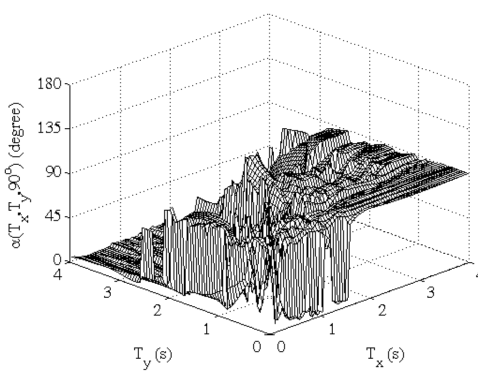

(f) $\alpha(T_x, T_y, 90^\circ)$

Figure B-158 Pseudo acceleration spectra and incident angles in various directions of Livermore earthquake, 57063 Tracy - Sewage Treatm Plant station

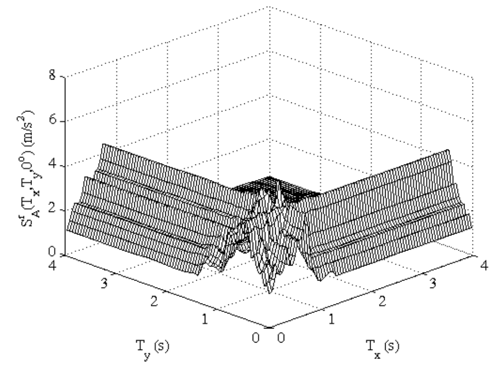

(a) $S_A^r(T_x, T_y, 0^\circ)$

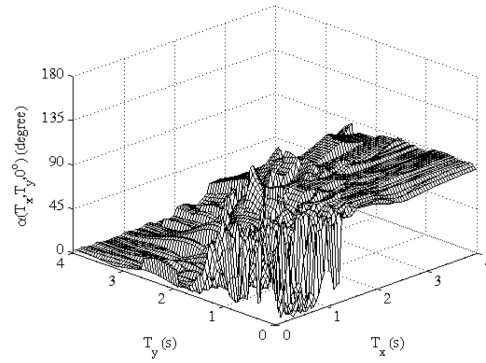

(b) $\alpha(T_x, T_y, 0^\circ)$

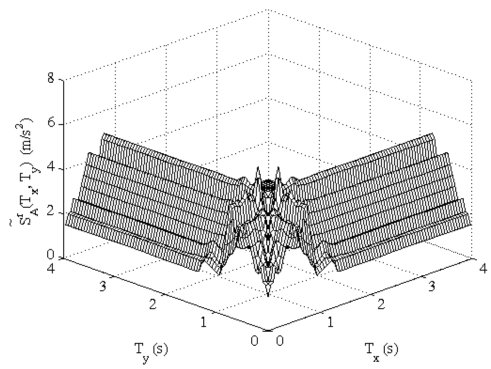

(c) $\widetilde{S}_A^r(T_x, T_y)$

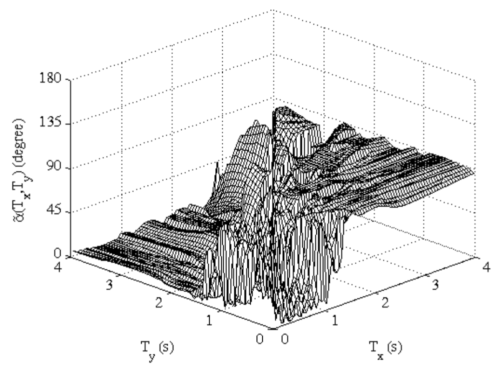

(d) $\widetilde{\alpha}(T_x, T_y)$

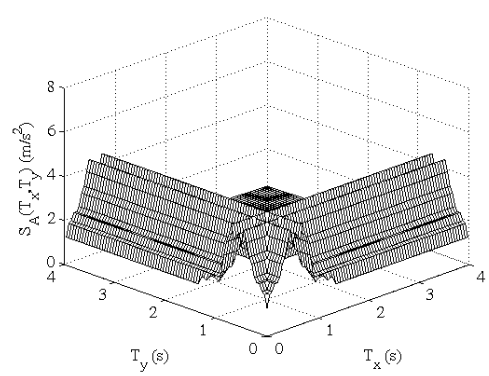

(e) $S_A(T_x, T_y)$

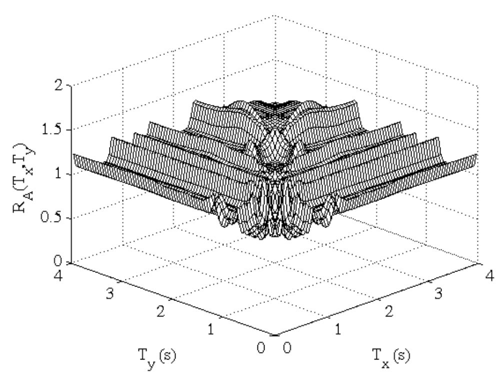

(f) $R_A(T_x, T_y)$

Figure B-159 Bi-directional responses of Loma Prieta earthquake, 57191 Halls Valley station

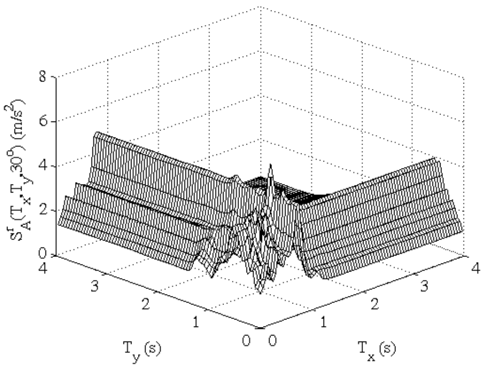

(a) $S_A^r(T_x, T_y, 30^\circ)$

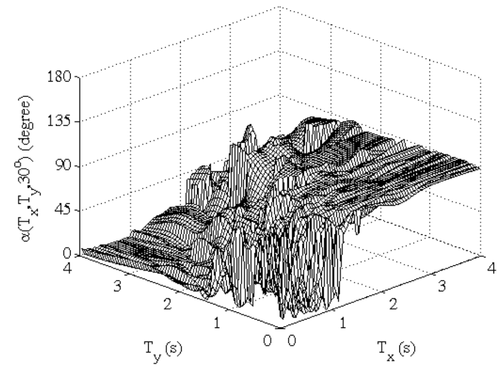

(b) $\alpha(T_x, T_y, 30^\circ)$

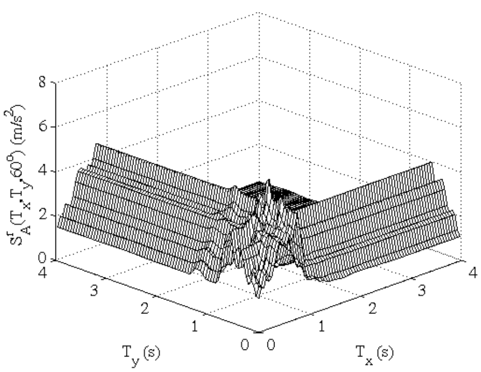

(c) $S_A^r(T_x, T_y, 60^\circ)$

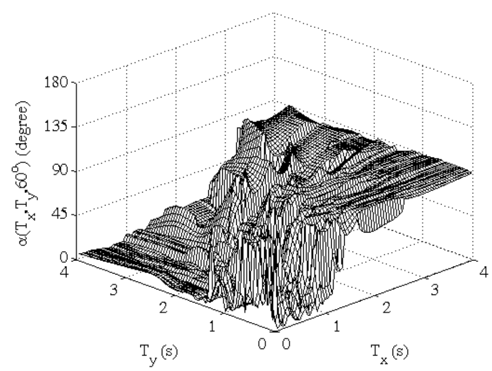

(d) $\alpha(T_x, T_y, 60^\circ)$

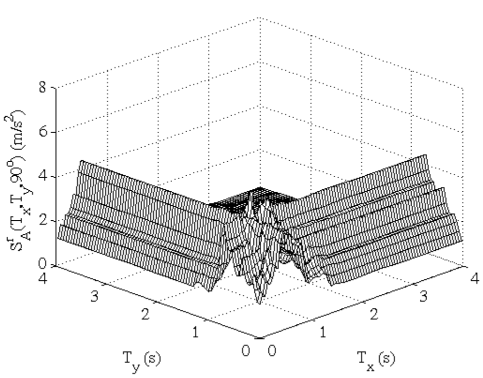

(e) $S_A^r(T_x, T_y, 90^\circ)$

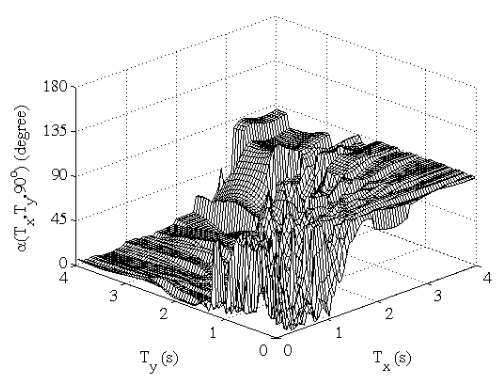

(f) $\alpha(T_x, T_y, 90^\circ)$

Figure B-160 Pseudo acceleration spectra and incident angles in various directions of Loma Prieta earthquake, 57191 Halls Valley station

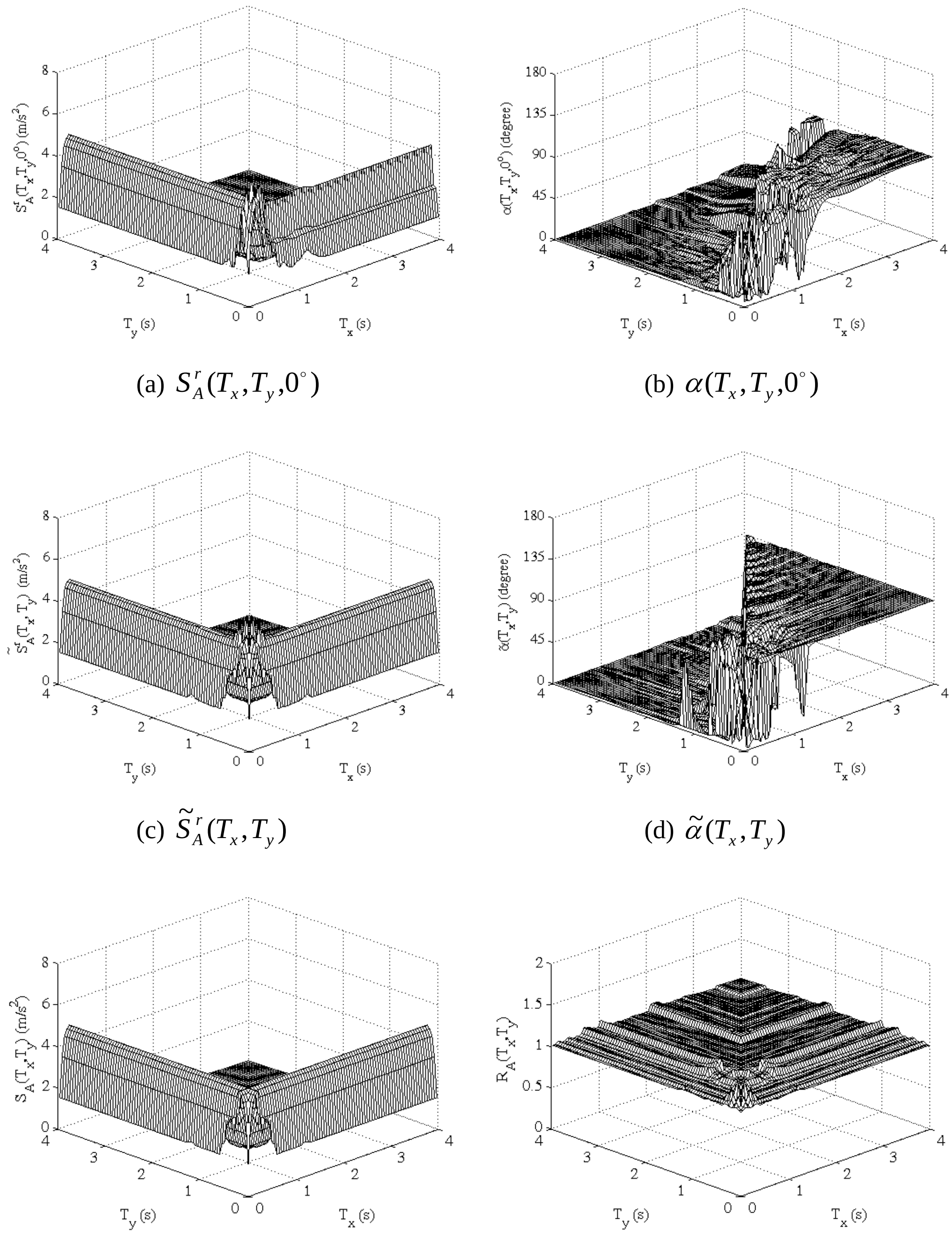

(a) $S_A^r(T_x, T_y, 0^\circ)$ (b) $\alpha(T_x, T_y, 0^\circ)$

(c) $\tilde{S}_A^r(T_x, T_y)$ (d) $\tilde{\alpha}(T_x, T_y)$

(e) $S_A(T_x, T_y)$ (f) $R_A(T_x, T_y)$

Figure B-161 Bi-directional responses of Morgan Hill earthquake, 47125 Capitola station

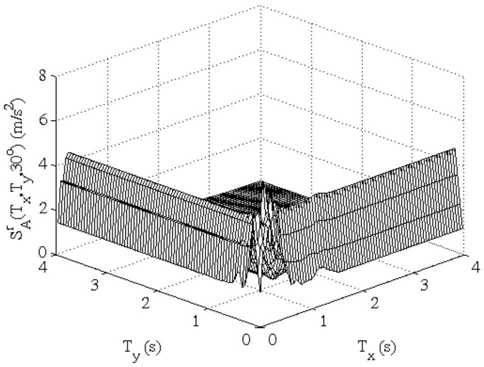

(a) $S_A^r(T_x, T_y, 30^\circ)$

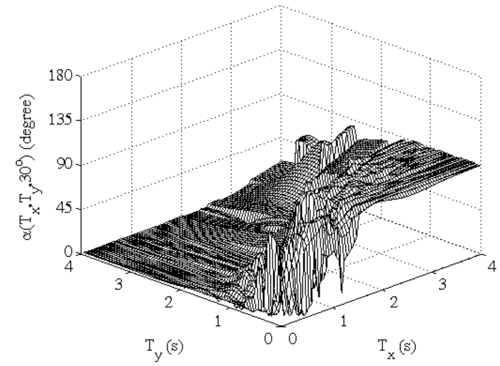

(b) $\alpha(T_x, T_y, 30^\circ)$

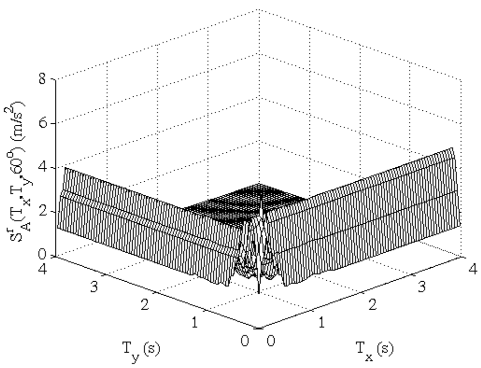

(c) $S_A^r(T_x, T_y, 60^\circ)$

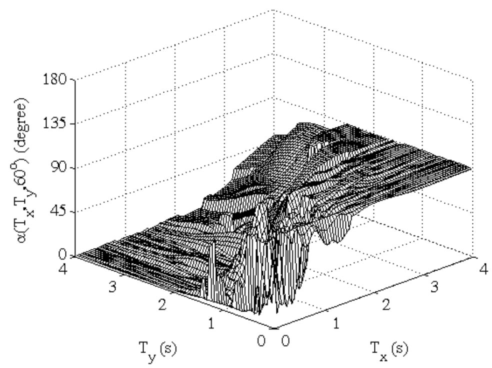

(d) $\alpha(T_x, T_y, 60^\circ)$

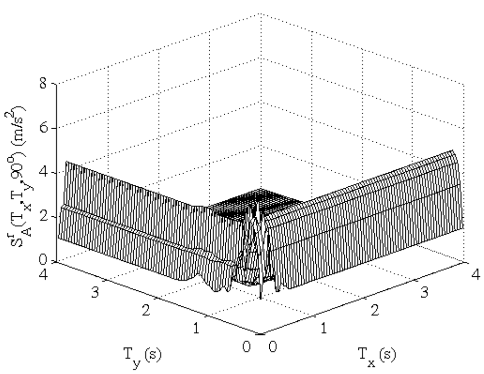

(e) $S_A^r(T_x, T_y, 90^\circ)$

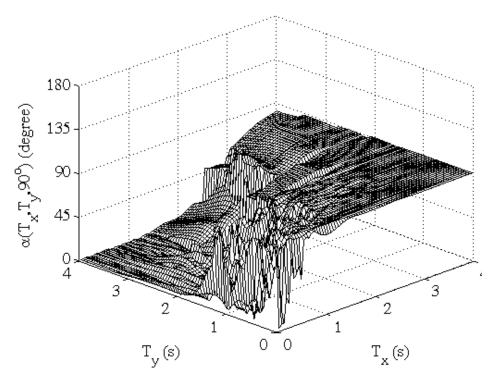

(f) $\alpha(T_x, T_y, 90^\circ)$

Figure B-162 Pseudo acceleration spectra and incident angles in various directions of Morgan Hill earthquake, 47125 Capitola station

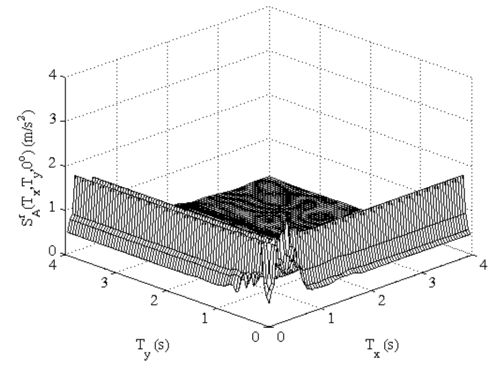

(a) $S_A^r(T_x, T_y, 0^\circ)$

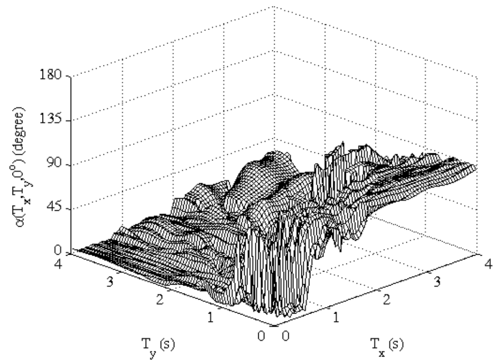

(b) $\alpha(T_x, T_y, 0^\circ)$

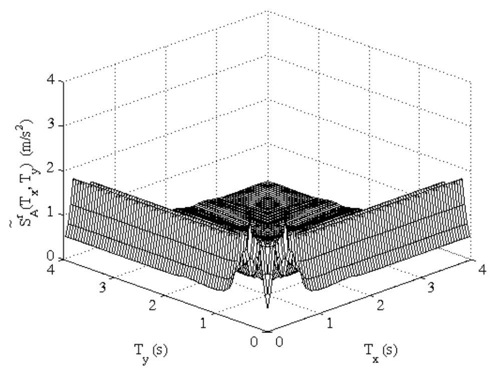

(c) $\tilde{S}_A^r(T_x, T_y)$

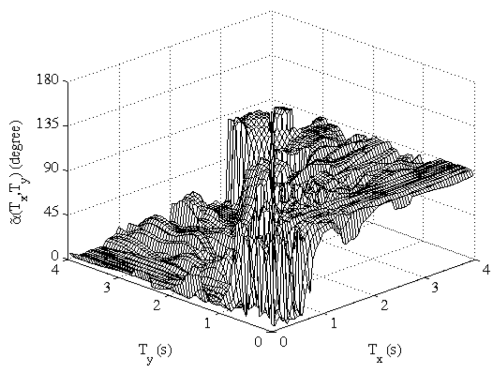

(d) $\tilde{\alpha}(T_x, T_y)$

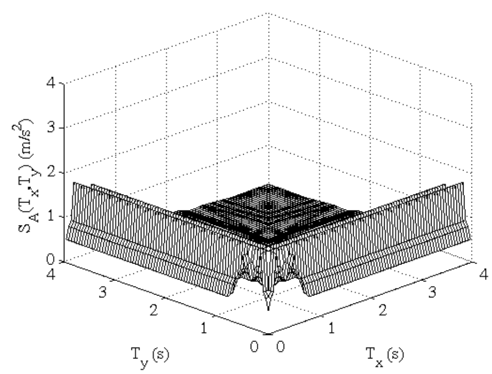

(e) $S_A(T_x, T_y)$

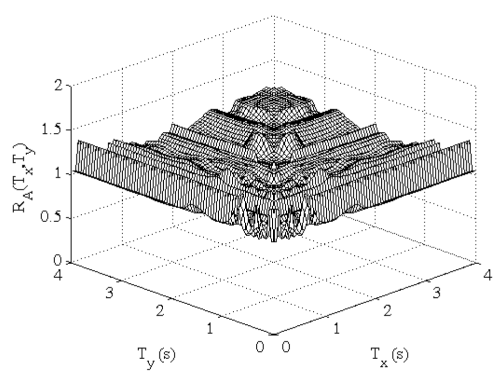

(f) $R_A(T_x, T_y)$

Figure B-163 Bi-directional responses of Northridge earthquake, 90090 Villa Park - Serrano Ave station

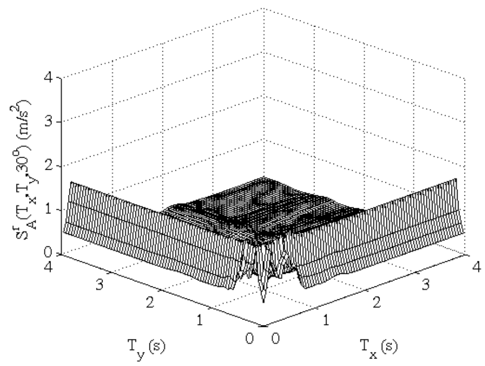

(a) $S_A^r(T_x,T_y,30^\circ)$

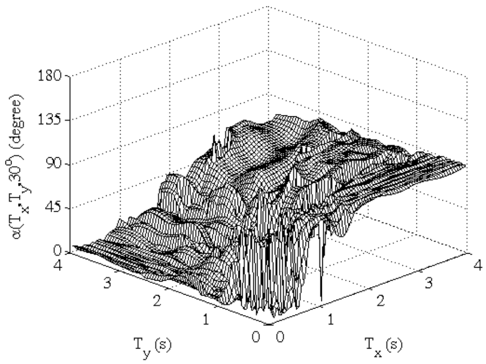

(b) $\alpha(T_x,T_y,30^\circ)$

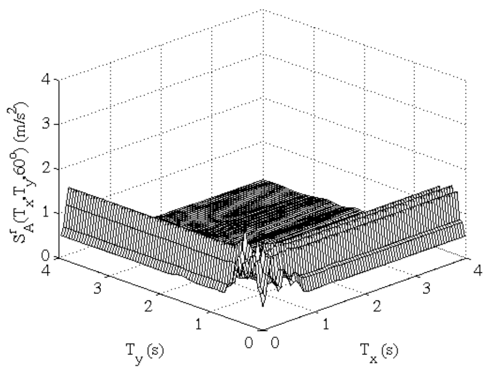

(c) $S_A^r(T_x,T_y,60^\circ)$

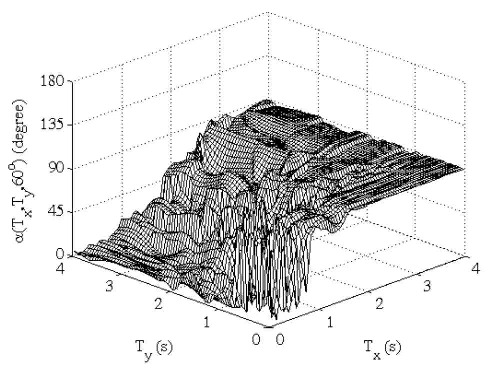

(d) $\alpha(T_x,T_y,60^\circ)$

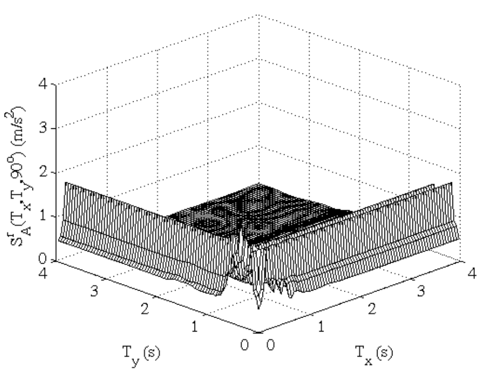

(e) $S_A^r(T_x,T_y,90^\circ)$

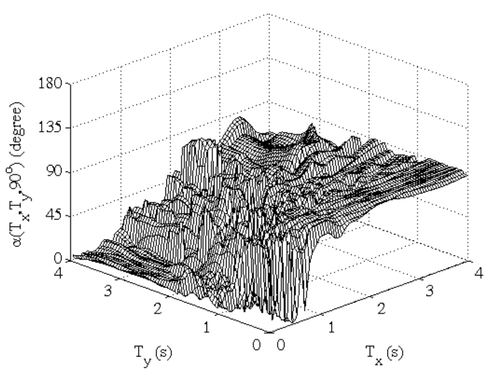

(f) $\alpha(T_x,T_y,90^\circ)$

Figure B-164 Pseudo acceleration spectra and incident angles in various directions of Northridge earthquake, 90090 Villa Park - Serrano Ave station

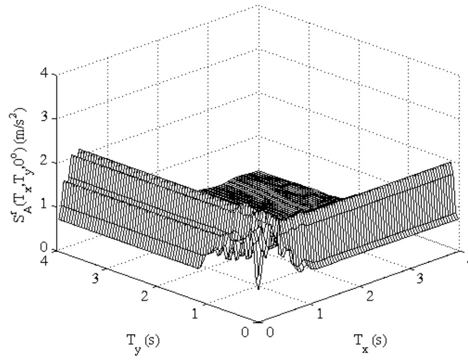

(a) $S_A^r(T_x,T_y,0^\circ)$

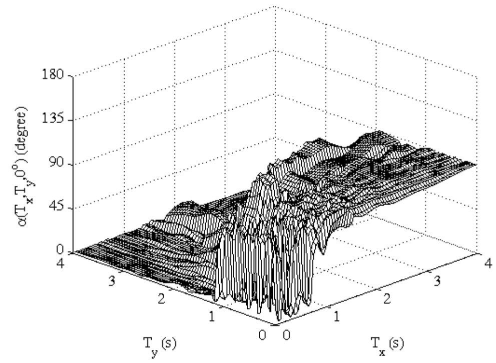

(b) $\alpha(T_x,T_y,0^\circ)$

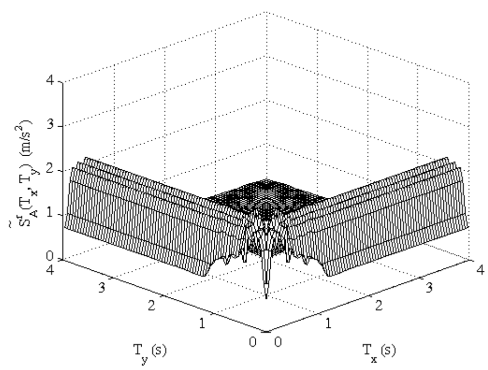

(c) $\tilde{S}_A^r(T_x,T_y)$

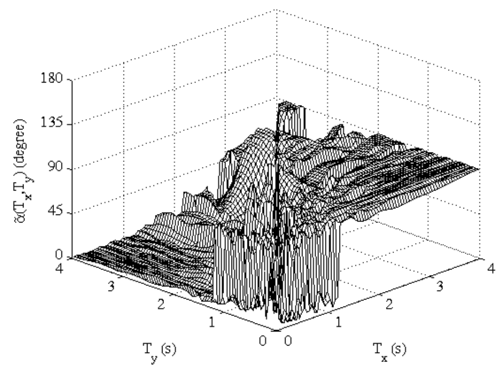

(d) $\tilde{\alpha}(T_x,T_y)$

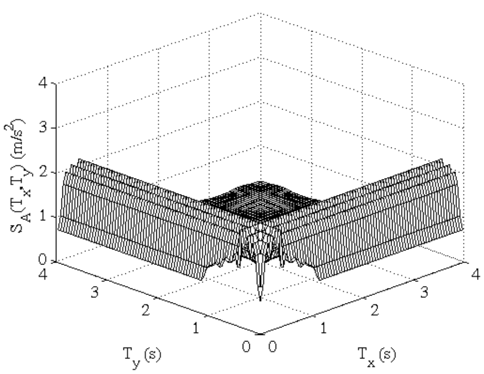

(e) $S_A(T_x,T_y)$

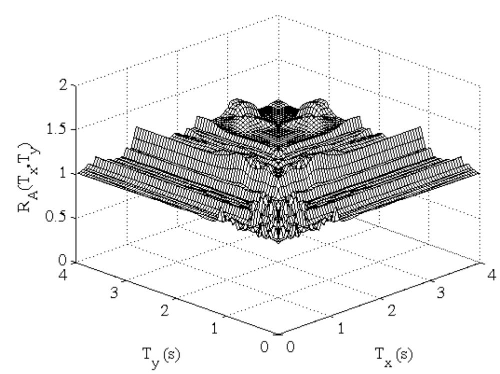

(f) $R_A(T_x,T_y)$

Figure B-165 Bi-directional responses of Northridge earthquake, 90071 West Covina - S. Orange Ave station

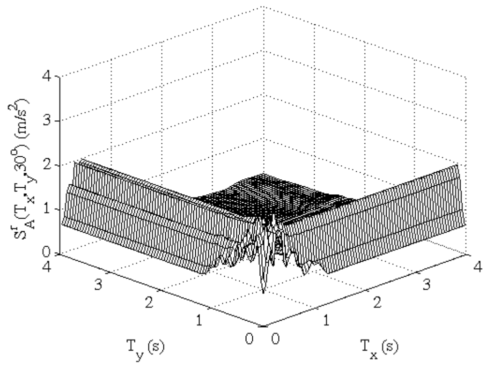

(a) $S_A^r(T_x, T_y, 30^{\circ})$

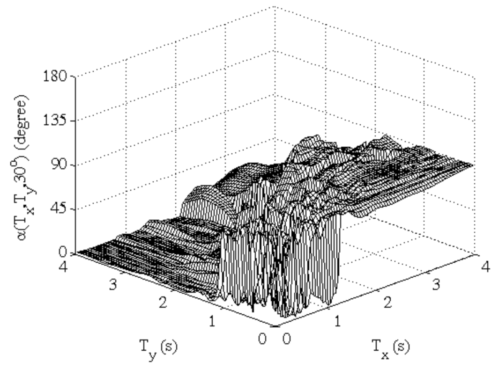

(b) $\alpha(T_x, T_y, 30^{\circ})$

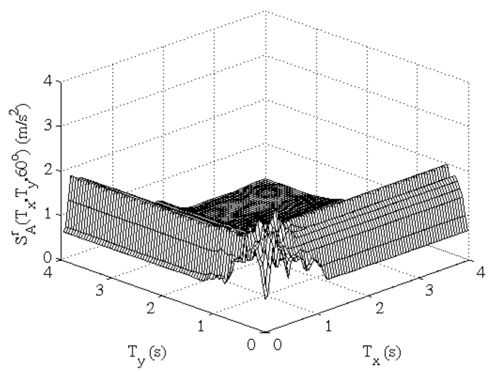

(c) $S_A^r(T_x, T_y, 60^{\circ})$

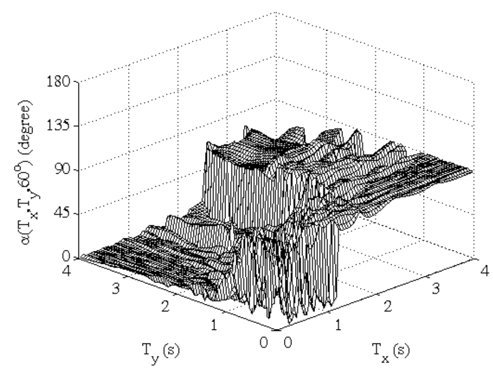

(d) $\alpha(T_x, T_y, 60^{\circ})$

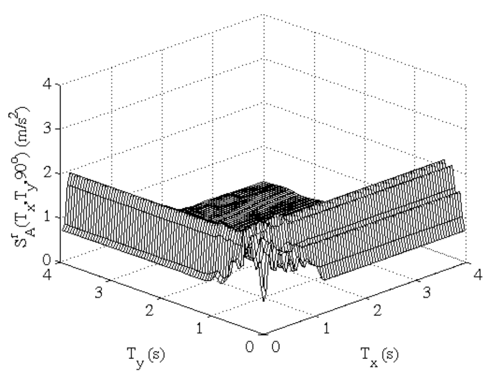

(e) $S_A^r(T_x, T_y, 90^{\circ})$

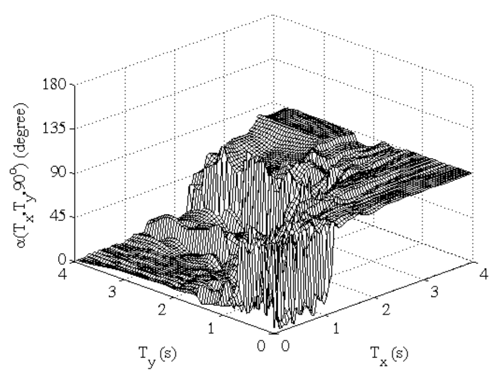

(f) $\alpha(T_x, T_y, 90^{\circ})$

Figure B-166 Pseudo acceleration spectra and incident angles in various directions of Northridge earthquake, 90071 West Covina - S. Orange Ave station

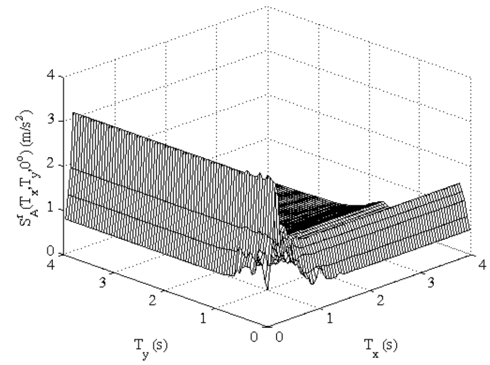

(a) $S_A^r(T_x, T_y, 0^\circ)$

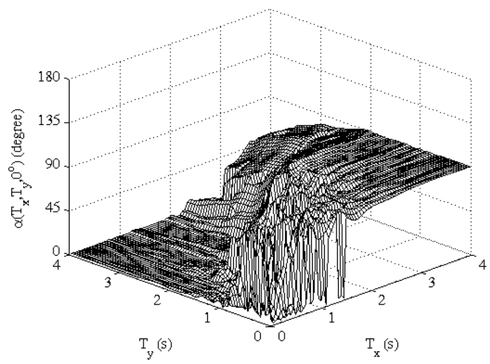

(b) $\alpha(T_x, T_y, 0^\circ)$

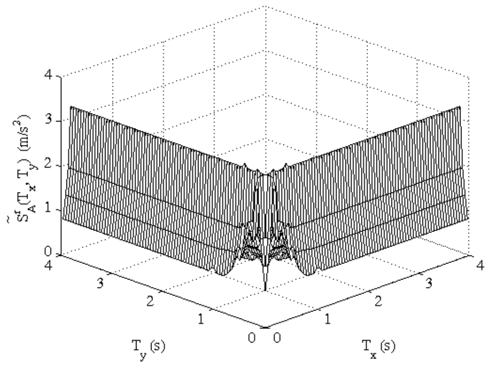

(c) $\widetilde{S}_A^r(T_x, T_y)$

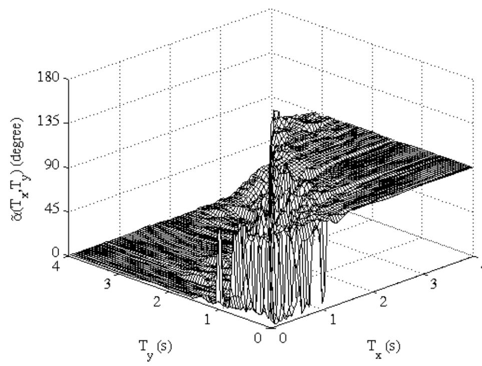

(d) $\widetilde{\alpha}(T_x, T_y)$

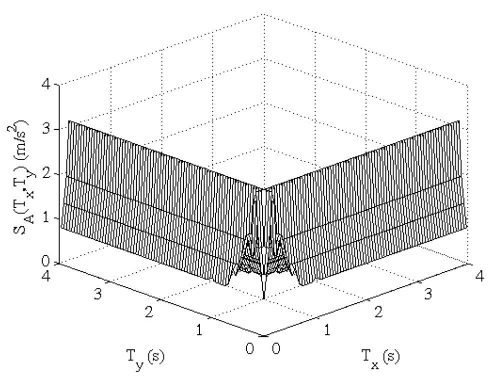

(e) $S_A(T_x, T_y)$

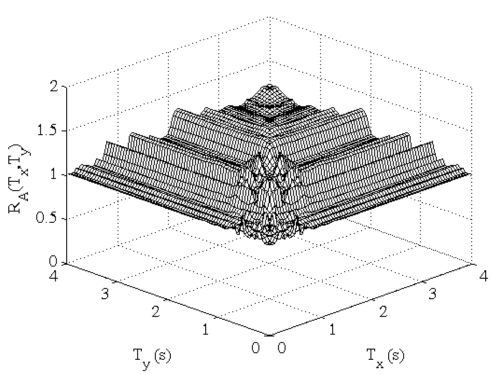

(f) $R_A(T_x, T_y)$

Figure B-167 Bi-directional responses of Northridge earthquake, 90073 Hacienda Hts - Colima Rd station

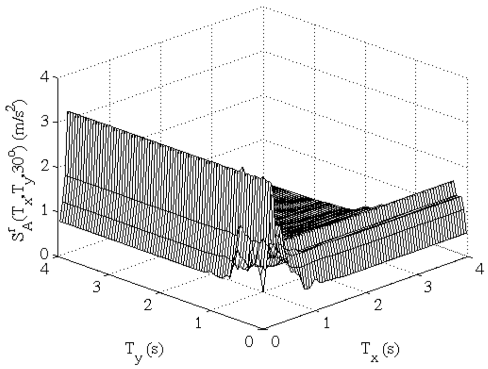

(a) $S_A^r(T_x, T_y, 30^\circ)$

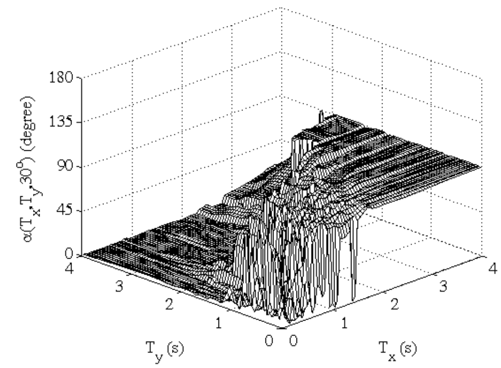

(b) $\alpha(T_x, T_y, 30^\circ)$

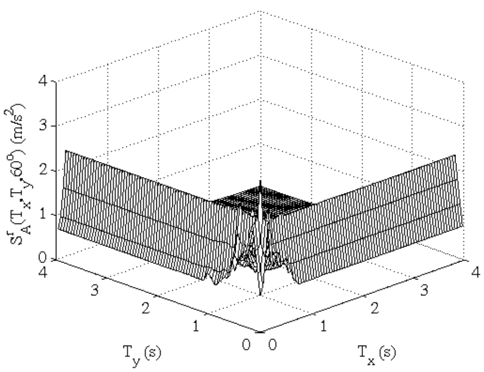

(c) $S_A^r(T_x, T_y, 60^\circ)$

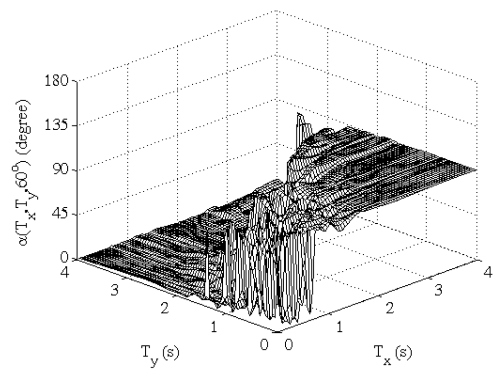

(d) $\alpha(T_x, T_y, 60^\circ)$

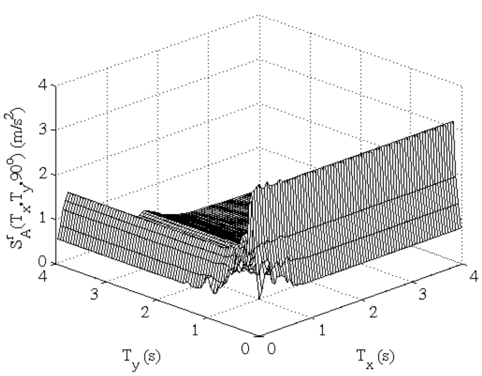

(e) $S_A^r(T_x, T_y, 90^\circ)$

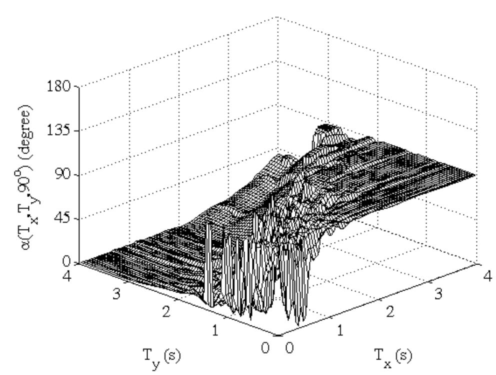

(f) $\alpha(T_x, T_y, 90^\circ)$

Figure B-168 Pseudo acceleration spectra and incident angles in various directions of Northridge earthquake, 90073 Hacienda Hts - Colima Rd station

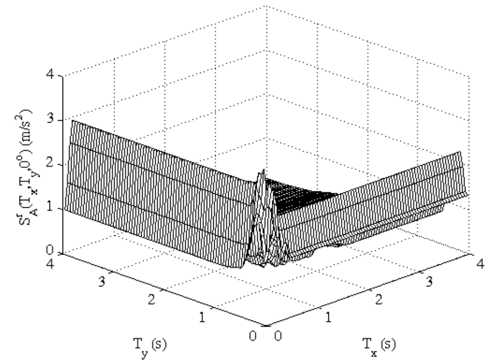

(a) $S_A^r(T_x, T_y, 0^\circ)$

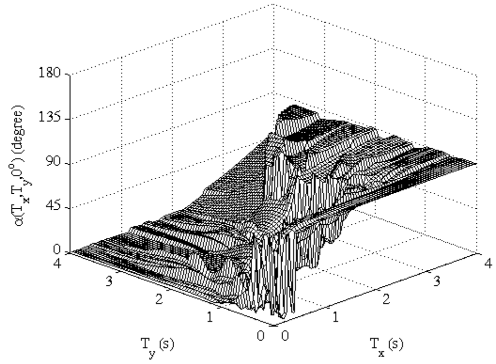

(b) $\alpha(T_x, T_y, 0^\circ)$

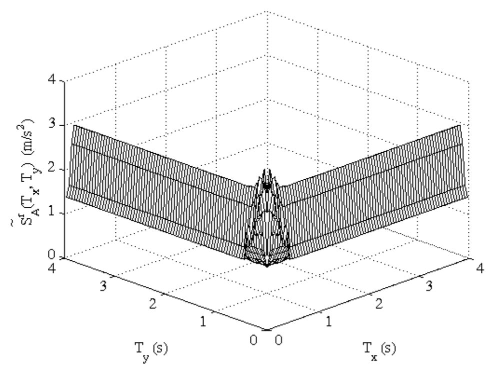

(c) $\widetilde{S}_A^r(T_x, T_y)$

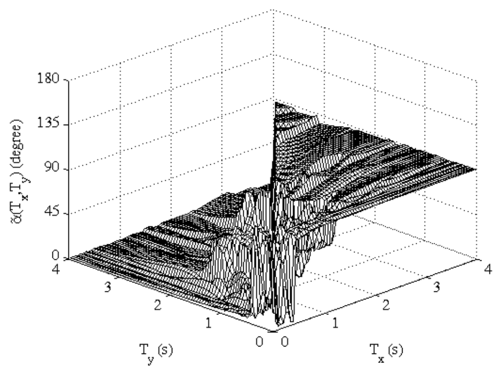

(d) $\widetilde{\alpha}(T_x, T_y)$

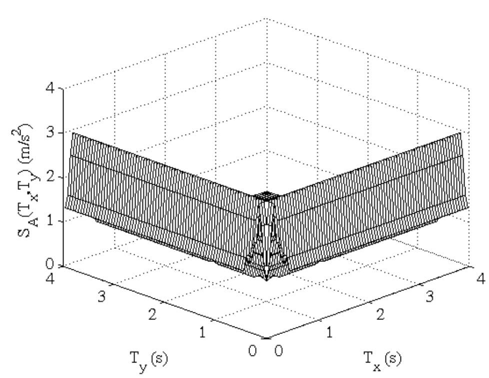

(e) $S_A(T_x, T_y)$

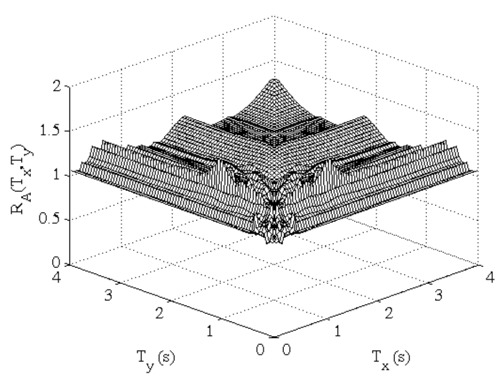

(f) $R_A(T_x, T_y)$

Figure B-169 Bi-directional responses of San Fernando earthquake, 994 Gormon - Oso Pump Plant station

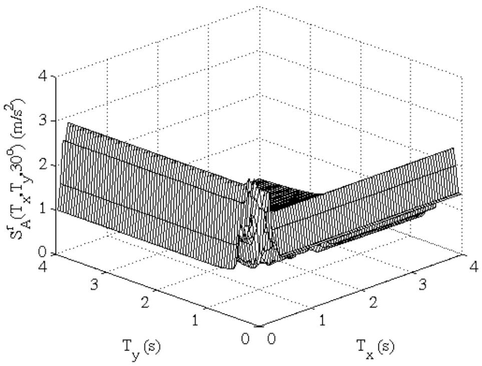

(a) $S_A^r(T_x, T_y, 30^\circ)$

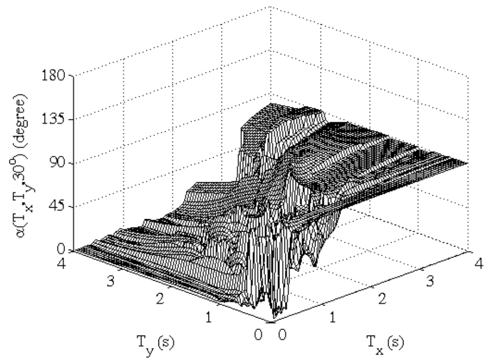

(b) $\alpha(T_x, T_y, 30^\circ)$

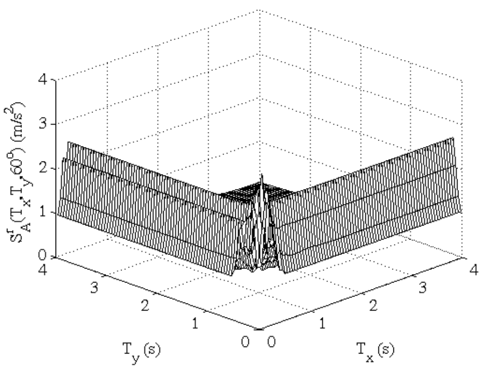

(c) $S_A^r(T_x, T_y, 60^\circ)$

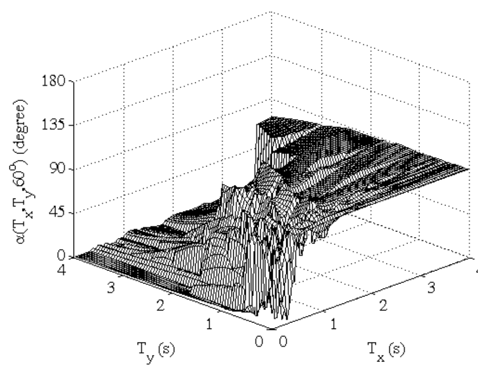

(d) $\alpha(T_x, T_y, 60^\circ)$

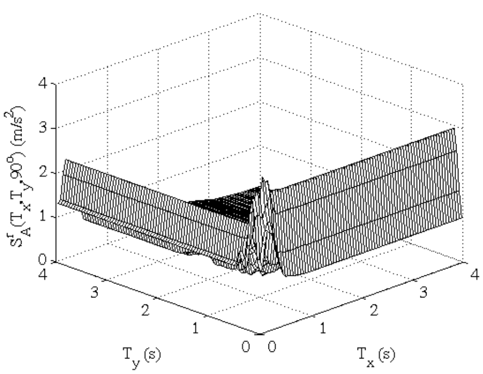

(e) $S_A^r(T_x, T_y, 90^\circ)$

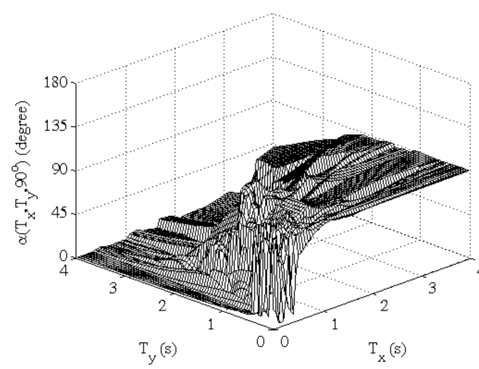

(f) $\alpha(T_x, T_y, 90^\circ)$

Figure B-170 Pseudo acceleration spectra and incident angles in various directions of San Fernando earthquake, 994 Gormon - Oso Pump Plant station

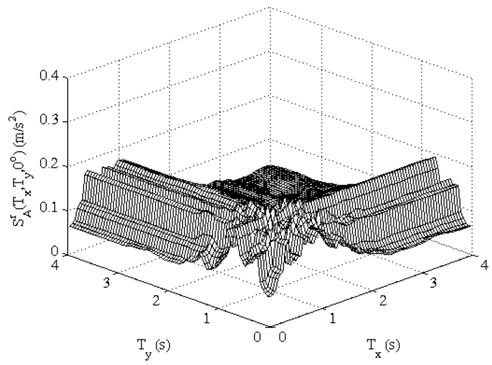

(a) $S_A^r(T_x, T_y, 0^\circ)$

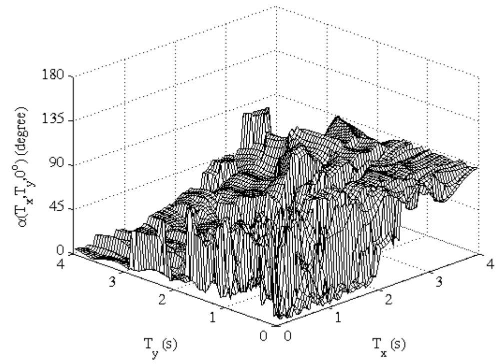

(b) $\alpha(T_x, T_y, 0^\circ)$

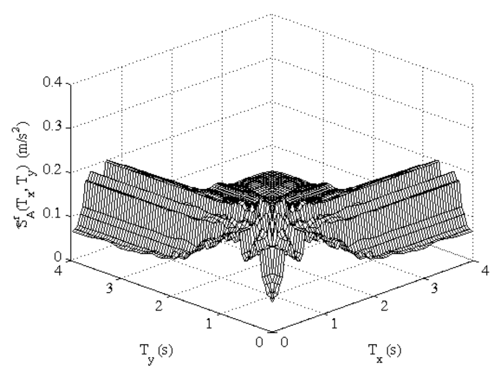

(c) $\tilde{S}_A^r(T_x, T_y)$

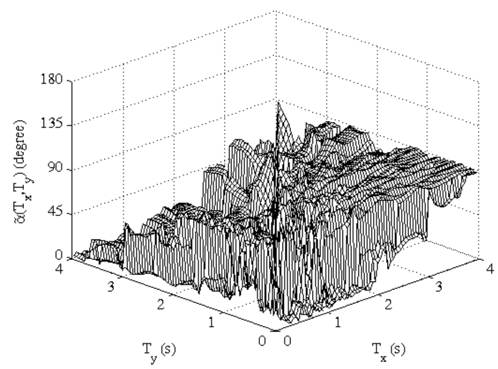

(d) $\tilde{\alpha}(T_x, T_y)$

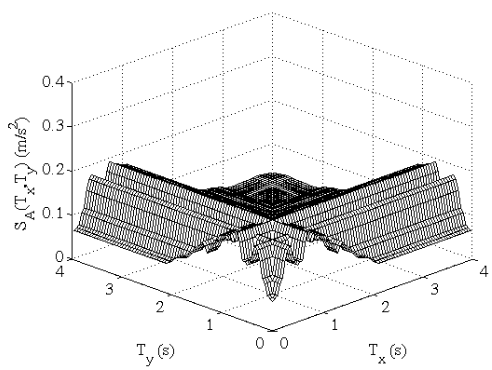

(e) $S_A(T_x, T_y)$

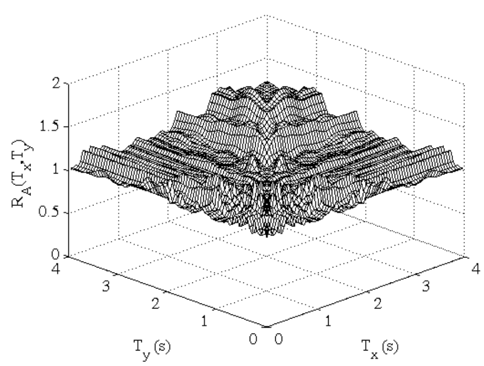

(f) $R_A(T_x, T_y)$

Figure B-171 Bi-directional responses of San Fernando earthquake, 1015 Cholame-Shandon Array #8 station

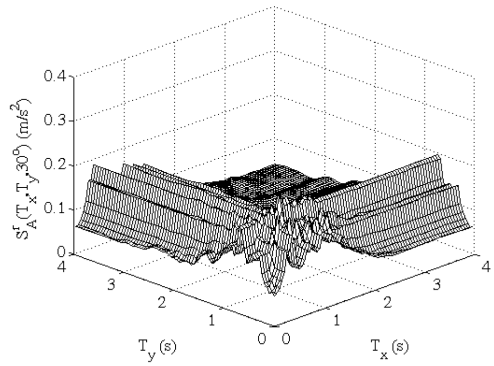

(a) $S_A^r(T_x,T_y,30^\circ)$

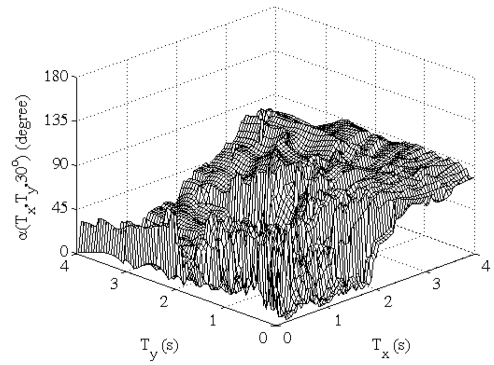

(b) $\alpha(T_x,T_y,30^\circ)$

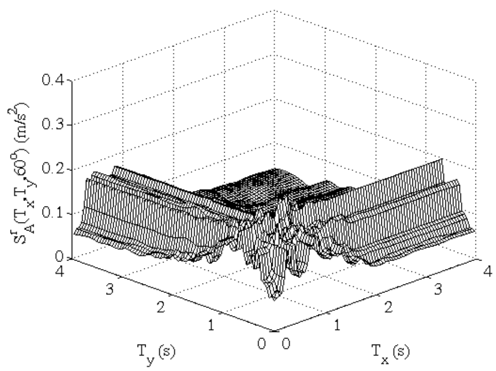

(c) $S_A^r(T_x,T_y,60^\circ)$

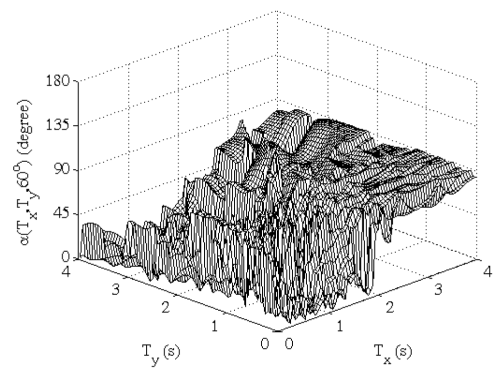

(d) $\alpha(T_x,T_y,60^\circ)$

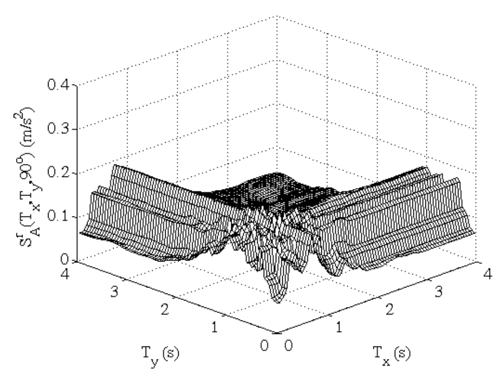

(e) $S_A^r(T_x,T_y,90^\circ)$

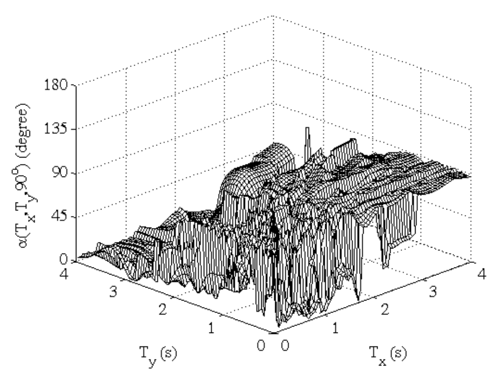

(f) $\alpha(T_x,T_y,90^\circ)$

Figure B-172 Pseudo acceleration spectra and incident angles in various directions of San Fernando earthquake, 1015 Cholame-Shandon Array #8 station

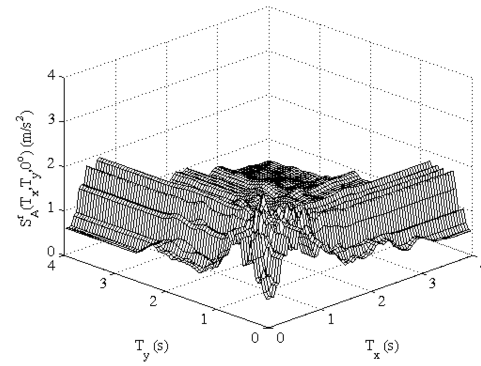

(a) $S_A^r(T_x, T_y, 0^\circ)$

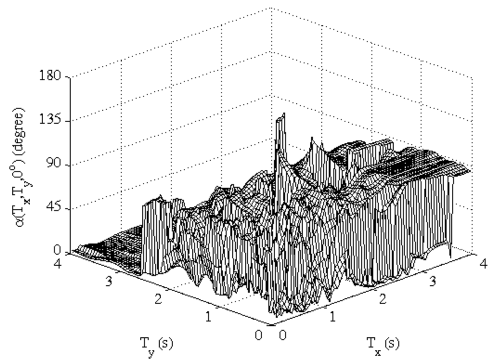

(b) $\alpha(T_x, T_y, 0^\circ)$

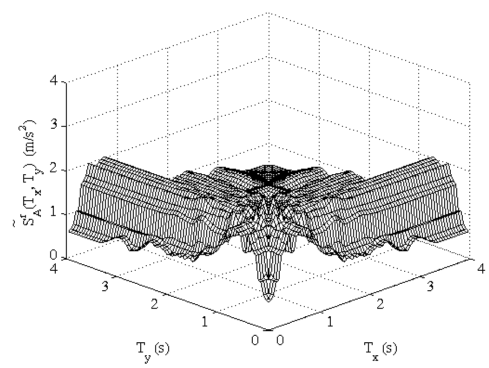

(c) $\tilde{S}_A^r(T_x, T_y)$

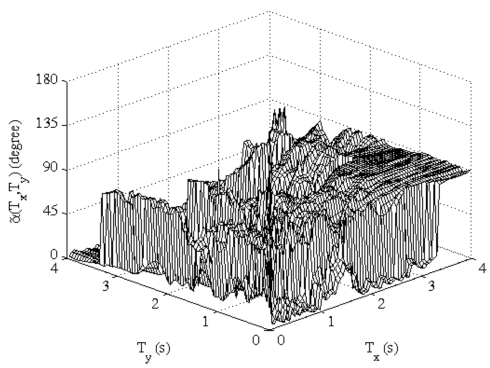

(d) $\tilde{\alpha}(T_x, T_y)$

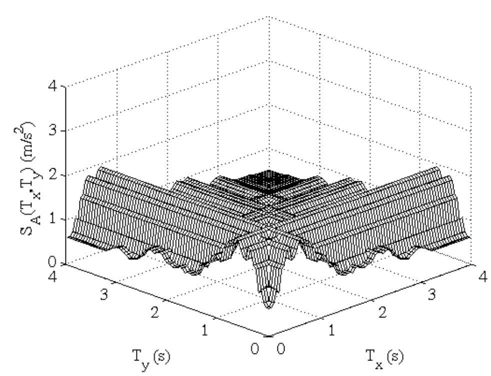

(e) $S_A(T_x, T_y)$

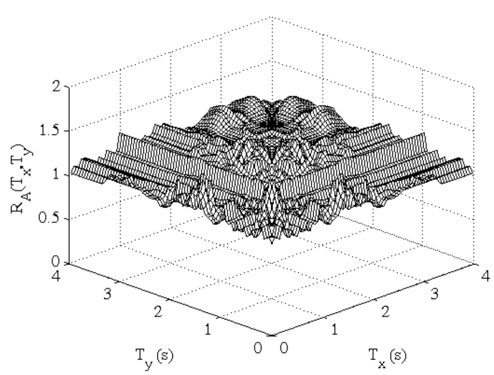

(f) $R_A(T_x, T_y)$

Figure B-173 Bi-directional responses of Chi-Chi, Taiwan earthquake, KAU011 station

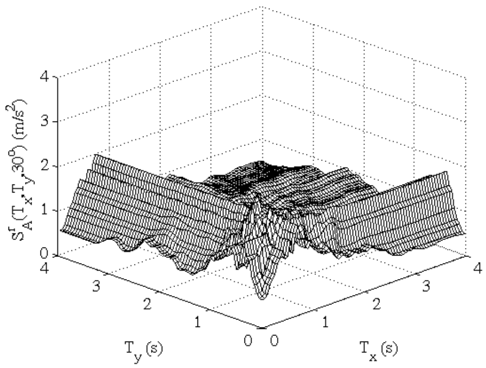

(a) $S_A^r(T_x, T_y, 30^\circ)$

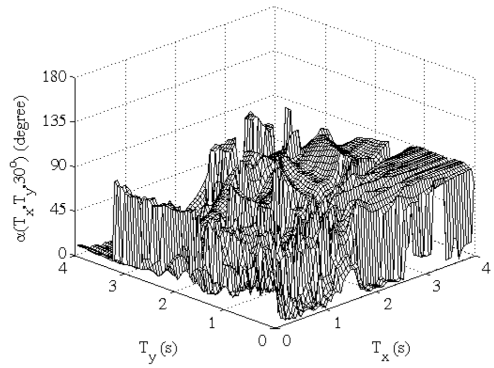

(b) $\alpha(T_x, T_y, 30^\circ)$

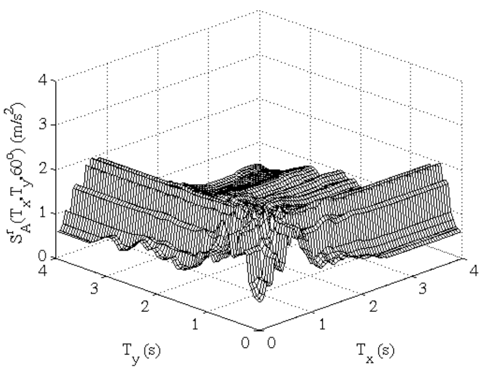

(c) $S_A^r(T_x, T_y, 60^\circ)$

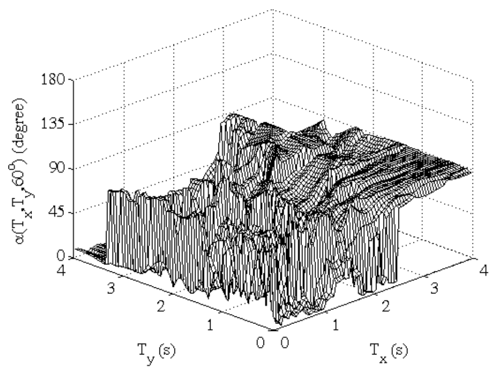

(d) $\alpha(T_x, T_y, 60^\circ)$

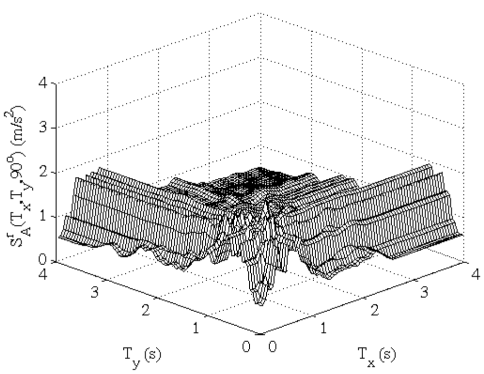

(e) $S_A^r(T_x, T_y, 90^\circ)$

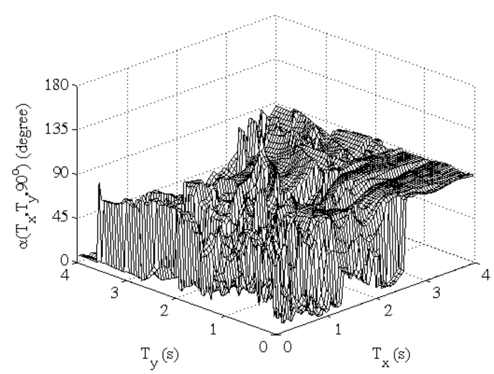

(f) $\alpha(T_x, T_y, 90^\circ)$

Figure B-174 Pseudo acceleration spectra and incident angles in various directions of Chi-Chi, Taiwan earthquake, KAU011 station

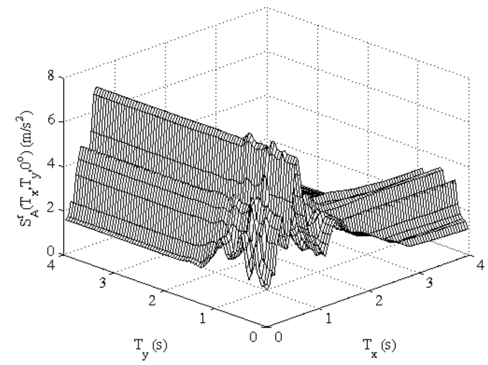

(a) $S^r_A(T_x,T_y,0^\circ)$

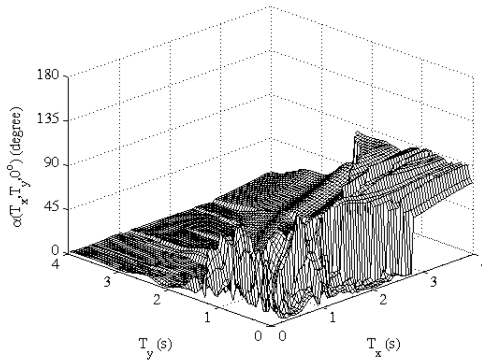

(b) $\alpha(T_x,T_y,0^\circ)$

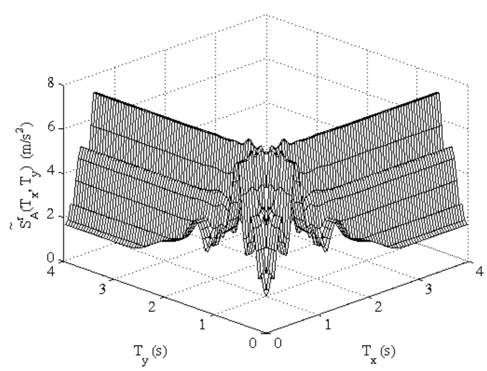

(c) $\tilde{S}^r_A(T_x,T_y)$

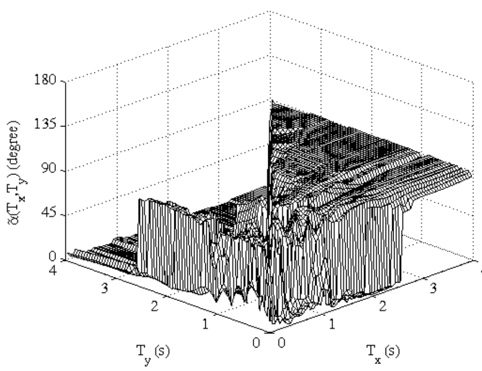

(d) $\tilde{\alpha}(T_x,T_y)$

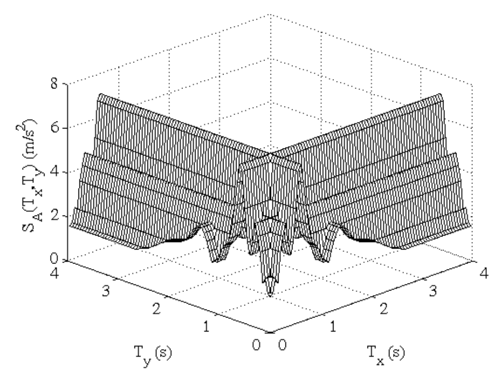

(e) $S_A(T_x,T_y)$

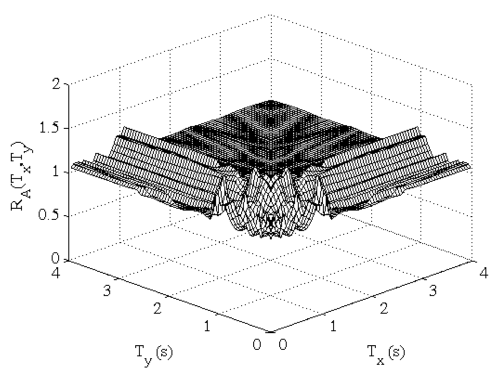

(f) $R_A(T_x,T_y)$

Figure B-175 Bi-directional responses of Loma Prieta earthquake, 58117 Treasure Island station

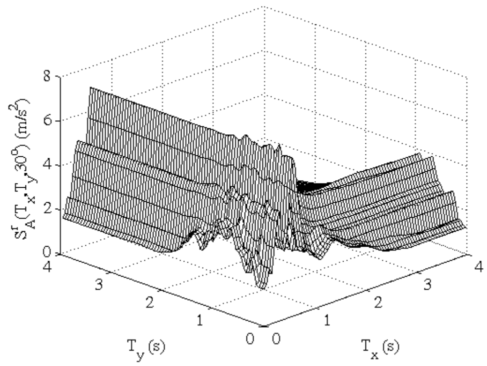

(a) $S_A^r(T_x, T_y, 30^\circ)$

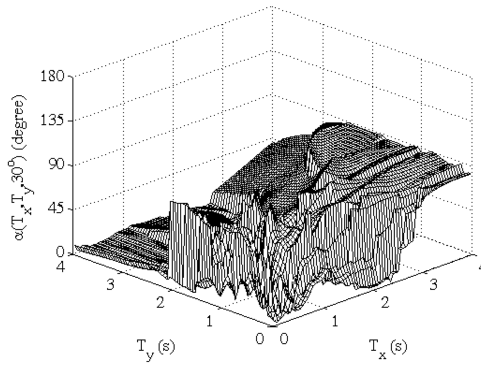

(b) $\alpha(T_x, T_y, 30^\circ)$

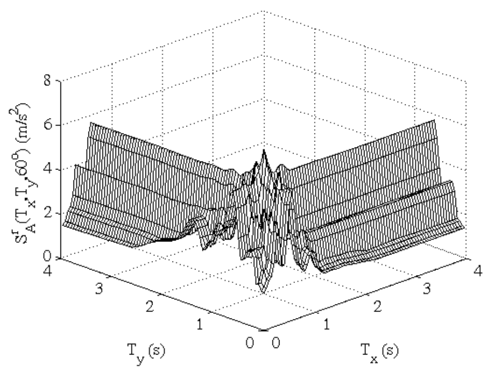

(c) $S_A^r(T_x, T_y, 60^\circ)$

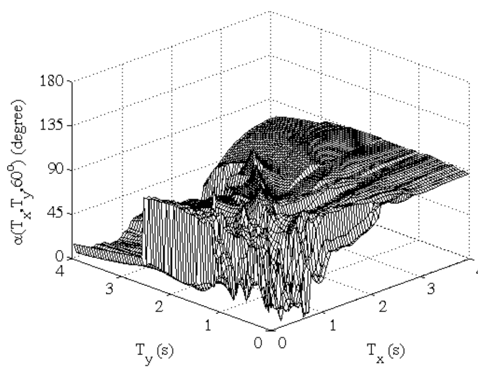

(d) $\alpha(T_x, T_y, 60^\circ)$

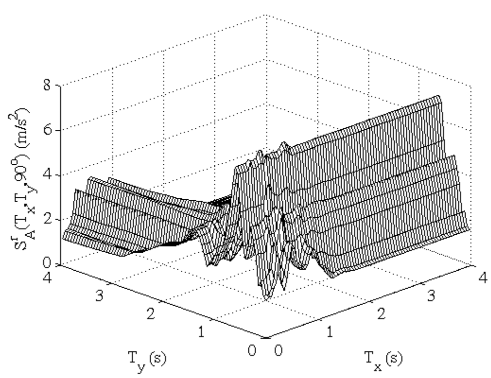

(e) $S_A^r(T_x, T_y, 90^\circ)$

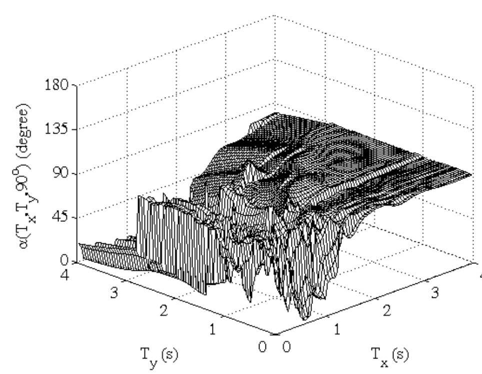

(f) $\alpha(T_x, T_y, 90^\circ)$

Figure B-176 Pseudo acceleration spectra and incident angles in various directions of Loma Prieta earthquake, 58117 Treasure Island station

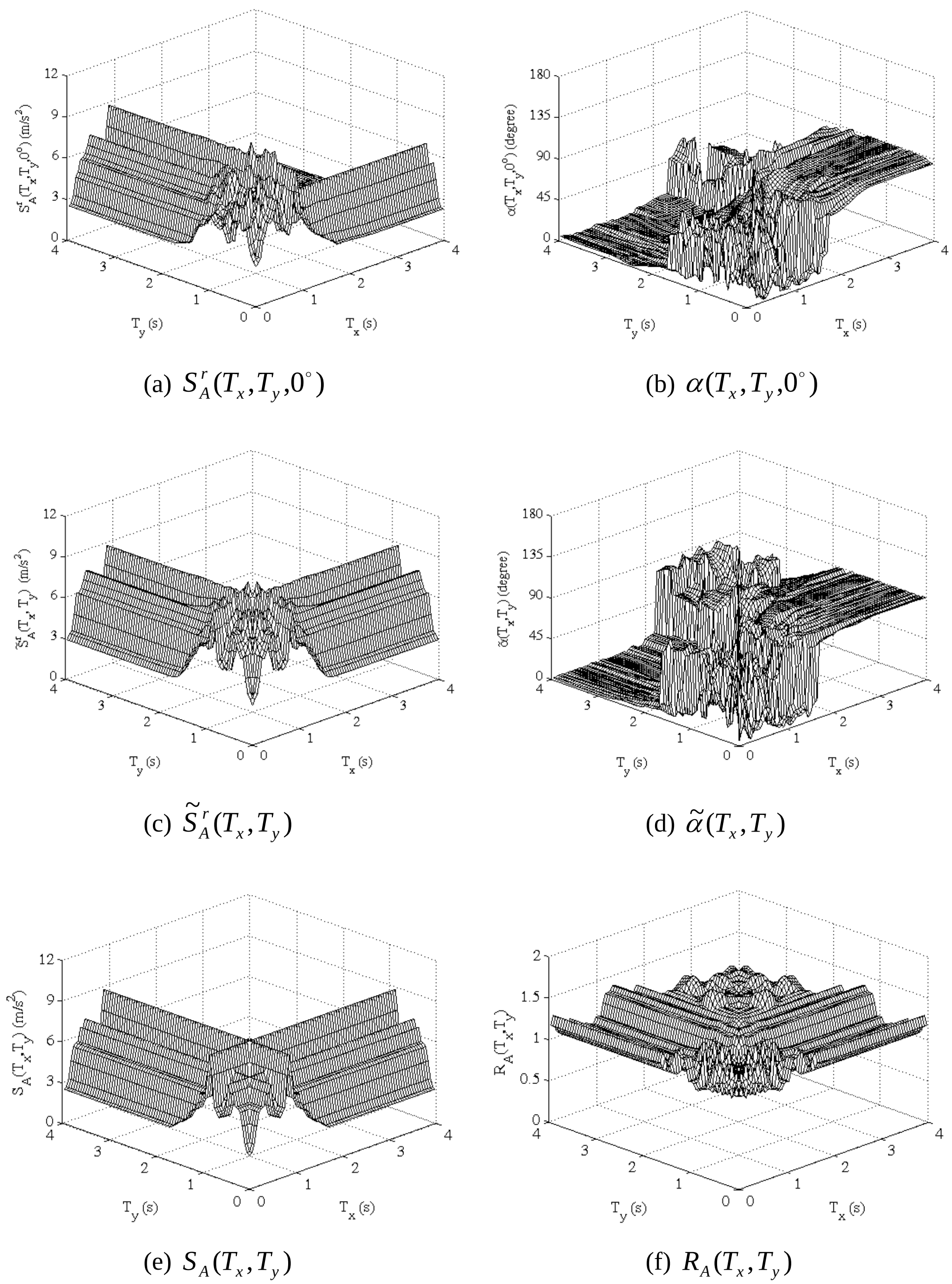

(a) $S_A^r(T_x, T_y, 0^\circ)$ (b) $\alpha(T_x, T_y, 0^\circ)$

(c) $\tilde{S}_A^r(T_x, T_y)$ (d) $\tilde{\alpha}(T_x, T_y)$

(e) $S_A(T_x, T_y)$ (f) $R_A(T_x, T_y)$

Figure B-177 Bi-directional responses of Kocaeli, Turkey earthquake, Ambarli station

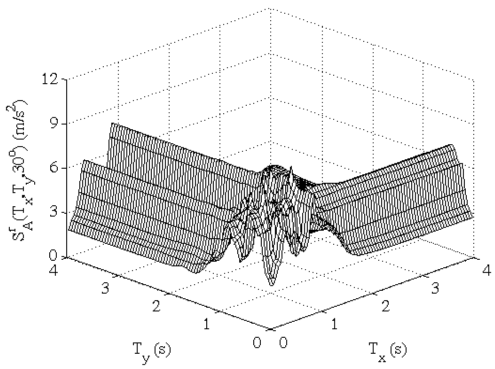

(a) $S_A^r(T_x, T_y, 30^\circ)$

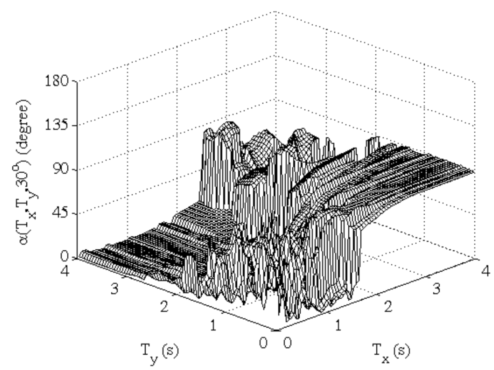

(b) $\alpha(T_x, T_y, 30^\circ)$

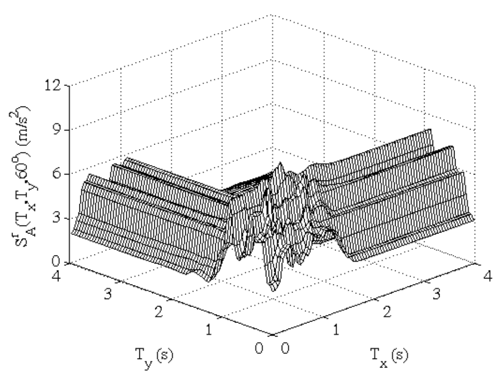

(c) $S_A^r(T_x, T_y, 60^\circ)$

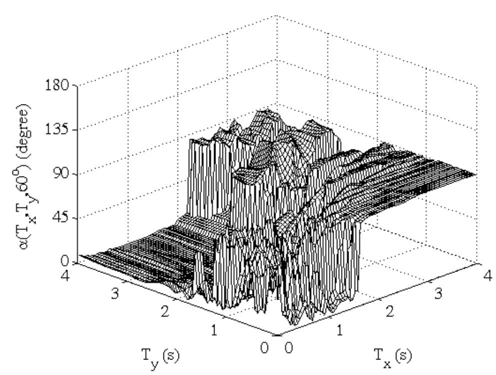

(d) $\alpha(T_x, T_y, 60^\circ)$

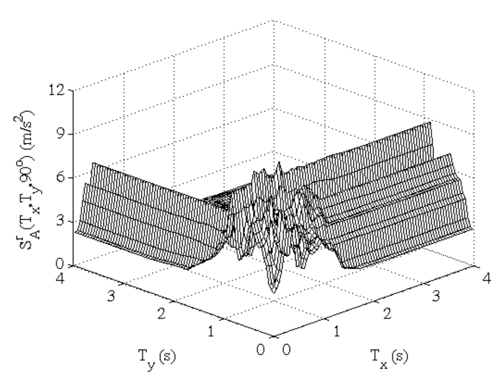

(e) $S_A^r(T_x, T_y, 90^\circ)$

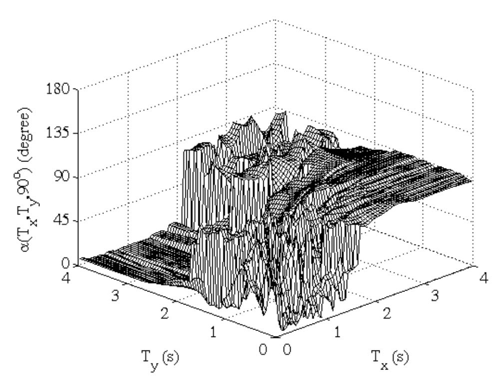

(f) $\alpha(T_x, T_y, 90^\circ)$

Figure B-178 Pseudo acceleration spectra and incident angles in various directions of Kocaeli, Turkey earthquake, Ambarli station

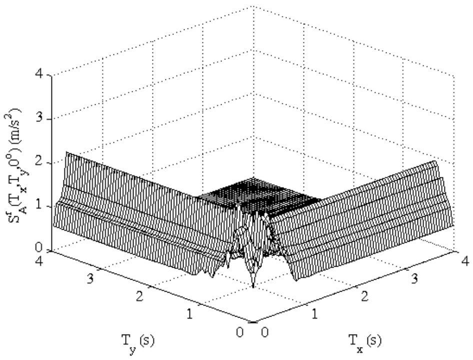

(a) $S_A^r(T_x, T_y, 0^\circ)$

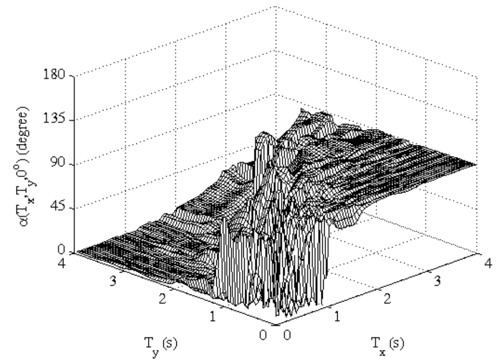

(b) $\alpha(T_x, T_y, 0^\circ)$

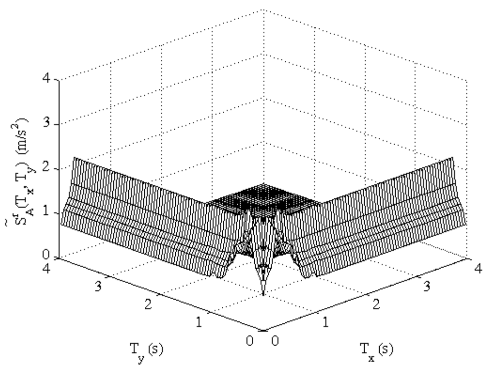

(c) $\tilde{S}_A^r(T_x, T_y)$

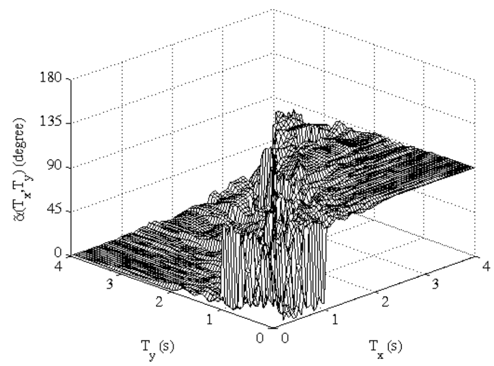

(d) $\tilde{\alpha}(T_x, T_y)$

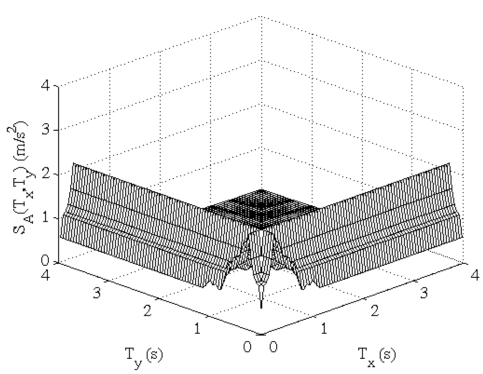

(e) $S_A(T_x, T_y)$

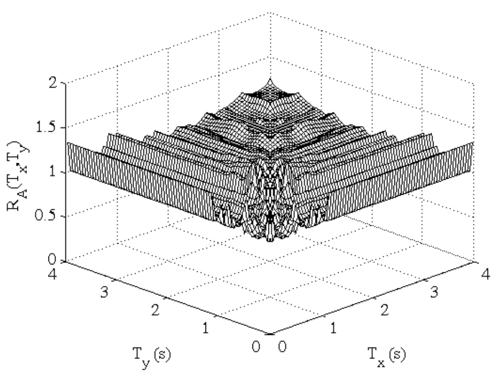

(f) $R_A(T_x, T_y)$

Figure B-179 Bi-directional responses of Morgan Hill earthquake, 58375 APEEL 1 - Redwood City station

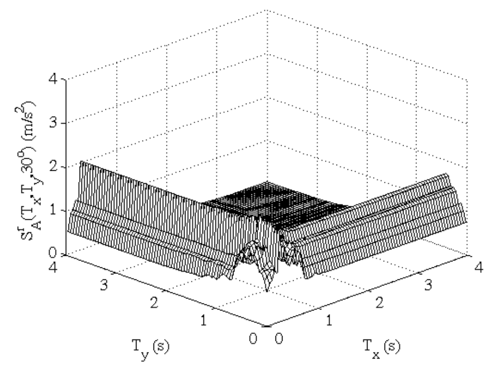

(a) $S_A^r(T_x, T_y, 30^\circ)$

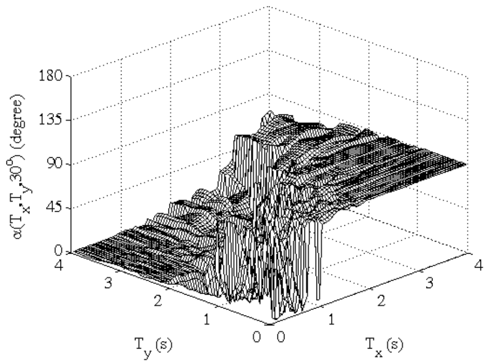

(b) $\alpha(T_x, T_y, 30^\circ)$

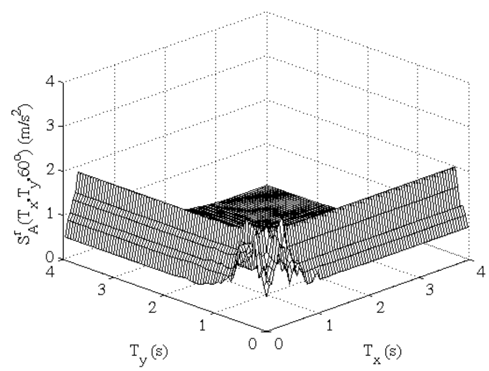

(c) $S_A^r(T_x, T_y, 60^\circ)$

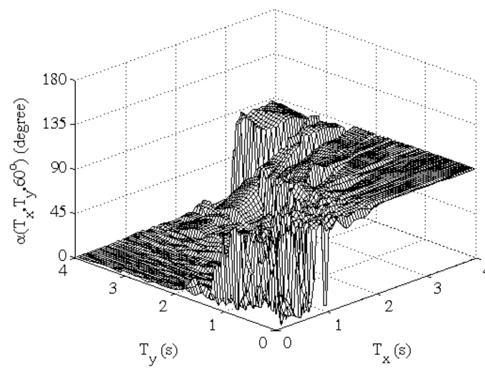

(d) $\alpha(T_x, T_y, 60^\circ)$

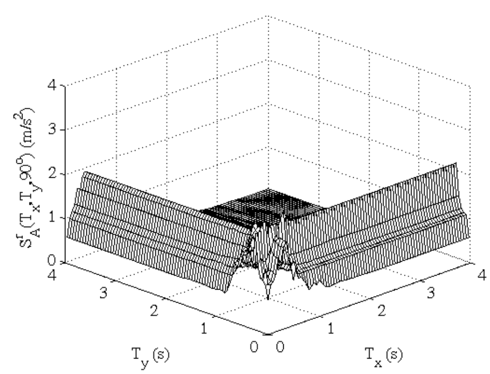

(e) $S_A^r(T_x, T_y, 90^\circ)$

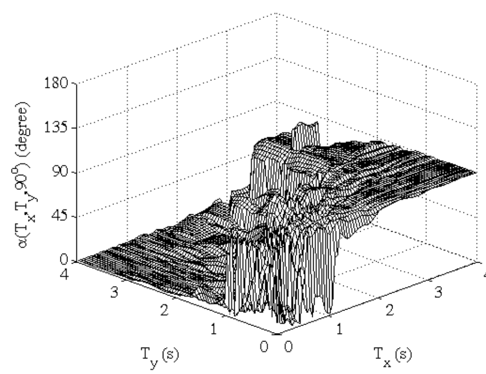

(f) $\alpha(T_x, T_y, 90^\circ)$

Figure B-180 Pseudo acceleration spectra and incident angles in various directions of Morgan Hill earthquake, 58375 APEEL 1 - Redwood City station

VITAE

Chitti Palasri was born in Bangkok, Thailand on June 1, 1982. The elementary and secondary schools where he studied were Premrudeesuksa School and Wat Suthiwararam School, respectively. He received the Bachelor of Civil Engineering degree in 2004 and the Master of Civil Engineering degree in 2007 from the Department of Civil Engineering, Chulalongkorn University, Thailand.

In 2011, he received the EU-NICE Erasmus Mundus scholarship to be a visiting research student at the University G. D'Annunzio Chieti-Pescara, Italy, from October, 2011 until October, 2012. His research interests include seismic hazard assessment, soil amplification, and response spectra.

Publication:

Palasri**,** C., and Ruangrassamee, A. (2010) "Probabilistic seismic hazard maps of Thailand," Journal of Earthquake and Tsunami, Vol. 4, No. 4, 369-386.

Conferences:

Palasri**,** C., and Ruangrassamee, A. (2009) "Relations among shear wave velocity, SPT N-value and undrained shear strength of soil in Bangkok and the north of Thailand," Proceedings of the 14th National Convention on Civil Engineering , Nakorn Ratchasima, Thailand.

Palasri**,** C., Ruangrassamee, A., and Siripala, S. (2010) "Bi-directional displacement response spectra," The 3rd ASIA Conference on Earthquake Engineering, Bangkok, Thailand.